Characterization and Modelling of the Thermomechanical and Ageing Behavior of PEKK and C/PEKK Composites for Aircraft Applications at High Temperatures (above the Glass Transition Temperature)

Giuseppe Pedoto

▶ **To cite this version:**

Giuseppe Pedoto. Characterization and Modelling of the Thermomechanical and Ageing Behavior of PEKK and C/PEKK Composites for Aircraft Applications at High Temperatures (above the Glass Transition Temperature). Other. ISAE-ENSMA Ecole Nationale Supérieure de Mécanique et d'Aérotechique - Poitiers, 2020. English. NNT : 2020ESMA0011 . tel-03079084

HAL Id: tel-03079084
https://theses.hal.science/tel-03079084

Submitted on 17 Dec 2020

HAL is a multi-disciplinary open access archive for the deposit and dissemination of scientific research documents, whether they are published or not. The documents may come from teaching and research institutions in France or abroad, or from public or private research centers.

L'archive ouverte pluridisciplinaire **HAL**, est destinée au dépôt et à la diffusion de documents scientifiques de niveau recherche, publiés ou non, émanant des établissements d'enseignement et de recherche français ou étrangers, des laboratoires publics ou privés.

THESE

Pour l'obtention du Grade de
DOCTEUR DE L'ECOLE NATIONALE SUPERIEURE DE MECANIQUE ET D'AEROTECHNIQUE
(Diplôme National – Arrêté du 25 mai 2016)

Ecole Doctorale :
Sciences et Ingénierie en Matériaux, Mécanique, Energétique

Secteur de Recherche : Mécanique des solides, des Matériaux, des Structures et des Surfaces

Présentée par :

Giuseppe PEDOTO

****

Characterization and modelling of the thermomechanical and ageing behavior of PEKK and C/PEKK composites for aircraft applications at high temperatures (above the glass transition temperature)

****
Directeur de thèse : Marco GIGLIOTTI
Co-directeur : Jean-Claude GRANDIDIER

****
Soutenue le 08 Octobre 2020

devant la Commission d'Examen

****

JURY

Président :
Nadia BALHOULI, Professeur, Université de Strasbourg
Rapporteurs :
Silvestre PINHO, Professeur, Imperial College London, UK
Laurent GORNET, Maître de Conférence, Ecole Centrale Nantes
Membres du jury :
Bruno FAYOLLE, Professeur, Ecole Nationale Supérieure d'Arts et Métiers, Paris
Alain VINET, Ingénieur de Recherche, AIRBUS SAS
Benoit BRULÉ, Ingénieur de Recherche, ARKEMA
Marco GIGLIOTTI
Jean-Claude GRANDIDIER

Index

INTRODUCTION **1**

CHAPTER 1 – LITERATURE SURVEY **6**

1.1. LITERATURE SURVEY 7
1.1.1. Composite Materials in aeronautical structures *7*
1.1.2. Crystallization mechanisms in PEKK polymers and PEKK based composites *10*
1.1.3. Effect of the crystallization on PEKK polymer and PEKK based composite mechanical properties *16*
1.1.4. PEEK and PEKK polymers and composites thermomechanical behavior *18*
1.1.5. Degradation (and oxidation) behavior of PEKK and PEKK based composites *22*
1.2. CONCLUSIONS AND AIM OF THE PRESENT WORK. 28

CHAPTER 2 - MATERIALS AND METHODS **32**

2.1. INTRODUCTION 33
2.2. MATERIALS 35
2.2.1. Manufacturing *36*
2.2.2. Specimens *38*
2.3. METHODS 42
2.3.1. Experimental equipment and methods *42*
2.3.2. Measurement system *53*
2.3.3. Numerical models *74*
2.4. CONCLUSIONS 82

CHAPTER 3 – PRELIMINARY ANALYSIS OF TENSILE AND CREEP THERMOMECHANICAL BEHAVIOR OF PEKK SC AND C/PEKK **83**

3.1. INTRODUCTION 84
3.2. TENSILE TESTS 86
3.2.1. Temperature effects *86*
3.2.2. Time effects *89*
3.2.3. Fiber rotation *92*
3.2.4. PEKK SC and C/PEKK engineering mechanical properties *93*
3.3. DMA TESTS 97
3.4. CREEP-RECOVERY TESTS 101
3.4.1. Creep-recovery test parameters *101*
3.4.2. Creep-recovery tests results *103*
3.4.3. Fiber rotation *108*
3.4.4. Fitting of the creep test curves *109*
3.4.5. Creep compliance mastercurve *114*
3.5. DSC TESTS 117
3.6. SEMI-ANALYTICAL HOMOGENIZATION-LOCALIZATION METHOD FOR THE INTERPRETATION OF TEST RESULTS 120
3.7. CONCLUSIONS 125

CHAPTER 4 – CHARACTERIZATION OF PEKK THERMOMECHANICAL AND CREEP BEHAVIOR ABOVE T_G **128**

4.1. INTRODUCTION 129
4.2. ANALYSIS OF THE PEKK SC THERMOMECHANICAL BEHAVIOR ABOVE T_G 131
4.2.1. Volumetric changes 131
4.2.2. Load-Unload-Reload tests 134
4.2.3. PEKK SC load-unload behavior 138
4.2.4. PEKK SC creep – recovery behavior 140
4.3. CRYSTALLIZATION KINETICS 144
4.4. DISCUSSION OF RESULTS 157
4.4.1. Thermal load 157
4.4.2. Thermomechanical load 158
4.5. ANALYTICAL 1-D MODEL FOR THE DESCRIPTION OF THE PEKK SC THERMOMECHANICAL BEHAVIOR ABOVE T_G 164
4.5.1. Load-Unload behavior 164
4.5.2. Creep-recovery behavior 166
4.5.3. Summary of the PEKK SC 1-D description and comparison with experimental curves. 171
4.6. PEKK 7002 AM BEHAVIOR AT T>TG 182
4.6.1. Tensile test 182
4.6.2. DMA tests 189
4.6.3. DSC tests on PEKK AM 190
4.6.4. Load – Unload – Reload tests 198
4.6.5. 1-D model applied to PEKK AM 199
4.7. CONCLUSIONS 202

CHAPTER 5 – SIMULATION OF THE C/PEKK THERMOMECHANICAL TENSILE AND CREEP BEHAVIOR 206

5.1. INTRODUCTION 207
5.2. SIMPLIFIED ANALYTICAL 3-D MODEL FOR THE DESCRIPTION OF PEKK SC THERMOMECHANICAL BEHAVIOR AT 200°C 209
5.2.1. PEKK 3-D formulation for tensile solicitation 211
5.2.2. PEKK 3-D formulation for tensile-creep solicitation 215
5.3. IMPLEMENTATION OF PEKK 3-D MODEL IN THE SEMI-ANALYTICAL HOMOGENIZATION/LOCALIZATION METHOD 218
5.3.1. Tensile 219
5.3.2. Creep 224
5.4. SIMULATION OF LAMINATES WITH DIFFERENT AND MULTIPLE PLY ORIENTATIONS 228
5.4.1. Multiple orientations in the stacking sequence 231
5.5. CONCLUSIONS 238

CHAPTER 6 – COUPLED OXIDATION-THERMOMECHANICAL-CREEP BEHAVIOR OF PEKK AND C/PEKK AT 200°C 240

6.1. INTRODUCTION 241
6.2. EFFECT OF THERMAL OXYDATION 243
6.2.1. Effect of ageing on PEKK SC 243
6.2.2. Effect of ageing on C/PEKK 248
6.3. COUPLING BETWEEN OXIDATION AND THERMOMECHANICAL LOAD 250
6.3.1. Effect of oxidation on the creep behavior 251
6.3.2. Effect of thermomechanical load on the oxidation 258
6.4. CONCLUSIONS 260

CONCLUSIONS AND PERSPECTIVES 263

PERSPECTIVES 266

ANNEX A – SPECIMENS GEOMETRIES 269

A.1. SPECIMEN TYPE "B" 269
A.2. SPECIMEN TYPE "D" 269

ANNEX B – IAT CORRECTIONS 270

B.1. LIGHT EXPOSURE CORRECTION 270
B.2. IMAGE SUBSET DEFINITION 272

ANNEX C – TRANSVERSAL ISOTROPY 276

C.1. TRANSVERSAL ISOTROPY FORMULATION 277
C.1.1. From stress to strain 277
C.1.2. From displacement to strain 279
C.1.3. Equality of formulations 279
C.2. VERIFICATION OF TRANSVERSAL ISOTROPY HYPOTHESIS 281

ANNEX D – LINEAR APPROXIMATION OF THE DISPLACEMENT FIELD 284

ANNEX E – 3-D STRAIN FIELD FORMULATIONS 288

E.1. TOTAL LAGRANGIAN FORMULATION 288
E.2. UPDATE LAGRANGIAN FORMULATION 291
E.3. EULERIAN FORMULATION 293

ANNEX F – IAT VALIDATION THROUGH DIC ANALYSIS COMPARISON 296

F.1. VALIDATION OF THE MEASURE OF THE DISPLACEMENT FIELD 297

ANNEX G – ANALYTICAL METHODS 301

G.1. LAMINATION THEORY 301
G.1.1. Ply plane stress stiffness matrix in the composite reference system 301
G.1.2. Composite plane stress stiffness matrix 303
G.2. LOCALIZATION METHODS 304

ANNEX H - SAHLM OUTPUT COMPARISON 308

BIBLIOGRAPHY 311

LIST OF TABLES 320

LIST OF FIGURES 323

1. RESUME ÉTENDU II

I - INTRODUCTION ET CONTEXTE II
II - MATÉRIAUX ET MÉTHODES V
III - ANALYSE PRÉLIMINAIRE DU COMPORTEMENT THERMOMÉCANIQUE EN TRACTION ET EN FLUAGE DU PEKK SC ET DU C/PEKK VIII
IV -CARACTÉRISATION DU COMPORTEMENT THERMOMÉCANIQUE ET EN FLUAGE DU PEKK AU-DESSUS DE TG XI
V - SIMULATION DU COMPORTEMENT THERMOMÉCANIQUE DES COMPOSITES C/PEKK EN TRACTION ET EN FLUAGE XIV
VI-COMPORTEMENT COUPLÉ OXYDATION-THERMOMÉCANIQUE-REPLACEMENT DES PEKK ET C/PEKK À 200°C XVII
CONCLUSIONS ET PERSPECTIVES XX

Acknowledgments

The present work pertains to the French government program "ImPEKKable" (reference ANR-15-CE08-0016) in collaboration with AIRBUS GROUP SAS Département Innovations, ARKEMA France, Ecole Nationale Supérieure d'Arts et Métiers - Laboratoire de Procédés et Ingénierie en Mécanique et Matériaux and the Ecole Nationale Supérieure de Mécanique et Aéronautique of Poitiers - Département de Physique et Mécanique de Matériaux.

The present work of thesis was carried out at the ENSMA of Poitiers, and it was possible thanks to the collaboration with many of its researchers, PhD students and members of the technical équipe.

I wish to thank my two supervisors, Marco Gigliotti and Jean-Claude Grandidier, for the almost blind trust, the possibility of express my creativity, their advices and the continuous challenges they put me in front of. The present work is the result of their constant support, not only in terms of scientific experience, as knowledge, ideas and guidance, but most of all, their moral support and human qualities.

Thanks to all the members of the jury, for their participation and the interesting discussion on the present work. I also wish to thank all the participants at the ImPEKKable project, which I had the chance to meet and work with in the past 3 years, for their precious insights and exchanges.

A grateful thank goes to all the technical staff of the ENSMA. I'd like to thank Médéric for the kindness of having always been there for "The Problem of Monday morning", weekly appointment in front of the testing machine, for all his advice and for having taught me all that I know about the thermomechanical testing, between a joke and a laughter. Thanks also to David, for the training in the DSC the DMA techniques and, most of all, for the help with the testing under conditioned atmosphere and the X-rays μ-tomographies, but also for his availability and sympathy. I want to thank Brigitte, Karine and Francine for their patience, their support and help in all the different administrative and bureaucratic parts, but most of all for their kindness. I wish to thank Gerald and Cedric for the informatic support, up to the very last minute.

I feel legally obliged to thank Azdine for the *convexhull* Matlab command, his precious mathematic reviews, for nothing (he knows) but most of all for his sympathy.

Because I spent the most part of my last 3 and half years in the lab, I'd like to thank those who basically became my new family, namely all the PhD students of the DPMM. Thanks for all the scientific exchange, the nonsense discussions, the volleyball matches, to having taught me how to play Coinche and then to systematically lose against me (kidding), for the parties, the jokes, thanks for having be there when needed, thanks for having made this experience fantastic, hence thanks to Cyril, Paul, Lucille, Luciana, Clément, Maxime, Natan, Romain, Coline, Blanche, Anil, Prasad, Sami, Happy, Sarah.

A special thanks goes to all the members of the B001, the 9-place open space office I worked in. The first time I entered it, I asked myself where did I come into, but sooner than I had the possibility of realize it, I was part of it, of all its craziness, its joy, its incredible atmosphere. That because of its members, those who were already there, but also those who came during the years.

These people, these friends, I sincerely wish to thank. Thanks Selim, for your peace-maker contribution and calmness, fundamental to limit possible escalations of craziness. Thanks Mahak, for all the infinite debates, for your humor: it was so strange of find someone, coming from the other part of the Earth so similar to me; thanks for your incredible strength. Thanks Ravi, I could not wish better for someone to

occupy the desk in front of mine: thank you for all the scientific exchanges, to be always ready for joking, for your positivity, you always be a Taklà. Thanks to Adèle, for all your help, especially in correcting my French and for being there when I needed you, thanks for making the effort of understanding me. Thank Satoshi, with whom I shared the strangest situations in France, one of which could be in a joke beginning with: "An Italian and a Japanese went to an Indian restaurant in France…". Thanks to Ciccio, also called François, for your contagious joy, in my opinion the main responsible of good vibes in the B001; thanks for all the nonsense Late late Night Shows episodes (which escalated quickly), but most of all, for the precious insights and exchanges. Thanks Nicò, for being who you are, thanks for helping me integrate, for your availability, your generosity; it took some times to understand each other, so different we are, but eventually we got there, and it was worth it; thanks to understand my way of joking, thanks for your exaggerated joy (especially during Christmas), thank you for your stubborn engagement in make the B001 the best workplace ever. A thanks also to the newcomers of the office, to whom goes the burden of continuing its traditions, Nathan, Tiphaine and Melanie.

The best for last, the queen of the self-proclaimed independent queendom of B001: a huge thanks goes to Marina, with whom I shared the Italian corner of the office. Her continuous help during the last years was for me fundamental. Thank you for having carried the burden of listening to all my complaints, all my (too many) "I finally got it", thanks for your delicious lunches and dinners, thank you for everything.

A special thanks to all the other Italian PhD students and not, Vincenzo, Barbara, Antonio, Flavio, Giovanna, which were there at my arrival in France. Thank you for all the beautiful moments spent together, thank you for being there, thank you for letting me feel like at home. A special thanks to Vincenzo for all his help and teachings on Matlab coding, in particular for the conception and development of the image analysis tool.

A great thanks to the "Canollians", Federico, Eleonora, Carolina and Marco, which really become a second family to me. There are no words for expressing my gratitude towards you, and your help on every level is so huge, I don't think I could have lived a similar experience without you. I could not have been luckier in meeting you and sharing the last years with you. Thanks to Federico, between everything, for the help in the carrying out of the experimental tests needed for the validation of the image analysis tool, and together with Marco and Carolina for all the precious insight and fruitful scientific exchanges.

A thanks goes to my family, for their constant support and encouragement, and even if at over 1500 Km away, I always felt them right next to me. I thank them, as all my friends, also for supporting and advising me to take this opportunity, and to them the present work is dedicated.

Grazie a tutti!

Giuseppe Pedoto

Introduction

The current trend in the use of materials in aeronautics is consistent with the aim of reducing the mass of structures by replacing the conventionally used metallic materials with lighter *organic matrix composites* (CMO). It can be estimated, for instance, that taking into account the density ratios between aeronautical aluminum and composite materials and the proper design of the replaced parts, a weight gain of 20% can be achieved. This weight gain may give a reduction in costs and ecological impact, notably through a reduction in fuel consumption and CO_2 emissions.

Since the first CMOs applications, thermosetting matrix reinforced composites were privileged, and in particular epoxy based composites, because of the lower cost of the epoxy resin compared to other polymers with similar mechanical properties. Nowadays, the composites with a thermosetting matrix constitute more than 90% of CMOs used in aeronautics.

However, their ecological impact, as well as the possibility of increase the CMOs temperature operative range, are behind the use of thermoplastics matrix based composites, which started relatively later and backs in the 80s-90s. The more complex behavior, as well the higher manufacturing cost of those polymers respect to epoxy resin, strongly impacted a larger employment and never lead to replace thermosetting ones.

Nowadays increased sensibility and awareness towards ecological issues, combined with the exponential increase in aeronautical traffic and active fleets, highlighted the problem tied to aircrafts ecological impact, in terms of polluting emissions but also in terms end-of-life disposal of structures.

Engine ameliorations in terms of materials and design, could reduce the polluting imprint, but loss weight still remains a principal issue in the reduction of fuel consumption. The replacement of CMO components, which still remain the best alternative to metallic components, with more environment-friendly materials, as bio-sourced polymers and fibers, is not yet always possible, due to the mechanical properties of such materials, not yet satisfying the structural need in aircraft structures.

This situation gave new impulse to the research and the employment of high performance semi-crystalline thermoplastic polymers as CMO matrix for aircraft applications. In the aeronautical field, the currently most employed (and studied) thermoplastic polymer is the *Poly-Ether-Ether-Ketone* (PEEK), (e.g. it is currently used in the CMO structural parts of A400M cockpit floor). Its cost, considerably higher than the epoxy resin, as well as the manufacturing temperature required (it has to reach its melting temperature, 400°C), prevent a wider employment.

For this reasons, other polymers were developed, as the *Poly-Ether-Ketone-Ketone* (PEKK), manufactured by Arkema with the commercial name of KEPSTAN™. This polymer has a chemical structure similar to PEEK, but a ~40°C lower melting temperature, which reduces its manufacturing cost and, while its properties and thermomechanical behavior could be considered similar to PEEK ones, it is significantly less studied.

Moreover, besides the recyclability of the thermoplastic polymers, they offer the possibility of increase the temperature operative range, respect to thermosetting ones. In fact, while the latter experience a degradation (after consolidation), if exposed at high temperatures, the thermoplastic polymers, also show a change of state, from solid to rubber-like. This phenomenon is generally associated with a loss of mechanical properties, but could be mitigated by the formation or the preexistence of ordered molecular structures in the material, the *crystals*, which do not undergo the same change of state, but stay solid.

The complex interaction between the change of state due to the high temperature, the crystal structure presence and/or formation, and the possible activation of degradation phenomena, is not deeply investigated in the PEKK polymer and it constitutes the aim of the ANR *ImPEKKable project*, carried out as a collaboration between Airbus SAS, Arkema, the ENSAM of Paris and the ISAE-ENSMA of Poitiers.

In particular, the ImPEKKable project aims to replace components of the aircraft pylon, (VINET ET AL. 2019), (FIG. 1-1), currently manufactured in carbon fibers IM/epoxy composites (AIRBUS SAS, ARKEMA, ENSMA - POITIERS, ENSAM - PARIS 2018), which operative conditions are listed in TAB. 1-1.

Fig. 1-1: Upper longeron of A350-1000 pylon, (Vinet et al. 2019)

Temperature specifications	
Operative conditions	<150°C for 10000h
Critical event	180°C for 15 min

Critical load specifications	
	5 min at 180°C 10 min at 0.7 Limit load

Tab. 1-1: Material's required operative specifications, (Airbus SAS, Arkema, ENSMA - Poitiers, ENSAM - Paris 2018)

The content and activities of the ImPEKKable project aim to study these phenomena for a new generation of thermoplastic matrix composites (C / PEKK) in order to allow an accurate part design, while ensuring the appropriate durability for each foreseen application, (approximately 80,000 hours on an aircraft).

In fact, the pylon spends most of the service life in relatively low temperature ranges, where degradation is limited and where creep generated by thermo-mechanical stresses could generate concerns about the appearance and propagation of damage. However, the occurrence of incidents leading to exposure to higher temperatures (even if remote) has to be taken into account for structure design: in these extreme conditions the structures must not fail under any circumstances. For this reason, the behavior of the foreseen employed material under those condition has to be investigated and understood.

The main issue of the present study is therefore to evaluate the C/PEKK composite structures long-term behavior under those critical event temperature ranges (180°C ±20°C, above its matrix *temperature of glass transition* (T_g)) and solicitations (*long-term creep*), also considering particular environmental condition (*oxidizing atmosphere*).

The understanding of the different mechanisms characterizing the material behavior only constitutes the first step for its employment for industrial applications. The modelling of

those mechanisms to define a behavior-predictive tool, employable for the simulation of different solicitations and configurations is equivalently of the outmost importance for structure conception and design, and constitutes a second objective of the present work.

In the present work, the experimental equipment and techniques, as well as the results of the experimental campaign aimed to characterize the PEKK thermomechanical and physical-chemical behavior at temperature above the PEKK T_g are presented.

The analysis of the experimental data allowed the identification and the analytical description of the different mechanisms characterizing the PEKK behavior, and a model of the PEKK behavior, valid at different temperatures and types of solicitation is presented.

This model is implemented in a semi-analytical method, written in Matlab code, which allows the simulation of the PEKK based composite (C/PEKK) behavior under different solicitations, validated through comparison with the experimental data and generalized to simulate different ply orientations and stacking sequences.

The investigation of the long term PEKK and C/PEKK behavior and the presence of degradation phenomena, completes the present work.

Chapter 1 – Literature Survey

This Chapter presents a literature survey concerning generalities of composite materials in aeronautical structures, the thermomechanical creep behavior of thermoplastic polymers and polymer composites and the degradation (and oxidation) behavior of PEKK and PEKK based composites.

1.1. Literature Survey

The present chapter aims to provide the reader with a general overview of the state of the art on the different subjects which constitutes the object of the present work. Because of the (at least) biphasic nature of the composite materials; the present work is structured at two levels:

- at the composite material (higher level);
- at matrix level (lower level), through the analysis of its constituent, the polymer.

Consequently, the present chapter follows this structure and a literature survey on the state of the art at the two different levels is presented.

However, while a vast literature is available on thermoplastic polymer and thermoplastic matrix based composites, less work is available on PEKK polymer and PEKK based composites, and even less investigation was carried out on their high temperature behavior.

For this reason and limited to specific aspects, the studies carried out on a similar material, the PEEK, will be presented: those results were employed as guideline for the investigation on the PEKK and PEKK composite, as the phenomena and mechanisms which could be expected to be found also for those materials. Nevertheless, the parallelism/differentiation between PEKK and PEEK is not the purpose of the present work.

1.1.1. Composite Materials in aeronautical structures

The employment of composite material in aeronautics structures is started in the 1940s, as replacement of structural components initially realized in metallic alloys, and continued throughout nowadays, becoming, in percentage, the principal constituent of the aeronautic structures, (FIG. 1-1).

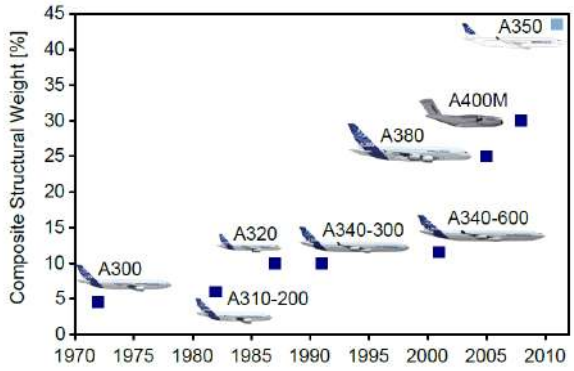

Fig. 1-1: Portion of composite materials in Airbus aircrafts (by courtesy of H. Assler, Airbus Deutschland GmbH) (Kaufmann 2008)

Considering the composites only constituted by fibers and matrix, a vast range of different materials were employed in the last decades as constituents, and between them, (NIU 2010):

- *fiber material*: glass, carbon, boron, metals, etc…
- *fiber geometry*: long, short;
- *matrix material*: organic (thermoset, thermoplastic polymers), metallic, ceramic, etc…

The composite specific properties, besides being provided by the combination of the matrix and fiber specific properties, depends also by the specific *manufacturing techniques* (e.g. poltrusion, resin transfer molding, etc…), which depends by the combination of the chosen composite constituents.

Moreover, those properties also depend on the different composite *architecture*: while the simplest architecture is constituted by a lamina with the fibers oriented all in the same direction (*unidirectional* or UD), textile preforms (woven, braid, knit, etc…), (RAMAKRISHNA 1997), can be realized.

The UD ply is an orthotropic material, which properties are higher in the fiber direction (dominated by the fiber's properties) than in the other 2 (dominated by the matrix's properties). The UD plies are employed in industrial applications within a stacking of different layers, generally employing different orientations: the most common stacking sequence is composed by a multiple of layers at 0° (vertical), 90° (horizontal) and ±45°. This particular configuration allows charging each layer in the fiber direction, optimizing the composite effectiveness, but also reducing the orthotropy of the composite, which is referred to as *quasi-isotropic* (QI). The consolidation of the stacking sequence is carried out applying specific temperature and pressure, inserting the structure in an autoclave.

In the aeronautical field, the configuration carbon fibers/epoxy matrix emerged and rapidly overcome all others: in fact, the carbon fibers have high specific properties and excellent thermal stability up to 1200°C (LAMOUROUX ET AL. 1999), while the epoxy has a low density, is relative inexpensive and has an operative temperature range up to 100°C. The resulting composite has a density significant lower than any metallic alloys employed for aeronautical application, allowing obtaining a better *Performance Index* (as the ratio between density and mechanical properties) respect to the metallic alloys.

The main drawbacks of the carbon/epoxy composite and generally of the composite are:

- operative temperature ranges considerably lower than many metallic alloys, limiting their application to "cold" aircraft structure up to 200°C (GABRION ET AL. 2016);
- the higher manufacturing cost respect to the metallic alloys which could be employed to realize the same parts, and the need of specific equipment: however, the gain in mass and consequently in fuel consumption, justifies their employment. Moreover, the larger diffusion and optimization of the manufacturing procedures, also contributed to significantly lower the cost;

- *damage scenarios* at different scale and different from metallic alloys, such a fiber-matrix debonding, inter-fiber cracking, ply delamination, fiber breakage, etc…, specific to the composite structures, influence their failure criterion and durability design. Moreover, impact toughness, water absorption, and oxidation can have a significant effect on the material's properties.
- the *end-of-life* is limited to down cycle, combustion and disposal of the material: this is the direct consequence of the *reticulation* phenomenon specific of thermoset polymers, which consists in the formation of non-reversible strong bonds between its macromolecular chains. This process is activated raising the temperature above its glass transition temperature during the consolidation in autoclave and, if from one side it confers to the material its mechanical properties, on the other side, it prevents the material to be recycled. Moreover, the single ply employed for the QI (*prepregs*), can be stocked only for a limited time.

In order to address those drawbacks, in the last 30 years, the possibility of replacing the matrix in the composites from thermoset to thermoplastic polymers was investigated. High performance polymers of the PAEK family where studied, in particular the *Poly-Ether-Ether-Ketone* (PEEK), and employed for aircraft applications (BIRON 2018), (GABRION ET AL. 2016), (MARTÍN ET AL. 2018), (TADINI ET AL. 2017), (PAPPADÀ ET AL. 2015). Between the advantages of employing those materials:

- the possibility of extending the maximum operation temperature to higher temperatures with respect to thermoset polymers: potentially these materials could work at temperatures above their glass transition temperatures. In fact, as discussed more in detail later, the thermoplastic polymers tend to form weak, reversible bonds within their macromolecular chains. Therefore, the exposure to temperature above T_g (but far from the melt) could not activate degradation mechanisms, as in the thermosets, but instead activate a phenomenon called *crystallization*, where the crystals, organized, stiffer molecular structures, increase the mechanical properties of the material;
- the *crystallization* mechanism, which is reversible, provide the possibility of recycling the material;
- the PAEK family polymers, and in particular the PEEK and PEKK show excellent corrosion and water absorption resistance. Moreover, the prepregs do not have an expiration date.

However, the thermoplastic polymers have a considerably higher cost respect to the epoxy resin, and require different manufacturing process for the realization of the prepregs. Moreover, also for the small scale production, the manufacturing process is less optimized and more expensive respect to one employed for epoxy based composites. Furthermore, even if the consolidation process can be carried out in autoclave, it requires the complete melt of the polymer (400°C for PEEK, 360°C for the PEKK, respect to the autoclave cure temperature of 180°C epoxy) and specific cooling rate and isothermal process to maximize the crystal formation in the material.

Those aspects are discussed more in detail in the next paragraphs.

1.1.2. Crystallization mechanisms in PEKK polymers and PEKK based composites

Thermoplastic polymers are composed by macromolecular chains, which internal chain bonds can produce rotation and bending in the chains themselves, and could lead to intertwining and entanglement with neighbor chains. The resulting random, highly irregular structure constitutes the polymer *amorphous phase*.

However, the movement of the chains could result in producing an ordered array, favoring the formation of covalent reversible bonds, which constitutes the polymer *crystalline phase*. This phase is different from metal crystalline structure, produced from atomic bonds, being produced by molecular ones. Moreover, because of the length of the polymer molecules, it is a local phenomenon, and the same macromolecular chain can be partially part of a crystal structure and partially amorphous. The resulting crystal structure is therefore dispersed in an amorphous region: this has the consequence that thermoplastic polymers cannot be totally constituted by crystals (as metals), and up to a certain percentage of crystals can be formed.

Moreover, chains could partially fold on themselves constituting ribbon-like structures called *lamellae*, which are separated between each others by amorphous region and, starting from a nucleation site, grow in a random direction, forming a larger, almost spherical structure called *spherulites*, as showed in FIG. 1-2, (WILLIAM D. CALLISTER 2007).

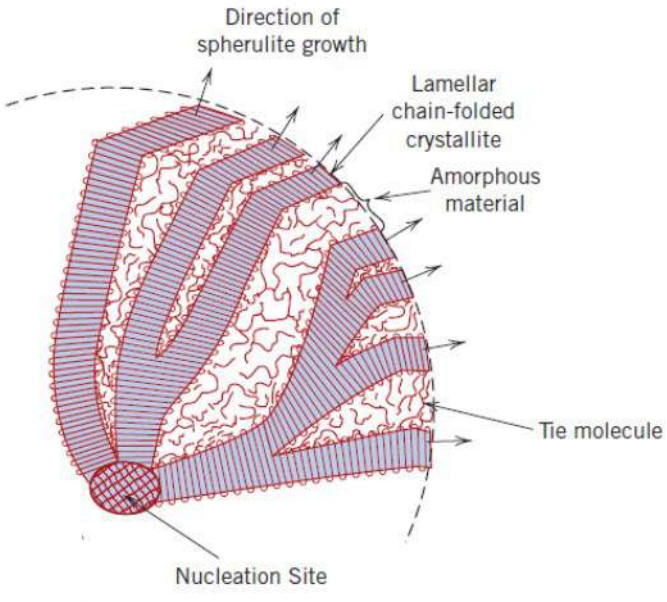

Fig. 1-2: Schematic representation of the detailed structure of a spherulite (William D. Callister 2007)

In case of spherulitic structure, the crystallization is constituted by 3 principal phases (HOFFMAN AND WEEKS 1962):

- **Nucleation**: the nucleation is function of the variation of enthalpy of a crystallized volume (constituted by defects in the polymer itself or by a different material or nucleation promoters) and by the supercooling degree. According to (KOSCHER AND FULCHIRON 2002), the density of nucleation sites can be evaluated through

$$ln(N) = a\,\Delta T + b \qquad \text{Eq. 1-1}$$

  where $\Delta T = T_{m0} - T$ is the supercooling degree, and T_{m0} the temperature of thermodynamic equilibrium;
- **Primary crystallization**: lamellae grow from the nucleation sites, integrating the surrounding amorphous phase in the crystal structure, in all directions, up to occupy the entire volume of the material. The growth rate is predicted by the theory of Lauritzen-Hoffman, (HOFFMAN AND WEEKS 1962) as:

$$G = G_0 \exp\left(-\frac{U^*}{R(T-T_\infty)}\right)\exp\left(-\frac{K_g}{T\Delta T}\right) \qquad \text{Eq. 1-2}$$

  where:

  - the activation energy U^*;
  - $T_\infty = T_g - 30°C$, the temperature below which the chains mobility is impossible;
  - G_0, K_g are two experimental constant and R is the universal constant of ideal gas.

  The theory of Lauritzen-Hoffman describes the crystallization mechanism which is active if $T_\infty = T_g - 30°C < T < T_{m0}$, meaning that crystallinity phase will form if the temperature is decreased from the melt state or increase from T_∞, with a crystallization growth rate G which has a Gaussian trend with the temperature, and a maximum in $\frac{(T_\infty + T_{m0})}{2}$.

  (KOLMOGOROV 1937) proposed a model to estimate the amount of relative primary crystallinity as function of the annealing time t, the density of nuclei N and the growth rate G, which for the case of isothermal, can be reduced to an (AVRAMI 1941) equation:

$$\alpha_1(t) = 1 - \exp(-K_1 t^n) \qquad \text{Eq. 1-3}$$

where:

- $n=3$ in case of spherulites;
- $K_1=K_{01}\ exp\left(-\frac{3U^*}{R(T-T_\infty)}\right) exp\left(-\frac{3K_{g1}}{T\Delta T}\right)$;
- $K_{01}=\frac{4\pi}{3}\ N_{01}\ G_{01}^3$.

- **Secondary crystallization**. As mentioned before, the spherulite structure is composed by lamellae growing in all direction, but also by amorphous phase between the lamellae (FIG. 1-2). The growth of primary crystallization involves extra-spherulitic amorphous phase and continue up to occupy the entire material volume. Towards the saturation, according to Avrami equation, the process slows down. At this stage, the mobility of chains activates intra-spherulitic crystallization, a slower and often minority mechanism compared to primary crystallization, which is not associated to nucleation nor to spherulitic growth. On the contrary it was observed to produce:
  - increase of lamellae thickness (MARAND AND HUANG 2004);
  - intra-lamellae crystallization (VERRNA, MARAND, AND HSIAO 1996), (BESSARD, ALMEIDA, AND BERNHART 2011), (BOYARD ET AL. 2017),(FIG. 1-3);
  - refinement of already crystallized region (Schultz et al. 1980).

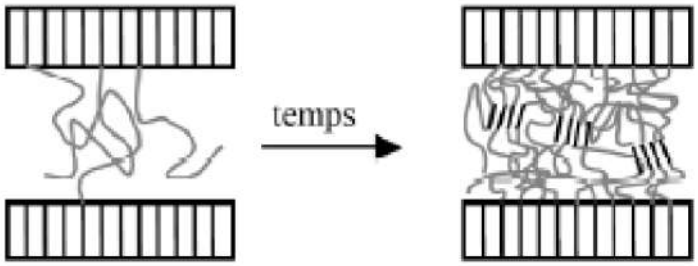

Fig. 1-3: Simplified schematization of interlamellar crystallization phenomenon, (Boyard et al. 2017)

Different models were developed to take into account also secondary crystallization, (VELISARIS AND SEFERIS 1986), (HILLIER 1965) and in the case of PEKK 70/30, (HSIAO, CHANG, AND SAUER 1991) found a good agreement with experimental results employing a modified Hillier model, describing primary crystallization (α_1) as in EQ. 1-3 and, in case of isothermal transformation, the secondary crystallization as:

$$\alpha_2(t)=\int_0^t \alpha_1 \frac{d}{dt}\left(1-\exp\left(-K_2(t-\theta)\right)\right) d\theta \qquad \textit{Eq. 1-4}$$

where:

- the Avrami exponent n=1;
- $K_2 = K_{02} \exp\left(-\frac{U^*}{R(T-T_\infty)}\right) \exp\left(-\frac{K_{g1}}{T\Delta T}\right)$;
- $K_{02}=N_{02}\, G_{02}$;
- $(t-\theta)$ is the delay in the activation of secondary crystallization.

Hence, the total crystallization can be calculated through the following rule of mixtures:

$$\alpha(t)=w_1\alpha_1(t)+(1-w_1)\alpha_2(t) \qquad \textit{Eq. 1-5}$$

where w_1 is a weight factor.

In different studies, in particular in (GARDNER ET AL. 1992), (CORTES ET AL. 2014), the presence of secondary crystallization on PEEK was observed, as a second endothermic peak, about at 10°C above the annealing temperature, in *Differential Scanning Calorimetry* (DSC) heat flow vs temperature curves, obtained testing the material after annealing,. This second peak was associated to the melt of secondary interlamellar crystallinity.

Recent works, carried out by (CHELAGHMA 2013) and (TANGUY CHOUPIN 2018), studied the crystallization kinetics employing Hillier modified model for PEKK. In particular, the latter, in the frame of ImPEKKable project, identified the parameters of the crystallization kinetics for isothermal transformations for PEKK 6002 and 7002, according to the modified Hillier model. The resulting kinetics of primary and secondary crystallization kinetics of PEKK 6002, for the case of crystallization at 230°C from the melt is showed in FIG. 1-4.

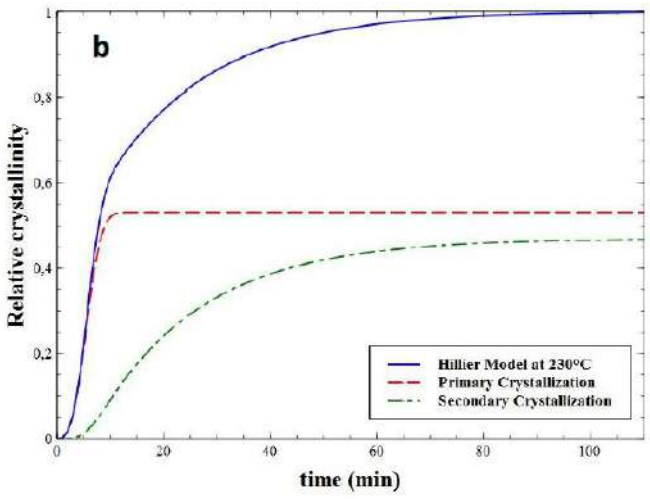

Fig. 1-4: Relative fraction crystallinity α(t) *vs tile with the Hillier model for the overall crystallization (solid curves), the primary (dashed curves) and the secondary crystallization (dashed dotted curves) at 230°C for neat PEKK 6002 crystallized from the melt, (Tanguy Choupin 2018)*

FIG. 1-4 shows the different contribution of the 2 mechanisms, and how the primary crystallization is dominant at the beginning up to almost its saturation, while the secondary crystallization starts when the primary slows down and has a slower kinetics. It is significant that at this temperature, the primary crystallization constitutes less than the 60% of the total relative crystallinity.

Moreover, (TANGUY CHOUPIN 2018) identified the parameters of the modified Hillier model describing the crystallization kinetics for PEKK 7002 from the melt state for isothermal transformations at any temperature between T_∞ and T_{m0}. Those parameters, listed in TAB. 1-1, allow the description of the *Time-Temperature-Transformation* (TTT) curves of crystallization showed in FIG. 1-5.

Kinetics parameters	PEKK 7002
T_{m0} [°C]	360
K_{01} [min^{-3}]	$1.79 \cdot 10^{16}$
K_{02} [min^{-1}]	$2.6 \cdot 10^{5}$
K_{g1} [K^2]	$4.0 \cdot 10^{5}$
K_{g2} [K^2]	$4.4 \cdot 10^{5}$
U^* [J mol^{-1}]	$4.7 \cdot 10^{3}$
w_1	0.78

Tab. 1-1: Parameters of the kinetic models for the crystallization rate constants (K_1 and K_2) and the weight factor (w_1) for PEKK 7002 crystallized from the melt, (Tanguy Choupin 2018)

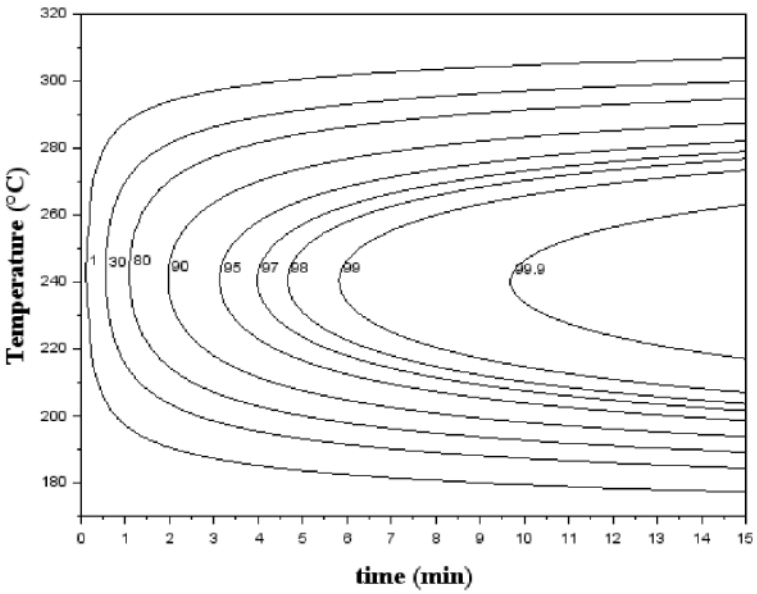

Fig. 1-5: TTT diagram of the relative crystallinity for the overall crystallization for PEKK 7002 crystallized from the melt, (Tanguy Choupin 2018)

FIG. 1-5 shows the maximum rate of crystallization for PEKK 7002, around 240°C, where the maximum achievable crystallinity could be obtained with a 10 min isothermal transformation.

In case of non-isothermal crystallization, the cooling rate plays a fundamental role on the crystallinity phase: in fact, as the cooling rate is increased, the crystal growth is slowed down up to be completely stopped in case of extremely fast cooling process, and allows obtaining a completely amorphous material at room temperature. Lower cooling rate, instead, allow the chains to organize and form crystals, (WILLIAM D. CALLISTER 2007).

For thermoplastic matrix composites, the fibers act as a preferential nucleation site and crystals growth perpendicular to the fiber direction has been observed (GAO AND KIM 2002), (JAR, CANTWELL, AND KAUSCH 1992), a phenomenon, called *transcrystallinity* . Both (CHELAGHMA 2013) and (TANGUY CHOUPIN 2018) showed the presence of transcrystallization on carbon fiber/PEKK composites (C/PEKK), as showed in FIG. 1-6.

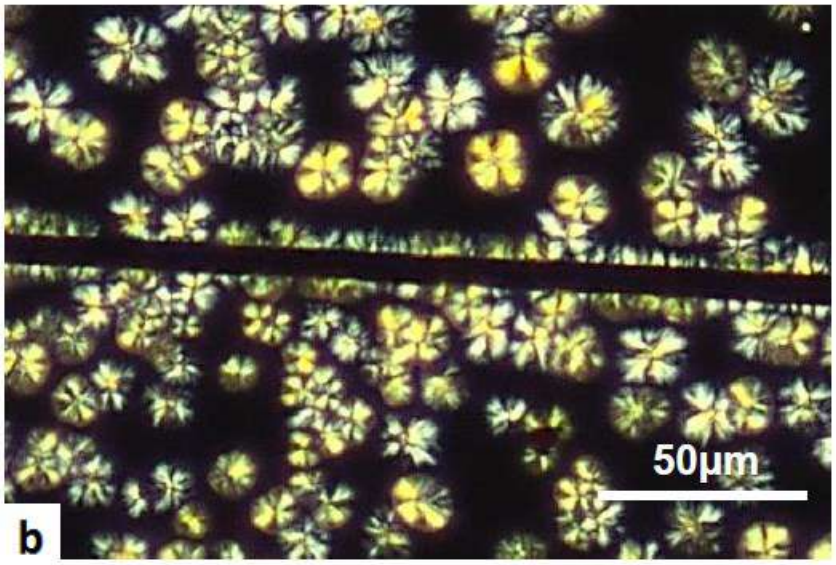

Fig. 1-6: Micrographs of PEKK 6002 with carbon fibers crystallized from the melt at 270°C during 2h, (Tanguy Choupin 2018)

The transcrystallinity impacts the fiber/matrix interface, and (LEE AND PORTER 1986) have found that it could ameliorate the adhesion between the two materials.

While the crystallization mechanisms could be activated at any temperature between $T_\infty = T_g - 30°C$ and T_{m0}, they play a fundamental role in particular in the manufacturing process, especially for the definition of the cooling kinetics from the melt state. During this phase of the manufacturing process, in fact, the amount of crystallinity phase in the materials is produced, from which the mechanical properties depend on, as described in the next paragraph.

1.1.3. Effect of the crystallization on PEKK polymer and PEKK based composite mechanical properties

The effect of the pre-existing crystalline phase on the mechanical properties of thermoplastic polymers and thermoplastic matrix composites was widely investigated (COWIE 2001), (SEFERIS 1986), (TALBOTT, SPRINGER, AND BERGLUND 1987), (PEACOCK AND MANDELKERN 1990), (PAWLAK AND GALESKI 2005), (GAO AND KIM 2002), showing an increase in Young modulus and a decrease in ductility.

The polymer behavior is strongly affected by the crystalline percentage, and while for an amorphous material, a linear viscoelastic model could describe its behavior, such model fails to correctly describe it, in case of semi-crystalline polymers (COWIE 2001). Moreover, at temperature below T_g, necking appears during tensile tests, causing the stress to drop due to the reduction in the specimens' cross section. In amorphous materials, however, an increase in stress was observed prior to failure, associated to the macromolecular chains alignment towards loading direction (*strain induced crystallinity*) (VAN MELICK, GOVAERT, AND MEIJER 2003), (WENDLANDT, TERVOORT, AND SUTER 2005), (NITTA AND NOMURA 2014).

The transition above T_g, produces a drop in the mechanical properties of thermoplastic polymers due to the amorphous change of state from solid to rubber-like. On the contrary, the crystalline phase remains in solid state, and produce a containment of such properties loss, which depends on the pre-existing crystalline phase.

In the case of PEKK, (TANGUY CHOUPIN 2018) investigated such phenomena, confirming the dependence of the mechanical properties on the crystalline percentage, as showed in FIG. 1-7.

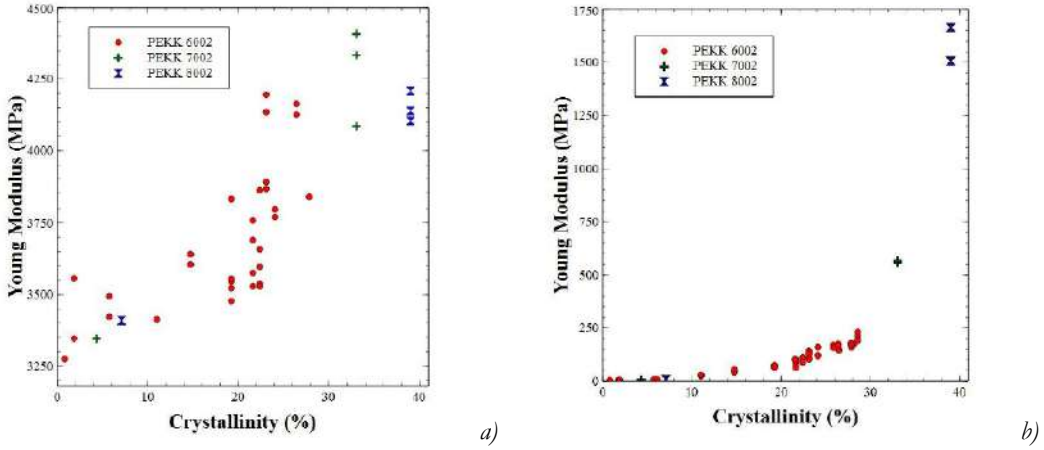

Fig. 1-7: Young modulus vs crystallinity at room temperature (a) and at 180°C (b) of neat PEKK crystallized at 230°C from the glassy state with a strain rate of 3.3 s^{-1}, (Tanguy Choupin 2018)

Moreover, FIG. 1-7 shows the loss of properties consequent to the passage above T_g, and the role of crystallinity in contain such loss for PEKK.

Semi-crystalline polymers could undergo plastic transformations, related to stress (strain) induced lamellar orientation towards loading direction, (G'SELL ET AL. 1999). This mechanism leads to the separation of the same lamellar structures and the consequent sliding of the obtained lamellar blocks, finally leading to orientation in loading direction (PEEBLES, L.H. 1974), (WILLIAM D. CALLISTER 2007), (FIG. 1-2). Pseudo-plastic phenomena, as the rupture of the lamella structures, (BOWDEN AND YOUNG 1974) or to phenomena related to the slide along slip plane, as the chain slide (G'SELL ET AL. 1999) were observed as well.

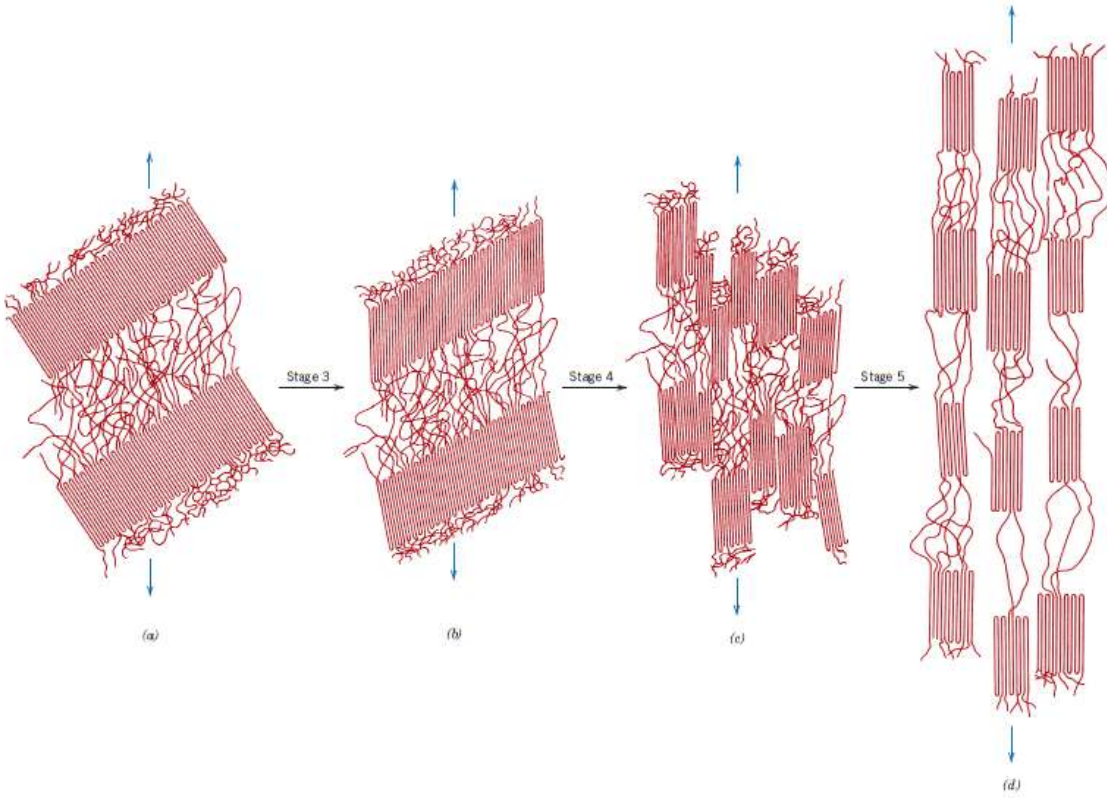

Fig. 1-8: Stages in the plastic deformation of a semicrystalline polymer. (a) Two adjacent chain-folded lamellae and interlamellar amorphous material after elastic deformation; (b) Tilting of lamellar chain folds. (c) Separation of crystalline block segments. (d) Orientation of block segments and tie chains with the tensile axis in the final plastic deformation stage, (William D. Callister 2007)

Above T_g, the above mentioned mechanisms are enhanced and accelerated by the increased chain mobility. Furthermore, if the material is not completely crystallized, crystallization mechanisms are activated, interacting with those mechanisms. The resulting coupling between thermomechanical load and crystallization affects the material thermomechanical behavior and consequently the polymer mechanical properties; this will be discussed more in detail in the next paragraph.

1.1.4. PEEK and PEKK polymers and composites thermomechanical behavior

PEEK has overall very good mechanical properties, but like any thermoplastic polymers, a drop in these properties is observed after at the glass transition temperature (MARTINEAU ET AL. 2016). However, tensile and flexural strength values are still acceptable up to around 250°C and 300°C, respectively. In addition, PEEK has very good behavior against friction and wear (DOBRACZYNSKI, A; TROTIGNON, J-P; VERDU, JACQUES; PIPERAUD 1996).

Different studies where carried out on its tensile, compression and shear behavior and different models where developed to describe its complexities: in particular, amongst the most recent ones:

- (GARCIA-GONZALEZ, ZAERA, AND ARIAS 2017) proposed a model taking into account the temperature and the strain rate effect, constituted by the parallel of two branches: the first taking into account the intermolecular resistance (describing the interactions between the crystalline and amorphous phases), associated with hyperelastic, viscoelastic and viscoplastic mechanisms, and a second branch, describing the network ("free" amorphous phase) hyperelastic behavior. The model, initially describing only the behavior at $T<T_g$, was also extended to describe the behavior above T_g by (BARBA, ARIAS, AND GARCIA-GONZALEZ 2020);
- (ZHENG ET AL. 2017) proposed an elastic – viscoplastic model, also taking into account the temperature and the strain rate effect, to describe the tensile behavior limited at $T>T_g$;
- (LI ET AL. 2019) proposed an alternative 2 branches model composed by a fast and a slow relaxing component, each constituted by different elastic and viscous constituents. This model was developed to describe PEEK monotonic tensile, compression and shear and shear cyclic behavior at $T<T_g$.

PEEK shows limited creep at room temperature and up to around 180°C, and has excellent resistance to fatigue (VILLOUTREIX AND ACETARIN 1998). Moreover, it is ductile and tough without notches, but the presence of moderate notches can considerably reduce its impact resistance.

The long – duration creep tests allowed the identification of the *physical ageing* phenomenon, which occurs at temperature below T_g, and it is characterized by the relaxations of macromolecular chains, which are not in thermodynamic equilibrium and tend to reach their closer equilibrium state, only producing an alteration of their spatial configuration and without involving chemical reactions (WHITE 2006), (FAYOLLE AND VERDU 2005). This phenomenon was extensively studied (STRUIK 1977) (MCKENNA AND KOVACS 1984)(KOVACS ET AL. 1979), (BRINSON AND GATES 1995), in particular in amorphous polymers, which undergo a quench to prevent the crystallinity phase to form and once below T_g, the superficial thermal equilibrium does not correspond to the thermodynamic

equilibrium. Moreover, the thermal gradient produced during the cooling provokes the development of residual stresses, and the progressively relaxation eventually reduced them: the change in residual stress over time could be considered another aspect of the physical ageing phenomenon (COXON AND WHITE 1980), (HAWORTH ET AL. 1982).

While the investigation was carried out more extensively on amorphous polymers, semi-crystalline ones also undergo such phenomenon, and while the crystals are less concerned by this phenomenon, the constraints applied by the crystals on the surrounding amorphous phase, strongly impact its relaxation and produce a far more complex scenario.

The relaxation behavior was employed to describe the creep behavior of amorphous polymers, through the Kohlrausch, Williams and Watt (KWW) function (G. WILLIAMS AND WATTS 1970):

$$J(t)=J_0 \exp\left(\frac{t}{t_0}\right)^m \qquad \textit{Eq. 1-6}$$

where J and J_0 are the creep compliance respectively at the time t and t=0, which led to the sum of exponentials form:

$$\sigma=\sum_j a_j \exp\left(-\frac{t}{\tau_j}\right) \qquad \textit{Eq. 1-7}$$

where a_j are the j weights, each corresponding to a τ_j characteristic relaxation time, which is employed to describe the linear viscoelasticy.

(BRINSON AND GATES 1995) showed how it is possible to obtain long term creep behavior for polymer and polymer based composites under T_g from short-term (*momentary*) creep tests, which difference is produced in fact by the physical ageing. Furthermore, starting from William-Landel-Ferry (M. L. WILLIAMS, LANDEL, AND FERRY 1955) formulation, they showed how to calculate the correction on the time-shift factor in order to obtain a time-temperature superposition of the long term creep compliances curves:

The literature on the elastoplastic and creep behavior of polymers and composites based on PEEK is relatively old (XIAO, HIEL, AND CARDON 1994), (D'AMORE, POMPO, AND NICOLAIS 1991), (KATOUZIAN, BRÜLLER, AND HOROSCHENKOFF 1995), (OGALE AND MCCULLOUGH 1987), (MA ET AL. 1997) and limited to temperature below T_g: in particular (D'AMORE, POMPO, AND NICOLAIS 1991), shows that the creep of amorphous PEEK is associated with physical aging.

Some differences between the viscoelastic behavior of pure resin (semi-crystalline PEEK) and the matrix in composites (APC-2 composites) have been highlighted (D'AMORE, POMPO, AND NICOLAIS 1991), but these aspects have not been sufficiently explored. Other authors (XIAO, HIEL, AND CARDON 1994) suggest the use of non-linear laws (non-linear viscoelastic Shapery model) for the description of the viscoelastic behavior of PEEK and PEEK-based composites at different temperature and stress regimes.

The development of new techniques for using thermoplastic polymers has aroused interest in the mechanical behavior at high temperatures of these materials (see (LEE AND PORTER 1991) concerning the creep-fatigue interaction in carbon-PPS composites), but there is very little recent work on PEEK and PEKK. A recent thesis from ISAE-ENSMA (DASRIAUX 2012) emphasized the importance of high temperature heat treatments (annealing) on "secondary" crystallization phenomena.

Whatever the conditions of use in service, the literature emphasizes - for composite materials based on thermoplastic polymer - the importance of taking into account deformations and residual manufacturing constraints (see reference (PARLEVLIET, BERSEE, AND BEUKERS 2007) for a state of fairly exhaustive art), for a correct estimate of the initial state of these materials / structures: the manufacturing temperature of these matrices being relatively high, the cooling phase at room temperature can generate residual deformations / stresses which can contribute not negligible at total deformations / stresses, in service.

The studies carried out on PEKK and PEKK composites thermomechanical behavior are significantly fewer and also relative old (I. Y. CHANG AND LEES 1988), (IKE Y. CHANG AND PRATTE 1991), (SUN, CHUNG, AND CHANG 1992), (PRATTE, KRUEGER, AND CHANG 1989), (KHAN ET AL. 1990). In particular, (SUN, CHUNG, AND CHANG 1992), investigated the PEKK composites behavior, describing their behavior below and above T_g with an elastic-viscoplastic model, as function of the fiber orientation: in fact, the mechanical behavior of thermoplastic composite could change with the fiber orientation, especially above T_g, because of fiber superior mechanical properties. Fibers could dominate the behavior, which could change from almost linear elastic (for 0° composites) to strongly non-linear (for 90°C composites)., as showed in FIG. 1-9A. Moreover, Sun found an analog loss of the mechanical properties in C/PEKK, (FIG. 1-9B) composites, similar to the one observed on PEEK, which varies along with the fiber orientation.

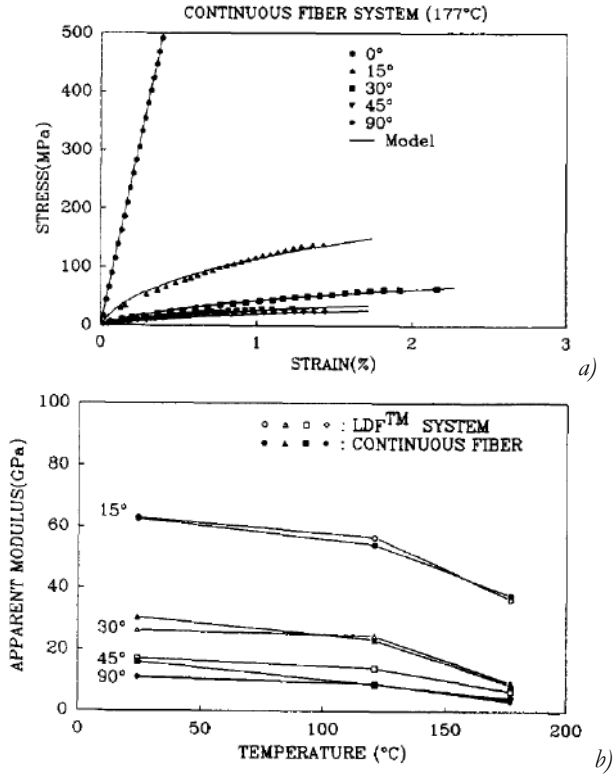

Fig. 1-9: (a) Stress/strain curves for off-axis specimens of continous fiber systems measured at 177°C (b) Variation of apparent moduli with respect to temperature for LDF (discontinous fiber) and continous fiber systems. (Sun, Chung, and Chang 1992)

This can be observed also for C/PEKK 7002 composites, from tensile tests carried out by (TANGUY CHOUPIN 2018) on 8 plies UD composites and $[\pm 45°]_{8s}$ composites, showed in FIG. 1-10.

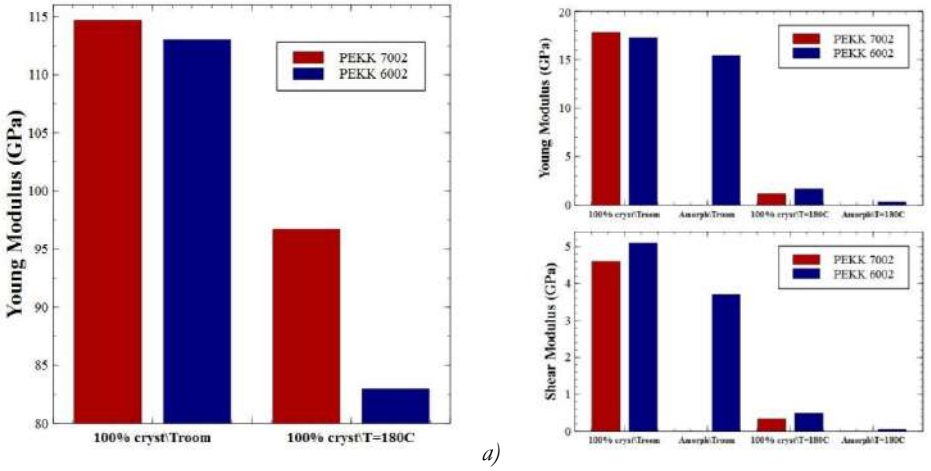

Fig. 1-10: (a) Evolution of the Young modulus of UD fully crystallized PEKK composites manufactured under autoclave tested at room temperature and at180°C.(b) Evolution of the Young modulus (upper figure) and shear modulus (lower figure) of ±45° fully crystallized from the melting state and amorphous PEKK composites manufactured under press tested at room temperature and at180°C (Tanguy Choupin 2018)

FIG. 1-10 shows, in any case, a loss of properties consequent to the transition above T_g; as observed in the neat polymer, more significant and similar to neat polymer for $[\pm 45°]_{8s}$ composites than for UD.

When the temperature is increased above T_g on PEKK and C/PEKK composites, as on other thermoplastic polymers and composites, if from one side the activation of physical ageing –related relaxation mechanisms is precluded, from the other side a loss of mechanical properties due to the polymer change of state is provoked and crystallization mechanisms can be activated, with a complex interaction between the two phenomena.

The higher temperature, however, especially combined with severe environmental conditions, could activate degradation mechanisms, which could have a significant effect on the thermomechanical properties of the materials, as discussed more in detail in the next paragraph.

1.1.5. Degradation (and oxidation) behavior of PEKK and PEKK based composites

Polymers and hence polymer based composites, could experience degradation (*ageing*) due to environmental effect, which could activate physic and/or chemical mechanisms. The main degradation phenomena are, (WILLIAM D. CALLISTER 2007):

- *swelling* and *dissolution*: those mechanisms are activated when polymers are exposed to liquids or solutes, such water, acid or alkaline solutions, which diffuse into the material, forcing the polymeric macromolecules to move apart. This mechanism causes the breaking of intermolecular bonds (*hydrolysis* if produced by water) and the material results softer and more ductile. Because of the PEKK good resistance to both water absorption and corrosive attacks, those phenomena are not observed.
- *bond rupture*: radiations, chemical reactions and heat (and a combination of them) could provoke the dissolution of the macromolecular chains' bond (*scission*) The resulting segment separates, reducing the polymer molecular weight, strongly impacting the physical-chemical properties of the material, as showed in FIG. 1-11.

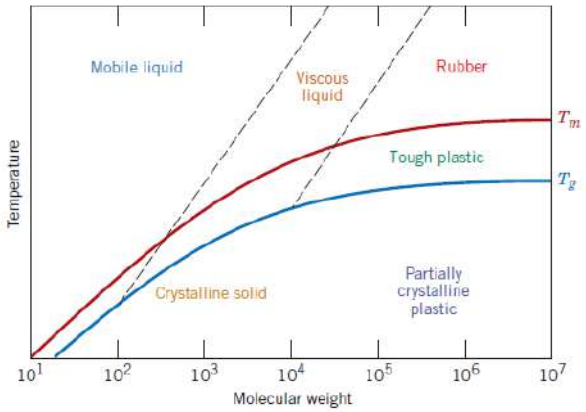

Fig. 1-11: Dependence of polymer properties as well as melting and glass transition temperatures on molecular weight. (From F.W. Billmeyer, Jr., Textbook of Polymer Science, 3rd edition. Copyright © 1984 by John Wiley & Sons, New York. Reprinted by permission of John Wiley & Sons, Inc.) (William D. Callister 2007)

In particular, the oxygen could form chemical reactions with the chains and accelerate the scissions. Because of the need of exposure to oxygen, this phenomenon is usually superficial, and it could result in the production of a film, protecting the core material form further reactions, or also cracks if the material is simultaneously under a stress state. Free radicals, also products of chain scission, are usually involved in these reactions.

Moreover, the exposure at high temperature could dissolve the macromolecular bonds (besides the wick bonds forming during crystallization in thermoplastic polymers): in those cases, chemical reaction occurs and gaseous species are produces. The contemporary presence of high oxygen concentrations, accelerate the phenomenon, while inert atmosphere slows it down.

The TAB. 1-2 lists the effect of the previously described phenomena.

Phenomenon	Effect	Consequence
Chemical reactions	• Film production • Chain scission • Free radical production	• Mass loss • Molecular weight decrease • Acceleration of the phenomena
Heat	• Chain scission • Gaseous species production	• Mass loss • Molecular weight decrease
	• Crosslinking • Branching	• Molecular weight increase

Tab. 1-2: Bond rupture phenomena and their consequence on the material properties

A vast literature is available, where the swelling and dissolution phenomena are investigated: PEEK has good chemical resistance, covering many products (organic or not), as well as water or many hydraulic fluids (GIRAUD 2011), although a certain number of diffusion anomalies have been measured during wet ageing (MENSITIERI ET AL. 1989), (DEL NOBILE ET AL. 1994). At room temperature, no solvent can dissolve it. Sulfuric acid and nitric acid can alter the polymer. The first dissolves it, while the second only degrades it, just like the brominated compounds. Secondary crystallization phenomena have been observed during the diffusion of chemical solvents (liquid solutions of methylene chloride or methylene chloride / n-heptane), (MENSITIERI ET AL. 1990). The work of (XIN, SHEPHERD, AND DEARN 2013) has shown that sterilization or ageing at 90°C for a hundred days do not modify the properties of the material very much. On the other hand, PEEK-based composites have shown residual properties, after wet ageing, clearly superior to those of carbon-epoxy composites, (LUCAS AND ZHOU 1993). A recent laboratory internship at the PPRIME Institute, ISAE-ENSMA, (BUKOWSKI R. 2014), has confirmed the low environmental sensitivity of PEEK. At high temperature, nitrobenzene and methyl ethyl ketone degrades it severely, (VILLOUTREIX AND ACETARIN 1998). The fact that it has an aromatic nucleus makes it sensitive to ultraviolet radiation, but it is very stable to β, γ and X rays, (DOBRACZYNSKI, A; TROTIGNON, J-P; VERDU, JACQUES; PIPERAUD 1996).

Recent studies were carried out on PEKK thermal ageing, at temperature close to the melt temperature, (T. CHOUPIN ET AL. 2018), (TADINI ET AL. 2017): because of the composite manufacturing process, which requires the complete melt of the polymeric matrix to the consolidation, the investigation of the thermal ageing effect is fundamental to the definition of the manufacturing process, since the matrix degradation could undermine the matrix and hence the composite properties.

It has been observed that, at 400°C ($>T_m$=330°C) in nitrogen atmosphere, macromolecular scission mechanisms activate, with the formation of free radicals: after further chemical reactions, the radicals rearrange with nearby radicals and form link between the chains (*crosslinking*) or ramifications (*branching*) (FIG. 1-12).

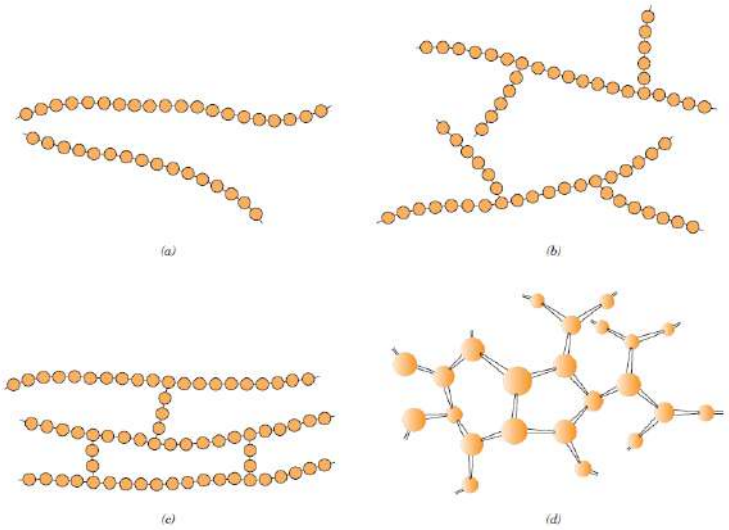

Fig. 1-12: Schematic representations of (a) linear, (b) branched, (c) crosslinked, and (d) network (three-dimensional) molecular structures. Circles designate individual repeat units, (William D. Callister 2007).

The crosslinks and branched structures alter the PEKK viscosity, its molecular weight and its T_g, as well as its crystallization kinetics and they decrease the crystallinity in the polymer.

In the context of the ANR project ImPEKKable, the ENSAM Paris carried out the investigation of the high temperature degradation of PEKK, from 200°C to T_m. All the tests were carried out on amorphous PEKK films of 50 µm films under air. FIG. 1-13 shows the evolution of the color in the films after exposure at 280°C up to 845 h.

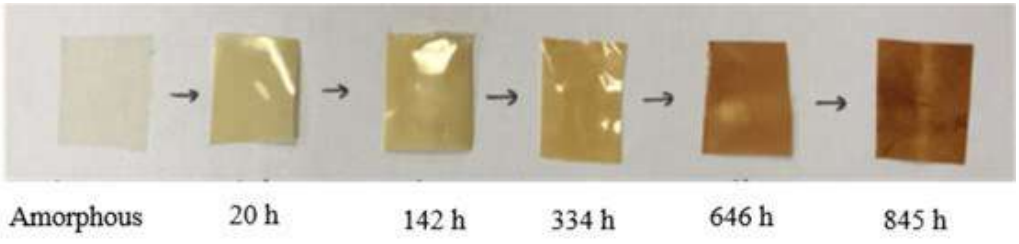

Fig. 1-13: PEKK 7002 AM films aged at 280°C on air (ENSAM Paris) (Roland and Fayolle 2020)

FIG. 1-13 shows a progressive change of color towards brownish color tones, which indicates the activation of degrading phenomena and the formation of an oxidized layer.

According, to TAB. 1-2, different indicators of the polymer degradation were tracked along the exposure time (up to over 10000 h) at different temperatures (200°C, 250°C, 280°C and 300°C): the mass loss, the fluorenone (gaseous species produced because of chemical reactions), the branching and the molar mass. Their evolution with the exposure time is showed in FIG. 1-14.

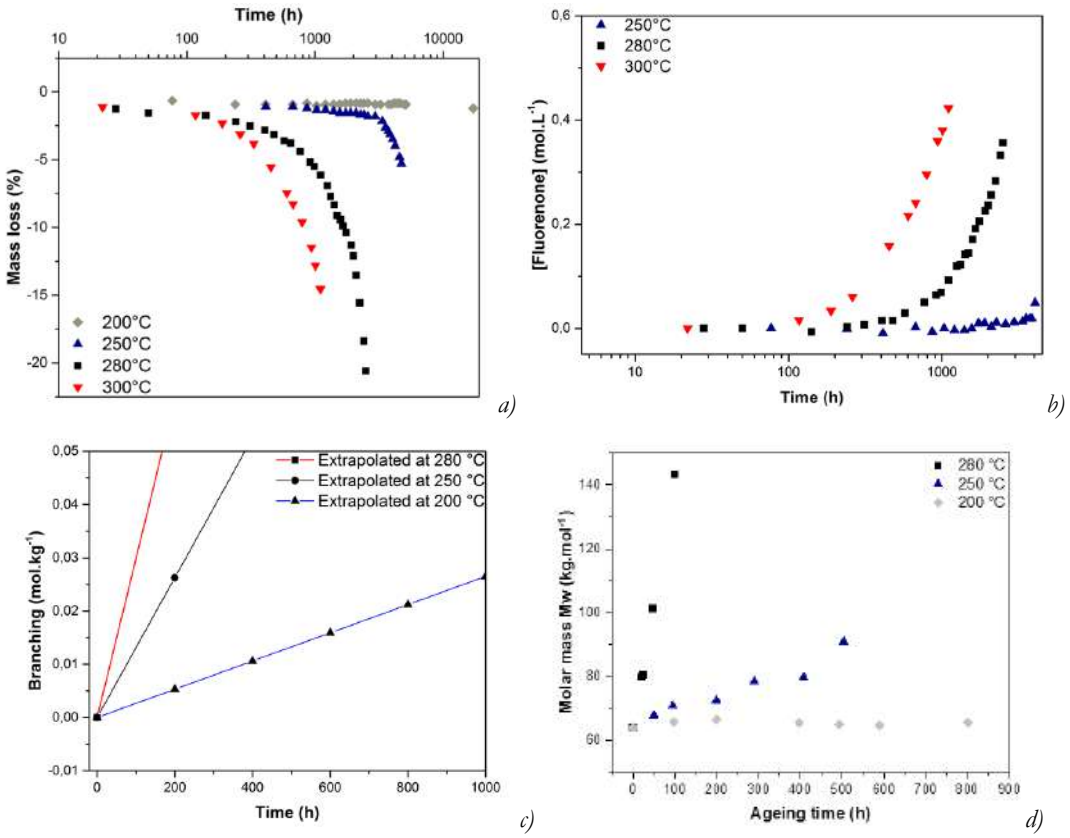

Fig. 1-14: Mass loss (a), fluorenone concentration (b), the branching (c) and the molar mass (d) evolution with the exposure time at 200°C (grey), 250°C (blue), 280°C (black), 300°C (red) (Roland and Fayolle 2020)

FIG. 1-14 shows the effective presence of the indicators of the ageing phenomena described before, but their magnitude and significant increases and their kinetics accelerates with the temperature. In particular, at 200°C, after over 10000h (>1.14 years), the indicators show no significant presence of ageing phenomena.

In order to highlight the phenomena, the property of the oxygen to accelerate the ageing phenomena was exploited, and the samples were aged at 200°C under 5 bar of O_2 up to 4000h (>166.5 days). The mass loss and the fluorenone concentration were tracked along the tests, and the results are showed in FIG. 1-15.

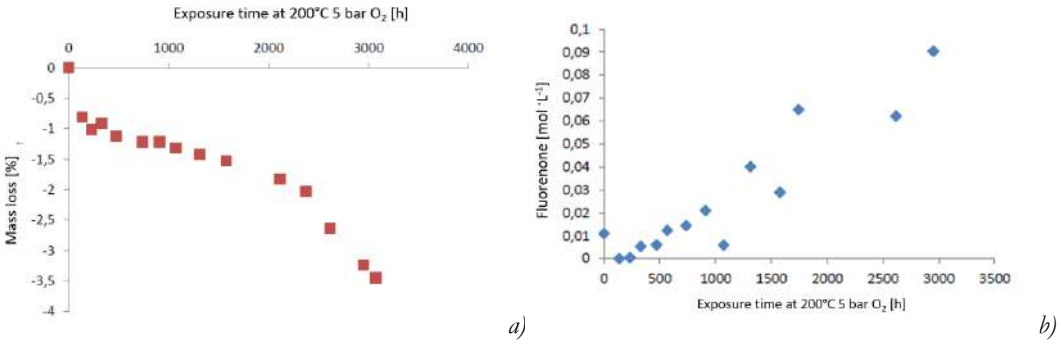

Fig. 1-15: Mass loss (a) and fluorenone concentration (b) evolution with the exposure time at 200°C under 5 bar of O_2 (Roland and Fayolle 2020)

FIG. 1-15 shows that the exposure to O_2 conditioned atmosphere significantly enhanced the degradation phenomena and accelerate them: considering the mass loss, the curve obtained at 200°C under 5 bar of O_2, is similar to the one obtained at 250°C under air. The effect of acceleration produced by the O_2 at 200°C is not simply quantifiable, because of the almost flat curve of the mass loss at 200°C under air. Considering the last point (at ~20000h of ageing at 200°C under air) as the first increment, the acceleration factor can be esteemed between 10 and 20 times.

1.2. Conclusions and aim of the present work.

In the previous chapter the main phenomena known from the literature are presented. For the PEKK and PEKK composites, as for any thermoplastic polymer and thermoplastic matrix composite, 3 main categories of investigation can be identified:

- crystallization mechanism;
- thermomechanical behavior;
- degradation mechanisms.

Moreover, 3 ranges of temperature can be identified:

- *Range 1*: $T<T_g$, where the material has a glassy behavior: this constitutes the actual operative range of temperature, in which no temperature induced crystallinity phenomena could take place, the thermomechanical behavior is known (also from similarities with PEEK) and physical ageing has to be taken into account;
- *Range 2*: $T_g < T<T_m$ where the material has a rubber behavior: in this range an extension of the operative range of temperature is looked for. The temperature induced crystallization mechanism could activate, which kinetics is known; the thermomechanical behavior is not fully known, as well as the activation of degradation mechanisms, such thermal ageing and oxidation. Furthermore, while the effect of the crystallinity percentage on the mechanical behavior is known, it is unknown the interaction of the thermomechanical behavior on the crystallization kinetics, and if activated, the interaction between degradation phenomena on both the crystallinity and thermomechanical behavior;
- *Range 3*: $T>T_m$ where the material has a liquid behavior: in this range of temperature the polymer and the composite are manufactured, and while crystallinity phenomena are not activated, the presence of degradation phenomena is known as well as their effect on the crystallinity kinetics and the resulting thermomechanical properties at lower temperature.

In FIG. 1-16 the range of temperature for which the different phenomena are/could be active, as well as the known and unknown aspects of the PEKK and PEKK composite behavior are schematized.

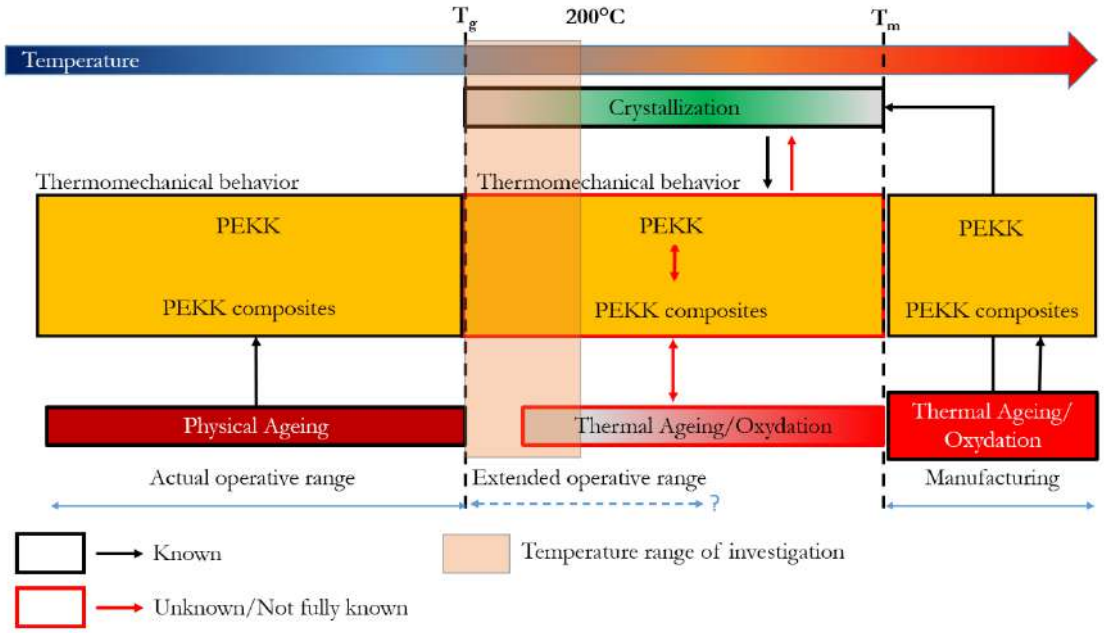

Fig. 1-16: Schematization of the different known and unknown aspects of the PEKK and PEKK composite behavior, for the different ranges of temperature.

The present works aims to investigate the PEKK and PEKK composite thermomechanical tensile and creep behavior at temperature between T_g (~160°C) and 200°C, at ±20°C from the targeted temperature of 180°C, as discussed in the introduction. Moreover, the interaction with the crystallization and degradation mechanisms is investigated.

The similarities in tensile and creep behavior between the composite's matrix and the neat polymer are also investigated: verified those similarities, the composite behavior could be reconstructed only starting from the polymer one. This kind of approach, if from one side prevents to obtain a direct ply or composite behavior model, has the advantage of being completely generalized, being independent on the fiber volumetric fraction, the number of ply or their stacking sequence. Hence, the composite response could be simulated for any combination of those variables.

The approach employed in the present work can be summarized in following points and each of them is presented more in detail in each of the following chapters.

CHAPTER 2. an extensive experimental campaign was carried out on the PEKK and C/PEKK composites, to characterize their thermomechanical behavior below and, most of all, above their T_g, as well as their physical-chemical behavior;

CHAPTER 3. the experimental data were analyzed to assess the similarities between the PEKK and PEKK composites;

CHAPTER 4. proven the previously mentioned relation, the PEKK data were employed for the identification of the different physical mechanisms characterizing its

behavior under the different experimental loading conditions above T_g and their analytical description;

CHAPTER 5. the resulting analytical model for the PEKK behavior, is implemented in a semi-analytical model to reconstruct and simulate the PEKK composites behavior above T_g;

CHAPTER 6. the presence of ageing mechanisms is investigated at 200°C, and accelerated through the exposure to 5 bar of O_2 conditioned atmosphere for longer test durations.

Chapter 2 - Materials and methods

The present chapter presents materials, equipment, techniques and methods employed for the characterization of the PEKK polymer and C/PEKK composite behavior. This includes: high temperature traction, load-unload-reload, creep, DMA, DSC, thermomechanical-oxidation coupled tests. A novel strain measurement image analysis based tool (IAT) is presented and compared with existing measurement setup. Numerical methods used for interpretation of experimental results and for the definition of a semi-analytical Homogenization / Localization methods employed for simulations, are also described.

2.1. Introduction

The Literature Survey presented in the previous chapter defines a complex work perimeter and an articulated set of objectives.

The expected complexity of the semi-crystalline thermoplastic PEKK polymer and C/PEKK composite behavior, already widely documented for temperatures below the glass transition temperature (T_g), where physical ageing phenomena take place, asks for the setup and the development of dedicated techniques for monitoring the behavior at temperatures higher than T_g. At these temperatures, due to the rearrangement of the amorphous phase at glass transition, a complex thermomechanical behavior may be expected, calling for the setup of complex solicitation test paths at high temperature, such traction, load-unload-reload and creep-recovery tests. DMA and DSC protocol tests must also be developed for monitoring the transition and possible material evolution. The possible occurrence of material degradation of chemical nature (due, for instance, to the emergence of thermo-oxidation phenomena) requires the setup of complex coupled thermomechanical-oxidation tests accounting for the possible interaction and synergy between thermomechanical behavior above T_g and chemical degradation.

This complex test scenario at high temperature, under oxidative environment, calls for the development of adequate monitoring systems, long-distance non-contact strain measurement systems which must face possible degradation. This justifies the development of a new Image analysis tool (IAT) adapted to this type of applications.

Moreover, the expected complex response calls for the development of opportune analysis methods, for test interpretation and simulation. In particular, the characterization of the response of the polymer matrix within the composite, requires the development of dedicated models capable to represent through modeling the in-situ behavior of polymer within the composite, such as semi-analytical Homogenization / Localization models.

All these methods will be presented in the following sections, in particular:

- in CHAP. 2.2, the materials studied in this work are presented, describing more in detail:
  - their manufacturing process (CHAP. 2.2.1);
  - the geometry of the specimens employed for the different tests (CHAP. 2.2.2).

- in CHAP. 2.3 the different methods employed are introduced:
  - CHAP. 2.3.1 is focused on experimental methods and details the experimental equipment and testing protocols employed during the experimental campaign carried out to evaluate the materials behavior above their T_g, under air (CHAPTER 3) and coupled with accelerated oxidation, under 5 bars of O_2 (CHAPTER 6);
  - in CHAP. 2.3.2 the strain measuring system employed during the tests (IdPix) is illustrated, as well as its advantages and drawbacks. A new image analysis tool (IAT)

for post-test image treatment is proposed, in order to be employed in couple with IdPix and to result in a robust measurement system;

- in CHAP. 2.3.3 the analytical methods employed for data analysis and C/PEKK simulations are described, (Homogenization and Localization methods), (CHAPTER 3 and CHAPTER 5).

2.2. Materials

An experimental campaign was carried out during this work on *Poly – Ether – Ketone - Ketone* (PEKK), a high performance thermoplastic polymer of the *Poly – Aryl – Ether - Ketone* (PAEK) family. Its chemical structure is represented FIG. 2-1.

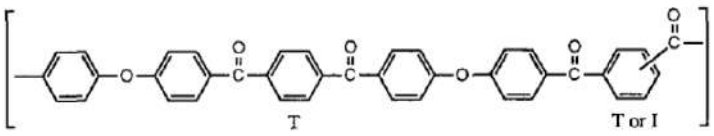

Fig. 2-1: Chemical structure of a monomer of PEKK.

Different configurations of PEKK can be produced varying the ratio (T/I) between the terephtalic acid (T) and the isopthalique acid (I) of which is composed. In the present work PEKK 7002, with a T/I ratio of 70/30, is studied.

The experimental campaign was carried out on 3 different configurations of PEKK:

- the amorphous (AM) PEKK 7002 (nominal 5% of crystalline phase, minimum achievable during cooling process), manufactured by Arkema;
- the semicrystalline (SC) PEKK 7002 (nominal 24% of crystalline phase, maximum achievable during cooling process), manufactured by Arkema;
- the $[(\pm 45)_2, +45]_s$ composite (C/PEKK), manufactured by Airbus SAS from prepregs of SC PEKK 7002 and AS4C carbon fibers, with a strong crystalline phase (nominal 28% of crystalline phase, maximum achievable during the cooling process).

The properties of the different materials are listed in TAB. 2-1.

Property - 7002 PEKK	Value
Glass transition temperature - T_g	160°C
Melting temperature – T_m	330°C
Crystalline phase % - χ - AM	5% (min)
Crystalline phase % - χ - SC	24% (max)
Density	~1.30 g/cm^3

Property - C/PEKK	Value
Crystalline phase % - χ – C/PEKK	28% (max)
Fibers volume fraction	0.6
Density	1.60 g/cm^3

Property - AS4C	Value
Tensile Modulus	231 GPa
Fiber diameter	6.9 μm
Fiber density	1.78 g/cm^3

Tab. 2-1: Materials properties

As discussed in Literature Survey, besides the fiber content and orientation, the properties of C/PEKK composites directly depends on the crystallinity percentage present in the matrix at the end of the manufacturing process. This dependency is even more pronounced in neat polymer.

Because the initial crystallinity percentage present in the materials (TAB. 2-1) depends on the manufacturing process, the specific manufacturing process employed for the different material is described in the following paragraph.

2.2.1. Manufacturing

2.2.1.1 PEKK 7002

The manufacturing process for PEKK 7002 was carried out by Arkema, injecting PEKK in form of powder in steel plates (showed in FIG. 2-2), previously heated at 230°C.

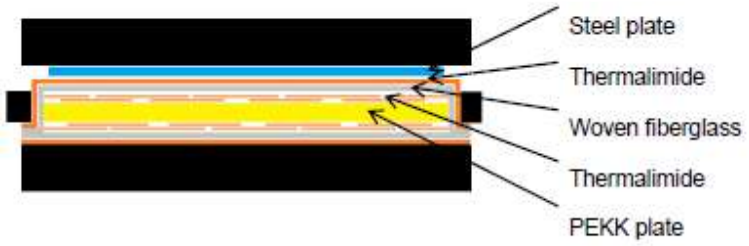

Fig. 2-2: PEKK plates environment for crystallization from the melt (Tanguy Choupin 2018)

PEKK SC is obtained from an isothermal transformation at 230°C, while PEKK AM is produced from a high cooling rate non isothermal transformation.

2.2.1.2 $[(\pm 45)_2, +45]_s$ composite (C/PEKK)

The $[(\pm 45)_2, +45]_s$ composite (C/PEKK) was manufactured by Airbus SAS from prepregs provided by Arkema, whose properties are listed in TAB. 2-2. The prepregs were stacked, according to the sequence showed in FIG. 2-3, allowing obtaining a symmetric composite.

Property	Value
Fibers	AS4
Volumetric fraction	60%
Average fibers surface mass	155 g/m^2
Prepregs surface mass	228 g/ m^2
Prepregs thickness	150 µm

Tab. 2-2: Prepregs properties

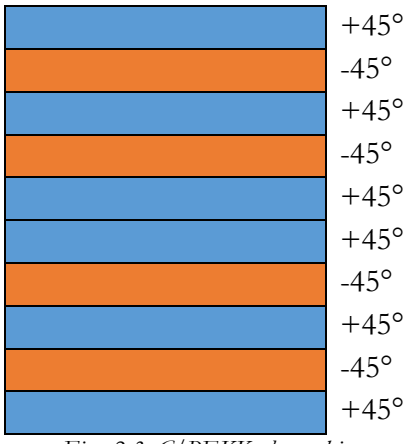

Fig. 2-3: C/PEKK ply stacking

The thermal protocol (FIG. 2-4), (TANGUY CHOUPIN 2018), employed for the composite manufacturing was chosen in order to obtain the maximum achievable crystallinity percentage (28% nominal).

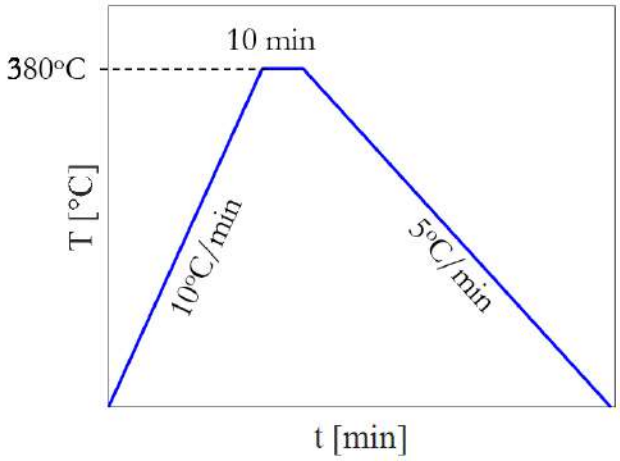

Fig. 2-4: C/PEKK manufacturing thermal protocol

The thermal protocol showed in FIG. 2-4 was carried out in a press under 7 bars and is composed by the following phases:

1. heating of the stacked plies up to 380°C (above PEKK 7002 T_m ~340°C) at 10°C/min;
2. isothermal at 380°C for 10 min to allow the complete melting of the matrix;
3. cooling to room temperature at 5°C/min to allow the complete crystallization.

2.2.2. Specimens

The PEKK 7002 was provided in form of 100 mm x 100 mm x 2.10 mm plates which were cut in order to obtain different specimen geometries, according to the different tests needs. The C/PEKK composite specimens were directly provided. The different specimens geometry are showed in FIG. 2-5 and listed in TAB. 2-3.

Fig. 2-5: Specimens employed for the experimental campaign

Type of specimen	Material	Dimensions	Type of test
a	PEKK 7002	70x10x2.11	DMA
b	PEKK 7002	ANNEX A.1	Tensile, Creep-recovery
c	C/PEKK $[(\pm 45)_2, +45]_s$	90x12.5x1.44	DMA

d	C/PEKK $[(\pm 45)_2, +45]_s$	ANNEX A.2	Tensile, Creep-recovery
e	C/PEKK $[(\pm 45)_2, +45]_s$	250x25x1.44	Creep under O_2
f	PEKK 7002, C/PEKK $[(\pm 45)_2, +45]_s$	Cut from other specimens to obtain 8 mg ± 0.1 mg samples	DSC

Tab. 2-3: Specimen geometries employed for the experimental campaign.

The specimens listed in TAB. 2-3 were employed in different tests, which can be divided as showed in TAB. 2-4:

Tests for the thermomechanical characterization	Tensile
	Creep-recovery
	Load-Unload-Increase
Tests for the physical-chemical characterization	DMA
	DSC
Test for estimate the effect of oxidation:	Ageing
	µtomography

Tab. 2-4: Schematization of the experimental campaign

All the tests carried out on the different materials are summarized in TAB. 2-5.

Tensile tests				
Test Temperatures [°C]	**Displacement speed [mm/min]**	**PEKK AM**	**PEKK SC**	**C/PEKK**
RT	1	Yes	Yes	Tests carried out by Airbus SAS
100	1	Yes	Yes	
150	1	Yes	Yes	
165	0.1	No	Yes	Yes
	1	Yes	Yes	Yes
	10	No	Yes	Yes
180	0.1	No	Yes	Yes
	1	Yes	Yes	Yes
	10	No	Yes	Yes
200	0.1	No	Yes	Yes
	1	No	Yes	Yes

	10	No	Yes	Yes

Creep – Recovery tests				
Test Temperatures [°C]	**Creep stress**	**PEKK AM**	**PEKK SC**	**C/PEKK**
165	Stress 1	No	0.7 σ_{th}	0.5 σ_u
	Stress 2	No	0.5 σ_{th}	$\sigma_{matrix} = \sigma_{th}$
	Stress 3	No	0.3 σ_{th}	No
180	Stress 1	No	0.7 σ_{th}	0.5 σ_u
	Stress 2	No	0.5 σ_{th}	$\sigma_{matrix} = \sigma_{th}$
	Stress 3	No	0.3 σ_{th}	No
200	Stress 1	No	0.7 σ_{th}	0.5 σ_u
	Stress 2	No	0.5 σ_{th}	$\sigma_{matrix} = \sigma_{th}$
	Stress 3	No	0.3 σ_{th}	41 MPa
	Stress 4	No	No	41 MPa, 5 bar O_2

Load – Unload - Increase tests				
Test Temperatures [°C]	**Displacement speed [mm/min]**	**PEKK AM**	**PEKK SC**	**C/PEKK**
165	1	0.15, 0.2, 0.25, 0.3, 0.4	0.3, 0.5, 0.7 σ_{th}	No
180	1	No	0.3, 0.5, 0.7 σ_{th}	No
200	1	No	0.3, 0.5, 0.7 σ_{th}	No
		No	0.3, 0.5, 0.7 σ_{th} + Recovery	No

DMA			
Condition	**PEKK AM**	**PEKK SC**	**C/PEKK**
As received	Yes	Yes	Yes
Aged 5 bar O_2	No	Yes	No

DSC			
Condition	PEKK AM	PEKK SC	C/PEKK
As received	Yes	Yes	Yes
After tensile tests	Yes	Yes	No
After creep-recovery test	No	Yes	No
After Load-Unload-Increase tests	No	Yes	No
Aged 5 bar O_2	No	Yes	No

µtomography			
Condition	PEKK AM	PEKK SC	C/PEKK
As received	No	No	Yes
Aged 5 bar O_2	No	No	Yes
After creep test 200°C 5 bar O_2	No	No	Yes

Tab. 2-5: List of the tests carried out during the experimental campaign

For each of the tests listed in TAB. 2-5, a specific experimental equipment and test protocol was employed, presented in the next paragraph.

2.3. Methods

The experimental campaign carried out in the present work and composed by the tests summarized in TAB. 2-5, required for each type of test and depending on the material:

- a specific geometry of the specimen, (TAB. 2-3);
- a specific experimental equipment;
- a specific test protocol.

All the instrumentation and techniques employed are described in the present paragraph.

Moreover, for the tests aimed to the thermomechanical characterization, a particular focus was dedicated to the strain measure, because of the severe test conditions applied to the materials: a section of the next paragraph is dedicated to the employed strain measurement system.

The last part of the paragraph is dedicated to numerical models employed to analyze the data obtained from the C/PEKK and correlated them to the data obtained from tests carried out on PEKK SC.

2.3.1. Experimental equipment and methods

For the experimental campaign, the tests listed in TAB. 2-4 were carried out and, for each of them, the employed equipment and test protocol is described below. Moreover, a drying protocol is added, which was carried out prior to each test.

2.3.1.1 Drying protocol

All specimens of each material were dried in an oven at 120°C for 48 h as specified by the manufacturer. This procedure allowed the escaping of water and volatile substances trapped in the material during the manufacturing process.

2.3.1.2 Tensile and creep-recovery tests

Tensile and creep-recovery tests were carried out on an Instron 4505 servo-hydraulic machine, equipped with a regulated oven to allow carrying tests at temperature higher than room temperature. The Instron 4505 properties are listed in TAB. 2-6.

Property	Value
Loading cell capacity	0.5/2/5/50/100 KN
Max displacement speed	500 mm/min
Oven temperature range	-100°C up to 200°C

Tab. 2-6: Instron 4505 properties

The machine is run through a computer and has a touch screen panel to easy the user control during the tests. A camera, connected to a dedicated computer, was employed, allowing real time measurements of strains (Video-extensometer Technique, see CHAP. 2.3.2.1). The whole testing equipment is showed in FIG. 2-6.

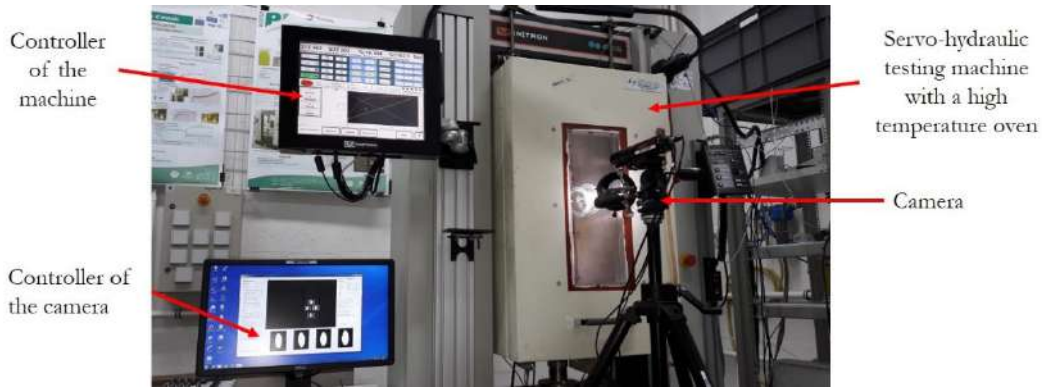

Fig. 2-6: Tensile, load-unload-reload and creep-recovery tests experimental equipment

All tests on both PEKK and C/PEKK composite samples were carried out at different temperatures from room temperature to 200°C, on specimens type *b* and *d* respectively (FIG. 2-5), at different constant displacement rate of 0.1, 1 or 10 mm/min.

Heating phase

Each test at temperature higher than room temperature was preceded by a *heating phase*, needed for allowing the oven to reach the thermal equilibrium once the test temperature was reached. The employed thermal protocol is showed in FIG. 2-7.

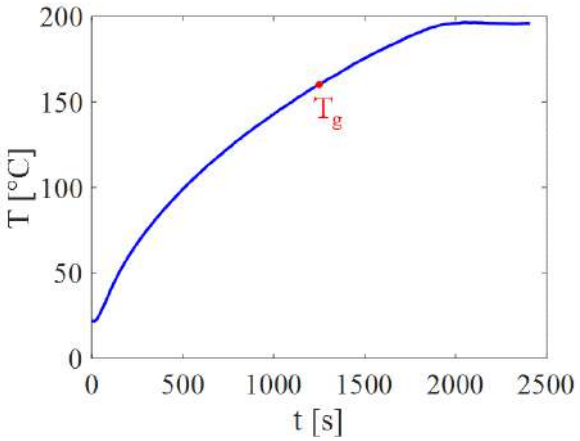

Fig. 2-7: Thermal protocol

During this preliminary phase, the test is force driven keeping the force constant at 0.3 N for 41 min (≈ 2500 s), time needed to reach a stabilized value of 200°C. 2500 s has been chosen as the longest time the PEKK 7002 AM can be exposed at 180°C (max test temperature for PEKK AM) under 0.3 N without crystallize (CHAP. 4.6.1.1).

Tensile tests

Tensile tests were carried out at different constant displacement speeds and at different temperatures from room temperature to 200°C. The testing protocol employed for tensile tests is showed in FIG. 2-8.

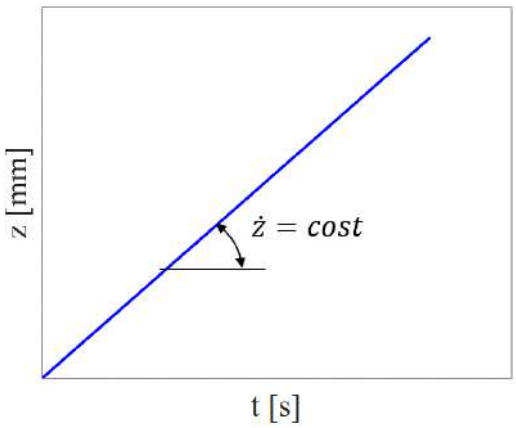

Fig. 2-8: Tensile test protocol

The test temperatures and displacement speeds employed are detailed in CHAPTER 3.

Creep-recovery tests

Creep-recovery tests were carried out only at temperature above PEKK's T_g, according to the following protocol:

2. Loading phase. Once the heating phase is completed, the test is displacement driven at 1 mm/min until the creep stress is reached.
3. Creep phase. The control is switched to stress driven and the creep stress is kept constant for 48 h.
4. Unload phase. The control is switched to displacement driven at -1 mm/min and the force is decreased to 0.15 MPa, in order to avoid entering in compression state.
5. Recovery phase. The control is switched to stress driven and the stress is kept constant for 60 h.

The testing protocol employed for creep-recovery tests is showed in FIG. 2-9.

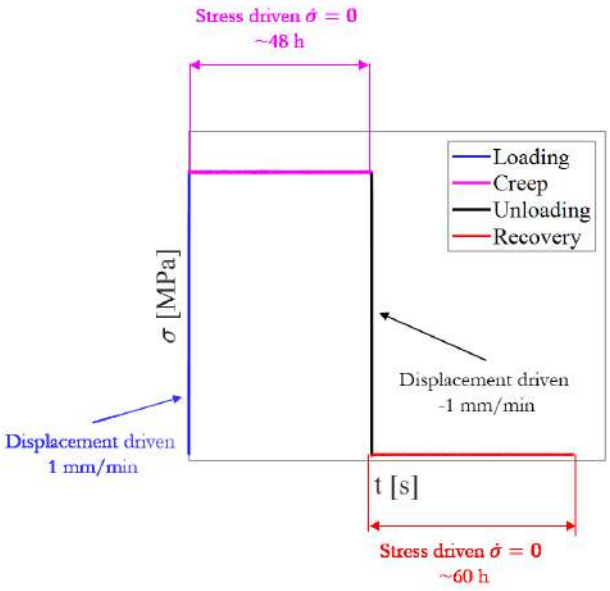

Fig. 2-9: Creep-recovery test protocol

PEKK SC creep-recovery tests were driven in true stress during creep and recovery phases, while C/PEKK creep-recovery tests were driven in nominal stress. 3 creep stress level were chosen for PEKK SC and 2 creep stress level for C/PEKK composites. All tests conditions are detailed in CHAPTER 3.

Load – unload-reload tests

Load – unload - reload tests were carried on PEKK SC at 165°C, 180°C and 200°C at 1 mm/min. During the tests, 3 load-unload loops are described. Each loop consists in two phases:

1. Loading phase. Once the heating phase is completed, the test is displacement driven at 1 mm/min until the lowest of the 3 creep stress is reached.
2. Unload phase. The control is switched to displacement driven at -1 mm/min and the force decreased until almost 0 N is reached, in order to avoid entering in compression state.

The loop is repeated 2 more times, one for each remaining creep stress level (employed for creep-recovery tests at the same test temperature), followed by one final tensile test.

The testing protocol employed for load – unload -increase tests is showed in FIG. 2-10.

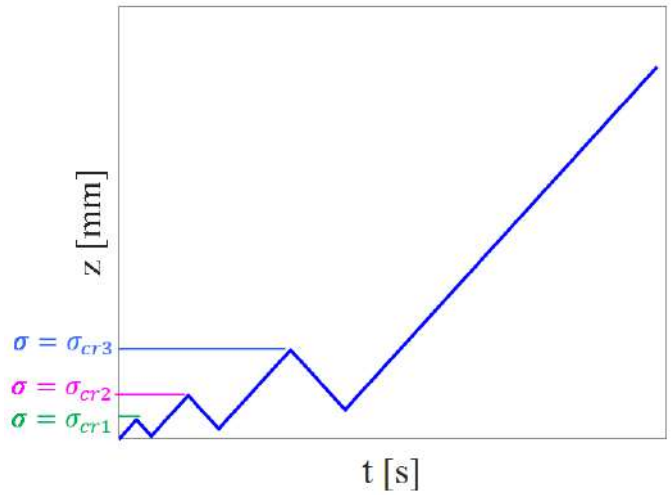

Fig. 2-10: Load-unload-reload protocol

A variation of the Load-Unload-Reload test was carried out, where at the end of each unload, a recovery phase, similar to the phase 4 of the creep-recovery tests, was carried out. Contrary to creep-recovery tests, in the case of Load-Unload-Reload test, the recovery phase had different duration for each loop, and it was stopped when no significant variations were observed in the recovered strain.

All tests conditions are detailed in CHAPTER 4.

2.3.1.3 DMA tests

All the *Dynamical Mechanical Analysis* (DMA) tests were carried out on a TA Instrument DMA Q800 (FIG. 2-11), which properties are listed in TAB. 2-7.

Fig. 2-11: TA Instrument DMA Q800

Property	Value
Temperature range	-150°C ÷ 600°C
Applicable force range	0.0001 N ÷ 18 N
Frequency range	0.1°C/min ÷ 20°C/min
Type of DMA test	tensile, single cantilever, 3 point bending, shear

Tab. 2-7: TA Instrument DMA Q800 properties

The testing protocol employed for DMA tests is showed in FIG. 2-12.

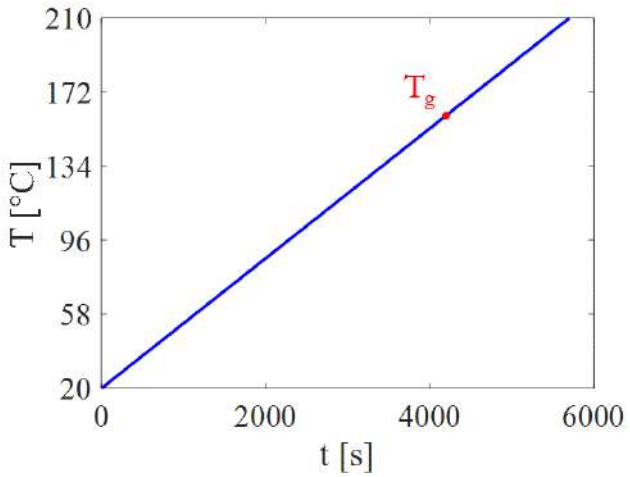

Fig. 2-12: DMA test protocol

3-point-bending DMA tests were carried out on both specimens *a* (PEKK) and *c* (C/PEKK), respectively, (FIG. 2-5), varying the temperature from 20°C to 200°C, at 2°C/min heating rate, at 1 Hz, imposing an amplitude of strain of 0.01% (PEKK) or 15μm (C/PEKK).

2.3.1.4 DSC tests

All the *Differential Scanning Calorimetry* (DSC) tests were carried out on the *TA Instruments DSC Q20* machine (FIG. 2-13A). The DSC Q20 employs a constantan heath flow sensor and chromel/constantan thermocouple both under the sensor and in the middle of it (*Tzero* technology), as showed in FIG. 2-14. The DSCQ20 was employed combined with the Refrigerated Cooling System *RCS 90* (FIG. 2-13B), which properties are listed in TAB. 2-8.


a) b)

Fig. 2-13: TA Instruments DSC Q20 (a) and RCS 90(b)

Fig. 2-14: Q20 heath flow sensor

Property	Value
Temperature range	-90°C ÷ 550°C
Tzero technology	Yes
Type of Analysis	Standard, modulated

Tab. 2-8: TA Instruments DSC Q20 properties

For the DSC tests, *f* type specimens were employed, (FIG. 2-5), cut from as received material (which constitutes the reference) and from the *b* and *d* specimens previously tested under tensile and creep-recovery conditions. .

The FIG. 2-15 shows the DSC test temperature kinetics during the tests.

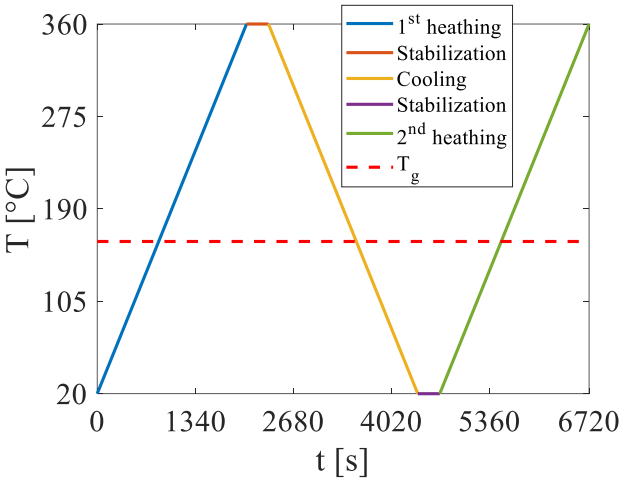

Fig. 2-15: DSC test protocol

The DSC test consists in 5 phases:

1. 1st heating, from 20°C to 360°C at 10°C/min. The maximum temperature was chosen above the melting temperature (340°C), as a compromise between a temperature high enough to allow the complete melting of the sample in a brief time, but not too high to cause material degradation;
2. stabilization, at 360°C for 5 min, to ensure the complete melting of the sample;
3. cooling, from 360°C to 20°C at 10°C/min;
4. stabilization, at 20°C for 5 min, to allow the sample to reach the thermodynamic equilibrium;

2nd heating, from 20°C to 360°C at 10°C/min

2.3.1.5 Thermomechanical behavior – oxidation coupling

In order to evaluate the effect of long-term exposure to high temperature, two types of test were carried out:

- a first test for investigating the effect of the sole environment and the possible presence of oxidation phenomena on the PEKK behavior,
- a second fully coupled thermomechanical-oxidation test.

For the first test, 6 PEKK 7002 SC specimen type *a* and a C/PEKK specimen type *e* , (FIG. 2-5), were exposed at 200°C under 5 bars of O_2, for 6 weeks (CHAPTER 6).

The specimens were conditioned in a TOPIN 2344 (FIG. 2-16), which is constituted by an oven allowing exposure under controlled atmosphere. Its properties are summarized in TAB. 2-9.

Fig. 2-16: TOPIN 2344

Property	Value
Temperature range	Up to 350°C
Pressure	Up to 5 bars
Conditioning atmosphere	Air, N_2, O_2

Tab. 2-9: TOPIN 2344 properties

The evaluation of the coupled effect produced by thermomechanical load and oxidation is evaluated through a creep test carried out on a C/PEKK specimen type *e* (FIG. 2-5), at 200°C under 5 bars of O_2, for 6 weeks (CHAPTER 6).

The creep test was carried out in a Instron 1251 COMPTINN (FIG. 2-17), which is a servo-hydraulic machine equipped with climatic chamber developed to enable carrying out mechanical test in controlled environment. Along with a loading cell mounted externally to the climatic chamber in series with the static head, a second loading cell is mounted in series with the moving head: this setup avoids the weight of the climatic chamber to influence the measure of the force. Moreover, to ensure the watertightness of the climatic chamber, the second load cell is directly mounted in the same cooling block which contain the moving head (and thus the second load cell is referred to as *internal*). The properties of the Instron 1251 are listed in TAB. 2-10.

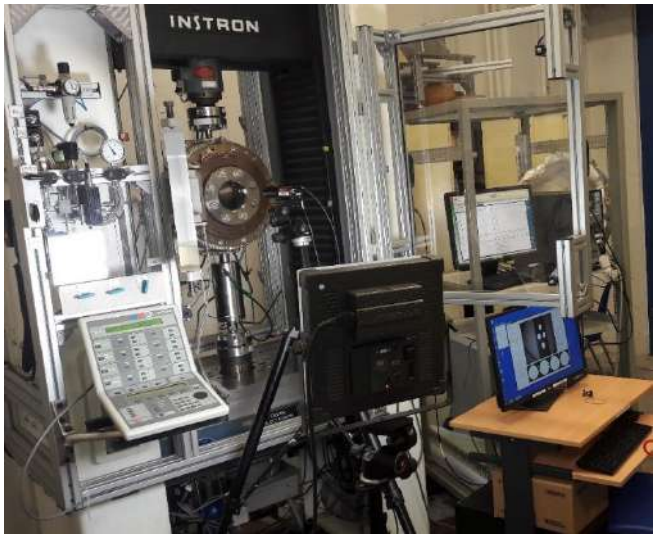

Fig. 2-17: Instron 1251

Property	Value
Temperature max	350°C
Pressure max	5 bars
Conditioning atmosphere	Air, N_2, O_2
Internal Load cell	100 KN
Max displacement	15 mm

Tab. 2-10: Instron 1251 properties

Only in the case of coupled test carried out employing the Instron 1251, a creep test was carried out at 200°C under 5 bars of O_2.

The test protocol employed for creep tests in conditioned atmosphere is showed in FIG. 2-18.

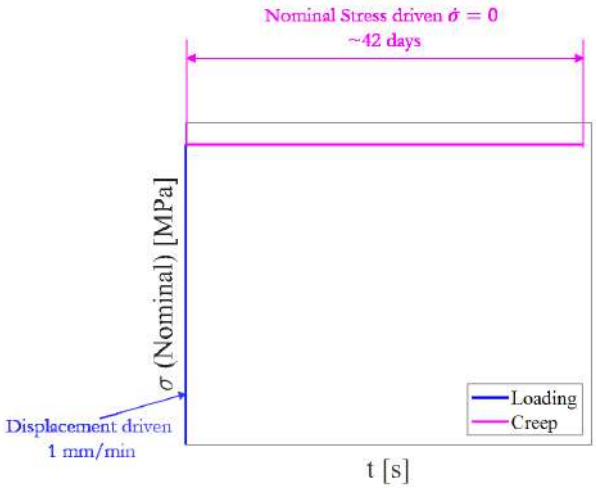

Fig. 2-18: Creep test under 5 bars of O_2 test protocol

The creep test protocol showed in the image above is similar to the creep-recovery test protocol CHAP. 2.3.1.2, where the last two phases are removed and the remaining changed as follows:

1. Loading phase. Once the heating phase is completed, the test is displacement driven at 1 mm/min until the creep stress is reached;
2. Creep phase. The control is switched to nominal stress driven (controlled by the internal load cell) and the creep stress is kept constant for 6 weeks.

2.3.1.6 μ-Computed Tomography

In order to assess the damage scenario on the C/PEKK composites produced by O_2 exposure and thermal load, or combined also with mechanical loads, X-Rays technique were employed. μ-Computed Tomography, in particular, allows obtaining a sequence of X-Rays scans at different heights, which can be reconstructed to recreate a 3D image of the specimen. Segmentation techniques then allow the separation of the different components (matrix, fibers and eventually cracks), through binarization-based or image gradient-based techniques, (FOTI 2017).

For the tomography, a RX Solution UltraTom XL was employed (FIG. 2-19), which properties are listed in TAB. 2-11.

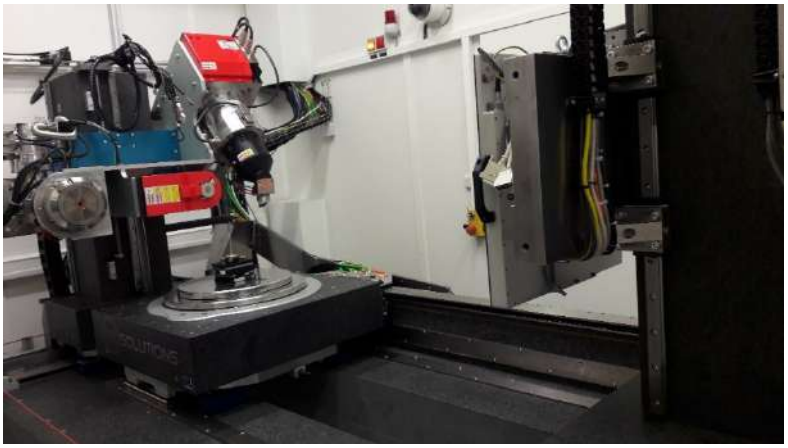

Fig. 2-19: RX Solution UltraTom XL

Property	Value
Max Power	75 W
Min resolution	1920 pixels x 1536 pixels, 127 μm/pixel
Max resolution	4008 pixels x 2624 pixels, 5.9 μm/pixel
Acquisition	Circular, helicoidal

Tab. 2-11: RX Solution UltraTom XL properties

For the tomography, the parameters listed in TAB. 2-12 were employed.

Property	Value
Voltage	70 kV
Power	12.6 W
Resolution	12 μm/pixel
Frame Rate	4 pps
Acquisition	Helicoidal

Tab. 2-12: Parameters for X-Rays tomography

The images acquired during the scans were reconstructed through the software X-Act (CHAPTER 6).

2.3.2. Measurement system

For all the tests aimed to the thermomechanical characterization (TAB. 2-4), the employed equipment allowed the measure in real time:

1. Testing temperature, measured by a thermocouple, which output, in Volt, can be converted in Celsius degrees through the following equation:

$$T=48.5(0.9889\,T_{Volt}+0.0072)-185 \qquad \textit{Eq. 2-1}$$

2. Displacement or traverse position, measured by a LVDT;
3. Force, measured by a load cell;
4. Longitudinal and transversal true strain, longitudinal true stress, measured by the software *IdPix*, described more in detail in the next paragraph.

As described more in detail in the following paragraph, all the measurements were obtained with IdPix software, with a Video-extensometer technique. This technique was employed from each test from room temperature to 200°C, under air or in conditioned atmosphere. The cases where the material underwent the most severe conditions, however, were also the most detrimental for this technique and in some cases exceeding its limits of employability. Because the recurrence of this situation during all the tests at temperature above PEKK T_g, an alternative to IdPix was investigate, not forcedly aiming to replace it, but at least to be complementary to IdPix and validate its measurements.

2.3.2.1 IdPix

The Video-extensometer Technique is a non-contact measurement system, which requires that markers or stickers are applied on the specimen surface. The latter is recorded during the test with a camera and the images are sent to a computer, where a software is able to evaluate the distance, in pixels, between the markers both in space and time, measuring the strain, (G'SELL ET AL. 1992).

In all tensile, creep – recovery and load-unload test, this technique was employed and in order to measure both longitudinal and transversal strains, 4 markers were painted on the specimens as the 4 vertex of a rhombus, (FIG. 2-24A).

The images were processed with *IdPix* software, developed at the ISAE-ENSMA, Poitiers. On IdPix graphics interface, the user has to manually define a box around each marker (FIG. 2-21). The area inside each box is binarized with a specific threshold automatically identified by the software through Otsu algorithm, (OTSU 1979). From the binarized image (boxes in the bottom of FIG. 2-21), the software is able to identify the marker contour and hence to calculate the coordinates of its center of mass. The identification has to be launched before the test is started to define the initial position of the markers.

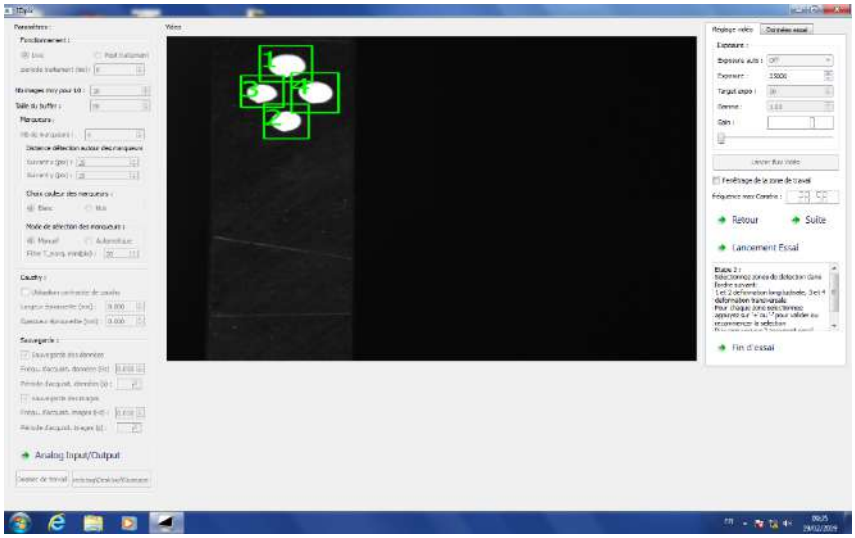

Fig. 2-20: IdPix graphic interface and box definition around the markers

During the test, IdPix self regulates the exposure and the size of the box (which act as searching windows) around each markers and registers their evolution (FIG. 2-21).

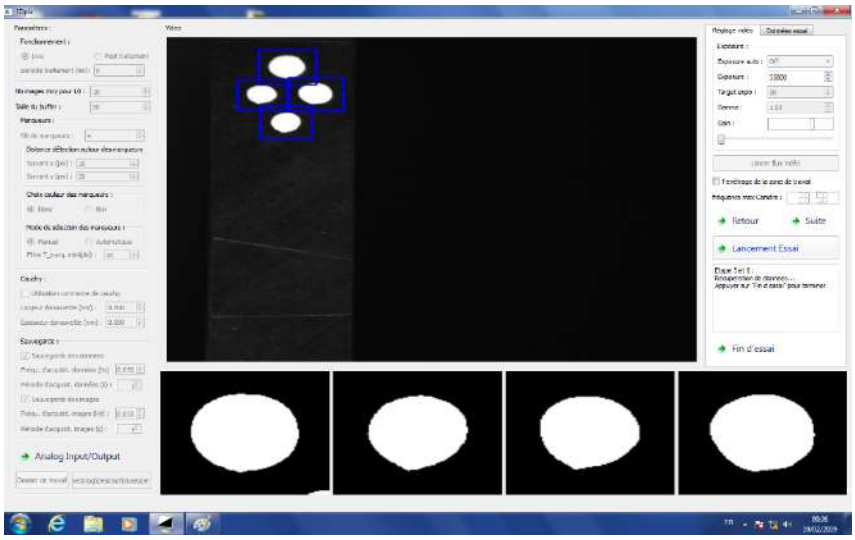

Fig. 2-21: IdPix graphic interface and markers monitoring during the test

In this way, it is able to evaluate, in real time:

- the distance between the 2 vertical markers L, (FIG. 2-22), from which it calculates the *longitudinal logarithmic strain* as:

$$\varepsilon_{xx} = \frac{\Delta L}{L_0} \qquad \textit{Eq. 2-2}$$

- the distance between the 2 horizontal markers *B*, (FIG. 2-22), from which it calculates the *transversal logarithmic strain* as:

$$\varepsilon_{yy} = \frac{\Delta B}{B_0} \qquad \textit{Eq. 2-3}$$

- once provided with the initial cross-section area S_0 and the instantaneous value of the measured load *F*, IdPix is also able to calculate the *true stress* in the applied load direction (under the transversal isotropy hypothesis) as:

$$\sigma_{xx} = \frac{F}{S_0}\left(-\exp\left(2\varepsilon_{yy}\right)\right) \qquad \textit{Eq. 2-4}$$

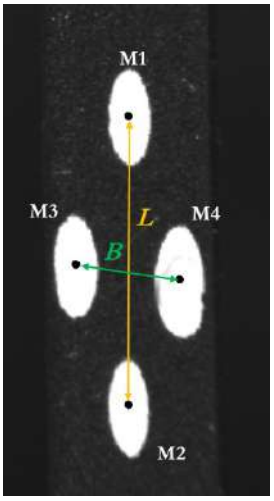

Fig. 2-22: IdPix measures on the specimen surface

Advantages and drawbacks of IdPix

IdPix does not require high-resolution images (a 1 MP camera was employed during the tests, which registers 1024 pixels x 1024 pixels images) and it has a fast processing algorithm, which allows having the above-mentioned measures displayed in real time on the Instron 4505 control display (FIG. 2-23). Thanks to real time measurements, it is also possible to carry out stress driven creep tests, adjusting the applied load during creep tests in order to keep constant the measured true stress.

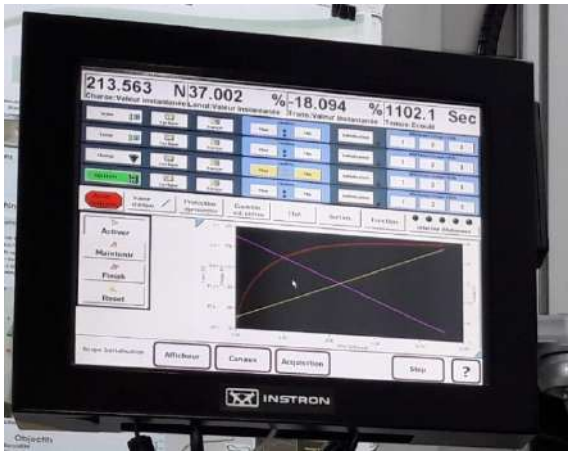

Fig. 2-23: Control screen of the tensile test machine: on the top there are the real time values of applied force, longitudinal and transversal strain; in the bottom, their curves against the time.

IdPix greatest weakness, however, is the accuracy of the measures, depending on the perimeter of the markers: holes in the perimeter and degradation of the marker paint (FIG. 2-24), due to the testing temperature, environment exposure and high strains, could induce a shifting of the center of mass, producing variations in the calculated strains, and hence in the calculated stress. Markers more severe degradation could result in leading IdPix to follow only a part of the markers, leading to an abruptly variation on the measured strain or in the complete "loss of the marker", where the software in so no longer able to identify the marker position, causing the end of strain measurement.

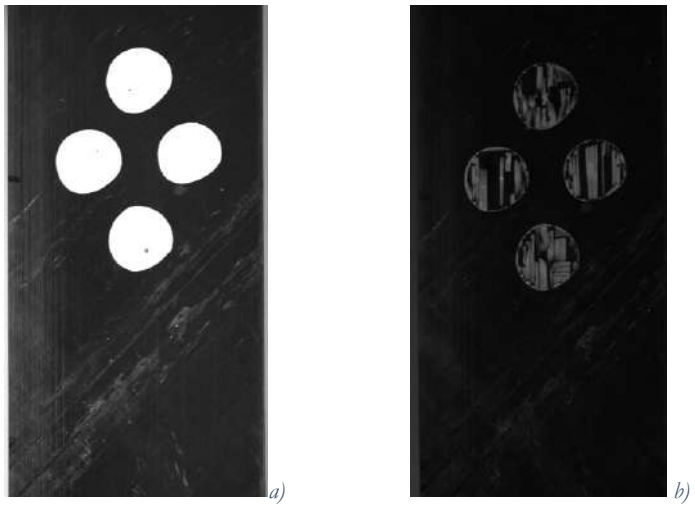

Fig. 2-24: Marker degradation: comparison of marker at the beginning (a) and at the and (b) of a test

Fluctuations in the camera signal or modification of the light exposure (as produced by the movement of the marker area along the specimen longitudinal axis while the light source is fixed during the test) could randomly affect the calculation of the marker center of mass.

A possible solution could be the increase of the marker size, directly painting a larger one, but the width of the specimen limits in some cases the actual size of the marker.

Another solution could be increasing the camera magnification, but, besides focus and resolution problems (which could be improved with a higher resolution camera), the maximum zoom depends also on the distance between the camera's objective and the specimen surface. This is strongly limited by the employing of the oven for high temperature tests, whose door is set at around 20 cm from the specimen surface and constitutes the minimum camera distance (FIG. 2-25).

Fig. 2-25: Camera in front of the oven employed during high temperature tests.

Carefully setting those factors, it was possible to achieve an absolute error of ±0.01 mm/mm in the strain measure for the range of 0.1 ÷ 0.8 mm/mm of longitudinal strain. However, if the maximum strain is lower than 0.1 mm/mm, the measured percent error is even of the 50%.

In all the cases, the size of the marker limits the duration of the test: the magnification factor sets the maximum strain that could be recorded without the markers exiting the camera acquisition field. The camera cannot be moved to keep following the test, because this would affect the measures. Also, the acquisition cannot be stopped and restarted once a new camera setup is defined, otherwise the initial reference system would be changed in favor of a new one and no link could be easily established between the first and second set of images.

To extend the acquisition field (and thus the test duration), the only solution is to reduce the magnification, but this strongly leads the measures to be affected by the above-mentioned fluctuation.

Moreover, since IdPix only measures 4 points, it is only possible to employ a finite difference formulation of the strains: it is not possible to evaluate the displacement or strain field on the whole gauge length, but only an average value.

The advantages and the drawbacks of the IdPix are summarized in TAB. 2-1.

Advantages	Drawbacks
Low resolution camera (low data volume and low analysis time)	High sensitiveness to marker degradation
Real time true stress and true strain measurement (True stress driven tests possible)	High sensitiveness to light exposure changes
	No displacement/strain field calculation (only average value)

Tab. 2-13: Advantages and drawbacks of IdPix

The combination of the applied high temperature and the measured large strains produced marker degradation during almost every test. Those two aspects question the accuracy of the measures: in order to verify them, a suitable second image analysis tool was looked for.

2.3.2.2 Digital Image Correlation (DIC)

A possible second image analysis tool could be the *Digital Image Correlation* (*DIC*) technique, (PETERS AND RANSON 1982).

Contrary to IdPix, the DIC requires high definition images, but with a 12 MP camera it is possible to transfer an image to the computer at least every 6 s (0.1 Hz minimum image acquiring frequency, while it is 0.01 Hz for IdPix) and there is no implemented algorithm for DIC real time analysis: these aspects make real time measurement impossible to achieve with DIC. Since real time measurements were necessary for carrying out creep-recovery tests, DIC could be employed only as complementary, post-test measurement system.

The DIC requires a larger number of markers in the form of small drops of paint (with an average diameter of *10÷100 μm*), as shown in FIG. 2-26.

Fig. 2-26: Pattern painted on the specimen gauge length

The employing of markers during the test, however, precluded the possibility of verifying the results obtained from IdPix with any DIC software. In fact, since the objective, employing IdPix, is to binarized the images, the acquired images are optimized for this purpose and present a great contrast between the markers and the rest of the gauge length. This aspect is instead detrimental to the DIC point of view: while for IdPix the images should

be as much smooth and uniform as possible, for the DIC they should have a richer texture instead. In the same way, the pattern painted for employing DIC techniques prevents from using IdPix.

The incompatibility between IdPix and DIC precludes the employment of the latter even as post-test measurement system, unless to double each test.

Moreover, the pattern could undergo the same degradation due to the temperature, which could affect the markers and even if such degradation has a lower impact on the measure, since calculated on more points, it is still remain an issue.

From the pattern, the software *Correla* (developed at the P'Prime D3, Poitiers, (GERMANEAU, DOUMALIN, AND DUPRÉ 2007) is able to reconstruct the displacement field of the observed gauge length and then to calculate the strain field, up to the fourth order of derivation of the strain gradient, allowing getting a localized description of the deformation field itself.

Considering the calculation part, the DIC employs a searching window that need a predictive formulation to estimate the subsequent position of the searching window itself, (SCHREIER, ORTEU, AND SUTTON 2009): tests with Correla (ANNEX F) showed that, because of the large strain produced during the tests and the non-linearity between displacement and strain, the software is not able to analyze the images acquired during the test as whole, but it forces to divide them in subset and to a posteriori reconstruct the displacement field along the test duration.

The advantages and the drawbacks of the DIC are summarized in TAB. 2-14.

Advantages	Drawbacks
Lower sensibility to degradation	High resolution camera
Displacement/strain field calculation	No real time measures
	No image compatibility with VT
	High sensibility to non-linearity between displacement and strain

Tab. 2-14: Advantages and drawbacks of DIC

2.3.2.3 A new image analysis tool (IAT)

The capability of obtain real time measures, together with a low data volume and a relatively simple set up (markers are more easy to be paint than pattern) make IdPix unreplaceable. At the same time, the incompatibility with IdPix, the higher data volume required and moreover the need of doubling the tests lead to exclude DIC even as post-test measurement system.

Therefore, a new post-test procedure, *Image Analysis Tool* (IAT), was developed, which cannot replace IdPix but is perfectly complementary to it, acting as post-test validation or correction measurement system.

The IAT requires the same images acquired during the test where IdPix was employed and it is capable to solve the principal drawbacks of IdPix: in fact, it is capable to reconstruct the degraded markers and to correct lights effects.

High order formulations are implemented, allowing the same calculation possible with DIC, with the advantage that IAT does not require a mobile searching window, because it researches the marker in the whole image or in a fixed subset of it. This analysis is still faster than DIC analysis, because of the lower images size acquired for IdPix.

The advantages and the drawbacks of the IAT are summarized in TAB. 2-15.

Advantages	Drawbacks
Low resolution camera (same images than IdPix)	Real time true stress and true strain measurement (post-test only)
Marker reconstruction	
Light changes correction	
No searching window	
Displacement/strain field calculation	
No sensibility to non-linearity between displacement and strain (no searching window)	

Tab. 2-15: Advantages and drawbacks of IAT

The IAT algorithm is composed by to subsequent part:

1. *Image analysis*: where IAT reads the images acquired during the test and, for each of them, calculates the coordinates of different points on the surface of the specimen;
2. *Calculation*: starting from the coordinates and comparing them to a reference (changing according of the chosen formulation), it calculates the average value of the strain (as IdPix) or the full displacement and strain fields.

Image Analysis algorithm

The Image analysis algorithm, written in Matlab code, is a semi-automatic algorithm, composed of the following parts:

1. *Definition of an image subset*. The initial original image is superposed to the last one and an image subset is defined by the user, deleting all the unnecessary areas to speed the analysis, (FIG. 2-27).

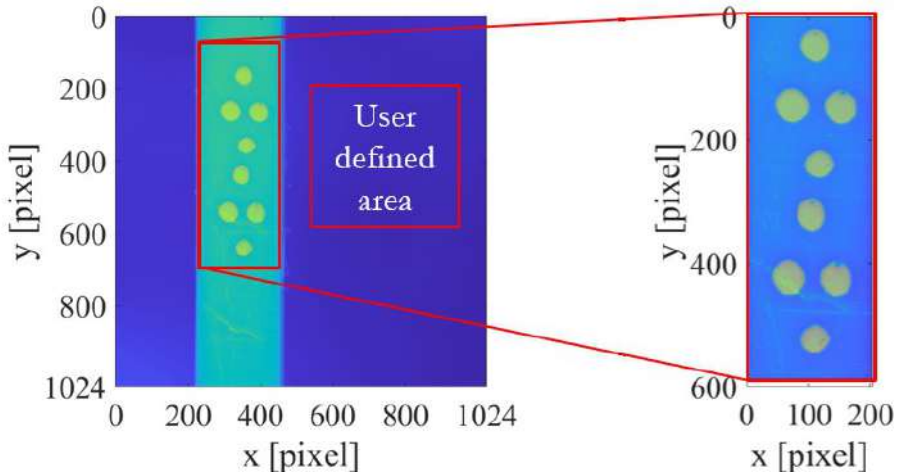

Fig. 2-27: User defined area

2. *Image binarization*. An image is read by Matlab as a matrix of the same dimensions, whose elements contain the color information of their respective pixel, as a number between 0 (black) and 255 (white). The algorithm asks the user to choose a *threshold value* s_0 on the first image of the test: every pixel with a value higher than the threshold is set to white (and given a value of 1) and the others to black (and given a value of 0). To ease the user's choice, different versions of the binarization are showed, at different values of threshold.

3. *Light exposure correction*. Since the light source is fixed during the test and positioned under the camera (FIG. 2-25), it can results, especially in the case of high strains, that the area of the gauge length, where the markers are painted, move from a lower exposure zone towards a higher exposure zone, as it moves towards the area directly in face of the light source. This leads to the fact that the initial threshold value could no longer be suitable for the subsequent images. To correct this effect, the image histogram is calculated for each processed image. The mean of the histogram, in terms of color value, is calculated for each image and employed to correct the initial threshold value s_0, according to EQ. 2-7. The result of this operation is a threshold value $s(i)$ which is optimized for each image i, as shown in FIG. 2-28.

$$\text{Mean(i)} = \sum_{1}^{N} \frac{Count(i)\ \ Color\ Value(i)}{\sum_{1}^{N} Count(i)} \qquad \textit{Eq. 2-5}$$

$$\Delta_0 = s_0 - Mean_0 \qquad \textit{Eq. 2-6}$$

$$s(i) = \Delta_0 + Mean(i) \qquad \textit{Eq. 2-7}$$

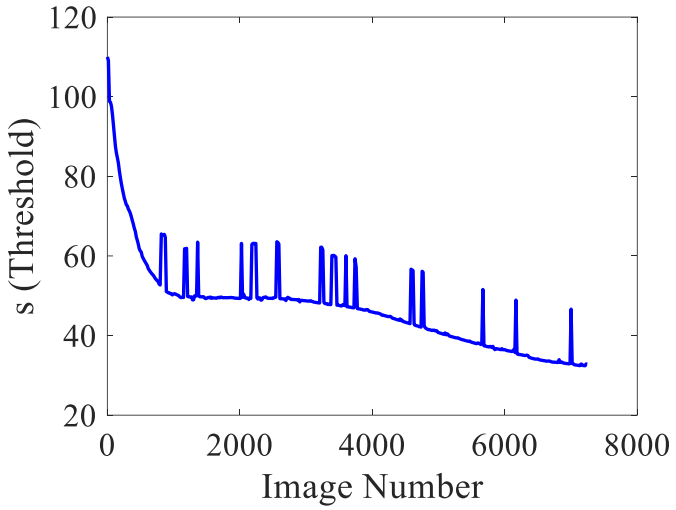

Fig. 2-28: Threshold value vs image number

4. *Connectivity analysis*. The generic element *e* of the resulting binarized matrix is surrounded by 8 other elements, as the center of a 3 by 3 square matrix. The *bwconncom* Matlab command considers connected to *e* each element of the 8 around it, if it has the same value (1 or 0) of *e*. In this way, the algorithm is able to find a certain number of connected groups of elements. The markers should represent the groups with the largest number of connected elements. To improve the results, the image is polished by artefacts (due to imperfection on the paint, spots hit by the light, etc...) which result in groups with fewer elements than the markers. In order to eliminate those groups, a second threshold value is defined, which sets the minimum number of connected elements forming a group and eliminating all the groups with less elements than the threshold, so that 4 markers only are recognized as connected object.

5. *Markers reconstruction*. Each of the remaining 4 group is analyzed and the operations listed in TAB. 2-16 are applied to it.

	Matlab Command	Effect
1	*imfill*	fill holes inside the perimeter of the marker
2	*bwconvhull*	reconstruct the edge of the marker if it is degraded, creating a convex hull of it
3	*edge*	the elements constituting the perimeter of the marker are isolated

Tab. 2-16: Matlab commands for marker reconstruction

6. *Ellipses approximation*. A matrix containing the pixel coordinates constituting each marker perimeter are input in an algorithm, (GAL 2003), which fits the perimeter itself with an ellipse. The algorithm evaluates a cost function and it minimizes it, through its derivation with respect of each parameter of the ellipse conic function (EQ. 2-8).

$$ax^2 + bxy + cy^2 + dx + ey + f = 0 \qquad \text{Eq. 2-8}$$

The first attempt is made trying to fit the marker with a non-tilted ellipse (its vertical and horizontal axes are aligned with the image reference system); then the algorithm is set to show the original image with the overlapped ellipse, and waits the user input, asking him if an ellipse rotation is needed to better fit the marker. Since the marker were handmade, their orientation could have been misaligned respect to the specimen reference system.

In any case, the initial angle is kept constant for all other images, in the assumption that no rotation (besides rigid one, directly neglected during the derivative calculation) could happen during the tests carried out during tensile or creep tests.

The employment of the ellipse fitting has the purpose to measure the coordinates of multiple points from each marker instead of just its center of mass, as obtainable from IdPix. Multiple points allow the evaluation of and average the finite difference on different area of the specimens, compensating the errors, but they as well allow describing the displacement field. In the IAT only the coordinates of the ellipses axes ends and their centers of mass are stored, for a total of 20 points.

The Image analysis algorithm is summarized in FIG. 2-29.

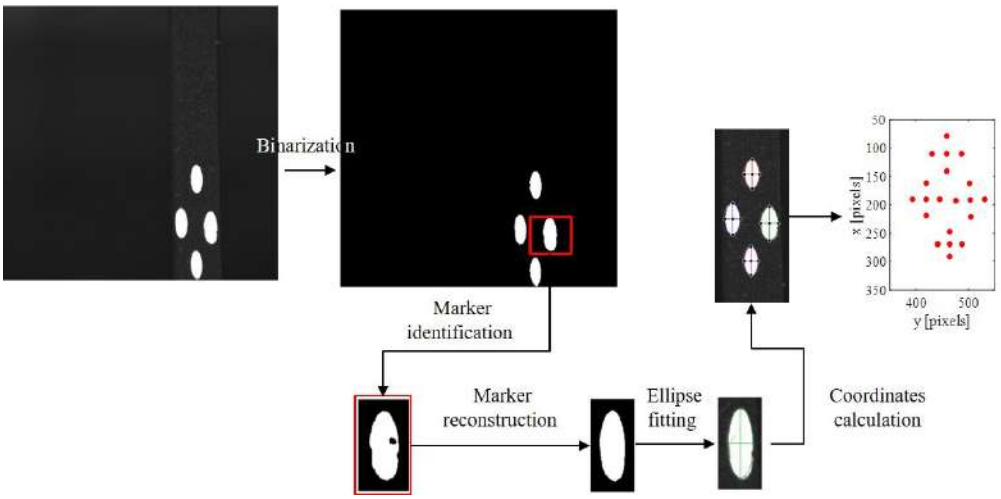

Fig. 2-29: IAT Image analysis algorithm

Since the choice of the binarization threshold value can be more or less arbitrary, some pixel around the marker perimeter can or cannot being above the threshold as consequence of the user's choice. This results in a change of the perimeter of the marker and consequently of the points coordinates. In order to evaluate the effect produced, a random error up to 5 pixels is added to each point coordinate (considering the average marker size during the test of 100 pixels – major axis - x 50 pixels – minor axis). The analysis, more detailed in ANNEX B.1, shows a maximum absolute error of maximum ±0.02 mm/mm in both longitudinal and transversal strain.

In the case of extreme marker degradation, which occurred under exposure to 5 bars of O_2 and at 200°C (see CHAPTER 6), each marker could be constituted by several non-connected groups of pixels, instead than just one. In that case, IAT algorithm can be modified to consider as part of the marker each group belonging to a specific subset of the image. The subset definition is achieved by plotting the two diagonal of the image: the procedure is discussed in detail in ANNEX B.2.

Calculation algorithm

The Calculation algorithm, written in Matlab code, can be divided in two part:

1. *Finite difference calculation*. It simply calculate logarithmic strains at time *i* from the coordinates of the 20 points measured by the image analysis algorithm on the *i*-th image respect to their coordinates on the 1st images (reference).

2. *3D formulations*. 2nd order strain fields according to Total and Update Lagrangian and Eulerian formulations are calculated at time *i* from the coordinates of the 20 points calculated by the image analysis algorithm on the *i*-th image, with following procedure:

a. The displacement field $\mathbf{u}=\{U, V, W\}$ is calculated as difference between the coordinates of the *i*-th image respect to the reference image (according to the chosen formulation).

b. Each directional component of displacement field of the *i*-th image is fitted through a bilinear polynomial function (discussed more in detail in ANNEX D) of the reference initial coordinates, as:

$$\mathbf{u}=\begin{cases} U=U(x,y,z)=a_U+b_U x+c_U y+d_U z \\ V=V(x,y,z)=a_V+b_V x+c_V y+d_V z \\ W=W(x,y,z)=a_W+b_W x+c_W y+d_W z \end{cases} \qquad \textit{Eq. 2-9}$$

c. Deriving to the 1st order the directional component of the displacement field and exploiting the transversal isotropy hypothesis (which is discussed more in detail in ANNEX C.1, and verified experimentally in ANNEX C.2), the gradient of displacement field **H** and the strain gradient **F** can be calculated for the *i*-th image (only the Total Lagrangian formulation is described so on, the other formulations are detailed in ANNEX E) as:

$$H_{ij}=\frac{\partial u_i}{\partial X_j} \quad \overset{\text{TIH}}{\Longrightarrow} \quad \mathbf{H}=\begin{bmatrix} \frac{\partial U}{\partial x_0} & \frac{\partial U}{\partial y_0} & \frac{\partial U}{\partial y_0} \\ -\frac{\partial U}{\partial y_0} & \frac{\partial V}{\partial y_0} & 0 \\ -\frac{\partial U}{\partial y_0} & 0 & \frac{\partial V}{\partial y_0} \end{bmatrix} \qquad \textit{Eq. 2-10}$$

$$\mathbf{F}=\mathbf{I}+\mathbf{H} \Rightarrow F_{ij}=\delta_{ij}+\frac{\partial u_i}{\partial X_j} \quad \overset{\text{TIH}}{\Longrightarrow}$$

$$\overset{\text{TIH}}{\Longrightarrow} \mathbf{F}=\begin{bmatrix} 1+\frac{\partial U}{\partial x_0} & \frac{\partial U}{\partial y_0} & \frac{\partial U}{\partial y_0} \\ -\frac{\partial U}{\partial y_0} & 1+\frac{\partial V}{\partial y_0} & 0 \\ -\frac{\partial U}{\partial y_0} & 0 & 1+\frac{\partial V}{\partial y_0} \end{bmatrix} \qquad \textit{Eq. 2-11}$$

d. From the strain gradient it is possible to calculate the 1st order strain field as:

$$\boldsymbol{\epsilon}=\frac{1}{2}\left(\mathbf{F}+\mathbf{F}^{\mathrm{T}}\right)-\mathbf{I} \qquad \textit{Eq. 2-12}$$

and the 2nd order strain field (Green-Lagrange strain) as:

$$\mathbf{C}=\mathbf{F}^{T}\cdot\mathbf{F} \qquad \textit{Eq. 2-13}$$

$$\mathbf{E}=\frac{1}{2}(\mathbf{C}-\mathbf{I}) \qquad \textit{Eq. 2-14}$$

e. Furthermore, from the strain gradient it is also possible to calculate the Volume variation (EQ. 2-15), the surface variation (through Nanson' formula), (EQ. 2-16), and if provided with the force value at time i, also the 1st component of both Cauchy stress (EQ. 2-17) and 2nd Piola-Kirchhoff stress tensor (EQ. 2-18).

$$\Theta=\frac{dv-dV}{dV}=det(\boldsymbol{F})-1=J-1 \qquad \textit{Eq. 2-15}$$

$$\frac{da}{dA}=J\sqrt{\mathbf{N}^{T}(\mathbf{C})^{-1}\mathbf{N}} \qquad \textit{Eq. 2-16}$$

$$\sigma_{11}=\frac{F}{A\cdot\frac{da}{dA}} \qquad \textit{Eq. 2-17}$$

$$S_{11}^{PK2}=J\,\mathbf{F}^{-1}\cdot\boldsymbol{\sigma}\cdot\mathbf{F}^{-T} \qquad \textit{Eq. 2-18}$$

The Calculation algorithm is schematized in FIG. 2-29.

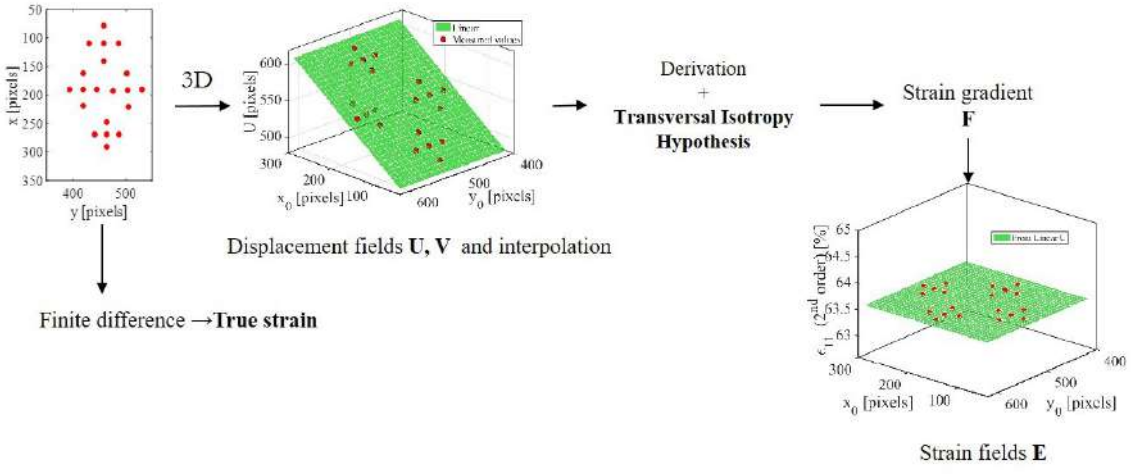

Fig. 2-30: IAT Calculation algorithm

The complete IAT algorithm is schematized in FIG. 2-31, while the different formulations implemented are listed in TAB. 2-17.

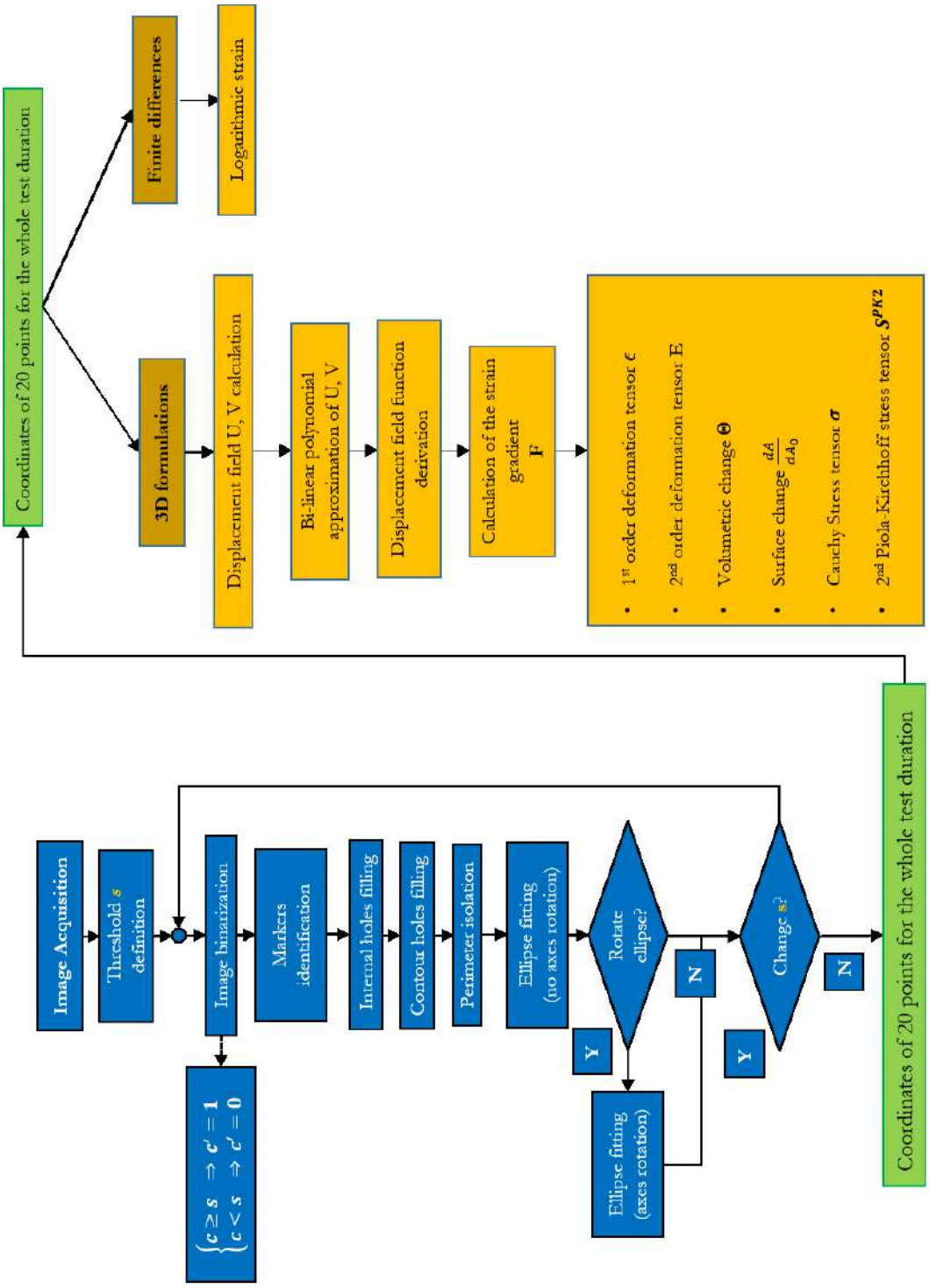

Fig. 2-31: IAT Complete algorithm

	Total Lagrangian Formulation	***Update Lagrangian Formulation***	***Eulerian Formulation***	***Logarithmic Formulation***	***Engineering Formulation***
Displacement field	$\mathbf{U}(x_0,t)=\mathbf{x}(x_0,t)-\mathbf{x_0}$	$\mathbf{U}(x_0,t)=\mathbf{U_R}(x_R,t)+\mathbf{U}(x_0,t)=$ $=(\mathbf{x}-\mathbf{x_R})+(\mathbf{x_R}-\mathbf{x_0})$	$\mathbf{U}(x,t)=\mathbf{x}-\mathbf{x_0}(x,t)$	/	/
Displacement field gradient	$\mathbf{H}=\frac{\partial \mathbf{U}}{\partial \mathbf{x_0}}$	$\mathbf{H_R}=\frac{\partial \mathbf{U_R}}{\partial \mathbf{x_R}}$ *at* t_0, $\mathbf{H_R}(0)=\mathbf{0}$.	$\mathbf{H}=\frac{\partial \mathbf{U}}{\partial \mathbf{x}}$	/	/
Deformation gradient	$\mathbf{F}=\mathbf{I}+\mathbf{H}$	$\mathbf{F_R}=\mathbf{I}+\mathbf{H_R}$ *at* t_0, $\mathbf{F_R}(0)=\mathbf{I}$. $\mathbf{F}(t_i)=\mathbf{F_R}(t_i)\cdot\mathbf{F}(t_{i-1})$	$\mathbf{F}^{-1}=\mathbf{I}-\mathbf{H}$	/	/
1st order deformation field	$\boldsymbol{\epsilon}=\frac{1}{2}(\mathbf{F}+\mathbf{F}^{T})-\mathbf{I}$		$\boldsymbol{\epsilon}=\mathbf{I}-\frac{1}{2}(\mathbf{F}^{-1}+\mathbf{F}^{-T})$	$\varepsilon(t_i)=\ln\left(\frac{l(t_i)}{l(0)}\right)$	$\boldsymbol{e}(t_i)=\left(\frac{l(t_i)-l(0)}{l(0)}\right)$
2nd order deformation field	$\mathbf{C}=\mathbf{F}^{T}\cdot\mathbf{F}$ $\mathbf{E}=\frac{1}{2}(\mathbf{C}-\mathbf{I})$		$\mathbf{c}=\mathbf{F}^{-T}\cdot\mathbf{F}^{-1}$ $\mathbf{E}=\frac{1}{2}(\mathbf{I}-\mathbf{c})$	/	/
Volumetric variation	$\Theta=\frac{dv-dV}{dV}=det(\boldsymbol{F})-1=J-1$			$\frac{\Delta V}{V_0}=\varepsilon_{11}+2\varepsilon_{22}$	$\frac{\Delta V}{V_0}=\varepsilon_{11}+2\varepsilon_{22}$
Surface variation	$\frac{da}{dA}=J\sqrt{\mathbf{N}^{T}(\mathbf{C})^{-1}\mathbf{N}}$			$\frac{da}{dA}=\exp(2\varepsilon_{22})$	/
Longitudinal stress	$\sigma_{11}=\frac{F}{A\cdot\frac{da}{dA}}$			$\sigma_{11}=\frac{F}{A\cdot\frac{da}{dA}}$	$\sigma_{11}=\frac{F}{A}$
2nd Piola-Kirchhoff	$S_{11}^{PK2}=J\,\mathbf{F}^{-1}\cdot\boldsymbol{\sigma}\cdot\mathbf{F}^{-T}$			/	/

Tab. 2-17: IAT different formulations implemented in the calculation algorithm

IAT validation

The IAT was validated through comparison with both IdPix and DIC output, in order to verify, respectively, the logarithmic and 3-D strain field measurements.

The comparison with IdPix consists in processing the images acquired during a tensile test at 200°C and 1 mm/min on a type *b* (FIG. 2-5) PEKK 7002 SC specimen, where the markers were painted on the specimen gauge length, with both IdPix (during the test) and IAT (post-test). The FIG. 2-32 shows the comparison in terms of searching area (A) and initial coordinates measured (B).

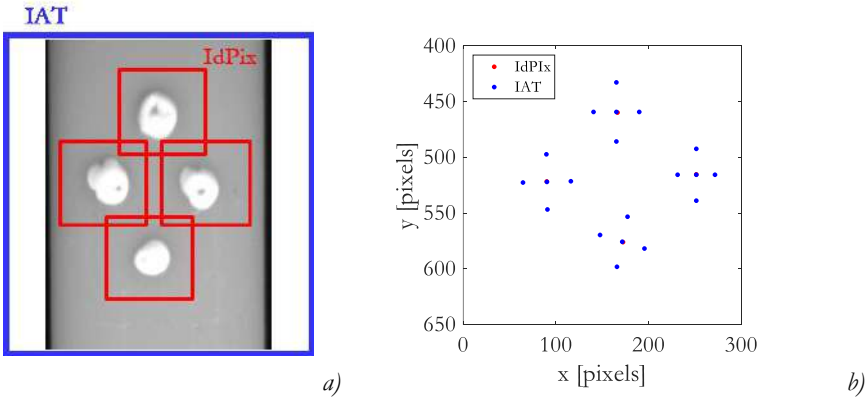

Fig. 2-32: IAT (blue) and IdPix (red) searching areas (a) and correspondent initial coordinates measured (b)

The distance between the centers of mass calculated by IdPix and IAT is showed in FIG. 2-33 and it does not exceed 2 pixels on a 1024x1024 pixels image. Considering the different binarization methods, the light exposure correction, IAT's markers reconstruction and ellipse fitting and the low resolution camera employed, this result already validates the IAT logarithmic strains measurement.

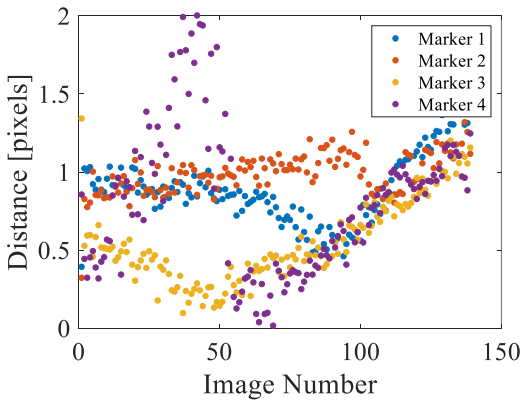

Fig. 2-33: Difference between each markers center mass position calculated by IAT and IdPix along the tensile test

As confirmation, FIG. 2-34 shows the comparison of measured logarithmic strains in longitudinal and transversal directions.

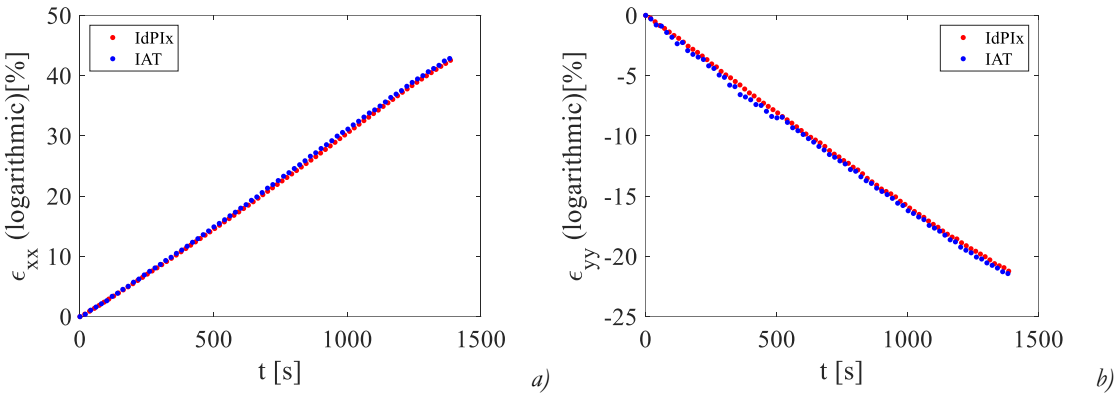

Fig. 2-34: Comparison between the logarithmic longitudinal (a) and the transversal (b) strains measured by IdPix and IAT.

The comparison with DIC software Correla consists in processing the images acquired during a tensile test at 200°C and 1 mm/min on a type *b* (FIG. 2-5) PEKK 7002 SC specimen where both IdPix markers and DIC pattern markers were painted on the specimen gauge length, with both Correla (post-test) and IAT (post-test).

The FIG. 2-35 shows the comparison in terms of searching area (A) and initial coordinates measured (B). The FIG. 2-35 shows also that markers and pattern are not in the same area. The configuration chosen is in fact a compromise, where the pattern occupies the first half the gauge length (from the clamps to the mid-height) and the markers just below it: in this way the presence of the pattern does not interfere with the calculation on the markers (altering their contour) and the markers do not create a vast homogeneous area that cannot be processed by Correla. During this test, the images were acquired with a 12 MP camera which transferred the images acquired each 6 s: this prevent to also employ IdPix and no real time measurement was possible.

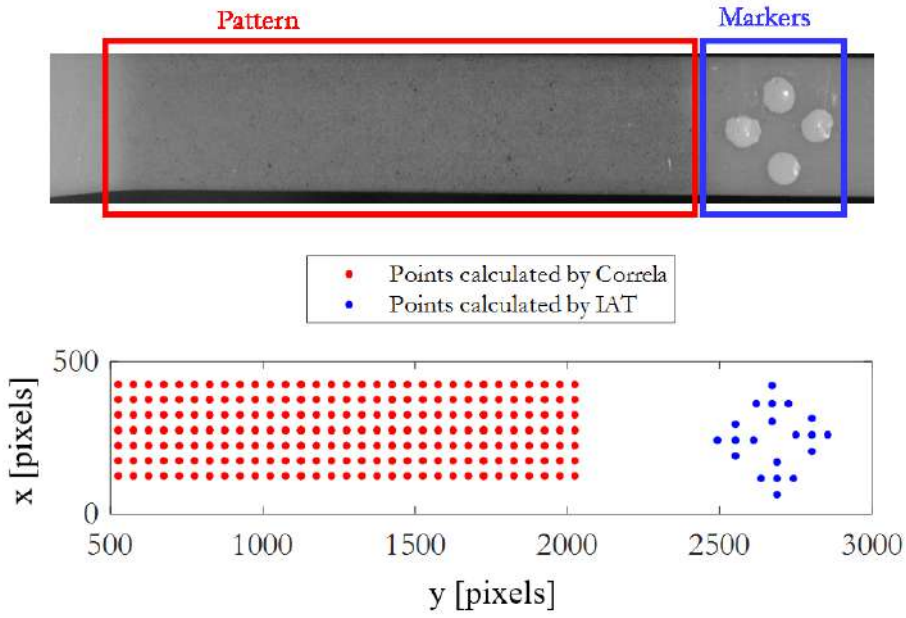

Fig. 2-35: IAT (blue) and Correla (red) searching areas (a) and correspondent initial coordinates measured (b)

Since it was not possible to process all the acquired images at once with Correla, the images where processed in groups: therefore, the displacement field measure was limited to the time interval each image group referred to and at each following restarting of the analysis (on different group of images) the initial coordinates of the points were changed.

The validation of IAT followed a 2 step procedure (discussed more in detail in ANNEX F):

- *validation of the calculation*, comparing the strains measured from Correla and IAT, calculating the strain fields with different formulation, on the same displacement field measured by Correla on a specific group of images;
- *validation of the measurement of the displacement field* reconstructing the displacement field from the different images group (ANNEX F.1).

The FIG. 2-36 shows the comparison of the longitudinal strain calculated by Correla and IAT, according both Total Lagrangian and Eulerian formulations, on the reconstructed displacement fields: the superposition of the curves in both cases validates IAT measurements.

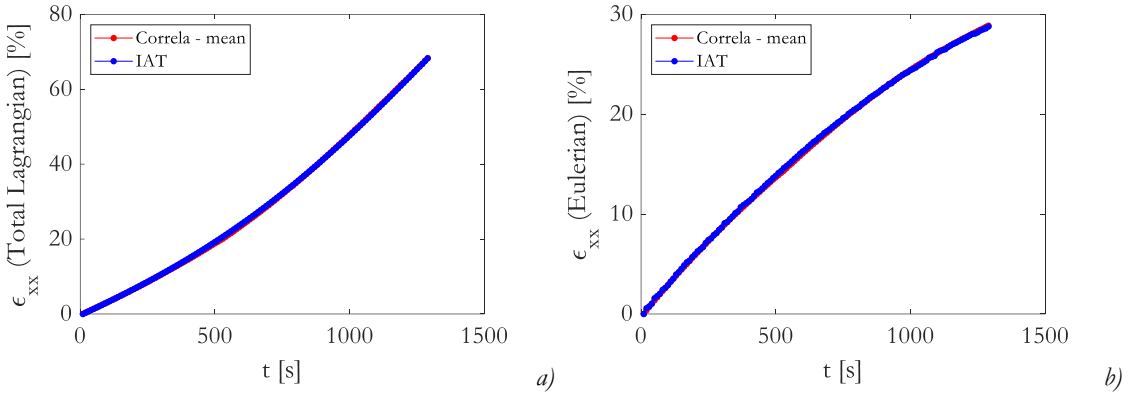

Fig. 2-36: Total Lagrangian(a) and Eulerian (b) longitudinal strains, calculated by Correla (red) and IAT (blue).

2.3.2.4 Employed measurement system

The employment of both IdPix and IAT assures a robust measurement tool: while the first provides with real time measures, the second can act as verification system and in some cases also as backup, preventing the user to re-carry out the test. FIG. 2-37 resumes the employed measurement system during all tensile, load-unload-increase and creep-recovery tests.

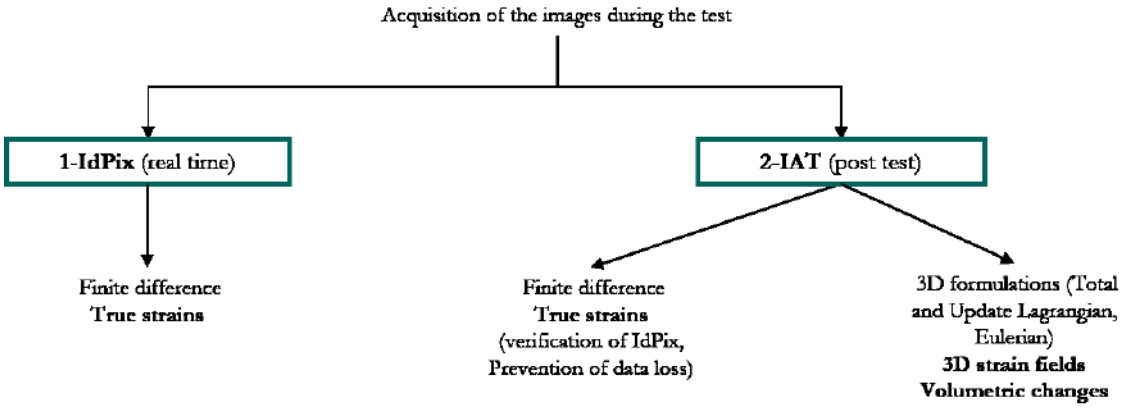

Fig. 2-37: Employed measurement system

In the case of creep test at 200°C and under 5 bars of O_2 exposure for 6 weeks (see CHAPTER 6), the marker underwent an extreme level of degradation, which provoked the failing of IdPix shortly after the beginning of the test: since this degradation was produced only by the environmental effects, it cannot be avoided. Therefore, only the employment of IAT as post-test analysis (combined to the nominal stress driven test, which did not require real time measure) avoided to stop the test and completely changing the measurement system.

2.3.3. Numerical models

As discussed in Literature Survey, the approach chosen to characterize the behavior of C/PEKK composite is based to its reconstruction starting from the neat polymer behavior, once verified the similarities in behavior between the composite matrix and the neat polymer itself.

This approach, as well the test interpretation, requires the development of a semi-analytical dedicated method, capable of modeling the in-situ behavior of polymer within the composite. While their detailed description is presented respectively in CHAPTER 3 and CHAPTER 5, its basic components are presented in the present paragraph.

The analytical methods have the advantage of requiring low computational resources but they are able to provide only first order, averaged values. Homogenization methods (to calculate the average ply and composite properties) and Localization methods (to evaluate the average strain stress in the matrix and in the fibers) were employed.

2.3.3.1 Homogenization methods

Homogenization methods allow the evaluation, starting from matrix and fiber properties, of the averaged ply properties (through *Micromechanics* methods) and according to the ply stacking sequence and orientation, the composite properties (through *Lamination Theory* methods). A schematization of the homogenization method employed is showed in FIG. 2-38.

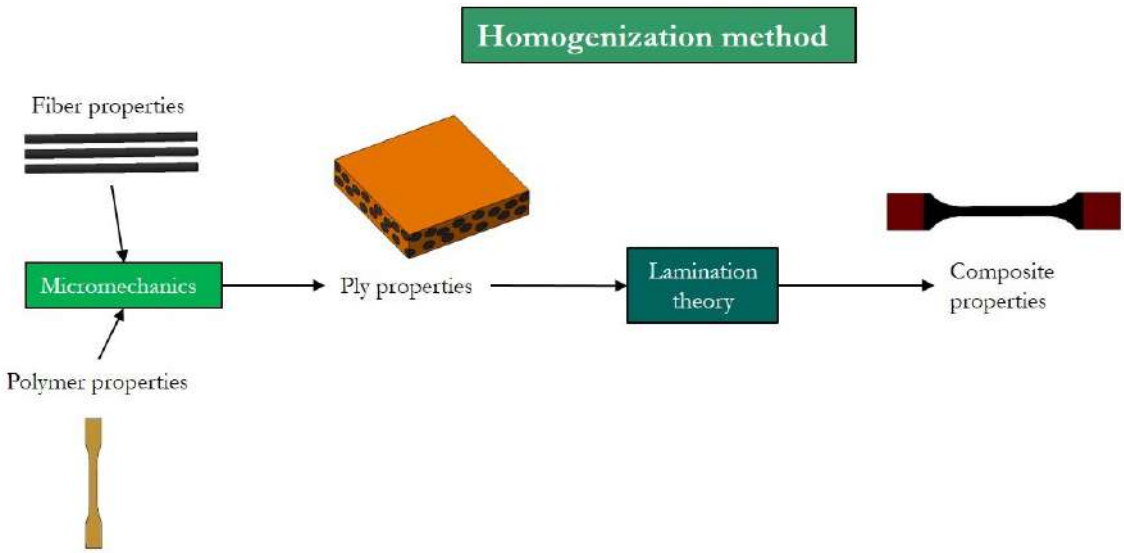

Fig. 2-38:Schematization of the homogenization method

The Halpin and Tsai, (HALPIN 1969) micromechanics method was employed: it allows the evaluation of the ply properties starting from elastic consideration on a simplified two-phases element (*slab model*, showed in FIG. 2-39) where, according to the property which has to be evaluated, a specific stress field is applied (e.g. a σ_{11} is applied on the slab model to evaluate the ply properties in *direction 1*, according to the reference system showed in FIG. 2-39).

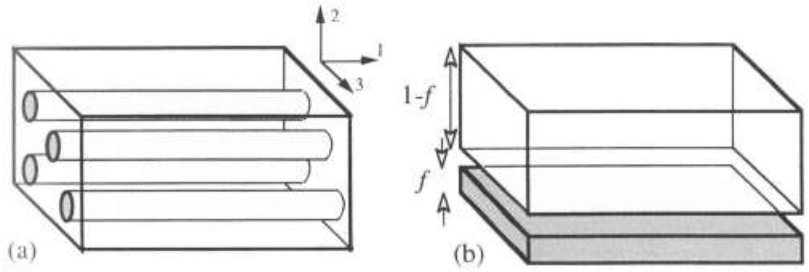

Fig. 2-39: Schematization of a ply with continuous long fibers (a) and representation of bonded slabs of fiber and matrix materials (b) (Hull and Clyne 1996)

Halpin and Tsai method modifies the calculation in some cases, replacing it with semi-empirical formulation in order to better represent experimental results (HULL AND CLYNE 1996).

Under the hypothesis of linear transversal isotropic material, from the constitutive equation (EQ. 2-19), according to Hook's law, the ply compliance matrix is expressed by EQ. 2-20.

$$\{\varepsilon\}_1=[S]\{\sigma\}_1 \qquad \textit{Eq. 2-19}$$

$$[S]=\begin{bmatrix} \frac{1}{E_{11}^p} & -\frac{\nu_{12}^p}{E_{11}^p} & -\frac{\nu_{12}^p}{E_{11}^p} & 0 & 0 & 0 \\ -\frac{\nu_{12}^p}{E_{11}^p} & \frac{1}{E_{22}^p} & -\frac{\nu_{23}^p}{E_{22}^p} & 0 & 0 & 0 \\ -\frac{\nu_{12}^p}{E_{11}^p} & -\frac{\nu_{23}^p}{E_{22}^p} & \frac{1}{E_{22}^p} & 0 & 0 & 0 \\ 0 & 0 & 0 & \frac{1}{G_{23}^p} & 0 & 0 \\ 0 & 0 & 0 & 0 & \frac{1}{G_{12}^p} & 0 \\ 0 & 0 & 0 & 0 & 0 & \frac{1}{G_{12}^p} \end{bmatrix} \qquad \textit{Eq. 2-20}$$

where the index *p* refers to ply and the index *ij* refer to the direction, according to the reference system (identified by a *1* outside the bracket in matrix notation) showed in FIG. 2-40A.

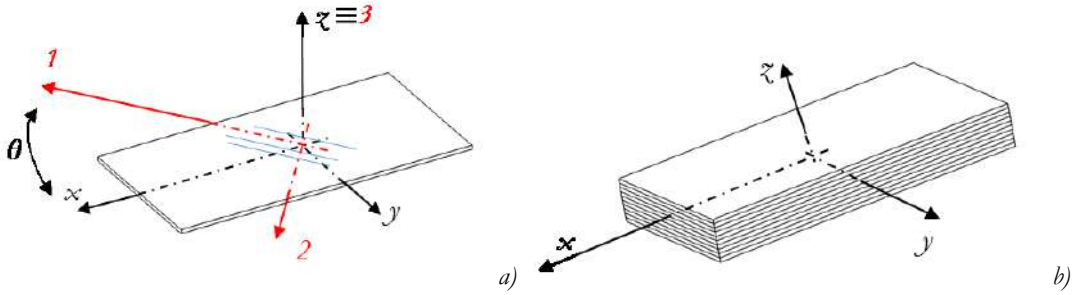

a) *b)*

Fig. 2-40: Ply reference system (a) and composite reference system (b)

The transversal isotropy hypothesis reduce to 6 the unknown properties defining the ply, which can be evaluated according to Halpin and Tsai with the formulations summarized in TAB. 2-18, where index *m* refers to matrix, *f* to the fibers and V_f is the fiber volumetric fraction. Both matrix and fiber are assumed as transversal isotropic materials.

• Longitudinal (direction-1) elastic modulus of the ply, E_{11}^{p}	$E_{11}^{p}=V_f E_{11}^{f}+(1-V_f)E_{11}^{m}$	*Eq. 2-21*
• Transversal (direction-2) elastic modulus of the ply, E_{22}^{p}	$\begin{cases} E_{22}^{p}=E_{22}^{m}\dfrac{1+\xi_E \eta_E V_f}{1-\eta_E V_f} \\ \xi_E=2+40V_f^{10} \\ \eta_E=\dfrac{\left(\frac{E_{22}^{f}}{E_{22}^{m}}-1\right)}{\left(\frac{E_{22}^{f}}{E_{22}^{m}}+\xi_E\right)} \end{cases}$	*Eq. 2-22*
• Poisson's coefficient between direction-1 and direction-2 of the ply, ν_{12}^{p}	$\nu_{12}^{p}=V_f \nu_{12}^{f}+(1-V_f)\nu_{12}^{m}$	*Eq. 2-23*

• Shear modulus between direction-1 and direction-2 of the ply, G_{12}^{p}	$\begin{cases} G_{12}^{p}=G_{12}^{m}\dfrac{1+\xi_G\,\eta_G\,V_f}{1-\eta_G\,V_f} \\ \xi_G=1+40V_f^{10} \\ \eta_G=\dfrac{\left(\frac{G_{12}^{f}}{G_{12}^{m}}-1\right)}{\left(\frac{G_{12}^{f}}{G_{12}^{m}}+\xi_G\right)} \end{cases}$	*Eq. 2-24*
• Poisson's coefficient between direction-2 and direction-3 of the ply, ν_{23}^{p}	$\begin{cases} \nu_{23}^{p}=1-\nu_{21}^{p}-\dfrac{E_{22}^{p}}{3K} \\ \nu_{21}^{p}=\nu_{12}^{p}\dfrac{E_{22}^{p}}{E_{11}^{p}} \\ K=\left(\dfrac{V_f}{K_f}+\dfrac{(1-V_f)}{K_m}\right)^{-1} \\ K_f=\dfrac{E_{11}^{f}}{3\left(1-\nu_{12}^{f}\right)} \\ K_m=\dfrac{E_{11}^{m}}{3(1-\nu_{12}^{m})} \end{cases}$	*Eq. 2-25*
• Shear modulus between direction-2 and direction-3 of the ply, G_{23}^{p}	$G_{23}^{p}=\dfrac{E_{22}^{p}}{2\left(1+\nu_{23}^{p}\right)}$	*Eq. 2-26*

Tab. 2-18: Halpin and Tsai formulation for ply properties calculation

Once the ply properties are evaluated, the ply compliance tensor can be calculated, according to EQ. 2-20. Lamination theory methods can be employed to obtain the composite properties, according to the ply stacking sequence. Herakovich's formulation (HERAKOVICH 1988) was employed (discussed more in detail in ANNEX G.1), which consists in the following procedure:

1. the ply properties (stiffness tensor, $\mathbf{C}=\mathbf{S}^{-1}$) are re-written in the composite reference system ($\overline{\mathbf{C}}$) (identified by a x outside the bracket in matrix notation and showed in FIG. 2-40B) and under the hypothesis that each ply is in plane stress ($\overline{\mathbf{Q}}$).

$$\overline{Q}_{ij}=\overline{C}_{ij}+\frac{\overline{C}_{i3}\overline{C}_{3j}}{\overline{C}_{33}} \quad \text{with } i,j=1,2,6 \qquad \textit{Eq. 2-27}$$

2. The composite stiffness matrix $[A]$, can be evaluated according to EQ. G- 16. However, it results that $[A]$ is independent of the stacking sequence, therefore, since the C/PEKK composite is constitute by 6 plies with orientation +45° and 4 plies with orientation -

45° (see FIG. 2-3), all with thickness t_k, symmetrically stacked, EQ. G- 16 can be written as:

$$[A]=6t_k[\overline{Q}]_{+45}+4t_k[\overline{Q}]_{-45} \qquad \textit{Eq. 2-28}$$

Hence the composite compliance matrix **a***, can be written as:

$$[a^*]=10t_k[A]^{-1} \qquad \textit{Eq. 2-29}$$

From the composite compliance matrix, the composite properties can be evaluated and are listed in TAB. 2-19.

• Longitudinal (direction-x) elastic modulus of the composite, E^c_{xx}	$E^c_{xx}=\frac{\bar{\sigma}_{xx}}{\varepsilon^0_{xx}}=\frac{1}{a^*_{11}}$	*Eq. 2-30*
• Transversal (direction-y) elastic modulus of the composite, E^c_{yy}	$E^c_{yy}=\frac{\bar{\sigma}_{yy}}{\varepsilon^0_{yy}}=\frac{1}{a^*_{22}}$	*Eq. 2-31*
• Poisson's coefficient between direction-x and direction-y f the composite, ν^f_{xy}	$\nu^f_{xy}=-\frac{\varepsilon^0_{yy}}{\varepsilon^0_{xx}}=-\frac{a^*_{22}}{a^*_{11}}$	*Eq. 2-32*
• Shear modulus between direction-x and direction-y of the composite, G^c_{xy}	$G^c_{xy}=\frac{\bar{\tau}_{xy}}{\gamma^0_{xy}}=\frac{1}{a^*_{66}}$	*Eq. 2-33*

Tab. 2-19: Composite properties form Lamination theory

Poisson's coefficient between the direction-x and the direction-z, ν^f_{xz}, and between the direction-y and the direction-z, ν^f_{yz}, (out of plane), can be evaluated with the following formulation:

$$\nu^f_{xz}=-\frac{A^*_{11}F_1+A^*_{12}F_2+A^*_{16}F_6}{10t_kA^*_{11}} \qquad \textit{Eq. 2-34}$$

$$\nu^f_{yz}=-\frac{A^*_{21}F_1+A^*_{22}F_2+A^*_{26}F_6}{10t_kA^*_{22}} \qquad \textit{Eq. 2-35}$$

where:

$$F_i = \sum_{k=1}^{N} \left(\bar{S}_{13}^k \bar{C}_{1i}^k + \bar{S}_{13}^k \bar{C}_{1i}^k + \bar{S}_{13}^k \bar{C}_{1i}^k \right) t_k \qquad i=1,2,6 \qquad \text{Eq. 2-36}$$

The presented formulation allows calculating the ply and composite properties, starting from the matrix and fibers one. Moreover, it allows the calculation of ply strain and stress, if the composite ones are known.

The formulation, however, is written under the hypothesis that matrix and fiber have linear elastic behavior: in the case of PEKK SC (CHAPTER 3), especially above T_g, this hypothesis is not valid, revealing the formulation not sufficient to describing the C/PEKK behavior.

Moreover, it does limit to ply stress and strain and no information could be obtained about the matrix stress and strain, which, instead, can be linked to the evolution of properties. For this reason, localization methods were also employed.

2.3.3.2 Localization methods

Localization methods acts in the opposite way than homogenization methods, allowing assessing the strain and stress tensors inside the matrix and the fibers, starting from the strain tensor applied to the ply.

(FRÉOUR, JACQUEMIN, AND GUILLÉN 2005) adapted the self-consistent method employed in metals to distinguish between matrix and precipitates: this method was originally developed for spherical precipitates, (MORRIS 1970), and then generalized for ellipsoidal ones, (TANAKA AND MORI 1970). If one of the axis is extended to infinite, the ellipsoidal phase become a cylindrical and could be suitable for the representation of the fibers inside the composite. A schematization of the localization method employed is showed in FIG. 2-38.

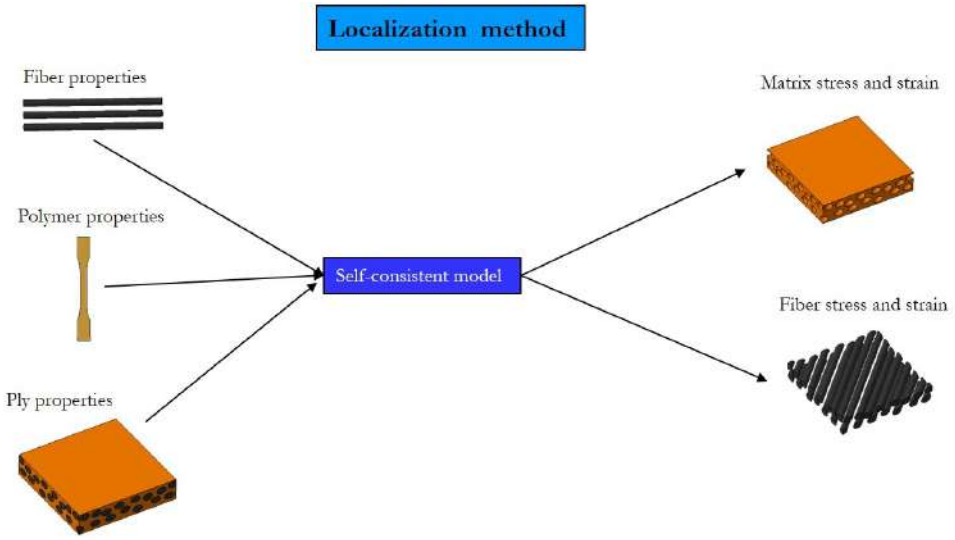

Fig. 2-41: Schematization of the localization method

The method (discussed more in detail in ANNEX G.2) consists in evaluating a *localization matrix* $[L]^m$, function of the matrix and ply properties, which is applied to the ply strain tensor $\{\varepsilon\}^p$ to evaluate the matrix strains tensor $\{\varepsilon\}^m$, according to:

$$\{\varepsilon\}^m=[L]^m\{\varepsilon\}^p \qquad \textit{Eq. 2-37}$$

where

$$[L]^m=\begin{bmatrix} 1 & 0 & 0 & 0 & 0 & 0 \\ \frac{B}{F} & \frac{C}{F} & \frac{D}{F} & 0 & 0 & 0 \\ \frac{B}{F} & \frac{C}{F}+H & \frac{D}{F}-H & 0 & 0 & 0 \\ 0 & 0 & 0 & A & 0 & 0 \\ 0 & 0 & 0 & 0 & G & 0 \\ 0 & 0 & 0 & 0 & 0 & G \end{bmatrix} \qquad \textit{Eq. 2-38}$$

- $A=\frac{2C^p_{55}}{C^p_{55}+C^m_{44}}$
- $B=\left(C^p_{12}-C^m_{12}\right)$
- $C=\left(\frac{C^p_{22}\left(C^p_{22}\left(5C^m_{11}-C^m_{12}+3C^p_{22}\right)-C^p_{23}\left(3C^m_{11}+C^m_{12}+4C^p_{22}\right)+\left(C^p_{23}\right)^2\right)}{\left(\left(3C^p_{22}-C^p_{23}\right)\left(C^m_{11}-C^m_{12}\right)+\left(C^p_{22}\right)\right)^2-\left(C^p_{23}\right)^2}\right)$ *Eq. 2-39*
- $D=\frac{\left(C^p_{22}\left(C^p_{22}\left(C^m_{11}-5C^m_{12}-C^p_{22}\right)+C^p_{23}\left(C^m_{11}+3C^m_{12}+4C^p_{22}\right)-3\left(C^p_{23}\right)^2\right)\right)}{\left(3C^p_{22}-C^p_{23}\right)\left(C^m_{11}-C^m_{12}\right)+\left(C^p_{22}\right)^2-\left(C^p_{23}\right)^2}$

- $F = C^m_{11} + C^m_{12} + C^p_{22} - C^p_{23}$
- $G = \frac{2C^p_{22}(C^p_{22} - C^p_{23})}{2(C^p_{22})^2 + Cp_{23}(C^p_{44} + C^m_{44}) + C^p_{22}(3C^m_{44} - 2C^p_{23} - 3C^p_{44})}$
- $H = -\frac{4C^p_{22}(C^p_{22} - C^p_{23})}{(C^p_{22})^2 + 3C^p_{22}(C^m_{11} - C^m_{12}) - C^p_{23}(C^m_{11} + C^p_{23} - C^m_{12})}$

The stress inside the matrix can be evaluated through the matrix constitutive equation (inverse of EQ. 2-19) from:

$$\{\sigma\}^m = [C^m]\{\varepsilon\}^m \qquad \textit{Eq. 2-40}$$

Localization methods overcome the limit of homogenization methods and allow the evaluation of the evolution of matrix stress and strain depending to the evolution of ply stress and strain. But, as the latter, localization methods have the limit of supposing a linear elastic behavior of both matrix and fibers.

The connection of both methods, however, is employed for obtaining a new analytical method (presented in the next chapter), which allows not only to calculating the matrix stress and strain evolution as function of the applied composite stress and strain, but also updating the matrix properties as function of the calculated matrix stress.

2.4. Conclusions

The 1st part of the present chapter has been dedicated to the description of all the tested materials, their manufacturing process and the geometry of the specimen employed for the experimental campaign, along with a summary of all the tests carried out, divided in test needed for thermomechanical characterization and the physical-chemical characterization.

The 2nd part has been composed by:

- the description, or each test, of the experimental equipment and the employed testing protocol, with the latter chosen in order to ensure the maximum test reproducibility.
- a particular focus on the strain measurement system and the description of a new image analysis tool developed to compensate the lacks of the preexisting one.

The last part of the chapter has been dedicated to the analytical methods, needed to the analysis of the composite material and to link its matrix to the polymer, and to development of semi-analytical methods employed for the simulations of the composite behavior.

Chapter 3 – Preliminary analysis of tensile and creep thermomechanical behavior of PEKK SC and C/PEKK

This chapter presents a preliminary analysis of the results obtained from tensile, creep-recovery, DMA and DSC tests carried on PEKK 7002 SC and on C/PEKK composites in order to investigate the change in behavior produced increasing the temperature above their T_g. The main issues related to material behavior are outlined and a simplified analysis, based on the study, and the comparison of the engineering constants is presented. In order to compare the behavior of the neat polymer and that of the matrix in the composite, a semi-analytical Homogenization / Localization model is presented.

3.1. Introduction

As discussed in the Literature Survey, presented in the first chapter, thermoplastic polymers exhibit a change of state from solid to rubber behavior, when the temperature is increased above their T_g. This phenomenon inevitably leads to a mechanical properties loss, which could be mitigated by the presence of crystalline phase.

As particularly stressed in the Literature Survey, the evolution of the mechanical properties with the crystallinity percentage was studied through tensile tests for different T/I ratio PEKK (including 7002) by (TANGUY CHOUPIN 2018), which showed a significant loss of properties when the temperature is increased above T_g and a greater impact of the crystallinity percentage above T_g compared to room temperature.

Because of the activation of crystallization mechanisms above T_g, the mechanical properties could also depend on the exposition time at those temperatures, producing a complex coupling with the thermomechanical properties which requires a detailed analysis. However, those phenomena are more significant in low crystalline percentage thermoplastic polymers, with higher macromolecular chains mobility, and should be prevented in fully crystallized ones. This implies that PEKK SC mechanical properties are more stable above T_g compared to PEKK AM.

Moreover, the presence of the fibers also could affect the behavior of the polymer, and in particular, for C/PEKK, this could depend by the composite manufacturing process (CHAP. 2.2.1.2), which requires that the stacked prepregs are heated at 380°C (> PEKK 7002 T_m), impacting the crystallinity phase in:

- percentage: because of difference in the cooling phase produced by the fiber presence, different crystallization percentage are measured in PEKK SC (24%) and in the composite, (28%), (TAB. 2-1);
- morphology: trans-crystallinity was observed on C/PEKK composite (TANGUY CHOUPIN 2018), (CHELAGHMA 2013), which could affect the matrix-fiber interface, and hence the global composite behavior.

The above described scenario is quite complex and calls for a complete and systematic characterization. In view of this obvious complexity, this characterization was split in two separate – though complementary – parts. The present Chapter will be focused on PEKK SC and C/PEKK composite, aiming to provide the outlines of the changing behavior from below to above T_g. For this analysis, and employing the specimen geometries, equipment and test protocols described in the previous chapter, the results of the following tests are presented:

- Tensile test;
- Creep-recovery tests;

- DMA tests;
- DSC tests.

The analysis of this preliminary characterization is performed in a simplified manner – through an engineering approach, coherent with the industrial framework of the present research - by employing engineering constants as gross indicators of the observed behavior. This analysis is of benefit in order to have an early look at the mean features and issues of the observed behavior. It will also allow determining a first order of magnitude for all the main material properties.

Moreover, in order to compare the behavior of the neat polymer and that of the matrix in the composite, two actions are carried out:

- a preliminary comparison between polymer and composite behavior is performed. Besides a qualitative comparison of the curves relative to the specified tests, the results obtained from creep-recovery tests are compared through a 3 parameter power law, and employed to define a creep compliance master-curve, through a time-temperature superposition. In this way, the possibility of a rheological simple behavior – evocated in the Literature Survey - is investigated, which could be directly related to a linear viscoelastic creep behavior.

- a semi-analytical homogenization / localization model is developed and used, aiming at correlating the properties of the polymer properties with those of the matrix in the composite. The model takes into account the polymer properties during a tensile test, relating them to the matrix behavior and updating the composite properties. The simulated composite tensile behavior is then compared to the experimental curves, giving a first account of the behavior of the matrix within the composite.

A more complete characterization of the polymer and of the composite behavior will be provided, respectively, in CHAPTER 4 and CHAPTER 5.

In order to simplify the exposition, a specific color code is assigned to each test temperature, as resumed in TAB. 3-1.

Test temperature	Color
Room temperature	Red
100°C	Blue
150°C	Grey
165°C	Green
180°C	Gold
200°C	Black

Tab. 3-1: Color code employed for defining each test temperature

3.2. Tensile tests

The first step in the thermomechanical characterization of both PEKK SC and C/PEKK is constituted by carrying out of tensile test, respectively on specimen type *b* and $[(\pm 45)_2, +45]_s$ C/PEKK composite specimens type *d* (FIG. 2-5), according to the testing protocol described in CHAP. 2.3.1.2. Different test conditions were applied to both materials, which were tested at:

- different temperature below and above T_g, from room temperature to 200°C, to investigate the mechanical properties dependency on temperature during the change of state linked to the passage of T_g;
- and at different displacement rate ($\dot{z}$), to investigate time effects on the mechanical properties above T_g.

The tensile test conditions are resumed in TAB. 3-2:

T [°C]	$\dot{z}$ [mm/min]
20	1
100	1
150	1
165	0.1
	1
	10
180	0.1
	1
	10
200	0.1
	1
	10

Tab. 3-2: Tensile test conditions

Other information is obtained from these tests, in terms of ultimate stress and failure mode, and, through the analysis of the initial part of the curve, the pseudo-elastic moduli are calculated.

3.2.1. Temperature effects

The tensile tests carried out on PEKK SC specimens at 1 mm/min at room temperature, 100°C, 150°C and 200°C are compared in FIG. 3-1 (the tests at 165°C and 180°C were stopped once the camera's acquisition window was exceeded). The results for the whole test durations are presented in form of force vs displacement (or machine head position) curves:

in fact, a necking appears in all samples at every temperature. Hence starting from the necking appearance, the global values of true stress and strain are no more representative. Moreover, those tests were carried out up to the specimen failure or up to the maximum machine stroke, exceeding the camera's acquisition window, so that no post-test analysis could be carried out either.

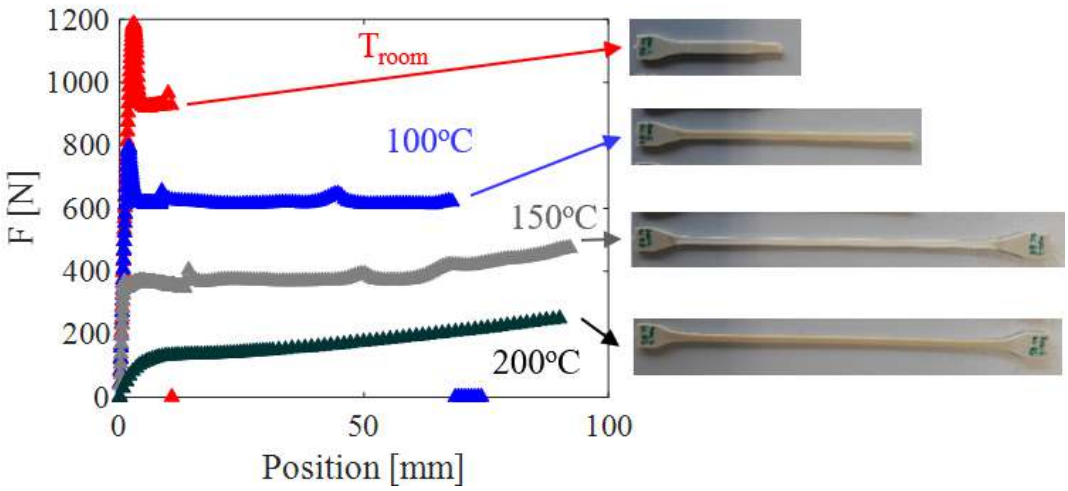

Fig. 3-1: Force vs displacement curves at different temperature at 1 mm/min on PEKK 7002 SC specimens

FIG. 3-1 shows clear effects of the temperature on PEKK SC, producing, as it increases:

- a decrease of the apparent stiffness;
- a decrease of the maximum stress;
- an increase in ductility;
- an increase in strain at rupture.

The failure mode also changes with the temperature:

- at room temperature, a localized and sharp necking appears (in correspondence of the peak), which shortly extends along the gauge length before failure;
- increasing the temperature, the necked area extends progressively until it covers the whole gauge length (150°C) and no failure could be induced because of testing limits;
- above T_g, however, the necking is more diffused and gradual along the overall gauge length and no peak appears in the force vs position curve; as consequence, no start of necking could be clearly identified. At every temperature above T_g, the failure could not be reached for testing limits ($\varepsilon \gg 200\%$).

The comparison between the true stress vs true strain curves at 1 mm/min at room temperature, 100°C, 150°C, 165°C, 180°C and 200°C is showed in FIG. 3-2, (for test temperature below T_g, the analysis is stopped before the necking appearance and in all cases up to the limit of the camera's acquisition window).

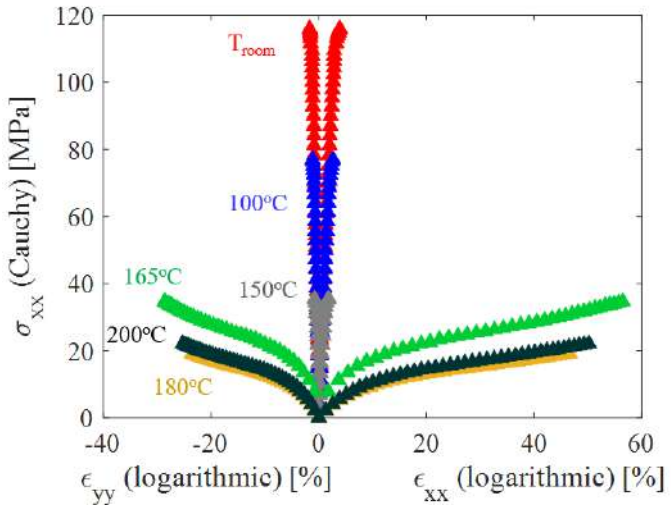

Fig. 3-2: True stress vs longitudinal and transversal true strains from tensile tests at different temperature at 1 mm/min on PEKK 7002 SC specimens

An analogue investigation is carried out on C/PEKK, and tensile tests are carried out on C/PEKK at 1 mm/min at room temperature, 100°C, 150°C, 165°C, 180°C and 200°C. The results are compared in FIG. 3-3. Because of its structure, the transversal isotropy hypothesis is no longer valid for the composite, hence the measure of the strain in the thickness direction is needed in order to evaluate the true stress. The results are therefore presented in the form of nominal stress vs nominal longitudinal strain.

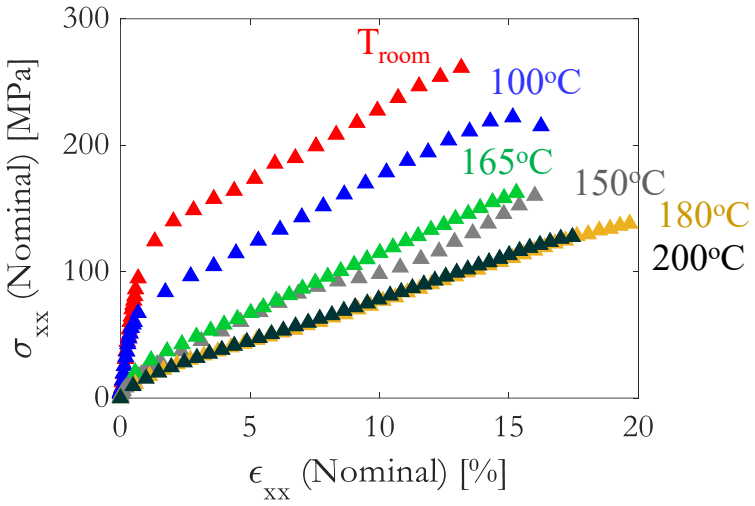

Fig. 3-3: Nominal stress vs longitudinal nominal strains from tensile tests at different temperature at 1 mm/min on C/PEKK specimens

Similar to PEKK SC, the temperature produces on C/PEKK, as it increases:

- a decrease of the apparent stiffness;
- a decrease of the maximum stress;
- an increase in ductility;
- an increase in strain at rupture.

The tensile behavior of PEKK SC and C/PEKK shows some similarity, and both exhibit a significant dependence on the test temperature and a pronounced change in behavior in the passage above T_g, which produces in both materials a severe loss in mechanical properties. However, sufficiently far from T_g, the temperature dependence seems to reduce.

3.2.2. Time effects

Other tensile tests were carried out at 3 temperatures above T_g (165°C, 180°C and 200°C) at different displacement speeds (0.1, 1 and 10 mm/min) to investigate time effects.

In FIG. 3-4 the true stress vs true strain curves obtained for PEKK SC are compared.

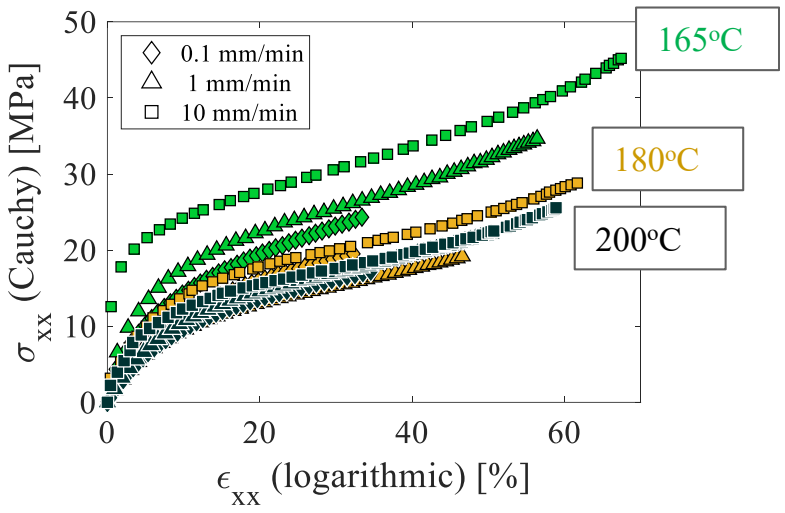

Fig. 3-4: Stress vs strain curves obtained from tensile test on PEKK 7002 SC and at 165°C, 180°C and 200°C at 0.1 mm/min, 1 mm/min and 10 mm/min

From FIG. 3-4, it can be concluded that:

- no pure elastic region is clearly identifiable at any condition of temperature and displacement speed.
- when the temperature is close to around T_g (at 165°C = T_g +5°C), the increase of displacement speed produces an increase of the apparent stiffness.
- at higher temperatures, the material shows less sensitiveness to time and temperature effects.

Tensile tests were carried out on C/PEKK specimens at the same 3 temperatures above T_g and 3 displacement speeds applied to the PEKK SC. FIG. 3-5 shows the comparison of the nominal stress vs strain curves obtained.

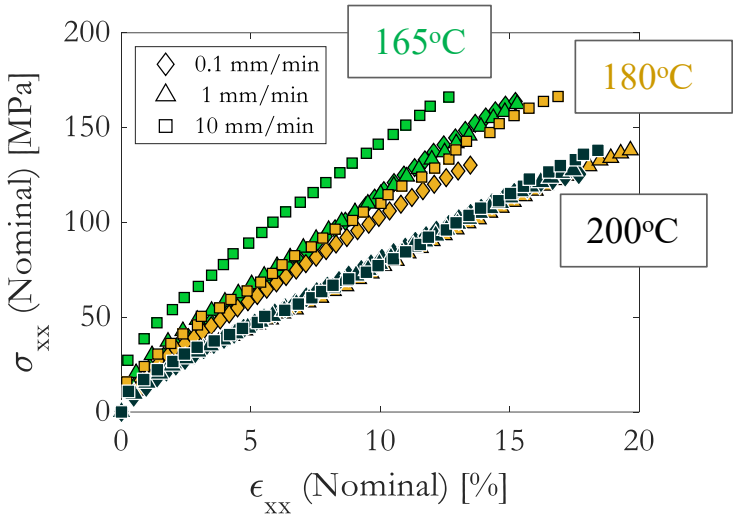

Fig. 3-5: Nominal stress vs nominal strain obtained from tensile tests on C/PEKK at 165°C, 180°C and 200°C at 0.1 mm/min, 1 mm/min and 10 mm/min

Similarly to PEKK SC, the following consideration can be made:

- when the temperature is close to around T_g (at 165°C = T_g +5°C), the increase of displacement speed produces an increase of the apparent stiffness.
- at higher temperatures, the material shows less sensitiveness to time and temperature effects.
- no linear elastic region is clearly identifiable at any condition of temperature and speed. At low strains, the C/PEKK shows a non-linear behavior, similar to PEKK SC, while at higher strains a more linear behavior presents. This facts suggests not only that there could be a similarity in behavior between the matrix and the polymer, but also that the composite behavior is matrix dominated at low strains (FIG. 3-6A) and fiber dominated at high strains (FIG. 3-6B).

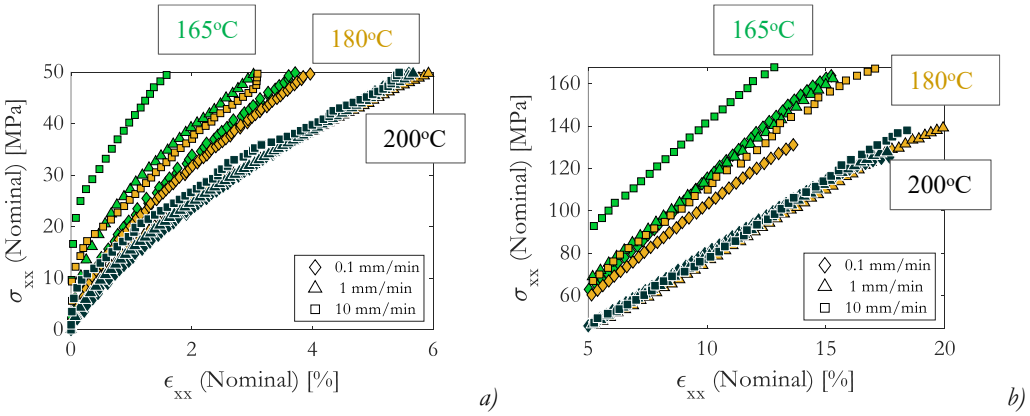

Fig. 3-6: C/PEKK matrix dominated region (a) and fiber dominated region (b)

Both PEKK SC and C/PEKK revealed similar time effects, limited to low strain in C/PEKK, up to around 6%: this represents the strain range in which the similarity in behavior of PEKK SC and C/PEKK can be investigated.

3.2.3. Fiber rotation

The surface of C/PEKK specimens (FIG. 3-7a) distinctly shows the external ply fibers, this allows measuring their orientation for the all test durations: FIG. 3-7B shows the measure of angle Θ, complementary to the fiber orientation angle (β). During tensile tests above T_g, up to 15° fiber rotation is measured, and, for Θ, a quadratic dependency on the applied nominal stress can be established (FIG. 3-8). The parameters describing the fibers rotation at 165°C, 180°C and 200°C are resumed in TAB. 3-3.

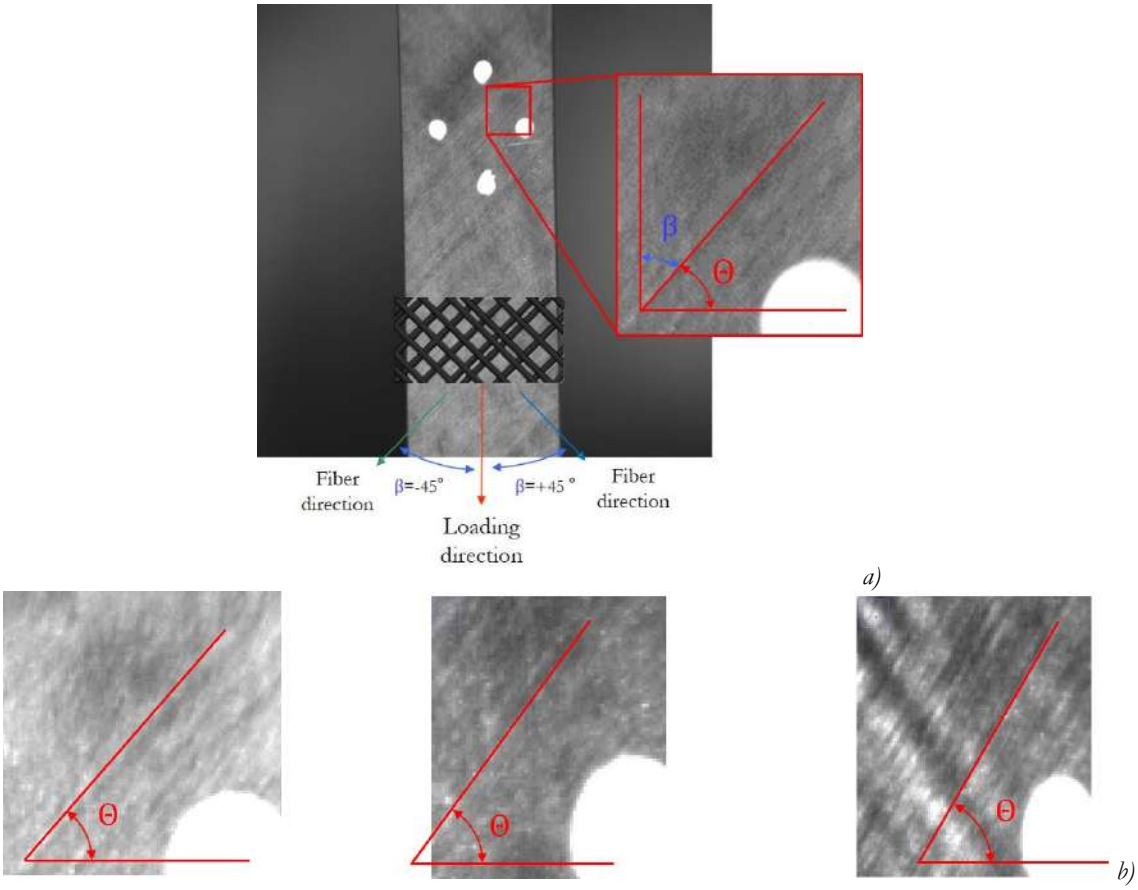

Fig. 3-7: C/PEKK specimen's surface (a) and fiber rotation at different times during tensile test (b)

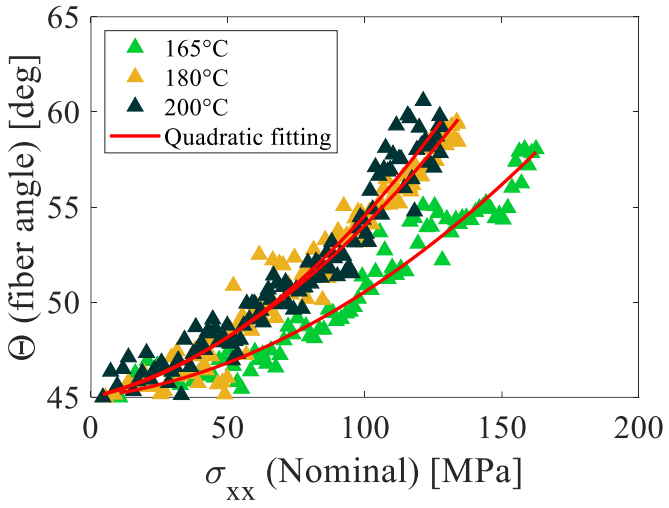

Fig. 3-8: C/PEKK Fiber orientation vs nominal stress measured during tensile tests at 165°C, 180°C, 200°C

$\Theta = a\,\sigma_C^2 + b\,\sigma_C + c$				
ż [mm/min]	**T [°C]**	**a [deg ·MPa^{-2}]**	**b [deg ·MPa^{-1}]**	**c [deg]**
1	165	0.000382	0.0173	45
	180	0.000544	0.0361	45
	200	0.000640	0.0317	45

Tab. 3-3: C/PEKK Fiber rotation parameters as function of the tensile tests nominal stress at 165°C, 180°C and 200°C

This phenomenon is coherent with the progressive reduction of properties in the polymer as the stress (strain) is increased, visible in the progressive reduction of apparent stiffness in FIG. 3-4. The final part of the composite stress vs strain curves (FIG. 3-6B) shows a linear behavior, while the angle keep increasing: a rotation towards the loading direction should increase the material apparent stiffness. A possible explanation is the contemporary matrix reduction of properties is compensated by the fiber rotation.

3.2.4. PEKK SC and C/PEKK engineering mechanical properties

The most evident effect resulting in the transition above T_g, for both PEKK SC and C/PEKK is the mechanical properties loss. Since no linear elastic part could be clearly identifiable, because of the non-linear behavior observed in both materials, in order to quantify this loss of properties, the engineering properties (*pseudo-elastic moduli*) were measured through a linear regression of the stress vs strain curves closest to their beginning.

The PEKK SC pseudo-elastic moduli are evaluated at each temperature through a linear regression of the true stress vs true strains curve, between 0.1% and 0.4% true strain, (FIG.

3-9). The values corresponding to all tensile tests at 1 mm/min are resumed in TAB. 3-4 and showed in FIG. 3-10.

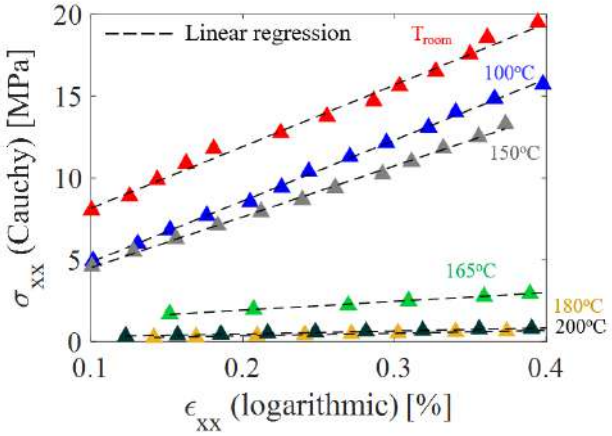

Fig. 3-9: Linear regression between 0.1% and 0.4% of PEKK 7002 SC true strain vs longitudinal true strain curve at different temperature at 1 mm/min

ż [mm/min]	T [°C]	Pseudo-elastic modulus [MPa]	Poisson's Coefficient
1	20	3793	0.45
	100	3750	0.44
	150	3126	0.43
	165	543	>0.5
	180	171	>0.5
	200	178	>0.5

Tab. 3-4: Pseudo-elastic moduli and Poisson's coefficient obtained from tensile test on PEKK 7002 SC and from room temperature to 200°C at 1 mm/min

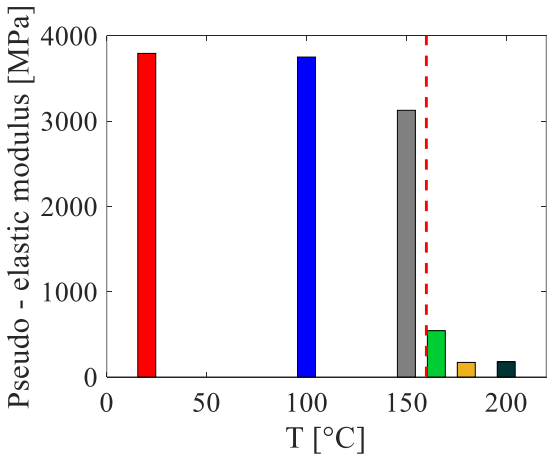

Fig. 3-10 Pseudo-elastic moduli vs temperature obtained from tensile test on PEKK 7002 SC from room temperature to 200°C at 1 mm/min

The C/PEKK pseudo-elastic moduli are resumed in TAB. 3-5 and calculated through a linear regression of the nominal stress vs nominal strain curves, between 0.01% and 0.3% nominal strain from all tensile tests at 1 mm/min (FIG. 3-11). FIG. 3-12A shows the pseudo-elastic modulus evolution vs the test temperature.

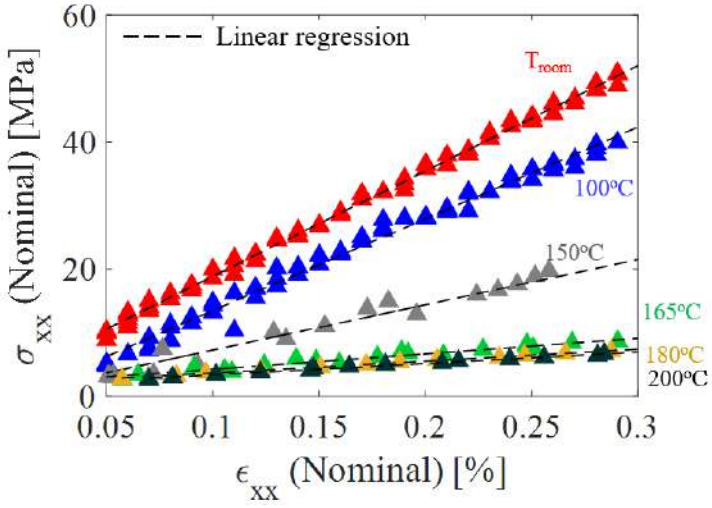

Fig. 3-11: Linear regression between 0.05% and 0.3% of C/PEKK nominal strain vs longitudinal nominal strain curve at different temperature at 1 mm/min

The ultimate nominal stresses obtained from 1 mm/min tensile tests are also listed in TAB. 3-5. In order to apply always the same test protocol to the C/PEKK, all the C/PEKK specimens at temperature above T_g were tested with a 2000 N load cell: this prevented to reach the failure of the specimen at 165°C, because the required force value exceeded the load cell capacity. In TAB. 3-5 the last measured value is reported, which is also employed for FIG. 3-12B to show its order of magnitude compared to other temperatures.

ż [mm/min]	T [°C]	Pseudo-elastic modulus [MPa]	Ultimate Nominal Stress [MPa]
1	20	16558	254.4
	100	14436	223.5
	150	7090	170.6
	165	2425	>169
	180	1868	139
	200	1795	128

Tab. 3-5: Pseudo-elastic moduli and ultimate nominal stresses obtained from tensile test on C/PEKK and from room temperature to 200°C at 1 mm/min

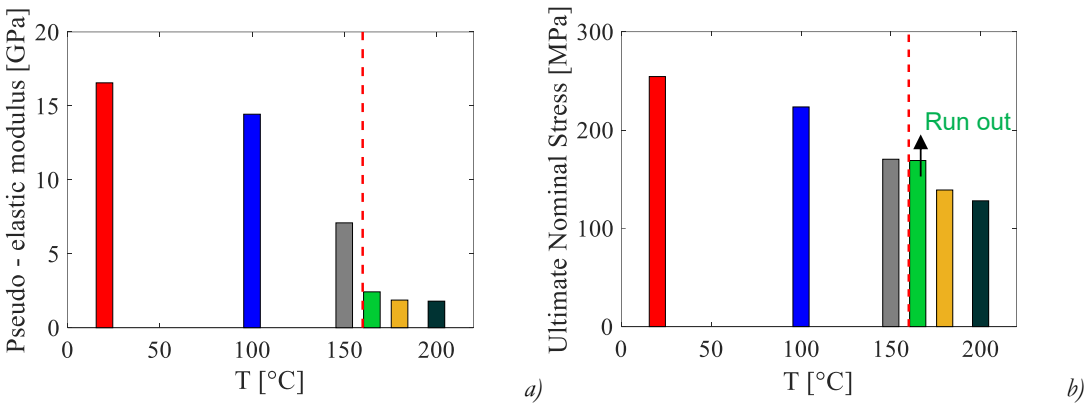

Fig. 3-12: Pseudo-elastic moduli (a) and ultimate nominal stresses (b) vs temperature obtained from tensile test on C/PEKK from room temperature to 200°C at 1 mm/min

From the images and the tables above, it can be concluded that:

- The fibers presence does not avoid the loss of mechanical properties produced in the transition above T_g;
- The temperature dependence of the pseudo-elastic moduli is similar in PEKK SC and C/PEKK, while the rupture mode and final strength is not, coherently to the high strain fiber dominated region observed in C/PEKK specimen.

The mechanical properties dependency on the temperature is more clearly investigated through DMA tests, which results are showed in the next paragraph.

3.3. DMA tests

DMA tests were carried out at constant frequency and varying the temperature, and provided valuable information about the mechanical properties dependency on the temperature, even if the resulting moduli cannot be exactly correlated to the material Young modulus.

In order to simplify the exposition, at each material is assigned a specific color resumed in TAB. 3-6.

Material	Color
PEKK SC	Orange
C/PEKK	Dark Grey

Tab. 3-6: Color code employed for defining each as received material

3-point-bending DMA tests were carried out on PEKK 7002 SC specimen type *a* (FIG. 2-5), according to the testing protocol described in (CHAP. 2.3.1.3).

The DMA storage modulus *E'*, (FIG. 3-14A), shows a T_g onset of 156.1°C, close to the nominal value of 160°C and a severe decrease of mechanical properties (around 90%) as the temperature is increased above T_g.

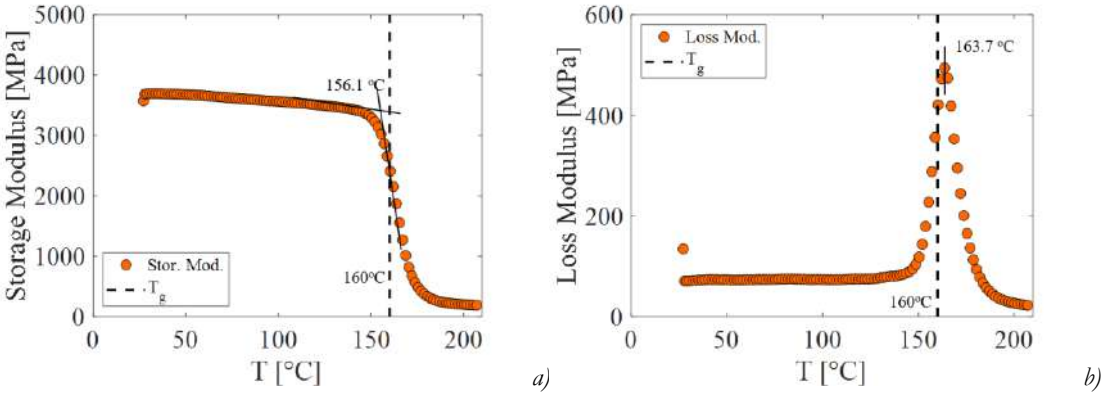

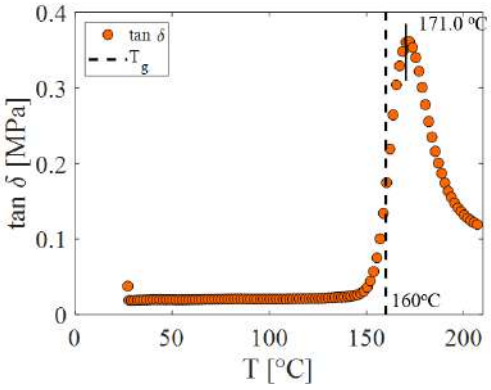

Fig. 3-13: 3-point bending DMA storage modulus (a), loss modulus (b) and tan delta (c) for PEKK 7002 SC

Such properties loss is a confirmation of the tensile tests results (see CHAP. 3.2.1): FIG. 3-14 shows that the storage modulus vs temperature curve almost superposes to the pseudo-elastic moduli obtained from tensile tests (TAB. 3-4). Moreover, the storage modulus vs temperature confirms the different sensibility to temperature effects resulting from tensile tests:

- at 165°C, a variation of ±1°C produce a variation of ±200 MPa of storage modulus (transition region);
- at 180°C, a variation of ±1°C produce a variation of ±40 MPa of storage modulus (end transition region);
- at 200°C, a variation of ±1°C produce a variation of ±4 MPa of storage modulus (low temperature sensitiveness region).

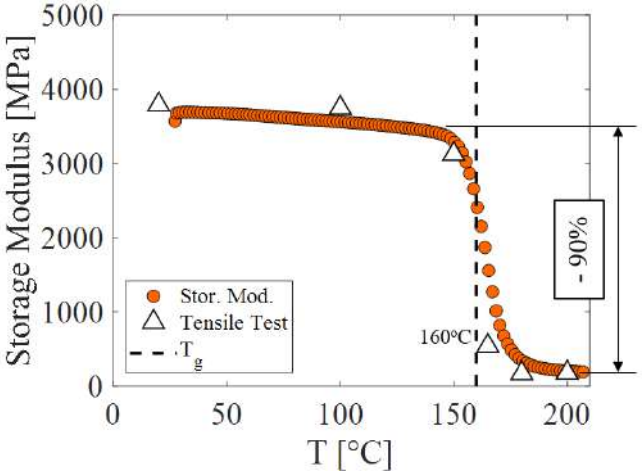

Fig. 3-14: DMA storage modulus between 20°C and 200°C, compared with pseudo-elastic moduli

3-point-bending DMA tests were carried out on C/PEKK 7002 SC specimen type *c* (FIG. 2-5), according to the testing protocol described in (CHAP. 2.3.1.3).

The DMA storage modulus *E'*, (FIG. 3-15), shows a T_g onset of 150.0°C, 6°C lower than PEKK SC one and a severe decrease of mechanical properties as the temperature is increased above T_g.

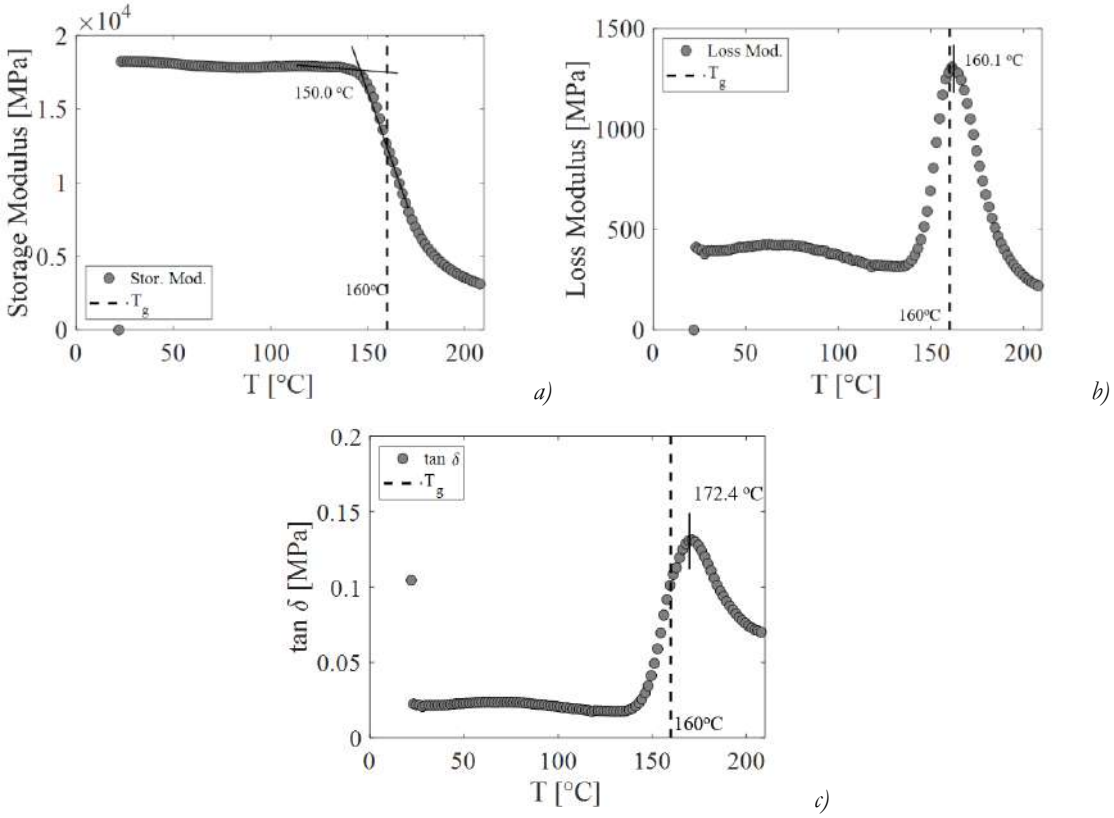

Fig. 3-15: 3-point bending DMA storage modulus (a), loss modulus (b) and tan delta (c) for C/PEKK

In FIG. 3-16A, the C/PEKK storage modulus is compared with the pseudo-elastic moduli, and the results obtained from DMA on PEKK SC. To better compare the results, all the measured values have been normalized respect to their initial value (FIG. 3-16B).

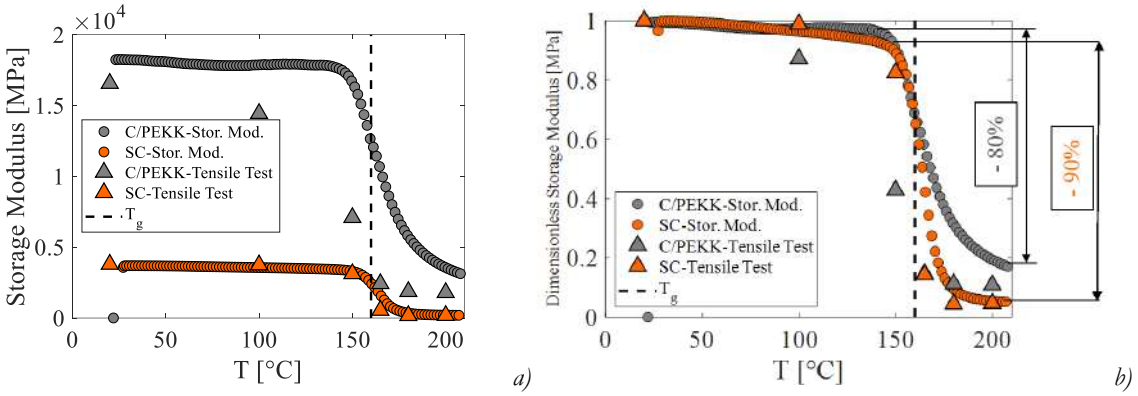

Fig. 3-16: Comparison between C/PEKK SC (grey) and PEKK SC (orange) DMA storage modulus between 20°C and 200°C, compared with pseudo-elastic moduli as measured values(a) and as ratio respect to initial values (b).

FIG. 3-16B, shows that, even if the global trend between PEKK SC and C/PEKK is similar, some differences can be seen in the storage modulus evolutions: during the transition above T_g, the C/PEKK storage modulus decreases sooner but more gradually compared to PEKK SC one, losing around the 80% of its mechanical properties, a slightly lower reduction of the mechanical properties compared to that of PEKK SC (90%). This imply that for ±45° ply orientation, the fiber mitigated effect in properties loss is rather limited. Those results similar to those found by (TANGUY CHOUPIN 2018) and showed in the Literature Survey, which described instead a loss of almost 90% for ±45°.

In case of C/PEKK, the pseudo-elastic moduli obtained from tensile tests do not superpose to DMA storage modulus curve, as for the neat polymer. On the contrary, the pseudo-elastic moduli describe a faster evolution with the temperature and reach lower values above T_g, respect to the storage modulus, more coherent to the 90% mechanical loss found by Choupin. This could imply an intrinsic error in DMA on C/PEKK, possibly linked to the composite difference between tensile - bending behavior linked to the anisotropy in the thickness direction. This does not appear in neat polymer, possibly because of its isotropic behavior. The above-mentioned comparison, therefore, seems to point out the more reliable results in terms of mechanical properties evolution of C/PEKK composite obtained from tensile tests, rather than DMA ones.

3.4. Creep-recovery tests

The previous paragraphs investigated the general outline of the PEKK SC and C/PEKK tensile behavior, revealing a complex dependency on temperature and time. However, all those tests have a limited duration (less than 5 h, in the case of tensile tests at the lowest displacement rate). Those durations of exposition to thermomechanical loads could be considerably far from the duration foreseen for industrial applications. Creep-recovery tests were designed to provide information about longer exposition to thermomechanical load, as well as information about the amount of recovered strain when the mechanical load is removed.

In those test, however, the activation of viscous mechanisms (viscoelastic if all the strain can be recovered, or viscoplastic, if part of the induced strain is permanent), implies the presence of time-dependent phenomena, which could be related to the same mechanisms driving the tensile time-dependency, or the activation of different ones.

Moreover, the possible degradation of the polymer promoted by the prolonged exposition to thermomechanical load, could affect the matrix-fiber interface in composite.

The presented scenario could result in an increase of complexity in the PEKK SC and C/PEKK behavior, and it will be investigated more in detail in the next chapter. The present paragraph shows the general outline of the creep-recovery behavior obtained from tests carried out on PEKK 7002 SC specimen type *b* and C/PEKK specimen type *d* (FIG. 2-5), according to the testing protocol described in (CHAP. 2.3.1.2).

Preliminarily to the presentation of the results, the definition of tests parameters is detailed.

3.4.1. Creep-recovery test parameters

In order to carry out the creep-recovery tests, 3 parameters were needed to be set:

1. *Temperature*. The tests were carried out at the same 3 test temperatures chosen for the tensile tests, 165°C, 180°C and 200°C.

2. *Displacement speed during loading and unloading phases*. 1 mm/min was chosen as displacement speed, as a compromise between being low enough to allow seeing its effect on the material and fast enough to reduce the tests duration.

3. *Creep stress*. 3 stress levels were chosen for the PEKK SC, initially as the 30%, 50% and 70% of the yield stress obtained from a tensile test at 1 mm/min for each test temperature. However, as showed in FIG. 3-4, no yield stress can be clearly identified, therefore a *threshold stress* for each temperature is identified, as the *stress in correspondence of which the tangent modulus reaches the 15% of its initial value*. The 15% value is chosen as the minimum value that the dimensionless tangent modulus reach at every tensile test

condition. The tangent modulus is calculated at each point of the tensile stress vs strain curve, as the slope of the straight-line tangent the curve itself, according to the following procedure:

a. the stress vs strain curve is approximated with a complete 7th order polynomial function:

$$\sigma(\varepsilon)=\sum_{0}^{7} a_i \varepsilon^i \qquad \textit{Eq. 3-1}$$

b. the slope of the tangent straight line is the 1st derivative of the EQ. 3-1:

$$tangent(\varepsilon)=\frac{d\sigma}{d\varepsilon}\varepsilon+c \;\Rightarrow\; E_{tan}(\varepsilon)=\frac{d\sigma}{d\varepsilon}=\sum_{1}^{7} i\, a_i\, \varepsilon^{i-1} \qquad \textit{Eq. 3-2}$$

c. the initial tangent modulus is the value of EQ. 3-2 when ε=0:

$$E_{tan}(0)=a_1 \qquad \textit{Eq. 3-3}$$

The creep-recovery test parameters are resumed in TAB. 3-7:

$\dot{z}$ $\left[\frac{mm}{min}\right]$	T[°C]	σ_{th} [MPa]	% σ_{th}	σ_{creep} [MPa]
1	165	16.8	30	5
			50	8
			70	12
	180	15.2	30	4.5
			50	8
			70	11
	200	13.1	30	4
			50	7
			70	10

Tab. 3-7: Creep-recovery test parameters for PEKK 7002 SC

For the C/PEKK, instead, at each temperature, 2 levels of creep stress were chosen:

a. the 50% of the composite ultimate nominal stress at each test temperature (TAB. 3-5);
b. the stress in correspondence of which the matrix Von Mises stress is equal to the polymer threshold stress (TAB. 3-7)., evaluated through the semi-analytical method described in CHAP. 3.6.

The composite creep-recovery test parameters are resumed in TAB. 3-7 and the creep stresses are showed in FIG. 3-17.

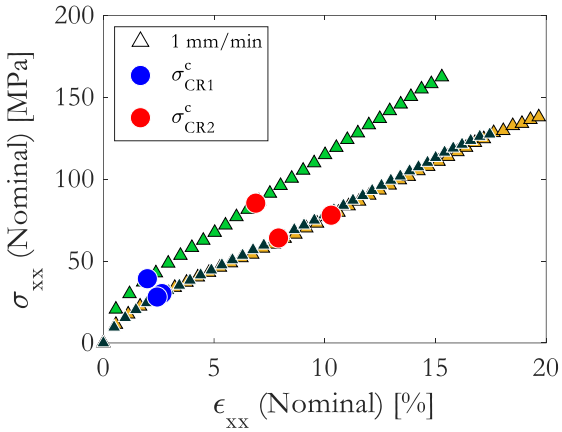

Fig. 3-17: Creep stress applied to the composite at 165°C, 180°C and 200°C

$\dot{z}\ \left[\frac{mm}{min}\right]$	T[°C]	Condition	F [N]	σ^C_{creep} [MPa]
1	165	$0.5\ \sigma^C_u$	974.7	85
		$\sigma^{VM}_m=\sigma^{th}_{poly}$	450.0	39
	180	$0.5\ \sigma^C_u$	896.5	78
		$\sigma^{VM}_m=\sigma^{th}_{poly}$	348.0	30
	200	$0.5\ \sigma^C_u$	743.6	64
		$\sigma^{VM}_m=\sigma^{th}_{poly}$	322.5	28

Tab. 3-8: Creep-recovery test parameters for C/PEKK

3.4.2. Creep-recovery tests results

From all the creep-recovery tests carried out on PEKK SC, a strain curve similar to the one showed in FIG. 3-18 is obtained.

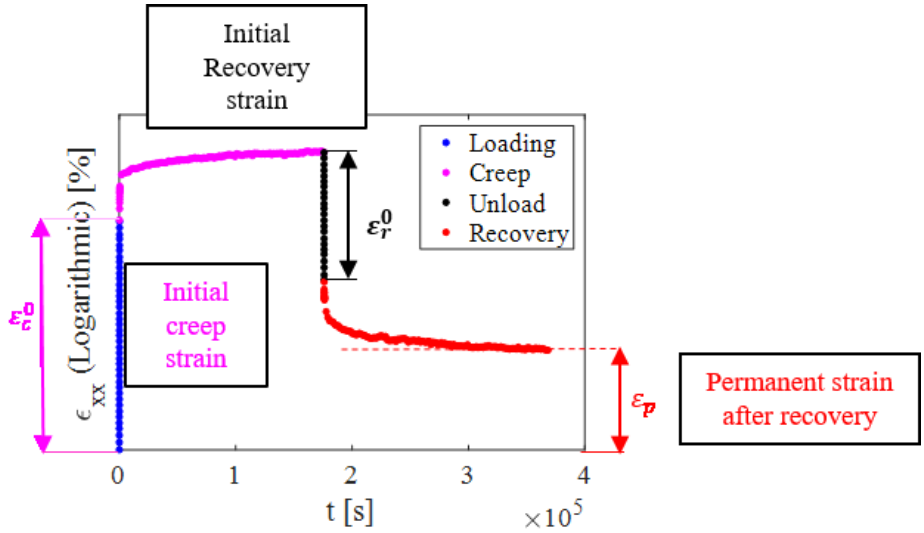

Fig. 3-18: True longitudinal strain vs time curve obtained from a creep-recovery test on PEKK 7002 SC.

From FIG. 3-18 it is clearly identifiable:

- the *initial creep strain*, or the amount of strain produced during the loading phase, before the beginning of the creep phase;
- the *initial recovery strain*, or the amount of strain recovered during the unloading phase, before the beginning of the recovery phase;
- the *permanent strain after recovery*, or the amount of strain left at the end of the test.

In FIG. 3-19, the strain curve relative only to the creep phase (A) and recovery phase (B) are showed in logarithmic scale.

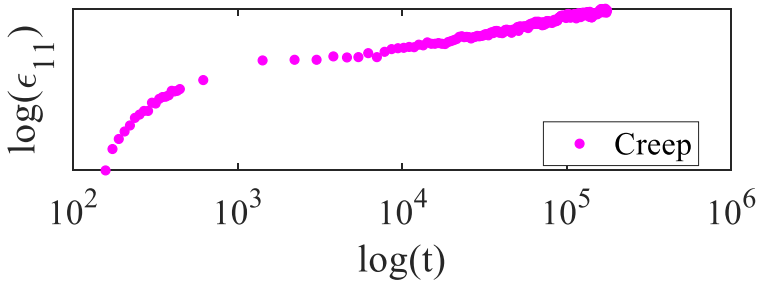

a)

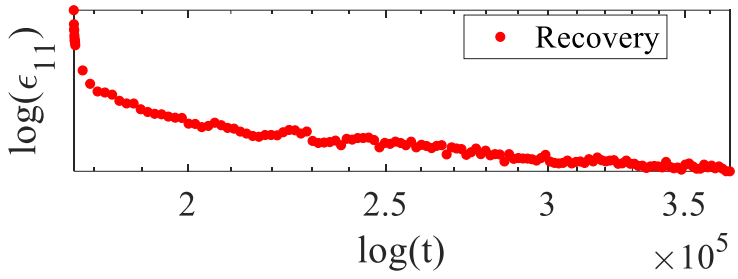

b)

Fig. 3-19: PEKK 7002 SC true longitudinal strain vs time curve of the creep phase (a) and recovery phase (b) plotted in logarithmic scale.

For both phases, an initial non-linear part (*primary creep*) and a final more linear part (*secondary creep*) can be identified. No *tertiary creep* (leading to sudden failure) is observed on PEKK 7002 SC sample at any test condition. The strain curve relative to the recovery phase, does not reach an asymptotic value, suggesting that the recovery phase duration is insufficient to the complete relaxation of the material.

The permanent strains after the recovery (values are resumed in TAB. 3-9) are plotted in function of the temperature and the creep stress, respectively in FIG. 3-20A and B.

T[°C]	% σ_{th}	Permanent strain after recovery [%]
165	30	0.10
	50	0.70
	70	4.60
180	30	1.40
	50	3.10
	70	5.40
200	30	0.20
	50	2.00
	70	5.60

Tab. 3-9: PEKK 7002 SC Permanent strain after recovery for each creep-recovery test condition

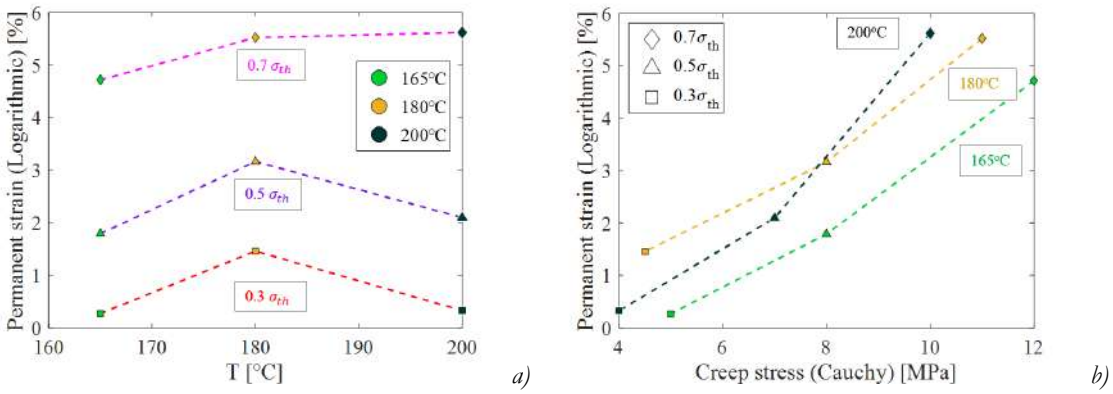

Fig. 3-20: PEKK 7002 SC Permanent strain after recovery vs test temperature (a) and creep stress (b)

No clear trend of the permanent strain with respect to temperature can be identified, while, as expected, the permanent strain increases as the creep stress increases. The absence of a clear trend could be a hint of the complex mechanisms active in the different phases of the creep-recovery tests, but it could be influenced as well by the fact that the recovery duration is not sufficient and further strain could be recovered. It has to be pointed out that in almost all tests, the recovery strain vs time curve does not reach an asymptotic value (FIG. 3-19B) and any attempt to fit it with an equation allowing estimating an asymptotic value was unsuccessful. The values resumed in TAB. 3-9 are obtained from the last value of the curve showed in FIG. 3-19B once smoothed to eliminate the noise in the strain measure.

From all the creep-recovery tests carried out on C/PEKK, a strain curve similar to the one showed in FIG. 3-21 was obtained.

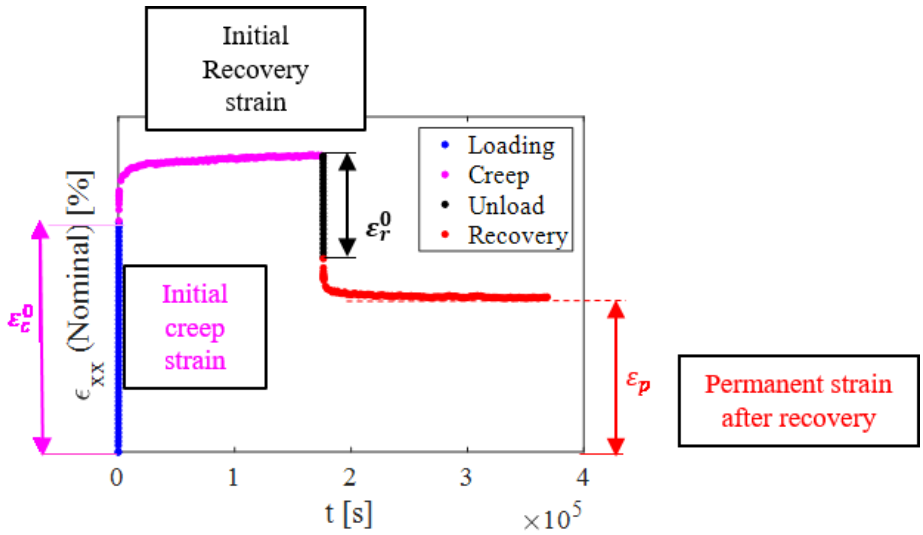

Fig. 3-21: Nominal longitudinal strain vs time curve obtained from a creep-recovery test on C/PEKK.

The C/PEKK typical strain curve is similar to PEKK SC one (FIG. 3-18), and, also for C/PEKK, the *initial creep strain*, the *initial recovery strain* and the *permanent strain after recovery* can be clearly identified on the strain vs time curve.

The strain curve relative only to the creep phase (A) and recovery phase (B) are showed in logarithmic scale in FIG. 3-22.

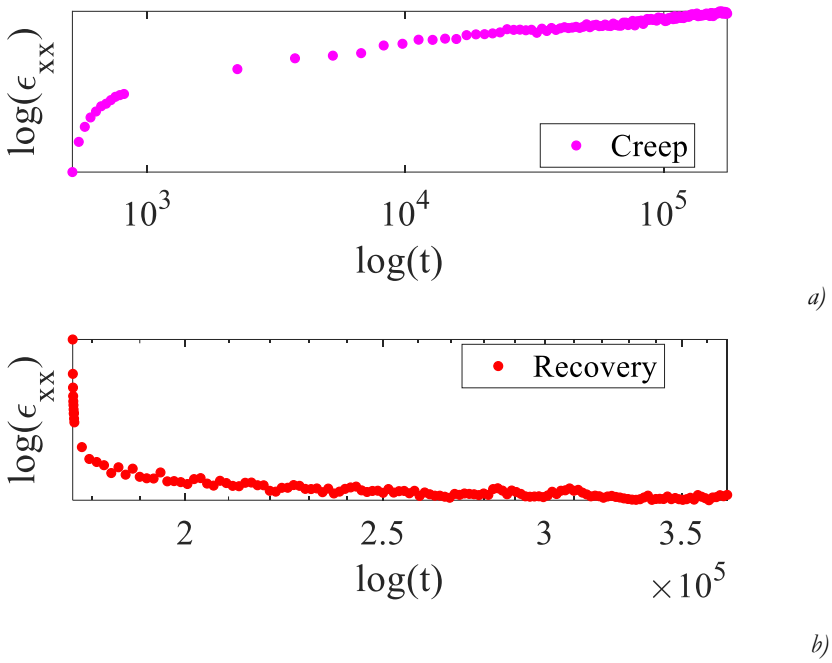

Fig. 3-22: C/PEKK true longitudinal strain vs time curve of the creep phase (a) and recovery phase (b) plotted in logarithmic scale.

For both phases, as for PEKK SC, an initial non-linear part (*primary creep*) and a final more linear part (*secondary creep*) can be identified. No *tertiary creep* (leading to sudden failure) was observed on C/PEKK sample at any test condition as well. The strain curve relative to the recovery phase, does not reach an asymptotic value, and the same considerations made for PEKK SC can be made also for C/PEKK.

The permanent strains after the recovery (values are resumed in TAB. 3-10), are plotted in function of the temperature and the creep stress, respectively in FIG. 3-23A and FIG. 3-23B.

T[°C]	Condition	Permanent strain after recovery [%]
165	$0.5\ \sigma_u^C$	3.72
	$\sigma_m^{VM}=\sigma_{poly}^{th}$	1.58

180	$0.5\ \sigma_u^C$	4.93
	$\sigma_m^{VM}=\sigma_{poly}^{th}$	0.90
200	$0.5\ \sigma_u^C$	5.53
	$\sigma_m^{VM}=\sigma_{poly}^{th}$	1.20

Tab. 3-10 C/PEKK Permanent strain after recovery for each creep-recovery test condition

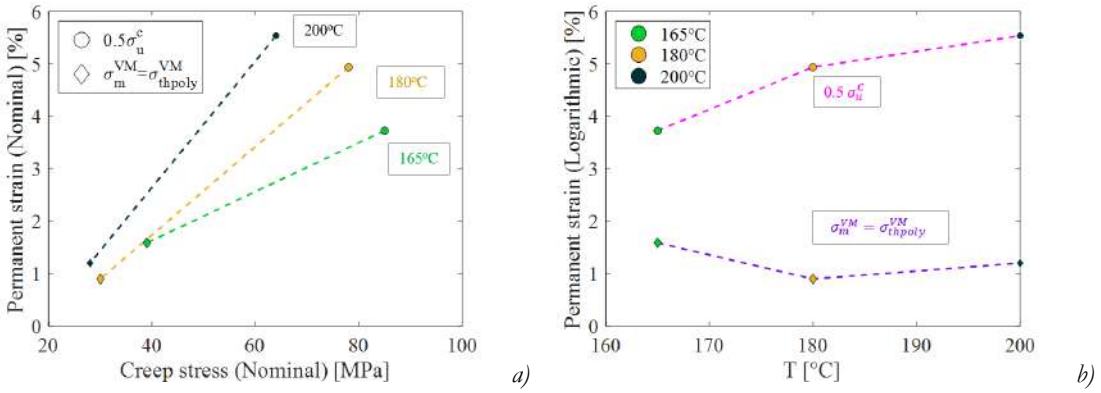

Fig. 3-23: C/PEKK Permanent strain after recovery vs test temperature (a) and creep stress (b)

No clear trend of the permanent strain with respect to the temperature can be seen, while, as expected, the permanent strain increases as the creep stress increases. The same considerations made for PEKK SC are valid for the C/PEKK.

The analysis of the permanent strain on the recovery, which could offer valuable information of the materials behavior and suggests the presence of viscoplastic behavior, is not sufficient to correlate the different curves nor to the temperature nor to the applied creep stress at iso-temperature.

3.4.3. Fiber rotation

During the creep-recovery tests on C/PEKK, similarly than for tensile tests, the fiber evolution along the test duration was measured on the specimen surface.

As example, FIG. 3-24 shows the fiber angle evolution during the creep-recovery test carried out on C/PEKK at 180°C, at creep stress equal to 0.5 σ_u^C.

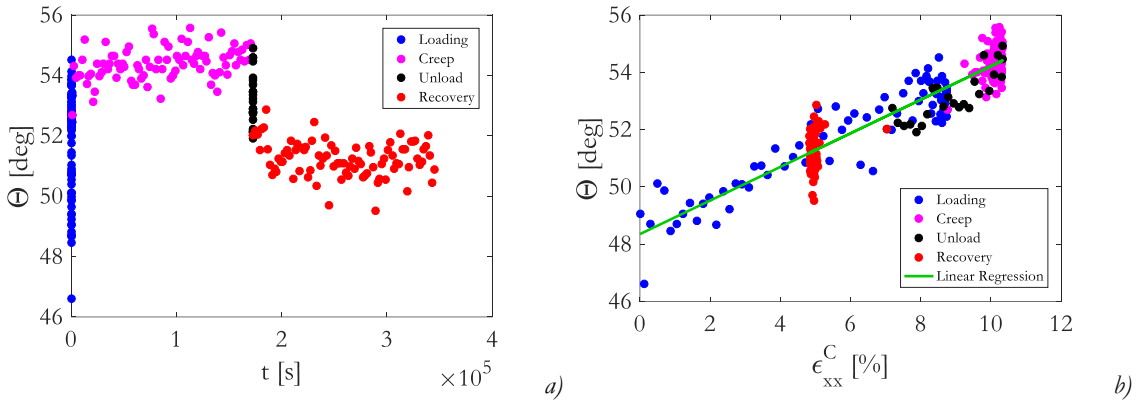

Fig. 3-24: C/PEKK Fiber orientation vs time (a) and nominal strain (b) measured during creep test at 180°C , at creep stress equal to 0.5 σ_u^C.

Comparing the fiber angle evolution during the creep-recovery test (FIG. 3-24A) with the evolution of the composite strain (FIG. 3-21), a similarity can be found. Plotting the fiber angle vs the composite strain (FIG. 3-24B) this trend is confirmed and a direct proportionality (through linear regression) can be established.

This proportionality excludes a dependence of the fiber angle on the composite nominal stress (since during creep it should result a constant angle). Moreover, considering that the composite viscous phenomena during creep are mainly due to the matrix ones, the fiber angle evolution seems strongly dependent on the matrix evolution and cannot be due to kinematics effect alone.

3.4.4. Fitting of the creep test curves

The previous paragraphs presented the difficulties related to the direct comparison of the creep-recovery strain vs time curves, suggesting the employment of a different approach and the focusing on the creep strain vs time curves alone.

For these reasons, a first attempt to investigate PEKK SC creep behavior is carried out through the fitting of the creep strain vs time curve employing the Norton-Bailey (BETTEN 2008) 3-parameters power law:

$$\dot{\varepsilon}=(A\sigma^n t^m) \qquad \textit{Eq. 3-4}$$

This equation, written for the description of metals creep behavior, could not have a direct physical correlation with mechanisms active in polymers, but it can describe coherently the PEKK SC behavior. However, since EQ. 3-4 refers to the strain rate, it has to be integrated

to be employed and, exploiting the fact that during the creep phase the stress is independent of time, in the form:

$$\varepsilon = \frac{(A\sigma^n t^{m+1})}{m+1} \quad \text{for } m > -1 \qquad \textit{Eq. 3-5}$$

In order to simplify the analysis of the different creep conditions effects, one or two parameters are fixed, for the creep phase. For instance, the comparison between the measured data and the fitted curve is presented in FIG. 3-25, with one (*n*), (A), and two (*n* and *m*), (B), fixed parameters, relatively to the data obtained from creep tests at 180°C. The power law however is not sufficient to describe the whole creep behavior and its parameters can be chosen to best fit the beginning of the strain vs time curve (producing an overestimation of the stress at high times) or the overall trend (overestimating the beginning): the last approach is chosen.

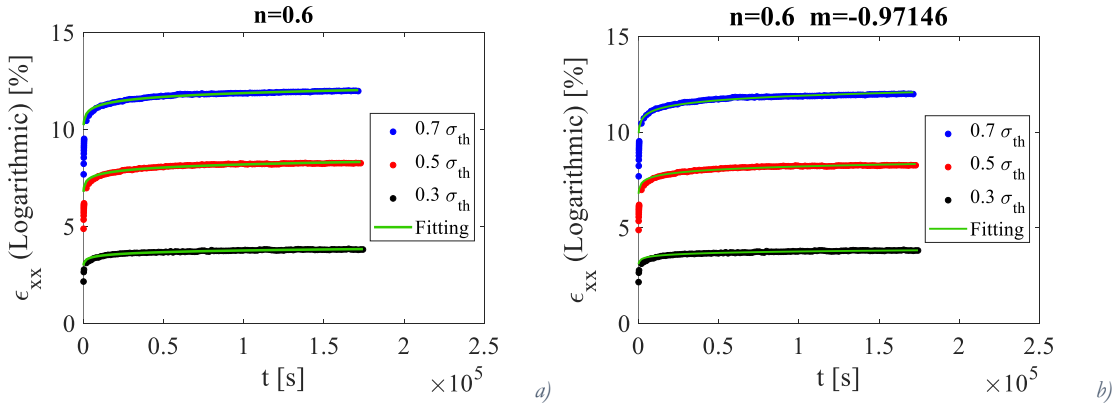

Fig. 3-25: Comparison between the PEKK 7002 SC measured data and the fitted curve, with one (n) (a), and two (n and m) fixed parameters (b), relatively at the data obtained from creep test at 180°C.

The parameters of the power law are listed in TAB. 3-11, while FIG. 3-26 shows the evolution of the free parameters with the temperature in both cases.

T[°C]	% σ_{th}	n=0.6 fixed		n=0.6 fixed, m averaged	
		A	m	A	m
165	70	0.0853	-0.9303	0.0853	-0.9304
	50	0.0576	-0.9274	0.0571	

180	30	0.0357	-0.9335	0.0361	-0.9715
	70	0.0510	-0.9762	0.0580	
	50	0.0480	-0.9718	0.0484	
	30	0.0348	-0.9664	0.0313	
200	70	0.0530	-0.9775	0.0573	-0.9749
	50	0.0332	-0.9775	0.0360	
	30	0.0247	-0.9697	0.0217	

Tab. 3-11: A, m and n parameters of creep power law for PEKK 7002 SC

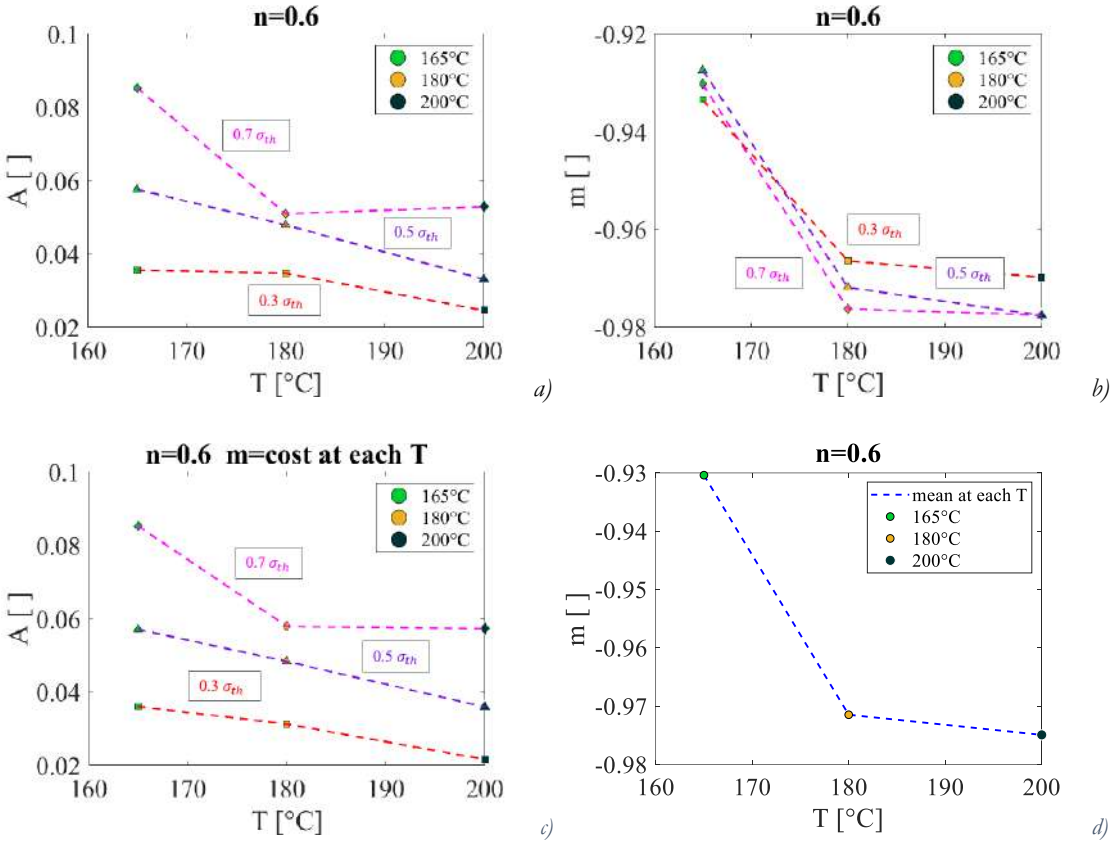

Fig. 3-26: PEKK 7002 SC A (a) and m (b) parameter of the power law plotted against the temperature (case of one fixed parameter) and A(c) parameter of the power law plotted against the temperature (case of m=cost at each temperature)

As the temperature increases, (FIG. 3-26):

- the *A* parameter, both in the cases of 1 and 2 fixed parameters (FIG. 3-26A and C) has a decreasing trend (at the same percentage of the threshold stress), and lower sensibility to the applied creep stress;
- the *m* parameter has a decreasing trend as well (FIG. 3-26B), with lower sensibility to temperature, at temperatures farer from T_g. Since it shows for any test temperature low sensibility to the applied creep stress, it is more suitable for been fixed than the *A*

parameter: hence, at each temperature, *m* is averaged and imposed for the fitting. FIG. 3-26D shows the averaged *m* parameter for each temperature, which trend is similar to the trend showed by the DMA storage modulus as the temperature increases, (CHAP. 3.3).

Several analogies observed in the creep-recovery behavior suggest a direct comparison between the creep-recovery strain vs time curve of PEKK SC and C/PEKK. Therefore, as for the PEKK SC, also the C/PEKK creep strain curves were fitted with the 3-prameters power-law described by EQ. 3-5, with both 1 and 2 fixed parameters, in both cases employing the same *n* parameter identified for PEKK SC.

For instance, the comparison between the measured data and the fitted curve is showed in FIG. 3-27, with one (*n*) (A) and two (*n* and *m*) (B) fixed parameters, relatively at the data obtained from creep tests at 180°C.

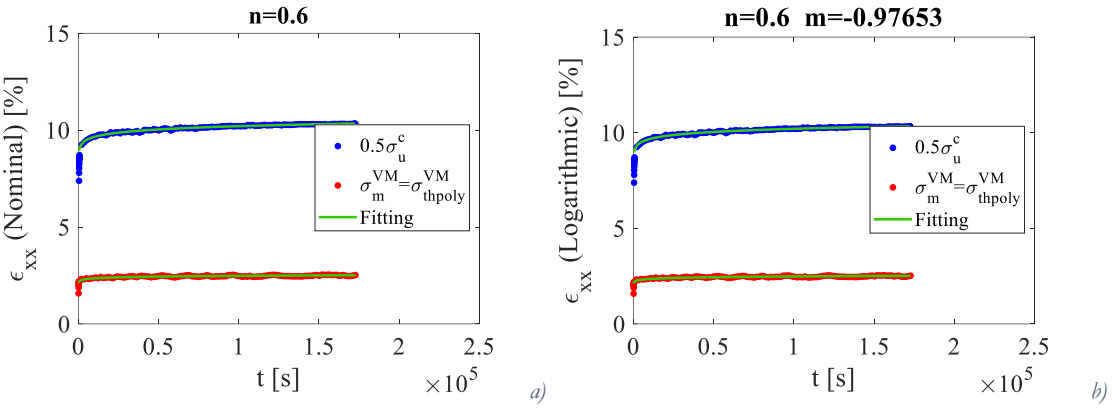

Fig. 3-27: Comparison between the C/PEKK measured data and the fitted curve, with one (n) and two (n and m) fixed parameters, relatively at the data obtained from creep test at 180°C.

The parameters of the power law are listed in TAB. 3-12, while FIG. 3-28 shows the evolution of the free parameters with the temperature in both cases.

T[°C]	Condition	n=0.6 fixed		n=0.6 fixed, m averaged	
		A	m	A	m
165	0.5 σ_u^C	0.0098	-0.9757	0.0105	-0.9732

	$\sigma_m^{VM}=\sigma_{poly}^{th}$	0.0094	-0.9707	0.0088	
180	$0.5\ \sigma_u^C$	0.0137	-0.9759	0.0134	-0.9765
	$\sigma_m^{VM}=\sigma_{poly}^{th}$	0.0056	-0.9772	0.0058	
200	$0.5\ \sigma_u^C$	0.0119	-0.9834	0.0139	-0.9797
	$\sigma_m^{VM}=\sigma_{poly}^{th}$	0.0068	-0.9759	0.0060	

Tab. 3-12: A, m and n parameters of creep power law for C/PEKK

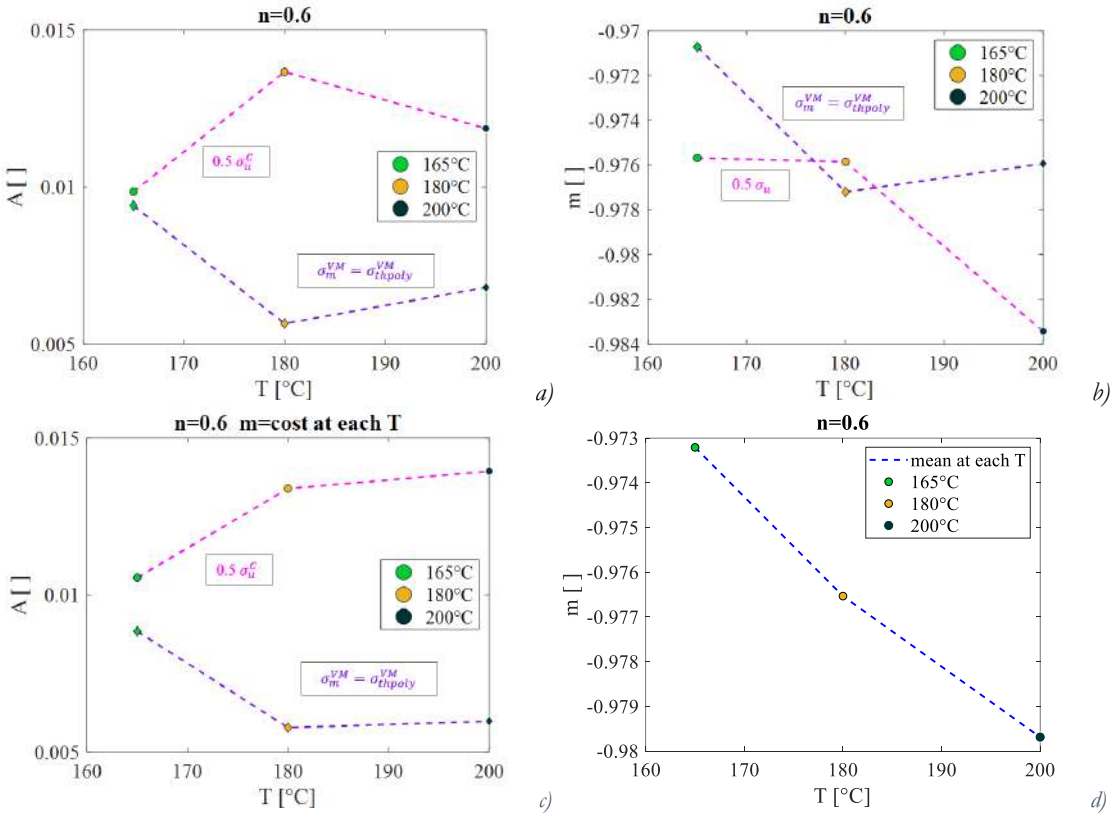

Fig. 3-28: C/PEKK A (a) and m (b) parameter of the power law plotted against the temperature (case of one fixed parameter) and A(c) parameter of the power law plotted against the temperature (case of m=cost at each temperature)

As the temperature increases, (FIG. 3-28):

- the A parameter, both in the cases of 1 and 2 fixed parameters (FIG. 3-28A and C) shows different trend for creep stress in the fibers region ($0.5\ \sigma_u^C$) and in the matrix region ($\sigma_m^{VM}=\sigma_{poly}^{th}$). The evolution of A in the matrix region with the temperature, in the case of 2 parameters fixed, is qualitatively identical to the PEKK SC A parameter (FIG. 3-26C) in the case of the highest creep stress ($0.7\sigma_{th}$): even if in the case of PEKK SC the fitting is on the logarithmic strain, while for C/PEKK is made on nominal strain, it has be noticed that the identified parameters are in a constant ratio of 1/10 at each temperature;

- the *m* parameter has a different trend as well (FIG. 3-28B), for 1st and 2nd creep stress levels. However, the range of values is smaller (0.014), compared to PEKK SC (0.06) (FIG. 3-26B): therefore, once averaged, the resulting fitting (FIG. 3-27B) is not far from the previous one, with free *m* parameter (FIG. 3-27A). Looking at the averaged *m* trend, (FIG. 3-28D) it is closer to a linear behavior with the temperature, compared to the PEKK SC one (FIG. 3-26D).

The fitting of the creep strain vs time curves with Norton-Bailey power law, provides with a valuable tool for the qualitative comparison of the creep strain curves of the same material, and it will be employed in CHAPTER 6 for the comparison of creep tests carried out on C/PEKK under different environmental conditions.

Even if a correspondence can be found between PEKK SC and C/PEKK, it could not be considered the definitive prove of a correlation between the two materials. Further and more detailed investigation is presented in the next chapter.

3.4.5. Creep compliance mastercurve

Once evaluated the PEKK SC creep compliance as:

$$J=\frac{\varepsilon_{xx}}{\sigma_{xx}} \qquad \textit{Eq. 3-6}$$

at each testing condition, a time-temperature superposition is evaluated, according to the Williams-Landel-Ferry (WLF) model (M. L. WILLIAMS, LANDEL, AND FERRY 1955). Since the creep tests were carried out at different stresses at different temperatures, a 2 steps procedure is employed:

1. a first WLF law is employed to find a superposition at each temperatures, through the equation

$$\mathrm{Log}_{10}(a_\sigma)=\frac{C_1(\sigma-\sigma_{min})}{C_2+(\sigma-\sigma_{min})} \qquad \textit{Eq. 3-7}$$

   where σ_{min} is the lowest creep stress applied and a_σ is the time shifting factor related to the applied creep stress;

2. a second WLF law is employed to superpose all the resulting curves, through the form:

$$\mathrm{Log}_{10}(a_t)=\frac{C_3(T-165°C)}{C_4+(T-165°C)} \qquad \textit{Eq. 3-8}$$

The coefficient values are listed in TAB. 3-13:

T [°C]	σ_{min} [MPa]	C_1	C_2	C_3	C_4
165	5	7	9.5		
180	4.5	12	14	10	35
200	4	45	35		

Tab. 3-13: .Coefficients of WLF law at each test temperatures

FIG. 3-29 shows the curve resulting employing the identified coefficients.

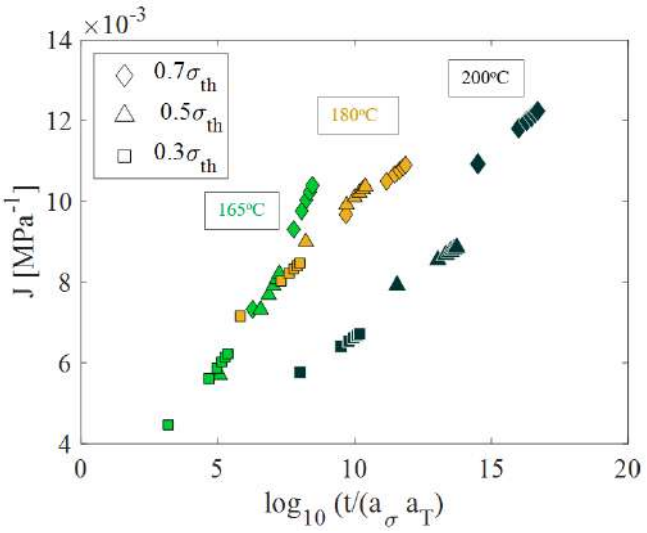

Fig. 3-29: WLF law applied to the creep compliance of the semicrystalline PEKK

As showed in FIG. 3-29, it is not possible to obtain a master curve of the creep compliance, and as consequence it can be concluded that PEKK SC is not rheological simple, and that it has a complex behavior instead.

An analogous attempt to identify the creep compliance mastercurve was carried out on C/PEKK creep compliances. The results are showed in FIG. 3-30 and the identified coefficient of the WLF laws are listed in TAB. 3-10.

T [°C]	σ_{min} [MPa]	C_1	C_2	C_3	C_4
165	39	2	1.2		
180	30	10	5	5	100
200	28	12	10		

Tab. 3-14: .Coefficients of WLF law at each test temperatures

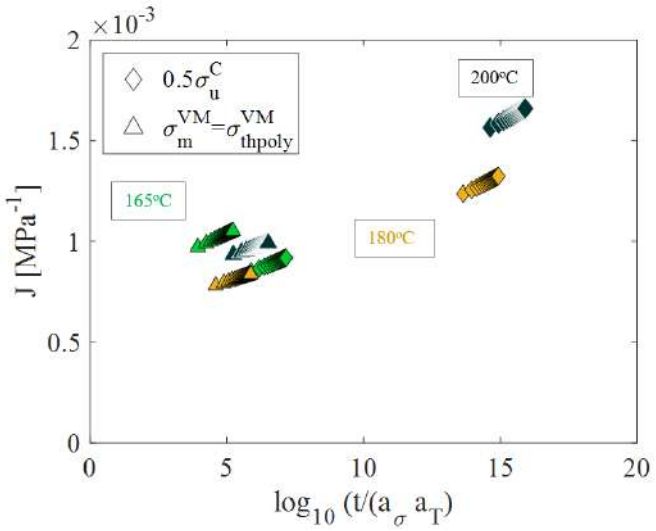

Fig. 3-30: WLF law applied to the creep compliance of the semicrystalline PEKK

In the case of C/PEKK the results are worse than for PEKK SC, because of the difference registered in the material response to the different creep stress levels (the first in the fiber dominated region and the second in the matrix dominated region), which appeared in the different A parameter trend (FIG. 3-28C).

This is however coherent with the results PEKK SC not rheological simple behavior, suggesting that also in presence of fibers, the matrix behavior strongly influences the composite behavior.

3.5. DSC tests

The previous paragraphs described the tests carried out on PEKK SC and C/PEKK for their thermomechanical characterization and the general outlines of their behavior. In order to complete their physical-chemical characterization, DSC tests carried out on both materials are presented below.

DSC tests were carried out on PEKK 7002 SC and C/PEKK specimen type *f* (FIG. 2-5), cut from as-received materials (*reference*), according to the testing protocol described in (CHAP. 2.3.1.4).

In FIG. 3-31, the typical heath flow vs temperature curve is showed.

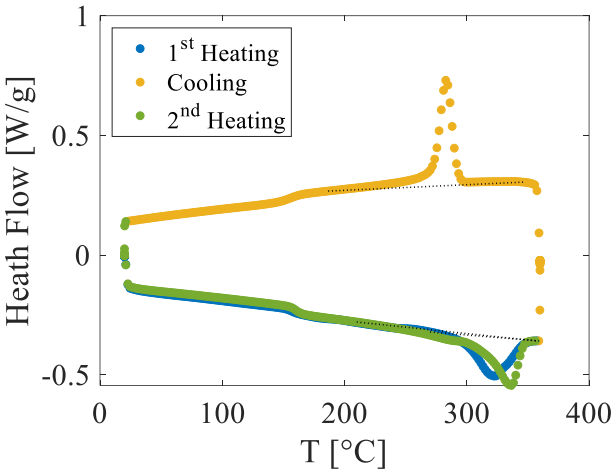

Fig. 3-31: Typical heath flow vs temperature curves obtained from DSC test on PEKK 7002 SC

Because of the presence of the fibers, it is not possible to precisely determine the mass of the matrix inside the samples, therefore the comparison with the DSC carried out on the PEKK SC, showed in FIG. 3-32, can only be qualitative.

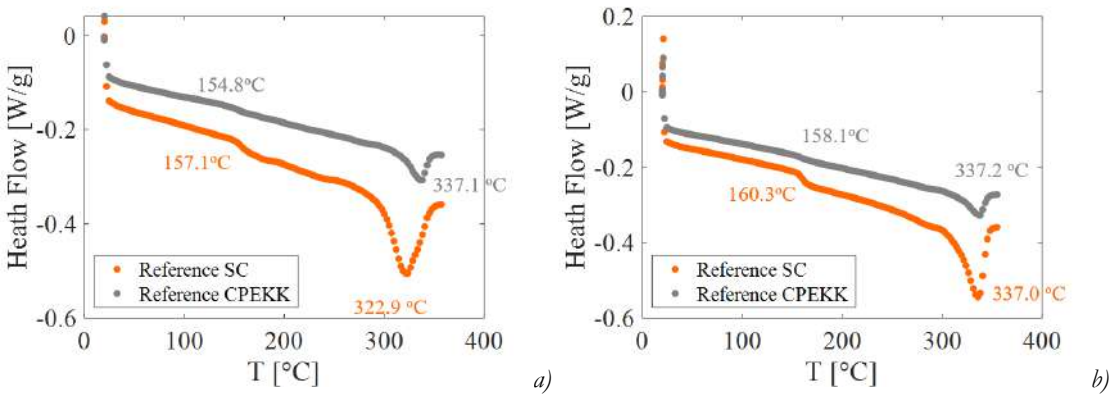

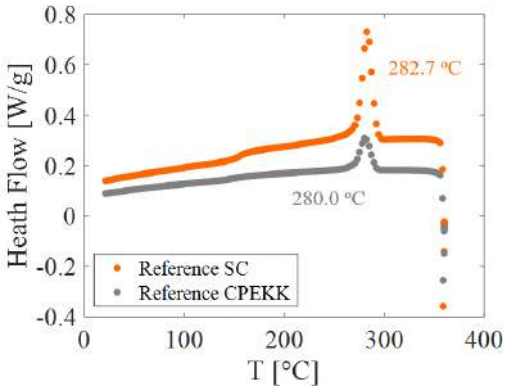

c)

Fig. 3-32: 1st (a), 2nd heating (b) and cooling (c) phases comparison from DSC test on C/PEKK and PEKK 7002 SC samples cut from as-received material

The measured values of T_g and T_m for 1st and 2nd heating and cooling phases; are listed in TAB. 3-15.

	PEKK SC As received	C/PEKK SC As received
1st Heating		
T_g [°C]	157.1	154.8
T_m [°C]	322.9	337.1
2nd Heating		
T_g [°C]	160.3	158.1
T_m [°C]	337.0	337.2
Cooling		
T_p [°C]	282.7	280.0

Tab. 3-15: T_g and T_m measured from DSC test on PEKK 7002 SC and C/PEKK samples cut from as-received material

Both PEKK SC and C/PEKK show no presence of the exothermic peak, suggesting that the matrix inside the composite, as in PEKK SC, reached the maximum crystallinity percentage during manufacturing process.

The heat flow vs temperature curves during 1st heating phase, (FIG. 3-32A), shows difference values of T_g (-3°C) and melting peak values (+15°C), possibly because of morphological difference in the crystal phases of the two materials.

Lower differences (< 2°C) appear in 2nd heating and cooling phases (FIG. 3-32B and C), possibly because the crystalline phase produced after the 1st melt is more similar than the one produced during the manufacturing process.

The comparison between 1st heating and the following cooling and 2nd heating seems to confirm difference exists between the composite matrix and the neat polymer. The difficulty

of measure the crystalline percentage in the composite matrix, exclude this parameter as indicator. However, information could be deduced from the differences in T_g and T_m, which suggest that a difference if not in amount, at least in morphology of the crystal structure is present between the matrix and the neat polymer.

3.6. Semi-analytical homogenization-localization method for the interpretation of test results

The similarity between PEKK SC and C/PEKK described in the previous paragraphs leads supposing that the matrix inside the composite behaves as the polymer, at least at macroscopic level. However, the manufacturing process employed for C/PEKK (CHAP. 2.2.1.2), which includes a complete matrix melting and a subsequent cooling, even if it carried out at cooling rate granting the reaching of the maximum crystallization phase, could affect the matrix behavior: this could lead to differences between the PEKK SC as pure polymer and as composite matrix, because of the interaction with fibers during the crystallization (TANGUY CHOUPIN 2018).

In order to assess if there is a similarity in behavior between matrix and pure polymer, the hypothesis that the composite matrix has the same properties of PEKK 7002 SC is made. Under that hypothesis, it should be possible to reconstruct the behavior of the C/PEKK starting from the properties of PEKK SC and considering:

- the fibers as a transversal isotropic linear elastic material;
- a perfect bond between matrix and fibers;
- that above T_g, the C/PEKK reaches its free stress temperature and no thermal effect appears;
- no interply effect;
- the stress in the matrix as averaged and constant in the space;
- the non-linearity in C/PEKK behavior depends only on the non-linearity in PEKK SC behavior.

In fact, because of the low strain non-linearity in C/PEKK tensile behavior, significant error is produced in the reconstruction of C/PEKK behavior starting from polymer and fibers properties through *homogenization* methods (HM) (CHAP. 2.3.3.1). Those methods, in fact, are developed under the hypothesis that the composite has a linear elastic behavior. Therefore, depending on the properties assigned to the matrix (supposed linear elastic), those methods allow obtaining reconstructed curves which could only be tangent or secant to the experimental C/PEKK curves.

The matrix non-linearity cannot be taken into account in homogenization methods, because they do not provide any information on matrix stress or strain, and no link could be established between the applied composite stress (or strain) and the matrix ones.

This can be instead achieved employing *localization* methods (LM) (CHAP. 2.3.3.2), which can easily be linked as showed in FIG. 3-33, obtaining a linear elastic analytical method.

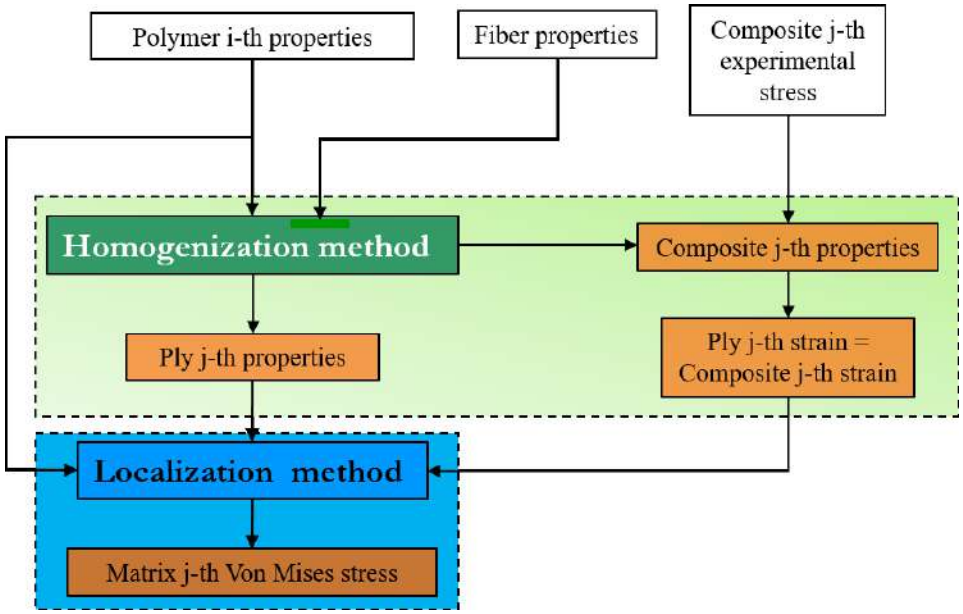

Fig. 3-33: Linear elastic analytical method algorithm

The resulting method, however, still allows inputing only one value of polymer properties and, for each value of the composite experimental stress, it calculates, as output:

- from HM, the composite properties and strain; the ply properties, strain and stress;
- from LM, the matrix stress and strain.

For a uniaxial composite stress applied, the resulting stress vs strain composite curve is a straight line (linear behavior) which slope is depending on the input matrix properties.

In order to introduce the polymer non-linearity in the method:

1- *the matrix stress has to be compared to the polymer stress.* In the ply reference system, the matrix stress resulting from the LM, because of the plane stress hypothesis in HM, has the form:

$$\boldsymbol{\sigma}_{\mathbf{m}} = \begin{bmatrix} \sigma_{11}^{m} & \tau_{12}^{m} & 0 \\ \tau_{12}^{m} & \sigma_{22}^{m} & 0 \\ 0 & 0 & \sigma_{33}^{m} \end{bmatrix} \qquad \textit{Eq. 3-9}$$

which is completely different form the uniaxial stress state produced in the polymer under tensile load. In order to compare it with the polymer stress state, only its deviatoric part, in the form of Von Mises stress (EQ. 3-10) is equalized to polymer Von Mises stress (which in the case of uniaxial tensile load is equal to the longitudinal stress, EQ. 3-11).

$$\sigma_m^{VM}=\sqrt{\frac{1}{2}\left[(\sigma_{11}^m-\sigma_{22}^m)^2+(\sigma_{22}^m-\sigma_{33}^m)^2+(\sigma_{33}^m-\sigma_{11}^m)^2+6\left(\tau_{12}^{m,2}+\tau_{23}^{m,2}+\tau_{31}^{m,2}\right)\right]} \qquad \textit{Eq. 3-10}$$

$$\sigma_{poly}^{VM}=\sigma_{xx}^{poly} \qquad \textit{Eq. 3-11}$$

2- *the polymer stress has to be related to the polymer properties*. In order to relate the polymer Von Mises stress (and hence its longitudinal stress) to its properties, the tensile test bijectivity property is exploited: in fact, during tensile test, the monotonic functions describing the resulting stress, strain and properties variation with time, can all be related to each other, such that at time *t(i),* a single value of stress, strain and properties results (FIG. 3-34). In the need of the model, this translate with the fact that for each value of longitudinal strain corresponds one and one only value of polymer properties (in the form of secant modulus E_{xx} and Poisson's coefficient ν_{xy}).

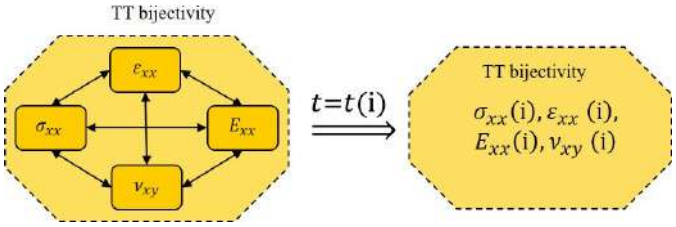

Fig. 3-34: Tensile test bijectivity property between stress, strain, secant modulus and Poisson's coefficient

The non-linearity is then introduced in method in the following way, for each *j*-th value of the composite stress:

- the fiber angle is evaluated from the *j*-th value of the composite stress, according to the experimental observations (CHAP. 3.2.3), and the equation and parameters showed in TAB. 3-3;
- a *i*-th guess of polymer properties is input, as in the linear elastic model, calculating the same outputs;
- the resulting matrix Von Mises stress is equalized to the polymer Von Mises stress, and exploiting tensile bijectivity, the correspondent values of polymer longitudinal secant modulus is evaluated. The latter is compared to the input polymer longitudinal secant modulus: if their difference is less than 2 MPa, the output are confirmed for the *j*-th value of the composite stress. Otherwise, the input polymer properties are update with the resulting ones and the loop is continued until convergence is reached (for the tested cases, the method takes less than 20 iterations).

The algorithm of the non-linear semi-analytical method is showed in FIG. 3-35.

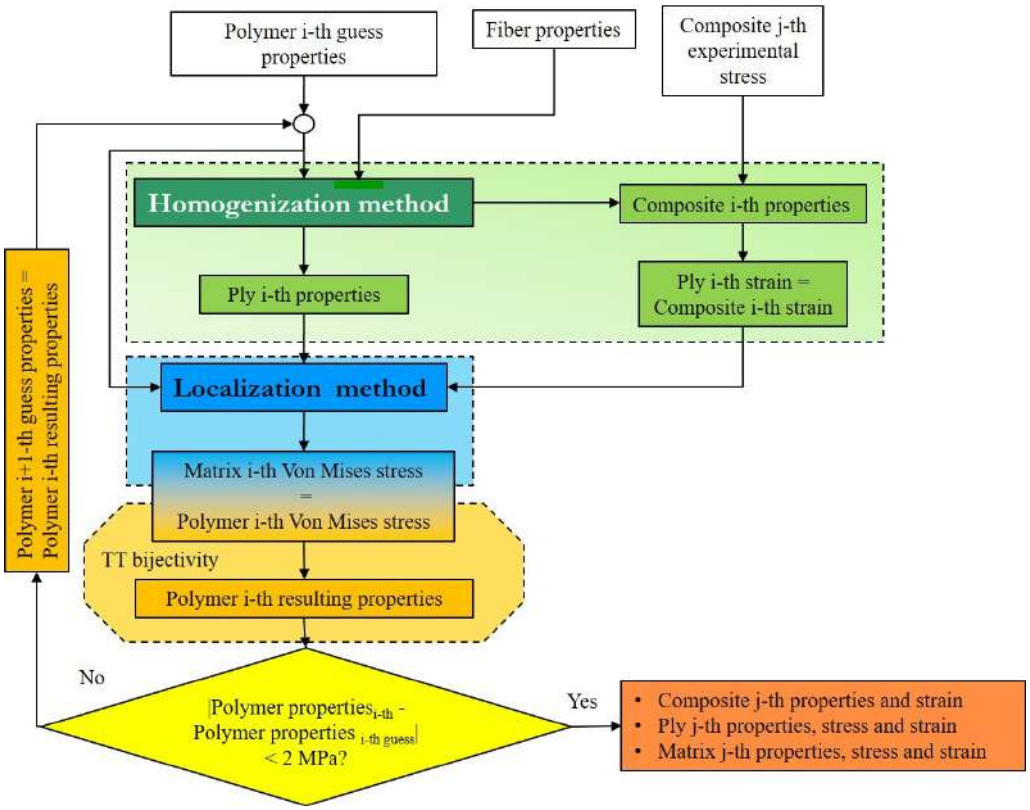

Fig. 3-35: Non-linear analytical method algorithm

The reconstructed C/PEKK tensile test curves at 1 mm/min and at 165°C, 180°C and 200°C are showed in FIG. 3-27.

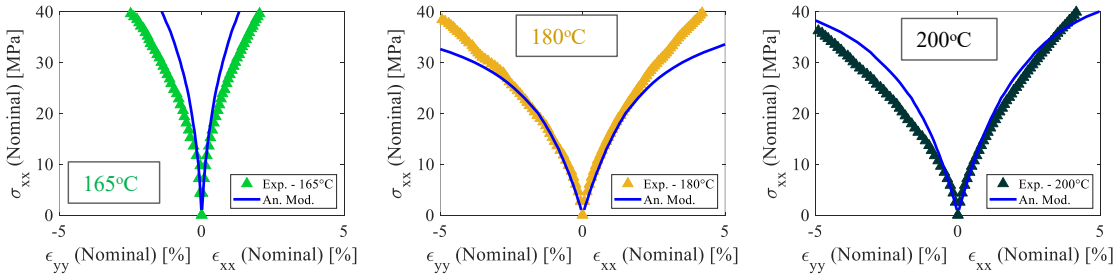

Fig. 3-36: Comparison between experimental tensile test on C/PEKK at 1 mm/min 165°C, 180°C and 200°C and the non-linear semi-analytical method

FIG. 3-27 shows that the model is capable of describing the initial part of the curves, diverging rapidly at middle strains, while at higher strains no convergence is reached.

The most important considerations deriving from the good agreement between the experimental results and the model, are that, even if physical – chemical tests showed differences between the composite matrix and the neat polymer behavior, at macroscopic

scale, those differences are limited. Moreover, this is valid to the small range strains in composite behavior, or until the fibers become dominant in the C/PEKK behavior, confirming the existence of a matrix dominated region.
The semi-analytical homogenization/localization method is capable of differentiate the stress state in the different oriented plies, as well as the composite and ply properties at each step of the calculation (ANNEX H).

3.7. Conclusions

The present chapter is focused on the characterization of the tensile and creep thermomechanical behavior of PEKK SC and C/PEKK composite in the transition from below to above T_g. Since the simplest tests, a complex behavior emerged in both materials, and only their general outlines are presented.

The present chapter is focused on the qualitative comparison of their behaviors. In particular:

- both material experience a significant loss of mechanical loss in the transition above T_g (-90% and -80% respectively), as emerged from tensile tests and confirmed through DMA tests;
- the PEKK SC shows a tensile non-linear behavior, with a complex temperature and time dependence. In C/PEKK, a matrix dominated (low strain) and a fiber dominated (high strain) regions can be identified: in the first, the same tensile behavior of PEKK SC can be identified, while the latter express a more linear behavior;
- creep-recovery tests, carried out in both materials shows significant similarities: both do not show tertiary creep failure, but the presence of permanent strain after recovery, suggesting the presence of pseudo-plastic phenomena in both materials;
- the creep strain fitting through the Norton-Bailey power law was employed for the comparison of the curves: while no clear trend of the fitting parameters emerged for both materials, a similarity can be found comparing the evolution of the parameters with the temperature in the most similar creep condition;
- DMA and DSC showed a similar global evolution with temperature but also differences in the measured values of T_g onset.

The previous considerations suggest that while physical-chemical differences between polymer and matrix are present, possibly due to differences in the crystal morphology and because oh the presence of the carbon fibers (the trans-crystallinity observed in C/PEKK), those same differences have a limited impact on the thermomechanical behavior, which is instead similar, in the limit of the composite matrix dominated region.

A prove of this hypothesis comes from the semi-analytical homogenization/localization method, allowing linking linear elastic homogenization and localization methods and taking also into account the matrix non-linearity. Through this method, starting from the PEKK SC tensile properties, the C/PEKK low strain tensile curve is reconstructed at all the temperatures above T_g and the ply and composite initial properties are calculated.

The semi-analytical model has the limit of requiring the PEKK SC experimental data and exploits the bijectivity intrinsically related to tensile tests, between stress – strain-properties, which is no more valid during creep stress.

However, it shows the connection between polymer and matrix, and the feasibility of an approach which presents the possibility of simulate different fibers percentage contents,

different ply orientation and/or different stacking sequences without needing a specific behavior law for each configuration.

The need of the neat polymer experimental data can be overcome if the different mechanisms active during each different loading phase are identified and analytically described, as it is proposed in the following chapter. Moreover, this allows also extending the capability of simulation to the creep phase. The implementation of the analytical description in the model and its simulation capabilities and limits are presented in CHAPTER 5.

Chapter 4 – Characterization of PEKK thermomechanical and creep behavior above T_g

The present chapter aims at the identification of the mechanisms activated by the different thermomechanical loads at temperatures above T_g, as experienced in tensile, load-unload-reload and creep-recovery tests. The crystallization kinetics between 165°C and 200°C is described and the coupling with thermomechanical solicitations is investigated. An analytical description of the identified mechanisms is proposed and it constitutes a 1-D model of PEKK 7002 SC, which is employed for understanding the experimental results. The 7002 AM behavior is investigated in order to support the understanding of PEKK SC behavior.

4.1. Introduction

The outlines of the PEKK SC behavior in the transition above T_g, as described in the previous chapter, revealed a complex scenario, where the material mechanical properties depend on the applied temperature, the stress (strain) and the time (stress (strain) rate).

In particular, during creep-recovery tests, viscous effect has to be expected, producing the activation of time-dependent mechanisms which could be different from the ones activated during tensile tests. The difficulties in obtaining of a time-temperature superposition excludes a creep linear viscoelastic behavior, while the presence of permanent strain at the end of creep-recovery tests suggests a rather viscoplastic behavior.

Moreover, the attained maximum crystallinity percentage during manufacturing process (CHAP. 2.2.1.1), does not exclude that the exposure to thermomechanical loading could affect the crystalline structure, modifying its morphology or providing the necessary energy to increase its percentage.

Furthermore, from the transition above T_g, the percentage of crystallinity phase in PEKK has an almost total dominance in the definition of its mechanical properties (CHAPTER 1) and hence any change in the crystalline phase could have a not-negligible effect on the material behavior. However, this would imply a material dependency also on the crystalline phase, which could be dependent itself by the applied temperature, the exposure time and by the interaction with the different load conditions.

In fact, according to the creep test protocol (CHAP. 2.3.1.2), 4 different load conditions can be identified:

1. *Load*;
2. *Creep*;
3. *Unload*;
4. *Recovery*.

Each phase could interact differently with the crystalline structure or could have no effect at all. The effect cannot be established a priori and, moreover, cannot be deduced directly by the tests showed in the previous chapter.

The tensile, creep-recovery tests, as well as DMA and DSC tests on as received material can provide with valuable information, but not sufficient to isolate and identify the different mechanisms, nor the interaction with the crystalline phase. In order to provide with the missing elements, complementary tests were carried out:

- *Load-unload-increase* tests, aimed to more precisely define the mechanisms involved during load (and hence reload) and unload and to differentiate them from the mechanism active during creep and recovery. In addition, Load-Unload-Reload tests, with recovery phase at end of each load-unload loop were carried out, enabling to distinguish the effect of the creep on the recovery;

- *DSC tests on previously tested specimens*, to compare the effect of the thermomechanical loads on the crystallinity phase. Those tests allow the description of the kinetics of crystallization at the different test temperatures above T_g and the coupling between thermomechanical loads and crystallinity variation.

Exploiting the results of all the above mentioned tests, the present chapter aims to provide with a more detailed analysis of PEKK SC behavior, and to identify and analytically describe the different mechanisms activated during the different thermomechanical conditions applied to PEKK SC and the effect of the latter on the crystalline structure.

The analysis allows the definition of a 1-D model for the analytical description of PEKK 7002 SC behavior from 165°C and 200°C. The model formalism is proposed as well as its comparison with the experimental data at the different temperatures.

In order to complete the analysis of PEKK SC, some aspects of the behavior of its amorphous phase of PEKK SC, are deduced from the characterization of PEKK 7002 AM composed by the results of tensile, load-unload-reload, DMA and DSC tests, presented in the last paragraph of the present chapter.

4.2. Analysis of the PEKK SC thermomechanical behavior above T_g

The tensile and creep-recovery tests presented in the previous chapter were carried out under monoaxial longitudinal load conditions. The strain measurement system employed during those tests (and described in CHAP. 2.3.2), allows registering both longitudinal and transverse behavior. Moreover, the verification of the transversal isotropy (ANNEX D), also allows deducing the behavior in the thickness direction.

In order to further investigate the behavior and define the relations between the elements composing the PEKK SC stiffness tensor, especially above T_g, the volumetric changes occurring because of thermal and thermomechanical loads are investigated.

4.2.1. Volumetric changes

During the tests, images of the specimen gauge length were acquired. Those images were processed with both IdPix and IAT and, under the transversal isotropy hypothesis, the volumetric changes are calculated both as the trace of the strain tensor, under the transversal isotropy hypothesis, according to:

$$\frac{\Delta V}{V_0} = \varepsilon_{xx} + 2\varepsilon_{yy} \qquad \textit{Eq. 4-1}$$

and employing IAT calculation algorithm, with the Total Lagrangian formulation, under the transversal isotropy hypothesis, according to EQ. 2-15.

As representative of thermal and thermomechanical load conditions, the volumetric changes during the heating phase (thermal load from room temperature to 200°C) and during the different tensile tests (thermomechanical load at different temperatures) are presented.

4.2.1.1 Volumetric changes during the heating phase

Each tensile test at temperature above the room temperature was preceded by the heating phase described in CHAP. 2.3.1.2, according to EQ. 2-15.

FIG. 4-1 shows the comparison between the volumetric changes occurring during the heating phases from room temperature up to 165°C, 180°C and 200°C, obtained from averaging the measures obtained from all the tests carried out up to the same temperatures. Because of the small strain measured and the progressively increased temperature, producing

variation in the markers paint, the IdPix measurement were significantly affected by noise, which was corrected through the employment of IAT. Only those results are showed.

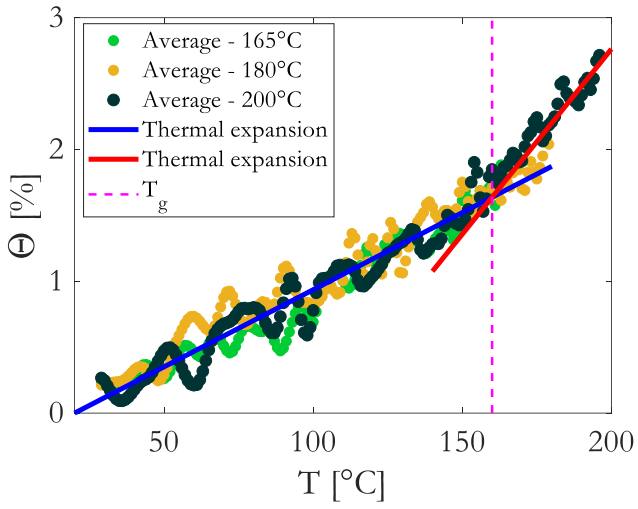

Fig. 4-1: PEKK 7002 SC Volumetric change measured during tensile tests heating phase

The curves showed in FIG. 4-1 show a change of slope at around 160°C, confirming the estimated value of T_g for PEKK SC at around 160°C. Moreover, this particular trend is coherent with the presence of physical ageing below T_g, as shown in (BRINSON AND GATES 1995).

The volumetric changes below and above T_g, can be approximated by linear regression, providing with the volumetric thermal expansion coefficients, as:

$$\Theta=\begin{cases}\alpha_{V1}\,(T-T_0) & \text{if } T\leq T_g\\ \alpha_{V2}\,(T-T_g)+\Theta_{T_g} & \text{if } T\geq T_g\end{cases} \qquad \textit{Eq. 4-2}$$

where T_0 = 20°C and $\Theta_{T_g}=\alpha_{V1}\,(T_g-T_0)=1.638\,\%$ is the value of the volumetric changes in correspondence of T_g, employed as continuity condition.

If the material is supposed to have isotropic thermal properties, the linear thermal expansion coefficients (α_i) can be obtained from the volumetric ones. The volumetric and linear thermal expansion coefficients are listed in TAB. 4-1.

	Thermal expansion coefficient $\left[\frac{10^{-6}}{°C}\right]$	
	$\alpha_i = \frac{1}{3}\alpha_{Vi}$	α_{Vi}
i=1	39.0	117.0
i=2	93.7	281.0

Tab. 4-1: PEKK 7002 SC Thermal expansion coefficients below and above T_g

4.2.1.2 Volumetric changes during the tensile tests

The analysis of the volumetric changes during the tensile tests is carried out starting from the end of the analysis of volumetric changes during the heating phase and shifting to zero all the measured values of strain. The values measured by IdPix and IAT are showed, respectively in FIG. 4-2A and FIG. 4-2B.

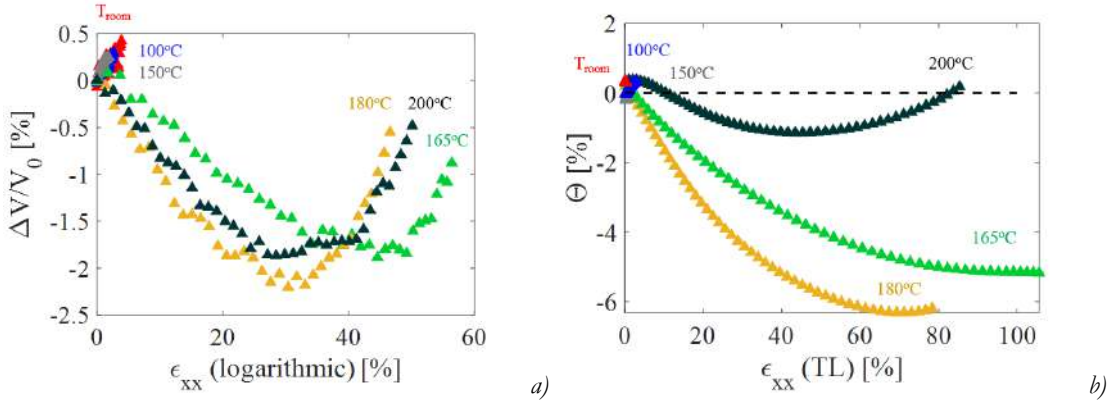

Fig. 4-2: PEKK 7002 SC volume change from tensile tests at different temperature at 1 mm/min, according to logarithmic formulation (a) and Total Lagrangian formulation (b)

From FIG. 4-2, it appears that, while a positive volume change is measured for test temperatures below T_g, this becomes negative for temperatures above T_g.

A negative volume variation is physically impossible according to classic mechanics and could be due to the necking along the overall gauge length, which affects the measures (especially in the transverse direction), to internal morphological changes (at iso-crystallinity) as crystal alignment towards the loading direction or to a change in crystal shape.

The ratio between the transversal and longitudinal strains allows the evaluation of the Poisson's coefficient between the two directions, according to:

$$\nu_{xy} = -\frac{\varepsilon_{yy}}{\varepsilon_{xx}} \qquad \textit{Eq. 4-3}$$

In FIG. 4-3, the comparison between the Poisson's coefficient at the different temperature is showed.

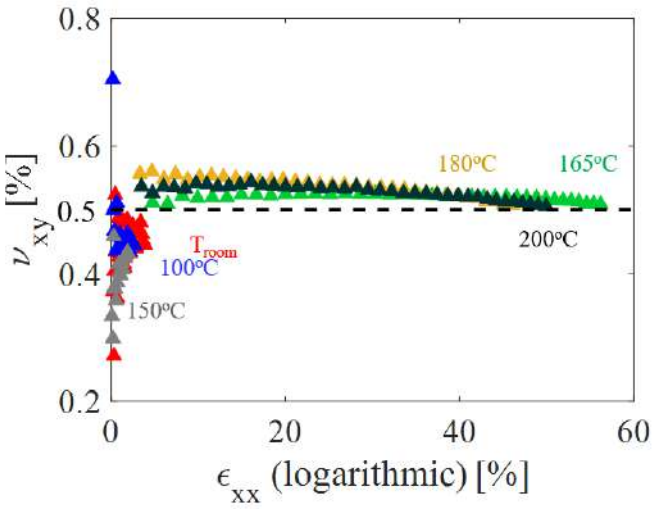

Fig. 4-3: PEKK 7002 SC Poisson's coefficients from tensile tests at different temperature at 1 mm/min

From FIG. 4-3 it appears that while the Poisson's coefficient is lower than 0.5 at temperature below T_g, it exceeds 0.5 above T_g, coherently with the measured negative volume variation.

Because of the previous considerations, and because of the small value exceeding 0.5, the Poisson's coefficient is considered close to 0.5 above T_g and hence PEKK SC is assumed to have an **incompressible behavior above T_g**.

The hypothesis of incompressibility leads to the consequence that the behavior in the transversal and in the thickness direction can be directly derived from the longitudinal behavior, significantly simplifying the analysis of PEKK SC behavior above T_g. For this reason, the following analysis is carried only on the longitudinal direction.

4.2.2. Load-Unload-Reload tests

As mentioned in the introduction of the present chapter, Load – unload - reload tests (CDP) are constituted by a combination of the same load conditions than tensile and creep tests, which can be directly compared with the other tests, as:

- first load and following reload, which can be compared with the tensile tests and investigate the effect of the unloads on the reloads: this comparison could provide with more elements to identify the mechanisms active during the load;
- unload, which can be compared to the unload after creep (in creep-recovery tests), to determine the effect of the creep on the unload and, going upward, to deduce the mechanisms active during creep.

Load – unload - reload tests (CDP) were carried out on PEKK 7002 SC specimen type *b* (FIG. 2-5), according to the testing protocol described in (CHAP. 2.3.1.2). The CDP test parameters are summarized in TAB. 4-2.

T [°C]	ż [mm/min]	%σ_{th}	σ_i [MPa]
165	1	30, 50, 70	5, 8, 12
180	1	30, 50, 70	4.5, 8, 11
200	1	30, 50, 70	4, 7, 10

Tab. 4-2: CDP test parameters for PEKK 7002 SC

The results of the CDP tests are summarized in FIG. 4-4, and compared with tensile tests at 1 mm/min at the same temperatures

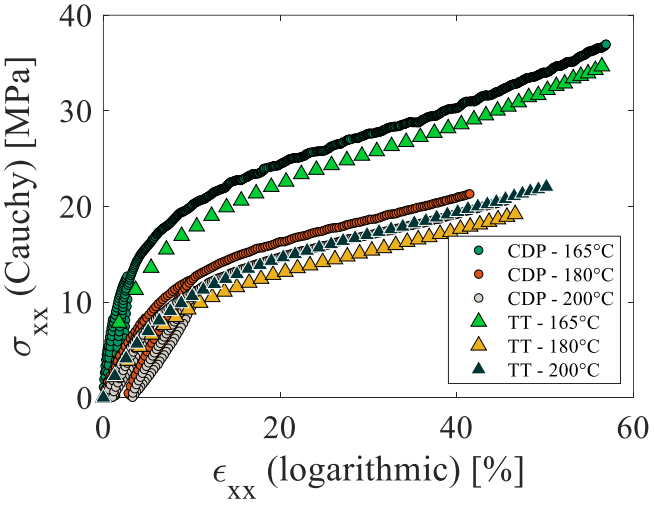

Fig. 4-4: Stress vs strain curves obtained from CDP test on SC PEKK and at 165°C, 180°C and 200°C, compared with the stress vs strain curves obtained from tensile test at 1 mm/mina at the same temperatures

FIG. 4-4 shows that:

- the CDP tests follow the tensile tests trend, superposing in the case of 200°C, after each loop, and the loop has no effect on the following behavior. This imply that the tensile behavior has no time dependency, and the PEKK SC reaches the same state in the stress vs strain domain after the time t_T (tensile) and t_T+t_L (t_L = time needed to carry out the loop). The differences showed at the other temperature can be due to the variability related to the temperature sensibility (CHAP. 3.3).
- the temperature effect showed on tensile tests, (CHAP. 3.2.1), is visible also for CDP tests, with lower temperature sensibility as the temperature is raised farer from T_g.

The test temperature of 200°C is the more stable in terms of material properties and testing reproducibility: moreover, it matches the maximum temperature of the Instron 4505 oven, and hence, less sensible to measurement errors.

FIG. 4-5 shows the comparison between CDP and tensile tests carried out at 200°C and 1 mm/min, limited to low strain.

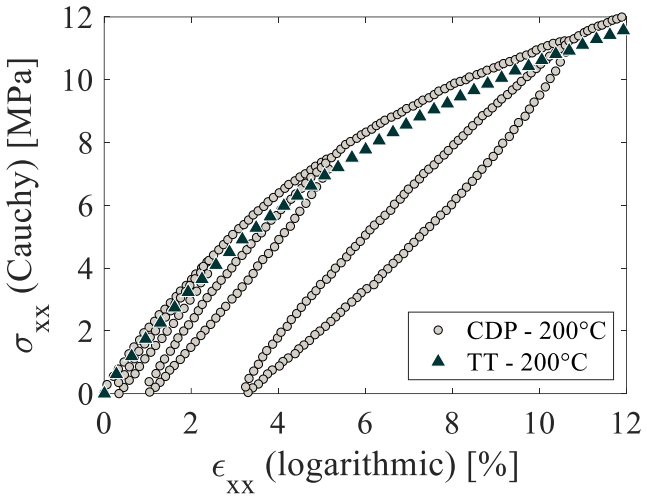

Fig. 4-5: Stress vs strain curves obtained from CDP and tensile tests on SC PEKK and at 200°C

From FIG. 4-5 it results that at the end of each loop (after the unloading phase), while the stress is set to 0, the strain does not return to zero. Moreover, after the first loop, the material shows an increase in apparent stiffness, up to the maximum value of stress of the previous loop, where it suddenly softens and again it superposes to the tensile test curve.

A different CDP test is carried out, keeping the stress constant at the end of each loop (CDP+R), similarly to the recovery phase carried out during creep tests (FIG. 4-6). The recovery phase in CDP+R test can be compared to the recovery phase in creep-recovery tests: such comparison could provide with the elements to deduce the mechanisms active during creep.

The duration of the recovery phase after each loop is variable and this phase is aimed at measuring the amount of strain at the end of each loop which is recovered. The test parameters are summarized in TAB. 4-3.

T [°C]	$\dot{z}$ [mm/min]	σ_i [MPa]
200	1	2.5, 6.5, 9.3
		9.3

Tab. 4-3: CDP +R test parameters for PEKK 7002 SC

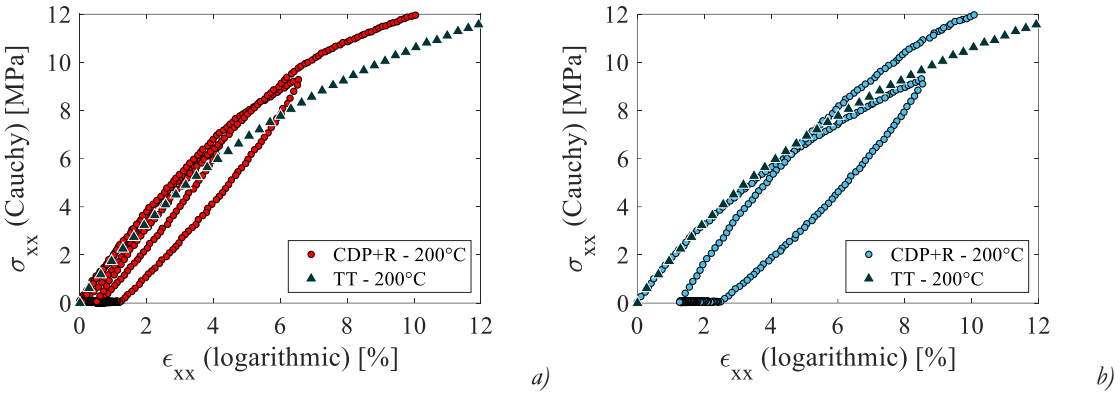

Fig. 4-6: Stress vs strain curves obtained from CDP+R and tensile tests on SC PEKK and at 200°C. a) maximum loop stress = 2.5, 6.5, 9.3 MPa and b) maximum loop stress 9.3 MPa

FIG. 4-6 shows that due to the addition of a recovery phase in the CDP tests, the curves do not superpose anymore to the tensile curves at the same temperature and displacement speed, but are parallel to it. During the initial part of the reload the curve superpose to each other.

The comparison of the different phases of the curves with tensile and creep-recovery phase is described in the following paragraph.

As previously mentioned, the tests carried out at 200°C show low sensitivity to test speed and temperature, since the material is sufficiently outside the transition region around T_g: this allows a clearer identification of the different mechanisms active at the different load conditions, and it is described in the following paragraphs. The same mechanisms can be identified at 180°C and partially at 165°C (respectively at the end and inside the transition region around T_g), and will be employed for confirming the identification.

4.2.3. PEKK SC load-unload behavior

The simplest load condition is the load (and reload): the mechanisms active during this phase can be identified through the comparison between tensile and CDP tests carried out at the same temperature and at the same displacement speed.

FIG. 4-7 SHOWS the reloads of the CDP (A) and CDP+R (B) curves

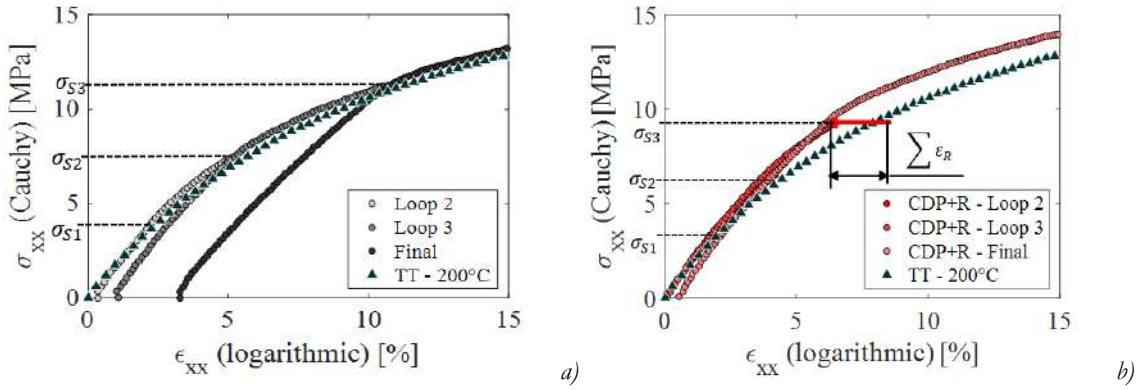

a) *b)*

Fig. 4-7: Reloads of CDP '(a) and CDP+R (b)

From the comparison it can be concluded that:

- the reload behavior changes abruptly when the previous maximum stress is reached and the material softens, superposing to the tensile curve at the same stress. Hence during the reload a **softening mechanism** is activated, when a threshold is passed: such threshold starts from 0 (the mechanism starts from the beginning of the test) and it is always equal to the maximum previous stress;
- the recovery has no effect on the softening mechanism, which is still activated when the threshold is passed, hence it is driven by the stress. Moreover, in the case of the CDP+R, the distance from the tensile curve is the sum of the previously recovered strains (ε_R).
- these phenomena could be associated with *pseudo-plastic phenomena*, as the rupture of the lamella structures, (BOWDEN AND YOUNG 1974) or to phenomena related to the slide along slip plane, as the chain slide (G'SELL ET AL. 1999).

All the initial parts of the reload, as mentioned in the previous paragraph, are superposed to each other (FIG. 4-6), if a recovery phase is carried out at the end of each loop. In order to investigate this phenomenon, all the reloads are shifted to 0 in stress and strain. The investigation is also extended to the unloads, which are shifted to 0 in both stress and strain, according to the shifts summarized in TAB. 3-15, where ε_R is the strain at the beginning of the reload, and max(σ) and max(ε) are the stress and strain at the beginning of the unload.

	Reload	Unload
Stress shift ($\measuredangle\sigma$)	σ	σ-max(σ)
Strain shift ($\measuredangle\varepsilon$)	ε-ε_R	ε-max(ε)

Tab. 4-4: Stress and strain shift for the CDP and CDP+R reloads and unloads

FIG. 4-8 shows the reload up to the previous maximum stress (A), the unload (B) and the comparison of both (C), obtained from CDP and CDP+R tests.

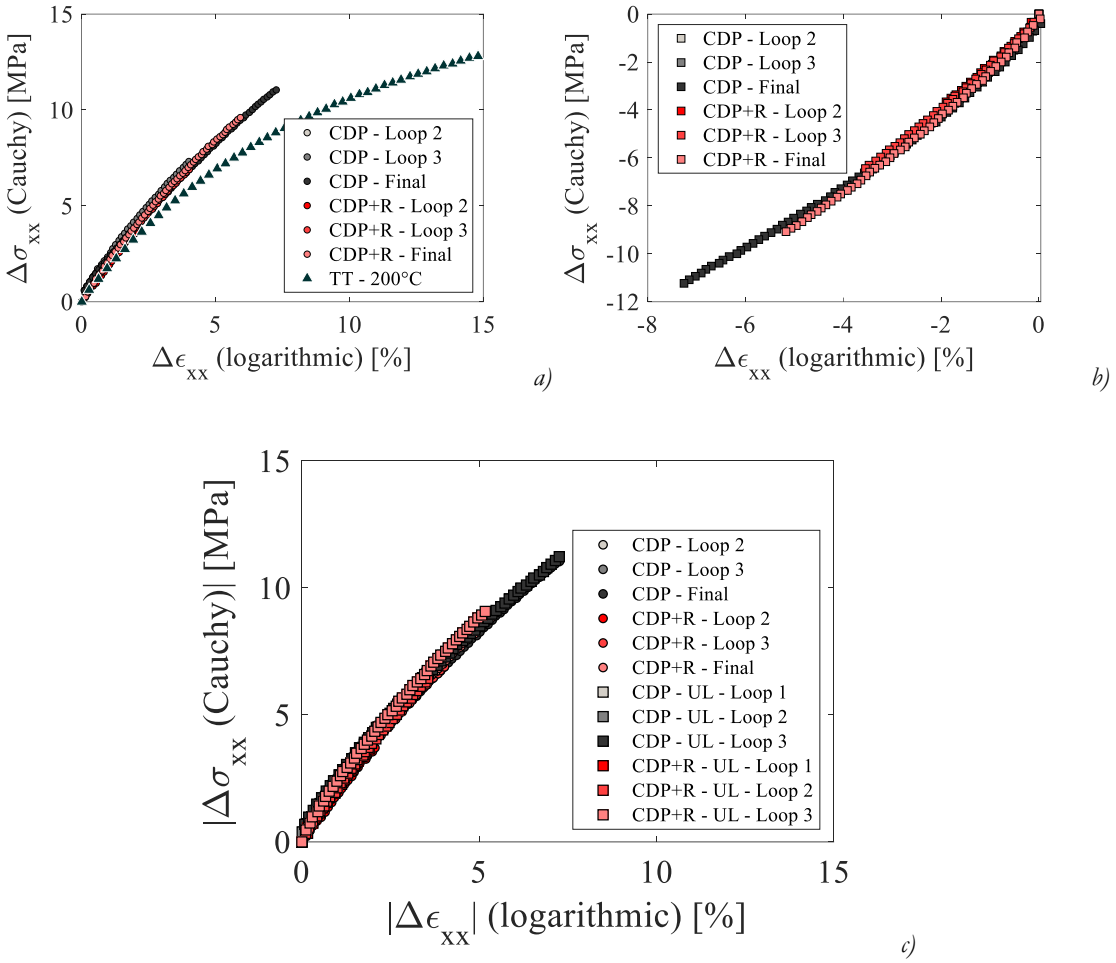

Fig. 4-8: Comparison of reload (a), unload (b) shifted to zero obtained from CPD and CDP+R tests on PEKK SC at 200°C at 1 mm/min, and overall comparison of both in absolute value (c)

From the comparison in FIG. 4-8, it can be concluded that:

- there is an increase in apparent stiffness respect to the first load (which superposes to the tensile test curve), produced during reload, up to the maximum previous applied stress; moreover, all the reloads superpose to each other, defining a *reloading path*;
- the unloads also superpose to each other and follow the same *unload path*;

- the reloads and the unloads (in absolute value) superpose to each other, hence the unload path is the inverse of the reloading path or during the reload a **hardening mechanism** is activated, which is reversed during the unload.
- the softening mechanism is not active during unload, because the unload behavior is completely described by the hardening mechanism only, while it is not sufficient to describe the initial load or the reload after the maximum previous stress is passed.
- the recovery has no effect on both the reloading and unloading path, hence they are driven by the stress;
- this mechanism is associated to the morphological *re-arrangement of the crystal structure*, leading the crystals initially random orientation to change in favor of an alignment toward the loading direction, as observed in PE and PEKK (G'SELL ET AL. 1999). This rotation is intrinsically favored by the rubber state amorphous phase, which low mechanical properties above T_g are not able to prevent the movement of the crystalline phase. This interpretation has been confirmed by WAXS observations, carried out at the ENSAM Paris, (ROLAND AND FAYOLLE 2020).

4.2.4. PEKK SC creep – recovery behavior

The mechanisms identified in the previous paragraph are sufficient to characterize the PEKK SC behavior during tensile, CDP tests and also the initial load phase of the creep-recovery tests, leaving to characterize the remaining creep, unload and recovery phases.

Since the creep phase shows complex interaction between concurrent mechanisms and the previous analysis provides its initial conditions, the final conditions can be derived by the analysis of the unload phase in the creep-recovery tests and its comparison with the unloads in CDP tests.

FIG. 4-9 shows the comparison of unloads obtained from CDP tests (A), creep-recovery tests (B) on PEKK SC at 200°C and the overall comparison (C). Each loop maximum stress corresponds to a creep stress, such that the difference between the two unloads starting from the same maximum stress, is the presence or absence of a creep phase.

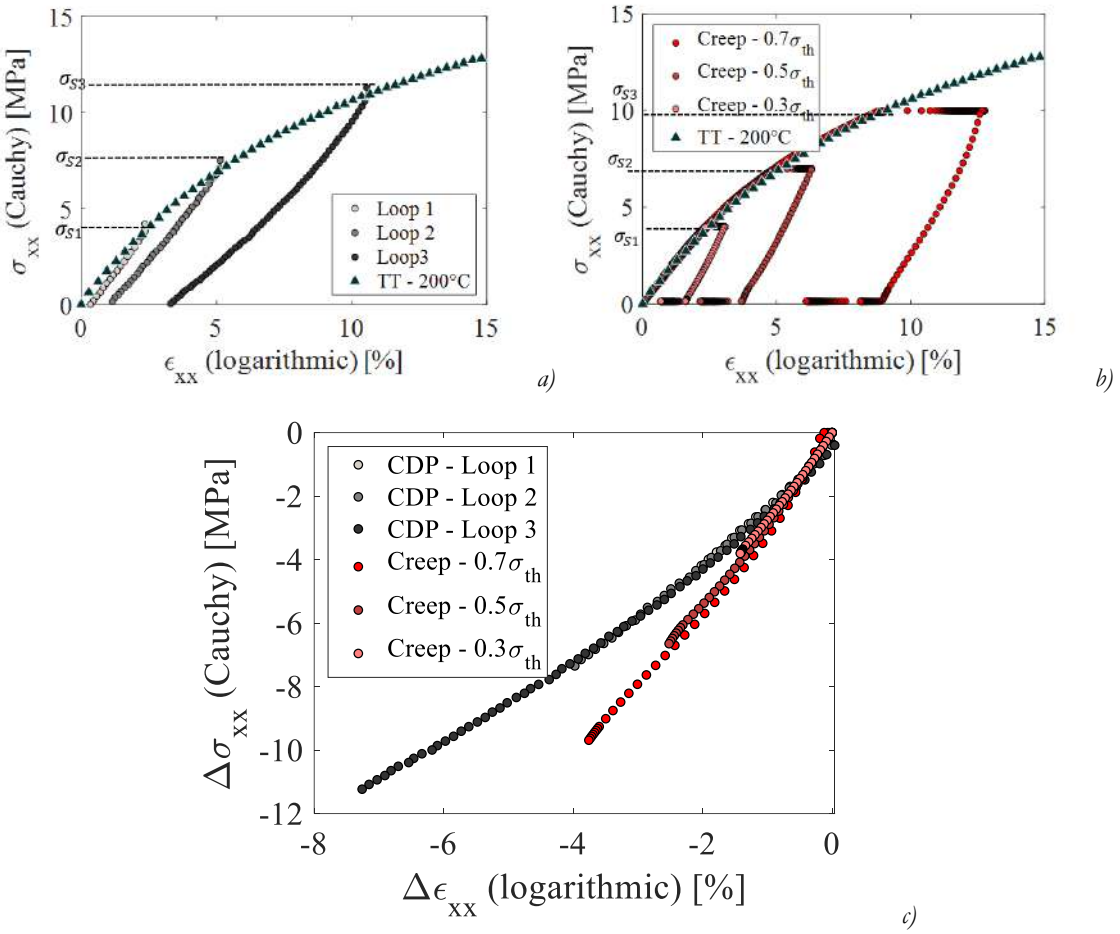

Fig. 4-9: Comparison of unload obtained from CDP tests(a), Creep-recovery tests (b) on PEKK SC at 200°C and overall comparison (c)

The comparison of the unload phases preceded or not by a creep phase (FIG. 4-9C), shows an increase in the apparent stiffness of the unload phase after creep with respect to unload directly after loading.

On the contrary, the stiffness (as the ratio between stress and strain) during creep is expected to decrease or at least be constant, according to the increase in strain showed in FIG. 3-25 and the constant applied stress. A possible explanation is that such increase in stiffness is produced by the increase in crystallinity during the creep phase.

To investigate the effect of creep on the following recovery, the recovery at the end of creep-recovery tests is compared with the recovery in CDP+R test.

FIG. 4-10A shows the comparison of strain vs time curve during recovery obtained from CDP+R tests and creep-recovery tests (CHAP. 3.4.2), and the fact that they have a similar trend. The tendency becomes clearer if each curve is divided by the maximum stress experienced by the material during the test (FIG. 4-10B).

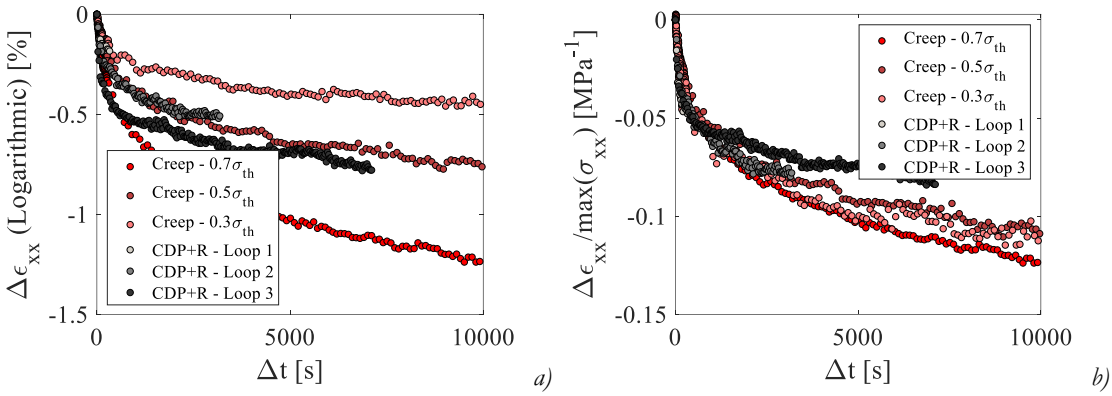

Fig. 4-10: Comparison of recovery strain vs time curves obtained from CDP+R tests and Creep-recovery tests (a) on PEKK SC at 200°C and comparison of the recoveries normalized respect to the maximum stress applied to the specimen(b)

All curves in FIG. 4-10B superpose, allowing concluding that:

- there is no difference between recovery preceded by creep and not, with the consequence that if there is no crystallization variation after CDP+R (FIG. 4-14) the mechanism active during recovery is directly proportional to the maximum (creep) stress.

The same analysis is carried out on the creep strain, normalized respect to the creep stress (compliance) and showed in FIG. 4-11.

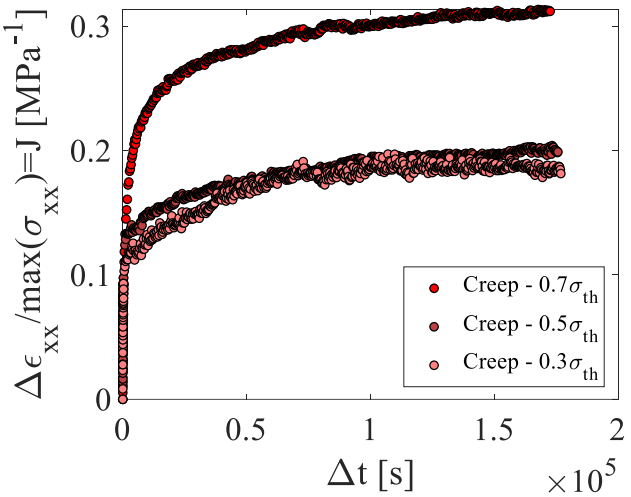

Fig. 4-11: Comparison of creep strain vs time curves obtained from Creep-recovery tests on PEKK SC at 200°C, normalized respect to the creep stress applied to the specimen(b)

FIG. 4-11 shows that the normalized creep strain (compliance) curves do not superpose to each other as observed for the recovery. This leads to conclude that the mechanism active during creep is not directly proportional to the creep stress and consequently:

- the creep compliance is not independent of the creep stress, hence is the material is not linear viscoelastic, coherently with the impossibility of a time-temperature superposition (CHAP. 3.4.5);
- other mechanisms are active during creep, which are not active in all other phases.

The conclusions drawn for PEKK SC at 200°C for loading-unloading and creep-recovery behavior are confirmed at 180°C and partially at 165°C.

4.3. Crystallization kinetics

The analysis described in the previous paragraph allows identifying the different mechanisms active during the different loading paths, and suggests the presence of additional mechanisms activated only during creep, which could affect the following unload, but are negligible during the recovery. All the drawn considerations suggest that a possible explanation could consist in an increase in crystalline phase active only during creep.

In order to verify it, DSC tests were carried out on PEKK 7002 SC specimen type *f* (FIG. 2-5), cut from previously tested specimens, according to the testing protocol described in (CHAP. 2.3.1.4). The results are compared with the DSC test carried out on the as received material, (CHAP. 3.5).

FIG. 4-12 shows the comparison between the heath flow vs temperature curve of DSC tests carried out on specimens

- cut from as-received material (orange curve),
- cut from a specimen previously tested under tensile condition at 1 mm/min and 200°C (most severe test conditions) (black curve)
- cut form a specimen exposed to only to 200°C for the tensile test duration (dummy sample), (grey curve).

For all 3 cases, the T_g, the T_m and the peak enthalpy are measured for 1st and 2nd heating and cooling phases; the measured values are listed in TAB. 3-15.

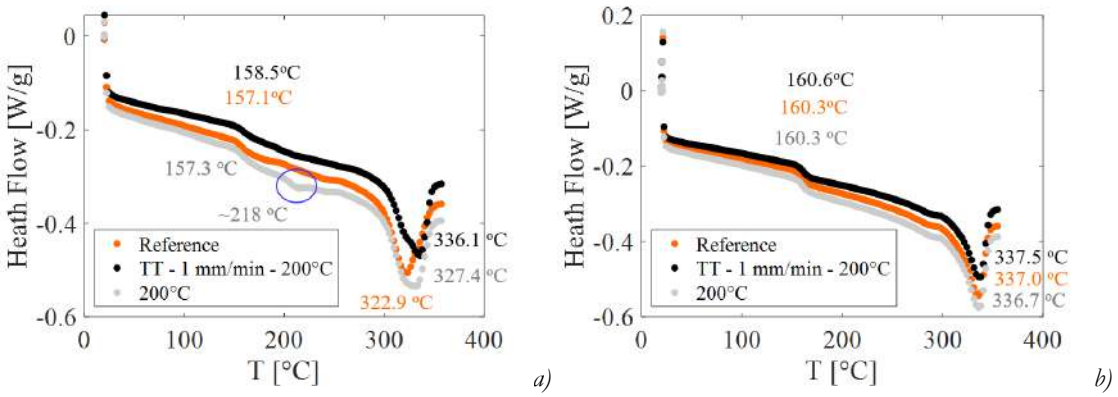

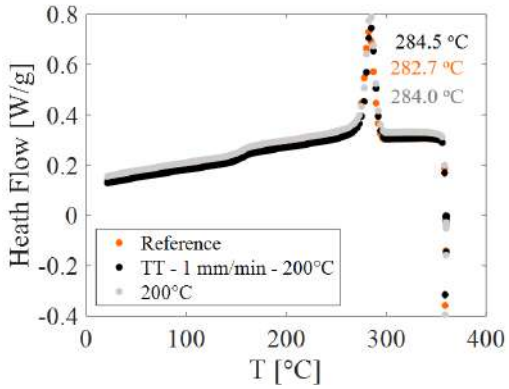

Fig. 4-12: 1st (a), 2nd heating (b) and cooling (c) phases comparison from DSC test on PEKK 7002 SC samples cut from as-received material, after tensile test at 1 mm/min and 200°C and dummy sample exposed at 200°C for the same duration of tensile test

	Reference	200°C	TT - 1 mm/min - 200°C
		1st Heating	
T_g [°C]	157.1	157.3	158.5
T_m [°C]	322.9	327.4	336.1
ΔH_f [J/g]	31.63	32.94	31.52
T_m [°C] (2nd peak)	No 2nd peak		218
ΔH_f [J/g] (2nd peak)			1.22
		2nd Heating	
T_g [°C]	160.3	160.3	160.6
T_m [°C]	337.0	336.7	337.5
ΔH_f [J/g]	29.86	31.07	30.21
		Cooling	
T_p [°C]	282.7	284.0	284.5
ΔH_c [J/g]	38.18	39.64	38.17

Tab. 4-5: Tg, Tm and peaks enthalpy measured from DSC test on PEKK 7002 SC samples cut from as-received material, after tensile test at 1 mm/min and 200°C and dummy sample exposed at 200°C for the same duration of tensile test

In particular, looking at the first heating, (FIG. 4-12A), it can be seen that there is:

- no presence of exothermic peak in any test, and therefore no presence of cold crystallization, suggesting that the maximum achievable crystallinity percentage is attaint during the manufacturing;
- a change of slope, corresponding to T_g, at 157.1°C for the reference and slightly higher on the other specimens, for both curves, proving that no significant T_g variation is induced by thermomechanical loads;

- an endothermic peak in correspondence of the melting temperature, which is of 323°C for the reference, 5°C higher in the dummy sample and 14°C higher in the tensile tested specimens, leading to the hypothesis that some morphological change has happened because of thermomechanical load. Measuring the area of the peak, it is also possible to measure the crystallinity percentage in the sample, according to:

$$\chi=\frac{\left(\Delta H_{melt}-\Delta H_{cold\ cryst}\right)}{\Delta H_{100}}\cdot 100 \qquad \textit{Eq. 4-4}$$

where:

- $\Delta H_{melt}=\frac{Area\ of\ the\ melting\ peak}{Heating\ rate}$ is the variation of the heath flow produced during the melting;
- $\Delta H_{cold\ crystl}=\frac{Area\ of\ the\ cold\ crystallization\ peak}{Heating\ rate}$ is the variation of the heath flow produced during the cold crystallization, which for PEKK 7002 SC is always zero;
- *Heating rate*=10°C/min;
- ΔH_{100}=130 $\frac{J}{g}$ is the theoretical variation of heath flow achievable if the material would have been completely crystallized.

		χ [%]
As received	1st heating	24.33
	2nd heating	22.97
	Cooling	29.36

Tab. 4-6: PEKK 7002 SC crystallinity percentage values measured through DSC test on as received specimens

- only on the curve obtained from the dummy sample, a 2nd endothermic peak (blue circle) in correspondence of 218°C, indicating the presence of a *secondary crystallization*. This 2nd family appears to be produced by thermal load only, while, under thermomechanical load, it is not produced.

The analysis of the 2nd heating phase (FIG. 4-12B) shows a less than 1°C difference in T_g and T_m between the reference and the specimens underwent thermal or thermomechanical loads, (for the reference, 160°C and 337°C respectively). Moreover, the heath flow vs temperature curves can be superposed, indicating that the loading history does not promote

chemical changes in the material. Looking at the crystallization percentages, a ±1% is registered around the reference value of 22.9%. The amount of crystalline phase is strictly related to the cooling rate, which is different from the PEKK 7002 SC manufacturing process, leading to the difference with the 1st heating.

The comparison of the cooling phases (FIG. 4-12C) leads to the same conclusions of the 2nd heating phases: in fact, it show less than 2°C of scatter around the crystallization peak (for the reference, 282.7°C) and ±1% is registered around the crystallization percentage (for the reference, 29.4%).

The comparison of the DSC curves showed in FIG. 4-12, seems to point out that thermal and thermomechanical loads have different effect on the crystallization kinetics: therefore the analysis is extended to the DSCs carried out on specimen cut after thermomechanical conditions different than tensile. Moreover, after the complete melt of the crystalline phase, the crystallinity kinetics is independent of the previous loading history and hence the analysis is limited to the 1st heating.

In FIG. 4-13 is showed the comparison between the 1st heating heath flow vs temperature curve of DSC tests carried out on specimens cut from as-received material (orange curve), and from specimens:

- cut from specimens previously tested under tensile condition at 200°C, 180°C and 165°C and at different speed and from the relative dummy samples (FIG. 4-13);
- cut from specimens previously tested under load-increase condition at 200°C (CHAP. 4.2.2) with recovery between each loop and without recovery (FIG. 4-14);
- cut from specimens previously tested under creep-recovery condition at 200°C,180°C and 165°C and at different creep stresses and from the relative dummy samples (FIG. 4-15);
- cut form a specimen aged at 200°C for 42 days under 5 bar of O_2 (CHAPTER 6) keeping as much surface as possible and removing as much surface as possible (FIG. 4-16).

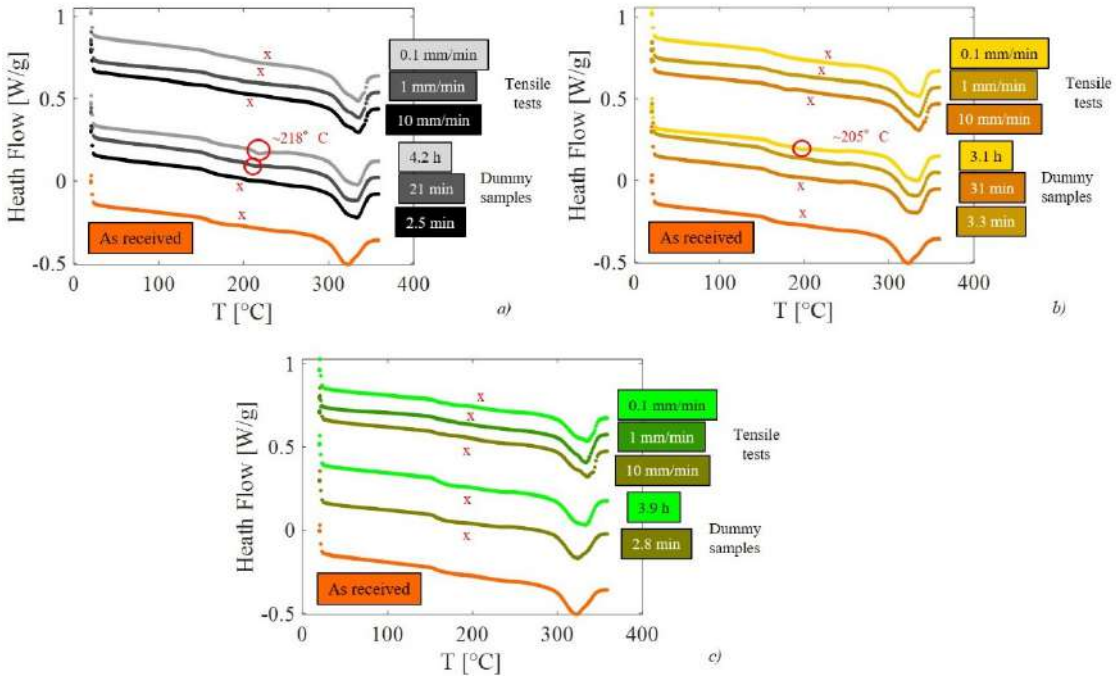

Fig. 4-13: 1st heating phases comparison from DSC test on PEKK 7002 SC samples cut from as-received material and after tensile tests and dummy samples at 200°C (a), 180)C (b) and 165°C (c)

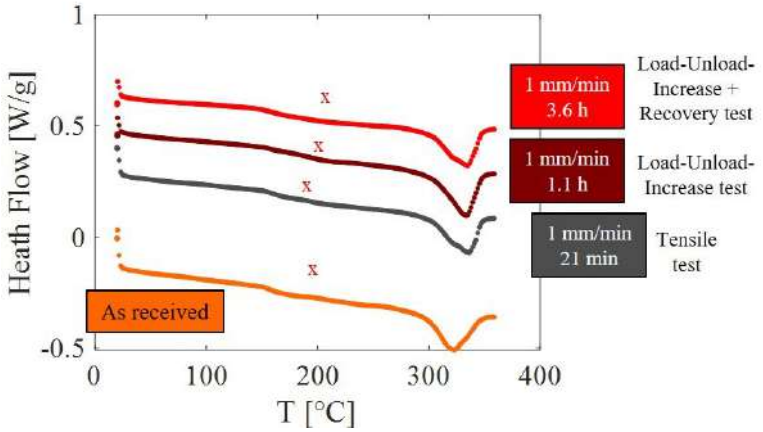

Fig. 4-14: 1st heating phases comparison from DSC test on PEKK 7002 SC samples cut from as-received material and Load-Unload-Reload with and without recovery at 200°C

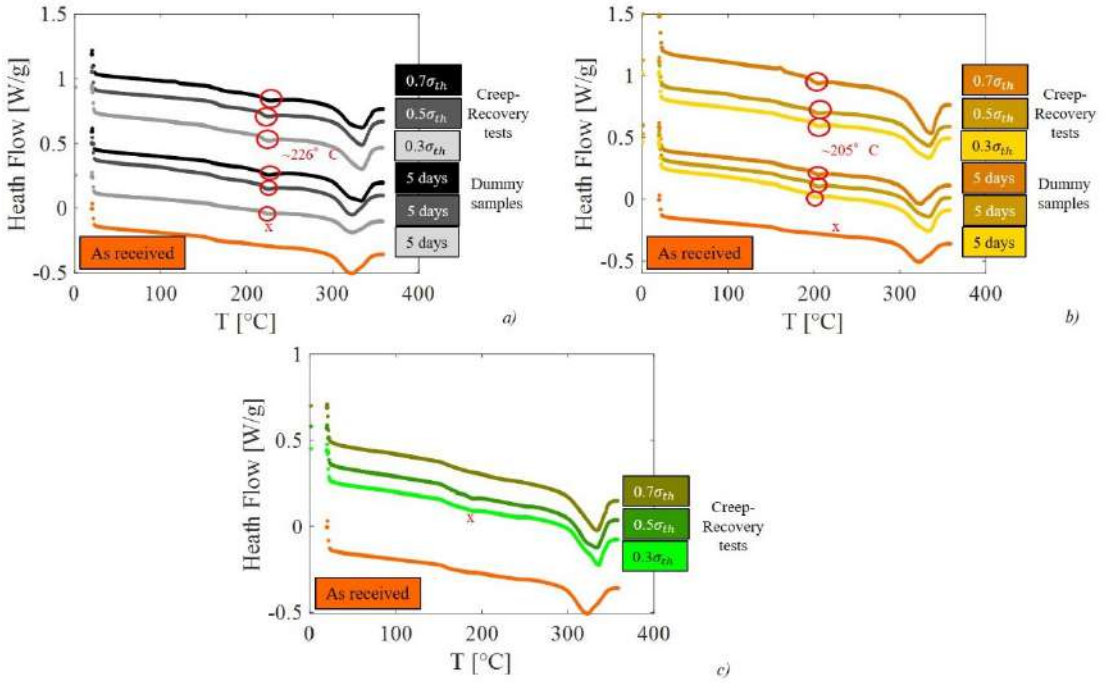

Fig. 4-15: 1st heating phases comparison from DSC test on PEKK 7002 SC samples cut from as-received material and after creep-recovery tests and dummy samples at 200°C (a), 180)C (b) and 165°C (c)

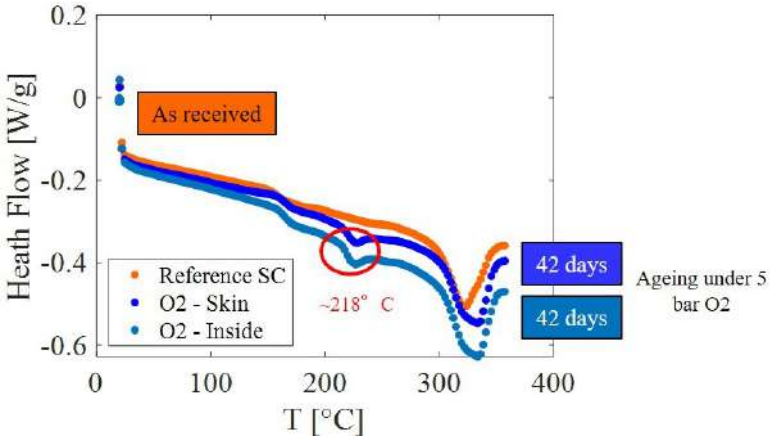

Fig. 4-16: 1st heating phases comparison from DSC test on PEKK 7002 SC samples cut from as-received material and after ageing under 5 bar of O_2 at 200°C

The red circle in the previous figures shows the presence of the secondary crystallization, which appears to be present at 180°C and 200°C, if the PEKK SC is exposed to thermal loading, after creep-recovery conditions, but not after tensile or CDP tests and never at 165°C.

The difference in behavior can be seen in FIG. 4-17, which shows the variation of the crystallinity percentage respect to the as received material:

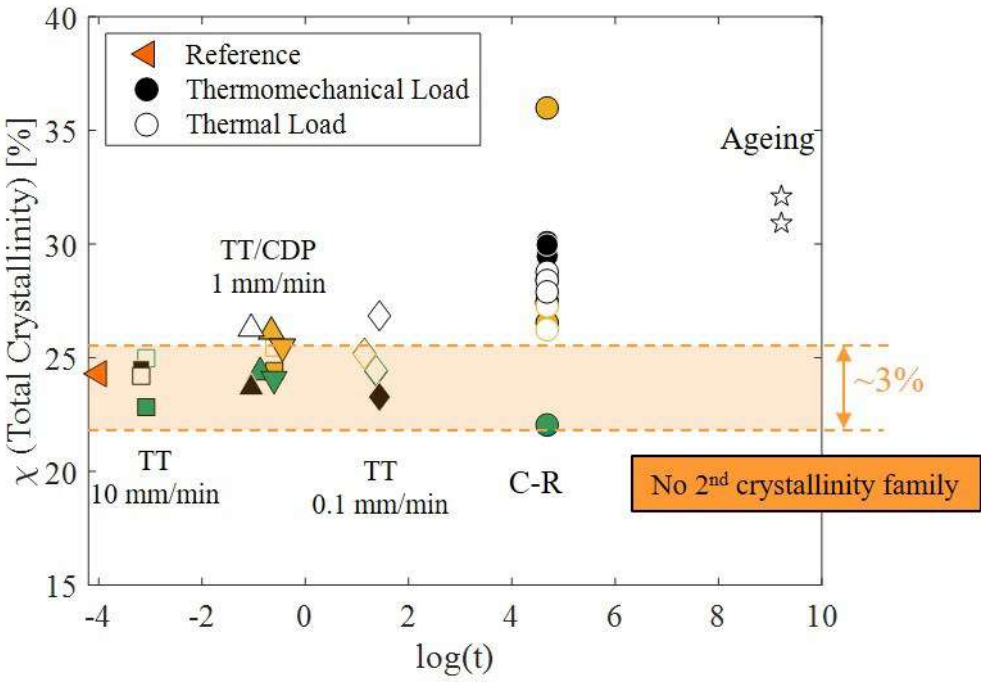

Fig. 4-17 PEKK SC measured crystallinity percentage vs test duration (solid marker) or exposure time (blank markers) at 165°C, 180°C and 200°C

The area colored in orange in FIG. 4-17 contains, in a 3% range of crystallinity, almost all the results obtained from the samples for which no secondary crystallinity is observed. Contrary to the measures of temperature (T_g, T_m, etc…), the measures of crystallinity percentage are depending on the measured mass of samples. Estimating the error can be difficult, considering that, besides the measure of the mass of the material, two more measures are carried out, on the two aluminum capsules needed for the preparation of the DSC samples.

The measured crystallinity percentage values are summarized in TAB. 4-7 and TAB. 4-8.

Test condition			Test duration	χ 1st peak [%]	χ 2nd peak [%]	χ_{TOT} [%]	Δχ [%]
TT	165°C	10 mm/min	0.046	22.83	/	22.83	/
		1 mm/min	0.417	24.37	/	24.37	/
		0.1 mm/min	3.934	24.41	/	24.41	/
	180°C	10 mm/min	0.055	24.42	/	24.42	/

		1 mm/min	0.518	26.15	/	26.15	/
		0.1 mm/min	3.14	25.20	/	25.20	/
	200°C	10 mm/min	0.0417	24.50	/	24.50	/
		1 mm/min	0.35	23.68	/	23.68	/
		0.1 mm/min	4.2	23.28	/	23.28	/
CDP	165°C	1 mm/min	0.55	24.07	/	24.07	/
	180°C	1 mm/min	0.64	25.49	/	25.49	/
	200°C	1 mm/min	1.10	25.05	/	25.05	/
		1 mm/min +R	3.60	24.57	/	24.57	/
C-R	165°C	0.7 σ_{th}	108	27.48	/	27.48	/
		0.5 σ_{th}	108	27.40	/	27.40	/
		0.3 σ_{th}	108	22.05	/	22.05	/
	180°C	0.7 σ_{th}	108	32.66	3.33	35.99	2.48
		0.5 σ_{th}	108	24.13	2.41	26.54	2.43
		0.3 σ_{th}	108	25.94	2.50	28.44	2.34
	200°C	0.7 σ_{th}	108	25.82	3.66	29.48	3.44
		0.5 σ_{th}	108	25.89	4.23	30.12	3.97
		0.3 σ_{th}	108	25.45	4.52	29.97	4.32

Tab. 4-7 PEKK 7002 SC crystallinity percentage values measured through DSC test on specimens cut from specimen after different thermomechanical loads

Test condition		Test duration	χ 1st peak [%]	χ 2nd peak [%]	χ_{TOT} [%]	Δχ [%]
TT	165°C	0.046	24.98	/	24.98	/
		0.417	/	/	/	/
		3.934	24.45	/	24.45	/
	180°C	0.055	25.45	/	25.45	/
		0.518	/	/	/	/
		3.14	24.63	0.54	25.17	0.53
	200°C	0.0417	24.20	/	24.20	/
		0.35	25.34	0.94	26.28	0.90
		4.2	24.63	2.22	26.85	2.19
CDP	165°C	0.55	/	/	/	/

	180°C	0.64	/	/	/	/
	200°C	1.1	/	/	/	/
		3.6	/	/	/	/
C-R	165°C	108	/	/	/	/
		108	/	/	/	/
		108	/	/	/	/
	180°C	108	24.35	1.89	26.24	1.89
		108	26.10	2.33	28.43	2.17
		108	25.94	1.34	27.28	1.26
	200°C	108	25.12	3.65	28.77	3.53
		108	24.73	3.67	28.40	3.61
		108	24.65	3.25	27.90	3.20
Ageing 5 bar O_2	200°C	1008	28.18	3.92	32.1.	4.05
		1008	26.50	4.42	30.92	3.38

Tab. 4-8 PEKK 7002 SC crystallinity percentage values measured through DSC test on specimens cut from specimen after different thermal loads

(TANGUY CHOUPIN 2018), (CHELAGHMA 2013) have characterized PEKK SC crystallization kinetics for temperature above T_g, according to Hillier modified model, (HSIAO, CHANG, AND SAUER 1991), including a primary spherulitic and a secondary intra-spherulitic crystallization: the primary crystallization is related to the endothermic peak close to the melting temperature, while the secondary crystallization is associated to an endothermic peak at around +10°C above the annealing temperature. Hillier model predicts a saturation time for both crystallizations, which is smaller for the primary crystallization from which the manufacturing protocol, showed in CHAP. 2.2.1.1 is derived, to ensure that the maximum crystallinity percentage is attained.

This is contrast of the results of the DSC tests summarized in TAB. 4-8, and not due to the additional energy provided by mechanical loads, since it was also observed after the exposition of thermal load. The increase in crystallinity could be explained by the fact that the complete saturation of secondary crystallization was not reached during the manufacturing.

Because of the faster saturation of the primary crystallization, it is assumed that only secondary crystallization is possible, which is evident from the presence of the 2nd endothermic peak. Thus, each value of crystallinity is normalized respect to the reference, implying that the endothermic peak close to T_m can have different shape respect to the reference one (due to morphological changes), but it has to have the same area: the difference in the measures are thus due to errors in the mass measurements.

Under such hypothesis, the crystallinity percentage of the 2nd peak can be normalized according to:

$$\chi_{norm,i}^{2^{nd}\,peak} = \chi_i^{2^{nd}\,peak} \frac{\chi_{ref}^{1^{st}\,peak}}{\chi_i^{1^{st}\,peak}} \qquad \text{Eq. 4-5}$$

Leading to the corrected crystallinity variation respect to the reference as showed in FIG. 4-18.

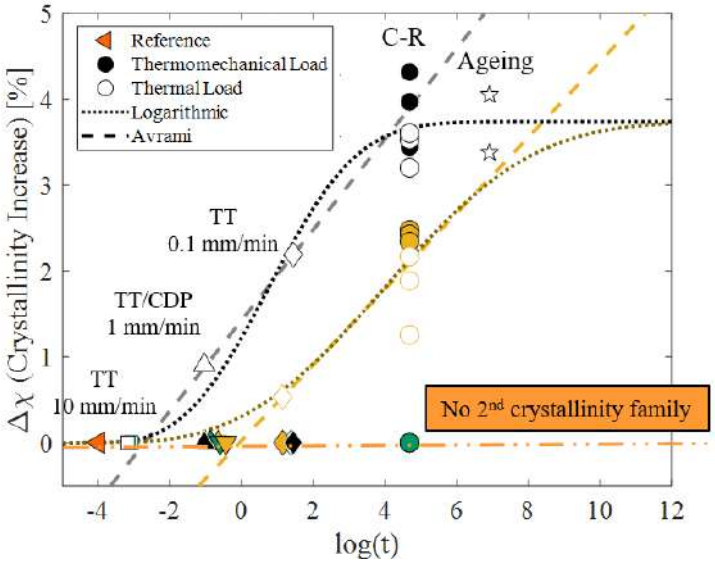

Fig. 4-18: PEKK SC corrected variation of crystallinity percentage vs test duration (solid marker) or exposure time (blank markers) at 165°C, 180°C and 200°C

From FIG. 4-18 it can be concluded that:

- the PEKK SC exposed only to the thermal load shows an increase in crystallinity, which can be approximated with an Avrami equation as, (AVRAMI 1941):

$$\Delta\chi = \chi_{max}\left(1 - \exp\left(-K\,(\ln t)^3\right)\right) \qquad \text{Eq. 4-6}$$

  which parameters are listed in TAB. 4-9:

T [°C]	χ_{max} [%]	K [ln(min)$^{-3}$]
180	3.789	0.01248
200		0.005792

Tab. 4-9: Parameters of the Avrami equation at the different test temperatures

EQ. 4-6, however, cannot be directly linked to the crystallization kinetics proposed by (TANGUY CHOUPIN 2018), because the latter does not take into account the possibility of stopping the crystallization and continuing it after a cooling to room temperature and a heating back to the annealing temperature. To simply the model, the crystallization kinetics is approximated with the natural logarithmic of the exposure time, according to:

$$\Delta\chi = \begin{cases} 0 & \text{if } t < t_0 = -\frac{d}{c} \\ c\ln(t) + d & \text{if } t_0 \le t \le t_1 \\ \chi_{max} & \text{if } t > t_1 = \frac{\chi_{max} - d}{c} \end{cases} \qquad \textit{Eq. 4-7}$$

which parameters are listed in TAB. 4-9:

T [°C]	χ_{max} [%]	c [ln(h)]	d [%]	t_0 [min]	t_1 [h]
180	3.789	0.4415	0.0256	56.6	4495.7
200		0.5276	1.4275	4	80

Tab. 4-10: Parameters of the Avrami equation at the different test temperatures

The plateau in FIG. 4-18 is coherent with the $\Delta\chi$ obtained from DSC after ageing for 42 days under 5 bar of O_2 at 200°C, which are close to the $\Delta\chi$ obtained from DSC after creep. This imply that the **PEKK SC was not completely crystalized during the manufacturing** and that the maximum crystallinity is not 24.3%, but ~**28%**. Considering that to not produce crystallinity increase at 165°C, the *K* parameter at 165°C should be at least 2 order of magnitude lower than its value at 180°C: this allows extrapolating the *K* value at the manufacturing crystallization temperature (230°C) of around 0.019 and estimating an increased exposure time, needed to fully crystallize the PEKK 7002, of 2÷3 h;

- the PEKK SC tested under tensile conditions does not show an increase in crystallinity, with all the measured value confined in a 3% scatter respect to the as received material, unlike the dummy samples exposed to only thermal load for the same durations than tensile tests. This could be due to the rotation of the crystalline structure, which prevents intra-spherulitic crystallinity to form, possibly continuously breaking the bond between intra-spherulitic amorphous chains. Moreover, it reduces the amorphous chain mobility, increasing the constraint on the intra-spherulitic amorphous phase, which could result in an increase in the activation energy required to activate the crystallization;
- the PEKK SC tested under Load-Unload-Reload with and without recovery between each loop, does not vary its crystallinity percentage as well, possibly suggesting that also during unload and recovery the previously described mechanism is active, or that the material suffers the resulting effect produced during the loading phase: from an

energetic point of view, during this phase, the thermal and mechanical energy provided to the material could be insufficient to reach the increased activation energy required to crystallize.

- the PEKK SC tested under creep-recovery condition, instead, appears to follow the trend of the PEKK SC exposed to thermal load, suggesting that:
  a. the material crystallizes during both creep and recovery (being the latter affected by the previous creep phase, which differentiates it from the recovery after load-unload);
  b. the material crystallizes only during creep and this has no impact on the following recovery;
  c. the material crystallizes only during recovery phase.

  Hypothesis *c* can be excluded because no increase in crystallinity can be observed after CDP+R tests, and since none was observed after tensile (load) and CDP (load-unload-reload), it can be concluded that no increase happens also during recovery.

  Moreover, in consideration of the superposition of the normalized recovery phases of both CDP+R and creep-recovery tests (FIG. 4-10), showing no difference between them and hence that the creep has no effect on the following recovery, also hypothesis *a* can be excluded, and hence it can be concluded that the **PEKK SC crystallizes only during creep.** This could be coherent with the fact that during creep the mechanical energy provided is sufficient to overcome the activation energy increased during the tensile part.

According to EQ. 4-6, and considering the total crystallinity as 28%, the percentage of total crystallinity can be evaluated as function of the exposure time, as:

$$\alpha = \frac{\chi_0 + \Delta\chi}{\chi_0 + \chi_{max}} 100 = \frac{\Delta\chi + 24.3}{28} 100 \qquad \textit{Eq. 4-8}$$

The resulting estimation for 180°C and 200°C is showed in FIG. 4-19.

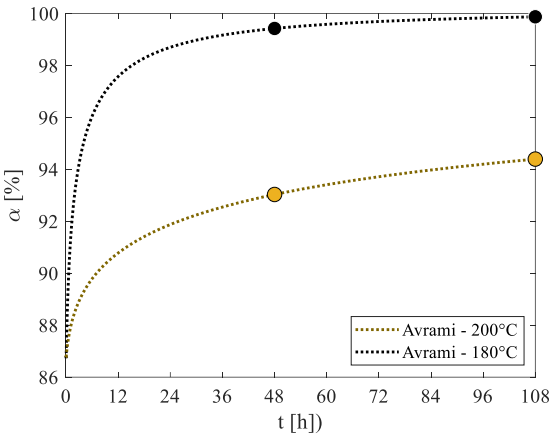

Fig. 4-19: Relative crystallinity vs exposure time at 180°C and 200°C

FIG. 4-19 allows concluding:

- the difference between the relative crystallization after 48 h (creep duration) and 108 h (creep-recovery duration) is less than 1%, explaining the ambiguity in defining the phases where the crystallization mechanism active and confirm that coherently it could be present during creep only;
- while after 108 h at 200°C, PEKK SC reaches the 99.7% of relative crystallinity (27.91%), exposed for the same duration at 180°C it reaches the 94.2% (26.3%) and it takes 2.8 years to reach the 99.7%;
- in order to be coherent to almost zero after 108 h, the EQ. 4-6 parameter *K*, should be at least 2 order of magnitude lower than its value at 180°C: this results in 0.15% increase in crystallinity after 10 years.

The description of the crystallization kinetics and its coupling with thermomechanical load allows completing the characterization of the different mechanisms defining PEKK SC behavior. A resuming of all the observed mechanism is proposed in the next paragraph.

4.4. Discussion of results

In the previous paragraphs the analysis carried out to identify the mechanisms controlling the PEKK SC behavior in load, unload, creep and recovery and the coupling with the crystallization kinetics at temperature above T_g is described.

Preliminarily, it is showed that:

- PEKK SC had not reached the maximum crystallinity percentage during manufacturing: in fact, the maximum crystallinity achievable is 28%, the initial 24.3% only constitutes its 86%, and 3.789% of crystallization is produced if the material is exposed to temperature above T_g. As resulting from DSC tests thermograms and coherently with (TANGUY CHOUPIN 2018), predicting that the 78% of total crystallinity is composed by spherulitic primary crystals, only secondary intra-spherulitic secondary crystals forms.
- above T_g PEKK SC has an incompressible behavior.

The analysis can be divided in two cases:

1. a thermal load is applied, or the impact of crystallization on the initial mechanical properties of PEKK SC
2. a thermomechanical load is applied, or the impact of crystallization on the evolution of mechanical properties (PEKK SC behavior) and, vice versa, the effect of the thermomechanical load on the crystallization kinetics.

4.4.1. Thermal load

Because of incomplete crystallization during manufacturing, if PEKK SC is exposed to temperature above T_g, the crystallization mechanism is activated and secondary crystallinity forms, as showed in FIG. 4-20.

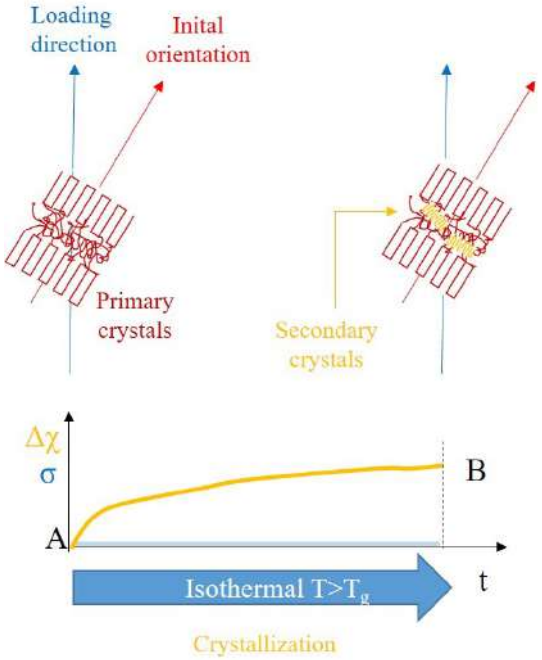

Fig. 4-20: Schematization of PEKK SC crystalline structure evolution during exposure to isothermal load at T> T_g

As showed in FIG. 4-20, secondary intra-spherulitic crystals forms from the amorphous chains contained between lamellae. The kinetics of crystallization can be described by Avrami's equation, and it has a sigmoidal trend with the exposure time, with an asymptotic value of around 3.8%. The 99.7% can be reached further exposing the material at 230°C for <3 h, at 200°C for 108 h and at 180°C for 2.8 years. At 165°C no crystallization increase was observed after 108 h (maximum time exposure), and therefore no identification of the crystallization kinetics parameters is possible: thus, the crystallization mechanism is considered not active at 165°C.

4.4.2. Thermomechanical load

The analysis of PEKK SC behavior in load, unload, creep and recovery conditions at T>T_g allowed the identification of 3 principal mechanisms:

- **Hardening mechanism**. This mechanism:
  - is associated with the re-orientation of the crystalline structure towards the loading direction;
  - is activated during the load and reload, and is completely reversible during the unload;
  - is stress driven, because it is independent of the initial reload strain (CDP+R tests) and an increase in the applied stress, increases the rotation angle of the crystals;

- is depending on the strain rate (and hence the stress rate), which increases the amplitude of the mechanism, or the amount of crystalline phase involved in the rotation, its saturation and its kinetics;
- has a complex dependency on the temperature. In fact, higher temperature should provide more energy to the system and enhance the mechanism, but its effect is compensated by the mechanical property loss, which reduces the mechanical contribution, in fact reducing the energy provided to the system. At the same time, an increase in temperature reduces as well the stress rate effect, coherently to the lower sensibility to time effect observed in PEKK SC tensile tests (CHAP. 3.2);
- is not active when the stress rate is zero, as during creep and recovery, and the orientation of the crystals is assumed to be fixed as long the stress is kept constant.

- **Softening mechanism.** This mechanism, present at low strains, becomes dominant once at middle-high strains, when the hardening mechanism saturates. This mechanism:
  - is associated with pseudo-plastic phenomena, as the rupture of the lamella structures, or to phenomena related to the slide along slip plane;
  - is activated during the load, is non reversible and not active during the unload;
  - is stress driven as the hardening, because it is independent of the initial reload strain (CDP+R tests) and it activated when a **threshold stress** (initially null), is passed: in CDP tests, the threshold is constituted by the maximum stress in correspondence of the *n-1* loop; when, during the *n*-th loop the stress is increase over it, the softening is activated and the threshold stress is update;
  - depends on the strain rate (and hence the stress rate), which increases the amplitude of the mechanism, as the hardening mechanism;
  - is not active only when the strain rate is strictly negative: because of the presence of permanent strain after recovery, and the not rheological simple creep behavior (which excluded linear viscoelastic mechanisms), the softening mechanism is active also during creep and recovery.

- **Crystallization mechanism.** This mechanism:
  - is not active during load (reload), unload and recovery. This could be explained by the increase in constraint which the intra-spherulitic amorphous phase undergoes due to the crystal structure re-orientation, resulting in lower chain mobility. From an energetic point of view, during the load (reload) this could produce an effect similar to the increase of the activation energy of crystallization, which cannot be reached by the thermal energy applied. Such increase could be proportional to the applied stress. The activation energy, increased during load, remains constant in other load conditions, but it cannot be reached during load and recovery, because the mechanical energy provided to system (always lower than the energy introduced at the end of the load), summed to the thermal energy, is not sufficient;

- is active during creep. From the energetic point of view, and coherently with the previous interpretation, the mechanical energy provided by the applied load, together with the thermal energy, is sufficient to pass the activation energy and enable the crystallization mechanism to activate. Because of the lacking of in situ continuous measurement of the crystallization increase during creep, the kinetics of crystallization during creep is supposed to be identical to the kinetics of crystallization observed during thermal loading. However, an acceleration of the kinetics produced by the applied mechanical energy cannot be excluded. Moreover, the increased crystallization produces an increase in the mechanical property, causing the increase in stiffness during the unload.

The above mentioned mechanisms are activated when specific load condition are verified. In order to clarify the interpretation, a schematization of the different analyzed solicitations is showed in the following figures.

During CDP test, as showed in FIG. 4-21, 4 different part can be identified, as summarized in TAB. 4-11.

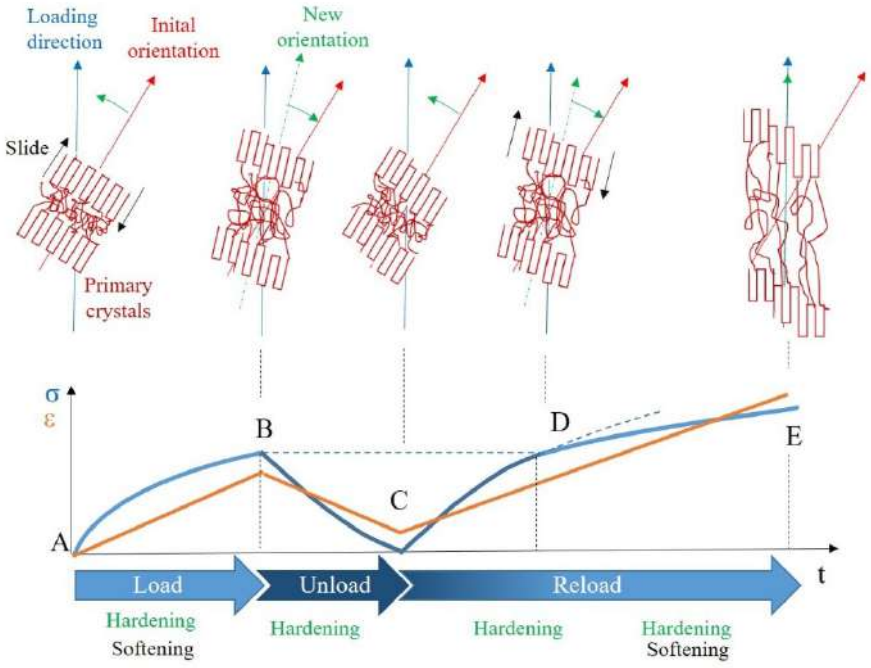

Fig. 4-21: Schematization of PEKK SC crystalline structure evolution during CDP tests at T> T_g

Part	Load condition	Hardening	Softening	Crystallization
A-B	*Load*	Active: • rotation towards load direction	Active: • initial threshold passed (0 MPa) • slide of crystals	Not active
B-C	*Unload*	Active: • rotation towards initial orientation	Not active: • previous plastic effect is maintained	Not active
C-D	*Reload*	Active: • rotation towards loading direction	Not active: • stress threshold not passed • previous plastic effect is maintained	Not active
D-E			Active: • stress threshold passed • slide of crystals	Not active

Tab. 4-11: Mechanisms activation loading conditions in CDP tests.

During creep-recovery tests, as showed in FIG. 4-25, 4 different part can be identified, as summarized in TAB. 4-12.

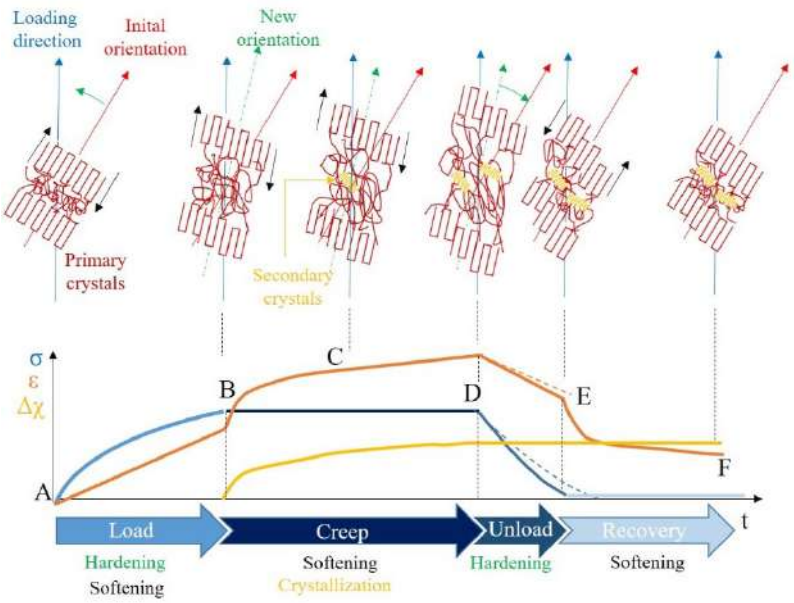

Fig. 4-22: Schematization of PEKK SC crystalline structure evolution during creep-recovery tests at T> T_g

Part	Load condition	Hardening	Softening	Crystallization
A-B	Load	Active: • rotation towards load direction	Active: • initial threshold passed (0 MPa) • slide of crystals	Not active
B-C **C-D**	Creep	Not active: • rotation blocked	Active: • viscoplastic phenomena	Active: • increase in material properties
D-E	Unload	Active: • rotation towards initial direction	Not active: • previous plastic effect is maintained previous plastic effect is maintained	Not active
E-F	Recovery	Not active: • initial orientation reached	Active: • viscoplastic phenomena	Not active

Tab. 4-12: Mechanisms activation loading conditions in creep-recovery tests.

While multiple clues, presented in the previous paragraphs, confirms the identification of the above mentioned mechanisms, the following considerations have to been made:

- the presence of other mechanisms besides the identified ones cannot be excluded, but their effect on the PEKK SC behavior can be considered negligible;
- the identification was carried out from the analysis of experimental tests, hence its validity is limited to the maximum test duration (108 h, corresponding to creep-recovery duration). Activation of different mechanisms or enhancing of mechanisms already active, but with negligible effect in the time – window investigated, during longer-term exposition to thermomechanical load cannot be excluded;
- the association between the effect of the identified mechanisms on the thermomechanical behavior and the modification in crystalline structure could not be completely verified: all the observations on the crystalline percentage and re-orientation of the crystals (the latter carried out by PIMM Paris) were carried out only before and after the tests. Hence, all the proposed kinetics are constituted by the mathematical models allowing linking the initial crystal structure configuration to its final configuration while best approximating the experimental data. A complete verification could be realized only through in situ measurement of the evolution of the crystalline structure during the application of thermomechanical loads.

The mechanisms identified constitutes the basis for a model of the PEKK SC behavior, constituted by their analytical description, proposed in the following paragraph.

4.5. Analytical 1-D model for the description of the PEKK SC thermomechanical behavior above T_g

The discussion in the previous paragraphs allows characterizing different mechanisms active during the different load paths and provides all the elements enabling to describe the behavior of PEKK SC. Exploiting the incompressibility hypothesis, deriving from the analysis of the volumetric changes, a 1-D description of the behavior is proposed. In order to simplify the notation, all the subscript index indicating the longitudinal components, are omitted.

Considering the material constituted by the amorphous and crystalline phases, the latter gives the material almost the totality of the mechanical properties above T_g, as can be deduced by the comparison of DMA storage modulus between PEKK SC and PEKK AM (FIG. 4-43). Moreover, above T_g, the amorphous phase is in a rubber state, (ROGUET 2006), compatible with a hyperelastic behavior, leading to assume for PEKK SC an initial behavior close to a filled elastomer one, (DORFMANN AND OGDEN 2004).

Because of the relatively small measured strain, compared to the typical large strain of hyperelastic behavior, (LENG ET AL. 2019), and because of the presence of a crystals, in order to simplify the description, the behavior of the PEKK SC is approximated with an elastic behavior, which Young's modulus is depending on the crystalline phase content, besides of the temperature.

This leads to define a theoretical initial state of the material as:

$$\sigma_0 = E_0\,\varepsilon \qquad \textit{Eq. 4-9}$$

4.5.1. Load-Unload behavior

The load-unload behavior (schematized in FIG. 4-21)can be characterized according to the considerations deduced from the comparison of tensile and CDP tests, which showed the presence of a hardening and a softening mechanism. Moreover, the DSC tests carried out after tensile and CDP tests show the absence of crystallization mechanisms.

4.5.1.1 Hardening mechanism

The hardening mechanism defines the loop of the CDP tests and is characterized by:

- reload apparent stiffness higher than initial load (load = tensile behavior);
- equality between reload and unload path.

As the charge is applied on the material theoretical initial state, the hardening mechanism is activated, which expresses during reloads and unloads.

However, because in situ observations were not possible at the testing conditions, no link can be directly established between the rotation angle and the stress. Therefore, the mechanism could only be described as function of the strain, according to:

$$\sigma_H=\sigma_0+a\left(1-exp\left(-\frac{|\measuredangle\varepsilon|}{b}\right)\right)= \\ =E_0\,|\measuredangle\varepsilon|+a\left(1-\exp\left(-\frac{|\measuredangle\varepsilon|}{b}\right)\right) \qquad \textit{Eq. 4-10}$$

where:

- both a and b parameters are function of the strain rate and the temperature; in particular, a describes the amplitude and the asymptotic value of the mechanism, while b describes its kinetics.
- $|\measuredangle\varepsilon|=|\varepsilon-\bar{\varepsilon}|$, and $\bar{\varepsilon}$ is the strain at beginning of the load or the unload.

Following the schema of stress and strain shift showed in TAB. 4-4, the reload and unload paths (loops in CDP tests) can be described according to:

$$\sigma=\begin{cases} E_0\,|\measuredangle\varepsilon_L|+a\left(1-\exp\left(-\frac{|\measuredangle\varepsilon_L|}{b}\right)\right) & \text{if } \dot{\sigma}>0 \qquad \textit{Eq. 4-11} \\ \bar{\sigma}-E_0\,|\measuredangle\varepsilon_U|+a\left(1-\exp\left(-\frac{|\measuredangle\varepsilon_U|}{b}\right)\right) & \text{if } \dot{\sigma}<0 \qquad \textit{Eq. 4-12} \end{cases}$$

where:

	Initial stress	Initial strain	Δε
Reload	0	$\bar{\varepsilon}=\varepsilon_R$	$\measuredangle\varepsilon_L=\varepsilon-\bar{\varepsilon}$
Unload	$\bar{\sigma}=\max(\sigma)$	$\bar{\varepsilon}=\max(\varepsilon)$	$\measuredangle\varepsilon_U=\bar{\varepsilon}-\varepsilon$

Tab. 4-13: Reload and unload initial conditions

Referring to FIG. 4-21, EQ. 4-11 characterizes the hardening mechanism in parts A-B and C-D-E (load and reload), while EQ. 4-12 describes part B-D (unload).

4.5.1.2 Softening effect

In order to describe the softening effect, the same 3 parameter viscoplastic power law described in EQ. 3-10 is employed, once inverted in the form:

$$\sigma_S = \begin{cases} \left[\dfrac{\varepsilon(m+1)t^{(m+1)}}{A}\right]^{\frac{1}{n}} & \text{if } \dot{\sigma}>0 \cup \sigma \geq \sigma_{th} \\ 0 & \text{else} \end{cases} \qquad \textit{Eq. 4-13}$$

where:

- the parameters m and n depends on the temperature;
- the parameter A depends on the temperature and the strain rate;
- the condition defines the threshold of activation of the mechanism, and σ_{th} equals the previous maximum stress.
- the time stops if the condition is not satisfied: this is due to direct time dependency of EQ. 4-13, while the load-unload behavior of the material is not explicitly time dependent, but this is introduced by the stress (strain) rate.

Referring to FIG. 4-21, EQ. 4-13 characterizes the softening mechanism in parts A-B and D-E (load and reload after the stress threshold), while is not active in part B-D (unload).

Then, the total stress during load (tensile test), can be evaluated as:

$$\sigma = \sigma_H - \sigma_S \qquad \textit{Eq. 4-14}$$

The formulation in EQ. 4-13 implies that during the initial part of the reload and during the unload (constituting the loop in CDP tests and where $\sigma<\sigma_{th}$), $\sigma_S=0$.

4.5.2. Creep-recovery behavior

The complete description of the creep-recovery tests (composed by load – creep – unload – recovery, schematized in FIG. 4-22), requires:

- the definition of the effect crystallization kinetics on the mechanical properties during creep;
- the effect of creep on the following unload.

4.5.2.1 Creep

The DSC tests carried out on specimen after creep-recovery tests showed an increase in crystallinity, which is produced only during creep phase, (part B-C-D in FIG. 4-22). Moreover, it is assumed that the final amount of crystallinity percentage follow the crystallization kinetics described by DSC on specimens exposed at thermal load only, for different duration.

In order to take into account the effect of the crystallinity increase, the following hypotheses are made:

1. the kinetics of crystallization is independent of the crystal structure configuration (hence of its orientation) and it is exactly the same obtained exposing the material to thermal load (FIG. 4-18), which could be described by EQ. 4-7.
2. the increase in stiffness, produced by the increase of crystallinity, is similar to the one described in (TANGUY CHOUPIN 2018), relative to 180°C;
3. the crystallinity affects the elastic modulus E_0 (EQ. 4-9), but not the hardening mechanism, meaning that the new formed crystals are not re-oriented. E_0 vs χ curve (dashed black curve in FIG. 4-23) has to have a trend coherent to the curve obtained from (TANGUY CHOUPIN 2018).
4. the E_0 vs χ at 200°C is similar to the curve at 180°C, because of the PEKK 7002 SC low sensibility at temperature effect far from T_g, showed by DMA tests and confirmed by the initial tensile moduli evolution with the temperature, (FIG. 3-14).

Under the previously described hypothesis, the estimated increase of stiffness during creep for PEKK 7002 SC (FIG. 4-23) can be obtained from:

$$\Delta E_0(\chi) = E_0\,(\exp(g\,\chi) - 1) \qquad \textit{Eq. 4-15}$$

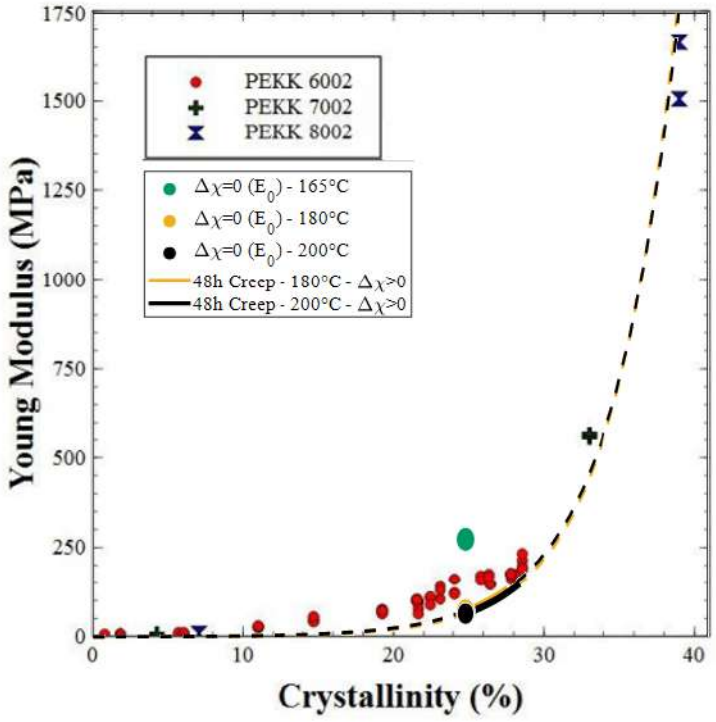

Fig. 4-23: Young modulus vs crystallinity at 180°C of neat PEKK crystallized at 230°C from the glassy state with a strain rate of 3.3 s^{-1}, (Tanguy Choupin 2018), PEKK 7002 SC E_0 at 165°, 180°C and 200°C(respectively green, yellow and black markers) at χ=24.3%, E_0 vs χ curve for PEKK 7002 SC at 180°C and 200°C for elastic stiffness (yellow and black dashed curve) and increase of E_0 during creep produced by exposure at 180°C and 200°C for 48h.

Following the hypothesis of crystals not being oriented during creep (when $\dot{\sigma}$=0), during creep, EQ. 4-10 becomes:

$$\sigma_H = \bar{\sigma}_H \qquad \textit{Eq. 4-16}$$

where $\bar{\sigma}_H$ is the value of σ_H at the beginning of the creep.

In order to satisfy EQ. 4-16, it follows that:

$$\begin{aligned} \Delta\sigma_H = 0 \cong E_0^{cr}\,\varepsilon^{cr} - E_0\,\bar{\varepsilon} &= \left(E_0 + \Delta E_0(\chi)\right)\,\varepsilon^{cr} - E_0\,\bar{\varepsilon} \\ \Rightarrow \Delta\varepsilon = \varepsilon^{cr} - \bar{\varepsilon} &= \left(\frac{E_0}{(E_0 + \Delta E_0(\chi))} - 1\right)\bar{\varepsilon} \end{aligned} \qquad \textit{Eq. 4-17}$$

where ε^{cr} is the total strain during creep and $\bar{\varepsilon}$ is the strain at the beginning of the creep.

A viscoplastic strain can be evaluated as:

$$\varepsilon_{VP} = \varepsilon - \Delta\varepsilon \qquad \text{Eq. 4-18}$$

Because $\Delta E(\chi)>0$, $\Delta\varepsilon(\chi)<0$, and hence $\varepsilon_{VP}>\varepsilon$, as it is showed in FIG. 4-24, where the total strain, $\Delta\varepsilon$ produced by the increase in crystallinity, and the viscoplastic strain are compared, evaluated for a creep test at 70% of σ_{th} and at 200°C.

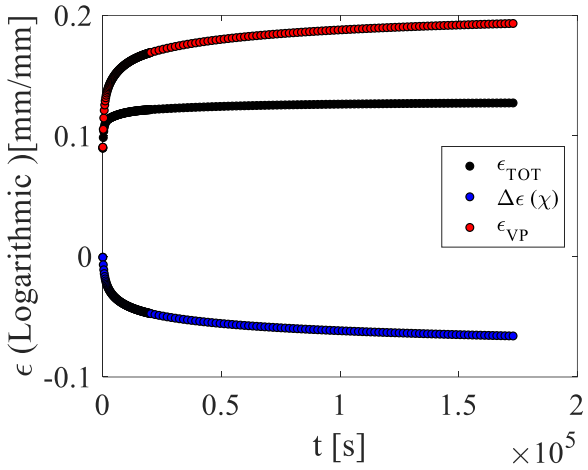

Fig. 4-24: Total strain (black), strain variation produced by crystallinity increase (blue) and resulting viscoplastic strain (red) for a creep test at 70% of σ_{th} and 200°C

Moreover, inverting EQ. 4-13, allows the estimation of the variation of the A parameter as function of the strain rate. FIG. 4-25 shows that evolution; which appears to be different compared to the one observed from tensile tests.

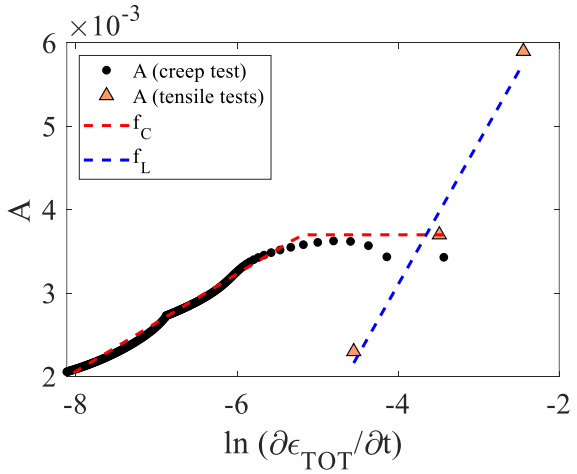

Fig. 4-25: Comparison of the A parameter vs strain rate from tensile tests (orange) and from creep tests (black). In dashed red the fitting for creep test

Thus, EQ. 4-13 can be corrected to take into account the crystallinity effect as it follows:

$$\sigma_S = \begin{cases} \left[\dfrac{\varepsilon(m+1)\, t^{-(m+1)}}{A_L(\dot{\varepsilon})}\right]^{\frac{1}{n}} & \text{if } \dot{\sigma}>0 \cup \sigma \geq \sigma_{th} \\ \left[\dfrac{\left(\varepsilon+\Delta\varepsilon(\chi)\right)(m+1)t^{-(m+1)}}{A_C(\dot{\varepsilon})}\right]^{\frac{1}{n}} & \text{if } \dot{\sigma}=0 \cup \sigma \geq \sigma_{th} \\ 0 & \text{else} \end{cases} \qquad \textit{Eq. 4-19}$$

with A_L an A_C the functions describing A as function of $\dot{\varepsilon}$ during loading and creep respectively:

$$A_L = h_{L1} \ln \dot{\varepsilon} + h_{L2} \qquad \text{if } \dot{\sigma}>0 \qquad \textit{Eq. 4-20}$$

$$A_C = \begin{cases} h_{C1} \ln \dot{\varepsilon} + h_{C2} & \text{if } \dot{\sigma}=0 \cup \dot{\varepsilon} \leq \dot{\varepsilon}_C \\ h_{C2} & \text{if } \dot{\sigma}=0 \cup \dot{\varepsilon} > \dot{\varepsilon}_C \end{cases} \qquad \textit{Eq. 4-21}$$

Referring to FIG. 4-22, the 1st condition in EQ. 4-19 describes the softening during load (part A-B), while the 2nd defines the softening during creep (part B-C-D) corrected of the increased crystallization.

4.5.2.2 Unload and Recovery after creep

The increase of elastic modulus E_0, produced by the increase of crystallinity during the creep, affects also the unload after creep. The increase of stiffness (showed in FIG. 4-9), respect to the unload preceded only by load, can be explained just by the increase in modulus due to the increase in crystallinity, leading to be able to employ the same formulation described in EQ. 4-10, corrected by the crystallization effect, as:

$$\sigma = \bar{\sigma} - (E_0 + \Delta E(\chi))\,|\Delta\varepsilon_U| + a\left(1 - \exp\left(-\frac{|\Delta\varepsilon_U|}{b}\right)\right) \qquad \textit{Eq. 4-22}$$

with the same initial conditions ($\bar{\sigma}$ and $\bar{\varepsilon}$) described in TAB. 4-13.

The following recovery can be described by the same formulation employed for creep, without the correction for the increase of crystallinity, (EQ. 4-19), under the hypothesis that:

1. there is no crystallinity increase during recovery;
2. there is no re-orientation of crystal phase (because $\dot{\sigma}=0$), hence the hardening follows EQ. 4-16, which implicitly includes the previous loading history effect.
3. the strain rate effect on A parameter is the same described for creep.

Those hypothesis leads to include a 3rd case in definition of the viscoplastic law, as follows:

$$\sigma_S = \begin{cases} \left[\dfrac{\varepsilon(m+1)t^{-(m+1)}}{A_L(\dot{\varepsilon})}\right]^{\frac{1}{n}} & \text{if } \dot{\sigma}>0 \cup \sigma \geq \sigma_{th} \\ \left[\dfrac{\left(\varepsilon+\Delta\varepsilon(\chi)\right)(m+1)t^{-(m+1)}}{A_C(\dot{\varepsilon})}\right]^{\frac{1}{n}} & \text{if } \dot{\sigma}=0 \cup \sigma \geq \sigma_{th} \\ \left[\dfrac{(\varepsilon)(m+1)t^{-(m+1)}}{A_C(\dot{\varepsilon})}\right]^{\frac{1}{n}} & \text{if } \dot{\sigma}=0 \cup \sigma=0 \\ 0 & \text{else} \end{cases} \qquad \textit{Eq. 4-23}$$

Referring to FIG. 4-22, the 1st condition in EQ. 4-23 describes the softening during load (part A-B), the 2nd defines the softening during creep (part B-C-D), corrected of the increased crystallization, while the 3rd the softening recovery (part E-F). Finally, the 4th condition describes it during unload (D-E). EQ. 4-22 describes the hardening effect during unload corrected of the crystallinity increase: in FIG. 4-22, it is showed the difference produced by the increase crystallinity in the unload (part D-E), respect to the unload not preceded by creep (dotted line).

4.5.3. Summary of the PEKK SC 1-D description and comparison with experimental curves.

The PEKK SC behavior in load, unload, reload, creep and recovery can be described by the combination of an elastic model, a hardening mechanism and a softening mechanism, corrected according to the crystallization kinetics. In this way, once provided with experimental time and longitudinal strain, the resulting model is able to calculate the correspondent total longitudinal stress, as:

$$\sigma = \sigma_H(\varepsilon, t) - \sigma_S(\varepsilon, t) \qquad \textit{Eq. 4-24}$$

where:

Crystallization kinetics		
$\Delta\chi=\chi-\chi_0=\begin{cases} \begin{cases} 0 & \text{if } t<-\frac{d}{c} \\ c\ln(t)+d & \text{if } -\frac{d}{c}\le t\le\frac{\chi_{max}-d}{c} \\ \chi_{max} & \text{if } t>\frac{\chi_{max}-d}{c} \end{cases} & \text{if } \dot{\sigma}=0 \cup \sigma=\sigma_{th} \\ \overline{\Delta\chi} & \text{else} \end{cases}$		Creep Load, reload, unload, recovery
	χ_0 = 24.3% (as-received) $\overline{\Delta\chi}$ = last value χ_{max} =3.789%	
$\Delta E_\chi=E_0\,(\exp(g\,\Delta\chi)-1)$		
$\Delta\varepsilon_\chi=\left(\frac{E_0}{(E_0+\Delta E_\chi)}-1\right)\overline{\varepsilon}_\chi$	$\overline{\varepsilon}_\chi$ = strain at beginning of crystallization	
Elasticity		
$\sigma_0=\begin{cases} (E_0+\Delta E_\chi)\,\lvert\Delta\varepsilon\rvert & \text{if } \dot{\sigma}>0 \\ \bar{\sigma}_0=\text{constant} & \text{if } \dot{\sigma}=0 \\ (E_0+\Delta E_\chi)\,\lvert\Delta\varepsilon\rvert & \text{if } \dot{\sigma}<0 \end{cases}$		Load, reload Creep, recovery Unload
	$\lvert\Delta\varepsilon\rvert=\lvert\varepsilon-\bar{\varepsilon}\rvert$ $\bar{\varepsilon}$ = strain when $\dot{\sigma}$ change of sign $\bar{\sigma}_0$= last value of σ_0	

Hardening

$$\sigma_H = \begin{cases} \sigma_0 + a\left(1 - \exp\left(-\dfrac{|\measuredangle\varepsilon|}{b}\right)\right) & \text{if } \dot{\sigma}>0 \quad \text{Load, reload} \\ \overline{\sigma_H} = \text{constant} & \text{if } \dot{\sigma}=0 \quad \text{Creep, recovery} \\ \bar{\sigma} - \sigma_0 - a\left(1 - \exp\left(-\dfrac{|\measuredangle\varepsilon|}{b}\right)\right) & \text{if } \dot{\sigma}<0 \quad \text{Unload} \end{cases}$$

$|\measuredangle\varepsilon| = |\varepsilon - \bar{\varepsilon}|$

$\bar{\varepsilon}$ = strain when $\dot{\sigma}$ change of sign

$\bar{\sigma}_H$ = last value of σ_H

Softening

$$\sigma_S = \begin{cases} \left[\dfrac{(\varepsilon)(m+1)\tilde{t}^{\,-(m+1)}}{h_{L1}\ln\dot{\varepsilon} + h_{L2}}\right]^{\frac{1}{n}} & \text{if } \dot{\sigma}>0 \cup \sigma \geq \sigma_{th} \quad \text{Load, reload after threshold} \\ \left[\dfrac{(\varepsilon - \measuredangle\varepsilon_\chi)(m+1)\tilde{t}^{\,-(m+1)}}{h_{C1}\ln\dot{\varepsilon} + h_{C2}}\right]^{\frac{1}{n}} & \text{if } \dot{\sigma}=0 \quad \text{Creep, recovery} \\ 0 & \text{else} \quad \text{Unload} \end{cases}$$

$\tilde{t}$ = cumulated time, increasing when softening is activated

According to the previous formulation, at each temperature, the PEKK SC load, unload, reload, creep and recovery behavior is function of 13 parameters, listed in TAB. 4-14.

Mechanism	Parameter	Value		
		T=165°C	T=180°C	T=200°C
Crystallization kinetics	c [ln(h)]$^{-1}$	0	0.4415	0.5276
	d [ ]	0	0.0256	1.4275
	g [ ]	0	0.23	0.24
Elasticity	E_0 [MPa]	275.1	72.36	64.84

Hardening	*a* [MPa]	(0.1 mm/min)	4.5	7.253	7.253
		(1 mm/min)	5	8	8.429
		(10 mm/min)	12	10.56	9.125
	b [mm/mm]	(0.1 mm/min)	0.01858	0.04945	0.05801
		(1 mm/min)	0.01858	0.037	0.05652
		(1 mm/min)	0.01172	0.03628	0.03628
Softening	*m* [ ]		-0.92	-0.852	-0.805
	n [ ]		0.795	0.79	0.6
	h_{C1} [ ]		-0.00002006	0.00008823	0.00025383
	h_{C2} [ ]		0.00324823	0.00381215	0.00673873
	$\dot{\varepsilon}_C$ [s^{-1}]		0.0005	0.000005	0.000005
	h_{L1} [ ]		0.00004877	0.00975228	0.00074161
	h_{L2} [ ]		0.00092279	0.11951135	0.00993437

Tab. 4-14: Parameters of the model at different temperatures

The evolution of the parameters with temperature is showed in FIG. 4-26.

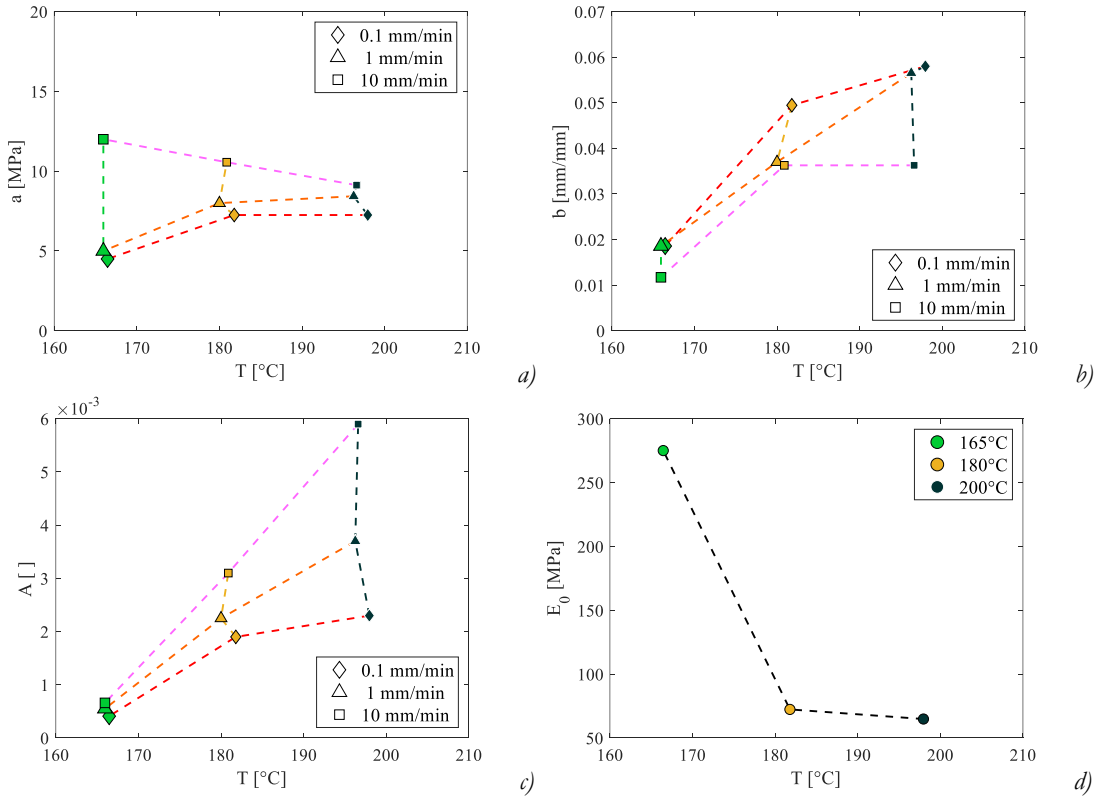

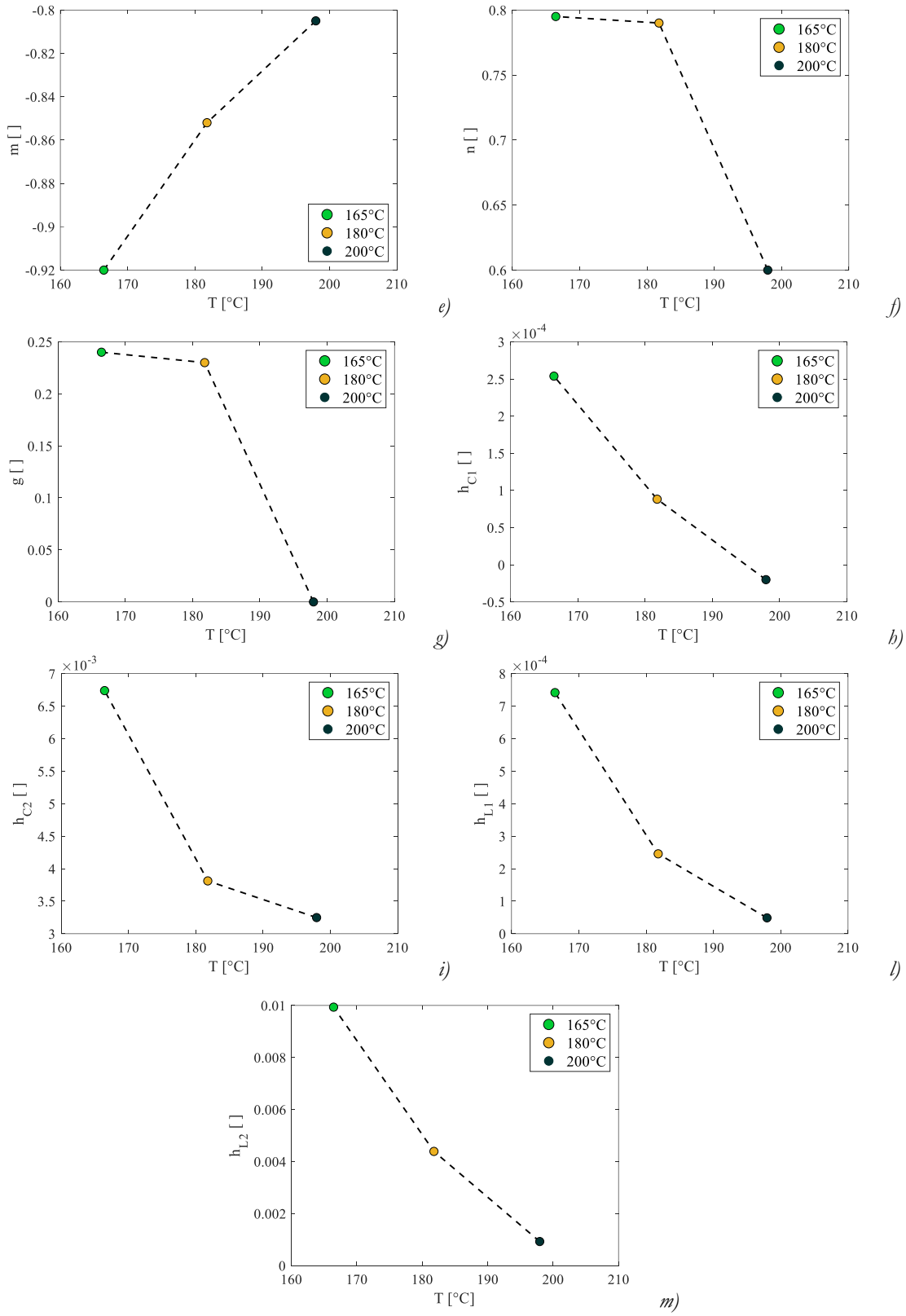

Fig. 4-26: Evolution of the parameters of the 1-D model with the temperature

Imposing the incompressibility hypothesis (ν=0.495), and employing the EQ. 4-14, the longitudinal and transversal behavior in tensile, CDP and creep-recovery condition can be reproduced. The comparison with experimental data is showed in following figures.

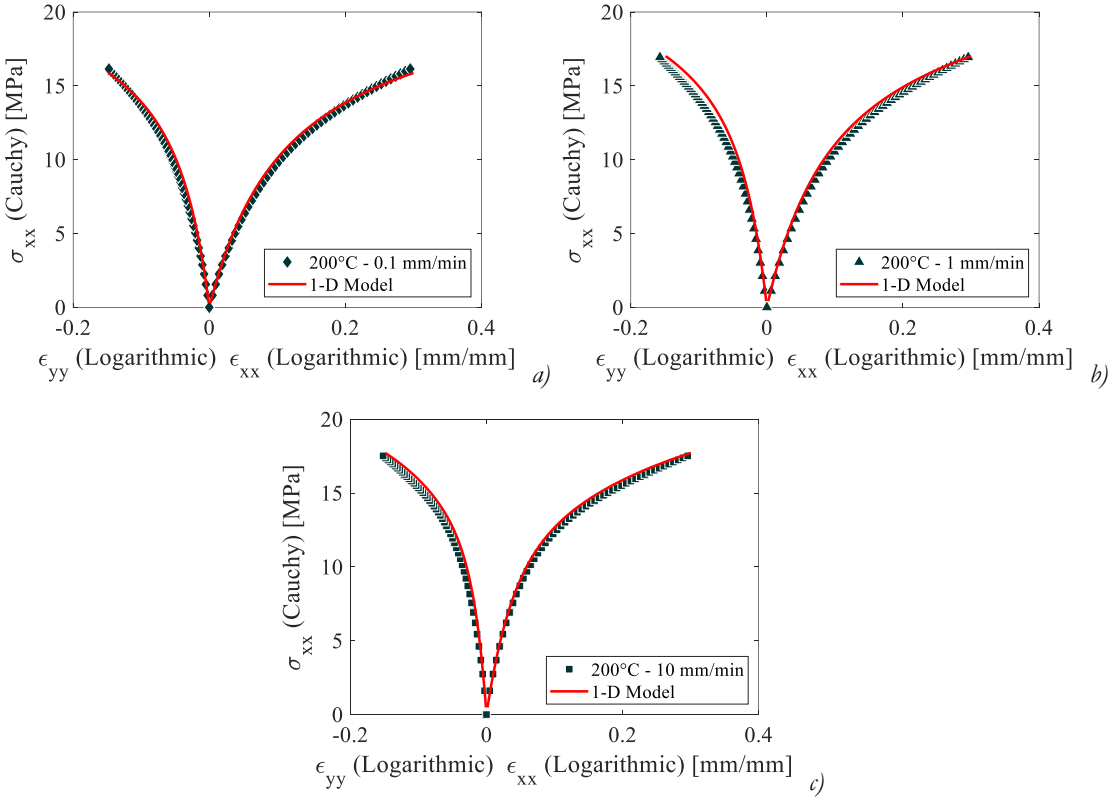

Fig. 4-27: Comparison between the 1-D model and the experimental tensile curves at 0.1 (a), 1 (b) and 10 (c) mm/min at 200°C

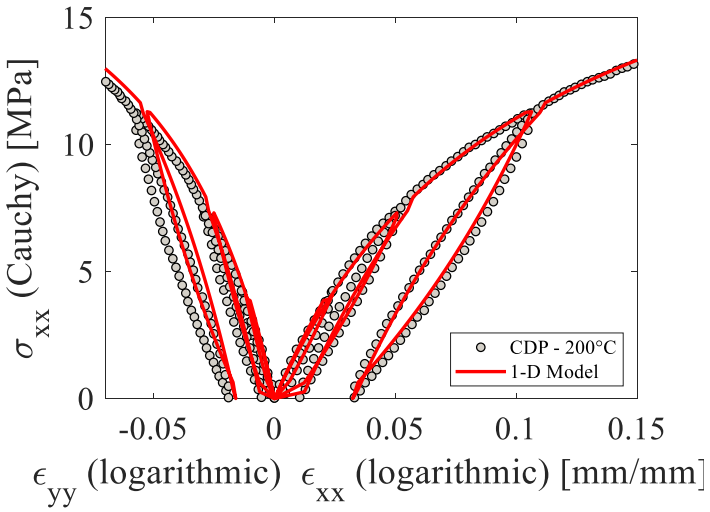

Fig. 4-28: Comparison between the 1-D model and the experimental CDP curve at 1 mm/min at 200°C

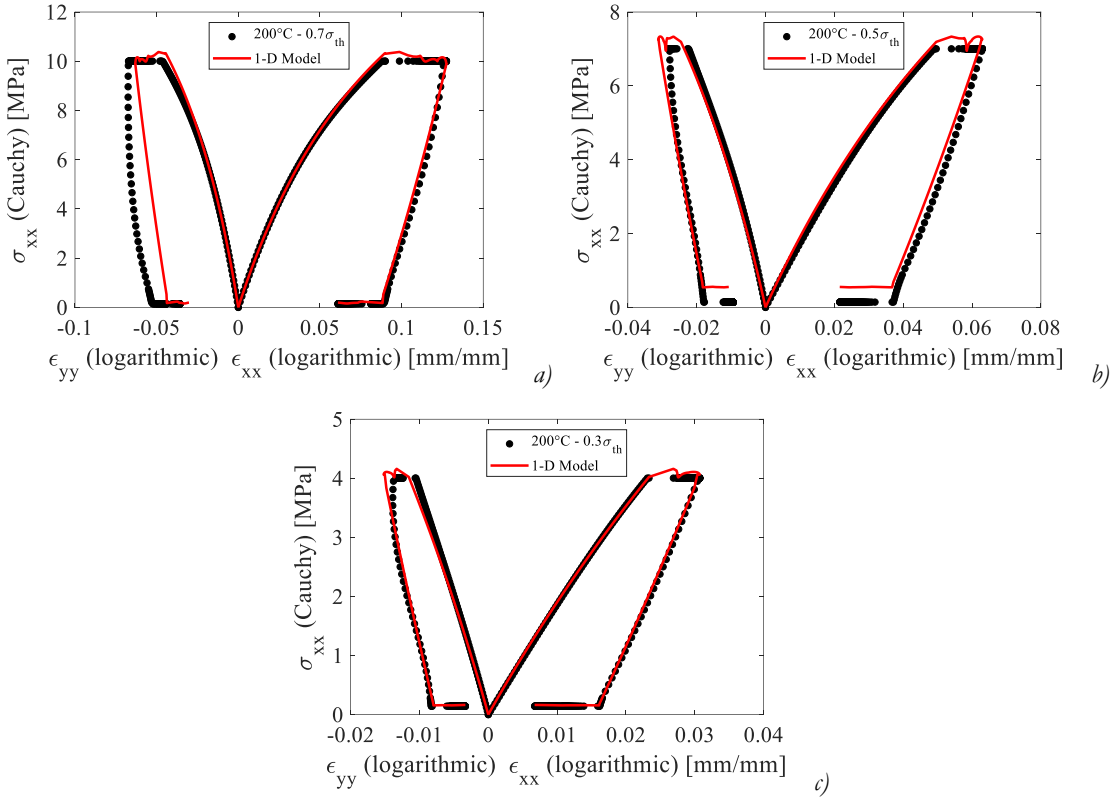

Fig. 4-29: Comparison between the 1-D model and the experimental creep-recovery curves at $0.7\sigma_{th}$ (a), $0.5\sigma_{th}$ (b) and $0.3\sigma_{th}$ (c) mm/min at 200°C

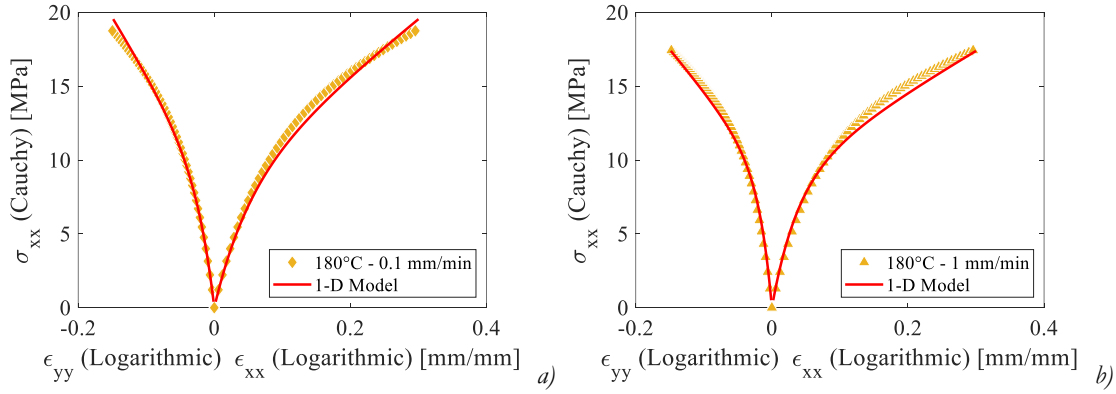

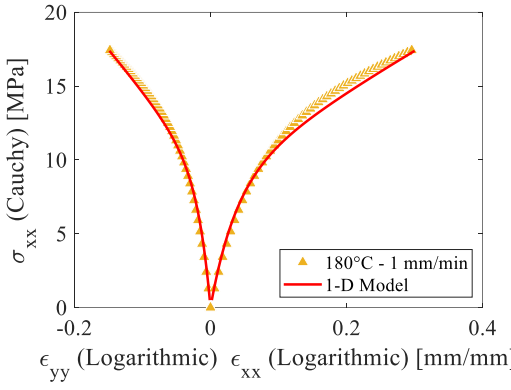

c)

Fig. 4-30: Comparison between the 1-D model and the experimental tensile curves at 0.1 (a), 1 (b) and 10 (c) mm/min at 180°C

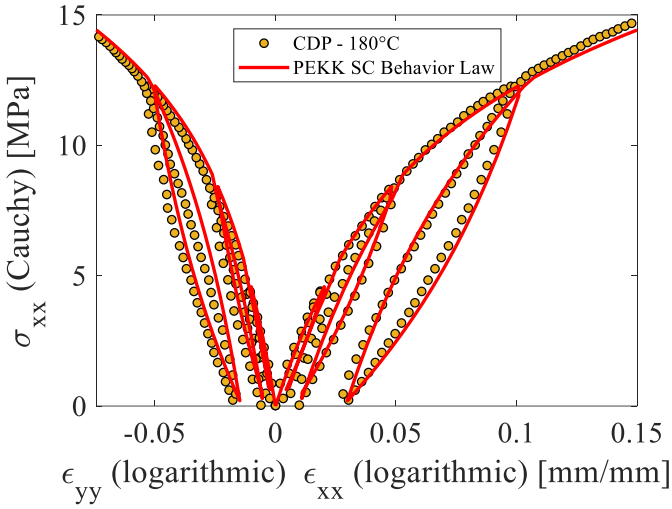

Fig. 4-31: Comparison between the 1-D model and the experimental CDP curve at 1 mm/min at 180°C

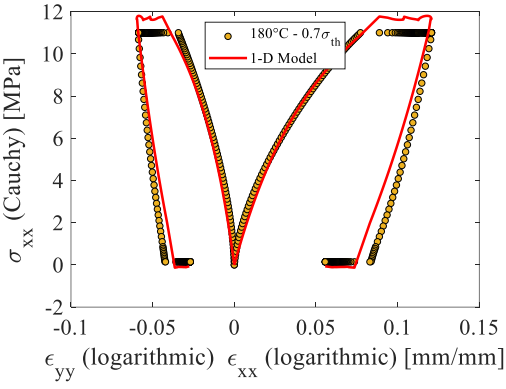

a)

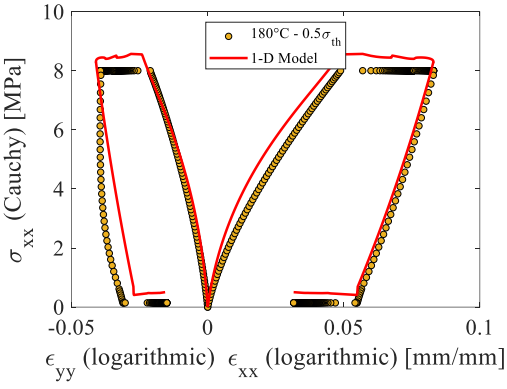

b)

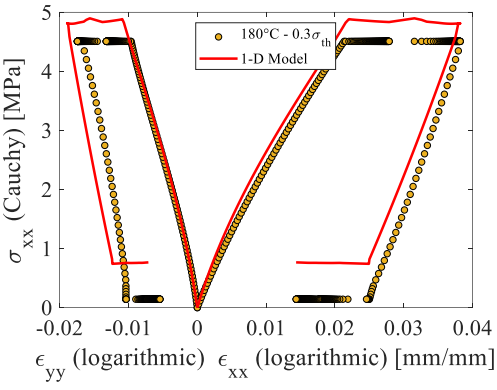

Fig. 4-32: Comparison between the 1-D model and the experimental creep-recovery curves at $0.7\sigma_{th}$ (a), $0.5\sigma_{th}$ (b) and $0.3\sigma_{th}$ (c) mm/min at 180°C

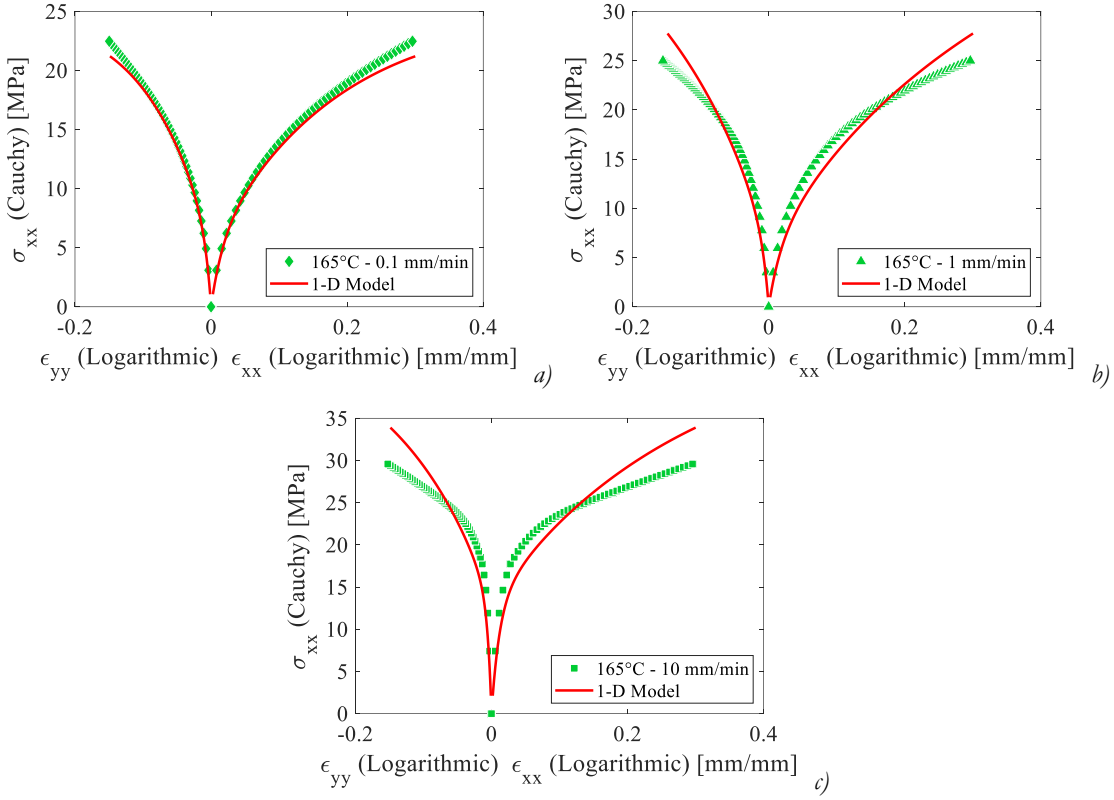

Fig. 4-33: Comparison between the 1-D model and the experimental tensile curves at 0.1 (a), 1 (b) and 10 (c) mm/min at 165°C

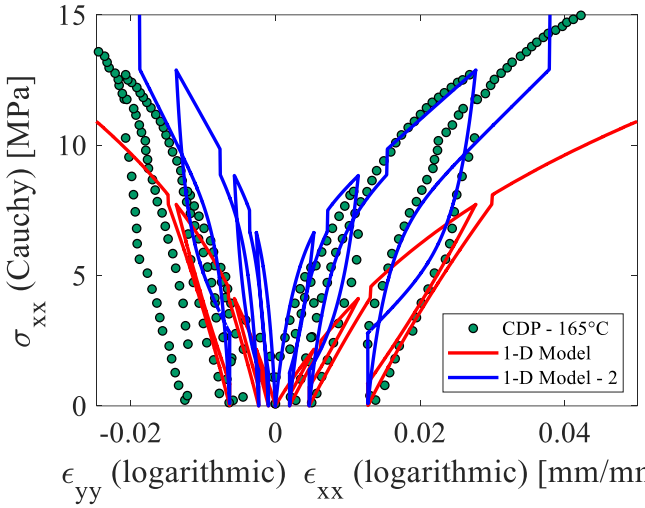

Fig. 4-34: Comparison between the 1-D model and the experimental CDP curve at 1 mm/min at 165°C

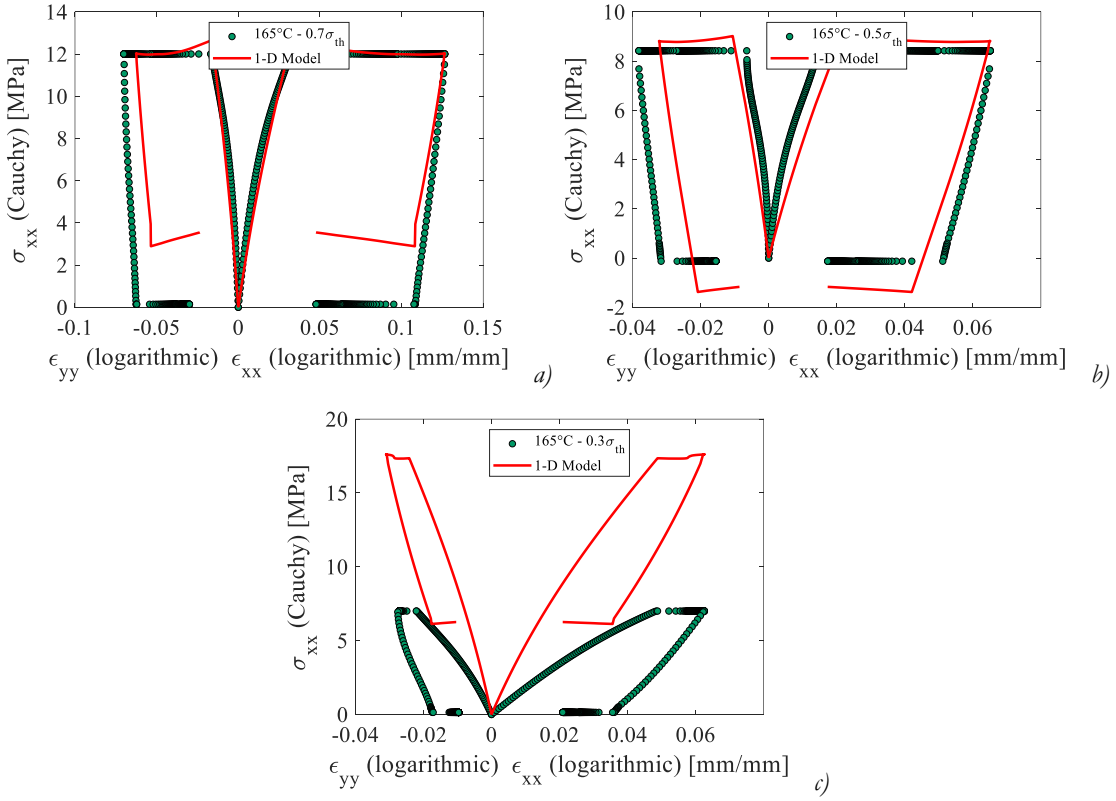

Fig. 4-35: Comparison between the 1-D model and the experimental creep-recovery curves at $0.7\sigma_{th}$ (a), $0.5\sigma_{th}$ (b) and $0.3\sigma_{th}$ (c) mm/min at 165°C

The 1-D model proposed for the PEKK 7002 SC behavior description can reproduce the tensile, CDP and C-R tests experimental curve at 180°C and 200°C. At 165°C, however, the model partially fails to reproduce the experimental curves, as for CDP tests, where different parameters are needed (blue curve in FIG. 4-31), and for creep-recovery tests.

Those differences could be due to the experimental low reproducibility (a ±1°C produce a ±50% of mechanical properties) of being still in the transition from below and above T_g, both could be possibly due to the presence of other mechanism that are not taken into account by the model.

The complexity in the interactions in the mechanisms active during load preceding the creep, which expresses the curves non-linearity, explains the difficulties in relating to each other the creep compliance curves (FIG. 4-11). Moreover, the combination of the crystallization mechanisms with different crystallization kinetics as function of the different test temperatures, combined to the viscoplastic phenomena present during creep, explains the impossibility of a time – temperature superposition showed in CHAP. 3.4.5.

While it is possible to modify the WLF formulation in order to obtain anyways a creep compliance mastercurve, no suitable physic-related alternative formulation could be found. Moreover, the data obtained at 165°C have to be excluded, as relative to the transition region from below to above T_g, reducing the suitable number of experimental data and preventing de facto from any further investigation.

The mechanisms identified in the previous paragraphs, which allow describing the behavior of PEKK SC, are depending on temperature, stress and, directly or indirectly (stress rate), on time. Because of the fact that all mechanisms are associated with phenomena related to the crystalline phase, a dependence on the crystalline percentage is probable. However, this could be assessed only if the analysis is extended to material with a different amount of initial percentage: therefore, in order to verify it, the analysis is extended to PEKK AM.

4.6. PEKK 7002 AM behavior at T>Tg

In order to extend the analysis on PEKK AM, a testing campaign similar to PEKK SC was carried out, with the same test conditions, protocols and equipment. In this way, the same analysis carried on PEKK SC and PEKK AM could be carried out also on PEKK AM. However, the latter is a material significantly different from the former, as discussed in the Literature Survey (CHAPTER 1) because of the different initial crystalline percentage, which impact:

- *the T_g*. The increase in crystalline percentage produces an increase in T_g, which for PEKK AM should be <160°C (=PEKK SC T_g). Therefore, because of the employment of the same test temperature, the comparison should be carried out considering the temperature respect to T_g and not in in absolute value;
- *the crystallization kinetics*. As proved in the previous paragraphs, in PEKK SC only secondary intra-spherulitic crystallinity can be produced exposing the material at T>T_g. Because of its initial low percentage content, in PEKK AM, also primary spherulitic crystallinity should be expected to form: the latter has a faster kinetics, such that PEKK AM crystallizes almost instantaneously as the temperature approaches 190°C. Hence, no tests could be carried out above this temperature. Furthermore, until the crystallinity percentage approaches the 78% of the maximum amount achievable (0.78 · 28%= 21.84%) and because of the delay in the formation of secondary crystallinity, it can be approximated that only primary crystallization forms;
- *the mechanical properties above T_g*. Because of the role of the crystalline percentage in containing the loss of properties above T_g, such loss is more significant in PEKK AM respect to PEKK SC: this leads to maximum stress measured in PEKK AM (<2 MPa at 165°C) significantly lower than in PEKK SC, which prevented to carrying out also creep-recovery tests on PEKK AM, because no difference could be established between creep and recovery phases.

Therefore, for PEKK AM the analysis is limited to tensile, CDP, DMA and DSC tests.

4.6.1. Tensile test

Tensile tests were carried out on PEKK 7002 AM specimen type *b* (FIG. 2-5), according to the testing protocol described in (CHAP. 2.3.1.2) at 5 of the 6 temperatures at which the SC was tested: in fact, at around 190°C, the crystallization process starts immediately in AM (CHAP. 4.6.3), with consequent modification of the internal stress state and the severe deformation of the specimen, which will become unemployable for testing, only because of temperature exposure; hence no test could be carried out at 200°C. The test conditions are summarized in TAB. 4-15.

$T\ [°C]$	$\dot{z}\ [mm/min]$
20	1
100	1
150	1
165	1
180	1

Tab. 4-15: PEKK 7002 AM tensile test conditions

4.6.1.1 Heating phase analysis

Each tensile test at temperature above the room temperature is preceded by the heating phase described in CHAP. 2.3.1.2. During the heating phase, after an initial linearity of the deformation (corresponding to a thermal expansion), once T_g is passed, the deformation starts increasing and the specimen undergoes a creep phase even under the applied load of 0.3N, which is not seen for SC. FIG. 4-36 shows the temperature and longitudinal strain kinetics during the heating phase.

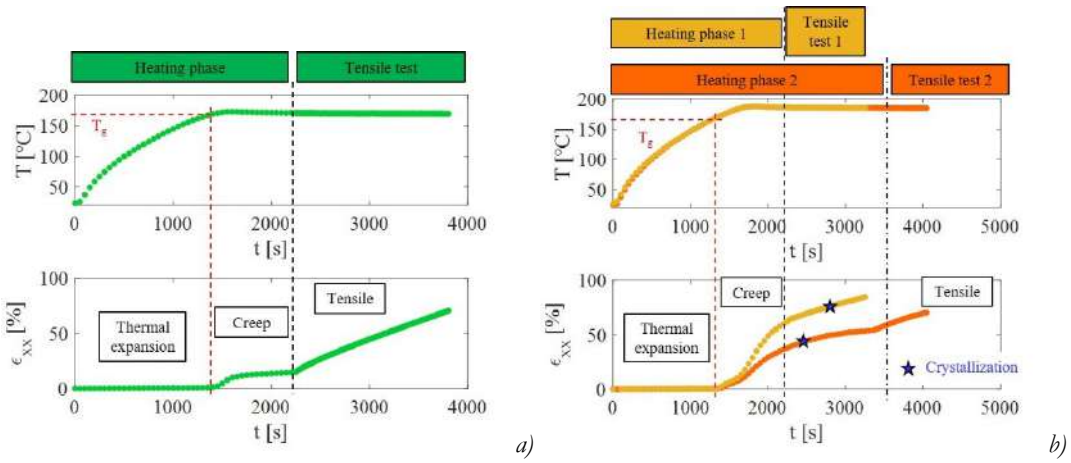

Fig. 4-36: Temperature and longitudinal strain curves plotted against time from for heating and tensile phases at 165°C (a) and180°C (b)

FIG. 4-36 show images taken at different times, during heating and tensile tests of the specimen gauge length, at 180°C, comparing the effect of different heating durations.

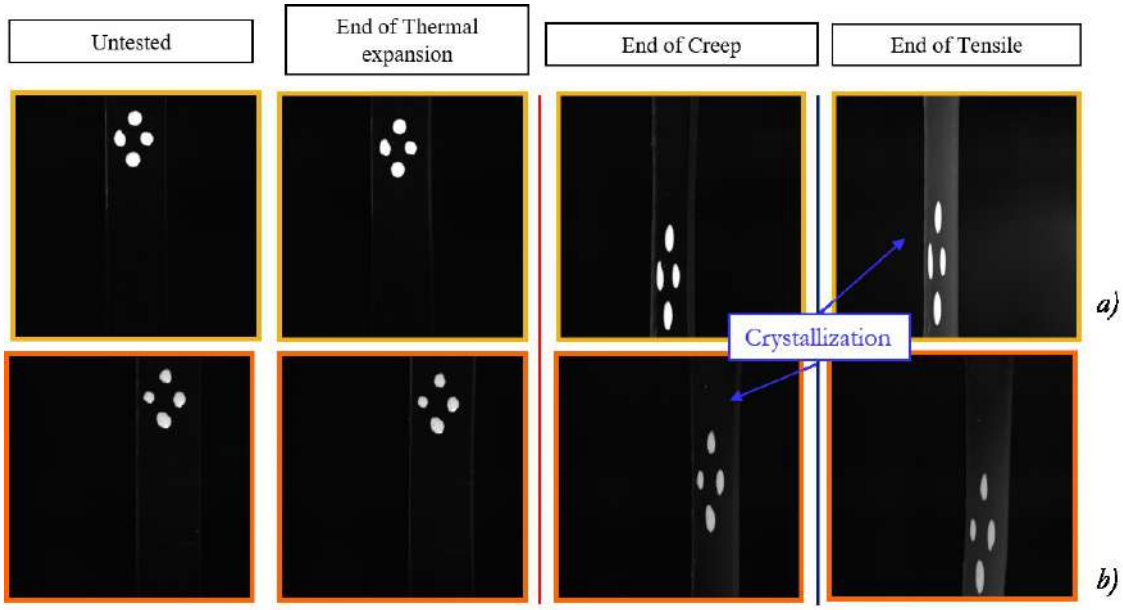

Fig. 4-37: Images acquired during heating phase up to 180°C of PEKK 7002 AM specimens

From the analysis of the heating phase data, it results that:

- after the heating phase up to 165°C, a creep strain of around 20% is measured (FIG. 4-36A) and no crystallization is observed;
- after the heating phase up to 180°C, a creep strain is measured (yellow curve in FIG. 4-36A) and no crystallization is observed; if the heating is prolonged over 2500 s (orange curve in FIG. 4-36B), crystallization appears in the specimens during the creep phase (FIG. 4-37B).

As appears from the images in FIG. 4-37, at 180°C, a great variability undermines the reproducibility of the tests (higher strain after lower heating duration), which could be due to out of plane deformations promoted by the beginning of crystallization processes, affecting the measurers and/or by small variations of the test temperature: therefore, all strain measures are employable just for qualitative comparison.

4.6.1.2 Temperature effects

The results obtained from tensile tests carried out at 1 mm/min at room temperature, 100°C, 150°C, 165°C and 180°C are showed in FIG. 4-38: in order to compare the results for the whole test durations, the behavior is presented in form of force vs displacement (or machine head position) curves.

The comparison of force vs displacement curves at different temperature at 1 mm/min on PEKK 7002 AM specimens is showed in FIG. 4-38 .

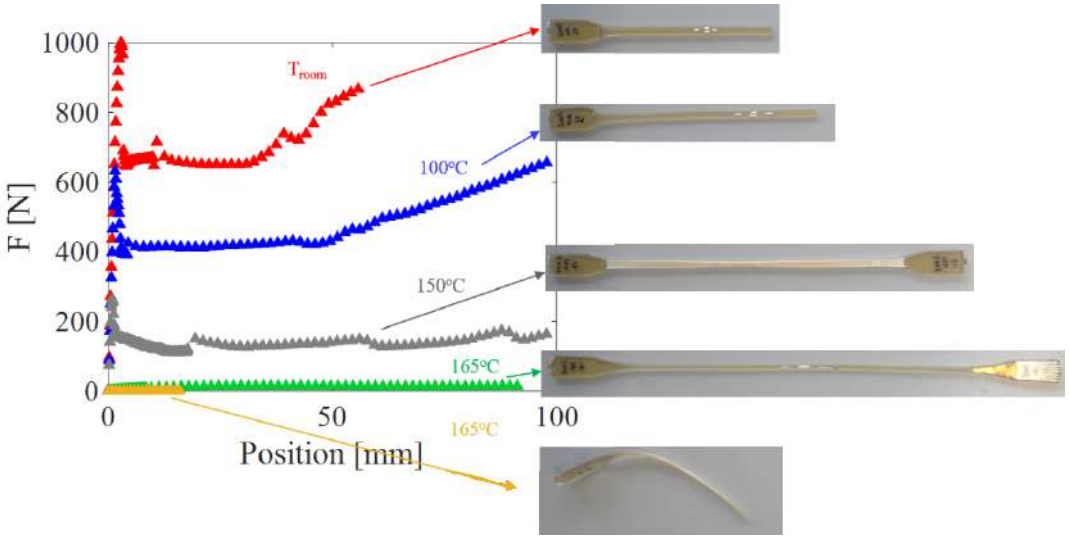

Fig. 4-38: Force vs displacement curves at different temperature at 1 mm/min on PEKK 7002 AM specimens

The FIG. 4-38 shows, on PEKK AM, the same effects of the temperature seen on PEKK SC, producing, as it increases:

- a decrease of the apparent stiffness;
- a decrease of the maximum stress;
- an increase in ductility;
- an increase in strain at rupture.

The failure mode also changes with the temperature:

- at room temperature and 100°C, a localized and sharp necking appears (in correspondence of the peak), which shortly extends along the gauge length before failure, as for PEKK SC;
- increasing the temperature, the necked area extends progressively until it covers the whole gauge length (150°C) and no failure could be induced because of testing limits; for PEKK AM, however, the all necked area changes color, become opaque, suggesting that crystallization phenomena appear;
- above T_g, at 165°C, the necking is more diffused and gradual along the overall gauge length as for PEKK SC. At this temperature:
  - a maximum value of only 13 N is measured, hence during the heating phase, the specimen undergoes a creep solicitation of 2.3% of maximum load;
  - no appreciable change in color appears;
  - the failure could not be reached for testing limits ($\varepsilon \gg 200\%$).
- at 180°C:

- a maximum value of only 1 N is measured, hence during the heating phase, the specimen undergoes a creep solicitation of 33% of maximum load;
- the specimen gradually changes color and, in the initial gradual necked area, crystallization appears from a crystallization nucleation site. The failure is reached, with out-of-plane strains, possibly due to the internal stress induced by the crystallization itself.

4.6.1.3 Volumetric changes during tensile tests

As for PEKK SC, the comparison between the true stress vs true strain curves of PEKK AM at 1 mm/min for each test temperature is stopped before the necking appearance and it is showed in FIG. 4-39.

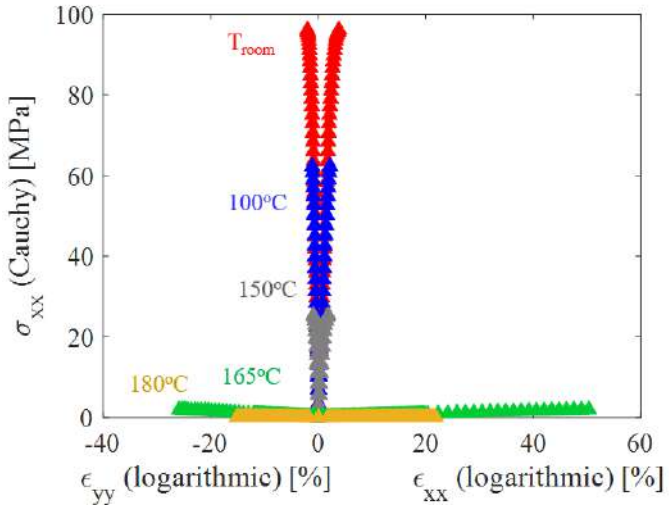

Fig. 4-39 True stress vs longitudinal and transversal true strains from tensile tests at different temperature at 1 mm/min on PEKK 7002 AM specimens

The volume change during tensile tests is measured as the trace of the strain tensor, under the transversal isotropy hypothesis, according to EQ. 4-1. The results are showed in FIG. 4-40: PEKK AM enhances the phenomena seen for PEKK SC, and for all tests the volume variation is negative.

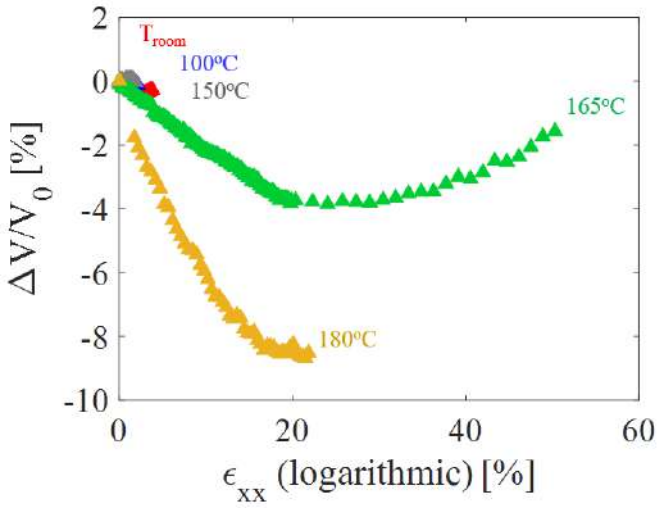

Fig. 4-40 PEKK 7002 AM volume change from tensile tests at different temperature at 1 mm/min, according to logarithmic formulation

The ratio between the transversal and longitudinal strains, allows evaluating the Poisson's coefficient between the two directions, according to EQ. 4-3, and coherently with the measured negative volume changes, it is higher than 0.5 at any temperature (FIG. 4-41).

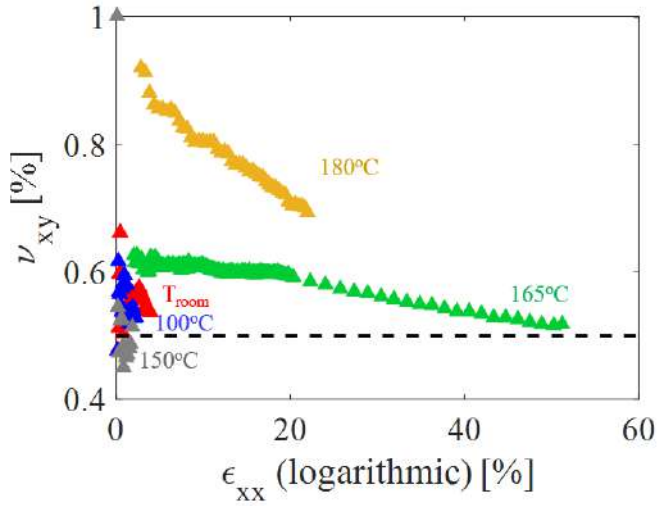

Fig. 4-41: PEKK 7002 AM Poisson's coefficients from tensile tests at different temperature at 1 mm/min

This seems to point out that the incompressibility hypothesis could generate errors in the transverse prediction of PEKK AM behavior but, as for PEKK SC, to comply to classic mechanics, such hypothesis will be made anyways.

4.6.1.4 PEKK AM engineering mechanical properties

As for PEKK SC, for PEKK AM the most evident effect resulting in the transition above T_g, is the mechanical properties loss. In order to compare such loss with the one observed in PEKK SC, the pseudo-elastic moduli are calculated for PEKK AM at the different test temperatures above and below T_g.

The pseudo-elastic tensile modulus is evaluated at each temperature through a linear regression of the true stress vs true strains curve between 0.1% and 0.5% true strain for temperature below T_g and between 1% and 4% true strain above T_g, (FIG. 4-39). The values corresponding to all tensile tests at 1 mm/min are summarized in TAB. 4-16 and showed in FIG. 4-42.

ż [mm/min]	T [°C]	Pseudo-elastic modulus [MPa]	Poisson's Coefficient
1	20	3757	>0.5
	100	3195	>0.5
	150	1968	>0.5
	165	4	>0.5
	180	0.5	>0.5

Tab. 4-16: Initial tensile moduli and Poisson's coefficient obtained from tensile test on PEKK 7002 AM and from room temperature to 180°C at 1 mm/min

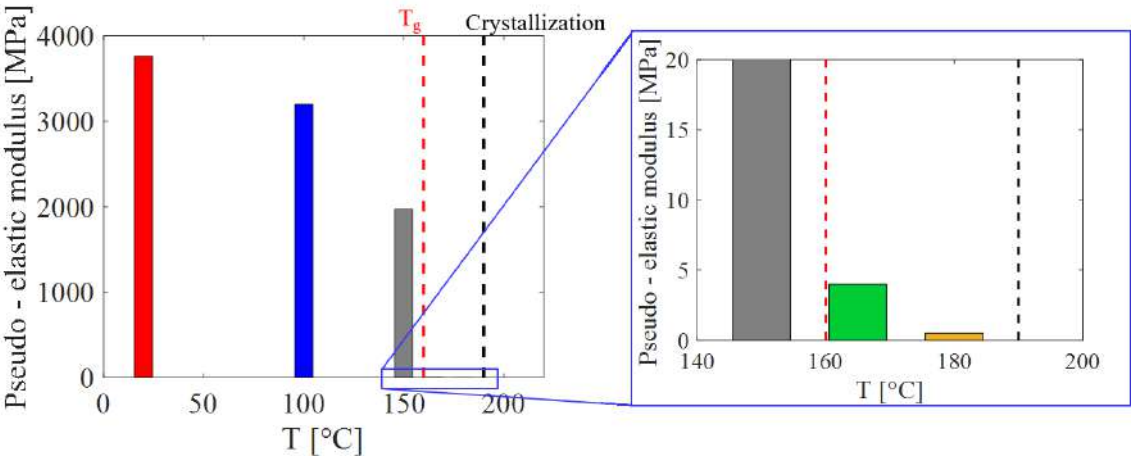

Fig. 4-42 Pseudo-elastic moduli vs temperature obtained from tensile test on PEKK 7002 AM from room temperature to 180°C at 1 mm/min

The measured value of pseudo-elastic moduli explains the need of changing the strain range in the calculation of the pseudo-elastic modulus: while below T_g, the values of PEKK AM pseudo-elastic moduli are of the same order of magnitude than for PEKK SC, above T_g, they are 2 orders of magnitude lower. In fact, for PEKK AM, the transition above T_g has a

dramatic effect on PEKK AM mechanical properties, which are almost completely lost (>-99%), showing at the same time the role of the crystalline phase in containing such loss.

4.6.2. DMA tests

In order to confirm the properties loss resulting from the comparison of pseudo-elastic moduli, 3-point-bending DMA tests were carried out on PEKK 7002 AM specimen type *a* (FIG. 2-5), according to the testing protocol described in (CHAP. 2.3.1.3).

The results, in terms of storage modulus and complete of the pseudo-elastic moduli, are compared to the respective value obtained on PEKK SC, in both absolute value and normalized respect to their initial values, respectively in FIG. 4-43A and B.

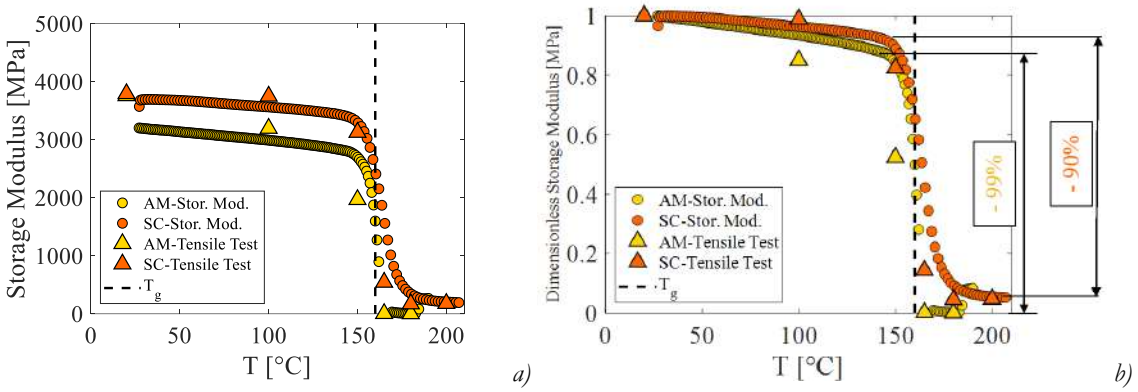

Fig. 4-43: Comparison between PEKK AM (yellow) and PEKK SC (orange) DMA storage modulus between 20°C and 200°C, compared with pseudo-elastic moduli as measured values(a) and as ratio respect to initial values (b).

Under T_g, PEKK AM and SC storage moduli have almost the same trend with the temperature (AM *E'* is around 300 MPa lower than SC *E'*). Above T_g, PEKK AM storage modulus decreases faster than PEKK SC storage modulus, losing almost completely its mechanical properties, and confirming the tensile tests results.

The comparison between the thermomechanical behavior PEKK SC and AM suggests a global similarity in behavior, with the latter scaled respect to the former because of the different crystallinity percentage, confirming the fundamental role of the crystalline structure in PEKK behavior.

Therefore, an investigation on PEKK AM crystallization kinetics is needed, and described in the following paragraph.

4.6.3. DSC tests on PEKK AM

As discussed in Literature Survey (CHAPTER 1), it is expected, for a not completely crystallized material, to activate crystallization mechanisms as the temperature is increased above T_g. Moreover, if the relative crystalline percentage is lower than 78% of the total (= 21.84%), also primary spherulitic crystallization mechanisms are expected to activate in PEKK.

The crystallization formed during tensile tests, showed in FIG. 4-38, already constitutes a major difference in behavior compared to PEKK SC, for which no crystallinity increase is observed during tensile tests, possibly confirming that different crystallization mechanisms are active in PEKK AM.

In order to verify it, DSC tests were carried out on PEKK 7002 AM specimen type *f* (FIG. 2-5), cut from as-received materials (reference) and previously tested specimens, according to the testing protocol described in (CHAP. 2.3.1.4).

FIG. 4-44 shows the comparison between the heath flow vs temperature curves of DSC tests carried out on specimens cut from PEKK AM and SC as-received material. For all materials, the T_g, the T_m and the peak enthalpy are measured for 1st and 2nd heating and cooling phases; the measured values are listed in TAB. 4-17.

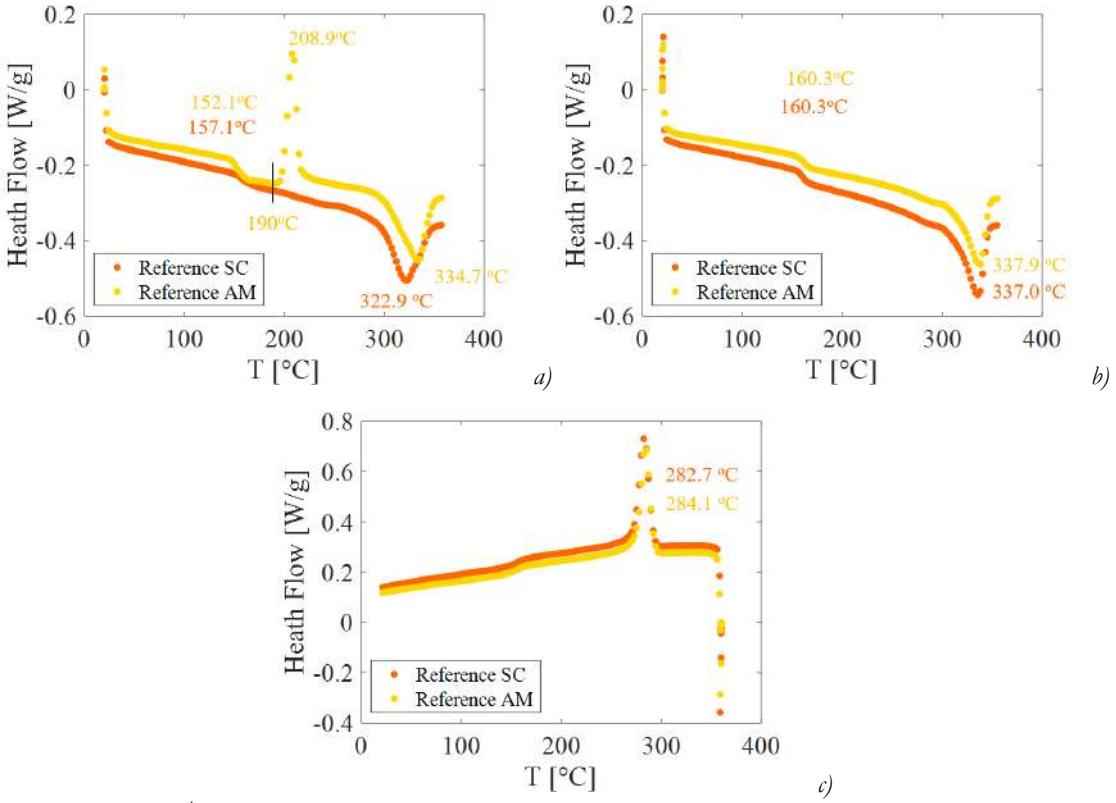

Fig. 4-44: 1st (a), 2nd heating (b) and cooling (c) phases comparison from DSC test on PEKK 7002 AM and SC samples cut from as-received material

	Reference SC	Reference AM
1st Heating		
T_g [°C]	157.1	152.1
T_m [°C]	322.9	334.7
ΔH_f [J/g]	31.63	31.22
T_{cc} [°C]	/	190
ΔH_{cc} [J/g]	/	25.88
2nd Heating		
T_g [°C]	160.3	160.3
T_m [°C]	337.0	337.0
ΔH_f [J/g]	29.86	39.64
Cooling		
T_p [°C]	282.7	284.1
ΔH_c [J/g]	38.18	35.76

Tab. 4-17 Tg, Tm and peaks enthalpy measured from DSC test on PEKK 7002 AM and SC samples cut from as-received material

The PEKK AM heath flow vs temperature curve referring to the 1st heating phase (FIG. 4-44A) shows the presence of an exothermic peak (*cold crystallization*) starting at around 190°C, which is not present in PEKK SC, and indicates the temperature at which the crystallization processes starts. Also a difference in the measured T_g (-5°C) and T_m (+12°C) is registered:

- the difference in T_g is coherent with the different initial crystalline percentage and with the nominal value of T_g (PEKK SC T_g = PEKK AM T_g +5°C). The difference in T_m could be instead explained by the difference in the crystalline morphology produced by the different crystallization kinetics, isothermal for PEKK SC at 230°C and non-isothermal during DSC for PEKK AM;
- the cold crystallization peak only prove the crystallization mechanism is activated, but no information about primary and secondary crystallization could be deduced, even if for the consideration made at the beginning of the present paragraph it should be for the most part primary.

The 2nd heating and cooling phase (respectively FIG. 4-44B and C), show that after the complete melting, there is no difference between PEKK AM and PEKK SC.

The crystallization occurring during tensile test is investigated through DSC test on PEKK 7002 AM samples cut from as-received material and after tensile tests at room temperature, 100°C, 150°C, 165°C and 180°C. FIG. 4-45 shows the comparison between the 1st heating phases obtained from those tests.

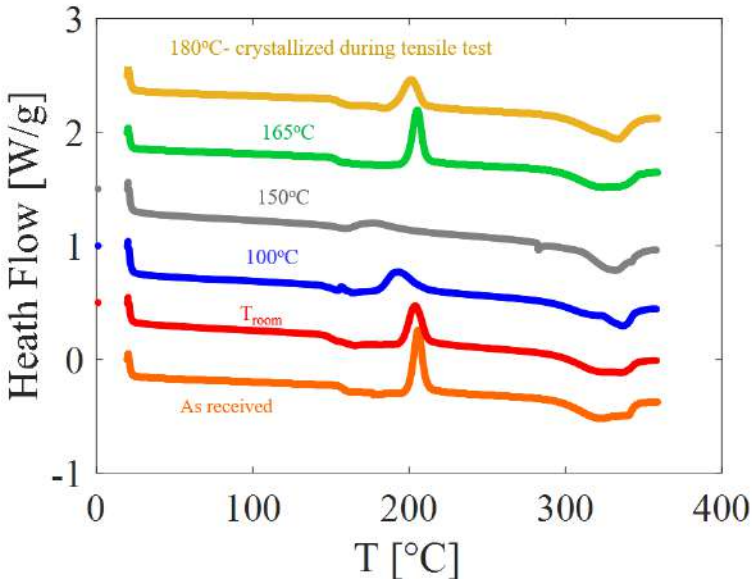

Fig. 4-45: 1st heating phases comparison from DSC test on PEKK 7002 AM samples cut from as-received material and after tensile tests at room temperature, 100°C, 150°C, 165°C and 180°C.

The exothermic peak after T_g progressively reduces if the temperature is increased up to T_g and shifts towards T_g, while the melting endothermic peak increases its area and shifts toward higher temperatures. Above T_g, the exothermic and the melting endothermic peaks have the same evolution with temperature than below T_g, but starting again from the as received material 1st heating curve.

The total crystallinity percentage measured after tensile test, according to EQ. 4-4, is showed in FIG. 4-46, and the values are listed in TAB. 4-18.

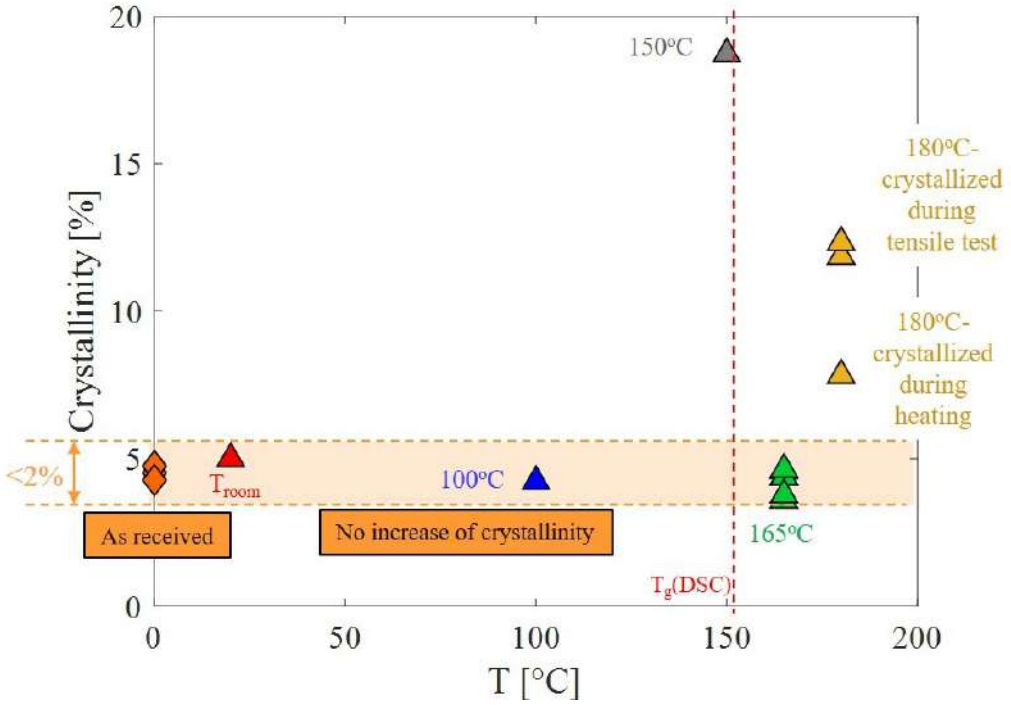

Fig. 4-46: PEKK AM measured crystallinity percentage vs test temperature from DSC test on samples cut after tensile tests at room temperature, 100°C, 150°C, 165°C and 180°C.

Test condition			χ_{TOT} [%]
As received (average)			4.52
TT	1 mm/min	RT	5.01
		100°C	4.23
		150°C	18.72
		165°C	3.60
			4.38
			3.78
			4.64
		180°C (>41 min heating)	7.84
		180°C (41min heating)	11.86
			12.34

Tab. 4-18: PEKK 7002 AM crystallinity percentage values measured through DSC test on specimens cut from specimen on as received material and after tensile tests at different test temperature

FIG. 4-46 shows the crystalline percentages after tensile tests, compared to the as received material: there is a considerable increase in crystallinity at 150°C (below T_g), while there is no increase of crystallinity at 165°C, confirming the optical observation of the color change in

the specimens (FIG. 4-38). An increase of crystallinity is observed at 180°C, with different value according to the employed heating protocol.

Since the measured crystallinity percentage is in all cases less than 21.74%, it can be considered that only primary crystallization was produced in the specimens. This allows the comparison with the modified Hillier model limited to primary crystallization (HSIAO, CHANG, AND SAUER 1991), which can be calculated as function of the time as:

$$\chi_1 = \chi_1^{max}(1 - \exp(-K_1(t)^3)) \qquad Eq.\ 4\text{-}25$$

where χ_1^{max}=21.74% is the maximum primary crystallization achievable and K_1 is calculated according to the parameter identification proposed by (TANGUY CHOUPIN 2018), with the hypothesis that:

- initially the 4.52% of crystallinity is present in the material and it is all primary crystallization;
- the kinetics continue from 4.52% and the exposure time is summed to the time needed at the temperature T to reach this value. While this is an overestimation, it produces a better result than considering that the kinetics starts from 0, because of the cubic dependence on the time. Hence the time inserted in EQ. 4-25 is equal to

$$t = t_{\chi 0} + \Delta t \qquad Eq.\ 4\text{-}26$$

  where:

  - $t_{\chi 0}$ is time needed to reach χ_0 =4.52% at a specific temperature;
  - Δt is the duration of the tensile test at the same temperature.

This lead to the comparison showed in FIG. 4-47, with the calculated values listed in TAB. 4-19.

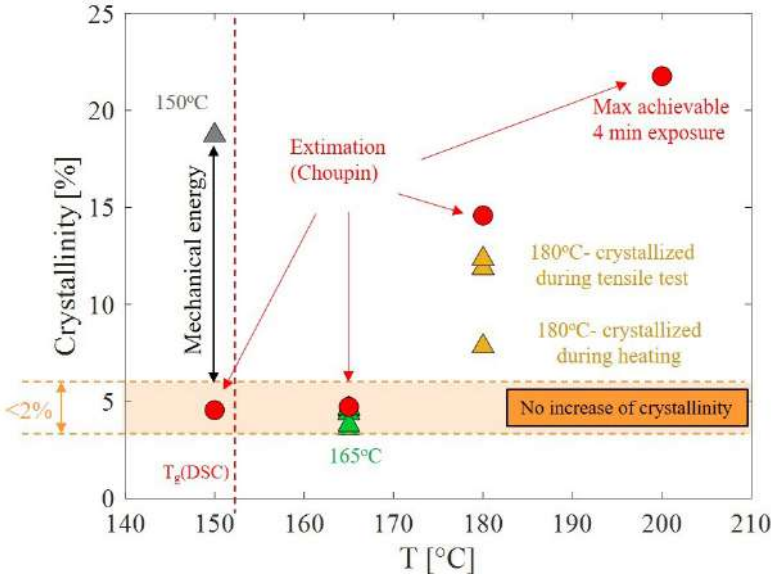

Fig. 4-47: Comparison between the total crystallinity measured on PEKK AM after tensile tests at 150°C, 165°C and 180°C and the esteemed crystallinity according to Choupin, at same temperature and for the same duration than tensile test (red markers). Estimation at 200C°, after 4 min of exposure

Temperature [°C]	K_1 [min]$^{-3}$	$t_{\chi 0}$ [min]	Δt [min]	χ_1 [%]
150	2.94E-21	4300000	25.72	4.55
165	2.40E-10	989	16.84	4.72
180	1.59E-05	24.5	16.61	14.58
200	2.41E-02	2.132	4	21.76

Tab. 4-19: Primary crystallization percentage produced after an isothermal duration of the same duration of tensile tests on PEKK AM, according to the PEKK 7002 crystallization kinetics proposed by (Tanguy Choupin 2018)

The comparison showed in FIG. 4-48 shows:

- a significant underestimation of the crystallinity measured after tensile test at 150C°;
- a good agreement with the value measured after tensile tests at 165°C (no increase in crystallinity);
- a small overestimation of the values after tensile tests at 180°C;
- it shows that only 4 min at 200°C are sufficient to produce the maximum achievable primary crystallization.

If the overestimation could be explained with the hypothesis made in the application of Hillier model, the underestimation at 150°C is not: this suggests that the *energy provided during the tensile test accelerates significantly the crystallization kinetics*. The fact that does not happen at higher temperatures, could be instead explained by the loss of mechanical properties showed in FIG. 4-43, in the transition above T_g: the maximum stress applied at 150°C is ~30 MPa, while it is <2 MPa at 165°C.

This scenario suggests that information could be extrapolated from the DSC and DMA tests: a total energy, composed by the sum of the mechanical and thermal energy, could be esteemed, as the energy provided to the system at the beginning of the tensile tests. In facts, DMA was carried out imposing only a 0.1% strain, while during the DSC a 10°C/min temperature rate was applied, such that the material is exposed at each temperatures ± 0.5°C for 6 s. Such conditions are coherent with the very beginning of the tensile tests.

The mechanical contribution can be obtained as the internal energy, according to:

$$\frac{dU_{mec}}{dV} = \frac{1}{2}\sigma\,\varepsilon \qquad \textit{Eq. 4-27}$$

where σ and ε are the stress and strain measured during the DMA tests on the as received material (CHAP. 4.6.2).

The thermal contribution as:

$$\frac{dU_{therm}}{dV} = -\,\varrho_{AM}\int q\ \mathrm{dt} \qquad \textit{Eq. 4-28}$$

where q is the heat flow measured during the DSC test showed in FIG. 4-44, multiplied for the density of the PEKK AM, ϱ_{AM} = 1.27 g/cm^3.

The total energy per unit of volume is then the sum of the two contribution as:

$$\frac{dU_{tot}}{dV} = \frac{dU_{mec}}{dV} + \frac{dU_{therm}}{dV} \qquad \textit{Eq. 4-29}$$

Employing the data obtained from the DSC and DMA tests carried out, FIG. 4-44 can be obtained, where the markers represent the value corresponding to the temperature chosen for the tensile tests on PEKK AM. The green curve shows the T_g resulting from DSC test.

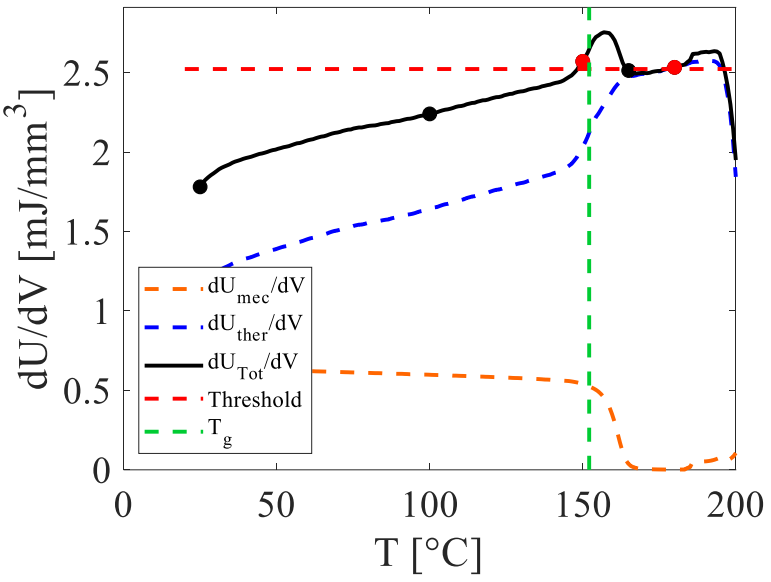

Fig. 4-49: Representation of the mechanical and thermal contribution to the crystallization energy for PEKK 7002 AM and the values corresponding to the temperature chosen for the tensile tests

FIG. 4-44 shows a peak of total energy between 150°C and 165°C, which could explain the difference of provided energy to the system which provoke the crystallization at 150°C and not 165°C. Moreover, the value calculated at 180°C is higher than the value at 165°C, (because of the increase thermal contribution), which allows drawing a crystallization threshold of energy, according to the results obtained from DSC tests (the red markers identify the value the value of total energy above the threshold).

Above 190°C, the PEKK AM starts crystallizing immediately by the provided thermal load alone: the new formed crystalline phase alters both the DSC and DMA test results, and therefore the analysis it is stopped at that temperature.

From the above described analysis it results for the PEKK AM a tensile behavior even more complex than for PEKK SC, where a different crystallization mechanism (primary instead than secondary) is activated: this mechanism is not only dependent on the temperature, but coupled with the mechanical load provided, which accelerates it. From an energetic point of view this has the effect of lowering the activation energy, exactly the contrary of the retardation effect the tensile load has on the secondary crystallization kinetics in PEKK SC.

The effective kinetics cannot be established if not with the carrying out of in situ WAXS tests during tensile tests.

This prevents the extension of the 1-D model defined for PEKK SC to PEKK AM, because it does not take into account the coupling with primary crystallization. However, because of the absence of crystallinity increase at 165°C, at this temperature PEKK AM behaves

similarly to PEKK SC. In order to verify it and moreover to verify if the same mechanisms are active, a CDP test was carried out at this temperature.

4.6.4. Load – Unload – Reload tests

The CDP test was carried out on PEKK 7002 AM specimen type *b* (FIG. 2-5), according to the testing protocol described in (CHAP. 2.3.1.2). The CDP test parameters are summarized in TAB. 4-20.

T [°C]	ż [mm/min]	σ_i [MPa]
165	1	0.15, 0.2, 0.25, 0.3, 0.4

Tab. 4-20: CDP test parameters for PEKK 7002 SC

FIG. 4-43 shows the comparison between the resulting true stress vs true strain of the CDP test at 165°C with the tensile test carried out at the same temperature and displacement speed.

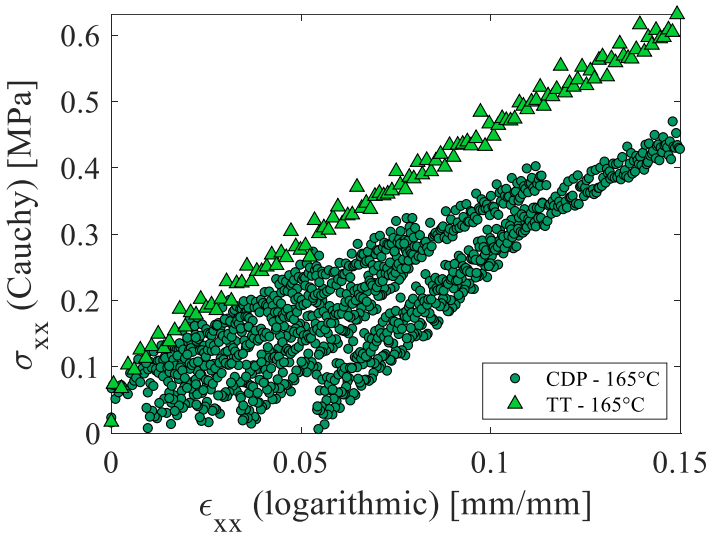

Fig. 4-50: Comparison between CDP and tensile test carried out on PEKK AM at 165°C and 1 mm/min

Considering a nominal value of 155°C for PEKK AM T_g, the test temperature of 165°C equals T_g+10°C, different than for PEKK SC (165°C=T_g+5°C): this explain the difference between tensile and CDP tests showed in FIG. 4-23, which are carried out at a temperature close to end of the transition region below-above T_g, but not yet out of it, hence still highly sensible to temperature variations. Thus, the comparison showed in FIG. 4-23 is more similar to PEKK SC behavior at 200°C than 165°C (FIG. 4-4).

Besides those considerations, the same mechanisms identified for PEKK SC are clearly identifiable also on PEKK AM, with the increase in reload stiffness compared to initial load, and the sudden softening as the threshold stress is passed, as described in CHAP. 4.2.3. This suggests that the model identified for PEKK SC could also describe PEKK AM behavior, if the crystallinity initial percentage is also taken into account.

4.6.5. 1-D model applied to PEKK AM

The 1-D model described in CHAP. 4.5.3, limited to the load – unload part is employed to reconstruct the PEKK AM tensile and CDP stress vs strain experimental curves.

The identified parameters at 165°C (= T_g+10°C) for PEKK AM are compared not in terms of absolute temperature, but as difference from T_g, to the PEKK SC corresponding ones at T_g+10°C = 170°C, extrapolated from TAB. 4-14.

The parameters are listed TAB. 4-14 in and the comparison between the model and the experimental curves are showed in the following figures.

Mechanism	Parameter		Value	
			PEKK AM T=165°C χ_0 = 4.5%	PEKK SC T=170°C χ_0 = 24.3%
Elasticity	E_0 [MPa]		4.88	140.00
Hardening	a [MPa]		0.0631	6.5
	b [mm/mm]		0.0015	0.0246
Softening	$h_{C1} \ln \dot{\varepsilon} + h_{C2}$ [ ]	TT	0.032	0.0021
		CDP	0.017	
	m [ ]		-0.93	-0.895
	n [ ]		0.8	0.69

Tab. 4-21: Comparison of the parameters of the model at the same distance from T_g for PEKK AM and PEKK SC

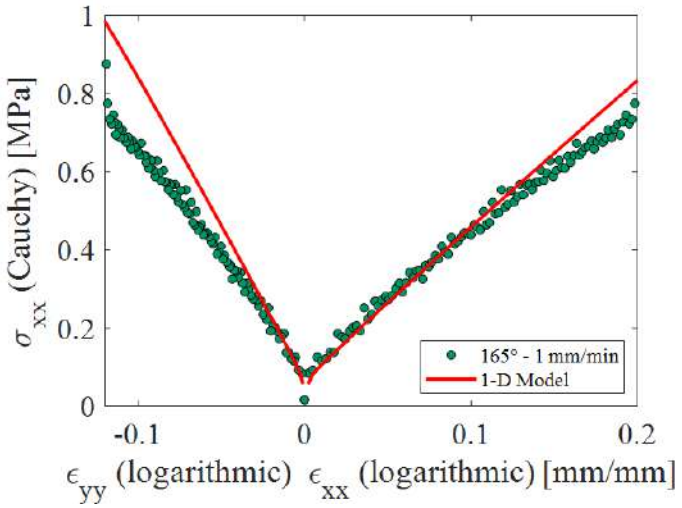

Fig. 4-51: Comparison between the 1-D model and PEKK AM experimental tensile curve at 1 mm/min at 165°C

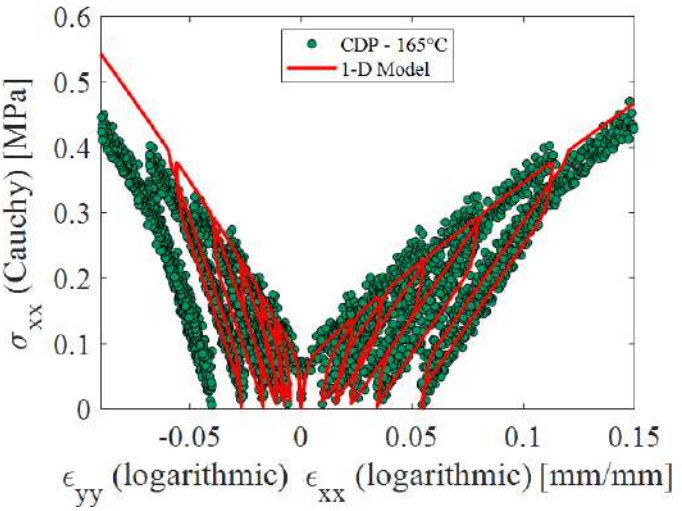

Fig. 4-52: Comparison between the 1-D model and PEKK AM experimental CDP curve at 1 mm/min at 165°C

The need of a different coefficient for the softening for the tensile and CDP description, as listed in TAB. 4-14, depends on the difference observed between the tensile and CDP experimental curves showed in FIG. 4-43, due to the fact that at165°C PEKK AM is still in the T_g transition region.

In both the above figures, while there is a good agreement in the description of the longitudinal behavior, the transversal one is not as well described: this is due to the fact that, for PEKK AM, the measured Poisson's coefficient is closer to 0.6 than 0.5, as showed in FIG. 4-41, producing the correspondence of the stress to lower value of transversal strain, if the incompressibility hypothesis is made.

Besides those errors, it can be concluded that:

- the same mechanisms observed in PEKK SC are present also in PEKK AM, and consequently, the model parameters depend also on the initial crystallinity percentage, besides temperature, stress and time;
- the elastic modulus is coherent to the evolution with the crystallinity percentage showed in FIG. 4-23;
- PEKK AM hardening mechanism parameters are 1÷2 orders of magnitude lower than PEKK SC ones, coherently with the physical interpretation of crystal re-orientation;
- PEKK AM softening mechanisms parameters are higher than PEKK SC ones, showing the role of the amorphous phase in this mechanism.

4.7. Conclusions

The present chapter is focused on the identification of the different mechanisms characterizing the PEKK SC behavior above T_g, enabling to complete description of the different thermomechanical load conditions which underwent experimentally.

Preliminarily, the analysis of the volumetric changes during the heating phase (thermal load from room temperature to 200°C) shows a change of slope at around 160°C, confirming the estimated value of T_g, and proves the presence of physical ageing below T_g. Above T_g, the material is considered incompressible, and its Poisson's coefficient as 0.5. Such hypothesis allows deriving the behavior of the PEKK SC in the transverse and in the thickness direction from the longitudinal one and allows considering only the latter in the analysis.

The addition of load-unload –reload tests to the tensile and creep –recovery tests, combined with DSC tests carried out after those tests, allowed the identification of 3 principal mechanisms:

- a *hardening* mechanism, producing an increase in stiffness in the reload respect to the initial load (or tensile test). This mechanism is dependent on the stress, the strain rate and on the temperature. Moreover, it activates only if the strain rate is not null. It is associated to the alignment of the initially random oriented crystal structure towards the loading direction, and it can be completely reversed during the unload;
- a *softening* mechanism, which causes the reload (stiffer than the initial load because of the hardening mechanism) to re-superpose on the tensile test (= initial load). As the hardening, the softening mechanism is dependent on the stress, the strain rate and on the temperature. Moreover, it does not activate if strain rate is strictly negative and if a threshold stress is not passed. It is associated with pseudo-plastic non-reversible phenomena occurring in the crystalline structure;
- a *crystallization* mechanism active only if a thermal load is applied or during creep. The increase of crystallinity appears as a 2nd endothermic peak at around 10°C more than the temperature at which the material was tested prior than DSC. The same peak was observed in PEKK SC cooling from melt and identified as secondary, intra-spherulitic crystallization. The kinetics of crystallization both in the case of thermal and creep conditions has a dependence on the time consistent with an Avrami model, leading to 2 conclusions:
  1. the material did not fully crystallize at the end of the manufacturing process and further 3.8% crystalline phase can be produced and cannot be observable through DSC on as-received material, because of the limited exposition to high temperatures (temperature rate during DSC = 10 °C/min);
  2. according to the Avrami model, no further increase in crystallinity appears after long exposure duration (ageing for 42 days).

The absence of crystallinity increase during load could be explained by the lower mobility imposed to intra-spherulitic amorphous chains due to the crystalline phase rotation, which has an analog effect to an increase in the crystallization energy, which keep increasing as the stress is increased. During unload and recovery, the energy provided to the material is insufficient to overcome this threshold, while the mechanical energy provided during creep allows it and activates the crystallization mechanism.

All the previous described mechanisms sum to an elastic behavior, which allows the defininition of the theoretical initial state of the material, depending on the initial crystalline phase as well as on the temperature.

The different mechanisms are described analytically and constitute a 1-D model of behavior for PEKK 7002 SC, which is able to reproduce the tensile, Load-Unload-Reload and creep-recovery experimental curves at 200°C and 180°C. Under the hypothesis of incompressibility, experimentally supported, also the transverse behavior can be reproduced, validating the considerations on the volume variation.

Some difference with the 165°C experimental curves are observed, possibly due to low experimental reproducibility or by the presence of other mechanisms that are not taken into account by the model.

In fact, the presence of other mechanisms besides the identified ones cannot be excluded, but their effect on the PEKK SC behavior can be considered negligible, at least at 180°C and 200°C. Moreover, the association with modification of the crystal structure has been observed only pre and post-test (crystallization and re-orientation) or just hypothesized (pseudo plastic and viscoplastic mechanisms): the proposed kinetics of those mechanisms, while is coherent with the initial and final state of the crystalline structure and allows a good agreement with the experimental data, can only be verified by in-situ tests.

The analysis is extended to PEKK 7002 AM, allowing the identification of the principal differences compared to PEKK SC:

- the mechanical properties loss, if the temperature is increased above T_g, is significant higher (-99% respect to -90%), confirming the role of the crystalline phase in piloting the mechanical properties above T_g;
- also primary crystallization mechanism is active, not only dependent on the temperature, but coupled with the provided mechanical load, which accelerates it. This has an effect analog to lowering the activation energy of crystallization, exactly the contrary of the retardation effect the tensile load has on the secondary crystallization kinetics in PEKK SC. Such phenomenon, respect to the crystallization kinetics proposed by (TANGUY CHOUPIN 2018), produces an increase in the predicted crystallization at 150°C, and coherently with the model an absence of increased crystallization at 165°C and again an increase at 180°C.

Because of the absence of crystallization increase during tensile tests, 165°C was a suitable temperature to extend the 1-D model to different values of initial crystallinity. In order to identify the model parameters, a CDP test at the same test conditions was carried out.

The good agreement between the model and the experimental curves confirmed that the same mechanisms active in PEKK SC can be identified in PEKK AM, and consequently those same mechanisms are not only dependent on temperature, time, stress and stress rate, but also on the initial crystallinity phase.

The whole analysis constitutes the basis for a 3-D model, describing PEKK SC behavior, which is employed for simulating the C/PEKK composite and it is described in the following chapter.

Chapter 5 – Simulation of the C/PEKK thermomechanical tensile and creep behavior

The present chapter aims at simulating the C/PEKK thermomechanical behavior through the employment of semi-analytical methods, starting from the PEKK thermomechanical behavior model. The PEKK 1-D model is extended to describe its 3-D behavior and implemented in the Semi - Analytical Homogenization / Localization Method (SAHLM). The SAHLM is validated through comparison with the C/PEKK experimental curves and employed for the simulation of the thermomechanical tensile and creep behavior of composite laminates with different stacking sequences.

5.1. Introduction

The similarities in tensile and creep behavior above T_g between the PEKK and the low-strain region of the C/PEKK, as emerges from the analysis described in CHAPTER 3, suggest the presence of a matrix dominated region in the composite, in which the matrix behaves as the neat polymer.

This latter consideration is the base of the chosen strategy for the simulation of the composite: the idea is to reconstruct the composite behavior starting from the the neat polymer (=matrix) behavior.

Within some limitations, and moreover limited only to tensile solicitations, this approach has been already exploited in CHAP 3.6, showing its validity: the composite tensile stress vs strain curves were obtained via a semi-analytical homogenization/localization method and the polymer behavior was introduced implicitly from the polymer experimental curves obtained from tests carried out in the same conditions.

In CHAPTER 4, the different mechanisms characterizing PEKK behavior were identified and, most of all, a 1-D analytical description of its behavior was provided.

This explicit description (once extended to a 3-D version) of the polymer behavior allows overcoming the limit of need the polymer experimental data. Moreover, it can be implemented in the semi- analytical homogenization/localization method: in fact, at the price of losing the local information on the matrix, such method provides with the required averaged information at the laminate level, and simultaneously at both ply and matrix ones. Moreover, it does not require the definition of model geometries or boundary conditions and has a negligible computational cost compared to Finite Element models. In order to obtained the same information via Finite Element, including the matrix local information, a multiscale model would have been required, which computational cost are orders of magnitude higher in both calculation time and resource, respect to the semi-analytical method.

Therefore, the chosen approach, described in the present chapter, could be summarized as follows:

1- extension of the PEKK 1-D thermomechanical model to the corresponding 3-D version;
2- implementation of the PEKK 3-D model in the semi-analytical homogenization/localization method;
3- setup and development of a tool for simulation of laminate with different ply orientations for tensile and creep solicitations: this tool, written in Matlab code, implements the modified semi-analytical method, and it allows running simulations with calculation times in the order of few minutes, without requiring particular computational resources.

4- validation of the approach through comparison with the composite experimental data, obtained from both the tensile and creep-recovery tests carried out on $[(\pm 45)_2, +45]_s$ C/PEKK composite at 200°C (CHAPTER 3);
5- simulation of the thermomechanical composite tensile and creep behavior for different stacking sequences.

5.2. Simplified analytical 3-D model for the description of PEKK SC thermomechanical behavior at 200°C

The analytical 1-D model of the PEKK behavior, proposed in CHAP. 4.5, was obtained with the purpose of providing with an analytical description of the different mechanisms identified.

In order to take into account all the different mechanisms, a rather complex formulation was obtained, which can be reduced to be function of solely:

- the longitudinal true strain;
- the time.

In order to extend such formulation to a 3-D description, and to proper describe the behavior of the matrix within the composite, the following elements should be taken into account:

1- the stress/strain state within the composite could be not mono-axial and could have shear components;
2- the polymer stress/strain rate could be of different magnitude respect to that of the matrix in the composite (which instead could be known from experimental tests), and could be not constant, even during tensile tests.

The 1st consideration implies the necessity to extend the 1-D model and, for this purpose, classical equivalent stress and strain are used to generalize it and the hydrostatic pressure is not taken into account. Experimental data are not sufficient to discern a non-linear influence of the pressure and employing a Poisson's ratio very close to 0.5 allows the deduction of the bulk modulus from the Young modulus. The classical equivalent stress and strain are calculated according to:

$$\begin{cases} \varepsilon^{VM} = \sqrt{\frac{2}{3}\boldsymbol{\varepsilon}^{\mathbf{dev}}:\boldsymbol{\varepsilon}^{\mathbf{dev}}} \\ \sigma^{VM} = \sqrt{\frac{3}{2}\boldsymbol{\sigma}^{\mathbf{dev}}:\boldsymbol{\sigma}^{\mathbf{dev}}} \end{cases} \qquad \textit{Eq. 5-1}$$

where:

$$\begin{cases} \boldsymbol{\varepsilon}^{\mathbf{dev}} = \boldsymbol{\varepsilon} - \frac{1}{3}\mathrm{tr}(\boldsymbol{\varepsilon})\mathbf{I} \\ \boldsymbol{\sigma}^{\mathbf{dev}} = \boldsymbol{\sigma} - \frac{1}{3}\mathrm{tr}(\boldsymbol{\sigma})\mathbf{I} \end{cases} \qquad \textit{Eq. 5-2}$$

and $\boldsymbol{\sigma}$ and $\boldsymbol{\varepsilon}$ are respectively the stress and strain tensors, and $\mathbf{I}$ is the identity tensor.

Moreover, the 1st consideration points out the need of a description of the shear behavior. This leads to face two main issues:

a) it can be assumed that the material is initially isotropic, but an orthotropic effect is expected because of the crystals re-orientation towards the loading direction. According to the analytic description (see hardening mechanism in CHAP. 4.5.3), the crystals re-orientation provokes an increase in stiffness in the loading direction which can be calculated and, at the same time, it can be assumed that this leads also to a difference in stiffness respect to the other 2 directions. However, the extension of such effect cannot be estimated from the experimental tests carried out, and requires multiaxial tests.
b) the PEKK shear behavior has not been investigated and no experimental tests are available.

In order to address the issues mentioned above, the following hypotheses are made:

- the behavior of the material is considered always close to isotropic and incompressible (this latter property has been validated in CHAP. 4.5.3);
- the shear behavior is deduced from the longitudinal one through equivalent quantities.

The 2nd consideration questions the time-dependence of the proposed 1-D formulation: in fact, because of the possible difference in strain rate between composite and matrix, and considering the equivalence between the matrix and the polymer, the correspondence between the time coordinates of the composite, the matrix and the polymer could not be a priori established. However, it could be possible to evaluate the matrix strain rate in the composite time coordinate as:

$$\dot{\varepsilon}_m^{VM}(i) = \frac{\varepsilon_m^{VM}(i) - \varepsilon_m^{VM}(i-1)}{t_C(i) - t_C(i-1)} \qquad \textit{Eq. 5-3}$$

where ε_m^{VM} and $\dot{\varepsilon}_m^{VM}$ are respectively the matrix equivalent strain and strain rate and t_C is the composite time coordinate. This possibility allows taking into account the time-dependence, but in an implicitly way.

5.2.1. PEKK 3-D formulation for tensile solicitation

The 3-D formulation is based on the above mentioned hypotheses, and it is developed starting from the 1-D formulation according to the following conditions:

- it has to be as close as possible to the 1-D formulation, in order to exploit the mechanisms description and the relative parameter identification;
- it can only be function of the strain and of the strain rate in order to facilitate its use in multi-scale methods.

Under those conditions, the PEKK 3-D formulation includes:

- an elastic isotropic incompressible state, defined by a *tangent modulus* E_0 and a constant Poisson's coefficient ν =0.495;
- an *hardening tangent modulus*, function of the equivalent strain, obtained as the derivative of the hardening stress without the elastic component over the strain, as:

$$E_H = \frac{\partial(\sigma_H - \sigma_0)}{\partial \varepsilon^{VM}} = \frac{a \exp\left(-\frac{\varepsilon^{VM}}{b}\right)}{b} \qquad \textit{Eq. 5-4}$$

where the coefficient a and b are the same of TAB. 4-14, written as function of the equivalent strain rate as:

$$\begin{cases} a = 0.386 \ \ln\left(\left(\varepsilon^{VM}\right)\right) + 11.377 \\ b = 0.059 \left(1 - \exp\left(-0.0055 \left(\left(-\ln\left(\varepsilon^{VM}\right)\right)^{3}\right)\right)\right) \end{cases} \qquad \textit{Eq. 5-5}$$

- a *softening tangent modulus*, function of the equivalent strain obtained as the derivative of the softening stress over the strain. Since the softening stress is explicitly function of the time, the formulation proposed in CHAP. 4.5, is replaced by a formulation analog to the hardening stress, resulting in:

$$E_s = \frac{\partial(\sigma_S)}{\partial \varepsilon^{VM}} = E_0 - \frac{a_S \exp\left(-\frac{\varepsilon^{VM}}{b_S}\right)}{b_S} \qquad \textit{Eq. 5-6}$$

where a_S=12 and b_S=0.239 are constant for any equivalent strain rate.

The hardening and softening tangent moduli are summed to the elastic tangent modulus, providing with the *total tangent modulus* E, from which is possible to calculate the shear modulus G, as:

$$\begin{cases} E=E_0+E_H-E_S \\ \nu=0.495 \\ G=\dfrac{E}{2(1+\nu)} \end{cases} \qquad \textit{Eq. 5-7}$$

and to define the 3-D PEKK compliance tensor, as:

$$[S_m]=\begin{bmatrix} \frac{1}{E} & -\frac{\nu}{E} & -\frac{\nu}{E} & 0 & 0 & 0 \\ -\frac{\nu}{E} & \frac{1}{E} & -\frac{\nu}{E} & 0 & 0 & 0 \\ -\frac{\nu}{E} & -\frac{\nu}{E} & \frac{1}{E} & 0 & 0 & 0 \\ 0 & 0 & 0 & \frac{1}{G} & 0 & 0 \\ 0 & 0 & 0 & 0 & \frac{1}{G} & 0 \\ 0 & 0 & 0 & 0 & 0 & \frac{1}{G} \end{bmatrix} \qquad \textit{Eq. 5-8}$$

EQ. 5-8 carries within the hypothesis that the material is always isotropic, as the same effect of hardening and softening is simultaneously applied to each direction and it defines its effects also on the shear components.

In this way, the property of the PEKK at the time i are defined, and it is possible to evaluate the stress tensor, through finite difference respect to the time $i-1$, and as function of the total strain tensor as:

$$\boldsymbol{\sigma}(i)=\left(\mathbf{S_m}(i)\right)^{-1}:(\boldsymbol{\varepsilon}(i)-\boldsymbol{\varepsilon}(i-1))+\boldsymbol{\sigma}(i-1) \qquad \textit{Eq. 5-9}$$

An important modification respect to the 1-D formulation is the following: while the 1-D formulation has the purpose to describe the PEKK behavior during creep, and hence to relatively small strains (<30%), in the composite matrix this range of deformation can be

easily overcome; moreover EQ. 5-7 leads, for $\varepsilon^{VM}\rightarrow\infty$ to E=0. Thus, to extend the validity of the formulation to higher strains the following criterion has been added:

$$\begin{cases} E=E_0+E_H-E_S & \text{if } \varepsilon_{VM}<20\% \\ E=26.6 \text{ MPa} & \text{if } \varepsilon_{VM}\geq 20\% \end{cases} \qquad \textit{Eq. 5-10}$$

The effect of the modification in the tangent modulus is investigated through comparison with the experimental data, through a simulation of the tensile test at 1 mm/min at 200°C where the strain is varied linearly up to 100% (ε) and the strain rate is kept constant to 0.000325 s^{-1} (mean strain rate during tensile test). The input total strain is $\{\varepsilon \quad -\nu\varepsilon \quad -\nu\varepsilon \quad 0 \quad 0 \quad 0\}^T$. The results of the simulations with restrained and unrestrained tangent modulus are compared with the experimental data and showed in FIG. 5-1.

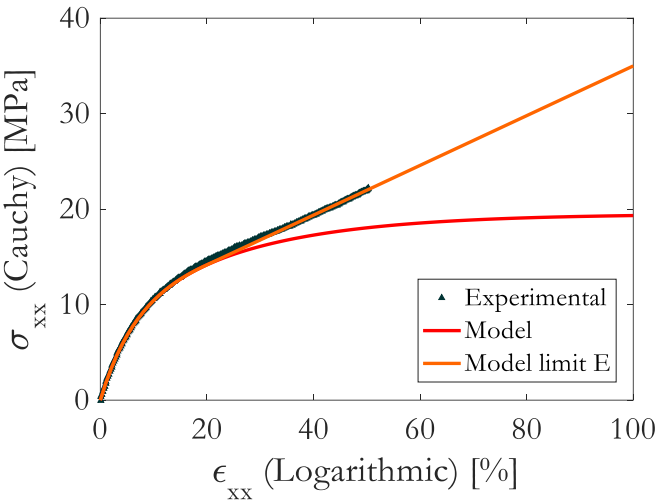

Fig. 5-1: Comparison between experimental data, obtained from a tensile test on PEKK SC at 1 mm/min and 200°C, and the simulation with not limited tangent modulus (red - Model) and limited tangent modulus (orange – Model limit E).

FIG. 5-1 shows that not providing a limit to the tangent modulus (as in 1-D formulation) allows a good approximation of the experimental curve, up to 30% strain, and the limit is needed to extend the approximation to higher strains.

A second simulation is carried out in order to assess the result in terms of shear. The same strain rate is employed and the total strain is $\{0 \quad 0 \quad 0 \quad 0 \quad 0 \quad \varepsilon\}^T$. The comparison with the tensile response is showed in FIG. 5-2.

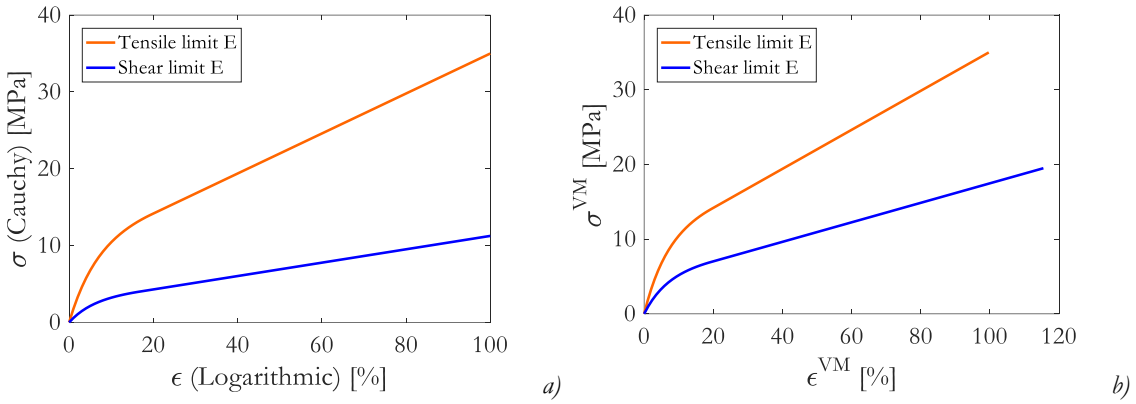

Fig. 5-2: Comparison between the simulation of tensile (orange) and shear (blue) solicitations with limited tangent modulus in term of true stress vs true strain (a) and equivalent stress vs equivalent strain (b).

FIG. 5-2 shows the differences produced by the different solicitations both in the case of true stress vs true strain (A) and equivalent stress vs equivalent strain (B) curves.

An equivalence can be established between the 2 cases, if an equivalent secant modulus is calculated:

$$\begin{cases} E_{eq}^{sec} = 3(1+\nu)\dfrac{\tau_{xy}}{\gamma_{xy}} = 2(1+\nu)\left(\dfrac{\sigma_{VM}}{\varepsilon_{VM}}\right)_{shear} \\ E_{eq}^{sec} = \dfrac{3}{2}\dfrac{\sigma_{xx}}{\varepsilon_{xx}} = (1+\nu)\left(\dfrac{\sigma_{VM}}{\varepsilon_{VM}}\right)_{tensile} \end{cases} \qquad \textit{Eq. 5-11}$$

The comparison of the equivalent secant moduli obtained in the case of tensile and shear solicitation is showed in FIG. 5-3.

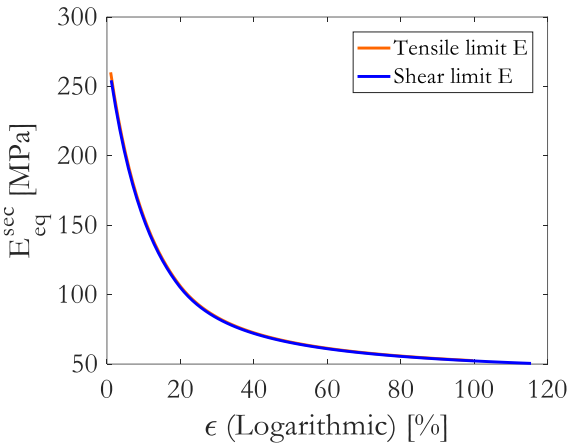

Fig. 5-3 Comparison between the equivalent secant modulus obtained from tensile (orange) and shear (blue) solicitation.

The equivalence showed in FIG. 5-3 provides with the possibility of describing any stress state in terms of equivalent secant modulus and, hence, the problem of not knowing a priori the stress state in the matrix is bypassed.

5.2.2. PEKK 3-D formulation for tensile-creep solicitation

Once defined the 3-D formulation for the tensile case, the creep phase can be approached: while the tensile solicitation constitutes a rather simple case, which does not require too many modification respect to the 1-D case, the creep presents several difficulties, which cannot be easily overcome in the 3-D description.

In fact, looking at the formulation described in CHAP. 4.5, while the hardening stress is kept constant during the creep, the softening stress:

- is directly dependent on the cumulated time, which increase only if $\dot{\sigma} \geq 0$ (in the case of tensile followed by creep solicitations coincides with the total time);
- is indirectly dependent on the time since the parameter A depends on the strain rate and in terms of $\measuredangle\varepsilon_\chi$, correlated to the activation of the crystallization mechanisms (also dependent on the time). Moreover, the functions describing A and $\measuredangle\varepsilon_\chi$ have opposite concavity and produce a non monotonic function (which introduces itself other convergence problem if implemented in an algorithm).

The most convenient choice to overcome the above-mentioned issues, generated by the intrinsic difficulty of obtaining a constant output (the creep stress), from the combination of different functions of non-constant input (the strain and the time), is to invert the problem and introducing the stress (constant) as input to obtain the strain.

This can be easily achieved by employing the Norton – Bailey formulation, as:

$$\varepsilon_{VM}=\frac{A_{cr}\,\sigma_{S,VM}^{n}\;t_{cr}^{m+1}}{m+1} \qquad \textit{Eq. 5-12}$$

where:

- $A_{cr}=(0.011\ t_{cr}^{-0.165})k$ is the proportional coefficient of the Norton-Bailey law;
- $t_{cr}=t-\bar{t}$ is the creep time, as difference between the total time and the time at the end of the tensile phase;
- $\sigma_{s,VM}=\overline{\sigma_{VM}}-\overline{\sigma_{H,VM}}$ is the equivalent softening stress, as difference of the total equivalent stress and the equivalent hardening stress at the end of the tensile phase. Because during creep, both the total stress and, according to the 1-D formulation, the hardening stress are constant, also their equivalent formulation is constant and hence the equivalent softening stress;
- $k=\frac{A_1}{0.011}$ is a continuity factor, needed to guarantee the continuity of the softening stress/strain from the tensile to the creep phase;
- $A_1=\frac{\left((m+1)\overline{\varepsilon_{VM}}\;1^{-(m+1)}\right)}{\overline{\sigma_{s,VM}}^{n}}$ is the value of the A parameter at beginning of creep (t_{cr}=1 s), such to match the equivalent softening stress.

In this way, at the price of eliminating the direct correlation with the mechanisms identified during creep, a simpler formulation can be obtained, which is monotonic and can be easier implemented. The new parameters were identified from the experimental creep curves at 200°C on PEKK SC.

With the above described formulation it is possible to simulate a tensile solicitation followed by a creep one, where the inputs and outputs of the model are listed in TAB. 5-1, according to the type of solicitation applied.

Type of solicitation	Input	Output
Tensile	• Strain tensor • Equivalent strain rate	• Total stress • Hardening stress
Creep	• Softening stress (constant) • Creep time	• Strain tensor

Tab. 5-1: Input and output of the PEKK 3-D model for tensile-creep solicitations

The schematization of the algorithm for the simulation of tensile-creep solicitation is showed in FIG. 5-4.

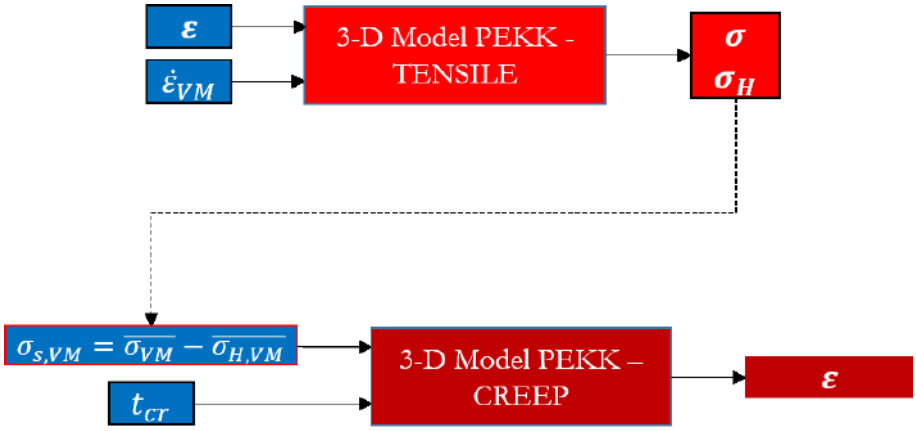

Fig. 5-4: Schematization of the algorithm for the simulation of the tensile-creep solicitations.

It has to be remarked that also for the creep, no information about the creep response under shear condition is available, and it is assumed that such response is analogue to the one observed in the case of load applied under longitudinal direction.

In order to validate the procedure, the following simulation was carried out, where the experimental longitudinal strain, measured during a creep test at 200°C and 10 MPa ($0.7\sigma_{th}$), is introduced in the model, as input during the tensile phase, and as comparison during the creep phase (where the strain is the output). The results are showed in FIG. 5-5.

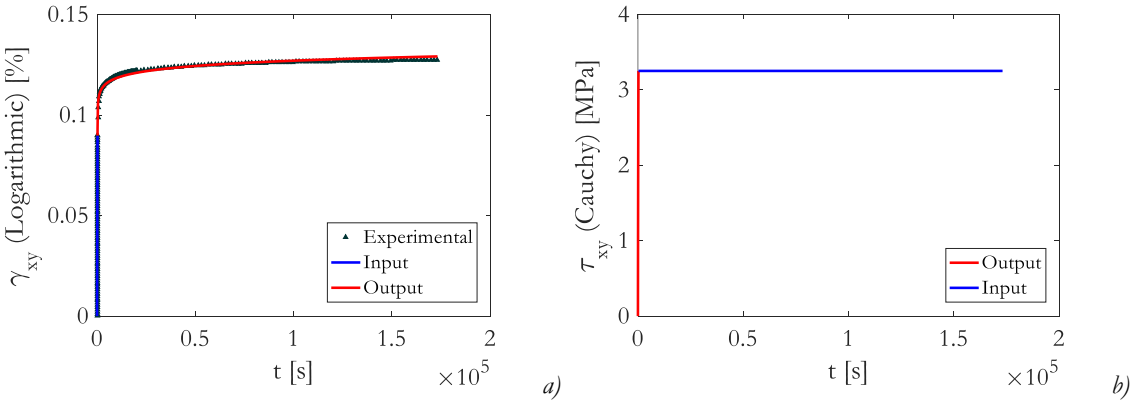

Fig. 5-5: Results of the tensile-creep simulation: comparison between the experimental longitudinal strain and the shear strain vs the time; b) stress vs time;the blue curves represent the inputs and the red ones the outputs of the model

The simulated creep strain of FIG. 5-5A (red curve) is in good agreement with the experimental curve (black), proving that EQ. 5-12 can replace the creep formulation employed in the 1-D model. However, the lack of creep tests with a shear load prevent from a proper validation, and limits to validate only the coherency of the model.

5.3. Implementation of PEKK 3-D model in the semi-analytical homogenization/localization method

The 3-D formulation of the PEKK behavior under tensile and creep solicitations, presented in the previous paragraphs, allows the employment of different methods for simulating the composite behavior.

In particular, the semi-analytical homogenization/localization method (SAHLM) proposed in CHAP. 3.6 is suited for the purpose and the 3-D formulation of the PEKK behavior allows overcoming the 2 main limits of this method:

1. the need of polymer experimental data;
2. the capability of being able to simulate only the composite tensile behavior.

Thus, the PEKK 3-D model can be implemented in the SAHLM as described in the following paragraphs. Since the only available tests at 200°C on the C/PEKK were carried out on $[(\pm 45)_{2s}, +45]_s$ specimens, in order to validate the results of the simulations through comparison with experimental data, the following discussion is focus on this particular lay-up.

The SAHLM is developed as multiscale method, which allows the calculation of the stress and strain tensor, as well as the properties at the 3 different levels of the composite: the laminate, the ply and the matrix level. For $[(\pm 45)_{2s}, +45]_s$ C/PEKK composite, the different levels are showed in FIG. 5-6, from images acquired at the optical microscope and as schematization.

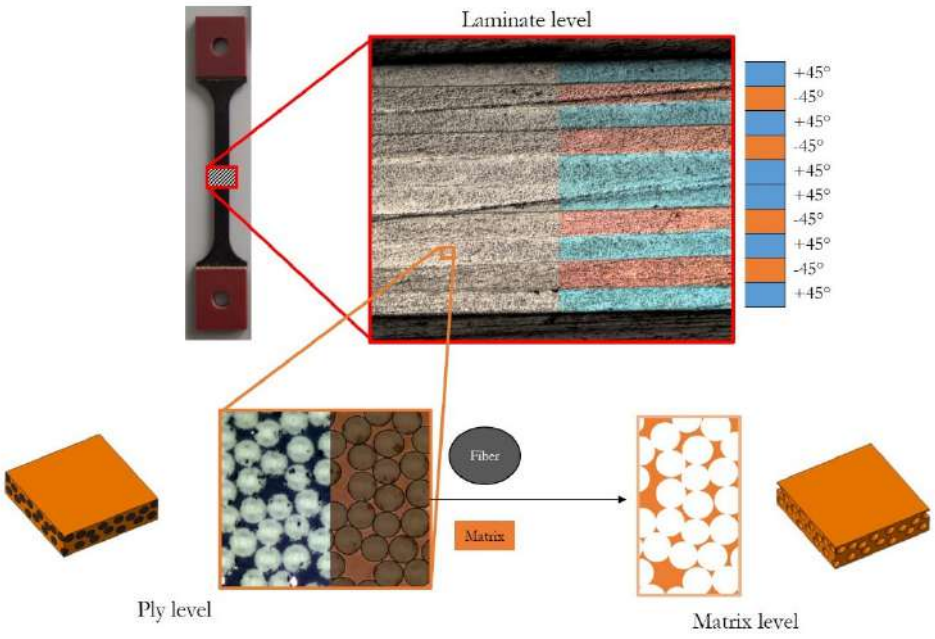

Fig. 5-6: Laminate, ply and matrix levels for the $[(\pm 45)_{2s}, +45]_s$ C/PEKK composite, from images acquired at the optical microscope and as schematization.

Moreover, all the hypothesis intrinsic to both the homogenization and localization methods, as well as their more detailed description, discussed in CHAP. 2.3.3, in ANNEX G and in CHAP. 3.6, will not be presented in the following paragraphs, which will only focus on the modifications and additional hypothesis on the pre-existing method.

5.3.1. Tensile

In case of the tensile solicitation, the SAHLM does not require substantial modifications respect to its previous version, schematized in FIG. 3-26. In fact, the 3-D model simply substitutes the database containing the pure polymer experimental data.

The schematization of the update version of SAHLM, where the PEKK 3-D model for tensile solicitation is showed in FIG. 5-7.

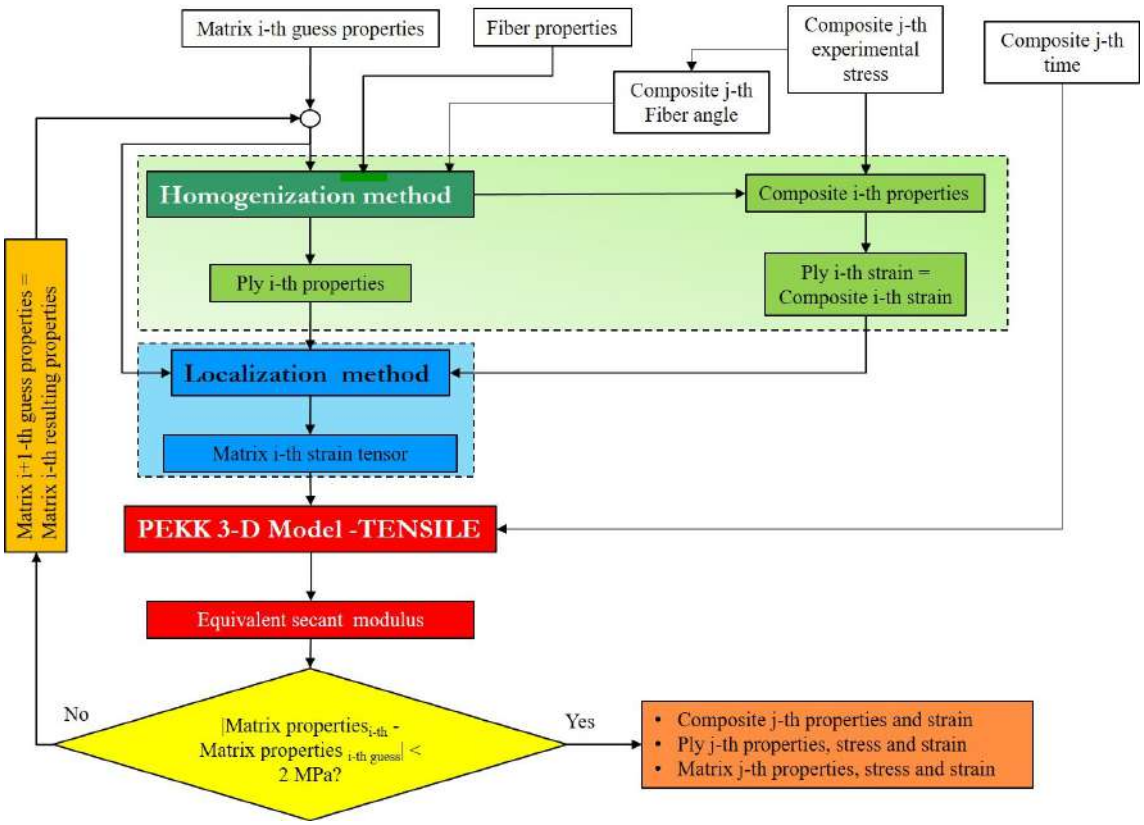

Fig. 5-7: Non-linear analytical method algorithm with the implementation of the PEKK 3-D model for tensile solicitations.

As in the previous version, the SAHLM workflow can be resumed as follows:

1. a 1st guess matrix properties value is introduced, as well as the fiber properties, the composite stress and the composite fiber angle (relative at the specific stress) in the homogenization method. Here the laminate and ply properties, strain and stress tensor are calculated;
2. from the homogenization method, the ply strain tensor and properties are introduced in the localization method, together with the matrix properties. This allows evaluation the matrix stress and strain tensors, and the matrix properties;
3. the matrix properties are compared with the 1st guess ones: if the convergence criterion is satisfied, the overall calculation is saved, otherwise, the new value of matrix properties replaces the 1st guess one and the calculation is started from the beginning, and so on, until the convergence is reached.

Two main modifications can be found with respect to the previous version:

1. the introduction of the **composite time coordinates** in the input list: this addition is needed to differentiate the tensile tests at different speed (in terms of displacement, strain rate or stress rate, all in bijectivity relation during tensile tests). Moreover, this is also needed to evaluate the matrix strain rate, according to EQ. 5-3, once the matrix strain tensor is obtained through Localization method;
2. the convergence criterion is introduced in terms of **matrix equivalent secant modulus**, evaluated through EQ. 5-11, as the longitudinal secant modulus was employed in the previous version. According to the 3-D model, the hypothesis of matrix incompressibility is maintained, and the Poisson's coefficient of 0.495 is employed.

As for the previous version, the fiber rotation in the composite is taken into account and calculated at each step as function of the composite longitudinal stress, according to the coefficients listed in TAB. 3-3. 2 important considerations on the fiber rotation have to be made:

1. as showed in FIG. 3-8, the fiber rotation is not constant at each temperature, and therefore this phenomenon is not only produced by kinematics effect and, even if this cannot be excluded, a direct correlation between fiber rotation and matrix loss of properties does exist and it is more pronounced as the temperature increases;
2. the fiber rotation angle during the tensile test (FIG. 3-8, re-showed below) is measured on the surface of the specimens and then refers to that specific ply only, but it is considered valid for every ply.

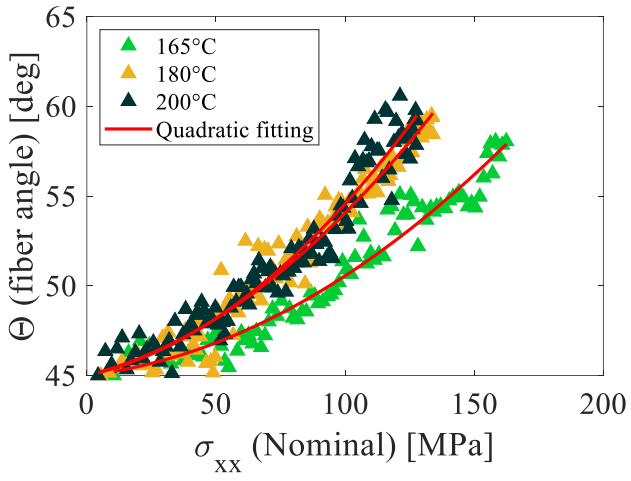

Fig. 3-8: C/PEKK Fiber orientation vs nominal stress measured during tensile tests at 165°C, 180°C, 200°C

Because of implementation needs, the fiber angle is described as function of the composite longitudinal stress with a quadratic fitting.

The results of the simulation of a tensile test at 200°C and 1 mm/min on a $[(\pm 45)_2, +45]_s$ laminate are showed in FIG. 5-8, and compared in the experimental results (CHAP. 3.2). FIG. 5-8A shows the results of a simulation where the fiber angle is set constant, while in FIG. 5-8B the fiber angle rotation is taken into account.

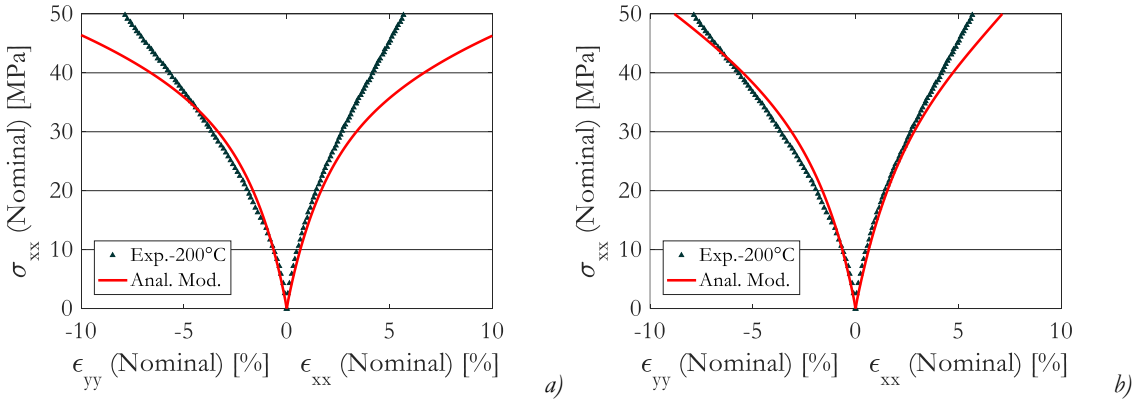

Fig. 5-8: Comparison between experimental tensile test on C/PEKK at 1 mm/min at 200°C and the simulation with SAHLM, not considering the fiber rotation (a) and taking the rotation into account (b).

From FIG. 5-8, it can be concluded that:

- the error, produced not taking into account the evolution of the fiber angle, is significant as the angle increases, but in both cases the model still diverges at some point: this could be due to an underestimation of the fiber rotation angle, because of error in the measure

and/or because of not having differentiate the angle in the different plies. However, a good approximation of the results can be achieved limited at the matrix dominated region and up to ~32 MPa;

- the employment of the PEKK 3-D model significantly improved the results respect to the previous version (FIG. 3-35C), most of all in the transversal direction.

FIG. 5-9 shows the ply stress vs the time and their ratio respect to the composite longitudinal stress.

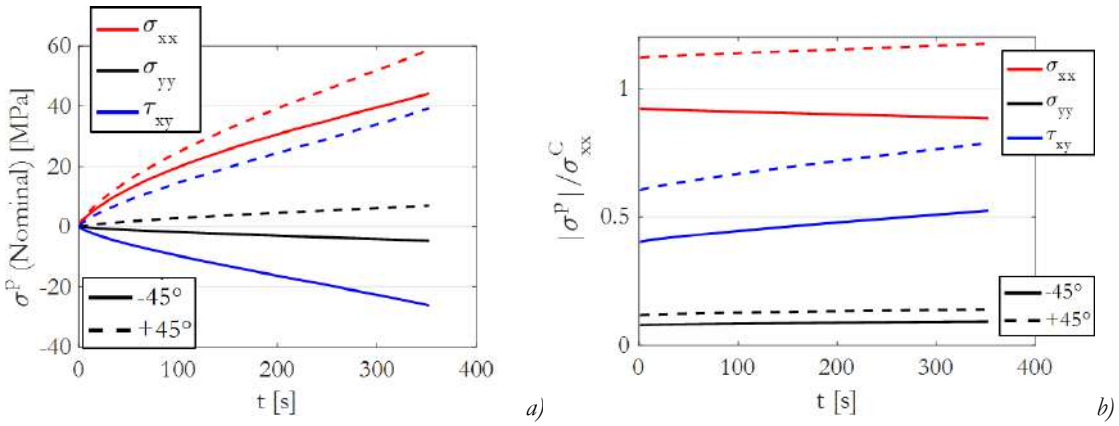

Fig. 5-9: a) Ply stress in global coordinates vs time; b) Ratio in absolute value between ply stress and longitudinal composite stress over time.

As showed in FIG. 5-9, the SAHLM is able to differentiate the resulting ply stress according to their orientation. This effect is even clearer in FIG. 5-9B, which shows the ratio, in absolute value, between each non-zero component of the ply stress tensor and the longitudinal composite stress and more on particular:

- at the beginning, the difference between ply of different orientation produced by the particular stacking sequence: in the case of equilibrate laminate, the absolute value of each component of the stress tensor of the +45° and -45° is the same;
- the variation of those differences with the time, produced by the variation of the fiber angle.

Looking at the matrix level, FIG. 5-10 shows the non-zero components of the matrix strain tensor and the equivalent strain rate, compared to the composite equivalent strain rate.

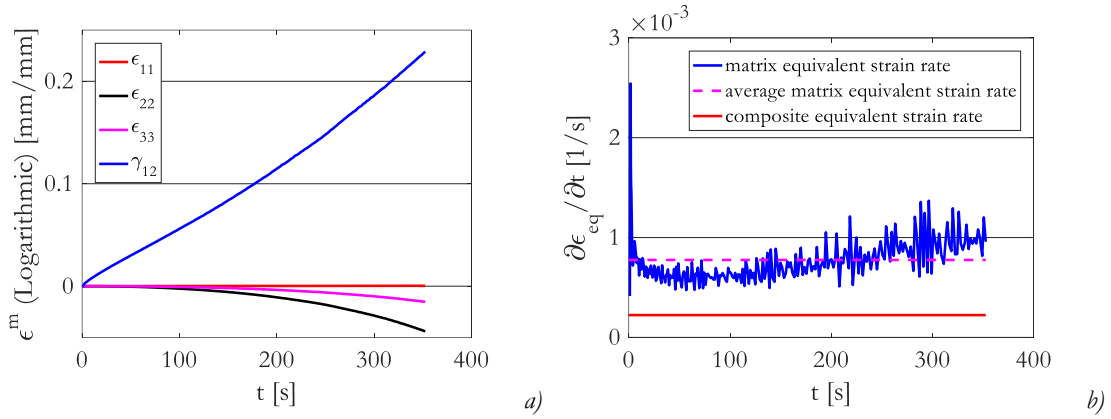

Fig. 5-10: a) Matrix non-zero components of the strain tensor vs time; b) matrix equivalent strain rate (blue), its mean (dotted magenta) and composite equivalent strain rate (red).

FIG. 5-10 shows that, in the case of $[(\pm 45)_{2s}, +45]_s$ laminates, the matrix is prevalently charged in shear, whose solicitation is at least one order of magnitude higher than the others. Moreover, the model diverges at less than 25% of strain. The explication for the divergence can possibly be found by looking at FIG. 5-10B, which shows the evolution of the strain rate along the simulation, which is over 3 times higher than the composite equivalent strain rate: at around 230 s, corresponding to 35 MPa, the strain rate shows higher fluctuations, and a general change of concavity. This is possibly due to the change between the matrix dominated region and the fiber dominated one, effect that the model fails to take into account.

FIG. 5-11 shows the stress vs strain matrix curves, in terms of shear and equivalent stress and the variation of the tangent and equivalent secant moduli over time.

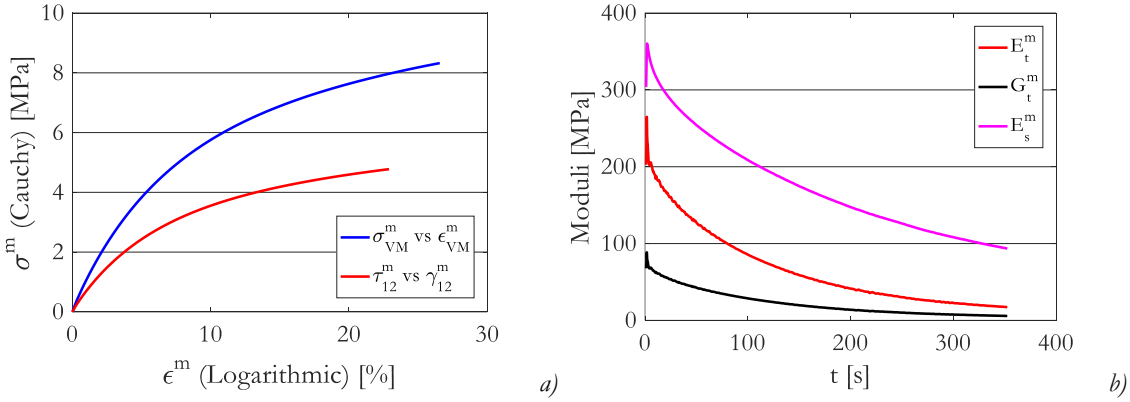

Fig. 5-11: a) Matrix equivalent stress vs equivalent strain (blue) and matrix shear stress vs shear strain (red); b) matrix equivalent equivalent secant modulus (Magenta), longitudinal (red)and shear (black) tangent moduli over time.

From FIG. 5-11 it clearly appears that the differences between the tangent and the secant properties of the matrix and their different evolution along the simulation: the fact that the

model diverges from the experimental strain, is not due to the 3-D model, as apparently, the secant model could still decrease and it verifies the condition of stability, being positive and different from 0 at each time.

The comparison with the experimental data, as well as the coherency of the results at each level, validates the SAHLM for tensile solicitations.

5.3.2. Creep

The extension of the 3-D model to the description of the creep phase, allows extending the SAHLM to the composite creep phase as well.

Because of the PEKK model formulation for creep, where the matrix stress is the input, contrary to the tensile phase, where the strain is the input, the architecture of SAHLM has to be modified. Moreover, the SAHLM can be considerably simplified if the hypothesis that when *composite is in creep solicitation also the matrix undergoes creep condition*, which means that when the composite stress is set constant, also the matrix stress is constant.

This hypothesis in fact, allows knowing directly the stress state of the matrix, as the last value during the tensile phase and it allows completely bypassing the localization part.

The resulting algorithm is schematized in FIG. 5-12.

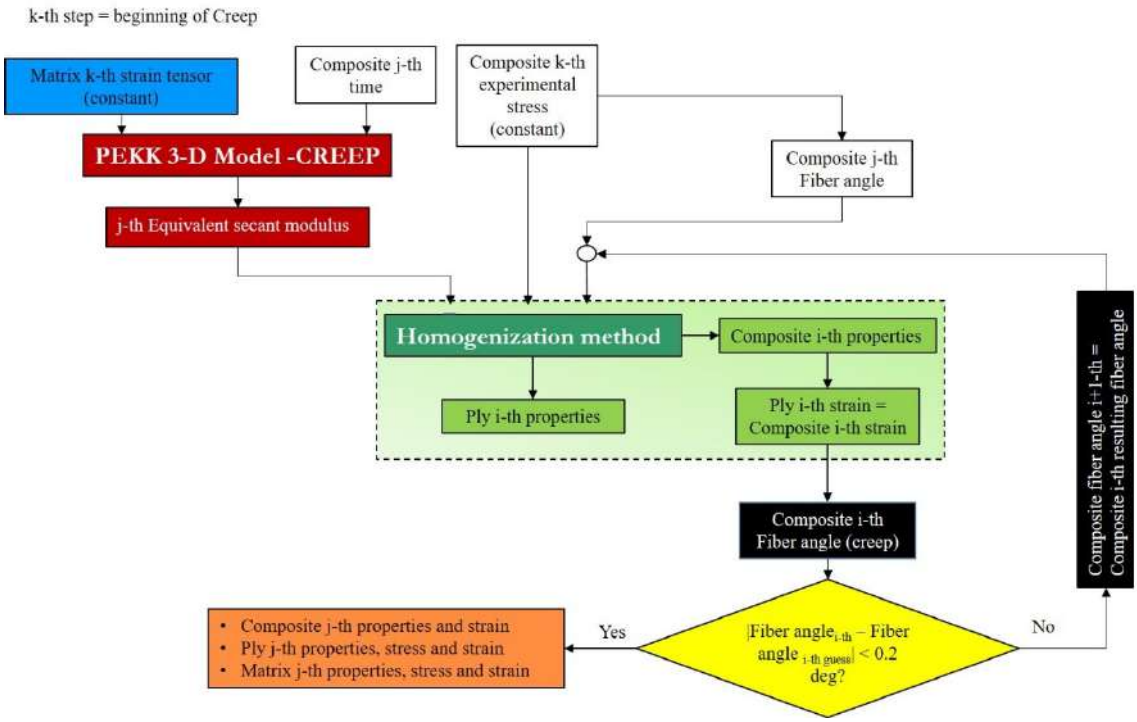

Fig. 5-12: Non-linear analytical method algorithm with the implementation of the PEKK 3-D model for creep solicitations.

The SAHLM workflow for the creep phase can be resumed as follows:

1. the matrix stress at the beginning of creep is set constant and employed to evaluate the matrix properties at each creep time;

2. the resulting matrix properties, as well as the fiber properties, the composite stress and the composite fiber angle (relative at the composite stress at the beginning of creep) in the homogenization method. Here the laminate and ply properties, strain and stress tensor are calculated;

3. the composite strain is employed to evaluate the new value of the fiber angle (discussed in detail below), and the latter is compared with the fiber angle resulting from the composite stress: if the convergence criterion is satisfied, the overall calculation is saved, otherwise, the new value of fiber angle replaces the previous employed one and a new calculation is started from point 2, and so on, until the convergence is reached.

More in detail:

- the beginning of the creep phase has to be known: this is particularly convenient, since the input in the model is the composite stress, and the beginning of creep can be easily identified as the time at which the stress is equal to its previous value. At this step, the matrix stress tensor at beginning of creep is calculated and set constant, and the time is re-initialized (creep time);
- the evolution of the properties is evaluated in terms of equivalent secant modulus, as during the tensile phase, but no convergence loop is carried out, since in the tensile part is needed to identified the matrix strain/stress state, which during the creep phase are already known;
- the fiber angle, however, because of its dependency on the composite stress, is constant, while it has observed its variation during the creep phase (CHAP. 3.4.3), and moreover its direct proportionality with the composite strain, (FIG. 3-24B). Therefore, the fiber angle is described as a linear variation of the creep strain as:

$$\Delta\Theta = -a_{\Theta}\ \Delta\varepsilon^{C}_{xx} \qquad \textit{Eq. 5-13}$$

The value of the a_{Θ} parameter is found through a linear regression on the experimental data, as showed in FIG. 5-13: the measure of the fiber angle were carried out on the images acquired during a creep test on C/PEKK at 200°C and 28 MPa ($\sigma^{m}_{VM}=\sigma^{poly}_{th}$, in black) and during a creep test on C/PEKK at 180°C and 78 MPa ($0.5\sigma^{C}_{u}$, in yellow): the latter is chosen as reference, because of the better quality of the images.

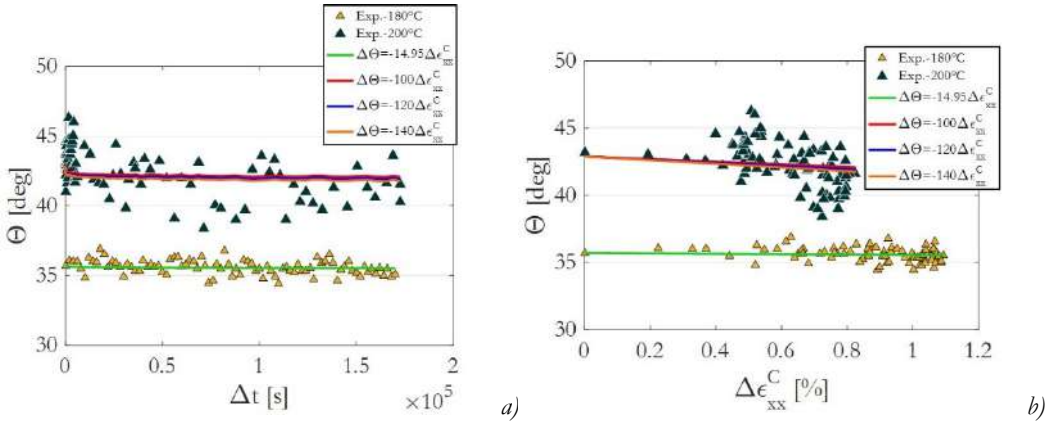

Fig. 5-13: Fiber rotation angle during creep phase vs creep time (a) and vs the longitudinal creep strain of the composite (b): in black the measurements on the creep test at 200°C, in yellow the measurements on the creep test at 180°C

As visible in FIG. 5-13, there is a considerable difference in the scatter on the measure of the fiber angle: this is due to the fact that the images were optimized for the observation of the markers and not for measurement on the fibers. However, considering the test at 180°C, a linear proportionality can be established with the composite longitudinal creep strain (as difference between the total strain and the strain at the beginning of the creep phase). Employing the same criterion, a similar proportionality can be found at 200°C, where the decrease of the angle is more pronounced with respect to 180°C, both coherently with the differences due to temperature effect and because of the difference in creep stress level: in fact, the test at 200°C was carried out at a creep stress in the matrix dominated region, contrary to the test at 180°C, confirming the not pure kinematic effect of the fiber rotation also during creep.

Because of the scatter in the test at 200°C, different values of a_Θ are possible, and its effect in the final output of the simulation is investigated.

In any case, the fiber rotation cannot be neglected. In order to take it into account, in the SAHLM, the composite strain tensor, obtained as output from the homogenization, is inserted in a convergence loop and employed to evaluate the new value of the fiber angle. Keeping constant all others variable, in the case that the convergence condition is not respected, the new value is introduced in the homogenization, and so on, up to reach convergence.

In order to validate the SAHLM also for the creep phase, the creep test carried on the C/PEKK at 200°C and 28 MPa for 48h has been simulated. The comparison of the results with the experimental data are showed in FIG. 5-14, in the case of neglecting the rotation of the fibers during the creep (A) and considering it with different values of the a_Θ parameter (B).

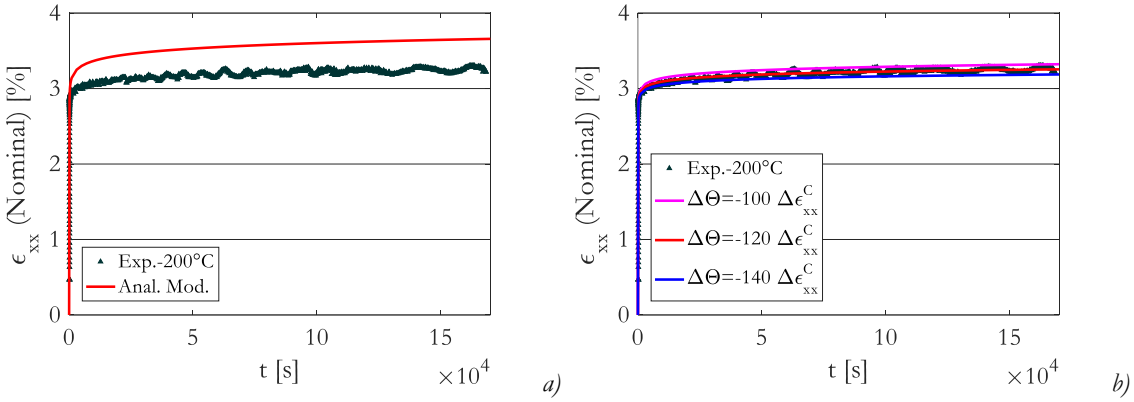

Fig. 5-14: Comparison between experimental creep test on C/PEKK at 200°C, 28 MPa for 48h and the simulation with SAHLM, not considering the fiber rotation during creep (a) and taking the rotation into account (b) with different values of a_Θ parameter.

FIG. 5-14A shows that neglecting the rotation of the fibers, the SAHLM overestimate the composite creep strain. However, looking at FIG. 5-14B, and considering a_Θ=120 (which ensure the best superposition with the experimental curve), variations of ±16.7% in the parameter produce a maximum variation of ±2.65% in composite strain.

At the different levels (laminate, ply and matrix), the same consideration made for the tensile part are valid and therefore will not be showed here.

More interestingly, the simulation range can be extended to the time coordinate, contrary to the tensile part, which is limited to the matrix region. An example of simulation is showed in FIG. 5-15, obtained with a_Θ=120 and extending the simulation time up to 42 days.

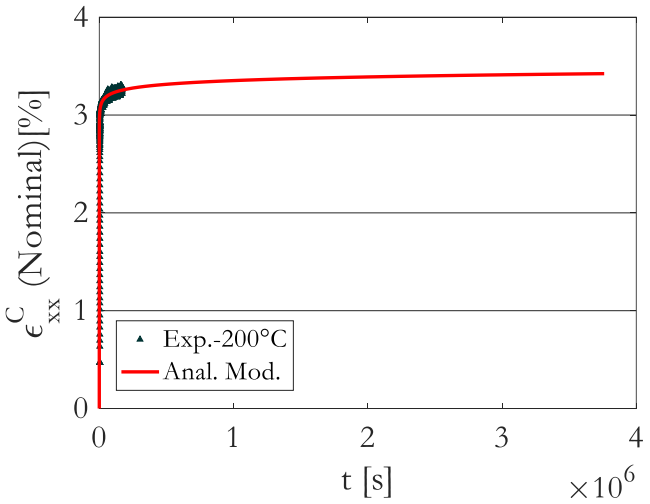

Fig. 5-15: Comparison between experimental creep test on C/PEKK at 200°C, 28 MPa for 48h and the simulation with SAHLM, considering a_Θ=120 and 42 days

5.4. Simulation of laminates with different and multiple ply orientations

The previous paragraph presented the modifications in the SAHLM model to accommodate the PEKK 3-D model for both tensile and creep solicitations. Thanks to those modifications, the model has been verified through the comparison with the experimental data obtained for tests carried out on C/PEKK composite with stacking sequence of $[(\pm 45)_2, +45]_s$.

The SAHLM can simulate, besides different fiber volumetric fractions, different stacking sequence and ply orientations. The model is capable of calculating the stress state in different plies, if the ply sequence is to be symmetric respect to the laminate mid-plane.

The main input elements of the model are:

- the composite stress state;
- the composite time coordinate, needed for the tensile phase to identify the creep strain rate (and hence the matrix one);
- the composite fiber angle, as a function of the composite strain (for the tensile phase) and as function of the composite strain (for the creep phase).

In the case of $[(\pm 45)_2, +45]_s$ laminates, these inputs are measured during the test or from the images, acquired during the tests, in post-treatment. In order to simulate different ply orientations and sequence, the lack of experimental data forces to make the following hypothesis:

- the composite strain rate is the same of the one measured experimentally, $\dot{\varepsilon}_{eq}^{C}=2.232\cdot10^{-4}\ s^{-1}$:this value has been chosen to allow a direct comparison with the case of $[(\pm 45)_2, +45]_s$. The composite time coordinate can be calculated as:

$$t(i)=\frac{\varepsilon_{eq}^{C}(i)-\varepsilon_{eq}^{C}(i-1)}{\dot{\varepsilon}_{eq}^{C}}-t(i-1) \qquad \textit{Eq. 5-14}$$

- the fiber angle is supposed to be constant: while, as it has been proven in the previous paragraph, neglecting the fiber angle can produce significant errors, in some particular case, as for 0° and 90°, it can be considered valid.

Under such hypothesis, the 0° and the 90° laminate were simulated. The results in terms of composite stress vs strain are showed in FIG. 5-16.

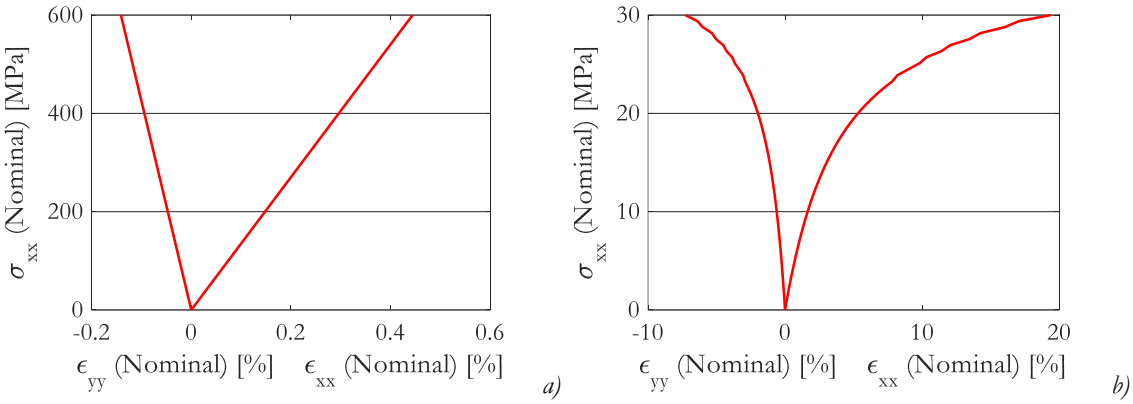

Fig. 5-16: Composite stress vs composite strain from simulations with SAHLM, of the 0° laminate (a) 90°laminate (b).

Because of the lack of experimental results, only qualitative considerations can be made:

- the results showed in FIG. 5-16, are consistent with what has to be expected: a quasi – linear behavior for the 0°, dominated by the fibers, and an important non-linearity in the 90°, which behavior is dominated by the matrix (direction perpendicular to the fibers);
- the maximum simulated composite stress vales are: 600 MPa for the 0° and only 30 MPa for the 90°. At higher composite stress, the SAHLM produces not-coherent results, suggesting that those are the limit between matrix and fiber dominated regions, for the 0° and 90° laminate respectively. However, compared to the ±45°, the latter behavior is between the 0° and 90° behavior, as expected. Furthermore, also the ductility of the ±45° is intermediate between the 90° (higher) and the 0° (lower) ones.

Looking at the ply level, the results are showed in FIG. 5-17, in terms of ply stress vs time.

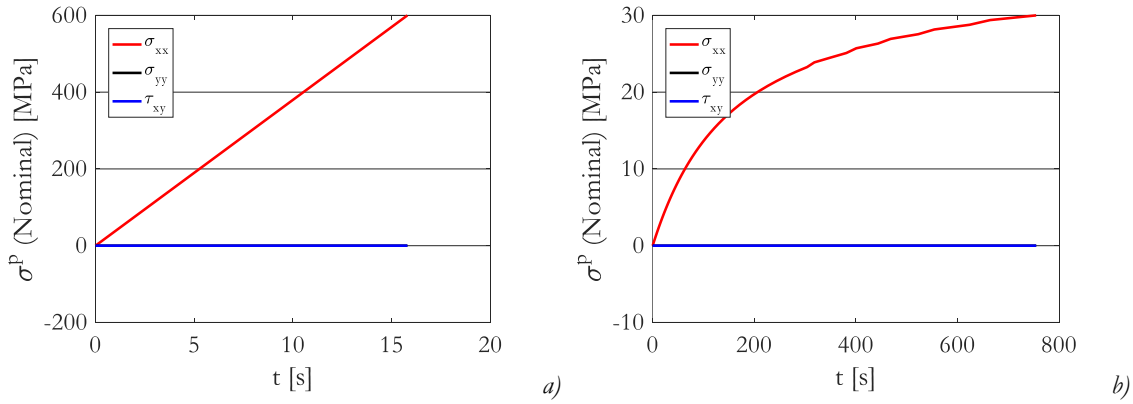

Fig. 5-17: Ply stress in global coordinates vs time from simulations with SAHLM, of the 0° laminate (a) 90°laminate (b).

Analyzing FIG. 5-17, the following consideration can be made:

- in both cases, only the component of stress tensor in the loading direction has non-zero values and, because of the absence of other ply orientations, it is exactly equal to the composite stress;
- the time coordinate is different in the two case, because of the different composite strain range, as discussed before, and because of the fact that the same composite strain rate was imposed. The ±45°-time coordinate is intermediate between the 0° and the 90° ones.

At the matrix level, the equivalent and deviatoric stress vs strain curves, the tangent and secant moduli vs time and the equivalent strain rate vs time are showed in FIG. 5-18.

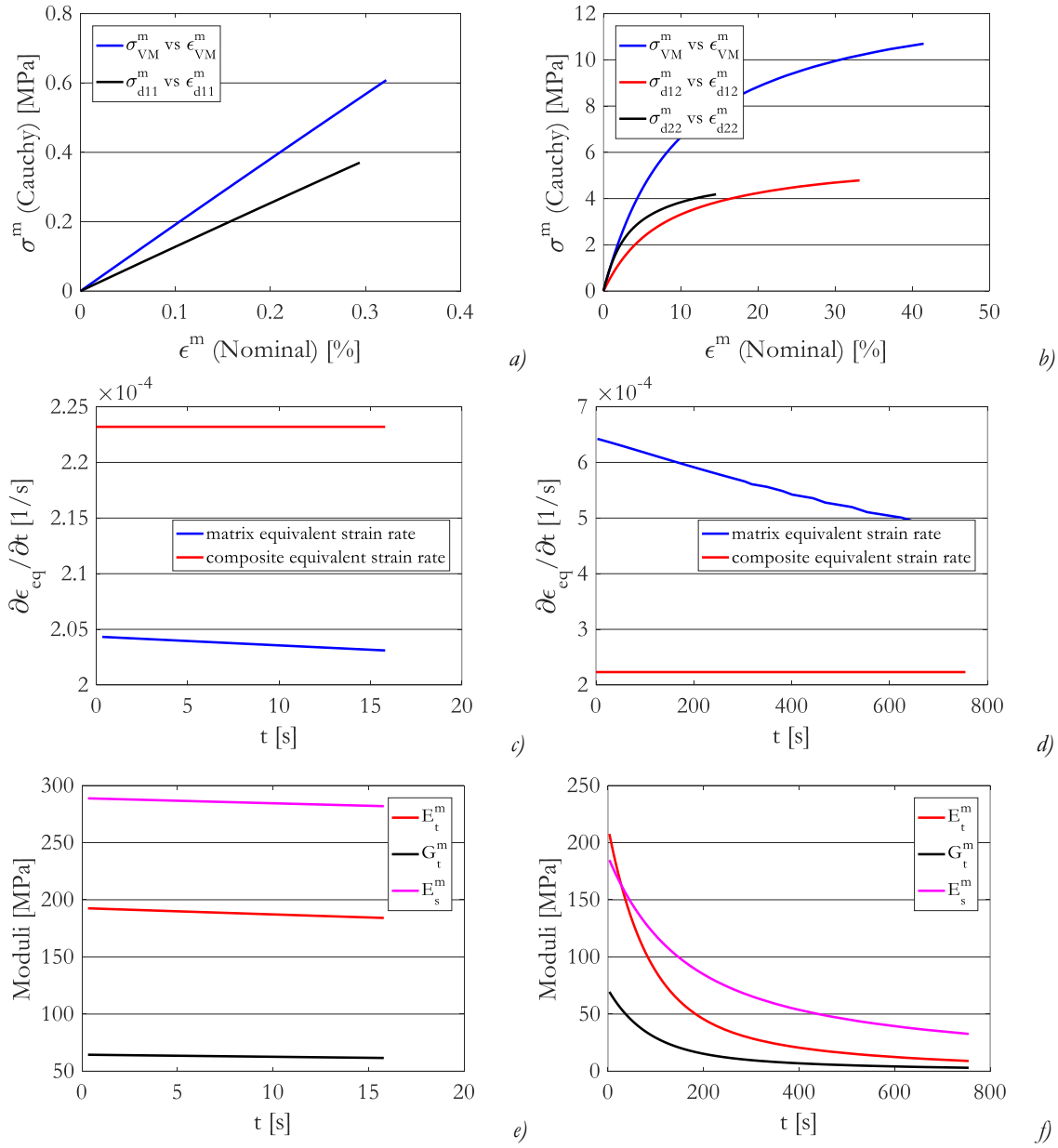

Fig. 5-18: Matrix equivalent and deviatoric stress vs strain, equivalent strain rate vs time and tangent andsecant moduli vs time curves, from simulations with SAHLM, of the 0° laminate (a,c,e respectilvely) 90°laminate (b,d,f respectilvely).

From FIG. 5-18, it appears:

- the same considerations, concerning the behavior at the laminate level, can be extended to the matrix level, where the matrix is more solicited in the case of the 90° (reaching ~40% of equivalent strain) respect than the 0° (~0.3%) (FIG. 5-18A and B). Moreover, in the case of the 0°, only the deviatoric component in the load direction has non zero value, while in the case of 90°, beside the component in the load direction (*22-direction* for the 90°), also a shear component it is present;
- the difference in matrix solicitation state in the 2 cases is due to their different matrix equivalent strain rate (FIG. 5-18C and D): because the time coordinate is introduced in the model from the composite equivalent strain rate (constant), the results of the simulation present less noise compared to the ±45° (FIG. 5-10B) and are monotonic, but not constant. Respect to the composite equivalent strain rate, the 90° matrix equivalent strain rate is higher and of the same order of magnitude than the ±45°, while for the 0°, the matrix equivalent strain rate is lower than the composite one, and ~75% lower than the ±45° one;
- the different matrix strain rate directly affects the matrix properties (FIG. 5-18E and F): in terms of value, the tangent properties are higher in the 90° (higher strain rate) than in the 0°, but the secant modulus is lower, because of the contribution of the shear component of the matrix strain and stress tensors. The different evolution of the moduli is produced by the different solicitation levels which the matrix undergoes in the different cases.

A limitation in the architecture of SAHLM consists in the capability of simulate only one fiber orientation at the time (only 1 $\pm\Theta$). This limitation can be easily overcome, modifying the SAHLM architecture, as described in the following paragraph.

5.4.1. Multiple orientations in the stacking sequence

In industrial applications the use of a monodirectional laminate is rare, and laminates composed by plies with multiple orientations are privileged, in order to obtain a better response of the material in case of multiaxial loads, but also in the case of uniaxial load, as safety precaution, for occasional loads occurring in off-axis directions.

Therefore, the capabilities of the SAHLM has been extended to simulate cases different from the monodirectional ply orientation. As general consideration, the SAHLM is modified to take into account the effect of the different ply orientation separately. Considering N different ply orientations, this difference produces modifications at each levels, and it is taken into account introducing N parallel branches, which all converges in the homogenization method to produce the composite response. More in detail:

- in the tensile algorithm the ply orientation is "called" at different levels:
  - at input level, to determinate the fiber angle from the composite stress;
  - at the ply level, to calculate both the ply strains and properties;
  - at matrix level, which properties, stress and strains depend on the input ply strain and properties.

  Each of the *N* equivalent moduli obtained, each corresponding to the *N*-th orientation, has to respect simultaneously the convergence condition that each difference with their previous value has to be lower than 2 MPa.

  The FIG. 5-19 shows a schematization of the SAHLM algorithm for tensile solicitations in the case of multiple ply orientations.

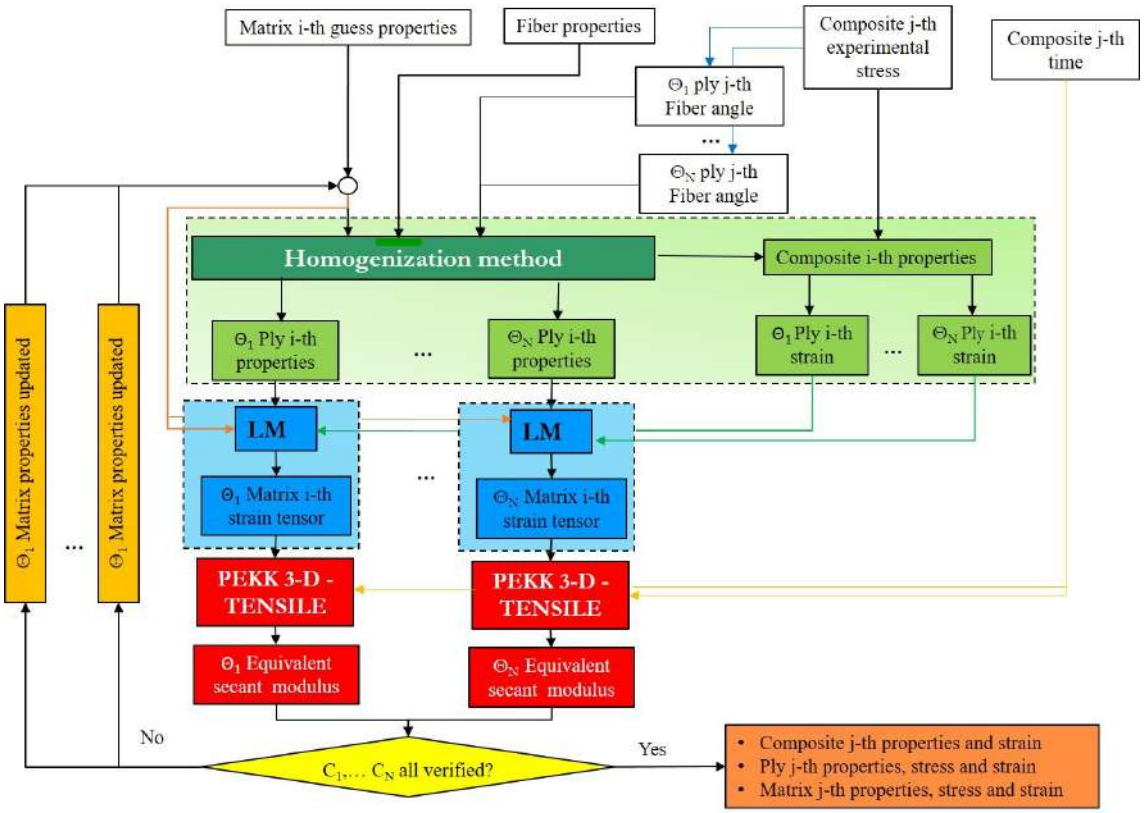

Fig. 5-19: SAHLM algorithm for tensile solicitations for multiple ply orientations.

The SAHLM workflow in the case of a laminate with *N* (> 1) ply orientation, under tensile solicitations, is similar to the ones described in CHAP 5.3.1, where the point 1 and 2 are repeated simultaneously *N* times, one for each ply orientation, and the point 3 is the same, only changing the convergence criterion, which is respected only if all the single branches convergence criteria are verified at once.

- in the creep algorithm:

- the matrix stress state resulting from each *N*-th ply at the beginning of the creep phase is considered separately and they produce *N* values of the equivalent secant modulus;
- each *N*-th ply strain tensor is employed to calculate the rotation of the angle in the creep phase, and all the differences with the previous value of the fiber angle have to simultaneously satisfy the convergence criterion of been lower than 0.2 deg.

The FIG. 5-20 shows a schematization of the SAHLM algorithm for creep solicitations in the case of multiple ply orientations.

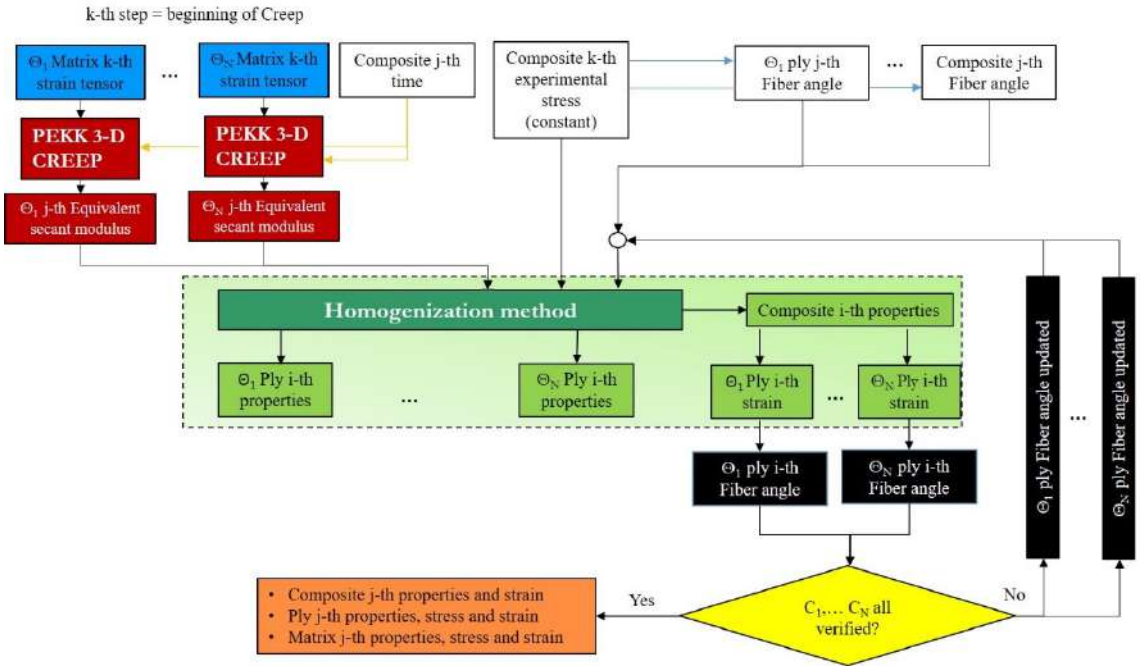

Fig. 5-20: SAHLM algorithm for creep solicitations for multiple ply orientations.

The SAHLM workflow in the case of a laminate with *N* (> 1) ply orientation, under creep solicitations, is similar to the ones described in CHAP 5.3.2, where the point 1 and 2 are repeated simultaneously *N* times, one for each ply orientation, and the point 3 is the same, only changing the convergence criterion, similarly to the tensile case.

Moreover, the following general hypothesis are made:

- the laminate has to be symmetric respect to the composite mid-plane;
- the ± *Θ* orientation count as 1 in the matrix level, instead than 2, even in the if the composite is not equilibrated (same number of +*Θ* and – *Θ* ply), and the differentiation of the cases is limited to the ply level, as for the case of $[(\pm 45)_{2s}, +45]_s$ described in CHAP. 5.3;

- the effect of the order in the ply sequence is not taken into account, or the effect on the ply behavior of being followed/preceded by a ply specific orientation, as well as the effect for a ply of being on the surface or in the core of the composite;
- interply interactions are not taken into account: in the case of C/PEKK, however, the manufacturing protocol, which requires the melt of the matrix during assembly, could play an important role and reduce this effect.

As example, the simulation of a quasi-isotropic (QI) composite $[0°/+45°/-45°/90°]_s$ was carried out, with the same hypothesis made for the simulations of the 0° and 90°, due to the lack of experimental tests for comparison. Therefore, also in this case the fiber rotation was neglected: even if this hypothesis can be considered valid for the 0° and 90° plies, it is certainly not valid for the ±45° plies, but because of the presence of the 0° and 90° plies, the variation of the fiber orientation could be different in the QI respect to the $[(\pm 45)_{2s}, +45]_s$ and therefore, since no hypothesis could be verified, the angle rotation was neglected.

The results of the simulations on a QI laminate, for a tensile solicitation, are showed in FIG. 5-21.

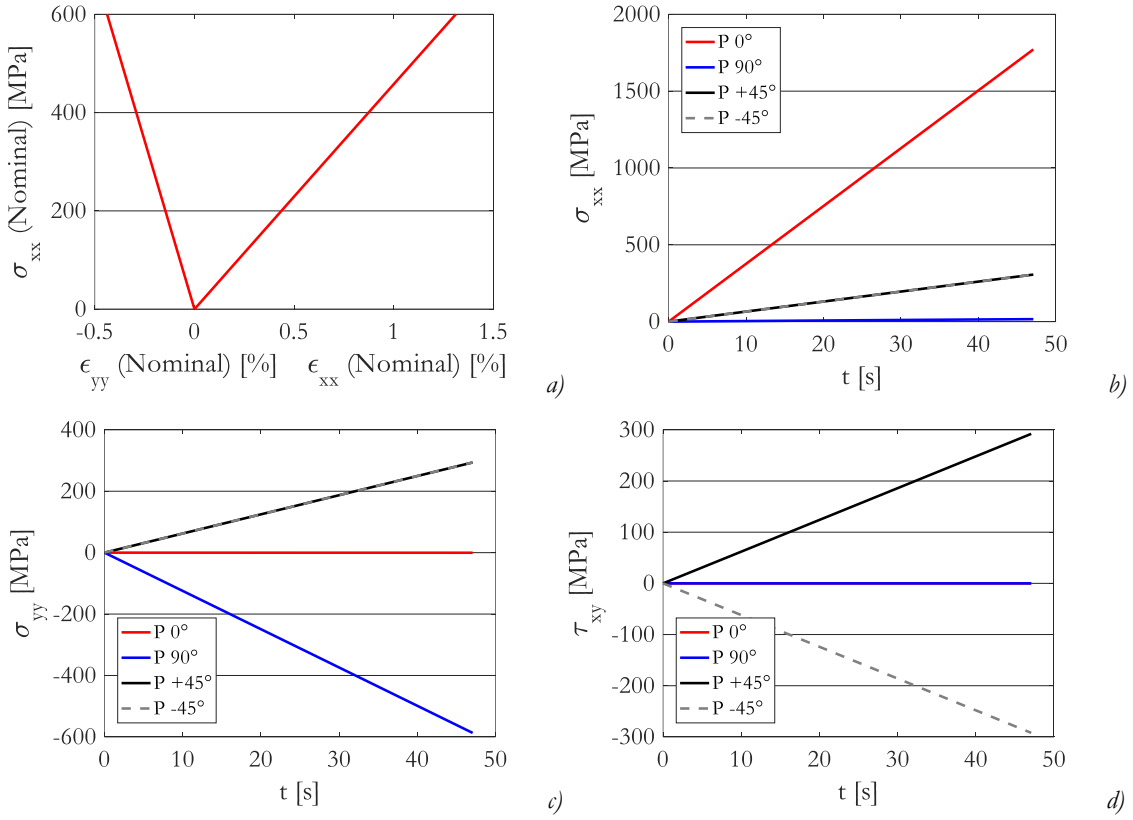

Fig. 5-21: QI simulations with SAHLM, of a QI laminate: composite stress vs composite strains (a) ply longitudinal(b), transversal (c) and shear (d) stress vs time for each ply orientation.

As showed in FIG. 5-21A, the QI behavior under tensile solicitation seems rather linear, similar to the results obtained for the 0° laminate (FIG. 5-16), but with higher ductility. Because of the presence of plies with different orientations:

- the plies with 0° orientation is 3 times more solicited than in the case of unidirectional laminate, at the same composite stress, and the only component of the stress tensor in the loading direction is non-zero;
- the plies with 90° orientation have non-zero component of the stress tensor only in the direction perpendicular to the loading direction (and hence parallel to the fiber direction), allowing it to undergo higher levels of solicitation respect than the case of laminate with only 90°: coherently with the charge only in the fiber direction, its behavior results similar to the 0° laminate;
- the plies with ±45° orientation have longitudinal, transversal and shear component of the stress tensor, which reduces to only longitudinal ones in the local coordinate system and hence in the fiber direction, for which the same consideration than the 90° plies can be applied.

At matrix level, the equivalent stress vs strain curves, the tangent moduli vs time and the equivalent strain rate vs time are showed in FIG. 5-22.

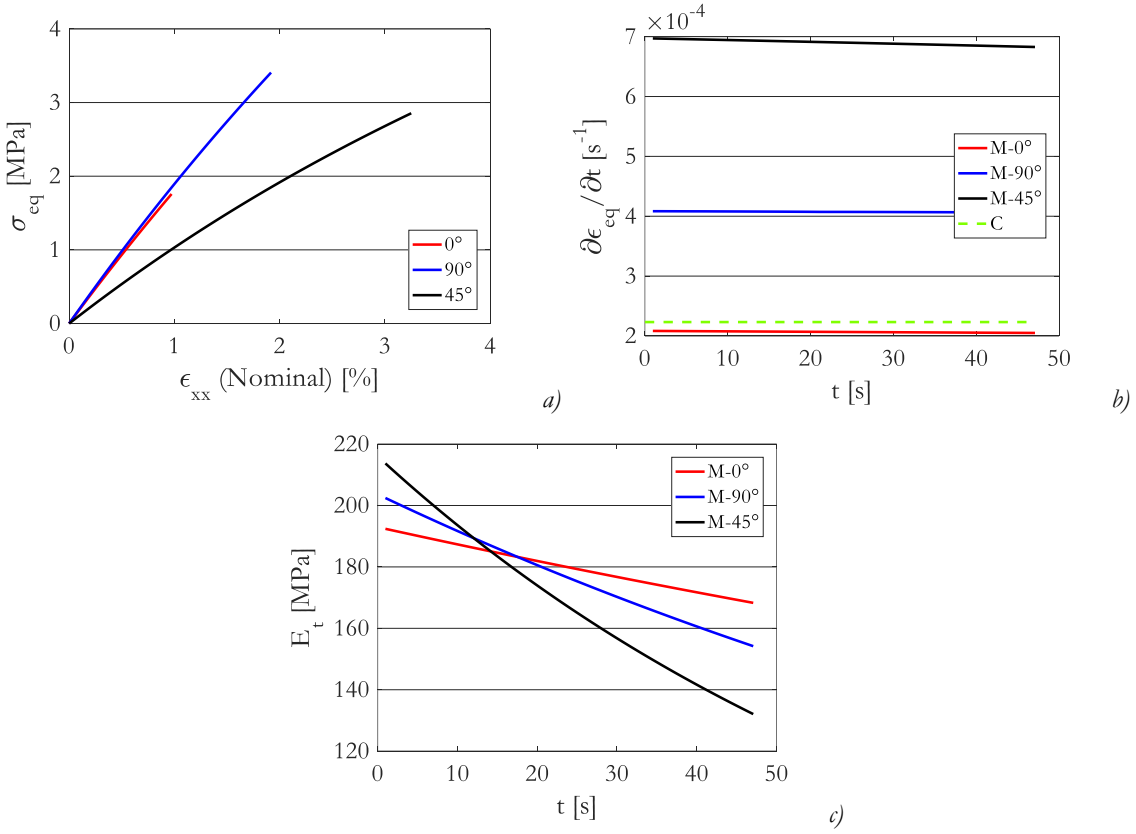

Fig. 5-22: Matrix equivalent stress vs strain (a), equivalent strain rate vs time (b) and tangent moduli vs time (c) curves, from simulations with SAHLM, of the QI laminate: comparison between the results of the matrix in the ply at 0° (red), 90° (blue), ±45° (black).

From FIG. 5-22, it appears that:

- the matrix level of solicitation is "averaged" and the values in the different plies are more similar to each other than in the case of monodirectional laminates: the matrix in the 0° plies is more solicited, while in the 90° and ±45° plies is considerably less solicited;
- the strain rate is different for the matrix in the differently-oriented plies, and while it is similar to the monodirectional laminates for the case of 0° and ±45° is almost the half in the case of 90°;
- the matrix initial tangent moduli reflect the strain rate results: because the strain rate is higher, the apparent stiffness in the equivalent stress vs strain curve for 90° is higher than the 0°; the ±45° has an even higher strain rate, but it has an apparent stiffness lower than the 0° and 90° because constituted only by shear components, (see FIG. 5-2).

The results of the simulations on a QI laminate, for a tensile-creep solicitation, are showed in FIG. 5-23.

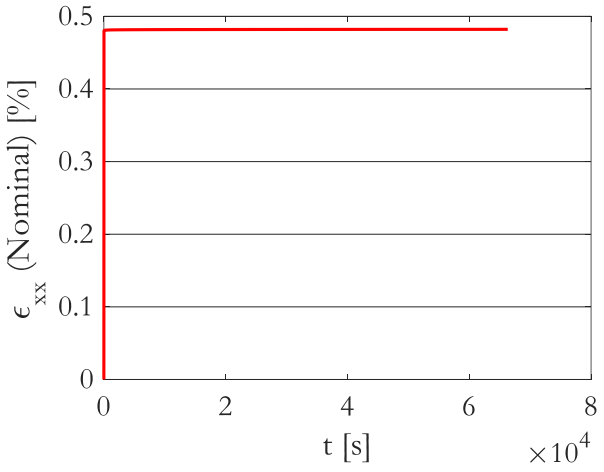

Fig. 5-23: QI simulation with SAHLM, of a QI laminate under tensile-creep solicitation: composite strain vs time

The simulation for the QI laminate shows that there is almost no increase due to creep solicitations. The creep stress in the ply are constant, as in the composite, and the ply strains, according to the laminate theory, are equal to the composite strains, and therefore are not showed.

At matrix level, the equivalent strain vs time curves, the secant moduli vs time are showed in FIG. 5-24.

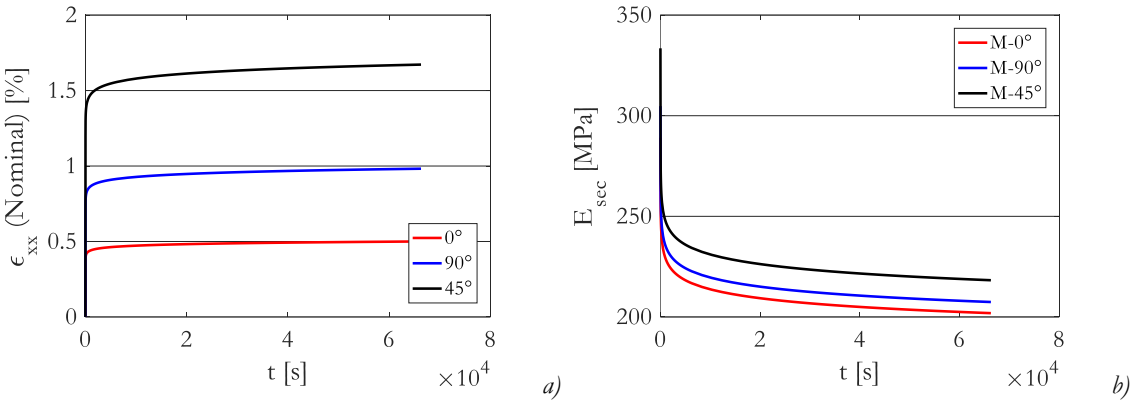

Fig. 5-24: Matrix equivalent strain vs time (a), secant moduli vs time (b) curves, from simulations with SAHLM, of the QI laminate: comparison between the results of the matrix in the ply at 0° (red), 90° (blue), ±45° (black).

From the FIG. 5-24, it can be seen that, despite the composite strain small increase during the creep phase, the matrix, however, shows indeed a more significant increase.

5.5. Conclusions

The implementation in the SAHLM of the PEKK 3-D model for tensile and creep behavior, allows the possibility of simulating both the tensile and creep behavior of the C/PEKK.

The comparison with experimental data obtained from tests at 200°C on the $[(\pm 45)_{2s}, +45]_s$ allowed the validation of the SAHLM and to identified its limits:

- the simulated curve is limited only to the matrix dominated region, and at higher composite stress, the model rapidly diverges from the composite behavior;
- the fiber rotation has to be taken into account, both for tensile and creep solicitations, and neglecting it can produce significant errors.

The model can simulate different ply orientations: because of the lack of experimental tests for comparison and fiber angle measurements, the hypothesis of constant angle is made. The results in case of monodirectional laminates with plies oriented at 0° or 90° showed a difference in the extension of the matrix dominated region and in ductility; at the matrix level, it shows difference in the solicitation and strain rate, both higher for the 90° than the 0° laminate. Moreover, at each level, the $[(\pm 45)_{2s}, +45]_s$ behavior, is intermediate between the two, as expected.

The SAHLM is modified to be able to simulate laminates with plies oriented in different directions: parallel branches to different part of the algorithm, where the effect of the different plies orientation intervenes, are implemented, and the convergence criterion is modified to be verified only when all single criteria are satisfied simultaneously.

As example, the results of a simulation of a QI laminate are presented, with the hypothesis of constant fiber angle and not taking into account the order of the plies sequence, nor their interaction. The results, both in terms of tensile and creep solicitations, show that the plies are all solicited in the fiber direction, as expected for the QI. Moreover, at matrix level, the SAHLM is able to differentiate the matrix in the solicitation and strain rate in each ply, according to the different orientations of the plies themselves, which are more similar to each other respect to the results obtained from simulating individually laminates constituted only by plies with the same orientation.

The results presented confirm the conclusion presented in CHAP. 3, confirming that the matrix behavior in the composite has a behavior similar to the polymer's one, and moreover that is possible to reconstruct the composite starting from the matrix behavior.

For the $[(\pm 45)_{2s}, +45]_s$, the conclusions can be only limited to the test durations (108 h). The SAHLM allows, however, the simulation of longer creep durations, implicitly extending the validity of the formulation over the 108 h. Degradation mechanisms could be activated due to the longer exposure to high temperature, modifying the materials thermomechanical behavior. Their presence, as well as their impact on the materials behavior are investigated in the next chapter, through longer-duration tests.

Chapter 6 – Coupled oxidation-thermomechanical-creep behavior of PEKK and C/PEKK at 200°C

The present chapter focuses on the characterization of the coupled oxidation-thermomechanical-creep behavior of PEKK and C/PEKK at 200°C. 42 days oxidation ageing under 5 bar O_2 was carried out on PEKK polymer and C/PEKK composite samples. Coupled oxidation-thermomechanical-creep tests were carried out on C/PEKK samples under a 5 bar O_2 environment for the same duration. Tests results discussion was supported by DMA and DSC scans. X-rays μ-tomography scans were performed on the tested specimens to investigate the possible occurrence of degradation and damage.

6.1. Introduction

The previous chapters presented the identification of the principal mechanisms controlling PEKK behavior under different loading conditions. In particular, (CHAP. 4.3) has shown for PEKK SC complex coupled thermomechanical-crystallization behavior. Moreover, it has been shown that PEKK SC was not fully crystallized and least 100h at 200°C are required to reach the saturation of crystallization. This suggests that no further crystallization mechanism should activate during longer exposures.

As mentioned before, the work presented so far has with 2 major limitations:

1. the presence of further mechanisms could not be excluded, even if, standing the whole interpretation, they could have marginal or negligible effects on PEKK behavior;
2. the proposed interpretation allows describing PEKK SC behavior in the time window investigated experimentally, up to a maximum duration of 108 h (corresponding to creep-recovery duration), and for duration significantly lower for the most part of the tests (a tensile test at 10 mm/min has a duration of few minutes), considerably shorter than the duration expected for engineering applications. While the behavior under longer exposures to thermomechanical loads could be extrapolated, it will implicitly suppose that no mechanisms manifest other than the ones observed during the experimental campaign described in the previous chapters.

As described in Literature Survey, long-term exposure was investigated through ageing at 200°C under air up to 17000h (~1.9 years), and no indicator of possible degradation mechanisms (as mass loss) has been observed.

However, the exposure to oxygen conditioned atmosphere, which has been proved to accelerate oxidation mechanisms, revealed possible signals of degradation at 200°C which start before 1000h of exposure. While it has to be pointed out that those tests were carried out on 50 μm film of amorphous PEKK, (on which also crystallization mechanism could be activated), hence in condition considerably different respect to the 2.1 mm – thick almost fully crystallized specimen employed in the present work, they could also reveal that for very long exposure, exceeding the 17000h, oxidation mechanism could be present.

In order to verify the presence of material degradation, experimental tests were carried out in the same testi conditions and durations of the above mentioned tests carried out on PEKK films. The investigation is carried out in two phases:

1. *Pure oxidation effect*: PEKK SC and C/PEKK samples were aged for 6 weeks at 200°C (maximum test temperature) under 5 bar O_2 conditioned atmosphere. Optical observations of the cross section, DSC and DMA tests on PEKK SC aged specimens were carried out to evaluate the presence of oxidation mechanisms and their effect on the physical-chemical and mechanical properties. A qualitative analysis was carried out also on C/PEKK specimens through the comparison of μ-tomographies on as received and aged C/PEKK specimens' damage scenario;

2. *Coupling between oxidation and thermomechanical load*: long term creep test with a duration of 6 weeks, at 200°C (maximum test temperature) under 5 bar O_2 conditioned atmosphere was carried out on a C/PEKK specimen. The effect of oxidation on C/PEKK thermomechanical behavior is investigated through the comparison with creep tests carried out at 200°C in not conditioned atmosphere (CHAP. 3.4). The effect of thermomechanical load on oxidation kinetics is investigated through the comparison of μ-tomographies on the creep tested specimen with the as received and aged C/PEKK specimens' damage scenario.

6.2. Effect of thermal oxydation

Preliminarily to the first phase of the investigation of the presence of oxidation mechanisms, the specimen listed in TAB. 6-1, were aged at 200°C under a 5 bar of O_2 conditioned atmosphere, according to the test protocol described in CHAP 2.3.1.5.

Material	Type of specimen (FIG. 2-5)	Ageing time [days]
PEKK SC	6 specimen type *a*	From 7 up to 42
C/PEKK	1 specimen type *e*	42

Tab. 6-1: Ageing conditions

6.2.1. Effect of ageing on PEKK SC

The 6 specimen type *a* of PEKK SC aged at 200°C in 5 bar of O_2 conditioned atmosphere for duration from 7 to 42 days are showed in FIG. 6-1.

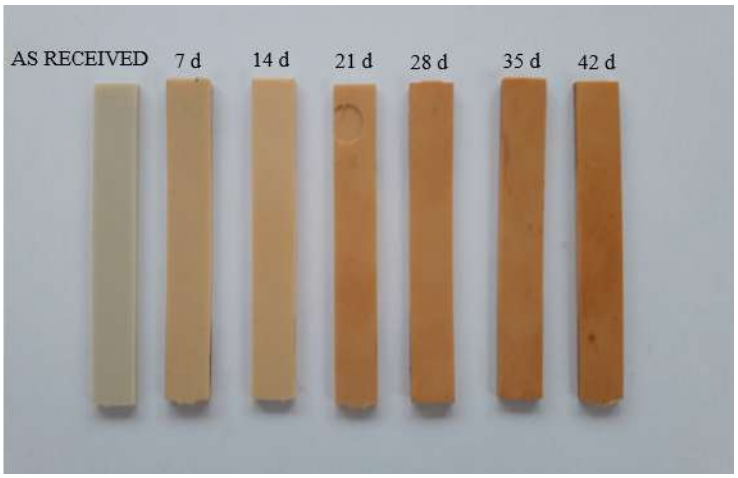

Fig. 6-1: PEKK SC specimen aged at 200°C in 5 bar of O2 conditioned atmosphere for duration from 7 to 42 days

Comparing the specimens to the as received material, it appears that the ageing produces a change in color on the surface of the aged specimens, gradually moving toward darker brownish shade as the exposure time is increased. Comparing them with the result obtained at ENSAM Paris, (ROLAND AND FAYOLLE 2020) on PEKK 7002 AM films, aged at 280°C in not conditioned atmosphere (showed in FIG. 1-13), the color tone after 42 days (1008 h) under 5 bar of O_2 is close to the color tone produced after 646 h at 280°C. Considering a factor 10 of acceleration produced by the oxygen, it can be esteemed an acceleration factor of over 15 of oxidation phenomena passing from 200°C to 280°C.

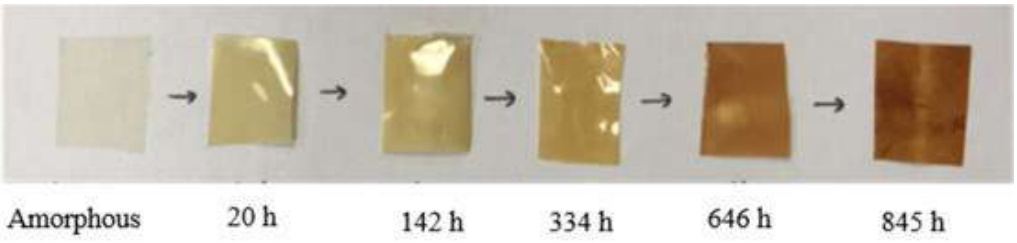

Fig. 1-13: PEKK 7002 AM film aged at 280°C on air (ENSAM Paris) (Roland and Fayolle 2020)

However, the difference in thickness between the specimens type *a* and the films (2.11 mm and 50 μm respectively), prevents to limit the investigation of ageing effect to the specimen surface, and therefore also the penetration of oxidation is investigated.

The specimen exposed for the longest duration was cut and its cross-section analyzed with the employment of an optical microscope. The acquired images were processed with image analysis techniques in order to evaluate the color gradient and to relate it to the oxidation penetration, on 2 levels:

1. the mean of the histogram at each value of each color of pixel (image *y*-direction) is evaluated and normalized respect to its maximum value;
2. the image *y*-direction gradient is evaluated, employing the Sobel operator: the directional *y* derivative (EQ. 6-2) of the image is evaluated after convolving 3x3 Sobel kernels (EQ. 6-1) applied on the image itself.

$$G_y = \begin{bmatrix} 1 & 2 & 1 \\ 0 & 0 & 0 \\ -1 & -2 & -1 \end{bmatrix} Imm \qquad \text{Eq. 6-1}$$

$$\frac{\partial Imm}{\partial y} = \frac{Imm(y+h) - Imm(y-h)}{2h} \qquad \text{Eq. 6-2}$$

Once the *y*-direction gradient is evaluated, the normalized mean of each column of pixels is evaluated, as for the original image.

The results are showed in FIG. 6-2, on two images acquired at different microscope magnifications of the specimen cross-section. The change of slope of the curve defined by the normalized mean of the histograms is taken as the limit of the change in color of the specimen cross-section. Considering this parameter directly linked to the penetration of oxidation inside the specimen, it suggests that the penetration stops at less than 50 μm from the surface, leaving more than the 93% of total cross-section unaffected by the ageing effect.

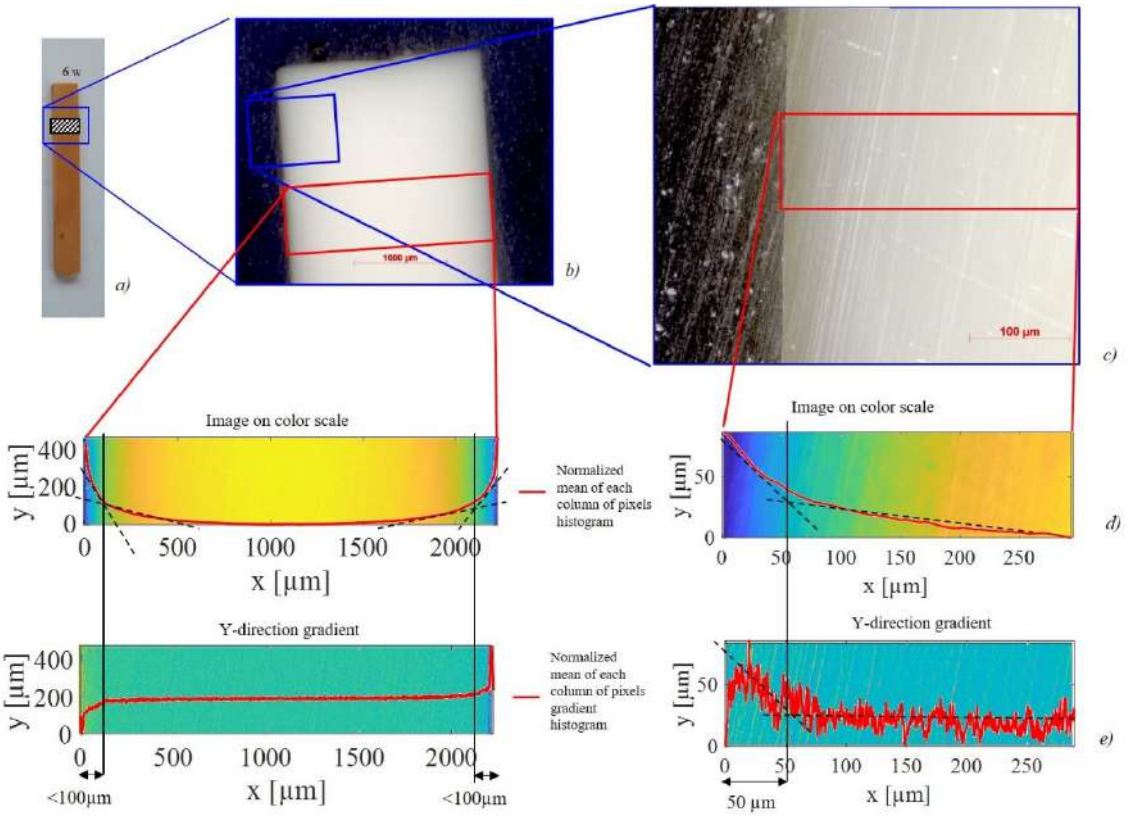

Fig. 6-2: PEKK SC specimen aged at 200°C under 5 bar of O2 for 42 days (a), images of its cross-section at different magnification factors (b and c), images color scale (d) and y-direction image gradients (e) and relative normalized means of each column of pixel

The effect of ageing on the physical-chemical and mechanical properties is investigated through DSC and DMA tests.

6.2.1.1 DSC tests on aged PEKK SC

DSC tests, according to the testing protocol described in (CHAP. 2.3.1.4), were carried out on 2 PEKK 7002 SC specimens type *f* (FIG. 2-5), cut from the specimen exposed for the longest duration at 200°C under 5 bar of oxygen (42 days): the first was cut trying to include in the sample as much skin as possible, while in the second the skin was removed as much as possible, to try and highlight the difference between skin and core. The results are compared with the DSC test carried out on the as received material, (CHAP. 3.4). and showed in FIG. 4-12

For all 3 cases, the T_g, the T_m and the peak enthalpy are measured for 1st and 2nd heating and cooling phases; the measured values are listed in TAB. 3-15.

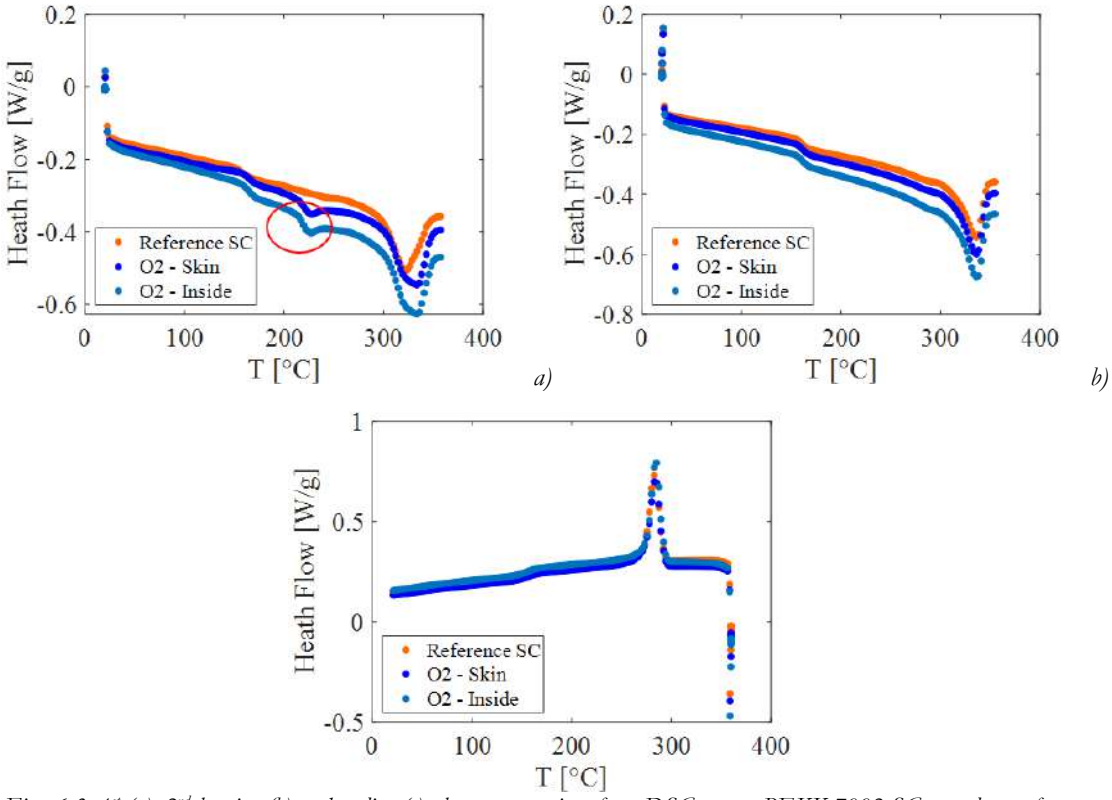

Fig. 6-3: 1st (a), 2nd heating (b) and cooling (c) phases comparison from DSC test on PEKK 7002 SC samples cut from as-received material, after ageing at 200°C and 5 bar of O2 for 42 days

	Reference	Ageing - Skin	Ageing -Inside
1st Heating			
T_g [°C]	157.1	165.04	164.74
T_m [°C]	322.9	333.51	333.25
ΔH_f [J/g]	31.63	34.50	36.64
T_m [°C] (2nd peak)	No 2nd peak	226.27	225.51
ΔH_f [J/g] (2nd peak)		2.236	2.671
2nd Heating			
T_g [°C]	160.3	161.15	160.44
T_m [°C]	337.0	336.37	337.10
ΔH_f [J/g]	29.86	33.11	34.20
Cooling			
T_p [°C]	282.7	283.52	284.5
ΔHc [J/g]	38.18	36.36	38.82

Tab. 6-2: T_g, T_m and peaks enthalpy measured from DSC test on PEKK 7002 SC samples cut from as-received material, after ageing at 200°C and 5 bar of O_2 for 42 days

In particular, looking at the first heating, FIG. 4-12A shows that there is:

- no significant difference between the curves obtained from skin and core of the most aged specimen, most possibly because the amount of oxidized layer has a small thickness compared to the whole specimen and its properties are hidden by the rest of the unaffected material;
- no presence of exothermic peak in any test, and therefore no presence of cold crystallization;
- the presence of the second endothermic peak after ageing, related to an increase of secondary crystallinity: in CHAP. 4.3 it has been pointed out how this increase is close to the value measured after creep-recovery tests carried out under air at 200°C for 108 h (~1/10 of effective exposure duration, ~1/100 considering the acceleration produced by the oxygen exposure), coherently to the saturation previewed by Hillier model of the crystallization kinetics and hence compatible with thermal effect alone;
- different values of T_g (+8°C) and melting peak values (+11°C) after the ageing, which, in consideration of the fact that most probably only the unaffected material (core) is tested, are likely produced by the increase in crystallinity percentage.

The second heating and the cooling curves (FIG. 4-12A and B), show no significant difference respect to the as received material, proving that all effect produced on the material during the ageing are annihilated after the complete melting.

6.2.1.2 DMA test on aged PEKK SC

3-point-bending DMA tests were carried out on the specimen exposed for the longest duration at 200°C under 5 bar of oxygen (42 days), according to the testing protocol described in (CHAP. 2.3.1.3). The results are compared to the DMA test carried out on the as received material (CHAP. 3.4) and showed in FIG. 6-4. The measured T_g onsets and the initial storage and loss moduli, as well as the initial *tanδ*, are summarized in TAB. 6-3.

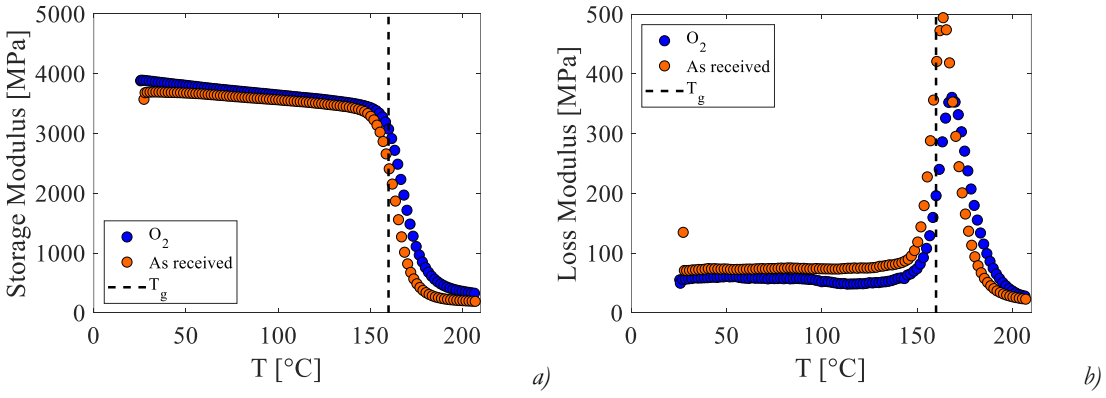

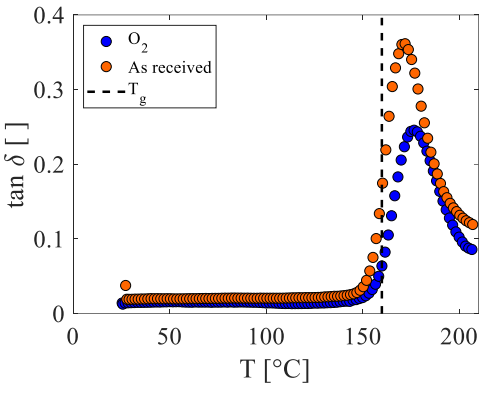

Fig. 6-4: 3-point bending DMA storage modulus (a), loss modulus (b) and tan delta (c) for PEKK 7002 SC as received (orange) and after ageing at 200°C and 5 bar of O2 for 42 days

	As received	Aged
T_g onset *E'* [°C]	155.96	158.95
E' @ 27°C [MPa]	3572	3889
T_g onset *E"* [°C]	163.73	168.17
E" @ 27°C [MPa	494.10	360.80
T_g onset *tanδ* [°C]	171.04	176.86
tanδ@ 27°C [MPa]	0.362	0.246

Tab. 6-3: T_g onsets and the initial storage and loss moduli, as well as the initial tanδ for PEKK 7002 SC as received (orange) and after ageing at 200°C and 5 bar of O_2 for 42 days

The comparison between the DMA on as received material and on aged samples, shows that the global trend is substantially unaffected by the ageing, but a +3÷5°C increase in the T_g onset is registered. Moreover, the storage modulus (TAB. 6-3), is slightly higher (+8%) at 27°C and such increase is more or less constant at any temperature: a similar effect is observed in the comparison between PEKK SC (χ = 24.3 %) and PEKK AM (χ = 4.5 %) storage moduli (FIG. 4-40), suggesting that all the variations respect to the as received material are produced by the increase in the crystallinity percentage.

6.2.2. Effect of ageing on C/PEKK

The not significant effect of ageing, which produced a layer confined to the surface, on PEKK SC physical-chemical properties, let exclude an analogue approach of investigation on C/PEKK: in fact, the presence of fibers prevents an optical analysis, and can hide any small change in physical-chemical properties.

In fiber reinforced polymers, the oxidation causes also the *shrinkage* of the matrix (LOÏC 2008), (GIGLIOTTI, MINERVINO, AND LAFARIE-FRENOT 2016), (POCHIRAJU, SCHOEPPNER, AND TANDON 2012), which results in matrix-fiber debonding and the

presence of cracks. Because the oxidation phenomenon starts as superficial (as it is observed also on PEKK SC), it is expected that the more external layer would be more affected than the core ones, resulting in a difference of damaging between the surface and the core of the composite.

This phenomenon allows the investigation of the oxidation effect on the C/PEKK with the employment of X-Rays techniques, and thus the sample aged at 200°C under 5 bar of O_2 was scanned with μ-tomography, as described in CHAP 2.3.1.6.

The results are compared with a μ-tomography carried out on an as received specimen, and showed respectively in FIG. 6-5 and FIG. 6-6. Because the specimens have a slight curvature (0.096 mm and 0.276 mm for as received and after ageing respectively), for the surface is chosen the last section of the specimen where all the central part is clearly visible (indicated with 0 μm) and the following images are chosen with a pace of 0.12 mm (10 images x 12μm of resolution) in the thickness direction. The last image, by consequence, shows the surface in the areas excluded from the first image: because of the exposure of both surface to the conditioned atmosphere, and considering no substantial variation between them, this choice should allow the complete representation of the superficial damaging scenario of the specimens.

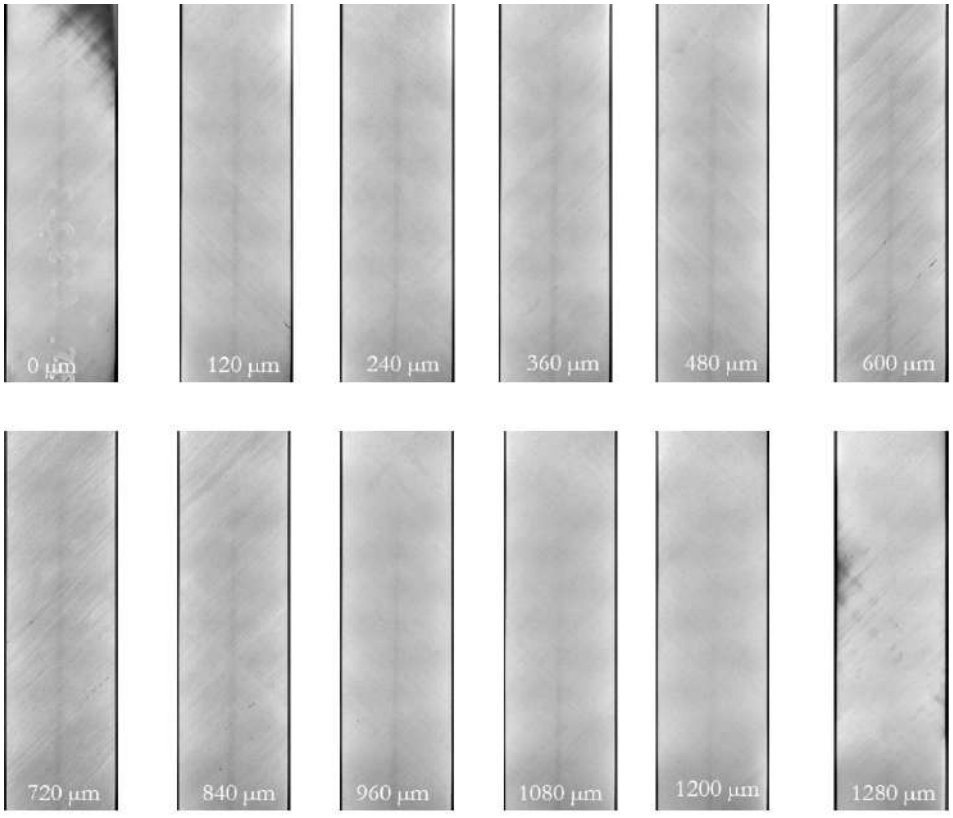

Fig. 6-5: C/PEKK as received specimen sections in the longitudinal-transverse plane, from one surface (first image) to the other (last image) in the thickness direction, obtained with μ-tomography

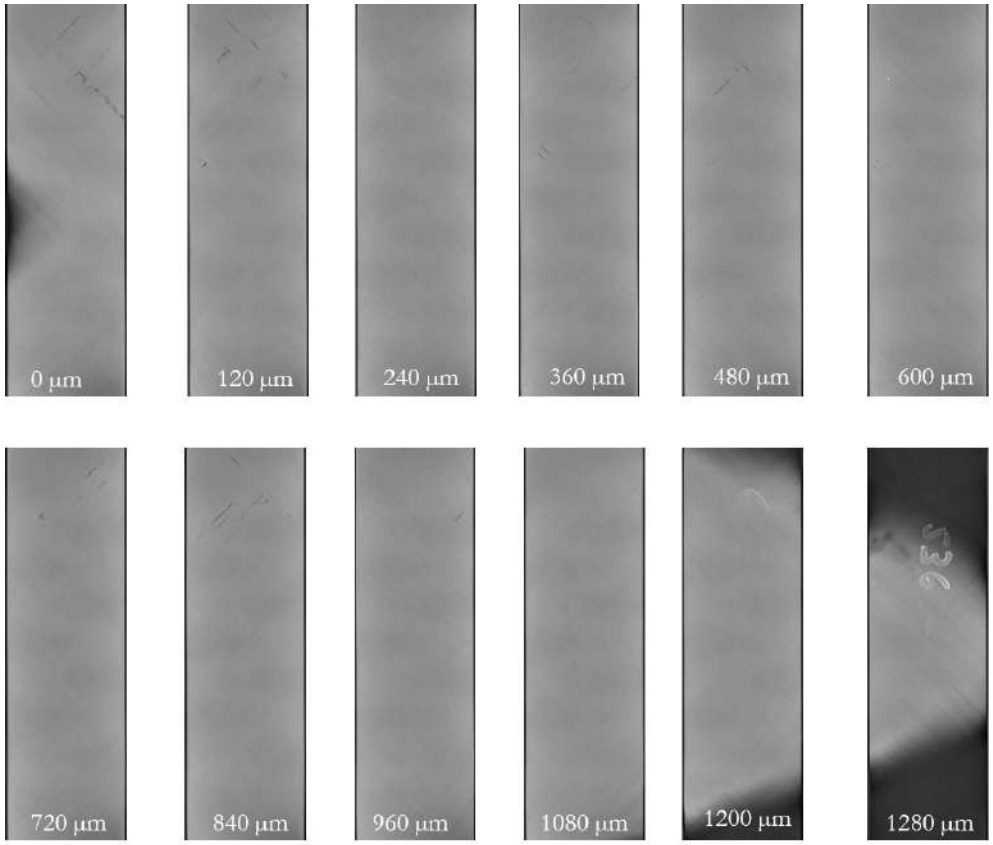

Fig. 6-6: C/PEKK aged at 200°C under 5 bar of O_2 for 42 days specimen sections in the longitudinal-transverse plane, from one surface (first image) to the other (last image) in the thickness direction, obtained with µ-tomography

The sections showed in FIG. 6-6, present a limited damaging scenario, with the presence of cracks in the upper part of the specimen which propagates through the thickness and in the different plies (changing direction). This could be due to the preexisting cracks in the specimen, produced before the ageing, which could help the propagation of oxygen in the specimen core. However, the rest of the specimen shows no damage at all, and no difference could be found respect to the as received one. This scenario confirms the limited effect of the oxidation on the PEKK SC, also in the composite.

6.3. Coupling between oxidation and thermomechanical load

In the previous paragraph, the activation of oxidation mechanisms after long term (1.15 years considering the acceleration produced by oxygen) is investigated and it is showed their limited impact on aged PEKK SC mechanical properties. On C/PEKK the observed damage scenario points out a similar conclusion.

However, the interaction with thermomechanical load, which itself produces a degradation of the interface between matrix and fiber, due to their different mechanical properties, could enhance the effect of the oxidation.

A long term creep test, carried out on C/PEKK for the same ageing test duration, temperature and environmental conditions, could provide the information about:

- *the effect of oxidation on the creep behavior*: a prove could be constituted by differences from the comparison between the long term creep strain and the creep strain extrapolated from shorter tests, carried out at the same creep stress and temperature under air.
- *the effect of thermomechanical load on the oxidation*: as discussed above, the damage induced by thermomechanical load could promote the penetration of oxidation mechanisms into the specimen's core: this could be assessed through the comparison of the damage scenario resulting after the long term creep test and after ageing.

6.3.1. Effect of oxidation on the creep behavior

Preliminarily to the long term test, needed for evaluating the effect of the oxidation on the C/PEKK creep behavior, there are needed:

1. **Comparison tests.** For the comparison, the initial part (load and creep phase only) of the creep-recovery tests carried out in not-conditioned atmosphere on C/PEKK presented in CHAP. 3.4 are employed. Since they were carried out at 2 levels of creep stress, a 3rd creep test was carried out at an intermediated creep stress, which parameters are summarized in TAB. 6-4.

$\dot{z}\ \left[\frac{mm}{min}\right]$	T[°C]	Condition	F [N]	σ^{C}_{creep} [MPa]	Test duration
1	200°C Air	41 MPa	468.6	41	108 h

Tab. 6-4: Creep test parameters for C/PEKK under air

All the creep strain curves are fitted with the Norton-Bailey power law (EQ. 3-10), changing the parameters values respect to the ones showed in TAB. 3-12 (needed for the comparison with PEKK SC), to better optimize the fitting. Also in this case the m and n parameter in EQ. 3-10 are fixed and the A parameter corresponding to each applied stress is identified. All the power law parameters are listed in TAB. 6-5.

Test condition	A	m	n	σ_{cr} [MPa]
Air 200°C	**0.04817**	-0.9706	0.01942	28
	0.117	-0.9706	0.01942	41
	0.2039	-0.9706	0.01942	64

Tab. 6-5: Power law parameters for the creep tests carried out at 200°C in not-conditioned atmosphere

The carrying out of a third creep test under air, at a creep stress intermediate to the 2 previous ones, allowed identifying a linear proportionality between the A parameter and the applied creep stress, as showed in FIG. 6-7 and according to EQ. 6-3.

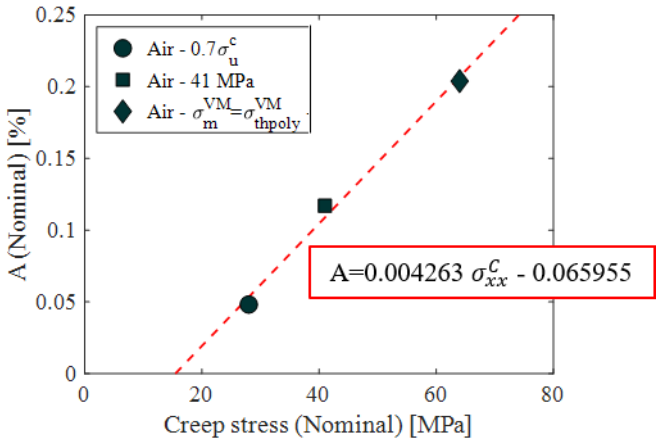

Fig. 6-7: Evolution of the A parameter of the Norton-Bailey equation with the creep stress for C/PEKK at 200°C under air

$$A=0.004263\ \sigma_{xx}^{C} - 0.065955 \qquad \textit{Eq. 6-3}$$

Employing EQ. 3-10 and EQ. 6-3, it is possible to extrapolate the creep behavior at 200°C for longer duration than the actual duration of the creep tests, for any value of the applied stress between 28 MPa and 64 MPa.

2. **Creep test parameters.** While the comparison with the C/PEKK aged specimen directly fixes the test temperature, duration and environmental conditions, for the creep stress, the value of 28 MPa is chosen, in order to limit the thermomechanical induced damage and to remain in the matrix dominated region. The testing condition are summarized in TAB. 6-6.

$\dot{z}\ \left[\frac{mm}{min}\right]$	T[°C]	Condition	F [N]	σ^{C}_{creep} [MPa]	Test duration
1	200°C 5 bar O_2	$\sigma_m^{VM}=\sigma_{poly}^{th}$	989	28	42 days

Tab. 6-6: Creep test parameters for C/PEKK for coupling with aging

The long duration creep test was carried out on C/PEKK specimen type *e* (FIG. 2-5), according to the testing protocol described in (CHAP. 2.3.1.5).

The extreme conditions of temperature combined with O_2, produced in the paint employed for the markers a consistent degradation, which prevented IdPix software to measure the strain, after around 10 h of testing.

The images where then post-treated with IAT (CHAP. 2.3.2.3), which allowed recovering the measure of strain, otherwise preventing the possibility of carrying out the test. The results of IAT's post-treatment, as well as the images of the progressively degradation of the markers are showed in FIG. 6-8.

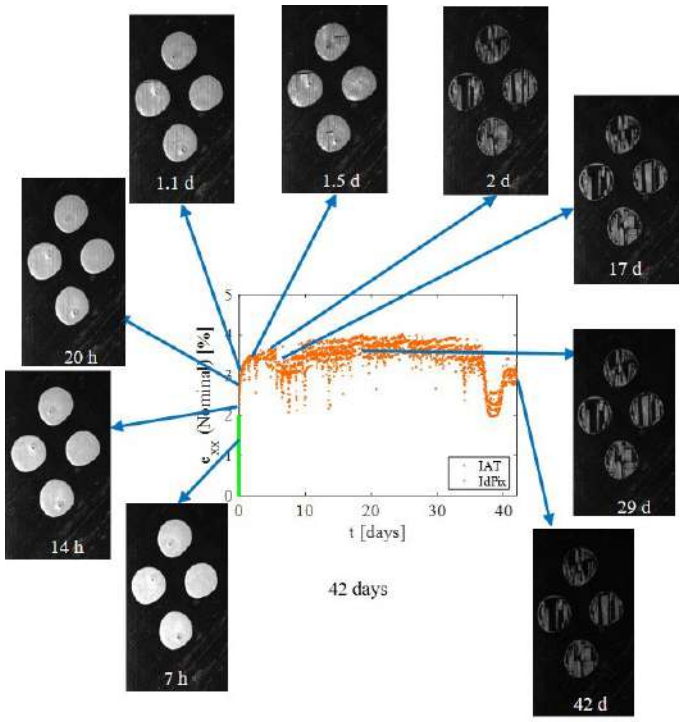

Fig. 6-8: Nominal longitudinal strain vs time curve obtained from creep test on C/PEKK at 200°C under 5 bar of O_2 and images of the progressive marker degradation.

The green markers indicate the point measured with IdPix, while the orange ones, the value measured with IAT, showing how IdPix stopped measuring the strain after less than 14 h.

FIG. 6-9 shows the comparison of the creep strain obtained from the different creep tests at 200°C.

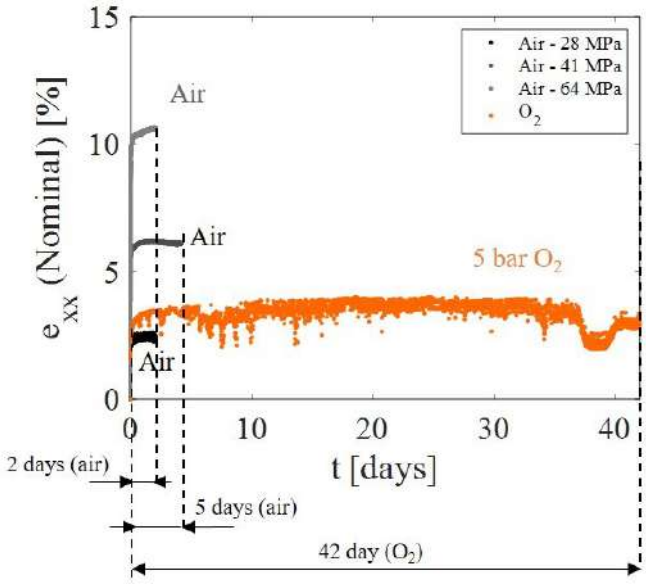

Fig. 6-9: Comparison of the creep strain carried out at 200°C in non-conditioned atmosphere (grey curves) and in conditioned atmosphere (orange curve).

The creep strain measured during the creep test carried out in conditioned atmosphere has greater magnitude than the creep strain measured under air. While an error in the strain measure cannot be excluded, because of the extreme marker degradation, the increase in creep strain is also compatible with oxidation phenomena, (FOTI 2017).

However, during the test, while the Instron 1251 internal load cell correctly registered the creep stress of 28 MPa, the external one registered higher, non-constant values, possibly because of friction between the internal load cell (encapsulated in the machine arm) and the machine arm itself. The position of the machine arm produced/was affected by such error (and by consequence the strain), as is it visible in FIG. 6-10, which shows negative peaks in both the nominal stress and the position vs time curve. Peaks can be found on the strain vs time curve in correspondence of the peaks of the nominal stress and position vs time curves.

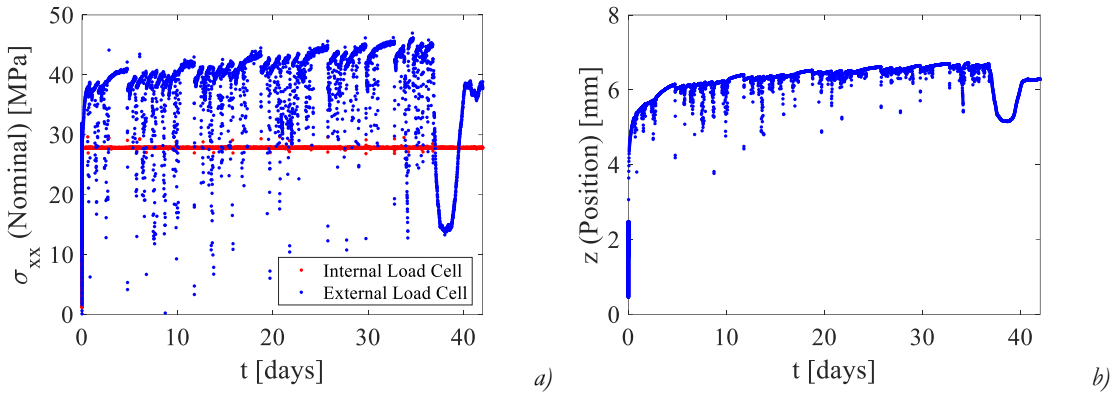

Fig. 6-10: Nominal stress vs time registered by the Instron 1251 internal (red) and external (blue) (a) and position vs time registered by Instron 1251 LVDT (b) during the creep test on C/PEKK at 200°C under 5 bar of O_2

FIG. 6-11 shows the comparison of the creep stress obtained from the different creep tests at 200°C.

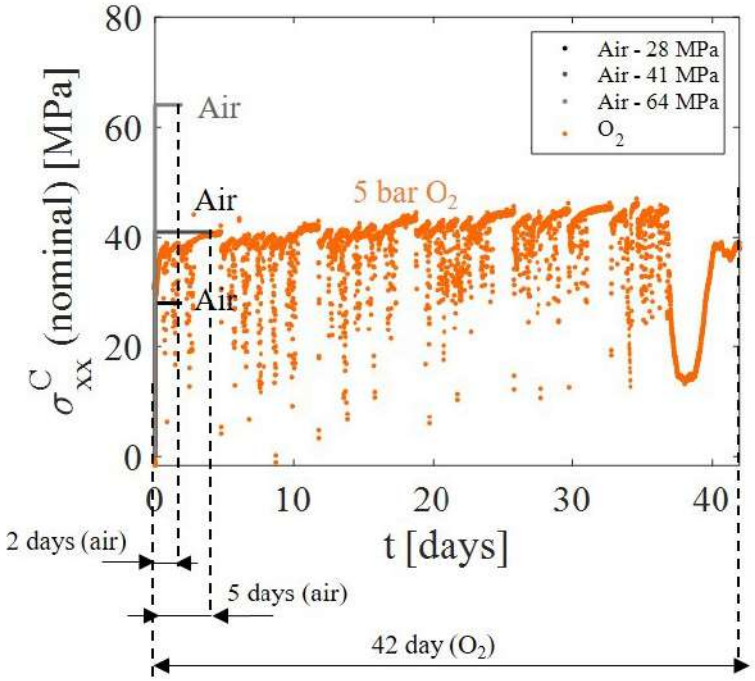

Fig. 6-11: Comparison of the creep stress carried out at 200°C in non-conditioned atmosphere (grey curves) and in conditioned atmosphere (orange curve).

An increase in the applied force on the specimen could justify an increase in the measured strain. However, while the creep strain obtained from the test carried out at 28 MPa in conditioned atmosphere is closer to the creep strain from the test carried out under air at 28 MPa than to the test at 41 MPa, (FIG. 6-9), the creep stress measured under O_2, is closer to

41 MPa than to 28 MPa, (FIG. 6-11). This could be provoked by the above mentioned friction between the internal load cell and the machine arm.

In order to verify if the increase if strain is due to the increase of stress or because of oxidation, the creep strain curves at 200°C are compared, exploiting the Norton-Bailey power low (EQ. 3-10) fitting, with the following procedure:

- the creep strain curves obtained from the test carried out under air (2 ÷ 5 days duration) are extrapolated to the duration of the test carried out under 5 bar O_2 (42 days);
- the creep strain curve obtained from the test carried out in conditioned atmosphere is reconstructed employing the measured values of the creep stress both for the calculation of the $A=(\sigma_{CR})$ parameter and the Norton –Bailey power law (EQ. 3-10), $\varepsilon=(A(\sigma_{CR}), \sigma_{CR}, T)$ employing the m and parameters listed in TAB. 6-5.

The comparison is showed in FIG. 6-12.

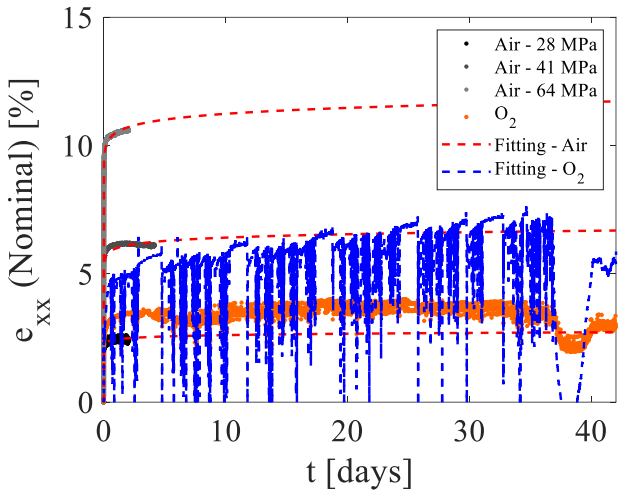

Fig. 6-12: Creep strain measured at 200°C in non-conditioned atmosphere (gray) and they respective fitting (red) and creep strain at 200°C under 5 bar of O_2 (orange), with calculated strain, taking into account the variable creep stress (blue)

The resulting reconstruction of the creep strain in conditioned atmosphere (blue curve in FIG. 6-12), overestimates the measured creep strain (in orange).

The calculated strain can be sensibly ameliorated if the friction between the internal load cell and the machine is taken into account: the measured creep stress is scaled to the nominal value of the creep stress, through:

$$\tilde{\sigma}^{C}_{xx} = \sigma^{C}_{xx} \frac{\sigma^{C}_{xx,\,NOM}}{<\sigma^{C}_{xx}>} \qquad \text{Eq. 6-4}$$

where:

- $\sigma^{C}_{xx,\,NOM}$ = 28 MPa, is the nominal value of the creep stress, as measured by the internal load cell;
- $<\sigma^{C}_{xx}>=\frac{\sum \sigma^{C}_{xx}\, t}{\sum t}$ = 37.41 MPa, is the time averaged creep stress measured by the external load cell.

The ratio $\frac{\sigma^{C}_{xx,\,NOM}}{<\sigma^{C}_{xx}>}=\frac{28}{37.41}$ = 0.7485, implying that the friction produce an overestimation of the applied stress of about the 25%.

The creep strain of the test carried out in conditioned atmosphere can be recalculated, according to the above mentioned procedure, but employing the corrected creep stress (EQ. 6-4), and compared with the extrapolated creeps strain curves obtained from tests carried out under air, as showed in FIG. 6-13.

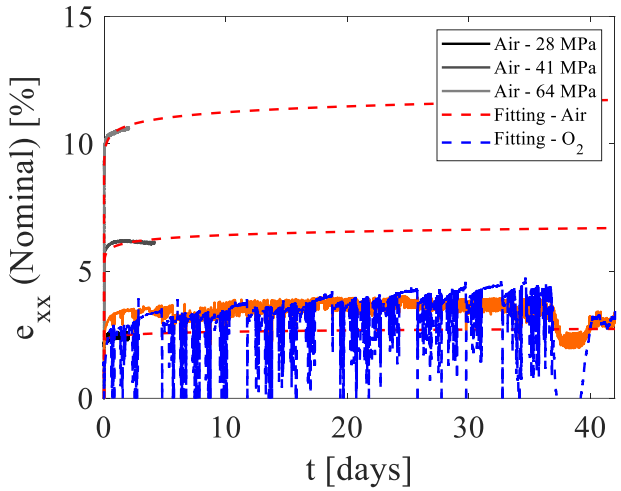

Fig. 6-13: Creep strain measured at 200°C in non-conditioned atmosphere (gray) and they respective fitting (red) and creep strain at 200°C under 5 bar of O_2 (orange), with calculated strain, taking into account the scaled variable creep stress (blue)

FIG. 6-13 shows that, once the measured creep is corrected stress of the friction effect, the reconstructed creep strain (blue curve) is superposing to the experimental curve (orange curve).

The capability of reconstructing the experimental creep strain curve obtained testing the C/PEKK in conditioned atmosphere with EQ. 3-10 and with the parameters identified fitting the creep strain curves obtained from not-conditioned atmosphere, proves that the increase in strain respect to the extrapolation of the test carried out under air is mainly produced by the increase in the applied stress and that degradation effect, as the oxidation, have a negligible effect.

6.3.2. Effect of thermomechanical load on the oxidation

The previously described analysis, showed that the oxidation has limited effect on the creep behavior of C/PEKK. In order to complete the investigation, the effect of thermomechanical load on the oxidation mechanisms are evaluated: the specimen tested at creep at 200°C under 5 bar of O_2 for 42 days was scanned whit μ-tomography, according to the procedure described CHAP 2.3.1.6.

As described in CHAP. 6.2.2, also for this specimen a curvature was observed (0.396 mm) and the same consideration described in the above mentioned paragraph can be applied to the this case too. The sections of the specimen are showed in FIG. 6-14.

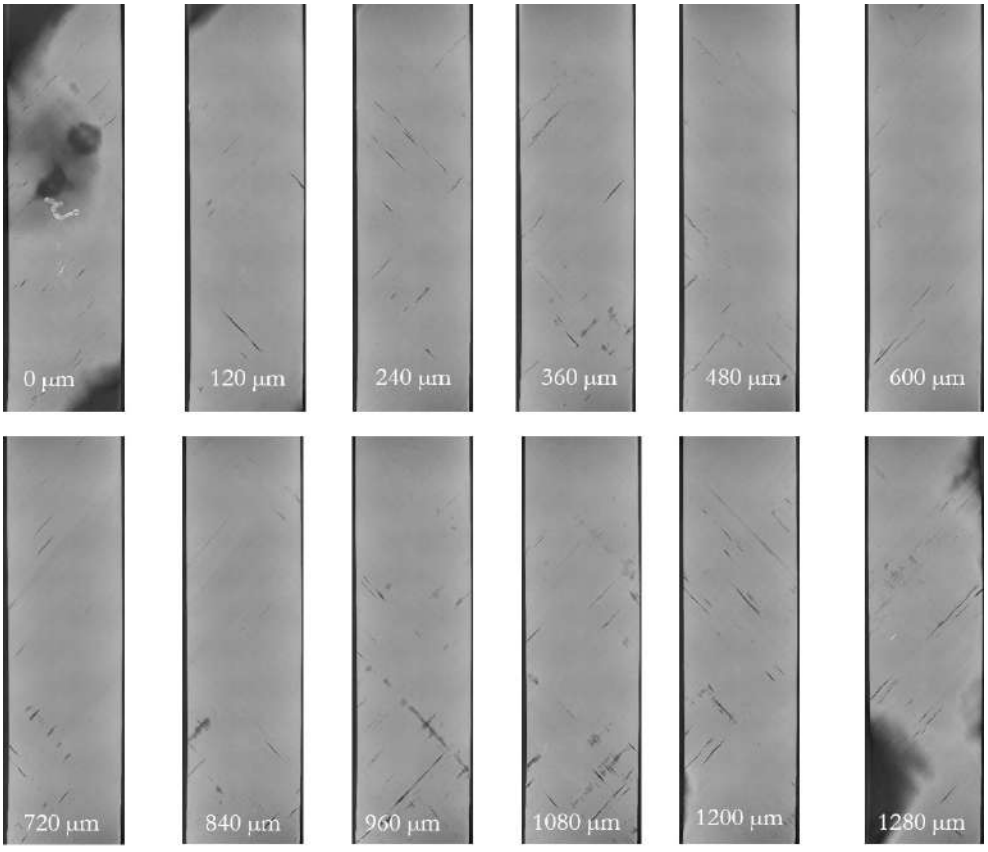

Fig. 6-14: C/PEKK tested at creep at 200°C under 5 bar of O_2 for 42 days specimen sections in the longitudinal-transverse plane, from one surface (first image) to the other (last image) in the thickness direction, obtained with μ-tomography

The specimen tested at creep under 5 bar of O_2, presents a more significant damage scenario respect to the as received (FIG. 6-5) and aged (FIG. 6-6) specimens: multiple cracks appear on the overall specimen gauge length and throughout the whole thickness, changing direction according to the ply orientation and parallel to the fibers. As after ageing, also after creep no

significant difference can be found comparing the specimen surfaces and its core, leading to conclude that the damage scenario is more compatible with the applied thermomechanical load than with oxidation mechanisms.

Hence, combining this results to the previous discussed capability of reconstruct the creep behavior under conditioned atmosphere, extrapolating it from the results obtained from tests under air, it emerges that the thermomechanical load alone is sufficient to describe both C/PEKK behavior and post-test damaging scenario. This suggests that at macroscopic level, the oxidation has very limited effect on C/PEKK.

Comparing also the damaging scenarios post-ageing and post-creep tests, it results that the thermomechanical load does not accelerates or enhance the oxidation effect.

Thus, while it cannot be excluded the presence of oxidation at microscopic/mesoscopic scale (as observed on the neat polymer cross-section), at macroscopic scale the oxidation at 200°C has a very limited, rather negligible effect on C/PEKK.

6.4. Conclusions

The present chapter investigates the interactions between thermomechanical loading and oxidation at 200°C, realized exploiting the accelerating effect produced by conditioning under 5 bar of O_2.

The investigation is carried out in 2 steps:

1. the evaluation of oxidation effect on as received material, through ageing at 200°C under 5 bar of O_2 for 42 days of both PEKK SC and C/PEKK specimens;
2. the evaluation of interactions with thermomechanical load through a creep test on C/PEKK under the same conditions and for the same duration.

The ageing of PEKK SC produced a less than 50 μm external brownish layer, identified with image analysis techniques, which, compared (in color tone) to aged film at 280°C, and considering the acceleration produced by employment of oxygen, lead to estimate an acceleration factor of over 15 of oxidation phenomena when passing from 200°C to 280°C.

Moreover, DSC showed an increase in crystalline percentage which could explain all the differences observed comparing DSC and DMA results with the results obtained from the same tests carried out on as received material. The increase in crystalline percentage, being the unaffected volume far greater than the oxidized one, could be directly linked to the thermal load alone (as showed in CHAP. 4.3), and allows neglecting the oxidation effects on physical-chemical and mechanical properties.

The effect of ageing on C/PEKK was investigated through X-Rays scans on both tested and as-received material, showing no difference between surface and core in the tested specimen (as saw for the polymer) and negligible differences with the as received specimen. Combined with the results on PEKK SC, it can be concluded that the oxidation produces negligible effect if a thermal load up to 200°C and 1.15 years (considering a factor of acceleration of 10 produced by conditioning under 5 bar of O_2) is applied on both PEKK SC and C/PEKK

The creep test carried out at 28 MPa, 200°C under 5 bar of O_2 for 42 days, produced a strain vs time curve with higher amplitude compared to a similar test carried out in the same test conditions but under air. The differences can be explained with an error in the machine control, which lead into apply a non constant higher stress during the test. If the creep stress is corrected of the friction produced between the internal load cell and the machine arm, to the nominal value, the whole strain vs time curve can be reconstructed employing the Norton-Bailey power law, which parameters are identified on the creep tests carried out under air: this implies that oxidation has limited effect on the C/PEKK creep behavior.

X-Rays scans of the specimen tested at creep under conditioned atmosphere show a more significant presence of cracks on both surface and core, throughout the whole gauge length, compared to the as-received and aged specimens. The absence of differences between

surface and core, leads to conclude that the damage scenario is compatible with the applied thermomechanical load alone and that the latter do not enhance oxidation mechanisms.

The overall analysis points out that oxidation has limited effect on both PEKK SC and C/PEKK at 200°C up to 1.15 years.

Conclusions and Perspectives

In the present work of thesis, the thermomechanical behavior under tensile and long-term creep solicitations of PEKK and C/PEKK composites consequent to the change of state due to exposition to temperature above T_g (between 165°C and 200°C), has been investigated, as well as its interaction with crystallization and degradation mechanisms.

Experimental test protocols were developed to ensure the maximum test reproducibility under different solicitations, particularly taking into account the preliminary heating phase needed for above room temperature tests.

Because of the high deformation experienced by the specimens and the severe test environmental conditions, for all high temperature mechanical tests (above T_g tensile, creep-recovery and load-unload tests), the optical contactless strain measurement system previously employed was significantly improved with the development of a new image analysis tool, the IAT.

The IAT, which exploit image analysis techniques, was developed in Matlab code, and employed post-test on the images acquired during the tests, which makes it complementary to the previous one. As particular feature, the possibility of digitally reconstructing the shape of the degraded markers employed for the strain measurement was implemented. This allowed the verification the strain measurements, to extend the measured strain range in case of progressive marker degradation, and even to recover the strain measurement, in the case of fast degradation, which otherwise would have led to the impossibility of carrying out the tests (e.g. in case of high temperature/oxygen exposure).

In fact, above T_g, the PEKK shows a non-linear rubber-like behavior, reaching high strains (up to 400% in the case of PEKK AM), and in most of the case, without reaching the failure up to the testing machine displacement capabilities.

Increased the temperature above T_g, a significant properties loss respect to below T_g is observed in PEKK AM, PEKK SC, and C/PEKK composite: while the amorphous configuration dramatically experienced an almost complete loss of properties (~-99%), the presence of a pre-existing crystalline phase, reduce such loss (~-90%), which is even lower in the case of ±45° composite (~-80%).

This particular ply orientation was chosen to enhance the effect of the matrix in the composite behavior, especially at low strains (matrix dominated region) and to assess a similarity in behavior between the polymer and the matrix in the composite.

These similarities extend to the creep-recovery behavior, in which a pseudo-plastic behavior could be identified in the permanent residual strains at the end of the tests, the possibility of employing a Norton-Bailey law to approximate the creep behavior and in the impossibility of establish a time-temperature superposition of the creep compliances for the polymer nor the composite.

The similarities where verified through a semi-analytical homogenization/localization method (SAHLM), written in Matlab code, allowing linking the linear elastic homogenization and the localization methods and taking also into account the matrix non-linearity. Through this method, starting from the PEKK SC tensile properties, the C/PEKK low strain tensile curve is reconstructed at all the temperatures above T_g and the ply and composite initial properties are calculated.

The analysis of tensile and creep-recovery tests, via comparison with load-unload and post-thermomechanical tests DSC tests, allowed identifying the main mechanisms characterizing the PEKK behavior above T_g:

- a *hardening* mechanism, associated to the alignment of the initially random oriented crystal structure towards the loading direction during a load solicitation, which can be completely reversed during the unload;
- a *softening* mechanism, associated with pseudo-plastic non-reversible phenomena occurring in the crystalline structure;
- a *crystallization* mechanism active only if a thermal load is applied or during creep, but not observed during other type of solicitations. Considering this increase as the formation of only secondary, intra-spherulitic crystallization, allowed the identification of its kinetics and its impact on the PEKK thermomechanical properties. Moreover, it shows that the material did not fully crystallize at the end of the manufacturing process and this process saturates after a specific exposure duration depending on the test temperature.

A similar analysis was carried out on PEKK AM, where also primary crystallization mechanism is active, not only dependent on the temperature, but coupled with mechanical loading. This effect is similar to lowering the activation energy of crystallization, and the

applied thermomechanical load provides the PEKK AM macromolecular chains sufficient energy to activate the mechanism.

The crystalline phase rotation during load solicitation increases the constraint level of the intra-spherulitic amorphous chains, reducing their mobility and it could explain the absence of crystallinity increase. This could also be interpreted as an increase of the crystallization energy, which keeps increasing as the stress is increased. During unload and recovery, the energy provided to the material is insufficient to overcome this threshold set during the previous load, while the mechanical energy provided during creep allows overcoming it and activates the crystallization mechanism.

All the previous described mechanisms sum to an elastic behavior, which allows defining the theoretical initial state of the material, depending on the initial crystalline phase as well as to the temperature.

The different mechanisms are described analytically and constitute a 1-D model of behavior for PEKK 7002 SC, which is able to reproduce the tensile, Load-Unload-Reload and creep-recovery experimental curves at 200°C and 180°C. Under the hypothesis of incompressibility, experimentally supported, also the transverse behavior can be reproduced, validating the considerations on the volume variation.

Some difference with the 165°C experimental curves are observed, possibly due to low experimental reproducibility or by the presence of other mechanisms that are not taken into account by the model.

The 1-D model of behavior for PEKK 7002 SC constitutes the base for the development of a 3-D model, where the matrix is considered always isotropic and uncompressible and its shear behavior is deduced from its longitudinal one (observed experimentally).

The 3-D model for the PEKK behavior is implemented in the SAHLM and the latter was employed for the simulation of the $[(\pm 45)_{2s}, +45]_s$ composite. The comparison with the experimental results, both for tensile and tensile-creep solicitations validates the SAHLM, which was further modified to simulate different ply orientations and stacking sequences than the $[(\pm 45)_{2s}, +45]_s$, proving its versatility and explaining the chosen simulation approach matrix-ply-laminate.

Neglecting the fiber rotation in the simulation, significant errors could produce: in the case of the $[(\pm 45)_{2s}, +45]_s$ composite, the measure obtained from the images acquired during tensile and creep-recovery tests were employed.

The validation of the SAHLM further validated the assumption that the matrix behaves, in the composite, as the neat resin. Moreover, the 1-D model, as well for the 3-D one, can be only validated for the duration of the tests carried out (108 h): because the identified mechanisms in this range of time are sufficient to describe the PEKK behavior, it can be assumed that the degradation phenomena, if present, have a very limited impact on the PEKK thermomechanical behavior.

In order to extend the validation to longer durations, more similar to the ones for industrial applications, both PEKK SC and C/PEKK where exposed at 200°C (max test temperature) for 1000h under 5 bar of O_2. In particular, the latter condition was proved to accelerate degradation phenomena.

The analysis of the specimens shows, in PEKK SC, the formation of ~50 μm brownish layer, which impact less than the 7% of the specimen thickness. Because of its low penetration, degradation phenomena do not have significant effect on the physical-chemical properties of the PEKK, and any variation can be attributed to the increase in crystallinity, already observed after lower exposure duration at the same temperature, which furthermore, do not increase because of the exposure to oxygen conditioned atmosphere.

The effect of ageing on C/PEKK was investigated through X-Rays scans on both tested and as-received material, showing no difference between surface and core in the tested specimen (as observed in the polymer) and negligible differences with the as received specimen.

The interaction between degradation mechanisms and C/PEKK thermomechanical behavior was investigated through a creep test at 200°C under 5 bar of O_2 for 1000 h. The results show a coherence with the analog tests carried out under air for shorter durations, and also the post-test μ-tomography presented a damage scenario compatible with the thermomechanical load, whit the appearance of multiple cracks, throughout the whole specimen gauge length, but uniformly in its thickness.

The overall investigation leads to conclude that degradation phenomena produce negligible effect on both PEKK and C/PEKK at 200°C, at least up to 1.15 years (considering a factor of acceleration of 10 produced by conditioning under 5 bar of O_2).

Perspectives

In the present study, the following aspects are left unanswered:

- the physical interpretation of the mechanisms was deduced from macroscopic tests, and, while it revealed the outmost importance of the crystal phase in the materials behavior, no experimental prove at microscopic level was possible to be carried out to confirm it. In particular, SAXS and WAXS in-situ tests could eventually confirm not only the presence of such phenomena, but also help describing their kinetics;
- this analysis could be extended to the interaction between thermomechanical load and crystallization mechanism: while the effect of the crystallization on the mechanical properties is known, the effect of the thermomechanical load on the crystallization it is not. In the present study, it was limited to the semi-crystalline, for which no crystallization is observed during load solicitation, while it is present for creep and thermal solicitations. More complex is the case of the PEKK AM, for which this interaction is more pronounced and appears also for load solicitation. An interpretation

was provided in the present work, but more investigation is needed to confirm or deny it.

- the 1-D formulation could be consequently ameliorated, and the mechanisms could be directly related to the crystal phase actual behavior;
- the shear behavior was deduced form the longitudinal one, and, while it can be considered a good 1st approximation, shear tests could ameliorate the understanding of the mechanisms and validate the made assumptions;
- the ensemble of longitudinal and shear tests could provide the elements to improve the 3-D formulation, verifying or confuting the isotropy hypothesis and providing with a behavior law deriving from the thermodynamics of the irreversible process.
- the study investigated the materials thermomechanical behavior up to 200°C, and no test was carried at higher temperatures, at which the identified mechanisms could have a lesser impact on the material behavior and other be more predominant; in particular degradation phenomena, which presence has been already proven, could strongly impact the thermomechanical behavior and vice versa;
- the fiber rotation has been proven to have a significant role in the composite simulation, and moreover, that it is not due only to kinematics effect, but it has an intrinsic interaction with the matrix properties. The identification of this link could overcome the need of experimental rotation angle measure, and improve the simulations, especially in the case of laminate with multiple orientations, where the measures cannot be directly obtained from observation of the surface: in this case, in-situ μ-tomographies could supply with the missing information;
- the better understanding of the mechanism responsible for the fiber rotation could extend the limit the capabilities of the SAHLM and enable to simulate the composite behavior also in the fiber dominated region.

Annex A – Specimens geometries

A.1. Specimen type “b”

From each plate of PEKK 7002, 6 dog-bone shape specimens was obtained, which specifics, according to the ISO 527-2 (specimen type 1BA), are showed in FIG. A- 1.

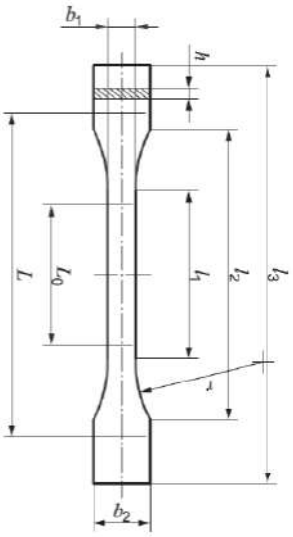

	Measure	Value [mm]
b_1	Width of the central area	5.0±0.5
b_2	Width of the clamped area	10.0 ±0.5
l_1	Length of the central area	30.0 ±0.5
l_2	Length of the clamped area	58.0 ±2.0
l_3	Total length	≥75.0
L_0	Gauge length	25.0 ±0.5
L	Initial distance between the clamps	$l_2\ {}^{+2}_{0}$
r	Connection radius	30.0
h	Thickness	≥2.0

Fig. A- 1: PEKK 7002 specimen type b

A.2. Specimen type “d”

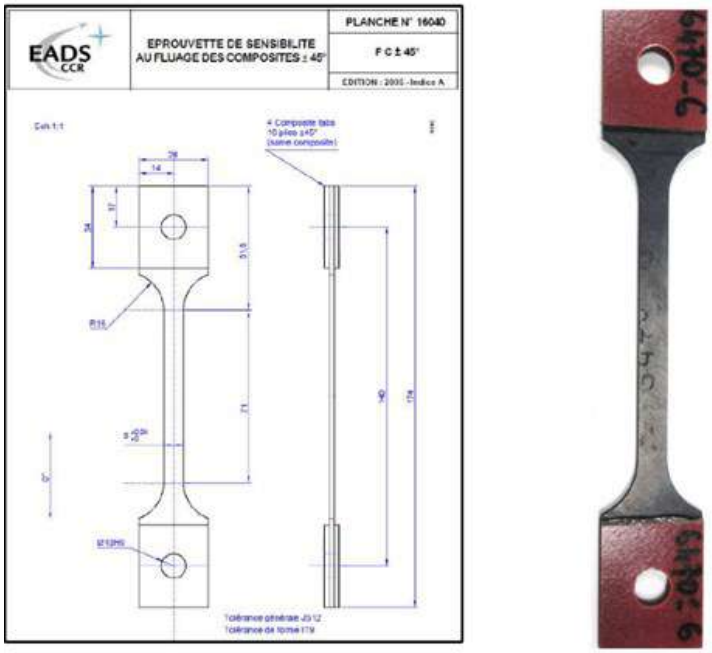

Fig. A- 2: C/PEKK specimen type d

Annex B – IAT corrections

B.1. Light exposure correction

Depending of the chosen binarization threshold value, some pixel around the marker perimeter are or not above the chosen threshold, as consequence of the user's choice. This results in a change of the perimeter of the marker and consequently of the coordinates of the calculated points.

In order to evaluate the error and its propagation, an error in the displacement field is introduced: the error cannot be equal and constant for each point (bias error), otherwise, it will constitute a rigid translation and it will be automatically neglected during the derivation of the displacement field.

Instead, a noise in the measure, constituted by the *random* function on Matlab, is more suitable to simulate a user or an unpredictable event (light hitting an imperfection on the surface, a scratch, etc…).

$$\begin{cases} U' = U + random(U) \\ V' = V + random(V) \end{cases} \qquad \textit{Eq. B- 1}$$

Random error from 1 pixel (highly probable, not depending by the binarization threshold) to 5 pixels (+20 color value error on the optimized binarization threshold) where chosen: considering an average size of the marker of around 100 pixels (major axis) x 50 pixels (minor axis), this produce a maximum error of ±5% in the measure of U and ±10% in the measure of V.

The FIG. B- 1 shows the difference of the two kind of error applied on the measured displacement field: the constant error causes just a shifting of the displacement field, while the random one adds noise to the measure.

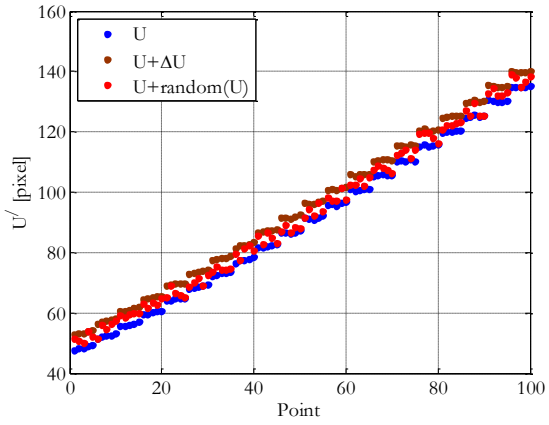

Fig. B- 1: Comparison between measured displacement field (blue), constant error (brown) and random noise (red)

The FIG. B- 2 shows the strain calculated from the displacement fields modified with random noise up to 5 pixels. The noise produces:

- on the Total Lagrangian longitudinal strain, up to ±0.02 mm/mm of maximum absolute error (image on bottom right of FIG. B- 2A) at 0.7 mm/mm of strain, which constitute ±2.8% of percentage error).

- on the Total Lagrangian transversal strain, up to ±0.02 mm/mm of maximum absolute error (image on bottom right of FIG. B- 2B) at -0.2 mm/mm of strain, which constitute ±10% of percentage error).

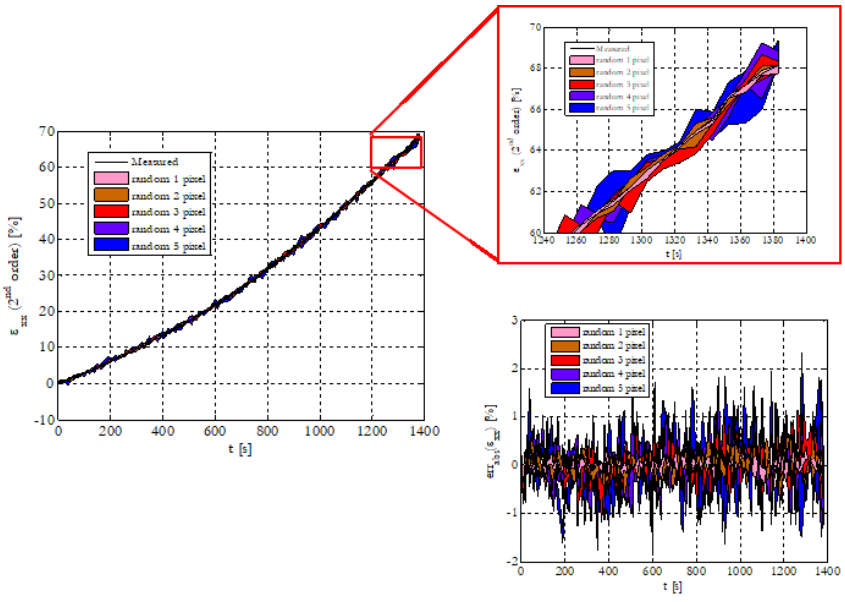

a)

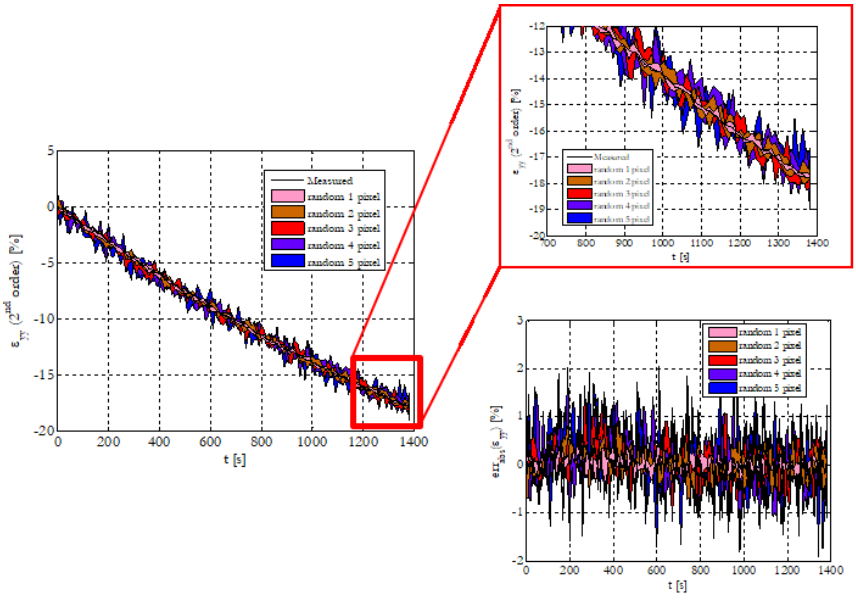

b)

Fig. B- 2: Effect of the different noise levels on the measure of longitudinal (a) and transversal (b) strains.

The different magnitude of the percentage error between longitudinal and transversal is due to the difference in amplitude of the directional components of the displacement fields: U is around 600 pixels, while V is around 50 pixels at maximum strains, leading V to be more sensible to random error than U.

The TAB. B- 1 resumes the measured error on the Total Lagrangian strain due to the adding of a random measurement error.

	ε_{xx} = 0.7 mm/mm		ε_{yy}=-0.2 mm/mm	
Random error [pixel]	**Absolute error [mm/mm]**	**Percentage error**	**Absolute error [mm/mm]**	**Percentage error**
±1	±0.005	±0.7 %	±0.005	±2.5 %
±5	±0.02	±2.8 %	±0.02	±10.0 %

Tab. B- 1: Absolute and percentage error produced by the random error on longitudinal and transversal strains, on the volumetric change and on the stress vs strain curve

B.2. Image subset definition

In the case of extreme marker degradation, FIG. B- 3A, the marker is no longer constituted by only one group of connected pixels, but by several groups, not connected between each other: FIG. B- 3B shows a red dot in correspondence of each connected group detected. In this case, both IdPix and IAT cannot measure the position of the marker center of mass. In fact, for both systems, the marker can be constituted by just one group and both identify the center of mass of the marker as the center of mass of the first connected group of pixel.

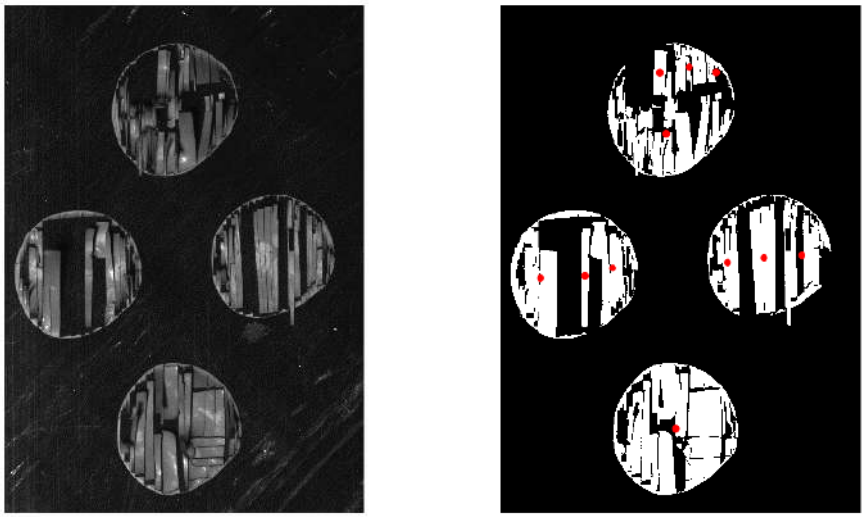

a) *b)*

Fig. B- 3: Marker extreme degradation (a) and center of mass (red dots) identified on connected groups (b)

To overcome this problem, the image is divided in 4 subsets, each one identifying the area where each marker should be in. The division is carried out through the definition of the image diagonals (EQ. B- 2), showed in FIG. B- 4.

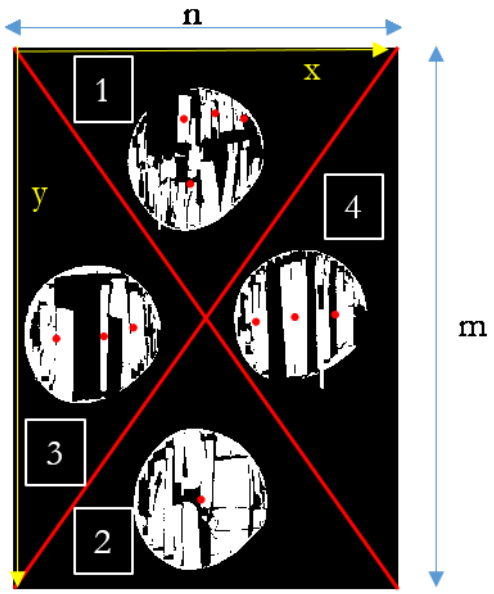

Fig. B- 4: Image subsets definition through image diagonals

$$\begin{cases} y_1 = \frac{m}{n} x \\ y_2 = -\frac{m}{n} x + m \end{cases} \qquad \textit{Eq. B- 2}$$

where m and n are the image dimension in pixels. Each group of pixel G_i has center of mass :

$$\mathrm{CM_i} = (x_i, y_i) \qquad \textit{Eq. B- 3}$$

If $y_1(x_i)$ and $y_2(x_i)$ are evaluated, then the following criteria can be imposed:

The i-th marker $(\mathrm{M_i})$ *is constituted by all the connected groups of pixels present in the i-th area between the two diagonals.*

Therefore, the conditions for all markers are defined as:

$$\begin{cases} \text{if } y_i < y_1(x_i) \cap y_i < y_2(x_i) & \mathrm{Group_i} \in \mathrm{Marker_1} \\ \text{if } y_i > y_1(x_i) \cap y_i > y_2(x_i) & \mathrm{Group_i} \in \mathrm{Marker_2} \\ \text{if } y_i < y_1(x_i) \cap y_i > y_2(x_i) & \mathrm{Group_i} \in \mathrm{Marker_3} \\ \text{if } y_i > y_1(x_i) \cap y_i < y_2(x_i) & \mathrm{Group_i} \in \mathrm{Marker_4} \end{cases} \qquad \textit{Eq. B- 4}$$

Once all the groups of pixels constituting each marker are identified, a convex hull operation is carried out on the ensemble of pixels so defined, which enable to obtain the whole contour of the marker, FIG. B- 5.

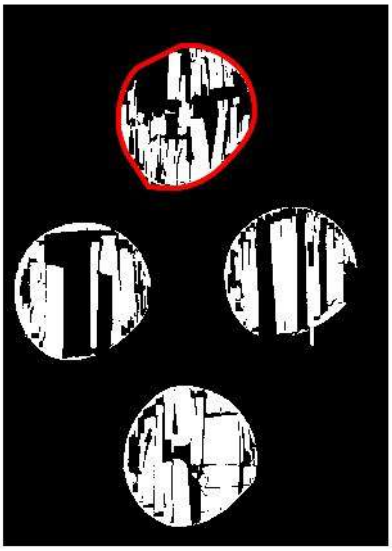

Fig. B- 5: Convex hull operation on all the groups of connected pixels constituting Marker 1

This procedure substitutes the marker reconstruction procedure described in CHAPTER 6

Annex C – Transversal Isotropy

The points identified by the IAT Image Analysis algorithm (see CHAP. 2.3.2.3) belong to the surface of the specimen corresponding to the $z=\frac{t}{2}$ plane (where t is the thickness of the specimen), in the specimen reference system (FIG. C- 1B), while they are acquired according to the camera reference system, (FIG. C- 1A).

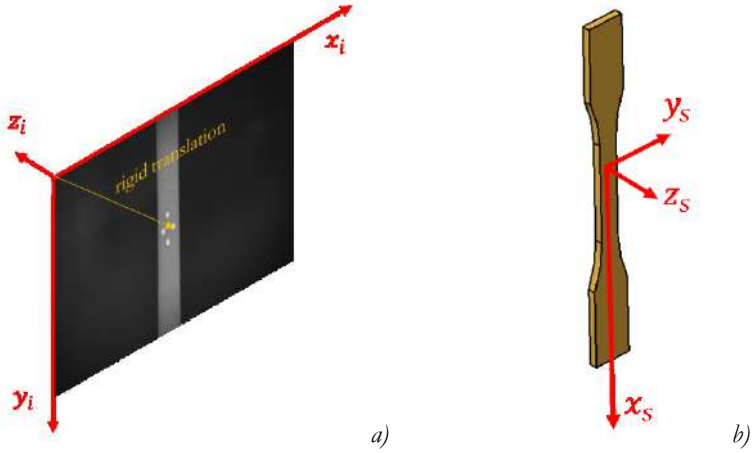

a) *b)*

Fig. C- 1: Image reference system (a) and specimen reference system (b)

To relate the two reference system, the following coordinates change was employed:

$$\begin{cases} x_S = y_i \\ y_S = x_i \\ z_S = -z_i \end{cases} \qquad \textit{Eq. C- 1}$$

The rigid translation from the top left corner to the center of specimen is omitted, because it would be automatically be neglected during the derivatives calculation.

The employment of optical extensometry equipment allows the calculation of the displacement field in both x and y directions (at a specific z value), but it provides with no information about its value in the third direction. The contemporary employment of a second camera could overcome this obstacle, but the oven employed during the tests, which has only one window (FIG. 2-25), prevents from observing more than one face of the specimen at once. Any other solution involves the re-execution of the tests.

In order to be able of evaluate the deformation field starting from the acquired images, without any other test, transversal isotropy hypothesis (TIH) was made.

C.1. Transversal Isotropy Formulation

From the reference system showed in FIG. C- 1, the displacement field can be defined as:

$$\mathbf{u}=\begin{cases} U=U(x_0,y_0,z_0) \\ V=V(x_0,y_0,z_0) \\ W=W(x_0,y_0,z_0) \end{cases} \qquad \textit{Eq. C- 2}$$

and moreover, the displacement gradient as:

$$\mathbf{H}=\begin{bmatrix} \frac{\partial U}{\partial x_0} & \frac{\partial U}{\partial y_0} & \frac{\partial U}{\partial z_0} \\ \frac{\partial V}{\partial x_0} & \frac{\partial V}{\partial y_0} & \frac{\partial V}{\partial z_0} \\ \frac{\partial W}{\partial x_0} & \frac{\partial W}{\partial y_0} & \frac{\partial W}{\partial z_0} \end{bmatrix} \qquad \textit{Eq. C- 3}$$

Observing only one face of the specimen, it is possible to evaluate only the first minor of **H**, since the displacement field W, its derivatives or any of the derivatives in the z-direction cannot be calculated .

In order to be able to impose some hypothesis, the strain tensor is evaluated starting from both the stress tensor and the displacement vector. Imposing the equivalence of both formulations allows obtaining the conditions to employing 3D formulations anyways.

C.1.1. From stress to strain

For an orthotropic material, Hooke's Law can be written as follows:

$$\boldsymbol{\sigma}=\mathbf{C}\cdot\boldsymbol{\epsilon} \quad \Rightarrow \quad \begin{bmatrix} \sigma_{11} \\ \sigma_{22} \\ \sigma_{33} \\ \tau_{12} \\ \tau_{23} \\ \tau_{31} \end{bmatrix} = \begin{bmatrix} C_{11} & C_{12} & C_{13} & 0 & 0 & 0 \\ C_{21} & C_{22} & C_{23} & 0 & 0 & 0 \\ C_{31} & C_{32} & C_{33} & 0 & 0 & 0 \\ 0 & 0 & 0 & C_{44} & 0 & 0 \\ 0 & 0 & 0 & 0 & C_{55} & 0 \\ 0 & 0 & 0 & 0 & 0 & C_{66} \end{bmatrix} \begin{bmatrix} \varepsilon_{11} \\ \varepsilon_{22} \\ \varepsilon_{33} \\ \gamma_{12} \\ \gamma_{23} \\ \gamma_{31} \end{bmatrix} \qquad \textit{Eq. C- 4}$$

Then the **C** tensor can be inverted and the strain can be written as function of the stress:

$$\boldsymbol{\epsilon}=\mathbf{S}\cdot\boldsymbol{\sigma} \quad \Rightarrow \begin{bmatrix}\varepsilon_{11}\\ \varepsilon_{22}\\ \varepsilon_{33}\\ \gamma_{12}\\ \gamma_{23}\\ \gamma_{31}\end{bmatrix}=\begin{bmatrix} S_{11} & S_{12} & S_{13} & 0 & 0 & 0\\ S_{21} & S_{22} & S_{23} & 0 & 0 & 0\\ S_{31} & S_{32} & S_{33} & 0 & 0 & 0\\ 0 & 0 & 0 & S_{44} & 0 & 0\\ 0 & 0 & 0 & 0 & S_{55} & 0\\ 0 & 0 & 0 & 0 & 0 & S_{66}\end{bmatrix}\begin{bmatrix}\sigma_{11}\\ \sigma_{22}\\ \sigma_{33}\\ \tau_{12}\\ \tau_{23}\\ \tau_{31}\end{bmatrix} \qquad \textit{Eq. C- 5}$$

where $\mathbf{C}^{-1}=\mathbf{S}$.

In the case of uniaxial tensile test, the stress tensor has only one component, and in Voigt notation the stress tensor can be written as:

$$\boldsymbol{\sigma}=\begin{bmatrix}\sigma_{11}\\ 0\\ 0\\ 0\\ 0\\ 0\end{bmatrix} \qquad \textit{Eq. C- 6}$$

If EQ. C- 6 is substituted in EQ. C- 5, the components of the strain tensor can be obtained, and, in Voigt notation have the form:

$$\begin{cases}\varepsilon_{11}=S_{11}\sigma_{11}\\ \varepsilon_{22}=S_{21}\sigma_{11}\\ \varepsilon_{33}=S_{31}\sigma_{11}\\ \gamma_{12}=\gamma_{23}=\gamma_{31}=0\end{cases} \qquad \textit{Eq. C- 7}$$

or alternatively, in tensor notation:

$$\boldsymbol{\epsilon}=\begin{bmatrix}S_{11}\sigma_{11} & 0 & 0\\ 0 & S_{21}\sigma_{11} & 0\\ 0 & 0 & S_{31}\sigma_{11}\end{bmatrix} \qquad \textit{Eq. C- 8}$$

C.1.2. From displacement to strain

The displacement field **u** can be expressed as showed in EQ. C- 2, and its spatial derivatives compose the displacement gradient **H**, as in EQ. C- 3. From the latter the strain gradient can be evaluated according to:

$$\mathbf{F}=\mathbf{I}+\mathbf{H} \Rightarrow F_{ij}=\delta_{ij}+\frac{\partial u_i}{\partial X_j}=\begin{bmatrix} 1+\frac{\partial U}{\partial x_0} & \frac{\partial U}{\partial y_0} & \frac{\partial U}{\partial z_0} \\ \frac{\partial V}{\partial x_0} & 1+\frac{\partial V}{\partial y_0} & \frac{\partial V}{\partial z_0} \\ \frac{\partial W}{\partial x_0} & \frac{\partial W}{\partial y_0} & 1+\frac{\partial W}{\partial z_0} \end{bmatrix} \qquad \textit{Eq. C- 9}$$

then the 1st order strain field results as:

$$\boldsymbol{\epsilon}=\frac{1}{2}\left(\mathbf{F}+\mathbf{F}^T\right)-\mathbf{I} \Rightarrow \epsilon_{ij}=\frac{1}{2}\left(F_{ij}+F_{ji}\right)-\delta_{ij}=\frac{1}{2}\left(u_{i,j}+u_{j,i}\right)=\frac{1}{2}\left(\frac{\partial u_i}{\partial X_j}+\frac{\partial u_j}{\partial X_i}\right) \Rightarrow$$

$$\Rightarrow \boldsymbol{\epsilon}=\begin{bmatrix} \frac{\partial U}{\partial x_0} & \frac{1}{2}\left(\frac{\partial U}{\partial y_0}+\frac{\partial V}{\partial x_0}\right) & \frac{1}{2}\left(\frac{\partial U}{\partial z_0}+\frac{\partial W}{\partial x_0}\right) \\ \frac{1}{2}\left(\frac{\partial U}{\partial y_0}+\frac{\partial V}{\partial x_0}\right) & \frac{\partial V}{\partial y_0} & \frac{1}{2}\left(\frac{\partial V}{\partial z_0}+\frac{\partial W}{\partial y_0}\right) \\ \frac{1}{2}\left(\frac{\partial U}{\partial z_0}+\frac{\partial W}{\partial x_0}\right) & \frac{1}{2}\left(\frac{\partial V}{\partial z_0}+\frac{\partial W}{\partial y_0}\right) & \frac{\partial W}{\partial z_0} \end{bmatrix} \qquad \textit{Eq. C- 10}$$

C.1.3. Equality of formulations

If the equality of the formulations obtained for the strain field (EQ. C- 7 and EQ. C- 10), the following of equivalence can be obtained:

$$\boldsymbol{\epsilon}=\begin{bmatrix} S_{11}\sigma_{11} & 0 & 0 \\ 0 & S_{21}\sigma_{11} & 0 \\ 0 & 0 & S_{31}\sigma_{11} \end{bmatrix}=\begin{bmatrix} \frac{\partial U}{\partial x_0} & \frac{1}{2}\left(\frac{\partial U}{\partial y_0}+\frac{\partial V}{\partial x_0}\right) & \frac{1}{2}\left(\frac{\partial U}{\partial z_0}+\frac{\partial W}{\partial x_0}\right) \\ \frac{1}{2}\left(\frac{\partial U}{\partial y_0}+\frac{\partial V}{\partial x_0}\right) & \frac{\partial V}{\partial y_0} & \frac{1}{2}\left(\frac{\partial V}{\partial z_0}+\frac{\partial W}{\partial y_0}\right) \\ \frac{1}{2}\left(\frac{\partial U}{\partial z_0}+\frac{\partial W}{\partial x_0}\right) & \frac{1}{2}\left(\frac{\partial V}{\partial z_0}+\frac{\partial W}{\partial y_0}\right) & \frac{\partial W}{\partial z_0} \end{bmatrix}\Rightarrow$$

$$\Rightarrow\begin{cases} \frac{\partial U}{\partial x_0}=S_{11}\sigma_{11} \\ \frac{\partial V}{\partial y_0}=S_{21}\sigma_{11} \\ \frac{\partial W}{\partial z_0}=S_{31}\sigma_{11} \\ \frac{1}{2}\left(\frac{\partial U}{\partial y_0}+\frac{\partial V}{\partial x_0}\right)=0 \;\Rightarrow\; \frac{\partial U}{\partial y_0}=-\frac{\partial V}{\partial x_0} \\ \frac{1}{2}\left(\frac{\partial U}{\partial z_0}+\frac{\partial W}{\partial x_0}\right)=0 \;\Rightarrow\; \frac{\partial U}{\partial z_0}=-\frac{\partial W}{\partial x_0} \\ \frac{1}{2}\left(\frac{\partial V}{\partial z_0}+\frac{\partial W}{\partial y_0}\right)=0 \;\Rightarrow\; \frac{\partial V}{\partial z_0}=-\frac{\partial W}{\partial y_0} \end{cases} \qquad \textit{Eq. C- 11}$$

In order to be able to obtain the unknown terms of the **H** tensor, the *Transversal Isotropy Hypothesis* (*TIH*) is made:

- the property of material in y-direction are equal to the property in z-direction, or:

$$S_{21}=S_{31} \;\Rightarrow\begin{cases} \frac{\partial V}{\partial y_0}=\frac{\partial W}{\partial z_0} & \textit{Eq. C- 12} \\ \frac{\partial U}{\partial z_0}=\frac{\partial U}{\partial y_0} & \textit{Eq. C- 13} \end{cases}$$

- the displacement field V is constant in the thickness direction:

$$\frac{\partial V}{\partial z_0}=0 \qquad \textit{Eq. C- 14}$$

Under the TIH, the displacement gradient **H** (EQ. C- 3) becomes:

$$\mathbf{H}=\begin{bmatrix} \frac{\partial U}{\partial x_0} & \frac{\partial U}{\partial y_0} & \frac{\partial U}{\partial y_0} \\ -\frac{\partial U}{\partial y_0} & \frac{\partial V}{\partial y_0} & 0 \\ -\frac{\partial U}{\partial y_0} & 0 & \frac{\partial V}{\partial y_0} \end{bmatrix} \qquad \textit{Eq. C- 15}$$

and all its components can be evaluated through measurement on only the *x-y* face of the specimen.

C.2. Verification of transversal isotropy hypothesis

In order to verify the TIH, two tensile test were carried out at 200°C and 1 mm/min, on type *b* PEKK 7002 SC specimens: in the first, the *x-y* face of the specimen was recorded and in the second, the Instron 4505 clamps were turned by 90°, and the *x-z* face of specimen was recorded (according to the reference system showed in in FIG. C- 2, and with consequent coordinate change described by EQ. C- 16).

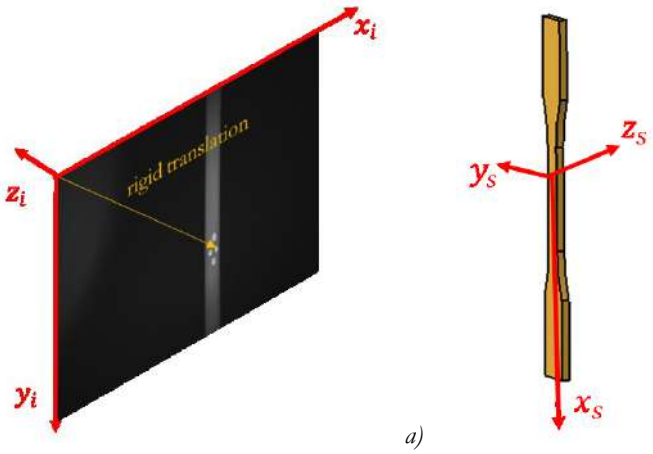

Fig. C- 2: Image reference system (a) and specimen reference system (b) recording the x-z face

$$\begin{cases} x_S = y_i \\ y_S = z_i \\ z_S = y_i \end{cases} \qquad \textit{Eq. C- 16}$$

In this case too, the rigid translation from the top left corner to the center of specimen is omitted, because it would be automatically neglected during the derivatives calculation.

The transversal isotropy hypothesis is verified if the following equality are satisfied:

$$
\begin{aligned}
&1)\ \frac{\partial U_{xy}}{\partial x_0} = \frac{\partial U_{xz}}{\partial x_0} \\
&2)\ \frac{\partial U_{xy}}{\partial y_0} = -\frac{\partial V_{xy}}{\partial x_0} \\
&3)\ \frac{\partial U_{xz}}{\partial z_0} = -\frac{\partial W_{xz}}{\partial x_0} \\
&4)\ \frac{\partial V_{xy}}{\partial y_0} = \frac{\partial W_{xz}}{\partial z_0} \\
&5)\ \frac{\partial U_{xz}}{\partial z_0} = \frac{\partial U_{xy}}{\partial y_0}
\end{aligned}
\qquad \textit{Eq. C- 17}
$$

where the index *ij* indicates the specimen face where the component of the displacement field is measured. The 1st equation corresponds to the congruence of measure, and imposes that the displacement field *U* has the same value if it is measured on face *x-y* or *x-z*; the 2nd and 3rd equation (from EQ. C- 11), derive from the strain gradient simplifications in the case of tensile test; the 4th and 5th equation (EQ. C- 12 and EQ. C- 13) derive from the transversal isotropy hypothesis.

A 6th equation could be added,

$$
6)\ \frac{\partial V_{xy}}{\partial z_0} = \frac{\partial W_{xz}}{\partial y_0} = 0 \qquad \textit{Eq. C- 18}
$$

which derive from the strain gradient simplifications in the case of tensile test (EQ. C- 11), but is still not verifiable, since it would require the recording of the plane *y-z* (the specimen cross section) during the test, which is not possible.Thus, under the transversal isotropy hypothesis (EQ. C- 14) both derivatives are neglected.

The comparison of the results is showed in the next figure.

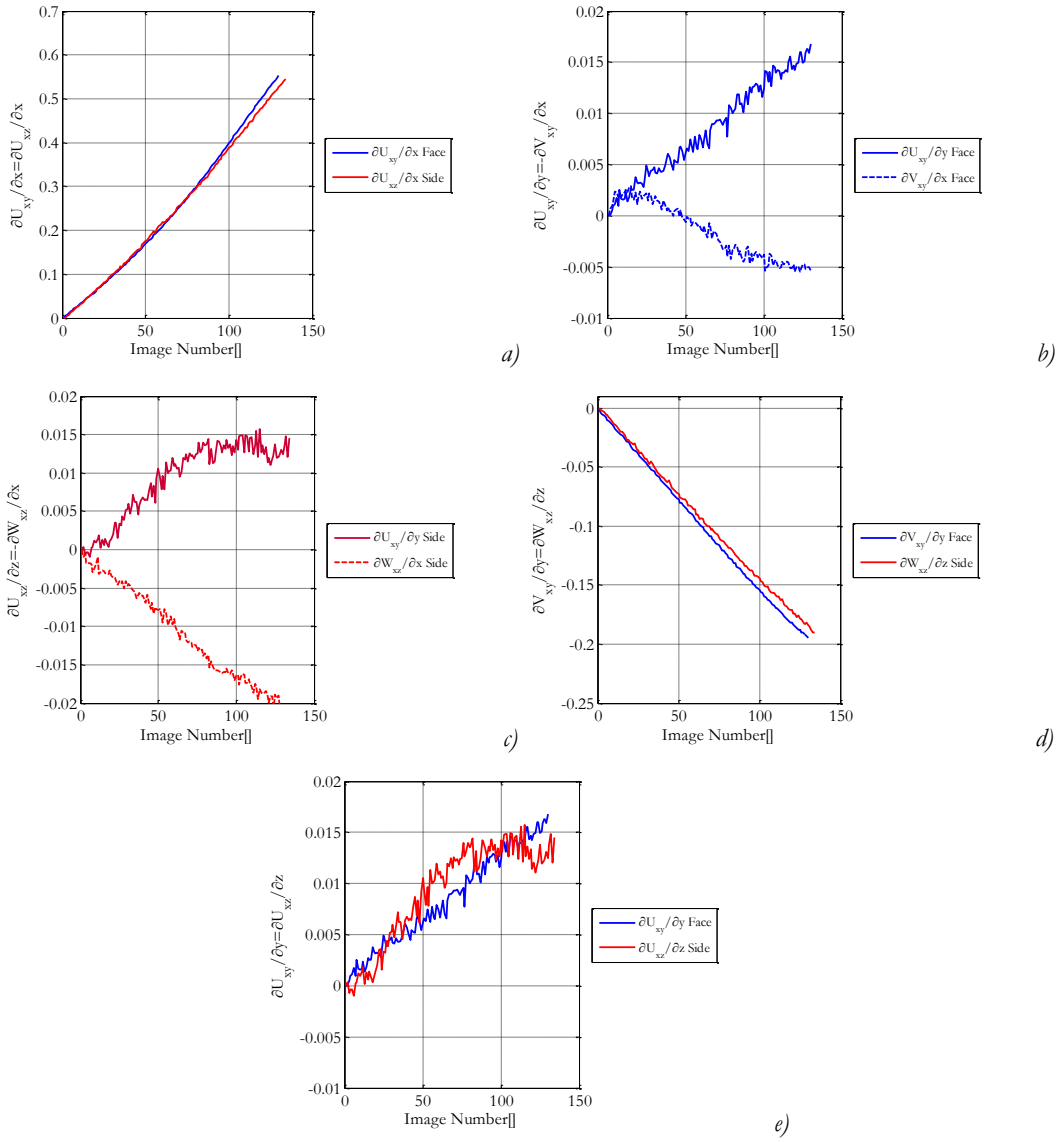

Fig. C- 3: Comparison of the derivatives of the displacement fields measured in the tensile tests recording the x-y face (blue curves) and x-z face (red curves)

The longitudinal (EQ. C- 15A) and transversal (EQ. C- 15D) derivatives almost superpose, while the out diagonal derivatives (EQ. C- 15B, EQ. C- 15C and EQ. C- 15E) show a greater scatter and are the most affected by the field approximation. However, the out of diagonal derivatives are at least one order of magnitude lower than diagonal derivatives and have negligible effects on the calculation.

Those considerations lead to confirm the validity of the transversal isotropy hypothesis.

Annex D – Linear approximation of the displacement field

Starting from the tensile test employed for validating the IAT, where both the pattern needed for DIC and the markers needed for VT were painted (FIG. 2-35), the displacement field along the most part of the gauge length can be reconstructed.

The displacement field can be obtained, subtracting from the coordinates of the points identified by Correla and IAT at the *i*-th image, the coordinates calculated at the 1st image.

In FIG. D- 1, the values, calculated for each point identified by IAT and Correla, of the longitudinal component of the displacement field, *U,* is showed at the *i*-th image as magenta round marker. All the values are fitted with a bi-cubic polynomial function of the initial coordinates (blue surface), which is the smallest degree of polynomial function able to fit all the points.

The area corresponding to the points identified by IAT, is then fitted with both a bi-cubical polynomial function (red surface), as shown in FIG. D- 1, and a bi-linear polynomial function (green surface), as showed in FIG. D- 2, which is much fast to calculate.

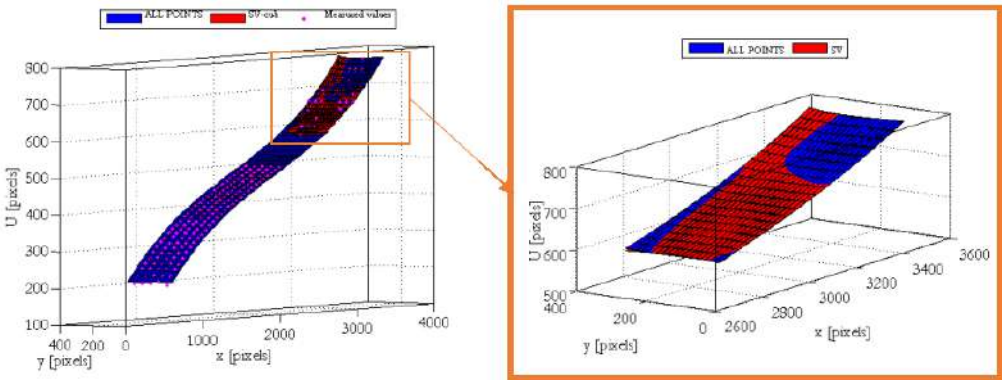

Fig. D- 1: Comparison between complete displacement field approximation and cubic approximated displacement field evaluated from the markers

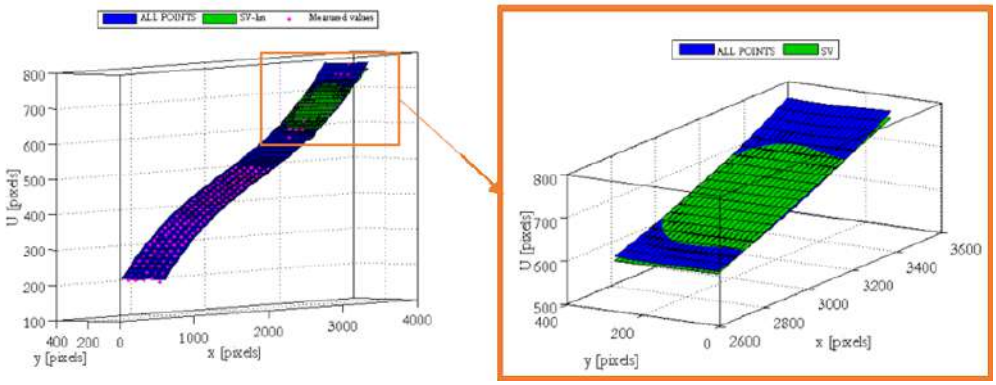

Fig. D- 2: Comparison between complete displacement field approximation and linear approximated displacement field evaluated from the markers

FIG. D- 1 and FIG. D- 2 show that the linear fitting is sufficient for approximating the markers displacement field. However, a bi-linear fit imply a constant strain field and in order to verify the difference produced by the different fittings, the derivatives of the employed function are compared.

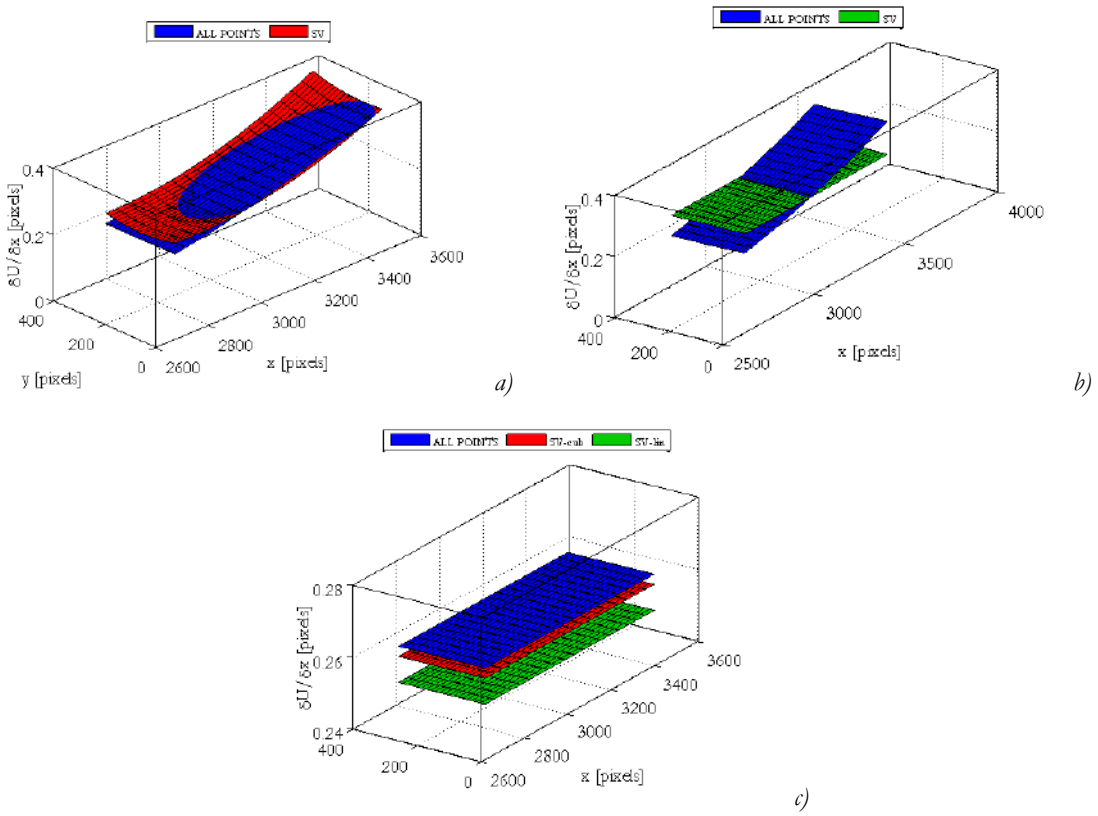

Fig. D- 3: Comparison of the first derivative in x direction of the complete displacement field and the displacement field evaluated from the markers approximated with cubic polynomial function (a) and linear one (b) and comparison of the averaged derivative (c)

FIG. D- 3 shows the comparison of the derivative respect to the longitudinal direction (1st element of the displacement gradient **H** diagonal): as expected, the derivative of the bi-cubic fitting superposes better the derivative of the global fitting than the derivative of the bi-linear fitting.

In fact, the strain field is non-linear, but it has to be evaluated at each point of the field. In order to have a macroscopic value of the strain, it has to be averaged, and thus, comparing the average of the derivatives, the difference between the two fitting sensibly diminish.

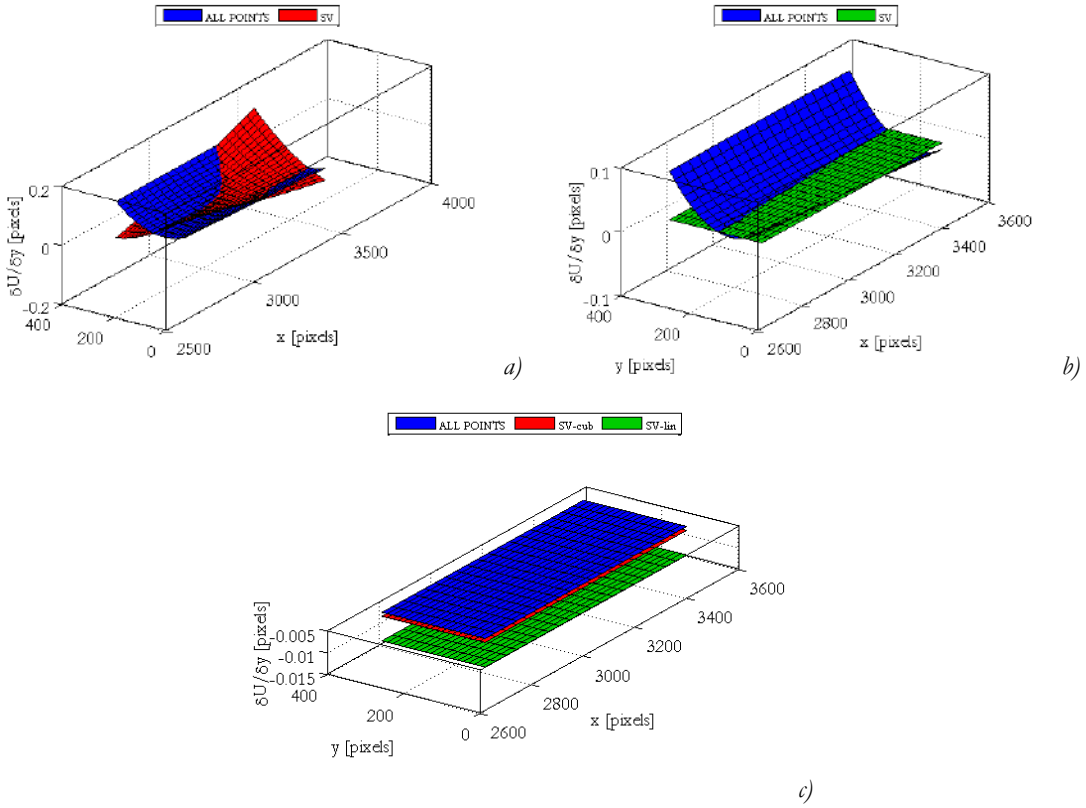

Fig. D- 4: Comparison of the first derivative in y direction of the complete displacement field and the displacement field evaluated from the markers approximated with cubic polynomial function (a) and linear one (b) and comparison of the averaged derivative (c)

FIG. D- 4 shows the comparison of the derivatives respect to the transversal direction (element outside the displacement gradient **H** diagonal): in this case, the derivatives of both the bi-cubic and bi-linear fitting do not superpose the derivative of the complete displacement field.

This analysis suggests that the employment of a bi-cubic fitting of the displacement field, can be advantageous only in the case of local measurement of the strain field.

However, the evaluation of the bi-cubic fitting coefficients and the calculation of the strain values at each point requires a factor 10 in calculation time compared to the bi-linear fitting (which derivative has not to be evaluated at each point, being constant). Such calculation time increase is not justifiable if after its calculation, the strain field is averaged.

Annex E – 3-D strain field formulations

In the IAT calculation algorithm, different 3-D formulations are implemented, which differs for the time (or image) taken as reference, as showed in FIG. E- 1.

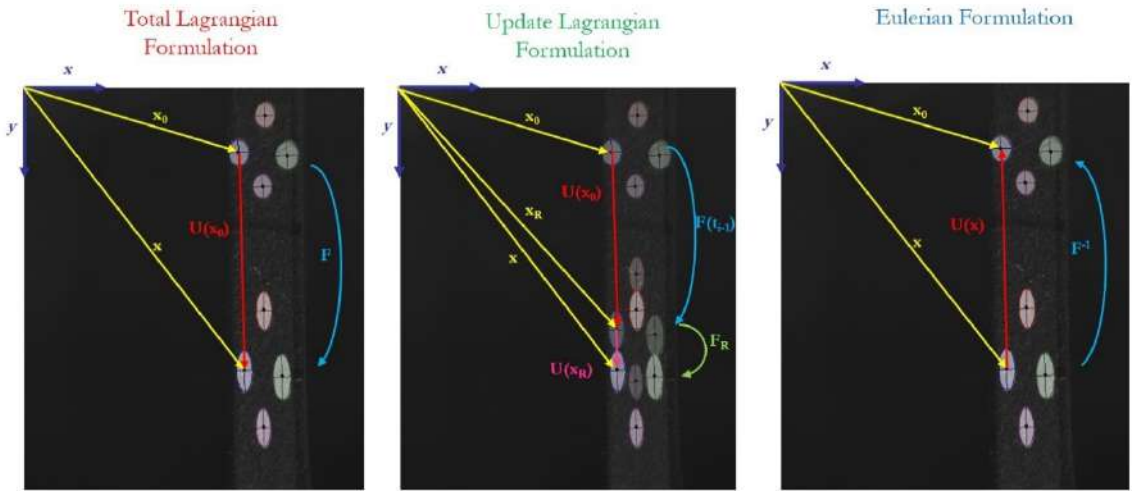

Fig. E- 1: Deformed and undeformed configuration for Total Lagrangian, Update Lagrangian and Eulerian formulations

In particular:

- for the Total Lagrangian Formulation, the tensor **F** (*strain gradient*) describes the transformation that the *deformed configuration* **x** at the generic time t_i underwent with respect to the *undeformed configuration* **X** at the time t_0;
- for the Update Lagrangian Formulation, the *deformed configuration* **x** at the generic time t_i is described with respect to the *deformed configuration* **x** at the time t_{i-1} by the tensor $\mathbf{F_R}$; the *deformed configuration* **x** at the time t_{i-1} is described as function of the *undeformed configuration* **X** at the time t_0 by the tensor $\mathbf{F_0}$.
- for the Eulerian Formulation, the *undeformed configuration* **X** at the time t_0 is described with respect to the *deformed configuration* at the generic time t_i by the tensor $\mathbf{F^{-1}}$.

The following paragraphs describe more in detail each formulation, (HUTTER AND JOHNK 2004).

E.1. Total Lagrangian Formulation

The *displacement field* **u** can be evaluated as the difference between the deformed and undeformed configuration:

$$\mathbf{u}(X,t)=\mathbf{x}(X,t)-\mathbf{X} \quad \Rightarrow \quad \begin{cases} U=x-x_0 \\ V=y-y_0 \\ W=z-z_0 \end{cases} \qquad \textit{Eq. E- 1}$$

The displacement field is then approximated through a function of the initial spatial coordinates, at least derivable once. The *gradient of displacement* **H**, in fact, can be evaluated deriving the displacement field and through the transversal isotropy hypothesis (TIH) (ANNEX C.1) reaches the form:

$$H_{ij}=\frac{\partial u_i}{\partial X_j}=\begin{bmatrix} \frac{\partial U}{\partial x_0} & \frac{\partial U}{\partial y_0} & \frac{\partial U}{\partial z_0} \\ \frac{\partial V}{\partial x_0} & \frac{\partial V}{\partial y_0} & \frac{\partial V}{\partial z_0} \\ \frac{\partial W}{\partial x_0} & \frac{\partial W}{\partial y_0} & \frac{\partial W}{\partial z_0} \end{bmatrix} \quad \overset{\text{TIH}}{\Longrightarrow} \quad \mathbf{H}=\begin{bmatrix} \frac{\partial U}{\partial x_0} & \frac{\partial U}{\partial y_0} & \frac{\partial U}{\partial y_0} \\ -\frac{\partial U}{\partial y_0} & \frac{\partial V}{\partial y_0} & 0 \\ -\frac{\partial U}{\partial y_0} & 0 & \frac{\partial V}{\partial y_0} \end{bmatrix} \qquad \textit{Eq. E- 2}$$

The *strain gradient* **F**, can be expressed as:

$$\begin{cases} \mathbf{x}=\mathbf{F}\,\mathbf{X} \quad \Rightarrow \quad F_{ij}=\frac{\partial x_i}{\partial X_j} \Rightarrow \quad \mathbf{F}=\mathbf{I}+\mathbf{H} \Rightarrow F_{ij}=\delta_{ij}+\frac{\partial u_i}{\partial X_j} \quad \overset{\text{TIH}}{\Longrightarrow} \\ \mathbf{u}=\mathbf{x}-\mathbf{X} \quad \Rightarrow \quad \mathbf{x}=\mathbf{u}+\mathbf{X} \end{cases}$$

$$\overset{\text{TIH}}{\Longrightarrow} \mathbf{F}=\begin{bmatrix} 1+\frac{\partial U}{\partial x_0} & \frac{\partial U}{\partial y_0} & \frac{\partial U}{\partial y_0} \\ -\frac{\partial U}{\partial y_0} & 1+\frac{\partial V}{\partial y_0} & 0 \\ -\frac{\partial U}{\partial y_0} & 0 & 1+\frac{\partial V}{\partial y_0} \end{bmatrix} \qquad \textit{Eq. E- 3}$$

and allows the calculation of:

1. The *1st order strain field*:

$$\boldsymbol{\epsilon}=\frac{1}{2}\left(\mathbf{F}+\mathbf{F}^T\right)-\mathbf{I} \Rightarrow \quad \epsilon_{ij}=\frac{1}{2}\left(F_{ij}+F_{ji}\right)-\delta_{ij}=\frac{1}{2}\left(u_{i,j}+u_{j,i}\right)=\frac{1}{2}\left(\frac{\partial u_i}{\partial X_j}+\frac{\partial u_j}{\partial X_i}\right) \quad \overset{\text{TIH}}{\Longrightarrow}$$

$$\overset{\text{TIH}}{\Longrightarrow} \boldsymbol{\epsilon}=\begin{bmatrix} \frac{\partial U}{\partial x_0} & 0 & 0 \\ 0 & \frac{\partial V}{\partial y_0} & 0 \\ 0 & 0 & \frac{\partial V}{\partial y_0} \end{bmatrix} \qquad \textit{Eq. E- 4}$$

2. The *2nd order deformation field* (*Green-Lagrange formulation*):

$$\mathbf{C}=\mathbf{F}^T\cdot\mathbf{F}=F_{ki}F_{kj} \qquad \textit{Eq. E- 5}$$

$$\mathbf{E}=\frac{1}{2}(\mathbf{C}-\mathbf{I}) \Rightarrow \quad E_{ij}=\frac{1}{2}\left(F_{ki}F_{kj}-\delta_{ij}\right)=\frac{1}{2}\left(u_{i,j}+u_{j,i}+u_{k,i}u_{k,j}\right)=\frac{1}{2}\left(\frac{\partial u_i}{\partial X_j}+\frac{\partial u_j}{\partial X_i}+\frac{\partial u_k}{\partial X_i}\frac{\partial u_k}{\partial X_j}\right) \Rightarrow$$

$$\Rightarrow \begin{cases} E_{xx}=\dfrac{\partial U}{\partial x_0}+\dfrac{1}{2}\left[\left(\dfrac{\partial U}{\partial x_0}\right)^2+\left(\dfrac{\partial V}{\partial x_0}\right)^2+\left(\dfrac{\partial W}{\partial x_0}\right)^2\right] \\ E_{yy}=\dfrac{\partial V}{\partial y_0}+\dfrac{1}{2}\left[\left(\dfrac{\partial U}{\partial y_0}\right)^2+\left(\dfrac{\partial V}{\partial y_0}\right)^2+\left(\dfrac{\partial W}{\partial y_0}\right)^2\right] \\ E_{zz}=\dfrac{\partial W}{\partial z_0}+\dfrac{1}{2}\left[\left(\dfrac{\partial U}{\partial z_0}\right)^2+\left(\dfrac{\partial V}{\partial z_0}\right)^2+\left(\dfrac{\partial W}{\partial z_0}\right)^2\right] \\ E_{xy}=\dfrac{1}{2}\left(\dfrac{\partial U}{\partial y_0}+\dfrac{\partial V}{\partial x_0}\right)+\dfrac{1}{2}\left[\dfrac{\partial U}{\partial x_0}\dfrac{\partial U}{\partial y_0}+\dfrac{\partial V}{\partial x_0}\dfrac{\partial V}{\partial y_0}+\dfrac{\partial W}{\partial x_0}\dfrac{\partial W}{\partial y_0}\right] \\ E_{xz}=\dfrac{1}{2}\left(\dfrac{\partial U}{\partial z_0}+\dfrac{\partial W}{\partial x_0}\right)+\dfrac{1}{2}\left[\dfrac{\partial U}{\partial x_0}\dfrac{\partial U}{\partial z_0}+\dfrac{\partial V}{\partial x_0}\dfrac{\partial V}{\partial z_0}+\dfrac{\partial W}{\partial x_0}\dfrac{\partial W}{\partial z_0}\right] \\ E_{yz}=\dfrac{1}{2}\left(\dfrac{\partial V}{\partial z_0}+\dfrac{\partial W}{\partial y_0}\right)+\dfrac{1}{2}\left[\dfrac{\partial U}{\partial y_0}\dfrac{\partial U}{\partial z_0}+\dfrac{\partial V}{\partial y_0}\dfrac{\partial V}{\partial z_0}+\dfrac{\partial W}{\partial y_0}\dfrac{\partial W}{\partial z_0}\right] \end{cases} \overset{\text{TIH}}{\Longrightarrow}$$

$$\overset{\text{TIH}}{\Longrightarrow} \mathbf{E}=\begin{bmatrix} \frac{1}{2}\left(\frac{\partial U}{\partial x_0}+1\right)^2+\left(\frac{\partial U}{\partial y_0}\right)^2-\frac{1}{2} & \frac{1}{2}\frac{\partial U}{\partial y_0}\left[\left(\frac{\partial U}{\partial x_0}+1\right)-\left(\frac{\partial V}{\partial y_0}+1\right)\right] & \frac{1}{2}\frac{\partial U}{\partial y_0}\left[\left(\frac{\partial U}{\partial x_0}+1\right)-\left(\frac{\partial V}{\partial y_0}+1\right)\right] \\ \frac{1}{2}\frac{\partial U}{\partial y_0}\left[\left(\frac{\partial U}{\partial x_0}+1\right)-\left(\frac{\partial V}{\partial y_0}+1\right)\right] & \frac{1}{2}\left(\frac{\partial V}{\partial y_0}+1\right)^2+\left(\frac{\partial U}{\partial y_0}\right)^2-\frac{1}{2} & \frac{1}{2}\left(\frac{\partial U}{\partial y_0}\right)^2 \\ \frac{1}{2}\frac{\partial U}{\partial y_0}\left[\left(\frac{\partial U}{\partial x_0}+1\right)-\left(\frac{\partial V}{\partial y_0}+1\right)\right] & \frac{1}{2}\left(\frac{\partial U}{\partial y_0}\right)^2 & \frac{1}{2}\left(\frac{\partial V}{\partial y_0}+1\right)^2+\left(\frac{\partial U}{\partial y_0}\right)^2-\frac{1}{2} \end{bmatrix} \qquad \textit{Eq. E- 6}$$

3. The *Volume variation* (volumetric change):

$$\Theta=\frac{dv-dV}{dV}=\det(\mathbf{F})-1=J-1 \quad \overset{\text{TIH}}{\Longrightarrow}$$

$$\overset{\text{TIH}}{\Longrightarrow} \Theta=\frac{\partial U}{\partial x_0}+2\frac{\partial V}{\partial y_0}+\frac{\partial U}{\partial x_0}\left(\frac{\partial V}{\partial y_0}\right)^2+2\left(\frac{\partial U}{\partial y_0}\right)^2\frac{\partial V}{\partial y_0}+2\left(\frac{\partial U}{\partial y_0}\right)^2+\left(\frac{\partial V}{\partial y_0}\right)^2+2\frac{\partial U}{\partial x_0}\frac{\partial V}{\partial y_0} \qquad \textit{Eq. E- 7}$$

4. The *Surface variation* (*Nanson's relation*):

$$\mathrm{d}a\cdot\mathbf{n}=J\,\mathrm{d}A\,\mathbf{F}^{-T}\mathbf{N} \quad \Rightarrow \quad \mathrm{d}a=\sqrt{\mathrm{d}a\cdot\mathrm{d}a}=J\,\mathrm{d}A\sqrt{\mathbf{N}^T\left(\mathbf{F}^T\cdot\mathbf{F}\right)^{-1}\mathbf{N}} \Rightarrow$$

$$\Rightarrow \quad \frac{\mathrm{d}a}{\mathrm{d}A}=J\sqrt{\mathbf{N}^T(\mathbf{C})^{-1}\mathbf{N}} \qquad \textit{Eq. E- 8}$$

where $\mathbf{N}$ is outward normal in the reference configuration of the y-z plane ($\mathbf{N}^T=[1 \quad 0 \quad 0]$).

5. The *longitudinal Cauchy stress*:

$$\sigma_{11}=\frac{F}{A\cdot\frac{\mathrm{d}a}{\mathrm{d}A}} \qquad \textit{Eq. E- 9}$$

6. The *longitudinal 2nd Piola-Kirchhoff Stress Tensor:*

$$S_{11}^{PK2}=J\,\mathbf{F}^{-1}\cdot\boldsymbol{\sigma}\cdot\mathbf{F}^{-T} \qquad \textit{Eq. E- 10}$$

E.2. Update Lagrangian Formulation

The deformed configuration $\mathbf{x}$ can be expressed as:

$$\begin{cases}\mathbf{x}(t_i)=\mathbf{F_R}(t_i)\mathbf{x_R}(t_i)\\ \mathbf{x_R}(t_i)=\mathbf{F_0}(t_i)\mathbf{X}(t_0)\end{cases} \Rightarrow \quad \mathbf{x}(t_i)=\mathbf{F_R}(t_i)\mathbf{F_0}(t_i)\mathbf{X}(t_0)=\mathbf{F}(t_i)\ \mathbf{X}(t_0) \qquad \textit{Eq. E- 11}$$

where the subscript index *R* refers to the reference configuration at the time t_i, which is the deformed configuration at the time t_{i-1}:

$$\mathbf{x_R}(t_i)=\mathbf{x}(t_{i-1}) \qquad \textit{Eq. E- 12}$$

The deformation gradient $\mathbf{F_R}$ is the function that allows the evaluatoion of the deformed configuration $\mathbf{x}(t_i)$ at the time t_i from the reference configuration ($\mathbf{x_R}(t_i)=\mathbf{x}(t_{i-1})$), while the deformation gradient $\mathbf{F_0}$ is the deformation gradient $\mathbf{F}$ at the time t_{i-1}, which is updated at each time:

$$\mathbf{F_0}(t_i)=\mathbf{F_R}(t_{i-1})\mathbf{F_0}(t_{i-1})=\mathbf{F}(t_{i-1}) \qquad \textit{Eq. E- 13}$$

The *displacement field* at the generic time t_i can be evaluated as:

$$\mathbf{u}=\mathbf{u_R}+\mathbf{u_0}=(\mathbf{x}-\mathbf{x_R})+(\mathbf{x_R}-\mathbf{X}) \quad \Rightarrow \begin{cases} U=U_R+U_0=(x-x_R)+(x_R-x_0)\\ V=V_R+V_0=(y-y_R)+(y_R-y_0)\\ W=W_R+W_0=(z-z_R)+(z_R-z_0)\end{cases} \qquad \textit{Eq. E- 14}$$

where at t_0, $U_R(0)=V_R(0)=0$.

The *Gradient of displacement* **H**, is then:

$$H_{R,ij}=\frac{\partial u_{R,i}}{\partial x_{R,j}} \quad \overset{\text{TIH}}{\Longrightarrow} \quad \mathbf{H_R}=\begin{bmatrix} \frac{\partial U_R}{\partial x_R} & \frac{\partial U_R}{\partial y_R} & \frac{\partial U_R}{\partial y_R}\\ -\frac{\partial U_R}{\partial y_R} & \frac{\partial V_R}{\partial y_R} & 0\\ -\frac{\partial U_R}{\partial y_R} & 0 & \frac{\partial V_R}{\partial y_R}\end{bmatrix} \qquad \textit{Eq. E- 15}$$

where at t_0, $\mathbf{H_R}(0)=\mathbf{0}$.

The *reference strain gradient*, $\mathbf{F_R}$:

$$\mathbf{x}=\mathbf{F_R}\mathbf{x_R} \quad \Rightarrow \quad F_{R,ij}=\frac{\partial x_i}{\partial x_{R,j}} \quad \Rightarrow \quad \mathbf{F_R}=\mathbf{I}+\mathbf{H_R} \Rightarrow F_{R,ij}=\delta_{ij}+\frac{\partial u_{R,i}}{\partial x_{R,j}} \overset{\text{TIH}}{\Longrightarrow}$$

$$\overset{\text{TIH}}{\Longrightarrow} \mathbf{F_R}=\begin{bmatrix} 1+\frac{\partial U_R}{\partial x_R} & \frac{\partial U_R}{\partial y_R} & \frac{\partial U_R}{\partial y_R} \\ \frac{\partial U_R}{\partial y_R} & 1+\frac{\partial V_R}{\partial y_R} & 0 \\ \frac{\partial U_R}{\partial y_R} & 0 & 1+\frac{\partial V_R}{\partial y_R} \end{bmatrix} \qquad \textit{Eq. E- 16}$$

where at t_0, $\mathbf{F_R}(0)=\mathbf{I}$.

The *total strain gradient* **F** is, therefore:

$$F_{ij}=F_{R,ik}F_{0,kj} \qquad \textit{Eq. E- 17}$$

The calculation of strain fields, volume and surface variation, and stress tensors, follows the equations showed for the Total Lagrangian formulation, only changing the strain gradient expressed in EQ. E- 3 with the one expressed in EQ. E- 17.

E.3. Eulerian Formulation

The *displacement field* **u** can be evaluated from the difference between the deformed and undeformed configuration:

$$\mathbf{U}(x,t)=\mathbf{x}\text{-}\mathbf{X}(x,t) \qquad \textit{Eq. E- 18}$$

The displacement field evaluated through the Eulerian formulation is equal to the displacement field evaluated through the Lagrangian formulation:

$$\mathbf{U}(x,t)=\mathbf{u}(X,t) \qquad \textit{Eq. E- 19}$$

The displacement field is then approximated through a polynomial function, in order to be able to derive it. Its derivation, allows the evaluation of the gradient of displacement field, **H**, as:

$$H_{ij}=\frac{\partial U_i}{\partial x_j} \quad \overset{\text{TIH}}{\Longrightarrow} \quad \mathbf{H}=\begin{bmatrix} \frac{\partial U}{\partial x} & \frac{\partial U}{\partial y} & \frac{\partial U}{\partial y} \\ \frac{\partial U}{\partial y} & \frac{\partial V}{\partial y} & 0 \\ \frac{\partial U}{\partial y} & 0 & \frac{\partial V}{\partial y} \end{bmatrix} \qquad \textit{Eq. E- 20}$$

and the strain gradient **F** as:

$$\begin{cases} \mathbf{X}=\mathbf{F}^{-1}\mathbf{x} & \Rightarrow \quad {F^{-1}}_{ij}=\frac{\partial X_i}{\partial x_j} \\ \mathbf{U}=\mathbf{x}-\mathbf{X} & \Rightarrow \quad \mathbf{X}=\mathbf{x}-\mathbf{U} \end{cases} \Rightarrow \quad \mathbf{F}^{-1}=\mathbf{I}-\mathbf{H} \Rightarrow {F^{-1}}_{ij}=\delta_{ij}-\frac{\partial U_i}{\partial x_j} \quad \overset{\text{TIH}}{\Longrightarrow}$$

$$\overset{\text{TIH}}{\Longrightarrow} \mathbf{F}^{-1}=\begin{bmatrix} 1-\frac{\partial U}{\partial x} & -\frac{\partial U}{\partial y} & -\frac{\partial U}{\partial y} \\ \frac{\partial U}{\partial y} & 1-\frac{\partial V}{\partial y} & 0 \\ \frac{\partial U}{\partial y} & 0 & 1-\frac{\partial V}{\partial y} \end{bmatrix} \qquad \textit{Eq. E- 21}$$

which allows the evaluation of the *1st order deformation field*:

$$\boldsymbol{\epsilon}=\mathbf{I}-\frac{1}{2}\left(\mathbf{F}^{-1}+\mathbf{F}^{-T}\right) \Rightarrow \quad \epsilon_{ij}=\delta_{ij}-\frac{1}{2}\left({F^{-1}}_{ij}+{F^{T}}_{ij}\right)=\frac{1}{2}\left(U_{i,j}+U_{j,i}\right)=\frac{1}{2}\left(\frac{\partial U_i}{\partial x_j}+\frac{\partial U_j}{\partial x_i}\right) \quad \overset{\text{TIH}}{\Longrightarrow}$$

$$\overset{\text{TIH}}{\Longrightarrow} \boldsymbol{\epsilon}=\begin{bmatrix} \dfrac{\partial U}{\partial x} & 0 & 0 \\ 0 & \dfrac{\partial V}{\partial y} & 0 \\ 0 & 0 & \dfrac{\partial W}{\partial z} \end{bmatrix} \qquad \textit{Eq. E- 22}$$

and the *2nd order deformation field* (Almansi formulation):

$$\mathbf{c}=\mathbf{F}^{-T}\cdot\mathbf{F}^{-1}=F^{-T}{}_{ki}F^{-1}{}_{kj} \qquad \textit{Eq. E- 23}$$

$$\mathbf{E}=\frac{1}{2}(\mathbf{I}-\mathbf{c}) \Rightarrow \quad E_{ij}=\frac{1}{2}\left(\delta_{ij}-F_{ki}F_{kj}\right)=\frac{1}{2}\left(U_{i,j}+U_{j,i}-U_{k,i}U_{k,j}\right)=\frac{1}{2}\left(\frac{\partial U_i}{\partial x_j}+\frac{\partial U_j}{\partial x_i}-\frac{\partial U_k}{\partial x_i}\frac{\partial U_k}{\partial x_j}\right) \quad \overset{\text{TIH}}{\Longrightarrow}$$

$$\overset{\text{TIH}}{\Longrightarrow}\mathbf{E}=\begin{bmatrix} \frac{1}{2}-\frac{1}{2}\left(\frac{\partial U}{\partial x}+1\right)^2-\left(\frac{\partial U}{\partial y}\right)^2 & \frac{1}{2}\frac{\partial U}{\partial y}\left[\left(\frac{\partial V}{\partial y}-1\right)-\left(\frac{\partial U}{\partial x}-1\right)\right] & \frac{1}{2}\frac{\partial U}{\partial y}\left[\left(\frac{\partial V}{\partial y}-1\right)-\left(\frac{\partial U}{\partial x}-1\right)\right] \\ \frac{1}{2}\frac{\partial U}{\partial y}\left[\left(\frac{\partial V}{\partial y}-1\right)-\left(\frac{\partial U}{\partial x}-1\right)\right] & \frac{1}{2}-\frac{1}{2}\left(\frac{\partial V}{\partial y}+1\right)^2-\left(\frac{\partial U}{\partial y}\right)^2 & -\frac{1}{2}\left(\frac{\partial U}{\partial y}\right)^2 \\ \frac{1}{2}\frac{\partial U}{\partial y}\left[\left(\frac{\partial V}{\partial y}-1\right)-\left(\frac{\partial U}{\partial x}-1\right)\right] & -\frac{1}{2}\left(\frac{\partial U}{\partial y}\right)^2 & \frac{1}{2}-\frac{1}{2}\left(\frac{\partial V}{\partial y}+1\right)^2-\left(\frac{\partial U}{\partial y}\right)^2 \end{bmatrix} \qquad \textit{Eq. E- 24}$$

The volume and surface variation, and stress tensor, follows the equations showed for the Total Lagrangian formulation.

Annex F – IAT validation through DIC analysis comparison

During a tensile test on PEKK 7002 SC at 200°C position driven at 1 mm/min where both the DIC pattern and the IdPix markers were painted on the specimen surface, 129 images were acquired with a 12 MP camera.

Those images were processed with DIC software Correla, which requires the definition, on the initial image, of a searching window and several sub windows (which are schematized in FIG. F- 1).

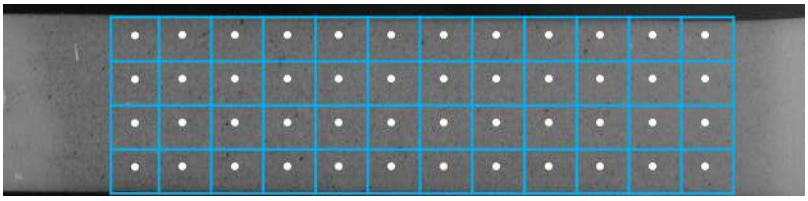

Fig. F- 1: Schematization of Correla searching window and sub windows

The software is then able to identify in the following image the new position of the deformed sub windows through a predictive algorithm, based on the measure of the displacement field and its derivatives, (SCHREIER, ORTEU, AND SUTTON 2009).

However, because of the non-linearity measured between the displacement and the strain and the high strain value registered, the software was not able to analyze the images all together, despite changing size and number of the sub windows.

The analysis was carried out setting the searching window with variable dimension to cover the major part of the pattern painted area and setting the sub-windows dimension to 50 pixels with both vertical and horizontal offset of 50 pixels.

It was possible to analyze the images only in small ranges, and trying to extend those ranges as much as possible, the analysis was carried out on 4 ranges of images:

- *Range 1*, from image 1 to 36;
- *Range 2*, from image 36 to 53;
- *Range 3*, from image 53 to 86;
- *Range 4*, from image 86 to 129.

In order to compare the results obtained with Correla to the results obtained from IAT, the validation procedure consisted in:

1. *validation of the calculation*. Each range of image was processed with Correla, obtaining its relative displacement and strain fields. Then, in order to validate the IAT calculation algorithm, the strain field was re-calculated from the displacement field measured by Correla.

2. *validation of the measurement* of the displacement field.

F.1. Validation of the measure of the displacement field

In order to compare the strains along the whole test duration, calculated by both Correla and IAT, the displacement field for the whole duration of the test is needed. While IAT achieved in providing with it, Correla could only measure it for each range of processed images.

The output results provided by Correla are, for each range of images:

a) the coordinates of the reference points, or the points found on the initial image of each range;
b) the displacement field of each point along the range of images.

Therefore, for the *Range 1* (images from 1 to 36), it is possible to plot the initial and final coordinates found by Correla, as shown in FIG. F- 2.

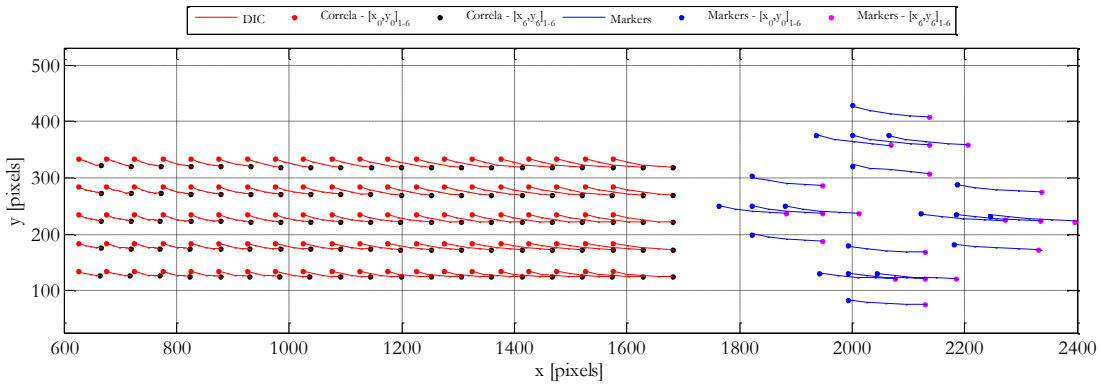

Fig. F- 2: Initial and final position of the points found by Correla (respectively in red and black) and by IAT (respectively in blue and magenta) for the Range 1 of images

where the subscript index *0* indicates the reference image, any other number indicates the actual image and the subscript numbers outside the brackets indicates the images of the range.

For the *Range 2*, however, it is not possible to impose, as initial coordinates, the final coordinates of the points of the *Range 1*, because, otherwise, the software would have been able to process all the images and there would have been no need to divide them in ranges. Furthermore, to analyze the same area, the size and position of the searching window was

changed, with the result of having more points respect to the previous range, as shown in FIG. F- 3.

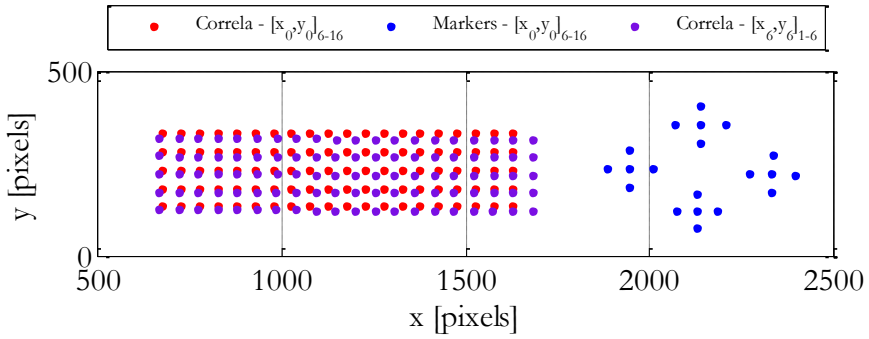

Fig. F- 3 Initial points found by Correla (in red) and by IAT (in blue) for the Range 2 of images, compared with the final points found by Correla (in purple) for the Range 1.

In order to reconstruct the displacement field, keeping as reference the first image of the *Range 1* across the other ranges of images, the following process was carried out:

1. the displacement field evaluated by Correla at each image *j* of the *Range i*, ($\{U_j\}_{R_i}$), is fitted with a bi-cubic polynomial function of the initial coordinates of the *Range i*, ($\{[x_0,y_0]\}_{R_i}$), hence:

$$\{U_j\}_{R_i} = f\{[x_0,y_0]\}_{R_i} \quad \text{with } j=1,\dots n_{R_i}$$
$$n_{R_i} = \text{number of images of } Range\ i \qquad \textit{Eq. F- 1}$$

2. each *Range i* begins with the last image of *Range i-1*: this allows fitting the 1st image of *Range i* with a bi-cubical polynomial function, in function of the final coordinates of the *Range i-1*:

$$\{U_1\}_{R_i} = f\{[x_0,y_0]\}_{R_i} = f\left\{\left[x_{n_{R_{i-1}}},y_{n_{R_{i-1}}}\right]\right\}_{R_{i-1}} \qquad \textit{Eq. F- 2}$$

3. The step 2 is then repeated for each *n* image of *Range i*. The displacement field of the *j-th* image of *Range i*, once fitted as function of the final coordinates of the *Range i-1,* can be seen as the increment of displacement:

$$f\left\{\left[x_{n_{R_{i-1}}},y_{n_{R_{i-1}}}\right]\right\}_{R_{i-1}} = \{\Delta U_k\}_{R_{i-1}} \qquad \textit{Eq. F- 3}$$

4. Then, the displacement field of *Range i* can be written as function of the initial coordinates of *Range i-1* simply summing it to the displacement of *Range i-1*. Applying this procedure to all *Range*s, it allows writing the displacement as function of the initial coordinates of *Range 1*, or to reconstruct the displacement field for all *k* images:

$$\begin{cases} \{U_k\}_{R_1} = \{U_k\}_{R_1} & \text{for } k \le n_{R_1} \\ \{U_k\}_{R_1} = \left\{U_{n_{R_1}}\right\}_{R_1} + \{\Delta U_k\}_{R_{i-1}} & \text{for } k > n_{R_1} \end{cases} \qquad \textit{Eq. F- 4}$$

The FIG. F- 4 shows the trajectories of the points in the *Range 2* and the reconstructed trajectories referred to the initial image of the *Range 1*.

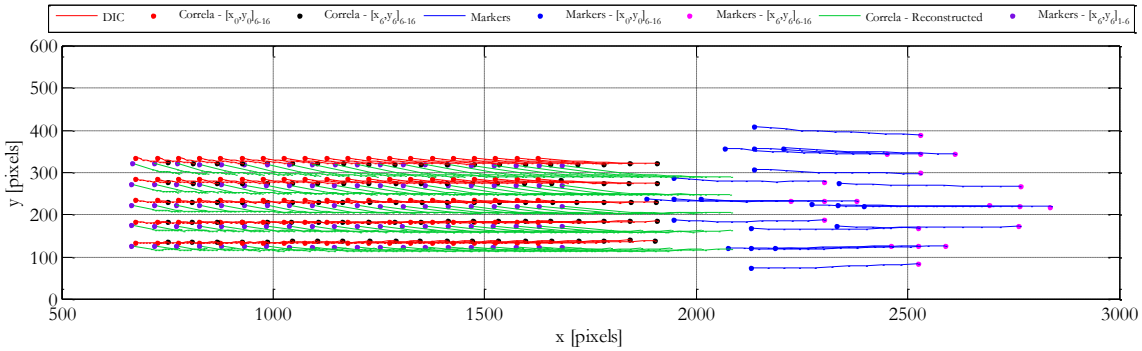

Fig. F- 4: Trajectories of the points evaluated by Correla in Range 2 (in red) and respect to the initial frame (in green), and the trajectory evaluated by IAT (in blue)

Since the points evaluated by Correla and by IAT are not in same area, it was not possible to directly compare the displacement fields evaluated by both software, but only a qualitative comparison was possible, as shown in FIG. F- 5. The reconstruction process led to obtain a displacement field which follows the same trend than the displacement field measured by IAT.

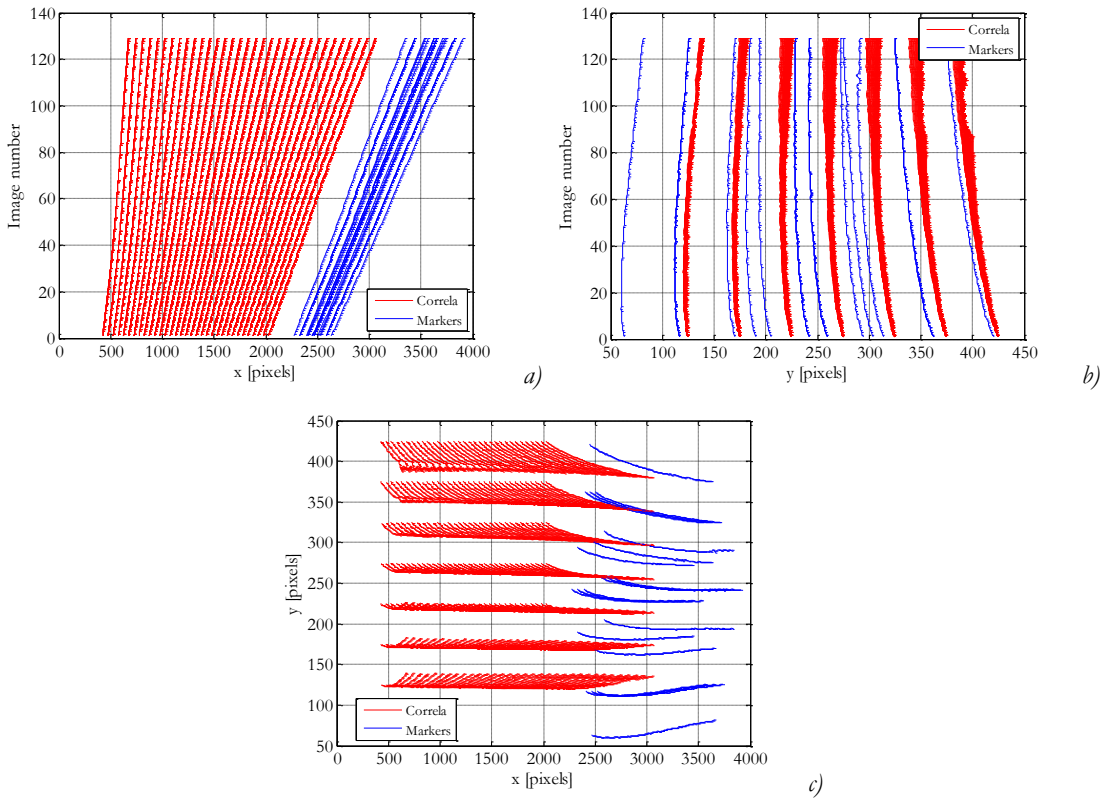

Fig. F- 5: Comparison of the trajectories evaluated by Correla (in red) and by IAT (in blue): a) longitudinal position of the points plotted against the time, b) transversal position of the points plotted against the time, c) longitudinal position points plotted against their transversal position

Exploiting the validation of IAT calculation algorithm, the strain field was evaluated starting from both the displacement field measured from the markers and the reconstructed one.

The results are showed in FIG. F- 6: for the fitting of the reconstructed displacement field, a bi-cubic polynomial function was employed, the resulting not constant strain field was averaged for the comparison with IAT's one.

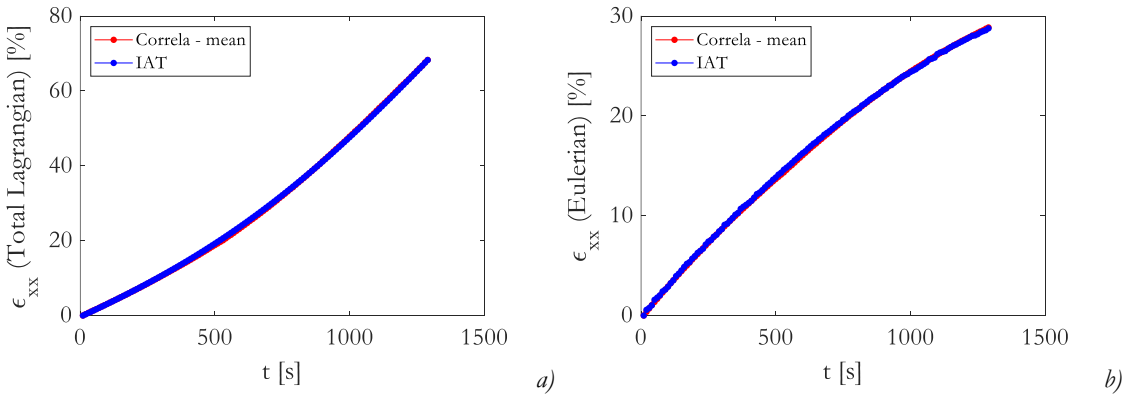

Fig. F- 6: Total Lagrangian(a) and Eulerian (b) longitudinal strains, calculated by Correla (red) and IAT (blue).

Annex G – Analytical methods

G.1. Lamination theory

The Lamination theory methods allow the calculation of the composite properties, starting from the ply properties and the stacking sequence.

According to Herakovich formulation (HERAKOVICH 1988), this can be achieved under the following hypothesis:

1. the plies are perfectly bonded;
2. each ply is a homogeneous transversal isotropic material;
3. each ply is in plane stress;
4. normal to the composite mid-plane are still normal to it after the deformation and do not change length (Kirchhoff-Love thin plates theory).

The procedure can be divided in two step:

1. evaluation of the ply plane stress stiffness matrix in the composite reference system ($\bar{\mathbf{Q}}$);
2. evaluation of the composite plane stress stiffness matrix (**a**).

G.1.1. Ply plane stress stiffness matrix in the composite reference system

In order to change the reference system (as showed in EQ. 2-27), a rotation around z-axis is needed for both stress and strain tensor. The formulation, following Voigt notation, is:

$$\begin{cases} \{\sigma\}_1 = [T_1]\{\sigma\}_x \\ \{\varepsilon\}_1 = [T_2]\{\varepsilon\}_x \end{cases} \qquad \textit{Eq. G- 1}$$

where $[T_1]$ and $[T_2]$ are the rotation matrix, which components are function of the angle Θ between the ply *1*-direction (fibers direction) and the composite x-direction (see FIG. 2-40). The rotation matrix can be expressed as follows, in Voigt notation:

$$[T_1] = \begin{bmatrix} m^2 & n^2 & 0 & 0 & 0 & 2mn \\ n^2 & m^2 & 0 & 0 & 0 & -2mn \\ 0 & 0 & 1 & 0 & 0 & 0 \\ 0 & 0 & 0 & m & -n & 0 \\ 0 & 0 & 0 & n & m & 0 \\ -mn & mn & 0 & 0 & 0 & m^2-n^2 \end{bmatrix} \qquad \textit{Eq. G- 2}$$

$$[T_2]=\begin{bmatrix} m^2 & n^2 & 0 & 0 & 0 & mn \\ n^2 & m^2 & 0 & 0 & 0 & -mn \\ 0 & 0 & 1 & 0 & 0 & 0 \\ 0 & 0 & 0 & m & -n & 0 \\ 0 & 0 & 0 & n & m & 0 \\ -2mn & 2mn & 0 & 0 & 0 & m^2-n^2 \end{bmatrix} \qquad \text{Eq. G- 3}$$

$$m=\cos\Theta$$
$$n=\sin\Theta \qquad \text{Eq. G- 4}$$

The ply constitutive equation (EQ. 2-27) could then be re-written, changing the reference system, as:

$$\begin{gathered} \{\varepsilon\}_1=[S]\{\sigma\}_1 \Rightarrow \\ \Rightarrow [T_2]\{\varepsilon\}_x=[S][T_1]\{\sigma\}_x \Rightarrow \\ \Rightarrow \{\varepsilon\}_x=[T_2]^{-1}[S][T_1]\{\sigma\}_x \Rightarrow \\ \Rightarrow \{\varepsilon\}_x=[\bar{S}]\{\sigma\}_x \end{gathered} \qquad \text{Eq. G- 5}$$

Hence, the compliance matrix, in the composite reference system ($\bar{\mathbf{S}}$), becomes:

$$[\bar{S}]=[T_2]^{-1}[S][T_1] \qquad \text{Eq. G- 6}$$

and from that, we could calculate the ply stiffness matrix in the composite reference system as:

$$[\bar{C}]=[\bar{S}]^{-1} \qquad \text{Eq. G- 7}$$

Introducing the plane stress hypothesis for the ply, the ply plane stress stiffness matrix in composite reference system ($\bar{\mathbf{Q}}$) can be written as follows:

$$\bar{Q}_{ij}=\bar{C}_{ij}+\frac{\bar{C}_{i3}\bar{C}_{3j}}{\bar{C}_{33}} \quad \text{with } i,j=1,2,6 \qquad \text{Eq. G- 8}$$

G.1.2. Composite plane stress stiffness matrix

The hypothesis made in Herakovich formulation lead to the decomposition of the strain tensor in the sum of mid-plane strains $\{\varepsilon_0\}_x$ and curvature $\{k\}_x$:

$$\{\varepsilon\}_x=\{\varepsilon_0\}_x+z\{k\}_x \qquad \textit{Eq. G- 9}$$

Following Hypothesis 3, only in-plane force, $\{N\}$, and moments, $\{M\}$, can be applied to the composite and they could be expressed as function of the stress inside each ply, $\{\sigma\}_x^k$, where the index k refers to the k-th ply:

$$\{N\}=\int_{-H}^{H}\{\sigma\}^k dz \qquad \textit{Eq. G- 10}$$

$$\{M\}=\int_{-H}^{H}\{\sigma\}^k z\, dz \qquad \textit{Eq. G- 11}$$

$$\{\sigma\}_x^k=[\bar{Q}]^k\{\varepsilon\}_x \qquad \textit{Eq. G- 12}$$

Substituting the strain decomposition (EQ. G- 9) in the ply stress constitutive equation (EQ. G- 12), and the resulting in both in plane force (EQ. G- 10) and moment (EQ. G- 11) definition, the following system can be obtained:

$$\begin{Bmatrix} N \\ M \end{Bmatrix}=\begin{bmatrix} A & B \\ B & D \end{bmatrix}\begin{Bmatrix} \varepsilon_0 \\ k \end{Bmatrix} \qquad \textit{Eq. G- 13}$$

The system in EQ. G- 13 implies that the application of a force on the composite, besides producing a *mid-plane effect* (a stretch or a compression, according to the force sign), also produce *curvature effect*; in the same way a moment besides producing a curvature on the composite, also produces mid-plane effects.

In the case of symmetric composite (if the ply stacking sequence is specular to the composite mid-plane), B=0, hence the effects of curvature are neglected for the in-plane force and the

mid-plane effects are neglected for the moments, thus the system expressed in EQ. G- 13, is decoupled and becomes:

$$\{N\}=[A]\{\varepsilon_0\} \qquad \textit{Eq. G- 14}$$

$$\{M\}=[D]\{k\} \qquad \textit{Eq. G- 15}$$

Furthermore, during both tensile and creep tests, only mid-plane forces are present, therefore, the analysis can refers only to EQ. G- 14.

The composite stiffness matrix can be evaluated as follows:

$$[A]=\sum_{k=1}^{N}[\bar{Q}]^k(z_k-z_{k-1}) \qquad \textit{Eq. G- 16}$$

where $(z_k-z_{k-1})=t_k$ is the ply thickness.

Imposing the equality of the in plane force defined in EQ. G- 10 and EQ. G- 14, and inverting them, the composite average stress $\bar{\boldsymbol{\sigma}}$ can be evaluated as:

$$\{\bar{\sigma}\}=\sum_k\{\sigma\}_x^k=\frac{1}{t}\{N\}=\frac{1}{t}[A]\{\varepsilon_0\} \qquad \textit{Eq. G- 17}$$

where t is the composite thickness.

Inverting EQ. 2-28the composite compliance matrix can be evaluated as:

$$[a^*]=t[A]^{-1} \qquad \textit{Eq. G- 18}$$

G.2. Localization methods

Localization methods (self-consistent methods) allow the evaluation of the average stress and strain of each phase of a two-phases material.

The 1st step of the method consists in evaluating Morris' tensor $\mathbf{E^p}$, which in (KRÖNER 1958) and (ESHELBY 1957) formalism, describes the interaction between ellipsoidal inclusion dispersed in an infinite medium:

$$E^{p}_{ijkl}=\frac{1}{4\pi}\int_0^{\pi}\sin\theta\,\mathrm{d}\theta\int_0^{2\pi}\gamma_{ikjl}\mathrm{d}\varphi \qquad \textit{Eq. G- 19}$$

where, for an orthotropic material:

- $\gamma_{ikjl}=K^{-1}_{ik}(\xi)\xi_j\xi_l$ *Eq. G- 20*

- $[K]=\begin{bmatrix} C^{p}_{11}\xi_1^2+C^{p}_{66}\xi_2^2+C^{p}_{55}\xi_3^2 & \left(C^{p}_{12}+C^{p}_{66}\right)\xi_1\xi_2 & \left(C^{p}_{13}+C^{p}_{55}\right)\xi_1\xi_2 \\ \left(C^{p}_{12}+C^{p}_{66}\right)\xi_1\xi_2 & C^{p}_{66}\xi_1^2+C^{p}_{22}\xi_2^2+C^{p}_{44}\xi_3^2 & \left(C^{p}_{23}+C^{p}_{44}\right)\xi_2\xi_3 \\ \left(C^{p}_{13}+C^{p}_{55}\right)\xi_1\xi_2 & \left(C^{p}_{23}+C^{p}_{44}\right)\xi_2\xi_3 & C^{p}_{55}\xi_1^2+C^{p}_{44}\xi_2^2+C^{p}_{33}\xi_3^2 \end{bmatrix}$ *Eq. G- 21*

- $\xi_1=\frac{\sin\theta\cos\varphi}{a_1}\qquad \xi_2=\frac{\sin\theta\sin\varphi}{a_2}\qquad \xi_3=\frac{\cos\theta}{a_3}$ *Eq. G- 22*

- a_1, a_2, a_3 are the ellipsoid axes;
- θ, φ are the ellipsoid integration variables.

If cylindrical inclusions are considered,

$$a_1\to\infty,\ a_2=a_3 \text{ and } \xi_1\ll\xi_2,\xi_3 \qquad \textit{Eq. G- 23}$$

which allow simplifying EQ. G- 21 as:

$$[\mathrm{K}]=\begin{bmatrix} C^{p}_{55}(\xi_2^2+\xi_3^2) & \left(C^{p}_{12}+C^{p}_{55}\right)\xi_1\xi_2 & \left(C^{p}_{12}+C^{p}_{55}\right)\xi_1\xi_2 \\ \left(C^{p}_{12}+C^{p}_{55}\right)\xi_1\xi_2 & C^{p}_{22}\xi_2^2+C^{p}_{44}\xi_3^2 & \left(C^{p}_{23}+C^{p}_{44}\right)\xi_2\xi_3 \\ \left(C^{p}_{12}+C^{p}_{55}\right)\xi_1\xi_2 & \left(C^{p}_{23}+C^{p}_{44}\right)\xi_2\xi_3 & C^{p}_{44}\xi_2^2+C^{p}_{33}\xi_3^2 \end{bmatrix} \qquad \textit{Eq. G- 24}$$

Considering the conditions over the dimensions (EQ. G- 23), and that the terms on **K** matrix diagonal have higher order of magnitude than the elements outside the matrix diagonal ($K_{ii} \gg K_{ij}$ with $i \neq j$), the inverse of tensor **K** can be approximated as follows:

$$[K^{-1}] \sim \begin{bmatrix} H_{11} & 0 & 0 \\ 0 & H_{22} & H_{23} \\ 0 & H_{23} & H_{22} \end{bmatrix} \qquad \textit{Eq. G- 25}$$

Employing the simplification expressed in EQ. G- 21 and EQ. G- 23, Morris' tensor **E** (EQ. G- 19), can be significantly simplified as:

$$[E^{p}] \sim \begin{bmatrix} 0 & 0 & 0 & 0 & 0 & 0 \\ 0 & \frac{3}{8C^{p}_{22}} + \frac{1}{4C^{p}_{22}-4C^{p}_{23}} & \frac{C^{p}_{22}+C^{p}_{23}}{8C^{p}_{22}C^{p}_{23}-8\left(C^{p}_{22}\right)^{2}} & 0 & 0 & 0 \\ 0 & \frac{C^{p}_{22}+C^{p}_{23}}{8C^{p}_{22}C^{p}_{23}-8\left(C^{p}_{22}\right)^{2}} & \frac{3}{8C^{p}_{22}} + \frac{1}{4C^{p}_{22}-4C^{p}_{23}} & 0 & 0 & 0 \\ 0 & 0 & 0 & \frac{1}{8C^{p}_{22}} + \frac{1}{4C^{p}_{22}-4C^{p}_{23}} & 0 & 0 \\ 0 & 0 & 0 & 0 & \frac{1}{8C^{p}_{55}} & 0 \\ 0 & 0 & 0 & 0 & 0 & \frac{1}{8C^{p}_{55}} \end{bmatrix} \qquad \textit{Eq. G- 26}$$

EQ. G- 26 allows the evaluation of the reaction tensor $\mathbf{R^p}$, which express the elastic interactions produced by the constituents morphology:

$$\mathbf{R^p} = (\mathbf{(L^p)^{-1}} - \mathbf{E^p}) : \mathbf{(E^p)^{-1}} \qquad \textit{Eq. G- 27}$$

In Fréour's work, in the matrix and ply constitutive laws definition, also hygrothermal dilation, produced by the composite moisture content, is taken into account. Since no moisture is assumed to be present both in PEKK and C/PEKK, because of the drying protocol carried out for each specimen and the high test temperature, the terms referring to hygrothermal dilatation are neglected.

In the same way, since the test temperatures considered for localization method application is above T_g, it is assumed that the composite free stress temperature is reached and no thermal effect is considered.

Thus, the constitutive laws for matrix and ply can be written respectively as:

$$\boldsymbol{\sigma}^{m}=\mathbf{C}^{m}:\boldsymbol{\varepsilon}^{m} \qquad \textit{Eq. G- 28}$$

$$\boldsymbol{\sigma}^{p}=\mathbf{C}^{p}:\boldsymbol{\varepsilon}^{p} \qquad \textit{Eq. G- 29}$$

If the difference between EQ. G- 28 and EQ. G- 29 is calculated:

$$\boldsymbol{\sigma}^{m}-\boldsymbol{\sigma}^{p}=-\mathbf{C}^{p}:\mathbf{R}^{p}:(\boldsymbol{\varepsilon}^{m}-\boldsymbol{\varepsilon}^{p}) \qquad \textit{Eq. G- 30}$$

EQ. G- 28 can be substituted in EQ. G- 30, leading to:

$$\boldsymbol{\varepsilon}^{m}=(\mathbf{C}^{m}+\mathbf{C}^{p}:\mathbf{R}^{p})^{-1}:[(\mathbf{C}^{p}+\mathbf{C}^{p}:\mathbf{R}^{p}):\boldsymbol{\varepsilon}^{p}] \qquad \textit{Eq. G- 31}$$

The explicit form of EQ. G- 31 is showed in EQ. 2-37, EQ. 2-38 and EQ. 2-39, and it allows the evaluation of the matrix strains. The matrix constitutive law, EQ. G- 28 allows the evaluation of the matrix stress.

However, EQ. G- 26 does not allow the evaluation of $(\mathbf{E}^{p})^{-1}$, since $\det(\mathbf{E}^{p})=0$, thus the matrix stress were evaluated directly through EQ. 2-37, EQ. 2-38 and EQ. 2-39.

Moreover, it is assumed that Hill's strain and stress average laws (HILL 1967) are valid, then fibers stress and strains can be evaluated from:

$$\boldsymbol{\sigma}^{f}=\frac{1}{V^{f}}\boldsymbol{\sigma}^{p}-\frac{V^{m}}{V^{f}}\boldsymbol{\sigma}^{m} \qquad \textit{Eq. G- 32}$$

$$\boldsymbol{\varepsilon}^{f}=\frac{1}{V^{f}}\boldsymbol{\varepsilon}^{p}-\frac{V^{m}}{V^{f}}\boldsymbol{\varepsilon}^{m} \qquad \textit{Eq. G- 33}$$

Employing both EQ. G- 32 and EQ. G- 33, however, leads to an incongruence with the fiber constitutive law and to obtain different values of the fiber stiffness matrix. For this reason, only matrix stress and strain were calculated.

Annex H - SAHLM output comparison

The particular stacking sequence chosen for the C/PEKK composite ($[(\pm 45)_2, +45]_s$), prevents for direct ply stress and strain calculation, as it would have been in the case of 8-ply stacking. In the latter case, in fact, and under the hypothesis of strain equality between composite and ply, the ply stress tensor in Voigt's notation has the exact solution showed in EQ. H- 1:

$$\boldsymbol{\sigma}^{\mathbf{P}} = \left[\sigma_{xx}^{C} \quad 0 \quad 0 \quad 0 \quad 0 \quad \pm\frac{\sigma_{xx}^{C}}{2}\right]^{T} \qquad \textit{Eq. H- 1}$$

However, the 10-ply stacking sequence and the fibers rotation taken into account, force to employ the HM to evaluate the stress distribution in the C/PEKK. FIG. H- 1 shows the results in correspondence of 5 MPa longitudinal composite stress (mean value of the linear regression employed for the evaluation of the composite properties), which are compared with 8-ply sequence distribution (black lines). The distribution is normalized respect to the applied composite longitudinal stress, and the values are resumed in TAB. H- 1.

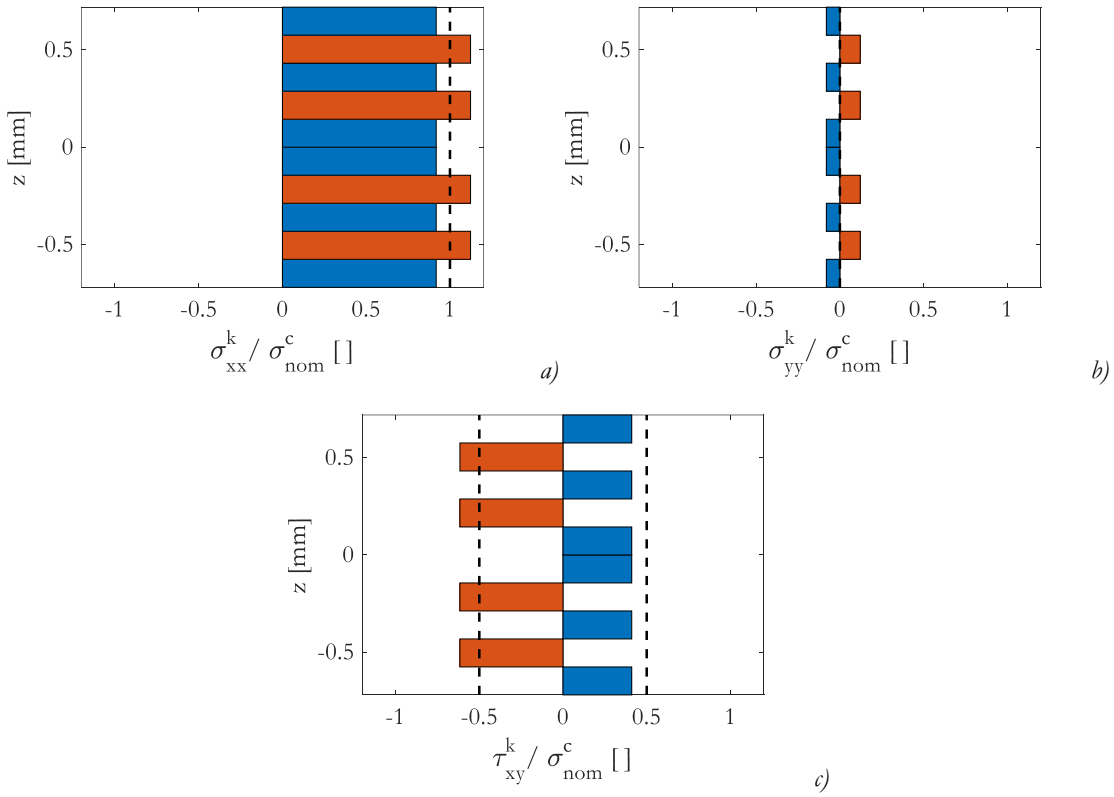

Fig. H- 1: C/PEKK stress distribution in the composite, normalized respect to the composite longitudinal stress and compared to the equivalent 8-ply stacking sequence stress distribution

Normalized stress	8-ply stacking sequence	10-ply stacking sequence	
	±45° ply	+45° ply	-45° ply
$\frac{\sigma_{xx}^{p}}{\sigma_{xx}^{C}}$	1	0.918	1.123
$\frac{\sigma_{yy}^{p}}{\sigma_{xx}^{C}}$	0	-0.081	0.121
$\frac{\tau_{xy}^{p}}{\sigma_{xx}^{C}}$	±0.5	0.411	-0.616

Tab. H- 1: C/PEKK normalized stress distribution compared to 8-ply stacking sequence

The semi-analytical method allows the evaluation of the composite and ply properties in the same range of the linear regression (CHAP. 3.2.4). However, the output properties are in terms of secant moduli, but exploiting the quasi-linearity of the region, the tangent moduli can be evaluated through the approximation:

$$E_{xx}^{tan} \approx \frac{\left(\sigma_{xx}(i)-\sigma_{xx}(i-1)\right)}{\frac{\sigma_{xx}(i)}{E_{xx}^{sec}(i)}-\frac{\sigma_{xx}(i-1)}{E_{xx}^{sec}(i-1)}} \qquad \textit{Eq. H- 2}$$

The composite and ply properties are resumed respectively in TAB. H- 2 and TAB. H- 3 respectively.

T [°C]	E_{xx}^{C} [MPa]	E_{yy}^{C} [MPa]	ν_{xy}^{C}	G_{xy}^{C} [MPa]	ν_{zx}^{C}	ν_{yz}^{C}
165	6944.5	6794.6	0.862	33763.3	0.177	0.189
180	1616.5	1532.9	0.988	33374.5	0.01	0.041
200	1727.9	1650.1	0.982	33379.3	0.016	0.045

Tab. H- 2: C/PEKK composite properties calculated through the semi-analytical method at 165°C, 180°C and 200°C

T [°C]	E_{11}^{p} [MPa]	E_{22}^{p} [MPa]	ν_{12}^{p}	G_{12}^{p} [MPa]	G_{23}^{p} [MPa]	ν_{23}^{p}
165	138680.5	2715.6	0.422	1809.3	1989.8	1.328
180	138656.5	782.5	0.384	398.1	362.2	1.174
200	138660.6	851.9	0.388	427.4	372.7	1.211

Tab. H- 3: : C/PEKK ply properties calculated through the semi-analytical method at 165°C, 180°C and 200°C

Bibliography

Airbus SAS, Arkema, ENSMA - Poitiers, ENSAM - Paris, ANR report. 2018. "IMPEKKABLE: Rapport d'activité Année 3."

Avrami, Melvin. 1941. "Granulation, Phase Change, and Microstructure Kinetics of Phase Change. III." *The Journal of Chemical Physics* 9(2): 177–84.

Barba, D., A. Arias, and D. Garcia-Gonzalez. 2020. "Temperature and Strain Rate Dependences on Hardening and Softening Behaviours in Semi-Crystalline Polymers: Application to PEEK." *International Journal of Solids and Structures* 182–183: 205–17.

Bessard, Emeline, Olivier De Almeida, and G. Bernhart. 2011. "Etude et Modélisation de La Cinétique de Cristallisation Du PEEK Lors de Refroidissements Isothermes et Anisothermes." *Comptes Rendus des JNC17*.

Betten, Josef. 2008. Creep Mechanics (Third Edition) *Creep Mechanics (Third Edition)*.

Biron, Michel. 2018. Thermoplastics and Thermoplastic Composites *Thermoplastics and Thermoplastic Composites*. Third. ed. William Andrew. Cambridge,: Elsevier Ltd.

Bowden, P. B., and R. J. Young. 1974. "Deformation Mechanisms in Crystalline Polymers." *Journal of Materials Science*.

Boyard, Nicolas et al. 2017. "Modélisation de La Cinétique de Cristallisation Dans Les Composites Fibreux à Matrice Thermoplastique." In *Compte Rendus Des JNC 20*,.

Brinson, L. Catherine, and Tom S. Gates. 1995. "Effects of Physical Aging on Long Term Creep of Polymers and Polymer Matrix Composites." *International Journal of Solids and Structures* 32(6–7): 827–46.

Bukowski R. 2014. "Vieillissement d'une Resine Thermoplastique « hautes Performances » Pour Applications Aéronautiques : Le PEEK." : 43.

Chang, I. Y., and J. K. Lees. 1988. "Recent Development in Thermoplastic Composites: A Review of Matrix Systems and Processing Methods." *Journal of Thermoplastic Composite Materials*.

Chang, Ike Y., and James F. Pratte. 1991. "LDF™ Thermoplastic Composites Technology." *Journal of Thermoplastic Composite Materials* 4(3): 227–52.

Chelaghma, Saber. 2013. "Fonctionnalisation de Composites C/PEKK Pour Application Aérospatiale : Caractérisation, Modélisation et Influence Sur Les Propriétés Du Composite." : 249. http://oatao.univ-toulouse.fr/9278/.

Choupin, T. et al. 2018. "Macromolecular Modifications of Poly(Etherketoneketone) (PEKK) Copolymer at the Melting State." *Polymer Degradation and Stability* 155: 103–10.

Choupin, Tanguy. 2018. "Mechanical Performances of PEKK Thermoplastic Tanguy Choupin To Cite This Version : HAL Id : Tel-01882121 l ' École Nationale Supérieure d ' Arts et M Étiers Mechanical Performances of PEKK Thermoplastic Composites Linked to Their Processing Parameters."

Cortes, Luis Quiroga, Antoine Lonjon, Eric Dantras, and Colette Lacabanne. 2014. "High-Performance Thermoplastic Composites Poly(Ether Ketone Ketone)/Silver Nanowires: Morphological, Mechanical and Electrical Properties." *Journal of Non-Crystalline Solids*.

Cowie, J. M. G. 2001. Contemporary Physics *Polymers: Chemistry and Physics of Modern Materials, 3rd Edition*.

Coxon, L. D., and J. R. White. 1980. "Residual Stresses and Aging in Injection Molded Polypropylene." *Polymer Engineering & Science*.

D'Amore, A., A. Pompo, and L. Nicolais. 1991. "Viscoelastic Effects in Poly(Ether Ether Ketone) (PEEK) and PEEK-Based Composites." *Composites Science and Technology* 41(3): 303–25.

Dasriaux, Marion. 2012. "Evolutions Microstructurales Du PEEK Au-Dessus de Sa Température de Transition Vitreuse Lors de Maintiens Sous Pression et Température." ISAE-ENSMA Ecole Nationale Supérieure de Mécanique et d'Aérotechique.

Dobraczynski, A; Trotignon, J-P; Verdu, Jacques; Piperaud, M. 1996. *Précis de Matières Plastiques : Structures-Propriétés, Mise En Oeuvre, Normalisation*. ed. Editions NATHAN.

Dorfmann, A., and R. W. Ogden. 2004. "A Constitutive Model for the Mullins Effect with Permanent Set in Particle-Reinforced Rubber." *International Journal of Solids and Structures* 41(7): 1855–78.

Eshelby, J. D. 1957. "The Determination of the Elastic Field of an Ellipsoidal Inclusion, and Related Problems." *Proceedings of the Royal Society of London. Series A. Mathematical and Physical Sciences*.

Fayolle, Bruno, and Jacques Verdu. 2005. "Am3150 - Vieillissement Physique Des Matériaux Polymères." *Techniques de l'ingénieur*.

Foti, Federico. 2017. "Effect of the Environment on the Fatigue Behaviour of Textile

Organic Matrix Composite Materials for Aircraft Applications." https://tel.archives-ouvertes.fr/tel-01724103%0Afile:///E:%5Ctelthese/tel-01724103.pdf.

Fréour, S., F. Jacquemin, and R. Guillén. 2005. "On an Analytical Self-Consistent Model for Internal Stress Prediction in Fiber-Reinforced Composites Submitted to Hygroelastic Load." *Journal of Reinforced Plastics and Composites* 24(13): 1365–77.

G'sell, C., A Dahoun, F X Royer, and M J Philippe. 1999. "The Influence of the Amorphous Matrix on the Plastic Hardening at Large Strain of Semicrystalline …." *MODELLING AND SIMULATION IN MATERIALS SCIENCE AND …*.

G'Sell, C., J. M. Hiver, A. Dahoun, and A. Souahi. 1992. "Video-Controlled Tensile Testing of Polymers and Metals beyond the Necking Point." *Journal of Materials Science* 27(18): 5031–39.

Gabrion, Xavier, Vincent Placet, Frédérique Trivaudey, and Lamine Boubakar. 2016. "About the Thermomechanical Behaviour of a Carbon Fibre Reinforced High-Temperature Thermoplastic Composite." *Composites Part B: Engineering* 95: 386–94.

Gal, Ohad. 2003. "Find the Best Fit for an Ellipse Using a given Set of Points (a Closed Contour)." https://www.mathworks.com/matlabcentral/fileexchange/3215-fit_ellipse.

Gao, Shang Lin, and Jang Kyo Kim. 2002. "Correlation among Crystalline Morphology of PEEK, Interface Bond Strength, and in-Plane Mechanical Properties of Carbon/PEEK Composites." *Journal of Applied Polymer Science*.

Garcia-Gonzalez, D., R. Zaera, and A. Arias. 2017. "A Hyperelastic-Thermoviscoplastic Constitutive Model for Semi-Crystalline Polymers: Application to PEEK under Dynamic Loading Conditions." *International Journal of Plasticity* 88: 27–52. http://dx.doi.org/10.1016/j.ijplas.2016.09.011.

Gardner, Kenn Corwin H., Benjamin S. Hsiao, Robert R. Matheson, and Barbara A. Wood. 1992. "Structure, Crystallization and Morphology of Poly (Aryl Ether Ketone Ketone)." *Polymer*.

Germaneau, Arnaud, P. Doumalin, and J. C. Dupré. 2007. "Full 3D Measurement of Strain Field by Scattered Light for Analysis of Structures." *Experimental Mechanics*.

Gigliotti, M., M. Minervino, and M. C. Lafarie-Frenot. 2016. "Thermo-Oxidative Induced Shrinkage in Organic Matrix Composites for High Temperature Applications: Effect of Fibre Arrangement and Oxygen Pressure." *Composite Structures*.

Giraud, Isabelle. 2011. "Elaboration d'ensimages Thermoplastiques Thermostables : Influence Sur Le Comportement Mécanique Des Composites PEEK / Fibres de Carbone." Centre Interuniversitaire de Recherche et d'Ingénierie des MATériaux (CIRIMAT), UMR 5085, Laboratoire de Physique des Polymères (LPP).

Halpin, J. 1969. Air Force Materials Lab Wright-Patterson AFB OH *Effects of Environmental Factors on Composite Materials*.

Haworth, B., C. S. Hindle, G. J. Sandilands, and J. R. White. 1982. "Assessment Of Internal Stresses In Injection-Moulded Thermoplastics." *Plastics and Rubber Processing and*

Applications.

Herakovich, Carl T. 1988. *Mechanics of Fibrous Composites*. ed. Ed. I. John Wiley & Sons.

Hill, R. 1967. "The Essential Structure of Constitutive Laws for Metal Composites and Polycrystals." *Journal of the Mechanics and Physics of Solids*.

Hillier, I. H. 1965. "Modified Avrami Equation for the Bulk Crystallization Kinetics of Spherulitic Polymers." *Journal of Polymer Science Part A: General Papers*.

Hoffman, John D., and James J. Weeks. 1962. "Melting Process and the Equilibrium Melting Temperature of Polychlorotrifluoroethylene." *Journal of Research of the National Bureau of Standards Section A: Physics and Chemistry*.

Hsiao, Benjamin S., Ike Y. Chang, and Bryan B. Sauer. 1991. "Isothermal Crystallization Kinetics of Poly(Ether Ketone Ketone) and Its Carbon-Fibre-Reinforced Composites." *Polymer*.

Hull, D., and T. W. Clyne. 1996. An Introduction to Composite Materials *An Introduction to Composite Materials*.

Hutter, Kolumban, and Klaus Johnk. 2004. *Continuum Methods of Physical Modeling*. Springer-Verlag Berlin Heidelberg.

Jar, P. Y., W. J. Cantwell, and H. H. Kausch. 1992. "Study of the Crystal Morphology and the Deformation Behaviour of Carbon Fibre Reinforced PEEK (APC-2)." *Composites Science and Technology*.

Katouzian, M., O. S. Brüller, and A. Horoschenkoff. 1995. "On the Effect of Temperature on the Creep Behavior of Neat and Carbon Fiber Reinforced PEEK and Epoxy Resin." *Journal of Composite Materials*.

Kaufmann, Markus. 2008. Technology *Cost / Weight Optimization of Aircraft Structures*.

Khan, S., J. F. Pratte, I. Y. Chang, and W. H. Krueger. 1990. "Composites for Aerospace Application from Kevlar Aramid Reinforced PEKK Thermoplastic." In *National SAMPE Symposium and Exhibition (Proceedings)*,.

Kolmogorov, Andrei Nikolaevich. 1937. "On the Statistical Theory of the Crystallization of Metals." *Bull. Acad. Sci. USSR, Math. Ser.*

Koscher, Emmanuelle, and René Fulchiron. 2002. "Influence of Shear on Polypropylene Crystallization: Morphology Development and Kinetics." *Polymer*.

Kovacs, A. J., J. J. Aklonis, J. M. Hutchinson, and A. R. Ramos. 1979. "Isobaric Volume Ad Enthalpy Recovery of Glasses - 2. A Transparent Multiparameter Theory." *J Polym Sci Polym Phys Ed*.

Kröner, Ekkehart. 1958. "Berechnung Der Elastischen Konstanten Des Vielkristalls Aus Den Konstanten Des Einkristalls." *Zeitschrift für Physik*.

Lamouroux, F. et al. 1999. "Oxidation-Resistant Carbon-Fiber-Reinforced Ceramic-Matrix Composites." *Composites Science and Technology* 59(7): 1073–85.

Lee, Youngchul, and Roger S. Porter. 1986. "Crystallization of Poly(Etheretherketone)

(PEEK) in Carbon Fiber Composites." *Polymer Engineering & Science*.

Lee, Youngchul, and Roger S. Porter. 1991. "Crystallization of Poly(Ether Ether Ketone) Oriented by Solid-State Extrusion." *Macromolecules*.

Leng, Dingxin et al. 2019. "A Hyper-Elastic Creep Approach and Characterization Analysis for Rubber Vibration Systems." *Polymers* 11(6).

Li, Wenlong et al. 2019. "Thermomechanical Model for Monotonic and Cyclic Loading of PEEK." *Mechanics of Materials* 129(June 2018): 113–38. https://doi.org/10.1016/j.mechmat.2018.11.005.

Loïc, Olivier. 2008. "Prévision Du Vieillissement Thermo-Oxydant de Composites à Matrice Organique Dédiés à l'aéronautique : Prise En Compte Des Couplages Multiphysiques." Ecole nationale supérieure de mécanique et d'aérotechnique (Chasseneuil-du-Poitou, Vienne, département).

Lucas, J. P., and J. Zhou. 1993. "The Effects of Sorbed Moisture on Resin-Matrix Composites." *JOM*.

Ma, C. C.M. et al. 1997. "Creep Behavior of Carbon-Fiber-Reinforced Polyetheretherketone (PEEK) [± 45]4S Laminated Composites (I)." *Composites Part B: Engineering* 28(4): 407–17.

Marand, Hervé, and Zhenyu Huang. 2004. "Isothermal Lamellar Thickening in Linear Polyethylene: Correlation between the Evolution of the Degree of Crystallinity and the Melting Temperature." *Macromolecules*.

Martín, M. I. et al. 2018. "On the Determination of Thermal Degradation Effects and Detection Techniques for Thermoplastic Composites Obtained by Automatic Lamination." *Composites Part A: Applied Science and Manufacturing*.

Martineau, L., F. Chabert, G. Bernhart, and T. Djilali. 2016. "Mechanical Behavior of Amorphous Peek in the Rubbery State." *ECCM 2016 - Proceeding of the 17th European Conference on Composite Materials* 2016(June).

McKenna, G. B., and A. J. Kovacs. 1984. "Physical Aging of Poly(Methyl Methacrylate) in the Nonlinear Range: Torque and Normal Force Measurements." *Polymer Engineering & Science*.

Van Melick, H. G.H., L. E. Govaert, and H. E.H. Meijer. 2003. "On the Origin of Strain Hardening in Glassy Polymers." *Polymer*.

Mensitieri, G. et al. 1990. "Solvent Induced Crystallization in Poly(Aryl-Ether-Ether-Ketone)." *Journal of Materials Science*.

Mensitieri, G., A. Apicella, J. M. Kenny, and L. Nicolais. 1989. "Water Sorption Kinetics in Poly(Aryl Ether Ether Ketone)." *Journal of Applied Polymer Science*.

Morris, Peter R. 1970. "Elastic Constants of Polycrystals." *International Journal of Engineering Science*.

Nitta, Koh Hei, and Hitomi Nomura. 2014. "Stress-Strain Behavior of Cold-Drawn Isotactic Polypropylene Subjected to Various Drawn Histories." *Polymer*.

Niu, Michael Chun-Yung. 2010. "Composite Airframe Structures." http://www.theeuropeanlibrary.org/tel4/record/3000042237733.

Del Nobile, M. A., G. Mensitieri, P. A. Netti, and L. Nicolais. 1994. "Anomalous Diffusion in Poly-Ether-Ether-Ketone." *Chemical Engineering Science*.

Ogale, A. A., and R. L. McCullough. 1987. "Influence of Microstructure on Elastic and Viscoelastic Properties of Polyether Ether Ketone." *Composites Science and Technology* 30(3): 185–201.

Otsu, Nobuyuki. 1979. "Threshold Selection Method From Gray-Level Histograms." *IEEE Trans Syst Man Cybern* SMC-9(1): 62–66.

Pappadà, Silvio et al. 2015. "Fabrication of a Thermoplastic Matrix Composite Stiffened Panel by Induction Welding." *Aerospace Science and Technology*.

Parlevliet, Patricia P., Harald E.N. Bersee, and Adriaan Beukers. 2007. "Residual Stresses in Thermoplastic Composites - a Study of the Literature. Part III: Effects of Thermal Residual Stresses." *Composites Part A: Applied Science and Manufacturing*.

Pawlak, Andrzej, and Andrzej Galeski. 2005. "Plastic Deformation of Crystalline Polymers: The Role of Cavitation and Crystal Plasticity." *Macromolecules*.

Peacock, A. J., and L. Mandelkern. 1990. "The Mechanical Properties of Random Copolymers of Ethylene: Force-elongation Relations." *Journal of Polymer Science Part B: Polymer Physics*.

Peebles, L.H., Jr. 1974. *Polymer Materials Science*. ed. Jerold M. Schultz. Englewood Cliffs: Prentice-Hall, Inc.

Peters, W. H., and W. F. Ranson. 1982. "Digital Imaging Techniques In Experimental Stress Analysis." *Optical Engineering*.

Pochiraju, Kishore V., Gregory A. Schoeppner, and Gyaneshwar P. Tandon. 2012. Long-Term Durability of Polymeric Matrix Composites *Long-Term Durability of Polymeric Matrix Composites*.

Pratte, James F., William H. Krueger, and Ike Y. Chang. 1989. "High Performance Thermoplastic Composites with Poly (Ether Ketone Ketone) Matrix." In *International SAMPE Symposium and Exhibition (Proceedings)*,.

Ramakrishna, S. 1997. "Analysis and Modeling of Plain Knitted Fabric Reinforced Composites." *Journal of Composite Materials* 31(1): 52–70.

Roguet, Eléonore. 2006. "Caracterisation Experimentale et Modelisation de l'etat Relaxé Dans Le Polyamide 11 à Hautes Témpératures." Ecole Nationale Superieure de Mecanique et d'Aeronautique.

Roland, S., and Bruno Fayolle. 2020. *Impekkable Project Results, to Be Published*. Paris.

Schreier, Hubert, Jean-José Orteu, and Michael A. Sutton. 2009. Image Correlation for Shape, Motion and Deformation Measurements *Image Correlation for Shape, Motion and Deformation Measurements*.

Schultz, J. M., E. W. Fischer, O. Schaumburg, and H. A. Zachmann. 1980. "Small-Angle X-Rray Scattering Studies of Melting." *Journal of polymer science. Part A-2, Polymer physics*.

Seferis, James C. 1986. "Polyetheretherketone (PEEK): Processing-structure and Properties Studies for a Matrix in High Performance Composites." *Polymer Composites*.

Struik, L. C.E. 1977. "Physical Aging in Plastics and Other Glassy Materials." *Polymer Engineering & Science*.

Sun, C. T., Islup Chung, and I. Y. Chang. 1992. "Modeling of Elastic-Plastic Behavior of LDF™ and Continuous Fiber Reinforced AS-4/PEKK Composites." *Composites Science and Technology* 43(4): 339–45.

Tadini, Pietro et al. 2017. "Thermal Degradation Analysis of Innovative PEKK-Based Carbon Composites for High-Temperature Aeronautical Components." *Aerospace Science and Technology*.

Talbott, Margaret F., George S. Springer, and Lars A. Berglund. 1987. "The Effects of Crystallinity on the Mechanical Properties of PEEK Polymer and Graphite Fiber Reinforced PEEK." *Journal of Composite Materials* 21(11): 1056–81.

Tanaka, K., and T. Mori. 1970. "The Hardening of Crystals by Non-Deforming Particles and Fibres." *Acta Metallurgica*.

Velisaris, Chris N., and James C. Seferis. 1986. "Crystallization Kinetics of Polyetheretherketone (Peek) Matrices." *Polymer Engineering & Science*.

Verrna, Ravi, Herve Marand, and Benjamin Hsiao. 1996. "Morphological Changes during Secondary Crystallization and Subsequent Melting in Poly(Ether Ether Ketone) as Studied by Real Time Small Angle X-Ray Scattering." *Macromolecules*.

Villoutreix, Josiane, and Jean-Dominique Acetarin. 1998. "Polyétheréthercétone (PEEK)." *Techniques de l'Ingénieur*.

Vinet, Alain et al. 2019. "Comportement Des Matrices PEKK En Oxydation To Cite This Version : HAL Id : Hal-02420678 Comportement Des Matrices PEKK En Oxydation." In *21ème Journées Nationales Sur Les Composites*, eds. ÉcoleNationaleSupérieured'Artset and Métiers (ENSAM). Bordeaux,Talence,France.

Wendlandt, Michael, Theo A. Tervoort, and Ulrich W. Suter. 2005. "Non-Linear, Rate-Dependent Strain-Hardening Behavior of Polymer Glasses." *Polymer*.

White, Jim R. 2006. "Polymer Ageing: Physics, Chemistry or Engineering? Time to Reflect." *Comptes Rendus Chimie* 9(11–12): 1396–1408.

William D. Callister, Jr. 2007. John Wiley & Sons, Inc. *Materials Science and Engineering 7th Ed. : An Introduction*.

Williams, Graham, and David C. Watts. 1970. "Non-Symmetrical Dielectric Relaxation Behaviour Arising from a Simple Empirical Decay Function." *Transactions of the Faraday Society*.

Williams, Malcolm L., Robert F. Landel, and John D. Ferry. 1955. "The Temperature Dependence of Relaxation Mechanisms in Amorphous Polymers and Other Glass-

Forming Liquids." *Journal of the American Chemical Society*.

Xiao, X. R., C. C. Hiel, and A. H. Cardon. 1994. "Characterization and Modeling of Nonlinear Viscoelastic Response of PEEK Resin and PEEK Composites." *Composites Engineering* 4(7): 681–702.

Xin, H., D. E.T. Shepherd, and K. D. Dearn. 2013. "Strength of Poly-Ether-Ether-Ketone: Effects of Sterilisation and Thermal Ageing." *Polymer Testing*.

Zheng, Bing et al. 2017. "Experimental Investigation and Constitutive Modeling of the Deformation Behavior of Poly-Ether-Ether-Ketone at Elevated Temperatures." *Polymer Testing* 63: 349–59. https://doi.org/10.1016/j.polymertesting.2017.08.020.

List of Tables

Tab. 1-1: Material's required operative specifications, (Airbus SAS, Arkema, ENSMA - Poitiers, ENSAM - Paris 2018) *3*
Tab. 1-1: Parameters of the kinetic models for the crystallization rate constants (K_1 and K_2) and the weight factor (w_1) for PEKK 7002 crystallized from the melt, (Tanguy Choupin 2018) *14*
Tab. 1-2: Bond rupture phenomena and their consequence on the material properties *23*
Tab. 2-1: Materials properties *36*
Tab. 2-2: Prepregs properties *37*
Tab. 2-3: Specimen geometries employed for the experimental campaign. *39*
Tab. 2-4: Schematization of the experimental campaign *39*
Tab. 2-5: List of the tests carried out during the experimental campaign *41*
Tab. 2-6: Instron 4505 properties *43*
Tab. 2-7: TA Instrument DMA Q800 properties *47*
Tab. 2-8: TA Instruments DSC Q20 properties *48*
Tab. 2-9: TOPIN 2344 properties *50*
Tab. 2-10: Instron 1251 properties *51*
Tab. 2-11: RX Solution UltraTom XL properties *53*
Tab. 2-12: Parameters for X-Rays tomography *53*
Tab. 2-13: Advantages and drawbacks of IdPix *59*
Tab. 2-14: Advantages and drawbacks of DIC *60*
Tab. 2-15: Advantages and drawbacks of IAT *61*
Tab. 2-16: Matlab commands for marker reconstruction *63*
Tab. 2-17: IAT different formulations implemented in the calculation algorithm *69*
Tab. 2-18: Halpin and Tsai formulation for ply properties calculation *77*
Tab. 2-19: Composite properties form Lamination theory *78*

Tab. 3-1: Color code employed for defining each test temperature 85
Tab. 3-2: Tensile test conditions 86
Tab. 3-3: C/PEKK Fiber rotation parameters as function of the tensile tests nominal stress at 165°C, 180°C and 200°C 93
Tab. 3-4: Pseudo-elastic moduli and Poisson's coefficient obtained from tensile test on PEKK 7002 SC and from room temperature to 200°C at 1 mm/min 94
Tab. 3-5: Pseudo-elastic moduli and ultimate nominal stresses obtained from tensile test on C/PEKK and from room temperature to 200°C at 1 mm/min 95
Tab. 3-6: Color code employed for defining each as received material 97
Tab. 3-7: Creep-recovery test parameters for PEKK 7002 SC 102
Tab. 3-8: Creep-recovery test parameters for C/PEKK 103
Tab. 3-9: PEKK 7002 SC Permanent strain after recovery for each creep-recovery test condition 105
Tab. 3-10 C/PEKK Permanent strain after recovery for each creep-recovery test condition 108
Tab. 3-11: A, m and n parameters of creep power law for PEKK 7002 SC 111
Tab. 3-12: A, m and n parameters of creep power law for C/PEKK 113
Tab. 3-13: .Coefficients of WLF law at each test temperatures 115
Tab. 3-14: .Coefficients of WLF law at each test temperatures 115
Tab. 3-15: T_g and T_m measured from DSC test on PEKK 7002 SC and C/PEKK samples cut from as-received material 118
Tab. 4-1: PEKK 7002 SC Thermal expansion coefficients below and above T_g 133
Tab. 4-2: CDP test parameters for PEKK 7002 SC 135
Tab. 4-3: CDP +R test parameters for PEKK 7002 SC 136
Tab. 4-4: Stress and strain shift for the CDP and CDP+R reloads and unloads 139
Tab. 4-5: Tg, Tm and peaks enthalpy measured from DSC test on PEKK 7002 SC samples cut from as-received material, after tensile test at 1 mm/min and 200°C and dummy sample exposed at 200°C for the same duration of tensile test 145
Tab. 4-6: PEKK 7002 SC crystallinity percentage values measured through DSC test on as received specimens 146
Tab. 4-7 PEKK 7002 SC crystallinity percentage values measured through DSC test on specimens cut from specimen after different thermomechanical loads 151
Tab. 4-8 PEKK 7002 SC crystallinity percentage values measured through DSC test on specimens cut from specimen after different thermal loads 152
Tab. 4-9: Parameters of the Avrami equation at the different test temperatures 153
Tab. 4-10: Parameters of the Avrami equation at the different test temperatures 154
Tab. 4-11: Mechanisms activation loading conditions in CDP tests. 161
Tab. 4-12: Mechanisms activation loading conditions in creep-recovery tests. 162
Tab. 4-13: Reload and unload initial conditions 165
Tab. 4-14: Parameters of the model at different temperatures 174
Tab. 4-15: PEKK 7002 AM tensile test conditions 183
Tab. 4-16: Initial tensile moduli and Poisson's coefficient obtained from tensile test on PEKK 7002 AM and from room temperature to 180°C at 1 mm/min 188

Tab. 4-17 Tg, Tm and peaks enthalpy measured from DSC test on PEKK 7002 AM and SC samples cut from as-received material *191*
Tab. 4-18: PEKK 7002 AM crystallinity percentage values measured through DSC test on specimens cut from specimen on as received material and after tensile tests at different test temperature *193*
Tab. 4-19: Primary crystallization percentage produced after an isothermal duration of the same duration of tensile tests on PEKK AM, according to the PEKK 7002 crystallization kinetics proposed by (Tanguy Choupin 2018) *195*
Tab. 4-20: CDP test parameters for PEKK 7002 SC *198*
Tab. 4-21: Comparison of the parameters of the model at the same distance from T_g for PEKK AM and PEKK SC *199*
Tab. 5-1: Input and output of the PEKK 3-D model for tensile-creep solicitations *216*
Tab. 6-1: Ageing conditions *243*
Tab. 6-2: T_g, T_m and peaks enthalpy measured from DSC test on PEKK 7002 SC samples cut from as-received material, after ageing at 200°C and 5 bar of O_2 for 42 days *246*
Tab. 6-3: T_g onsets and the initial storage and loss moduli, as well as the initial tanδ for PEKK 7002 SC as received (orange) and after ageing at 200°C and 5 bar of O_2 for 42 days *248*
Tab. 6-4: Creep test parameters for C/PEKK under air *251*
Tab. 6-5: Power law parameters for the creep tests carried out at 200°C in not-conditioned atmosphere *252*
Tab. 6-6: Creep test parameters for C/PEKK for coupling with aging *253*

Tab. B- 1: Absolute and percentage error produced by the random error on longitudinal and transversal strains, on the volumetric change and on the stress vs strain curve *272*

Tab. H- 1: C/PEKK normalized stress distribution compared to 8-ply stacking sequence *309*
Tab. H- 2: C/PEKK composite properties calculated through the semi-analytical method at 165°C, 180°C and 200°C *309*
Tab. H- 3: : C/PEKK ply properties calculated through the semi-analytical method at 165°C, 180°C and 200°C *309*

List of Figures

Fig. 1-1: Upper longeron of A350-1000 pylon, (Vinet et al. 2019)..... 3
Fig. 1-1: Portion of composite materials in Airbus aircrafts (by courtesy of H. Assler, Airbus Deutschland GmbH) (Kaufmann 2008)..... 7
Fig. 1-2: Schematic representation of the detailed structure of a spherulite (William D. Callister 2007) 10
Fig. 1-3: Simplified schematization of interlamellar crystallization phenomenon, (Boyard et al. 2017).. 12
Fig. 1-4: Relative fraction crystallinity at vs tile with the Hillier model for the overall crystallization (solid curves), the primary (dashed curves) and the secondary crystallization (dashed dotted curves) at 230°C for neat PEKK 6002 crystallized from the melt, (Tanguy Choupin 2018)..... 13
Fig. 1-5: TTT diagram of the relative crystallinity for the overall crystallization for PEKK 7002 crystallized from the melt, (Tanguy Choupin 2018)..... 14
Fig. 1-6: Micrographs of PEKK 6002 with carbon fibers crystallized from the melt at 270°C during 2h, (Tanguy Choupin 2018)..... 15
Fig. 1-7: Young modulus vs crystallinity at room temperature (a) and at 180°C (b) of neat PEKK crystallized at 230°C from the glassy state with a strain rate of 3.3 s^{-1}, (Tanguy Choupin 2018)..... 16
Fig. 1-8: Stages in the plastic deformation of a semicrystalline polymer. (a) Two adjacent chain-folded lamellae and interlamellar amorphous material after elastic deformation; (b) Tilting of lamellar chain folds. (c) Separation of crystalline block segments. (d) Orientation of block segments and tie chains with the tensile axis in the final plastic deformation stage, (William D. Callister 2007)..... 17
Fig. 1-9: (a) Stress/strain curves for off-axis specimens of continous fiber systems measured at 177°C (b) Variation of apparent moduli with respect to temperature for LDF (discontinous fiber) and continous fiber systems. (Sun, Chung, and Chang 1992)..... 21
Fig. 1-10: (a) Evolution of the Young modulus of UD fully crystallized PEKK composites manufactured under autoclave tested at room temperature and at180°C.(b) Evolution of the Young modulus (upper figure)

and shear modulus (lower figure) of ±45° fully crystallized from the melting state and amorphous PEKK composites manufactured under press tested at room temperature and at180°C (Tanguy Choupin 2018) 21
Fig. 1-11: Dependence of polymer properties as well as melting and glass transition temperatures on molecular weight. (From F.W. Billmeyer, Jr., Textbook of Polymer Science, 3rd edition. Copyright © 1984 by John Wiley & Sons, New York. Reprinted by permission of John Wiley & Sons, Inc.) (William D. Callister 2007)..... 23
Fig. 1-12: Schematic representations of (a) linear, (b) branched, (c) crosslinked, and (d) network (three-dimensional) molecular structures. Circles designate individual repeat units, (William D. Callister 2007). 25
Fig. 1-13: PEKK 7002 AM films aged at 280°C on air (ENSAM Paris) (Roland and Fayolle 2020) 25
Fig. 1-14: Mass loss (a), fluorenone concentration (b), the branching (c) and the molar mass (d) evolution with the exposure time at 200°C (grey), 250°C (blue), 280°C (black), 300°C (red) (Roland and Fayolle 2020)..... 26
Fig. 1-15: Mass loss (a) and fluorenone concentration (b) evolution with the exposure time at 200°C under 5 bar of O_2 (Roland and Fayolle 2020)..... 27
Fig. 1-16: Schematization of the different known and unknown aspects of the PEKK and PEKK composite behavior, for the different ranges of temperature. 29
Fig. 2-1: Chemical structure of a monomer of PEKK. 35
Fig. 2-2: PEKK plates environment for crystallization from the melt (Tanguy Choupin 2018)..... 36
Fig. 2-3: C/PEKK ply stacking 37
Fig. 2-4: C/PEKK manufacturing thermal protocol..... 37
Fig. 2-5: Specimens employed for the experimental campaign..... 38
Fig. 2-6: Tensile, load-unload-reload and creep-recovery tests experimental equipment..... 43
Fig. 2-7: Thermal protocol..... 44
Fig. 2-8: Tensile test protocol..... 44
Fig. 2-9: Creep-recovery test protocol..... 45
Fig. 2-10: Load-unload-reload protocol..... 46
Fig. 2-11: TA Instrument DMA Q800 47
Fig. 2-12: DMA test protocol..... 47
Fig. 2-13: TA Instruments DSC Q20 (a) and RCS 90(b)..... 48
Fig. 2-14: Q20 heath flow sensor 48
Fig. 2-15: DSC test protocol..... 49
Fig. 2-16: TOPIN 2344 50
Fig. 2-17: Instron 1251..... 51
Fig. 2-18: Creep test under 5 bars of O_2 test protocol..... 52
Fig. 2-19: RX Solution UltraTom XL..... 53
Fig. 2-20: IdPix graphic interface and box definition around the markers..... 55
Fig. 2-21: IdPix graphic interface and markers monitoring during the test 55
Fig. 2-22: IdPix measures on the specimen surface 56
Fig. 2-23: Control screen of the tensile test machine: on the top there are the real time values of applied force, longitudinal and transversal strain; in the bottom, their curves against the time. 57

Fig. 2-24: Marker degradation: comparison of marker at the beginning (a) and at the and (b) of a test 57
Fig. 2-25: Camera in front of the oven employed during high temperature tests. 58
Fig. 2-26: Pattern painted on the specimen gauge length..... 59
Fig. 2-27: User defined area..... 62
Fig. 2-28: Threshold value vs image number..... 63
Fig. 2-29: LAT Image analysis algorithm..... 65
Fig. 2-30: LAT Calculation algorithm..... 67
Fig. 2-31: LAT Complete algorithm..... 68
Fig. 2-32: LAT (blue) and IdPix (red) searching areas (a) and correspondent initial coordinates measured (b)..... 70
Fig. 2-33: Difference between each markers center mass position calculated by LAT and IdPix along the tensile test..... 70
Fig. 2-34: Comparison between the logarithmic longitudinal (a) and the transversal (b) strains measured by IdPix and LAT...... 71
Fig. 2-35: LAT (blue) and Correla (red) searching areas (a) and correspondent initial coordinates measured (b)..... 72
Fig. 2-36: Total Lagrangian(a) and Eulerian (b) longitudinal strains, calculated by Correla (red) and LAT (blue)...... 73
Fig. 2-37: Employed measurement system..... 73
Fig. 2-38:Schematization of the homogenization method..... 74
Fig. 2-39: Schematization of a ply with continuous long fibers (a) and representation of bonded slabs of fiber and matrix materials (b) (Hull and Clyne 1996) 75
Fig. 2-40: Ply reference system (a) and composite reference system (b)..... 76
Fig. 2-41: Schematization of the localization method..... 80
Fig. 3-1: Force vs displacement curves at different temperature at 1 mm/min on PEKK 7002 SC specimens 87
Fig. 3-2: True stress vs longitudinal and transversal true strains from tensile tests at different temperature at 1 mm/min on PEKK 7002 SC specimens..... 88
Fig. 3-3: Nominal stress vs longitudinal nominal strains from tensile tests at different temperature at 1 mm/min on C/PEKK specimens..... 89
Fig. 3-4: Stress vs strain curves obtained from tensile test on PEKK 7002 SC and at 165°C, 180°C and 200°C at 0.1 mm/min, 1 mm/min and 10 mm/min..... 90
Fig. 3-5: Nominal stress vs nominal strain obtained from tensile tests on C/PEKK at 165°C, 180°C and 200°C at 0.1 mm/min, 1 mm/min and 10 mm/min..... 91
Fig. 3-6: C/PEKK matrix dominated region (a) and fiber dominated region (b) 91
Fig. 3-7: C/PEKK specimen's surface (a) and fiber rotation at different times during tensile test (b)..... 92
Fig. 3-8: C/PEKK Fiber orientation vs nominal stress measured during tensile tests at 165°C, 180°C, 200°C..... 93
Fig. 3-9: Linear regression between 0.1% and 0.4% of PEKK 7002 SC true strain vs longitudinal true strain curve at different temperature at 1 mm/min..... 94
Fig. 3-10 Pseudo-elastic moduli vs temperature obtained from tensile test on PEKK 7002 SC from room temperature to 200°C at 1 mm/min 94

Fig. 3-11: Linear regression between 0.05% and 0.3% of C/PEKK nominal strain vs longitudinal nominal strain curve at different temperature at 1 mm/min *95*
Fig. 3-12: Pseudo-elastic moduli (a) and ultimate nominal stresses (b) vs temperature obtained from tensile test on C/PEKK from room temperature to 200°C at 1 mm/min *96*
Fig. 3-13: 3-point bending DMA storage modulus (a), loss modulus (b) and tan delta (c) for PEKK 7002 SC *98*
Fig. 3-14: DMA storage modulus between 20°C and 200°C, compared with pseudo-elastic moduli *98*
Fig. 3-15: 3-point bending DMA storage modulus (a), loss modulus (b) and tan delta (c) for C/PEKK *99*
Fig. 3-16: Comparison between C/PEKK SC (grey) and PEKK SC (orange) DMA storage modulus between 20°C and 200°C, compared with pseudo-elastic moduli as measured values(a) and as ratio respect to initial values (b). *100*
Fig. 3-17: Creep stress applied to the composite at 165°C, 180°C and 200°C *103*
Fig. 3-18: True longitudinal strain vs time curve obtained from a creep-recovery test on PEKK 7002 SC. *104*
Fig. 3-19: PEKK 7002 SC true longitudinal strain vs time curve of the creep phase (a) and recovery phase (b) plotted in logarithmic scale. *105*
Fig. 3-20: PEKK 7002 SC Permanent strain after recovery vs test temperature (a) and creep stress (b) *106*
Fig. 3-21: Nominal longitudinal strain vs time curve obtained from a creep-recovery test on C/PEKK. *106*
Fig. 3-22: C/PEKK true longitudinal strain vs time curve of the creep phase (a) and recovery phase (b) plotted in logarithmic scale. *107*
Fig. 3-23: C/PEKK Permanent strain after recovery vs test temperature (a) and creep stress (b) *108*
Fig. 3-24: C/PEKK Fiber orientation vs time (a) and nominal strain (b) measured during creep test at 180°C , at creep stress equal to 0.5 σuC. *109*
Fig. 3-25: Comparison between the PEKK 7002 SC measured data and the fitted curve, with one (n) (a), and two (n and m) fixed parameters (b), relatively at the data obtained from creep test at 180°C. *110*
Fig. 3-26: PEKK 7002 SC A (a) and m (b) parameter of the power law plotted against the temperature (case of one fixed parameter) and A(c) parameter of the power law plotted against the temperature (case of m=cost at each temperature). *111*
Fig. 3-27: Comparison between the C/PEKK measured data and the fitted curve, with one (n) and two (n and m) fixed parameters, relatively at the data obtained from creep test at 180°C. *112*
Fig. 3-28: C/PEKK A (a) and m (b) parameter of the power law plotted against the temperature (case of one fixed parameter) and A(c) parameter of the power law plotted against the temperature (case of m=cost at each temperature). *113*
Fig. 3-29: WLF law applied to the creep compliance of the semicrystalline PEKK *115*
Fig. 3-30: WLF law applied to the creep compliance of the semicrystalline PEKK *116*
Fig. 3-31: Typical heath flow vs temperature curves obtained from DSC test on PEKK 7002 SC *117*
Fig. 3-32: 1st (a), 2nd heating (b) and cooling (c) phases comparison from DSC test on C/PEKK and PEKK 7002 SC samples cut from as-received material *118*
Fig. 3-33: Linear elastic analytical method algorithm *121*

Fig. 3-34: Tensile test bijectivity property between stress, strain, secant modulus and Poisson's coefficient *122*
Fig. 3-35: Non-linear analytical method algorithm *123*
Fig. 3-36: Comparison between experimental tensile test on C/PEKK at 1 mm/min 165°C, 180°C and 200°C and the non-linear semi-analytical method *123*
Fig. 4-1: PEKK 7002 SC Volumetric change measured during tensile tests heating phase *132*
Fig. 4-2: PEKK 7002 SC volume change from tensile tests at different temperature at 1 mm/min, according to logarithmic formulation (a) and Total Lagrangian formulation (b) *133*
Fig. 4-3: PEKK 7002 SC Poisson's coefficients from tensile tests at different temperature at 1 mm/min *134*
Fig. 4-4: Stress vs strain curves obtained from CDP test on SC PEKK and at 165°C, 180°C and 200°C, compared with the stress vs strain curves obtained from tensile test at 1 mm/mina at the same temperatures *135*
Fig. 4-5: Stress vs strain curves obtained from CDP and tensile tests on SC PEKK and at 200°C ... *136*
Fig. 4-6: Stress vs strain curves obtained from CDP+R and tensile tests on SC PEKK and at 200°C. a) maximum loop stress = 2.5, 6.5, 9.3 MPa and b) maximum loop stress 9.3 MPa *137*
Fig. 4-7: Reloads of CDP '(a) and CDP+R (b) *138*
Fig. 4-8: Comparison of reload (a), unload (b) shifted to zero obtained from CPD and CDP+R tests on PEKK SC at 200°C at 1 mm/min, and overall comparison of both in absolute value (c) *139*
Fig. 4-9: Comparison of unload obtained from CDP tests(a), Creep-recovery tests (b) on PEKK SC at 200°C and overall comparison (c) *141*
Fig. 4-10: Comparison of recovery strain vs time curves obtained from CDP+R tests and Creep-recovery tests (a) on PEKK SC at 200°C and comparison of the recoveries normalized respect to the maximum stress applied to the specimen(b) *142*
Fig. 4-11: Comparison of creep strain vs time curves obtained from Creep-recovery tests on PEKK SC at 200°C, normalized respect to the creep stress applied to the specimen(b) *142*
Fig. 4-12: 1st (a), 2nd heating (b) and cooling (c) phases comparison from DSC test on PEKK 7002 SC samples cut from as-received material, after tensile test at 1 mm/min and 200°C and dummy sample exposed at 200°C for the same duration of tensile test *145*
Fig. 4-13: 1st heating phases comparison from DSC test on PEKK 7002 SC samples cut from as-received material and after tensile tests and dummy samples at 200°C (a), 180)C (b) and 165°C (c) *148*
Fig. 4-14: 1st heating phases comparison from DSC test on PEKK 7002 SC samples cut from as-received material and Load-Unload-Reload with and without recovery at 200°C *148*
Fig. 4-15: 1st heating phases comparison from DSC test on PEKK 7002 SC samples cut from as-received material and after creep-recovery tests and dummy samples at 200°C (a), 180)C (b) and 165°C (c) .. *149*
Fig. 4-16: 1st heating phases comparison from DSC test on PEKK 7002 SC samples cut from as-received material and after ageing under 5 bar of O_2 at 200°C *149*
Fig. 4-17 PEKK SC measured crystallinity percentage vs test duration (solid marker) or exposure time (blank markers) at 165°C, 180°C and 200°C *150*
Fig. 4-18: PEKK SC corrected variation of crystallinity percentage vs test duration (solid marker) or exposure time (blank markers) at 165°C, 180°C and 200°C *153*
Fig. 4-19: Relative crystallinity vs exposure time at 180°C and 200°C *156*

Fig. 4-20: Schematization of PEKK SC crystalline structure evolution during exposure to isothermal load at T> T_g *158*
Fig. 4-21: Schematization of PEKK SC crystalline structure evolution during CDP tests at T> T_g ... *160*
Fig. 4-22: Schematization of PEKK SC crystalline structure evolution during creep-recovery tests at T> T_g *161*
Fig. 4-23: Young modulus vs crystallinity at 180°C of neat PEKK crystallized at 230°C from the glassy state with a strain rate of 3.3 s^{-1}, (Tanguy Choupin 2018), PEKK 7002 SC E_0 at 165°, 180°C and 200°C(respectively green, yellow and black markers) at χ=24.3%, E_0 vs χ curve for PEKK 7002 SC at 180°C and 200°C for elastic stiffness (yellow and black dashed curve) and increase of E_0 during creep produced by exposure at 180°C and 200°C for 48h. *168*
Fig. 4-24: Total strain (black), strain variation produced by crystallinity increase (blue) and resulting viscoplastic strain (red) for a creep test at 70% of σth and 200°C *169*
Fig. 4-25: Comparison of the A parameter vs strain rate from tensile tests (orange) and from creep tests (black). In dashed red the fitting for creep test *169*
Fig. 4-26: Evolution of the parameters of the 1-D model with the temperature *175*
Fig. 4-27: Comparison between the 1-D model and the experimental tensile curves at 0.1 (a), 1 (b) and 10 (c) mm/min at 200°C *176*
Fig. 4-28: Comparison between the 1-D model and the experimental CDP curve at 1 mm/min at 200°C *176*
Fig. 4-29: Comparison between the 1-D model and the experimental creep-recovery curves at 0.7σ_{th} (a), 0.5σ_{th} (b) and 0.3σ_{th} (c) mm/min at 200°C *177*
Fig. 4-30: Comparison between the 1-D model and the experimental tensile curves at 0.1 (a), 1 (b) and 10 (c) mm/min at 180°C *178*
Fig. 4-31: Comparison between the 1-D model and the experimental CDP curve at 1 mm/min at 180°C *178*
Fig. 4-32: Comparison between the 1-D model and the experimental creep-recovery curves at 0.7σ_{th} (a), 0.5σ_{th} (b) and 0.3σ_{th} (c) mm/min at 180°C *179*
Fig. 4-33: Comparison between the 1-D model and the experimental tensile curves at 0.1 (a), 1 (b) and 10 (c) mm/min at 165°C *179*
Fig. 4-34: Comparison between the 1-D model and the experimental CDP curve at 1 mm/min at 165°C *180*
Fig. 4-35: Comparison between the 1-D model and the experimental creep-recovery curves at 0.7σ_{th} (a), 0.5σ_{th} (b) and 0.3σ_{th} (c) mm/min at 165°C *180*
Fig. 4-36: Temperature and longitudinal strain curves plotted against time from for heating and tensile phases at 165°C (a) and180°C (b) *183*
Fig. 4-37: Images acquired during heating phase up to 180°C of PEKK 7002 AM specimens *184*
Fig. 4-38: Force vs displacement curves at different temperature at 1 mm/min on PEKK 7002 AM specimens *185*
Fig. 4-39 True stress vs longitudinal and transversal true strains from tensile tests at different temperature at 1 mm/min on PEKK 7002 AM specimens *186*
Fig. 4-40 PEKK 7002 AM volume change from tensile tests at different temperature at 1 mm/min, according to logarithmic formulation *187*

Fig. 4-41: PEKK 7002 AM Poisson's coefficients from tensile tests at different temperature at 1 mm/min *187*
Fig. 4-42 Pseudo-elastic moduli vs temperature obtained from tensile test on PEKK 7002 AM from room temperature to 180°C at 1 mm/min *188*
Fig. 4-43: Comparison between PEKK AM (yellow) and PEKK SC (orange) DMA storage modulus between 20°C and 200°C, compared with pseudo-elastic moduli as measured values(a) and as ratio respect to initial values (b). *189*
Fig. 4-44: 1st (a), 2nd heating (b) and cooling (c) phases comparison from DSC test on PEKK 7002 AM and SC samples cut from as-received material *190*
Fig. 4-45: 1st heating phases comparison from DSC test on PEKK 7002 AM samples cut from as-received material and after tensile tests at room temperature, 100°C, 150°C, 165°C and 180°C. *192*
Fig. 4-46: PEKK AM measured crystallinity percentage vs test temperature from DSC test on samples cut after tensile tests at room temperature, 100°C, 150°C, 165°C and 180°C. *193*
Fig. 4-47: Comparison between the total crystallinity measured on PEKK AM after tensile tests at 150°C, 165°C and 180°C and the esteemed crystallinity according to Choupin, at same temperature and for the same duration than tensile test (red markers). Estimation at 200C°, after 4 min of exposure *195*
The comparison showed in FIG. 4-48 shows: *195*
Fig. 4-49: Representation of the mechanical and thermal contribution to the crystallization energy for PEKK 7002 AM and the values corresponding to the temperature chosen for the tensile tests *197*
Fig. 4-50: Comparison between CDP and tensile test carried out on PEKK AM at 165°C and 1 mm/min *198*
Fig. 4-51: Comparison between the 1-D model and PEKK AM experimental tensile curve at 1 mm/min at 165°C *200*
Fig. 4-52: Comparison between the 1-D model and PEKK AM experimental CDP curve at 1 mm/min at 165°C *200*
Fig. 5-1: Comparison between experimental data, obtained from a tensile test on PEKK SC at 1 mm/min and 200°C, and the simulation with not limited tangent modulus (red - Model) and limited tangent modulus (orange – Model limit E). *213*
Fig. 5-2: Comparison between the simulation of tensile (orange) and shear (blue) solicitations with limited tangent modulus in term of true stress vs true strain (a) and equivalent stress vs equivalent strain (b). ... *214*
Fig. 5-3 Comparison between the equivalent secant modulus obtained from tensile (orange) and shear (blue) solicitation. *215*
Fig. 5-4: Schematization of the algorithm for the simulation of the tensile-creep solicitations. *217*
Fig. 5-5: Results of the tensile-creep simulation: comparison between the experimental longitudinal strain and the shear strain vs the time; b) stress vs time;the blue curves represent the inputs and the red ones the outputs of the model *217*
Fig. 5-6: Laminate, ply and matrix levels for the $[(\pm 45)_{2s}, +45]_s$ *C/PEKK composite, from images acquired at the optical microscope and as schematization.* *219*
Fig. 5-7: Non-linear analytical method algorithm with the implementation of the PEKK 3-D model for tensile solicitations. *219*

Fig. 5-8: Comparison between experimental tensile test on C/PEKK at 1 mm/min at 200°C and the simulation with SAHLM, not considering the fiber rotation (a) and taking the rotation into account (b). *221*
Fig. 5-9: a) Ply stress in global coordinates vs time; b) Ratio in absolute value between ply stress and longitudinal composite stress over time. *222*
Fig. 5-10: a) Matrix non-zero components of the strain tensor vs time; b) matrix equivalent strain rate (blue), its mean (dotted magenta) and composite equivalent strain rate (red). *223*
Fig. 5-11: a) Matrix equivalent stress vs equivalent strain (blue) and matrix shear stress vs shear strain (red); b) matrix equivalent equivalent secant modulus (Magenta), longitudinal (red)and shear (black) tangent moduli over time. *223*
Fig. 5-12: Non-linear analytical method algorithm with the implementation of the PEKK 3-D model for creep solicitations. *224*
Fig. 5-13: Fiber rotation angle during creep phase vs creep time (a) and vs the longitudinal creep strain of the composite (b): in black the measurements on the creep test at 200°C, in yellow the measurements on the creep test at 180°C. *226*
Fig. 5-14: Comparison between experimental creep test on C/PEKK at 200°C, 28 MPa for 48h and the simulation with SAHLM, not considering the fiber rotation during creep (a) and taking the rotation into account (b) with different values of $a\Theta$ *parameter.* *227*
Fig. 5-15: Comparison between experimental creep test on C/PEKK at 200°C, 28 MPa for 48h and the simulation with SAHLM, considering $a\Theta$*=120 and 42 days* *227*
Fig. 5-16: Composite stress vs composite strain from simulations with SAHLM, of the 0° laminate (a) 90°laminate (b). *229*
Fig. 5-17: Ply stress in global coordinates vs time from simulations with SAHLM, of the 0° laminate (a) 90°laminate (b). *229*
Fig. 5-18: Matrix equivalent and deviatoric stress vs strain, equivalent strain rate vs time and tangent andsecant moduli vs time curves, from simulations with SAHLM, of the 0° laminate (a,c,e respectilvely) 90°laminate (b,d,f respectilvely). *231*
Fig. 5-19: SAHLM algorithm for tensile solicitations for multiple ply orientations. *232*
Fig. 5-20: SAHLM algorithm for creep solicitations for multiple ply orientations. *233*
Fig. 5-21: QI simulations with SAHLM, of a QI laminate: composite stress vs composite strains (a) ply longitudinal(b), transversal (c) and shear (d) stress vs time for each ply orientation. *234*
Fig. 5-22: Matrix equivalent stress vs strain (a), equivalent strain rate vs time (b) and tangent moduli vs time (c) curves, from simulations with SAHLM, of the QI laminate: comparison between the results of the matrix in the ply at 0° (red), 90° (blue), ±45° (black). *236*
Fig. 5-23: QI simulation with SAHLM, of a QI laminate under tensile-creep solicitation: composite strain vs time *236*
Fig. 5-24: Matrix equivalent strain vs time (a), secant moduli vs time (b) curves, from simulations with SAHLM, of the QI laminate: comparison between the results of the matrix in the ply at 0° (red), 90° (blue), ±45° (black). *237*
Fig. 6-1: PEKK SC specimen aged at 200°C in 5 bar of O2 conditioned atmosphere for duration from 7 to 42 days *243*

Fig. 6-2: PEKK SC specimen aged at 200°C under 5 bar of O2 for 42 days (a), images of its cross-section at different magnification factors (b and c), images color scale (d) and y-direction image gradients (e) and relative normalized means of each column of pixel *245*
Fig. 6-3: 1st (a), 2nd heating (b) and cooling (c) phases comparison from DSC test on PEKK 7002 SC samples cut from as-received material, after ageing at 200°C and 5 bar of O2 for 42 days *246*
Fig. 6-4: 3-point bending DMA storage modulus (a), loss modulus (b) and tan delta (c) for PEKK 7002 SC as received (orange) and after ageing at 200°C and 5 bar of O2 for 42 days *248*
Fig. 6-5: C/PEKK as received specimen sections in the longitudinal-transverse plane, from one surface (first image) to the other (last image) in the thickness direction, obtained with μ-tomography *249*
Fig. 6-6: C/PEKK aged at 200°C under 5 bar of O_2 for 42 days specimen sections in the longitudinal-transverse plane, from one surface (first image) to the other (last image) in the thickness direction, obtained with μ-tomography *250*
Fig. 6-7: Evolution of the A parameter of the Norton-Bailey equation with the creep stress for C/PEKK at 200°C under air *252*
Fig. 6-8: Nominal longitudinal strain vs time curve obtained from creep test on C/PEKK at 200°C under 5 bar of O_2 and images of the progressive marker degradation. *253*
Fig. 6-9: Comparison of the creep strain carried out at 200°C in non-conditioned atmosphere (grey curves) and in conditioned atmosphere (orange curve). *254*
Fig. 6-10: Nominal stress vs time registered by the Instron 1251 internal (red) and external (blue) (a) and position vs time registered by Instron 1251 LVDT (b) during the creep test on C/PEKK at 200°C under 5 bar of O_2 ..... *255*
Fig. 6-11: Comparison of the creep stress carried out at 200°C in non-conditioned atmosphere (grey curves) and in conditioned atmosphere (orange curve). *255*
Fig. 6-12: Creep strain measured at 200°C in non-conditioned atmosphere (gray) and they respective fitting (red) and creep strain at 200°C under 5 bar of O_2 (orange), with calculated strain, taking into account the variable creep stress (blue) *256*
Fig. 6-13: Creep strain measured at 200°C in non-conditioned atmosphere (gray) and they respective fitting (red) and creep strain at 200°C under 5 bar of O_2 (orange), with calculated strain, taking into account the scaled variable creep stress (blue) *257*
Fig. 6-14: C/PEKK tested at creep at 200°C under 5 bar of O_2 for 42 days specimen sections in the longitudinal-transverse plane, from one surface (first image) to the other (last image) in the thickness direction, obtained with μ-tomography *258*

Fig. A- 1: PEKK 7002 specimen type b *269*
Fig. A- 2: C/PEKK specimen type d *269*

Fig. B- 1: Comparison between measured displacement field (blue), constant error (brown) and random noise (red) *271*
Fig. B- 2: Effect of the different noise levels on the measure of longitudinal (a) and transversal (b) strains. *272*

Fig. B- 3: Marker extreme degradation (a) and center of mass (red dots) identified on connected groups (b) *273*
Fig. B- 4: Image subsets definition through image diagonals *273*
Fig. B- 5: Convex hull operation on all the groups of connected pixels constituting Marker 1 ..... *275*

Fig. C- 1: Image reference system (a) and specimen reference system (b) *276*
Fig. C- 2: Image reference system (a) and specimen reference system (b) recording the x-z face *281*
Fig. C- 3: Comparison of the derivatives of the displacement fields measured in the tensile tests recording the x-y face (blue curves) and x-z face (red curves) *283*

Fig. D- 1: Comparison between complete displacement field approximation and cubic approximated displacement field evaluated from the markers *284*
Fig. D- 2: Comparison between complete displacement field approximation and linear approximated displacement field evaluated from the markers *285*
Fig. D- 3: Comparison of the first derivative in x direction of the complete displacement field and the displacement field evaluated from the markers approximated with cubic polynomial function (a) and linear one (b) and comparison of the averaged derivative (c) *285*
Fig. D- 4: Comparison of the first derivative in y direction of the complete displacement field and the displacement field evaluated from the markers approximated with cubic polynomial function (a) and linear one (b) and comparison of the averaged derivative (c) *286*

Fig. E- 1: Deformed and undeformed configuration for Total Lagrangian, Update Lagrangian and Eulerian formulations *288*

Fig. F- 1: Schematization of Correla searching window and sub windows *296*
Fig. F- 2: Initial and final position of the points found by Correla (respectively in red and black) and by IAT (respectively in blue and magenta) for the Range 1 of images *297*
Fig. F- 3 Initial points found by Correla (in red) and by IAT (in blue) for the Range 2 of images, compared with the final points found by Correla (in purple) for the Range 1. ..... *298*
Fig. F- 4: Trajectories of the points evaluated by Correla in Range 2 (in red) and respect to the initial frame (in green), and the trajectory evaluated by IAT (in blue) *299*
Fig. F- 5: Comparison of the trajectories evaluated by Correla (in red) and by IAT (in blue): a) longitudinal position of the points plotted against the time, b) transversal position of the points plotted against the time, c) longitudinal position points plotted against their transversal position *300*
Fig. F- 6: Total Lagrangian(a) and Eulerian (b) longitudinal strains, calculated by Correla (red) and IAT (blue) *300*

Fig. H- 1: C/PEKK stress distribution in the composite, normalized respect to the composite longitudinal stress and compared to the equivalent 8-ply stacking sequence stress distribution *308*

1. Résumé étendu

I - Introduction et contexte

La tendance actuelle dans l'utilisation des matériaux en aéronautique est cohérente avec l'objectif de réduire la masse des structures en remplaçant les matériaux métalliques utilisés de manière conventionnelle par des composites à matrice organique (CMO) plus légers.

Depuis les premières applications des CMO, les composites renforcés à matrice thermodurcissable ont été privilégiés, et en particulier les composites à base de résine époxydique, en raison du coût inférieur de la résine époxydique par rapport à d'autres polymères ayant des propriétés mécaniques similaires. Aujourd'hui, les composites à matrice thermodurcissable constituent plus de 90% des CMO utilisés dans l'aéronautique.

Cependant, leur impact écologique, ainsi que la possibilité d'augmenter la plage de température de fonctionnement des CMO, sont à l'origine de l'utilisation de composites à matrice thermoplastique, qui a commencé relativement plus tard et remonte aux années 80-90.

Aujourd'hui, la sensibilité et la conscience accrues des questions écologiques, combinées à l'augmentation exponentielle du trafic aéronautique et des flottes actives, ont mis en évidence le problème lié à l'impact écologique des avions, en termes d'émissions polluantes mais aussi en termes d'élimination des structures en fin de vie. Ceci est d'autant plus vrai en 2020.

Cette situation a donné une nouvelle impulsion à la recherche et à l'emploi de polymères thermoplastiques semi-cristallins de hautes performances comme matrice CMO pour les applications aéronautiques. Dans le domaine aéronautique, le polymère thermoplastique le plus utilisé (et le plus étudié) est le poly-éther-éther-keton (PEEK). Son coût, considérablement plus élevé que celui de la résine époxydique, ainsi que la température de fabrication requise (il doit atteindre la température de fusion, 400°C), empêchent un emploi plus large.

Pour cette raison, d'autres polymères ont été développés, comme le poly-éther-keton-keton (PEKK), fabriqué par Arkema sous le nom commercial de KEPSTAN™. Ce polymère a une structure chimique similaire à celui du PEEK, mais une température de fusion inférieure d'environ 40°C, ce qui réduit son coût de fabrication et, bien que ses propriétés et son comportement thermomécanique puissent être considérés comme similaires à ceux du PEEK, il a été nettement moins étudié.

En outre, outre la recyclabilité des polymères thermoplastiques, ils offrent la possibilité d'augmenter la plage de température de fonctionnement par rapport aux thermodurcissables. En effet, alors que ces derniers subissent une dégradation (après consolidation), s'ils sont exposés à des températures élevées, la température de transition vitreuse constitue leur limite. Certains polymères thermoplastiques sont capables de conserver une rigidité à des niveaux

plus élevés de température sans se dégrader, mais ils présentent également un changement d'état, passant de l'état solide à l'état caoutchoutique. Ce phénomène est généralement aussi associé à une perte de propriétés mécaniques, mais pourrait être atténué par la formation ou la préexistence de structures moléculaires ordonnées dans le matériau, les cristaux, qui ne subissent pas le même changement d'état de transition vitreuse, mais restent rigides jusqu'à la fusion.

L'interaction complexe entre le changement d'état dû à la température élevée, la présence et/ou la formation de structures cristallines et l'activation éventuelle de phénomènes de dégradation n'a pas été étudiée en profondeur dans le PEKK et constitue l'objectif du projet ImPEKKable, réalisé en collaboration entre Airbus SAS, Arkema, l'ENSAM de Paris et l'ISAE-ENSMA de Poitiers.

En particulier, le projet ImPEKKable vise à remplacer des composants du pylône de l'avion, actuellement fabriqués en composites IM/époxy à base de fibres de carbone dont les conditions de fonctionnement sont répertoriées dans le TABLEAU 1.

Temperature specifications	
Operative conditions	<150°C for 10000h
Critical event	180°C for 15 min
Critical load specifications	
	5 min at 180°C 10 min at 0.7 Limit load

Tableau 1: Spécifications opérationnelles requises pour le matériel, (Airbus SAS, Arkema, ENSMA - Poitiers, ENSAM - Paris 2018)

Le contenu et les activités du projet ImPEKKable visent à étudier ces phénomènes pour une nouvelle génération de composites à matrice thermoplastique (C / PEKK) afin de permettre une conception optimale des pièces, tout en assurant la durabilité appropriée pour chaque application prévue, (environ 80.000 heures sur un avion).

Compte tenu des plages de température visées (environ 180°C) et des propriétés actuelles des matrices polymères, le principal enjeu de la présente étude est d'évaluer le comportement à long terme des structures composites thermoplastiques travaillant au-dessus de leur température de transition vitreuse (T_g) et dans des conditions de service de structures portantes (sous contrainte, température, atmosphère oxydante).

Pour le PEKK et les composites à matrice PEKK, comme pour tout polymère thermoplastique et les composites à matrice thermoplastique, 3 grandes catégories principales d'investigation peuvent être identifiées :

- mécanisme de cristallisation ;

- comportement thermomécanique ;
- mécanismes de dégradation.

La FIGURE 1 schématise la plage de température pour laquelle les différents phénomènes sont/peuvent être actifs, ainsi que les aspects connus et inconnus du comportement du PEKK et des composites à matrice PEKK.

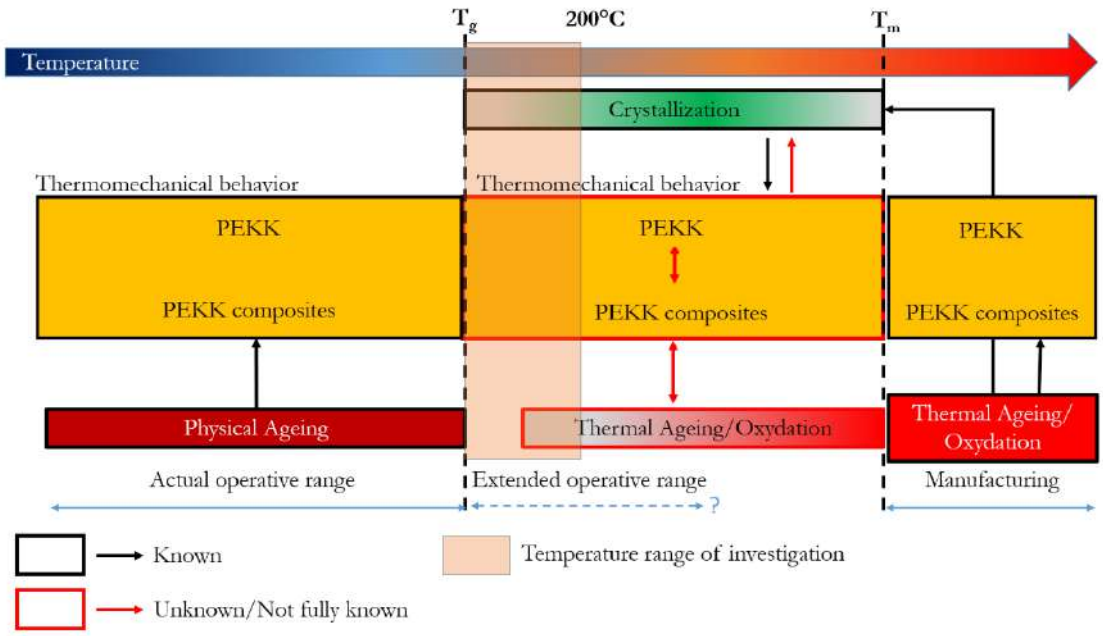

Figure 1: Schématisation des différents aspects connus et inconnus du comportement du PEKK et du composite C/PEKK, pour les différentes plages de température.

Le présent travail vise à étudier le comportement thermomécanique en traction et en fluage du PEKK et du composite C/PEKK à une température comprise entre T_g (~160°C) et 200°C, à ±20°C de la température ciblée de 180°C. Evidemment, l'interaction avec les mécanismes de cristallisation et de dégradation est étudiée.

Les similitudes de comportement en traction et en fluage entre la matrice du composite et le polymère pur sont également étudiées : une fois vérifiées ces similitudes, le comportement du composite a pu être reconstruit à partir de celui du polymère. Répondant à la question du comportement local de la matrice comparativement au comportement sous sa forme massive. Point essentiel dans les cas des thermoplastiques du fait de la structure cristalline.

II - Matériaux et méthodes

Une campagne expérimentale a été réalisée au cours de ce travail sur *le poly – éther – keton – keton* (PEKK), un polymère thermoplastique à haute performance de la famille des poly – aryle – éther - keton (PAEK). Sa structure chimique est représentée sur la FIGURE 2.

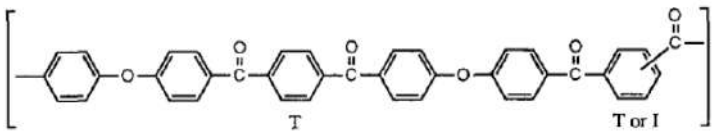

Figure 2: Structure chimique d'un monomère de PEKK.

Différentes configurations du PEKK peuvent être produites en faisant varier le rapport (T/I) entre l'acide téréphtalique (T) et l'acide isophtalique (I) qui le compose. Dans le présent travail, la PEKK 7002, avec un rapport T/I de 70/30, est étudiée.

La campagne expérimentale a été menée sur 3 configurations différentes du PEKK :

- PEKK 7002 amorphe (AM) (5% nominal de la phase cristalline, minimum réalisable pendant le processus de refroidissement), fabriqué par Arkema ;
- PEKK 7002 semi-cristalline (SC) (24% nominal de la phase cristalline, maximum réalisable pendant le processus de refroidissement), fabriqué par Arkema ;
- le composite $[(\pm 45)_2, +45]_s$ (C/PEKK), fabriqué par Airbus SAS à partir de pré imprégnés de fibres de carbone SC PEKK 7002 et AS4C, avec un taux de cristallinité fort (28% nominal de la phase cristalline, maximum réalisable pendant le processus de refroidissement).

Le comportement de ces matériaux est investigué à travers des essais de traction, fluage-recouvrance, charge-décharge, DMA et DSC pour caractériser le comportement et comprendre les mécanismes physiques sous-jacents.

Pour tous les essais visant à la caractérisation thermomécanique (traction, fluage-recouvrance et charge-decharge), l'équipement utilisé a permis de mesurer en temps réel :

- Température d'essai, mesurée par un thermocouple ;
- Déplacement, mesuré par un LVDT ;
- Force, mesurée par une cellule de charge ;
- Déformation longitudinale et transversale vraie, contrainte longitudinale vraie, mesurée par le logiciel IdPix, développé à l'ISAE-ENSMA, avec une technique de vidéo-extensomètrie.

Cette dernière technique a été utilisée pour chaque test, de la température ambiante à 200°C, sous air ou en atmosphère conditionnée : les conditions les plus sévères pour les matériaux sont également les plus préjudiciables pour cette technique et ont parfois dépassé ses limites

d'utilisation. En raison de la récurrence de cette situation pendant tous les tests à une température supérieure à la T_g du PEKK, une alternative à l'IdPix a été développée pour valider ses mesures et élargir leur champ d'applicabilité.

La capacité d'obtenir des mesures en temps réel, associée à un faible volume de données et à une mise en place relativement simple (faite en réalisant des marqueurs de peinture sur les échantillons) rendent IdPix irremplaçable.

D'autres techniques, comment la DIC ont été essayées, mais elles se sont montrées incompatibles avec IdPix. C'est la raison pour laquelle une nouvelle procédure de post traitement, l'IAT (*Image Analysis Tool*), a été élaborée, qui ne remplace pas IdPix mais qui lui est parfaitement complémentaire, agissant comme système de validation ou de correction.

L'IAT nécessite les mêmes images utilisées pendant le test par IdPix et la technique est capable de résoudre les principaux inconvénients d'IdPix : il est capable de reconstruire les marqueurs dégradés avec le temps et la température et de corriger les effets de lumière.

Des formulations lagrangienne et eulérienne ont étés implémentés, permettant de construire un champ comme avec une DIC . Contrairement à cette dernière, l'IAT ne nécessite pas de fenêtre de recherche mobile, puisqu'il recherche les marqueurs dans l'image entière ou dans un sous-ensemble fixe de celle-ci. Cette analyse est toujours plus rapide que l'analyse DIC, en raison de la taille inférieure des images acquises pour IdPix.

L'IAT a été validée par comparaison avec les résultats obtenus avec IdPix et la DIC, afin de vérifier, respectivement, les mesures logarithmiques et 3D du champ de déformation.

L'utilisation d'IdPix et de l'IAT permet d'obtenir un outil de mesure plus robuste : alors que le premier assure une mesure en temps réel, le second permet d'élargir le champ d'action, peut servir de système de vérification et, dans certains cas de sauvegarde, empêchant l'utilisateur de refaire les essais.

En ce qui concerne les méthodes numériques utilisées, les outils analytiques ont été choisis, car ils ont l'avantage de nécessiter moins de ressources de calcul par rapport à d'autres méthodes, comme les Eléments Finis, aux prix de ne pouvoir fournir que des valeurs moyennes des grandeurs simulées. Des méthodes d'homogénéisation (pour calculer les propriétés moyennes des plis et des composites) et des méthodes de localisation (pour évaluer la contrainte moyenne de déformation dans la matrice et dans les fibres) ont été utilisées.

Les méthodes d'homogénéisation permettent d'évaluer, à partir des propriétés de la matrice et des fibres, les propriétés moyennes des plis (par des méthodes de *micromécanique*) et, en fonction de la séquence et de l'orientation de l'empilement des plis, les propriétés du composite (par des méthodes de *théorie des stratifiés*). Une schématisation de la méthode d'homogénéisation utilisée est présentée à la FIGURE 3.

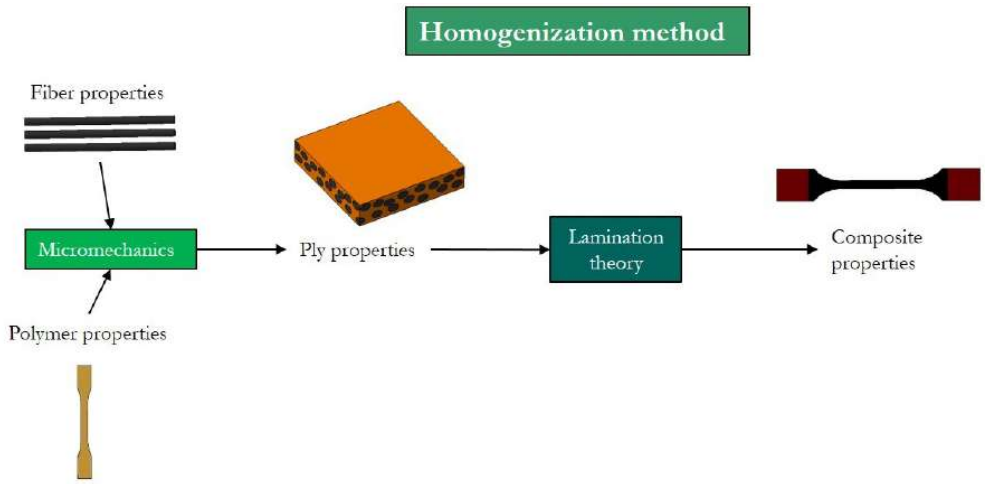

Figure 3: Schématisation de la méthode d'homogénéisation

Les méthodes de *localisation* agissent à l'opposé des méthodes d'homogénéisation, en permettant d'évaluer la contrainte à l'intérieur de la matrice et de la fibre, à partir de la déformation appliquée au pli. Une schématisation de la méthode de localisation employée est présentée à la FIGURE 4.

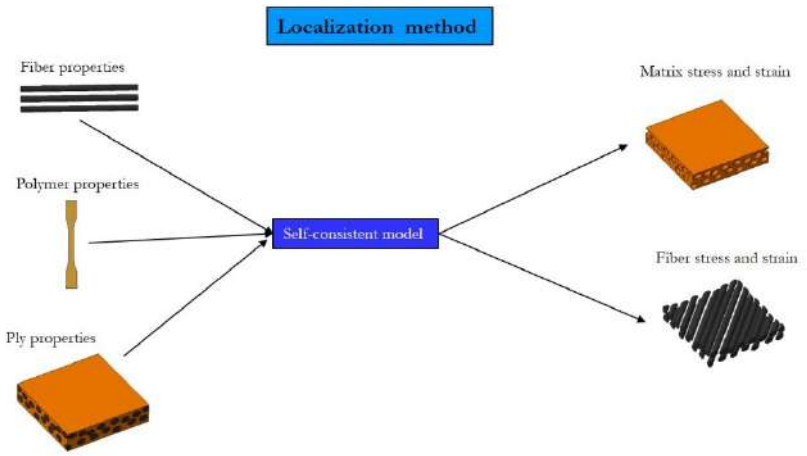

Figure 4: Schématisation de la méthode de localisation

III - Analyse préliminaire du comportement thermomécanique en traction et en fluage du PEKK SC et du C/PEKK

Pour la caractérisation du comportement thermomécanique en traction et en fluage du composite PEKK SC et C/PEKK, des essais ont été réalisés à des températures au-dessous et au- dessus de T_g. A partir des résultats des essais les plus simples DMA et traction, un comportement complexe est apparu dans les deux matériaux.

En comparant qualitativement leurs comportements, on peut observer :

- les deux matériaux subissent une perte mécanique significative pendant la transition (-90% et -80% respectivement) qui débute au-dessus de T_g, elle est apparue lors des essais de traction et confirmée par les essais DMA, (FIGURE 5) à des niveaux similaires ;

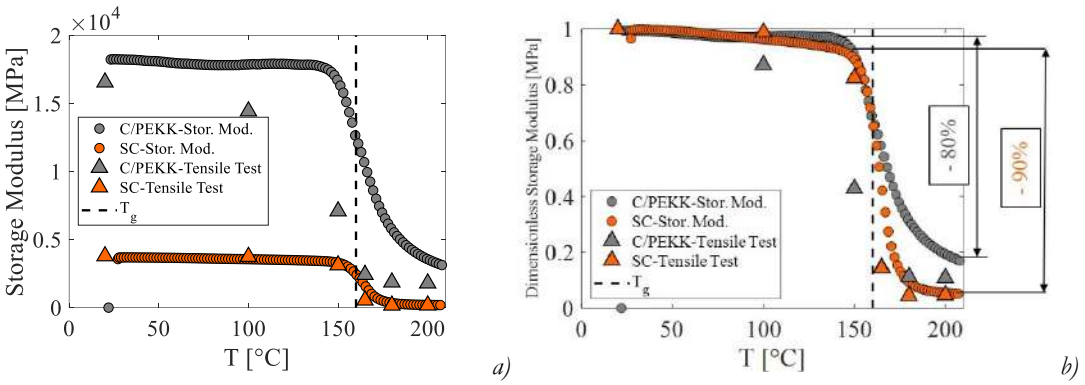

Figure 5: Comparaison entre le module de conservation mesuré en DMA, pour le C/PEKK SC (gris) et le PEKK SC (orange) entre 20°C et 200°C, comparé aux modules pseudo-élastiques comme valeurs mesurées (a) et comme rapport par rapport aux valeurs initiales (b).

- le PEKK SC montre un comportement non linéaire en traction, avec une dépendance complexe de la température et du temps (vitesse de déformations). Pour le C/PEKK, il est aisé d'identifier une région dominée par la matrice (faible déformation) et une région dominée par la fibre (forte déformation) : dans la première, on peut identifier le même comportement en traction de la PEKK SC, tandis que les secondes expriment un comportement plus linéaire, (FIGURE 6) ;

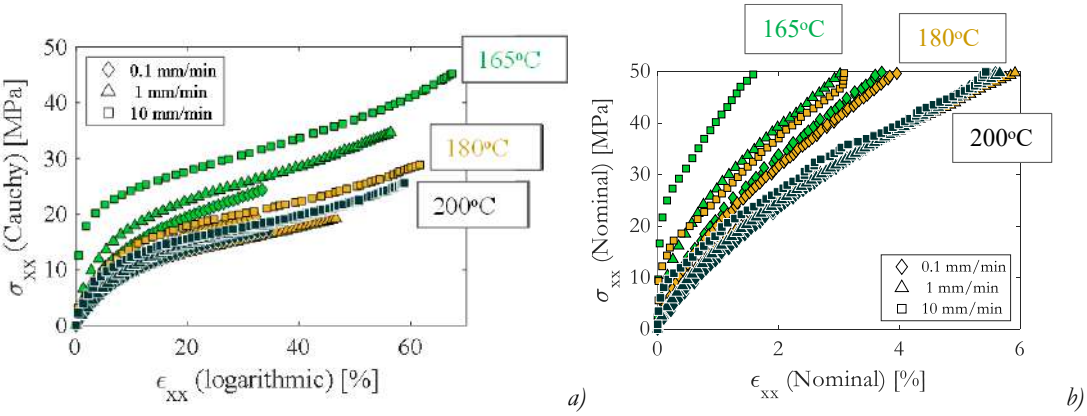

Figure 6: Courbes de contraint contre deformation obtenues des essais de traction à 165°C, 180°C et 200°C, à 0.1 , 1 et 10 mm/min sur le PEKK SC (a) et sur le C/PEKK (b)

- Les essais de fluage-recouvrance, montrent des similitudes significatives entre les deux matériaux : ils ne présentent pas d'accélération par fluage tertiaire, mais la présence d'une déformation permanente après la recouvrance, suggère la présence de phénomènes pseudo-plastiques dans les deux matériaux ;

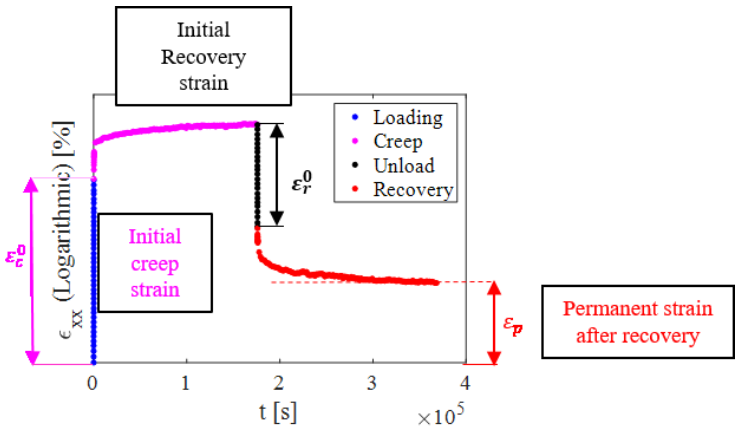

Figure 7: Courbes typique de déformation au cours d'un essai de fluage-recouvrance sur le PEKK SC et sur le C/PEKK

- Les essais de DMA et de DSC montrent une évolution globale similaire avec la température mais aussi des différences dans les valeurs mesurées du début de la T_g, (FIGURE 8).

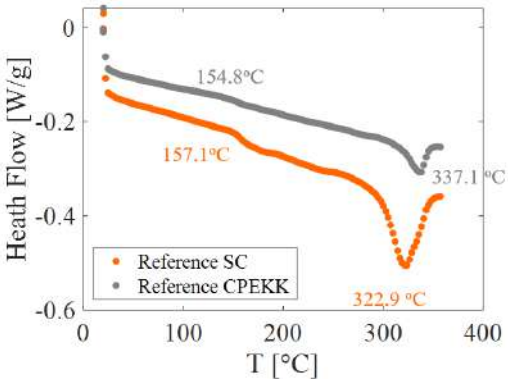

Figure 8: Flux de chaleur contre température, obtenue par une chauffe à 10°C/min réalisé en DSC sur le PEKK SC (orange) et C/PEKK (gris)

Les considérations précédentes suggèrent que si des différences entre le polymère et la matrice sont présentes, elles peuvent-être causées par une différence dans la morphologie des cristaux et/ou par la présence des fibres de carbone (*trans-cristallinité* observée dans C/PEKK). Ces différences sont toutefois limitées sur le comportement thermomécanique dans la plage de contraintes basses sollicitant la matrice du composite. Ce résultat suggère qu'à cette échelle, le polymère massif est assez proche de celui dans la matrice.

Une preuve supplémentaire de cette hypothèse vient de la méthode semi-analytique d'homogénéisation/localisation (SAHLM) (FIGURE 9), permettant de lier les méthodes d'homogénéisation élastique linéaire et de localisation et prenant également en compte la non-linéarité de la matrice. Grâce à cette méthode, à partir des propriétés de traction de PEKK SC, la courbe de traction à faible déformation C/PEKK est reconstruite à toutes les températures supérieures à T_g (FIGURE 10) et les propriétés initiales du pli et du composite sont calculées.

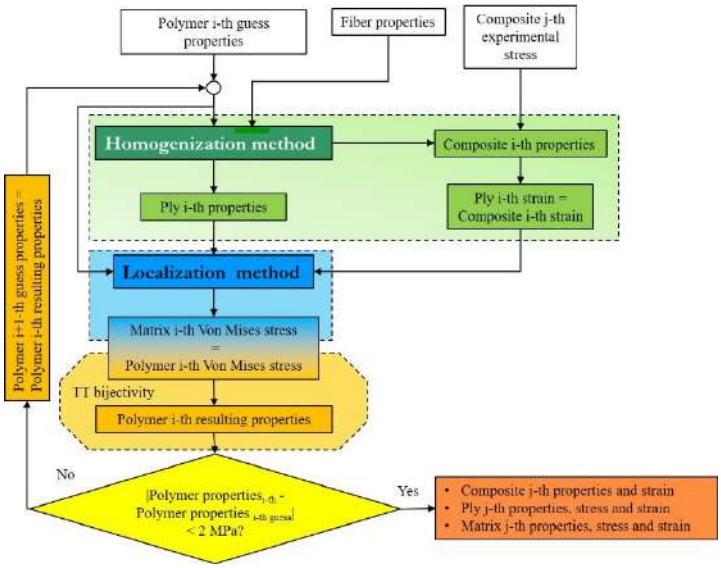

Figure 9: Algorithme de la méthode semi-analytique de homogénéisation/localisation

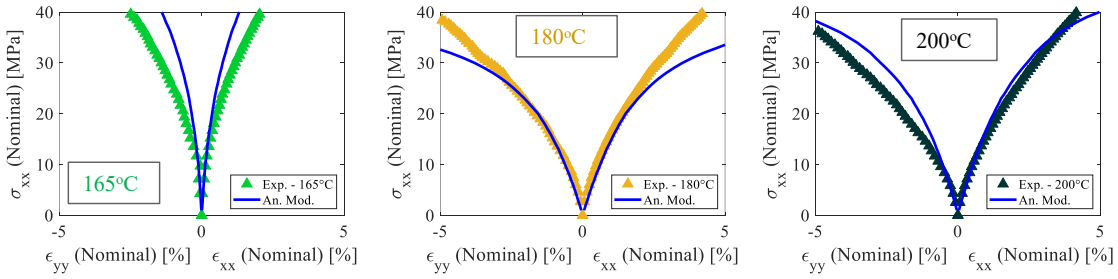

Figure 10: Comparaison entre les essais de traction expérimentales sur C/PEKK à 1 mm/min à 165°C, 180°C et 200°C et les simulations avec la méthode semi-analytique de homogénéisation/localisation

Le modèle semi-analytique confirme les similarités entre le polymère et la matrice, et la faisabilité d'une approche qui présente la possibilité de simuler différents pourcentages de fibres, différentes orientations de plis et/ou différentes séquences d'empilement sans avoir besoin d'une loi de comportement spécifique pour chaque configuration.

IV -Caractérisation du comportement thermomécanique et en fluage du PEKK au-dessus de Tg

L'ajout d'essais de charge-décharge-recharge (CDP) aux essais de traction et de fluage - recouvrance, combiné aux essais DSC effectués après chacun de ces essais, a permis d'identifier 3 mécanismes principaux :

- un mécanisme de *durcissement*, produisant une augmentation de la rigidité au départ de la recharge par rapport au début du chargement initial (correspondant à un essai de traction). Ce durcissement pilote le comportement soit pendant la recharge sous un seuil de plasticité amorçant le second mécanisme (décrit après), soit pendant la décharge, (FIGURE 11). Ce mécanisme est associé à l'alignement de la structure cristalline initialement orientée au hasard vers la direction de la charge, et il peut être complètement inversé pendant la décharge ;

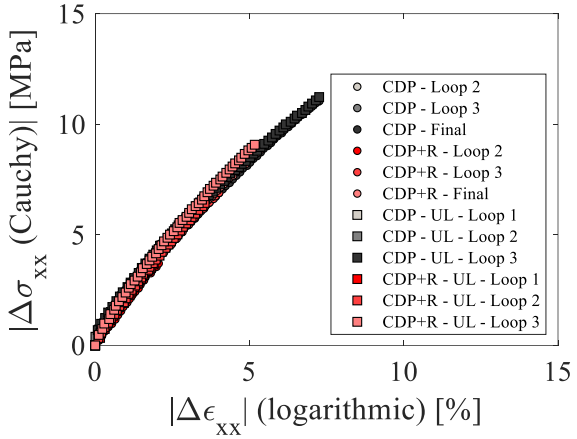

Figure 11: Comparaison des recharges et des décharges décalée vers zéro et en valeur absolue, obtenues à partir des essais CPD et CDP+R sur PEKK SC à 200°C à 1 mm/min

- un mécanisme d'*adoucissement*, qui fait que la recharge se superpose exactement à l'essai de traction lorsqu'un seuil de contrainte est dépassé. Ce seuil croit avec la charge (comme en plasticité classique). Il est associé à des phénomènes pseudo-plastiques non réversibles se produisant dans la structure cristalline ;
- un mécanisme de *cristallisation* qui n'est actif que si une charge thermique est appliquée ou lors du fluage. L'augmentation de la cristallinité apparaît comme un 2ème pic endothermique de cristallisation intra-sphélitique secondaire. La cinétique de la cristallisation montre alors une dépendance avec le temps conforme à un modèle d'Avrami, (FIGURE 12) et il montre que :

1. le matériau n'a pas complètement cristallisé à la fin du processus de fabrication et une phase cristalline supplémentaire de 3,8 % peut être produite ;

2. selon le modèle d'Avrami, l'augmentation de la cristallinité sature après une certain durée d'exposition.

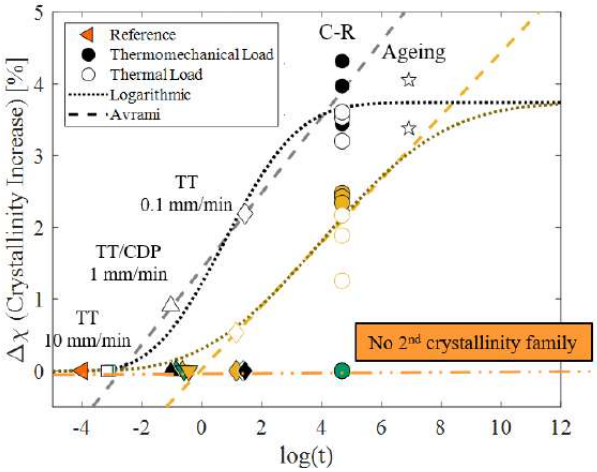

Figure 12: Variation du pourcentage de cristallinité corrigée du PEKK SC en fonction de la durée d'essai (marqueur solide) ou du temps d'exposition (marqueurs vides) à 165°C, 180°C et 200°C

L'absence d'augmentation de la cristallinité pendant la charge pourrait s'expliquer par un temps plus court qu'en fluage et par la moindre mobilité imposée aux chaînes amorphes intra-sphérulitiques en raison de la rotation de la phase cristalline qui la perturbe, ce qui a un effet analogue à l'augmentation de l'énergie de cristallisation, qui continue d'augmenter à mesure que la contrainte augmente. Lors de la décharge et de la recouvrance, l'énergie fournie au matériau est insuffisante pour dépasser ce seuil, tandis que l'énergie mécanique fournie lors du fluage permet de le dépasser et il active le mécanisme de cristallisation.

Tous les mécanismes décrits précédemment se superposent à un comportement élastique, qui permet de définir l'état initial théorique du matériau, en fonction de la phase cristalline initiale ainsi que de la température.

Les différents mécanismes sont décrits analytiquement et constituent un modèle 1-D du comportement du PEKK 7002 SC, qui est capable de reproduire les courbes expérimentales de traction, de CDP et de fluage-recouvrance à les différentes températures.

L'analyse est étendue à la PEKK 7002 AM, ce qui permet d'identifier les principales différences par rapport au PEKK SC :

- la perte de propriétés mécaniques si la température est augmentée au-dessus de T_g est plus significative (-99% par rapport à -90%), ce qui prouve le rôle de la phase cristalline sur des propriétés mécaniques au-dessus de T_g (FIGURE 13);

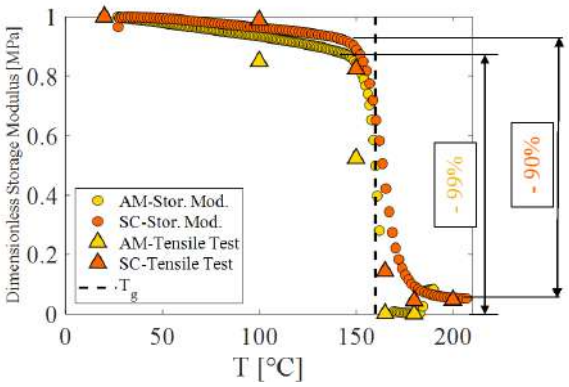

Figure 13: Comparaison entre les modules de conservation obtenus des essai de DMA sur le PEKK AM (jaune) et le PEKK SC (orange) entre 20°C et 200°C, comparés aux modules pseudo-élastiques normalisés par rapport aux valeurs initiales.

- Le mécanisme de cristallisation primaire est lui aussi actif, non seulement en fonction de la température, mais couplé à la charge mécanique fournie, qui l'accélère. Ce phénomène, par rapport à la cinétique de cristallisation proposée par (TANGUY CHOUPIN 2018), produit une augmentation de la cristallisation prédite à 150°C, une absence d'augmentation de la cristallisation à 165°C et à nouveau une augmentation à 180°C, (FIGURE 14).

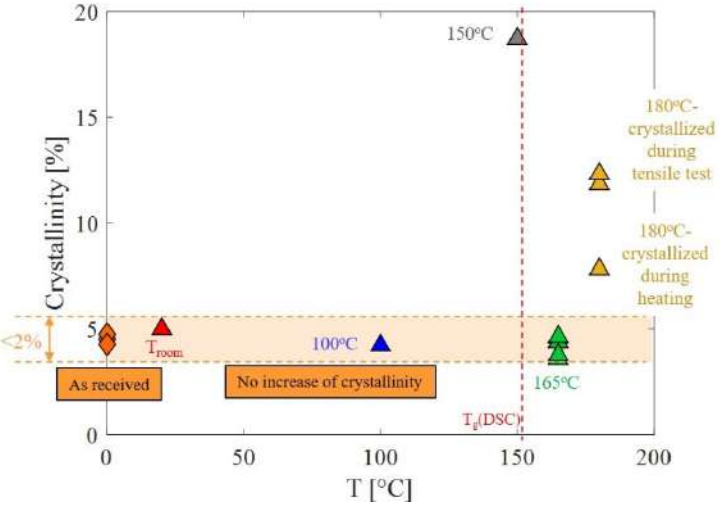

Figure 14: Taux de cristallinité du PEKK AM en fonction de la température obtenues des essais de DSC sur des échantillons découpés après des essais de traction à température ambiante, 100°C, 150°C, 165°C et 180°C.

Le modèle a été appliqué aussi au PEKK AM, et le bon accord avec les courbes expérimentales a confirmé que les mêmes mécanismes actifs dans PEKK SC peuvent être identifiés dans PEKK AM, et par conséquent ces mêmes mécanismes ne dépendent pas seulement de la température, du temps, de la contrainte et de la vitesse de contrainte, mais aussi de la phase de cristallinité initiale.

V - Simulation du comportement thermomécanique des composites C/PEKK en traction et en fluage

Le modèle décrivant le comportement du PEKK en 1-D a été généralisé au 3-D, en faisant l'hypothèse que pour la traction et le fluage le PEKK est isotrope et incompressible et le reste tout au long du processus. L'hypothèse d'isotropie étant la plus contestable car dans le modèle les cristaux changent d'orientation donc génèrent de l'anisotropie mais nous n'avons pas les données expérimentales pour l'appréhender.

Ce modèle 3-D a été implémenté dans le méthode semi-analytique d'homogénéisation/localisation (SAHLM) et permet de simuler à la fois le comportement en traction et en fluage du C/PEKK, (FIGURE 15).

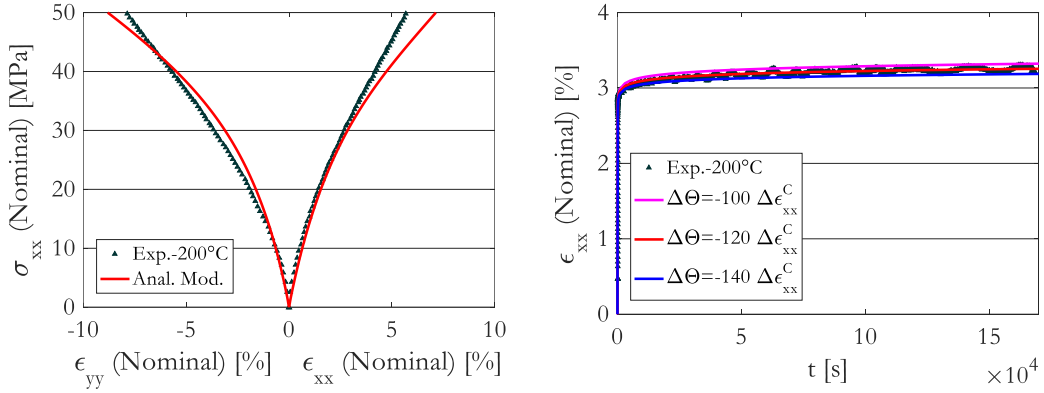

Figure 15: Comparaison entre l'essai de traction (a) et fluage (b) sur C/PEKK à 200°C et les simulation avec SAHLM.

La comparaison avec les données expérimentales obtenues lors des essais à 200°C sur les $[(\pm 45)_{2s}, +45]_s$ valide le SAHLM et permet d'évaluer ses limites :

- la courbe simulée est limitée uniquement à la région dominée par la matrice, et lorsque une contrainte composite plus élevée est simulé, le modèle diverge rapidement du comportement du composite ;
- la rotation des fibres dans le composite, (FIGURE 16) doit être prise en compte, tant pour les sollicitations en traction que pour le fluage, et la négliger peut produire une erreur significative. Dans ce travail une loi d'évolution est définie par interpolation de données expérimentales d'observations d'angle en surface.

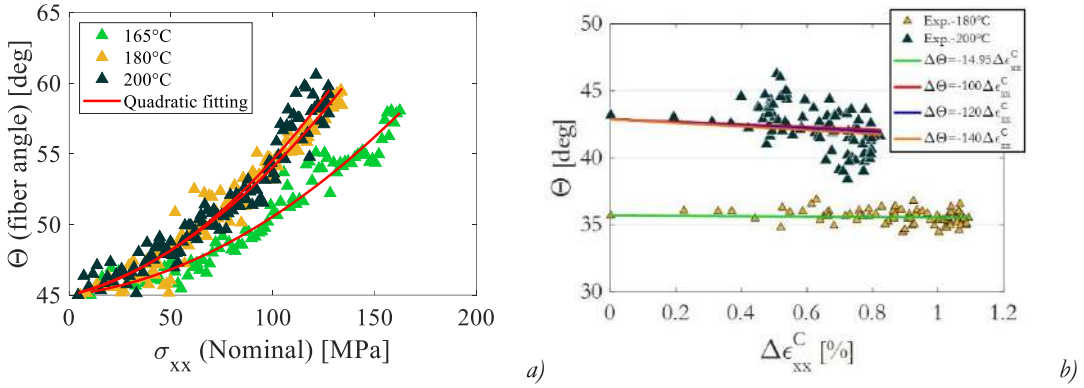

a) b)

Figure 16: Angle de rotation des fibre pendant la traction (a) et le fluage (b) à différents températures , mesurés à partir des images acquis pendant les respectives essais

Le modèle peut simuler différentes orientations des plis : les résultats dans le cas de stratifiés monodirectionnels avec des plis orientés à 0° ou 90° ont montré une différence dans l'extension de la région dominée par la matrice et dans la ductilité ; au niveau de la matrice, ils montrent une différence dans la sollicitation et le taux de déformation, tous deux plus élevés pour le laminé à 90° que pour celui à 0°. En outre, à chaque niveau, le comportement de $[(\pm 45)_{2s}, +45]_s$, est intermédiaire entre les deux, comme prévu.

Le SAHLM est modifié pour pouvoir simuler des composites avec des plis orientés dans différentes directions : des branches parallèles sont introduites dans l'algorithme où intervient l'effet des différentes orientations des plis, et le critère de convergence global est vérifié uniquement lorsque chaque critère de chaque pli est satisfait, (FIGURE 17).

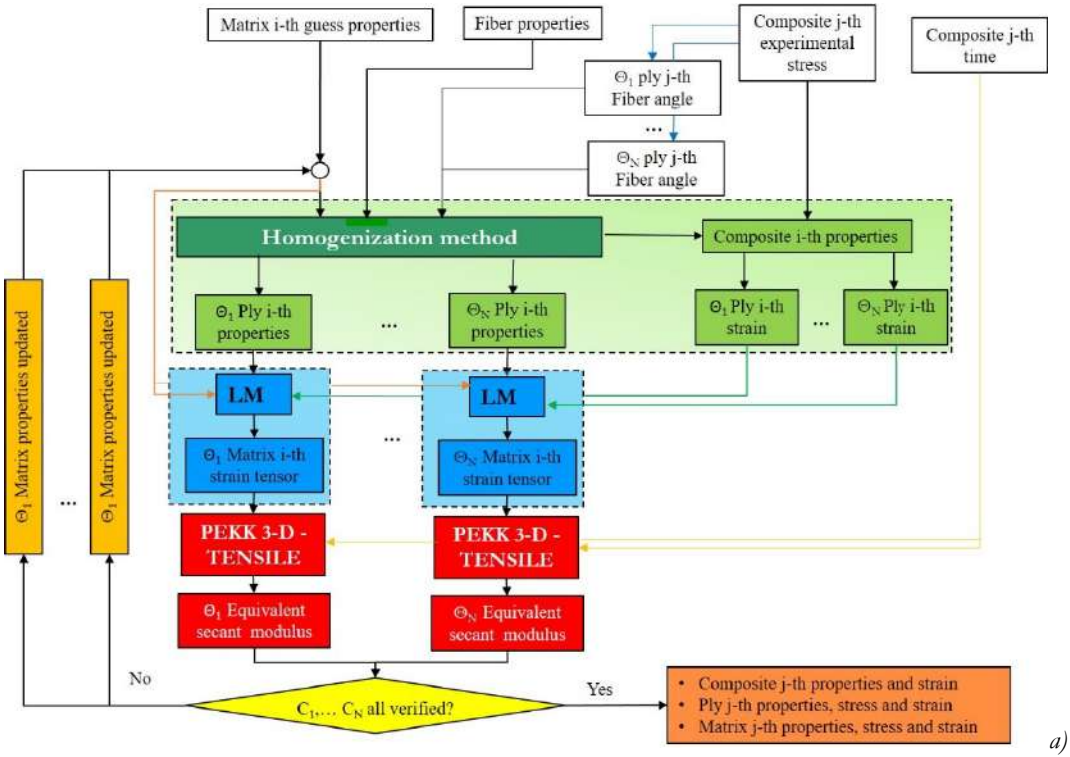

a)

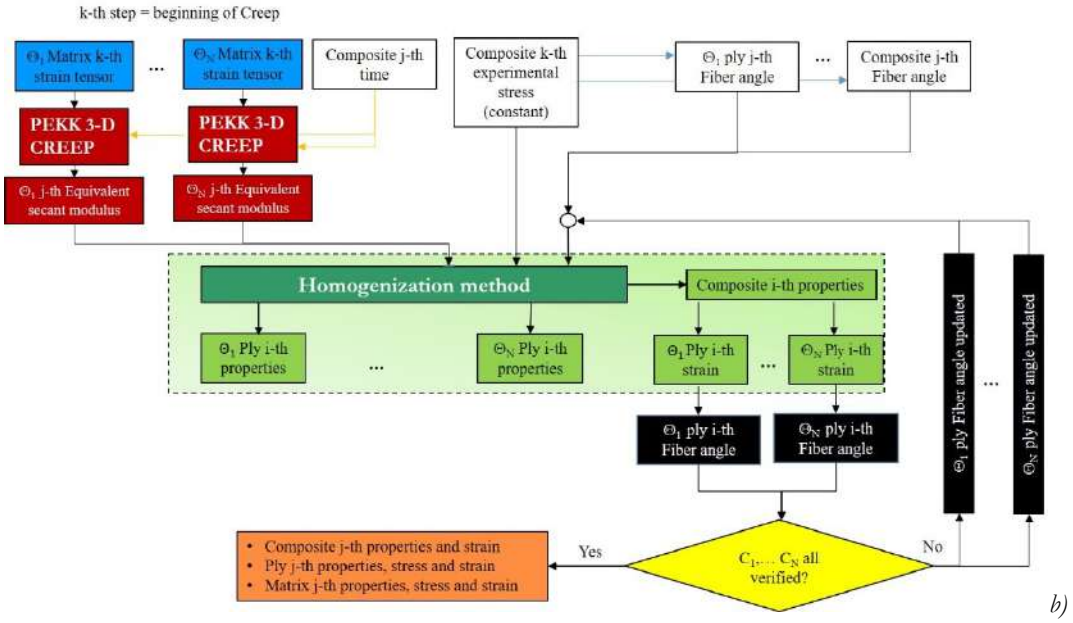

Figure 17: Schématisation du SAHLM pour un stratifié avec plis avec différents orientations pour simuler une sollicitation de traction (a) et de fluage (b).

A titre d'exemple, les résultats d'une simulation d'un laminé quasi isotrope (QI, $[0°/+45°/-45°/90°]_s$) sont présentés, (FIGURE 18), avec l'hypothèse d'un angle de fibre constant et sans tenir compte de l'ordre de la séquence des plis, ni de leur interaction. Les résultats, tant en termes de sollicitation en traction qu'en fluage, montrent que les plis sont tous sollicités dans la direction des fibres, comme prévu pour l'QI. En outre, au niveau de la matrice, le SAHLM arrive à différencier l'état de sollicitation et la vitesse de déformation dans la matrice, en fonction des différentes orientations des plis.

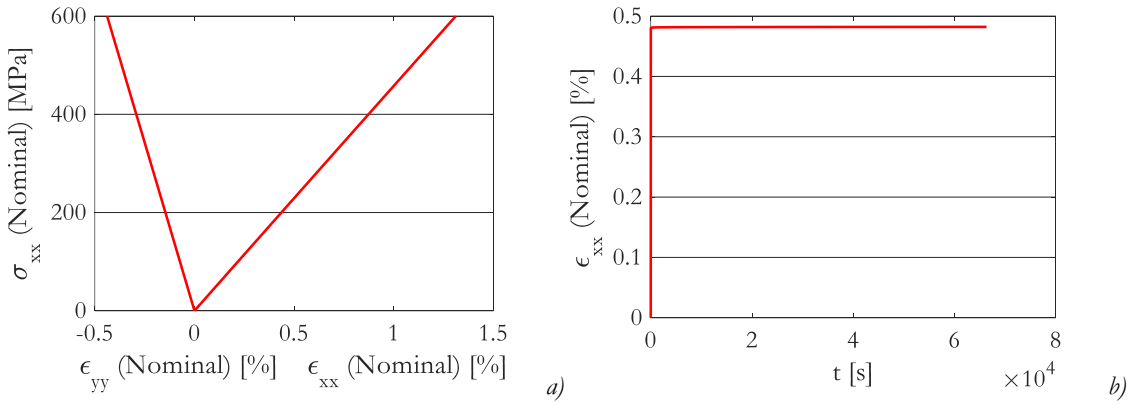

Figure 18: Simulation d'un QI avec SAHLM, en traction (a) et –fluage (b)

Les résultats des simulations confirmant que le comportement de la matrice dans le composite a un comportement similaire à celui du polymère, et de plus qu'il est possible de reconstruire le composite à partir du comportement de la matrice malgré son comportement complexe et les évolutions du réseau cristallin.

VI-Comportement couplé oxydation-thermomécanique-replacement des PEKK et C/PEKK à 200°C

Les interactions entre la charge thermomécanique et l'oxydation à 200°C a été étudié, en exploitant l'effet d'accélération produit par le conditionnement sous 5 bars d'O_2. L'étude est réalisée en 2 étapes :

1. l'évaluation de l'effet d'oxydation sur le matériau vierge, par vieillissement à 200°C sous 5 bars d'O_2 pendant 42 jours sur le PEKK SC et le C/PEKK ;

2. l'évaluation des interactions avec la charge thermomécanique à travers un essai de fluage sur le C/PEKK dans les mêmes conditions et pour la même durée.

Le vieillissement du PEKK SC a produit une couche externe brunâtre de moins de 50 µm, (valeur estimée par des techniques d'analyses d'images), qui comparée (en ton de couleur) à un film vieilli à 280°C, et compte tenu de l'accélération produite par l'emploi de l'oxygène, conduisent à estimer un facteur d'accélération des phénomènes d'oxydation de plus de 15 lors du passage de 200°C à 280°C.

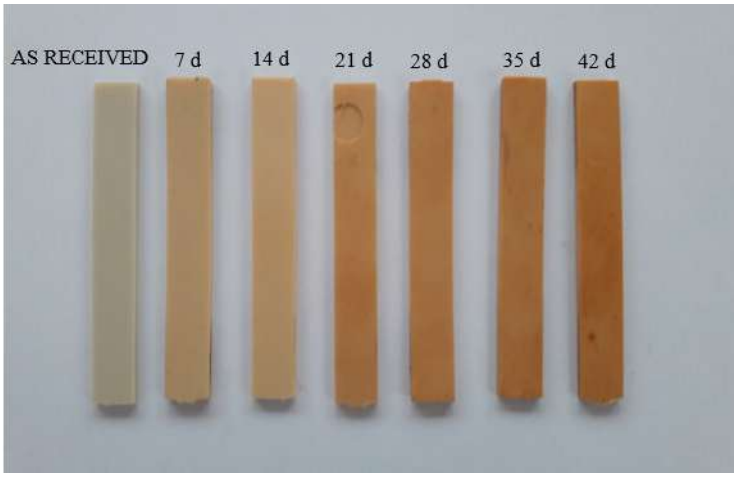

Figure 19: Échantillon de PEKK SC vieilli à 200°C sous 5 bars d'O_2 pendant une durée de 7 à 42 jours

De plus, des essais de DSC ont montré une augmentation du taux de cristallinité, ce qui pourrait expliquer toutes les différences observées par rapport au PEKK vierge. L'augmentation de la cristallinité peut être la conséquence de l'histoire thermique et/ou de l'oxydation. Toutefois la zone oxydée est très mince, donc la part de matériau oxydé dans les analyses de DSC est très faible voire inexistant lorsque l'on prélève la matière au centre. Ceci suggère fortement que la température est le principal moteur de l'évolution de la cristallinité.

L'effet du vieillissement sur le C/PEKK a été étudié par des µ-tomographie sur le matériau testé et sur le matériau vierge. Les images ne montrent aucune différence entre la surface et

le cœur de l'échantillon testé (comme observé pour le polymère) et les différences sont négligeables avec l'échantillon vierge (FIGURE 20).

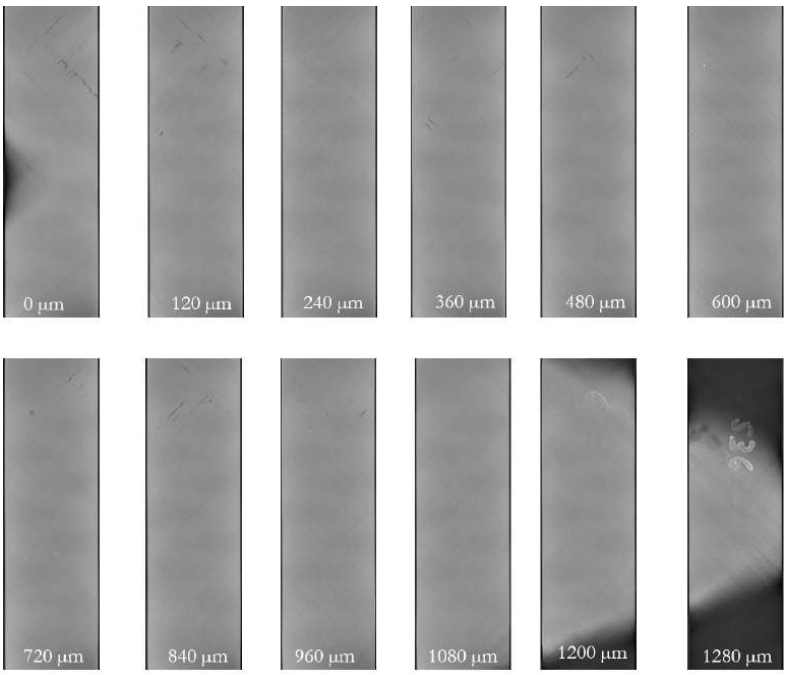

Figure 20: Coupes d'échantillons dans le plan longitudinal-transversal obtenues par µ-tomographie de C/PEKK vieillie à 200°C sous 5 bars d'O_2 pendant 42 jours, d'une surface (première image) à l'autre (dernière image) dans le sens de l'épaisseur,

L'essai de fluage réalisé à 28 MPa, 200°C sous 5 bar d'O_2 pendant 42 jours, a produit une courbe de déformation en fonction du temps qui peut être reconstruite en utilisant la loi de puissance de Norton-Bailey, dont les paramètres sont identifiés sur les essais de fluage effectués à l'air : cela implique que l'oxydation a un effet limité sur le comportement de fluage C/PEKK.

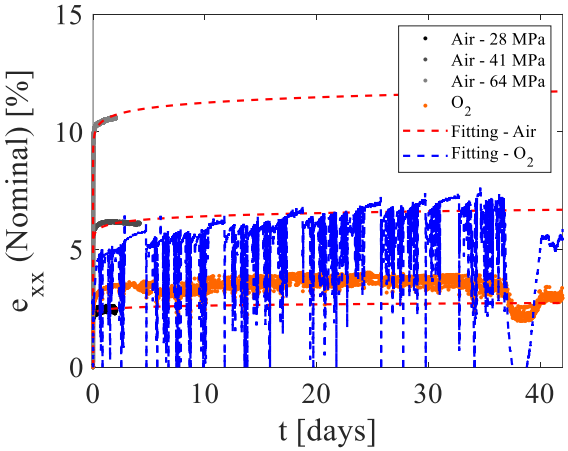

Figure 21: Déformation en fluage mesurée à 200°C en atmosphère non conditionnée (gris) et leurs respectifs fitting (rouge) et déformation de fluage à 200°C sous 5 bars d'O_2 (orange), avec déformation reconstruite, en tenant compte de la contrainte de fluage variable (bleu)

Les µ-tomographies de l'échantillon testé en fluage sous atmosphère conditionnée montrent une présence plus importante de fissures en surface et à cœur, sur toute la partie utile, par rapport aux spécimens vierge et vieilli. L'absence de différences entre la surface et le cœur permet de conclure que le scénario d'endommagement est inhérent à la seule charge thermomécanique appliquée et que cette dernière n'amplifie pas les mécanismes d'oxydation.

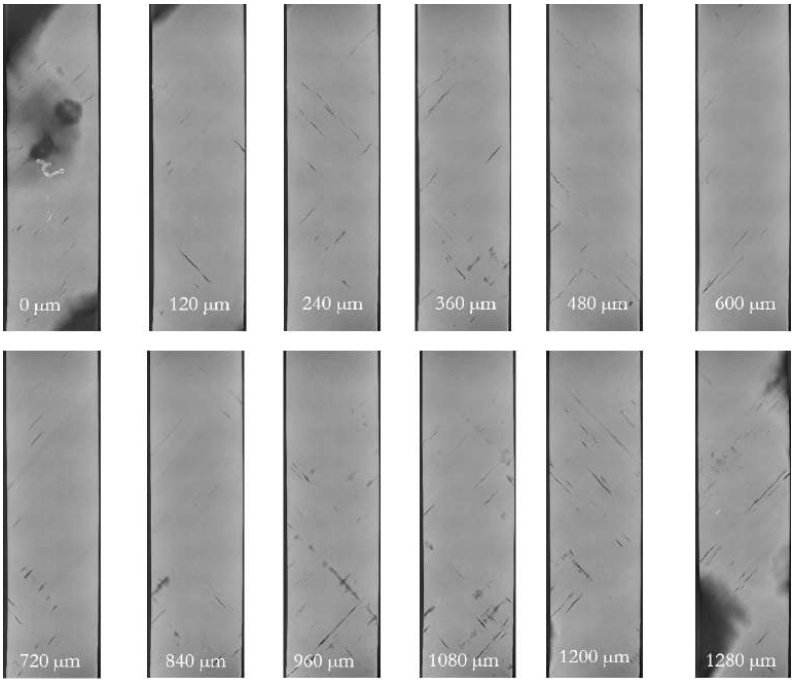

Figure 22: Coupes d'échantillons dans le plan longitudinal-transversal obtenues par µ-tomographie de C/PEKK testé en fluage à 200°C sous 5 bars d'O_2 pendant 42 jours, d'une surface (première image) à l'autre (dernière image) dans le sens de l'épaisseur,

L'analyse globale souligne que l'oxydation a un effet limité sur le PEKK SC et le C/PEKK à 200°C jusqu'à 1.15 ans.

Conclusions et perspectives

La présente étude est une première contribution à la connaissance du comportement du PEKK et du C/PEKK au-dessus de T_g, où de nombreux points restent encore inconnus. En particulier :

- l'interprétation physique du mécanisme a été déduite des essais macroscopiques, et, bien qu'elle ait révélé l'importance capitale de la phase cristalline dans le comportement des matériaux, aucune preuve expérimentale au niveau microscopique n'a pu être réalisée pour la confirmer. En particulier, des essais de SAXS et WAXS in-situ pourraient éventuellement confirmer non seulement la présence de tels phénomènes, mais aussi leur cinétique ;
- cette analyse pourrait être étendue à l'interaction entre le chargement thermomécanique et le mécanisme de cristallisation : si l'effet de la cristallisation sur les propriétés mécaniques est connu, l'effet de la charge thermomécanique sur la cristallisation ne l'est pas. Dans la présente étude, nous nous sommes limités au semi-cristallin, pour lequel aucune cristallisation n'est observée lors de la sollicitation de charge, alors qu'elle est présente pour le fluage et les sollicitations thermiques. Plus complexe est le cas du PEKK AM, pour lequel cette interaction est plus prononcée et apparaît également pour sous sollicitation thermo mécanique. Une première interprétation a été fournie dans le présent travail, mais une recherche plus approfondie est nécessaire pour la confirmer ou la repousser.
- la formulation 1-D pourrait être améliorée en conséquence, et les mécanismes pourraient être directement liés au comportement réel de la phase cristalline ;
- le comportement en cisaillement a été déduit du comportement en traction, et, bien qu'il puisse être considéré comme une première approximation raisonnable, des essais de cisaillement pourraient améliorer la compréhension des mécanismes et valider l'hypothèse faite ;
- l'ensemble des essais de taractionde cisaillement et de compression pourrait fournir les éléments pour améliorer la formulation 3-D, en vérifiant ou en confondant l'hypothèse d'isotropie et en fournissant une loi de comportement dérivant de la thermodynamique des processus irréversibles avec aussi une meilleure prise en compte de la pression hydrostatique.
- l'étude est limitée à 200°C, et aucun essai a été effectué à une température plus élevée, à laquelle les mécanismes identifiés pourraient avoir un impact moindre sur le comportement du matériau et d'autres pourraient être plus prédominants ; en particulier les phénomènes de dégradation, dont la présence a déjà été prouvée, ils pourraient par exemple fortement influencer le comportement thermomécanique et vice versa ;
- il a été prouvé que la rotation des fibres joue un rôle important dans la simulation des composites et, de plus, qu'elle n'est pas seulement due à un effet cinématique, mais qu'elle

découle d'une interaction forte avec l'évolution des propriétés de la matrice. L'identification de ce lien pourrait permettre de surmonter le besoin de mesurer expérimentalement l'angle de rotation et d'améliorer les simulations, en particulier dans le cas de stratifiés à orientations multiples, où les mesures ne peuvent pas être obtenues directement à partir de l'observation de la surface : dans ce cas, des μ-tomographies in-situ pourraient fournir les informations manquantes ; l'enjeu serait de coupler l'anisotrope évolutive du composite avec celle de la matrice.

- une meilleure compréhension du mécanisme responsable de la rotation des fibres pourrait étendre les limites des capacités du SAHLM et permettre de simuler le comportement du composite également dans la région où les fibres sont dominantes avec un simple outil prédictif.

Caractérisation et modélisation du comportement thermomécanique et du vieillissement du PEKK et des composites C/PEKK pour des applications à haute températures (au-dessous de la température de transition vitreuse)

Résumé :
La sensibilisation accrue aux questions environnementales concerne aujourd'hui les structures aéronautiques en termes d'impact environnemental et traitements de fin de vie. Dans cette optique, la possibilité de remplacer, dans les composites à matrice organique (CMO) utilisés pour des applications aéronautiques, leur matrice thermodurcissable non recyclable par une matrice thermoplastique recyclable est étudiée. En outre, les polymères thermoplastiques, tels que le PEKK, ont la possibilité d'être utilisés dans des structures plus chaudes (par exemple le pylône d'un avion), faisant l'objet de sollicitations de longue durée (fluage).
Les températures de service de ces structures plus élevées que celles de la température de transition vitreuse du PEKK : il en découle, dans le matériau, une perte de propriétés due au changement d'état de solide à caoutchoutique, et éventuellement l'activation de phénomènes de cristallisation et de dégradation, qui pourraient également interagir. Ce travail vise à identifier et à modéliser ces mécanismes caractérisant le comportement du PEKK, dans ces conditions extrêmes particulières. Ceci est réalisé à partir de l'analyse des résultats des essais thermomécaniques, physico-chimiques et thermomécaniques couplés avec l'oxydation. Le modèle analytique 1-D du comportement du PEKK qui résulte de l'analyse des essais est étendu en 3-D et implémenté dans une méthode d'homogénéisation/localisation semi-analytique multi-échelle pour simuler le comportement dans mêmes conditions de composites stratifiés à matrice PEKK, en faisant varier l'orientation des plis et la séquence d'empilement.

Mots clés : PEKK, Composites thermoplastiques, Fluage, Matériaux--Effets des hautes températures, Polymères—Détérioration, Polymères--Propriétés thermomécaniques, Analyse multiéchelle

Characterization and modelling of the thermomechanical and ageing behavior of PEKK and C/PEKK composites for aircraft applications at high temperatures (above the glass transition temperature

Abstract:
The nowadays increased awareness towards environmental issues concerns aircraft structures in terms of environmental impact and end-of-life disposal. In this optics, the possibility of replacing in the organic matrix composites (CMO) employed for aircraft applications the non-recyclable thermosetting matrix with a recyclable thermoplastic one is investigated. Moreover, thermoplastic polymers, such PEKK, have the possibility of being employed in warmer structures (e.g. the aircraft pylon), undergoing long duration solicitations (creep).
The service temperatures for those structures are higher than the PEKK glass transition temperature, provoking, in the material, a loss of properties deriving from a change of state from solid to rubber, and possibly the activation of crystallization and degradation phenomena, which could also interact. This work aims to identify and model the mechanisms characterizing PEKK behavior, under the structure operative service conditions. This is achieved from the analysis of the results of thermomechanical, physical-chemical and coupled thermomechanical/oxidation tests. The resulting 1-D analytical model of the PEKK behavior, is extended in 3-D and implemented in a multi-scale semi-analytical homogenization / localization method to simulate PEKK based composites under the same conditions, varying the plies orientation and stacking sequence.

Keywords: PEKK, Thermoplastic composites, Creep, Materials at high temperature, Polymers—Deterioration, Polymers--Thermomechanical properties.